frontiers | Research Topics

# New insights into schizophrenia-related neural and behavioral phenotypes

**Edited by**
Yuh-Man Sun and Ji Chen

**Published in**
Frontiers in Cellular Neuroscience

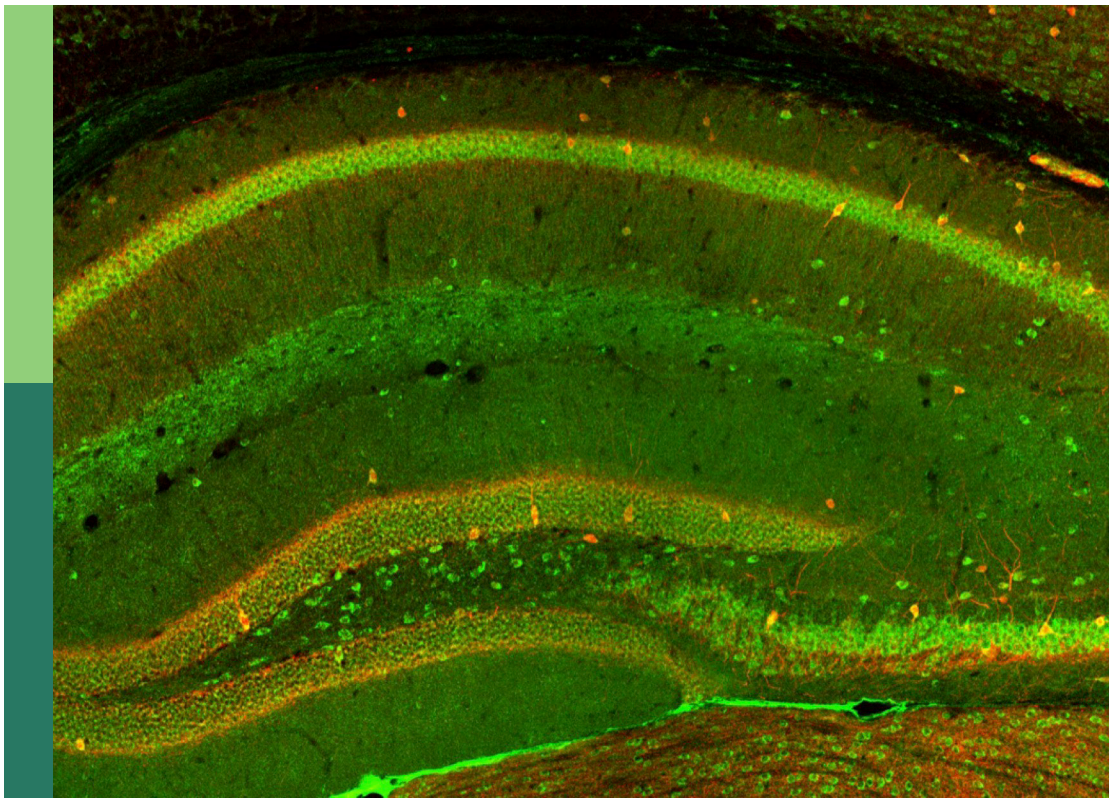

ISSN 1664-8714
ISBN 978-2-8325-2530-2
DOI 10.3389/978-2-8325-2530-2

## About Frontiers

Frontiers is more than just an open access publisher of scholarly articles: it is a pioneering approach to the world of academia, radically improving the way scholarly research is managed. The grand vision of Frontiers is a world where all people have an equal opportunity to seek, share and generate knowledge. Frontiers provides immediate and permanent online open access to all its publications, but this alone is not enough to realize our grand goals.

## Frontiers journal series

The Frontiers journal series is a multi-tier and interdisciplinary set of open-access, online journals, promising a paradigm shift from the current review, selection and dissemination processes in academic publishing. All Frontiers journals are driven by researchers for researchers; therefore, they constitute a service to the scholarly community. At the same time, the *Frontiers journal series* operates on a revolutionary invention, the tiered publishing system, initially addressing specific communities of scholars, and gradually climbing up to broader public understanding, thus serving the interests of the lay society, too.

## Dedication to quality

Each Frontiers article is a landmark of the highest quality, thanks to genuinely collaborative interactions between authors and review editors, who include some of the world's best academicians. Research must be certified by peers before entering a stream of knowledge that may eventually reach the public - and shape society; therefore, Frontiers only applies the most rigorous and unbiased reviews. Frontiers revolutionizes research publishing by freely delivering the most outstanding research, evaluated with no bias from both the academic and social point of view. By applying the most advanced information technologies, Frontiers is catapulting scholarly publishing into a new generation.

## What are Frontiers Research Topics?

Frontiers Research Topics are very popular trademarks of the *Frontiers journals series*: they are collections of at least ten articles, all centered on a particular subject. With their unique mix of varied contributions from Original Research to Review Articles, Frontiers Research Topics unify the most influential researchers, the latest key findings and historical advances in a hot research area.

Find out more on how to host your own Frontiers Research Topic or contribute to one as an author by contacting the Frontiers editorial office: frontiersin.org/about/contact

# New insights into schizophrenia-related neural and behavioral phenotypes

**Topic editors**

Yuh-Man Sun — Retired, United Kingdom

Ji Chen — Zhejiang University, China

**Citation**

Sun, Y.-M., Chen, J., eds. (2023). *New insights into schizophrenia-related neural and behavioral phenotypes*. Lausanne: Frontiers Media SA.

doi: 10.3389/978-2-8325-2530-2

# Table of contents

frontiers | Frontiers in Cellular Neuroscience

TYPE Editorial
PUBLISHED 10 May 2023
DOI 10.3389/fncel.2023.1202230



OPEN ACCESS

EDITED AND REVIEWED BY
Dirk M. Hermann,
University of Duisburg-Essen, Germany

*CORRESPONDENCE
Yuh-Man Sun
✉ yuhman.sun@gmail.com
Ji Chen
✉ ji.chen@zju.edu.cn

RECEIVED 07 April 2023
ACCEPTED 21 April 2023
PUBLISHED 10 May 2023

CITATION
Sun Y-M and Chen J (2023) Editorial: New insights into schizophrenia-related neural and behavioral phenotypes.
*Front. Cell. Neurosci.* 17:1202230.
doi: 10.3389/fncel.2023.1202230



# Editorial: New insights into schizophrenia-related neural and behavioral phenotypes

Yuh-Man Sun[1]* and Ji Chen[2,3]*

[1]Retired, London, United Kingdom, [2]Department of Psychology and Behavioral Sciences, Zhejiang University, Hangzhou, China, [3]Department of Psychiatry, The Fourth Affiliated Hospital, Zhejiang University School of Medicine, Yiwu, Zhejiang, China

KEYWORDS

**schizophrenia, excitation/inhibition (E/I) imbalance, extracellular vesicles (EVs), voltage-gated ion channels, (VIP)-expressing GABAergic neurons, human iPSC derived neurons, working memory (WM), Reelin**

Editorial on the Research Topic
New insights into schizophrenia-related neural and behavioral phenotypes

The etiology of schizophrenia (SCZ) is multifactorial and complex. Scientists employed animal models, human post-mortem tissue, imaging, bioinformatics, and recently human induced pluripotent stem cell (hiPSC)-based modeling to dissect the underlying multifaceted mechanisms of the disease. The emerging consensus is that cortical pathology is one of the fundamental features of schizophrenia (Selemon, 2001; Selemon and Zecevic, 2015; Parnanzone et al., 2017; Di Biase et al., 2019). The neocortex consists of around 80% of glutamatergic excitatory pyramidal neurons and 20% of GABAergic inhibitory interneurons (Harris and Shepherd, 2015; Lodato and Arlotta, 2015; Tatti et al., 2017; Musall et al., 2023). Mounting evidence suggests that aberrant connectivity of cortical macrocircuitry and microcircuitry plays a pivotal role in SCZ, especially excitation/inhibition (E/I) imbalance at the molecular, cellular, cell-type, and regional levels (Yizhar et al., 2011; Lisman, 2012; Marin, 2012; Gao and Penzes, 2015; Sohal and Rubenstein, 2019; Liu et al., 2021). The imbalance in excitatory and inhibitory information can cause disruption in sensory and working memory (Casanova et al., 2007; Opris and Casanova, 2014). The knowledge derived from the article collection in this Research Topic will be of help for understanding and unraveling the pathophysiology of SCZ under the framework of E/I imbalance.

At the molecular and cellular level, dysfunction of corticolimbic glutamatergic neurotransmission plays a critical role in the manifestations of schizophrenia (Coyle, 1996; Paz et al., 2008; Egerton et al., 2020). Glutamatergic neurons represent the primary excitatory afferent and efferent systems innervating the cortex, limbic regions (e.g., hippocampus and amygdala), and striatum (Coyle, 1996; Moghaddam, 2003). This orchestrates intricate interplays amongst neuronal networks (e.g., glutamatergic, GABAergic, dopaminergic, serotonergic neurotransmission, etc.). Dysfunction in one of those neuronal networks could alter an E/I balance (Belmer et al., 2016; Hayashi-Takagi, 2017; Sonnenschein et al., 2020). Let us now focus on the units of neuronal networks, i.e., neuronal synapses. It is well documented that synaptopathy underlies a variety of psychiatric disorders (Hayashi-Takagi, 2017; Obi-Nagata et al., 2019; Friston, 2023). Our study based on hiPSC modeling showed that an array of genes involving glutamatergic, GABAergic, dopaminergic, and cholinergic synapses are downregulated in the neurons derived from clozapine-responsive SCZ patients

(e.g., *GRIN2A, GRM1, VGLUT3, VGLUT2, GNB2, ADCY1, ADCY2, ADCY5, ADRBK1, GABBR2, GABBR3, GAT1, VGAT, GAD1, GABARAPL2, DRD1, CAMK2A, CAMK2B, PPP2R2C, PPP2CB, PPP2R5B, MAOA, MAPK11, KIF5A; CHRM3, KCNQ2*). The majority of those genes are restored by clozapine, especially the function of NMDA receptors (Hribkova et al., 2022). It was also observed a significant reduction in VGLUT1/PSD95-positive synapses in SCZ neurons (Hribkova et al., 2022). PSD95 plays critical roles in maintaining the balance between excitatory and inhibitory synapses, synapse development, and synaptic plasticity (Zeng et al., 2016; Lambert et al., 2017; Smith et al., 2017). In this Research Topic, Chen et al. report that defective dendritic spines and autism-like behaviors observed in the Fragile X messenger ribonucleoprotein 1 (*Fmr1*) knockout mice are rescued by dihydrotestosterone (DHT), whereby DHT increases PSD95 expression by abating the Fragile X messenger ribonucleoprotein (Fmrp)-mediated miR-125a/RISC inhibition of PSD95 productions. Moreover, neuronal extracellular vesicles (EVs) are also a key player in neuronal synapses. CD63 is one of the EV proteins and facilitates vesicular trafficking through endosomal pathways. Hendricks et al. find that Tsp42Ee and Tsp42Eg (Tsps), CD63 homologs in *Drosophila*, influence the synaptic cytoskeleton and membrane composition by regulating Futsch loop formation and synaptic levels of SCAR and PI(4,5)P 2. Tsps influence the synaptic localization of several vesicle-associated proteins including Synapsin, Synaptotagmin, and Cysteine String Protein. In a review article, Jiao et al. delineate the roles of neuronal EVs in cellular homeostasis, intercellular communication, and phenotypic changes in the recipient cells via sophisticated machineries. Aberrant EVs cause neuropathy and lead to neurological disorders, which echoes the EVs' role in SCZ (Wang et al., 2022). Others and we also observed abnormalities in EVs in SCZ. A study reported that peripheral EVs in psychotic patients contain higher levels of proteins involving the regulation of glutamatergic synaptic plasticity (Tunset et al., 2020). Our study showed that some of the genes responsible for synaptic vesicle cycle (e.g., *VGLUT2, VGLUT3, VGAT, CPLX2, RAB3A, STX1B1, and ATP6V1A*) are down-regulated in clozapine-responsive SCZ neurons (Hribkova et al., 2022).

Furthermore, synaptic ion channels also play a pivotal role in shaping synaptic communication and plasticity (Voglis and Tavernarakis, 2006; Burke and Bender, 2019) and accumulating data suggest that polymorphisms and mutations in ion channels link to the susceptibility or pathogenesis of psychiatric diseases (Imbrici et al., 2013). Our study also reveals that a score of genes encoding ion channels [e.g., *SLC4A4, SLC32A1, SLC13A4, SLC1A4, SLC17A8, SLC17A6, SCN2A, ATP1B1, SCN3A, ATP1A2, ATP1A3, SLC6A1, HCN4, KCNK10, KCNB1(Kv2.1), KCNH8 (Kv12.1), KCTD2, ATP1B1, KCNQ2 (Kv7.2), ATP1A2, ATP1A3, TMEM38A, KCNG1 (Kv6.1), KCNF1 (Kv5.1), KCNJ4 (Kir2.3), CACNG5, and CACNG8*] are down-regulated in clozapine-responsive SCZ neurons, in which some are restored by clazopine (Hribkova et al., 2022). Those studies suggest that the dysregulation of ion channel genes is associated with SCZ. Understanding the role of individual channels in SCZ is an insurmountable task due to the numerous constellations of subtypes. Therefore, computing and mathematical modeling would be useful tools to explore the involvement of ion channels in SCZ and for drug testing. In this Research Topic, Rathour and Kaphzan employ neuronal modeling to compute how variability of voltage-gated ion channels (VGICs), including fast $Na^+$, delayed rectifier $K^+$, A-type $K^+$, T-type $Ca^{++}$, and HCN channels, affects information transfer in neurons. They show that the A-type $K^+$ channel is the major regulator of information transfer. McGahan and Keener construct a novel mathematical model for heteromeric potassium channels that captures both α-subunit number and type present in each channel.

At the cell-type level, a review article by Apicella and Marchionni elucidate the role of vasoactive intestinal polypeptide (VIP)-expressing GABAergic neurons in the neocortical areas via disinhibitory and inhibitory effects on the intricate cortical circuits, which translates the external stimuli into underlying behaviors. The authors mentioned the effect of ErbB4 knockout mice on cortical microcircuits. ErbB4 ablation reduces the activity of VIP-expressing neurons also witnessed with an increase excitatory neuronal activity, suggesting a direct inhibitory effect of the VIP (Batista-Brito et al., 2017). ErbB4, a receptor of the schizophrenia-linked protein neuregulin-1, regulates glutamatergic synapse maturation, plasticity, NMDAR-mediated neurotransmission, and the migration of GABAergic interneurons (Flames et al., 2004; Li et al., 2007). The dopaminergic system plays a crucial role in the pathophysiology of schizophrenia (Collo et al., 2020; Martel and Gatti McArthur, 2020; Sonnenschein et al., 2020). It will be of interest to delineate the abnormalities in SCZ patient-specific dopaminergic neurons at the molecular and cellullar levels. Rakovic et al. generate a TH-mCherry iPSC reporter line by CRISPR/Cas9 technology to enrich the population of electrophysiologically mature $TH^+$ dopaminergic neurons. This method can be applied to SCZ patient-specific iPSC lines for underpinning the dysfunction of dopaminergic neurons.

At the regional level, limbic regions such as the hippocampus and amygdala are known to play a role in working memory processes, but the relationship between structural changes in these regions and cognitive deficits in schizophrenia is complex and influenced by various factors, including the severity of the condition. Three articles in this Research Topic provide new insights into this issue. Cheng et al. suggest that the disrupted integration of the default mode network (DMN) contributes to working memory deficits in SCZ patients with severe attention problems. They use graph theory to examine the network topology of the brain during a working memory task and at rest in SCZ patients with different levels of attention deficit severity. The results show that patients with severe attention deficits have a higher normalized path length of the DMN compared to those with mild attention deficits and healthy controls, which are not sustained during rest. These findings might provide reliable biomarkers for attention deficits during working memory tasks for schizophrenia patients. Peterson et al. show that structural atrophy in the head and tail of the hippocampus and widespread amygdala positively correlated with the severity of symptoms and inversely with working memory performance in SCZ patients. They suggest that patients in different severity groups might form a spectrum of severity, as

their working memory deficits and brain structural abnormalities follow similar patterns, but with varying degrees of severity. Delgado-Sallent et al. adopted a phencyclidine (PCP) mouse model to investigate the effects of NMDAR hypofunction on neural activities in the medial prefrontal cortex (mPFC) and the dorsal hippocampus (dHPC) during memory acquisition. They find that mice with subchronic PCP treatments exhibit impairments in short-term and long-term memory, which is associated with the disrupted mPFC-dHPC connectivity and the memory deficits are alleviated with Risperidone treatments by targeting this circuit. They suggest that this phenomenon might apply to SCZ patients with NMDAR hypofunction. An extracellular matrix protein Reelin is associated with SCZ in the human and mouse (Fatemi et al., 2001; Ishii et al., 2016; Negrón-Oyarzo et al., 2016). In this Research Topic, Pardo et al. report the effects of Reelin levels on adult brain's striatal structure and neuronal composition. They show that Reelin knockout mice (Cre fR/fR) from p45-60 onwards do not exhibit aberrant striatal structure and neuronal composition, whereas Reelin overexpressing (TgRln) mice display increases in the densities of striatal cholinergic interneurons and Parvalbumin interneurons in the ventral-medial striatum, dopaminergic projections in the ventral striatum, the number of dopaminergic synaptic boutons in the NAcc. They suggest those effects might play a counteracting role in the excitatory/inhibitory imbalance.

In closing, each SCZ study provides a piece of the puzzle. When many pieces of the puzzle fall into place, the pathophysiology of SCZ will be apparent. We hope that day is coming soon.

## Author contributions

All authors listed have made a substantial, direct, and intellectual contribution to the work and approved it for publication.

## Funding

This work was funded by the STI2030-Major Projects (No. 2022ZD0214000 [to JC]), the National Key R&D Program of China (No. 2021YFC2502200 [to JC]), and the National Natural Science Foundation of China (No. 82201658 [to JC]).

## Conflict of interest

The authors declare that the research was conducted in the absence of any commercial or financial relationships that could be construed as a potential conflict of interest.

## Publisher's note



## References

Batista-Brito, R., Vinck, M., Ferguson, K. A., Chang, J. T., Laubender, D., Lur, G., et al. (2017). Developmental dysfunction of VIP interneurons impairs cortical circuits. *Neuron* 95, 884–895.e889. doi: 10.1016/j.neuron.2017.07.034

Belmer, A., Lanoue, V., Patkar, O. L., and Bartlett, S. E. (2016). Excitatory/inhibitory balance of serotonergic axon connectivity in the brain. *J. Neurol. Neuromed.* 1, 18–22. doi: 10.29245/2572.942X/2016/9.1079

Burke, K. J. Jr., and Bender, K.J. (2019). Modulation of ion channels in the axon: mechanisms and function. *Front. Cell. Neurosci.* 13, 221. doi: 10.3389/fncel.2019.00221

Casanova, M. F., Switala, A. E., Trippe, J., and Fitzgerald, M. (2007). Comparative minicolumnar morphometry of three distinguished scientists. *Autism* 11, 557–569. doi: 10.1177/1362361307083261

Collo, G., Mucci, A., Giordano, G. M., Merlo Pich, E., and Galderisi, S. (2020). Negative symptoms of schizophrenia and dopaminergic transmission: translational models and perspectives opened by iPSC techniques. *Front. Neurosci.* 14, 632. doi: 10.3389/fnins.2020.00632

Coyle, J. T. (1996). The glutamatergic dysfunction hypothesis for schizophrenia. *Riv. Psichiatr.* 3, 241–253. doi: 10.3109/10673229609017192

Di Biase, M. A., Cropley, V. L., Cocchi, L., Fornito, A., Calamante, F., Ganella, E. P., et al. (2019). Linking cortical and connectional pathology in schizophrenia. *Schizophr. Bull.* 45, 911–923. doi: 10.1093/schbul/sby121

Egerton, A., Grace, A. A., Stone, J., Bossong, M. G., Sand, M., McGuire, P., et al. (2020). Glutamate in schizophrenia: neurodevelopmental perspectives and drug development. *Schiz. Res.* 223, 59–70. doi: 10.1016/j.schres.2020.09.013

Fatemi, S. H., Kroll, J. L., and Stary, J. M. (2001). Altered levels of Reelin and its isoforms in schizophrenia and mood disorders. *Neuroreport* 12, 3209–3215. doi: 10.1097/00001756-200110290-00014

Flames, N., Long, J. E., Garratt, A. N., Fischer, T. M., Gassmann, M., Birchmeier, C., et al. (2004). Short- and long-range attraction of cortical GABAergic interneurons by neuregulin-1. *Neuron* 44, 251–261. doi: 10.1016/j.neuron.2004.09.028

Friston, K. (2023). Computational psychiatry: from synapses to sentience. *Mol. Psychiatry* 28, 256–268. doi: 10.1038/s41380-022-01743-z

Gao, R., and Penzes, P. (2015). Common mechanisms of excitatory and inhibitory imbalance in schizophrenia and autism spectrum disorders. *Curr. Mol. Med.* 15, 146–167. doi: 10.2174/1566524015666150303003028

Harris, K. D., and Shepherd, G. M. (2015). The neocortical circuit: themes and variations. *Nat. Neurosci.* 18, 170–181. doi: 10.1038/nn.3917

Hayashi-Takagi, A. (2017). Synapse pathology and translational applications for schizophrenia. *Neurosci. Res.* 114, 3–8. doi: 10.1016/j.neures.2016.09.001

Hribkova, H., Svoboda, O., Bartecku, E., Zelinkova, J., Horinkova, J., Lacinova, L., et al. (2022). Clozapine reverses dysfunction of glutamatergic neurons derived from clozapine-responsive schizophrenia patients. *Front. Cell. Neurosci.* 16, 830757. doi: 10.3389/fncel.2022.830757

Imbrici, P., Camerino, D. C., and Tricarico, D. (2013). Major channels involved in neuropsychiatric disorders and therapeutic perspectives. *Front. Genet.* 4, 76. doi: 10.3389/fgene.2013.00076

Ishii, K., Kubo, K.-I., and Nakajima, K. (2016). Reelin and neuropsychiatric disorders. *Front. Cell. Neurosci.* 10, 229. doi: 10.3389/fncel.2016.00229

Lambert, J. T., Hill, T. C., Park, D. K., Culp, J. H., and Zito, K. (2017). Protracted and asynchronous accumulation of PSD95-family MAGUKs during maturation of nascent dendritic spines. *Dev. Neurobiol.* 77, 1161–1174. doi: 10.1002/dneu.22503

Li, B., Woo, R. S., Mei, L., and Malinow, R. (2007). The neuregulin-1 receptor erbB4 controls glutamatergic synapse maturation and plasticity. *Neuron* 54, 583–597. doi: 10.1016/j.neuron.2007.03.028

Lisman, J. (2012). Excitation, inhibition, local oscillations, or large-scale loops: what causes the symptoms of schizophrenia? *Curr. Opin. Neurobiol.* 22, 537–544. doi: 10.1016/j.conb.2011.10.018

Liu, Y., Ouyang, P., Zheng, Y., Mi, L., Zhao, J., Ning, Y., et al. (2021). A selective review of the excitatory-inhibitory imbalance in schizophrenia: underlying biology, genetics, microcircuits, and symptoms. *Front. Cell Dev. Biol.* 9, 664535. doi: 10.3389/fcell.2021.664535

Lodato, S., and Arlotta, P. (2015). Generating neuronal diversity in the mammalian cerebral cortex. *Annu. Rev. Cell Dev. Biol.* 31, 699–720. doi: 10.1146/annurev-cellbio-100814-125353

Marin, O. (2012). Interneuron dysfunction in psychiatric disorders. *Nat. Rev. Neurosci.* 13, 107–120. doi: 10.1038/nrn3155

Martel, J. C., and Gatti McArthur, S. (2020). Dopamine receptor subtypes, physiology and pharmacology: new ligands and concepts in schizophrenia. *Front. Pharmacol.* 11, 1003. doi: 10.3389/fphar.2020.01003

Moghaddam, B. (2003). Bringing order to the glutamate chaos in schizophrenia. *Neuron* 40, 881–884. doi: 10.1016/S0896-6273(03)00757-8

Musall, S., Sun, X. R., Mohan, H., An, X., Gluf, S., Li, S. J., et al. (2023). Pyramidal cell types drive functionally distinct cortical activity patterns during decision-making. *Nat. Neurosci.* 26, 495–505. doi: 10.1038/s41593-022-01245-9

Negrón-Oyarzo, I., Lara-Vásquez, A., Palacios-García, I., Fuentealba, P., and Aboitiz, F. (2016). Schizophrenia and reelin: a model based on prenatal stress to study epigenetics, brain development and behavior. *Biol. Res.* 49, 16. doi: 10.1186/s40659-016-0076-5

Obi-Nagata, K., Temma, Y., and Hayashi-Takagi, A. (2019). Synaptic functions and their disruption in schizophrenia: from clinical evidence to synaptic optogenetics in an animal model. *Proc. Jpn. Acad. Ser. B. Phys. Biol. Sci.* 95, 179–197. doi: 10.2183/pjab.95.014

Opris, I., and Casanova, M. F. (2014). Prefrontal cortical minicolumn: from executive control to disrupted cognitive processing. *Brain* 137, 1863–1875. doi: 10.1093/brain/awt359

Parnanzone, S., Serrone, D., Rossetti, M. C., D'Onofrio, S., Splendiani, A., Micelli, V., et al. (2017). Alterations of cerebral white matter structure in psychosis and their clinical correlations: a systematic review of diffusion tensor imaging studies. *Riv. Psichiatr.* 52, 49–66. doi: 10.1708/2679.27441

Paz, R. D., Tardito, S., Atzori, M., and Tseng, K. Y. (2008). Glutamatergic dysfunction in schizophrenia: from basic neuroscience to clinical psychopharmacology. *Eur. Neuropsychopharmacol.* 18, 773–786. doi: 10.1016/j.euroneuro.2008.06.005

Selemon, L. D. (2001). Regionally diverse cortical pathology in schizophrenia: clues to the etiology of the disease. *Schizophr. Bull.* 27, 349–377. doi: 10.1093/oxfordjournals.schbul.a006881

Selemon, L. D., and Zecevic, N. (2015). Schizophrenia: a tale of two critical periods for prefrontal cortical development. *Transl. Psychiatry* 5, e623. doi: 10.1038/tp.2015.115

Smith, K. R., Jones, K. A., Kopeikina, K. J., Burette, A. C., Copits, B. A., Yoon, S., et al. (2017). Cadherin-10 maintains excitatory/inhibitory ratio through interactions with synaptic proteins. *J. Neurosci.* 37, 11127–11139. doi: 10.1523/JNEUROSCI.1153-17.2017

Sohal, V. S., and Rubenstein, J. L. R. (2019). Excitation-inhibition balance as a framework for investigating mechanisms in neuropsychiatric disorders. *Mol. Psychiatry* 24, 1248–1257. doi: 10.1038/s41380-019-0426-0

Sonnenschein, S. F., Gomes, F. V., and Grace, A.A. (2020). Dysregulation of midbrain dopamine system and the pathophysiology of schizophrenia. *Front. Psychiatry* 11, 613. doi: 10.3389/fpsyt.2020.00613

Tatti, R., Haley, M. S., Swanson, O. K., Tselha, T., and Maffei, A. (2017). Neurophysiology and regulation of the balance between excitation and inhibition in neocortical circuits. *Biol. Psychiatry* 81, 821–831. doi: 10.1016/j.biopsych.2016.09.017

Tunset, M. E., Haslene-Hox, H., Van Den Bossche, T., Vaaler, A. E., Sulheim, E., Kondziella, D., et al. (2020). Extracellular vesicles in patients in the acute phase of psychosis and after clinical improvement: an explorative study. *Peer J.* 8, e9714. doi: 10.7717/peerj.9714

Voglis, G., and Tavernarakis, N. (2006). The role of synaptic ion channels in synaptic plasticity. *EMBO Rep.* 7, 1104–1110. doi: 10.1038/sj.embor.7400830

Wang, Y., Amdanee, N., and Zhang, X. (2022). Exosomes in schizophrenia: pathophysiological mechanisms, biomarkers, and therapeutic targets. *Eur. Psychiatry* 65, e61. doi: 10.1192/j.eurpsy.2022.2319

Yizhar, O., Fenno, L. E., Prigge, M., Schneider, F., Davidson, T. J., O'Shea, D. J., et al. (2011). Neocortical excitation/inhibition balance in information processing and social dysfunction. *Nature* 477, 171–178. doi: 10.1038/nature 10360

Zeng, M., Shang, Y., Araki, Y., Guo, T., Huganir, R. L., Zhang, M., et al. (2016). Phase transition in postsynaptic densities underlies formation of synaptic complexes and synaptic plasticity. *Cell* 166, 1163–1175.e12. doi: 10.1016/j.cell.2016. 07.008

frontiers in Cellular Neuroscience

REVIEW
published: 10 February 2022
doi: 10.3389/fncel.2022.811484

# VIP-Expressing GABAergic Neurons: Disinhibitory vs. Inhibitory Motif and Its Role in Communication Across Neocortical Areas

*Alfonso junior Apicella[1]* and Ivan Marchionni[2,3]**

[1] Department of Biology, Neurosciences Institute, University of Texas at San Antonio, San Antonio, TX, United States, [2] Department of Biomedical Sciences, University of Padova, Padua, Italy, [3] Padova Neuroscience Center (PNC), University of Padova, Padua, Italy

GABAergic neurons play a crucial role in shaping cortical activity. Even though GABAergic neurons constitute a small fraction of cortical neurons, their peculiar morphology and functional properties make them an intriguing and challenging task to study. Here, we review the basic anatomical features, the circuit properties, and the possible role in the relevant behavioral task of a subclass of GABAergic neurons that express vasoactive intestinal polypeptide (VIP). These studies were performed using transgenic mice in which the VIP-expressing neurons can be recognized using fluorescent proteins and optogenetic manipulation to control (or regulate) their electrical activity. Cortical VIP-expressing neurons are more abundant in superficial cortical layers than other cortical layers, where they are mainly studied. Optogenetic and paired recordings performed in *ex vivo* cortical preparations show that VIP-expressing neurons mainly exert their inhibitory effect onto somatostatin-expressing (SOM) inhibitory neurons, leading to a disinhibitory effect onto excitatory pyramidal neurons. However, this subclass of GABAergic neurons also releases neurotransmitters onto other GABAergic and non-GABAergic neurons, suggesting other possible circuit roles than a disinhibitory effect. The heterogeneity of VIP-expressing neurons also suggests their involvement and recruitment during different functions *via* the inhibition/disinhibition of GABAergic and non-GABAergic neurons locally and distally, depending on the specific local circuit in which they are embedded, with potential effects on the behavioral states of the animal. Although VIP-expressing neurons represent only a tiny fraction of GABAergic inhibitory neurons in the cortex, these neurons' selective activation/inactivation could produce a relevant behavioral effect in the animal. Regardless of the increasing finding and discoveries on this subclass of GABAergic neurons, there is still a lot of missing information, and more studies should be done to unveil their role at the circuit and behavior level in different cortical layers and across different neocortical areas.

**Keywords: GABAergic neurons, vasoactive intestinal polypeptide, cortex, inhibition, disinhibition, local circuit, long-range axons**

OPEN ACCESS

***Edited by:***
*Enrico Cherubini, European Brain Research Institute, Italy*

***Reviewed by:***
*Lisa Topolnik, Laval University, Canada*
*Dirk Feldmeyer, Helmholtz Association of German Research Centres (HZ), Germany*

***Correspondence:**
*Alfonso junior Apicella*
*alfonso.apicella@utsa.edu*
*Ivan Marchionni*
*ivan.marchionni@unipd.it*

***Specialty section:***
*This article was submitted to Cellular Neurophysiology, a section of the journal Frontiers in Cellular Neuroscience*

***Received:*** *08 November 2021*
***Accepted:*** *04 January 2022*
***Published:*** *10 February 2022*

***Citation:***
*Apicella Aj and Marchionni I (2022) VIP-Expressing GABAergic Neurons: Disinhibitory vs. Inhibitory Motif and Its Role in Communication Across Neocortical Areas. Front. Cell. Neurosci. 16:811484. doi: 10.3389/fncel.2022.811484*

## INTRODUCTION

The cortical processing is characterized by the interaction of excitatory/glutamatergic pyramidal neurons and the inhibitory/GABAergic neurons. Every cortical activity is shaped by two opposing and inseparable events: synaptic excitation and inhibition. In addition, these two opposing forces, together with their strength and temporal relationship, control the cortex's function in space and time.

The cortex contains about 70–80% of pyramidal neurons, while the remaining 20–30% is represented by a different population of GABA-releasing neurons (for review see Feldmeyer, 2012). Despite being a small fraction of the entire neocortical population, these GABAergic neurons are a very heterogeneous class given their anatomical, electrophysiological, and molecular properties.

Over the past 100 years, scientists have debated the classification and nomenclature of neurons. Despite all the effort, a satisfactory consensus has not been reached yet. This is particularly true for the cortical GABAergic neurons due to the enormous amount of morphological, molecular, and physiological data that has been accumulated on these neurons over the past two decades (for review see DeFelipe et al., 2013). In 2008, the Petilla Interneuron Nomenclature Group (PING) divided cortical GABAergic neurons based on the expression of specific molecular markers into five main groups: the parvalbumin (PV)-expressing neurons, including chandelier and basket GABAergic neurons, the Somatostatin (SOM)-expressing, such as Martinotti cells, the neuropeptide Y (NPY)-expressing but not SOM-expressing neurons, vasoactive intestinal polypeptide (VIP)-expressing neurons, and cholecystokinin (CCK)-expressing but not SOM-or VIP-expressing neurons (Petilla Interneuron Nomenclature Group, Ascoli et al., 2008). A more recent study from Tasic et al. (2016), using single-cell RNA sequencing (scRNAseq) and statistical clustering, identified 23 transcriptomic types of GABAergic neurons in the mouse visual cortex. In a subsequent study, Tasic (2018) ∼60 types of GABAergic neurons conserved between the visual and frontal cortex were identified. However, the major subclasses, types, and their hierarchical relationships are broadly consistent with previous studies in which the cortical GABAergic neurons can be subdivided into three non-overlapping subclasses of neurons: (1) Parvalbumin (PV)—expressing neurons, Somatostatin (SOM)—expressing neurons, and 5-hydroxytryptamine, or ionotropic serotonin receptor (5HT3aR)-expressing neurons (Rudy et al., 2011; Markram et al., 2015; Tremblay et al., 2016).

Based on the characteristic anatomical and wiring diagrams, the canonical circuit diagram has determined the following synaptic pattern between pyramidal and GABAergic neurons:

(1) The PV-expressing neurons, representing about 30–50% of all cortical GABAergic neurons, preferentially target the peri-somatic region of the pyramidal neurons, allowing these neurons to quickly control the spike output of the pyramidal neurons.
(2) The SOM-expressing neurons comprise approximately 30% of all cortical GABAergic neurons. These neurons target the dendrites of pyramidal neurons preferentially in order to control their distal inputs.
(3) Within the main three sub-classes of GABAergic neurons in the cortex, the Vasoactive Intestinal Polypeptide (VIP)-expressing neurons represent about 40% of the ionotropic serotonin receptor (5HT3aR) neurons. Recent studies have shown that their activity inhibits both PV-expressing neurons and SOM-expressing neurons, thereby controlling the activity of pyramidal neurons through the other two classes of GABAergic neurons (Rudy et al., 2011; Tremblay et al., 2016; Huang and Paul, 2019).

Cortical and subcortical brain structures are anatomically and functionally interconnected by long-distance axons. The dynamic interaction between different brain areas is a key component of the brain function that serves as the "decoding" and "coding" system to interpret the external world and influence our behavior. Then, local neuronal circuits within each brain area receive the stream of information from the distal region, process, and pass the processed information to downstream brain areas. Different excitatory and inhibitory cortical circuits control and modulate postsynaptic neuron activity. GABAergic inhibitory neurons directly inhibit excitatory neurons and make synaptic contacts with other GABAergic neurons, therefore producing a disinhibitory outcome on pyramidal neurons. Initially, the disinhibitory circuit motif involving VIP-expressing neurons controlling local microcircuits by preferentially targeting other GABAergic neurons was identified in the hippocampus (Acsady et al., 1996; Hajos et al., 1996). Since the initial discovery of this VIP-expressing neuron disinhibitory motif, numerous studies have focused their attention aimed to understand the neuronal connectivity (morpho-functional mapping of VIP-expressing neurons) of these neurons in the hippocampus (Chamberland et al., 2010; Donato et al., 2013; Tyan et al., 2014; Francavilla et al., 2018).

Here we address the role of VIP-expressing neurons in the mouse neocortex by first summarizing the recent anatomical and synaptic connectivity of this canonical disinhibitory motif and its function in behaving mice. Then, we will discuss alternative mechanisms complementary to the disinhibitory motif. Finally, we will discuss a new subclass of neocortical VIP-expressing neurons characterized by long-range GABAergic projection and their potential role in routing information across brain areas *via* an inhibitory and/or disinhibitory motif in healthy and diseased brains.

## ANATOMICAL, ELECTROPHYSIOLOGICAL, AND MOLECULAR PROPERTIES OF CORTICAL VIP-EXPRESSING NEURONS

Neuronal anatomy is strictly correlated to the neuron's function. The somato-dendritic compartments and the axonal arbor indicate how the specific neuron receives its input and

routes its output within the microcircuit and across different brain structures.

VIP-expressing neurons constitute only 1–2% of the entire cortical population. In general, these neurons span all the cortical layers even though they are more present in the supra-granular layers (layer 2/3), representing the most abundant subclass of GABAergic neurons (Pronneke et al., 2015, 2020; Zhou et al., 2017; Almasi et al., 2019; Guet-McCreight et al., 2020; Badrinarayanan et al., 2021). At the level of the supragranular layers (1 and 2/3), the VIP-expressing neurons share a similar, bipolar dendritic morphological pattern characterized by a dendritic arborization confined in the supra-granular layers reaching layer 1. On the other side, its organization becomes more heterogeneous in the deeper layers (4, 5, and 6) of the cortex, where additional studies revealed different dendritic morphology such as (1) multipolar single tufted, (2) bi-tufted, and (3) horizontally bipolar with dendrites that span all cortical layers (Vucurovic et al., 2010; Pronneke et al., 2015, 2020; Sohn et al., 2016; Emmenegger et al., 2018).

The morphological diversity of the dendritic arbors of the VIP-expressing neurons indicates that this type of neuron may be recruited by different intra- and inter-layer local inputs and from long-range inputs coming from different brain regions providing layer-specific inhibition. The local vs. long-range recruitment of the VIP-expressing neurons could influence, in principle, different local circuits of the cortex and might have an essential role in specific tasks during different behavioral states of the animal (Cirelli and Tononi, 2000).

Another interesting aspect of the morphological properties of the VIP-expressing neurons is that the axon often starts at dendrites oriented toward the white matter rather than the soma (Pronneke et al., 2015), giving a characteristic feature to this class of neurons and possibly an enhanced chance to elicit action potentials at lower activation threshold (Thome et al., 2014). In addition, in different cortical areas, the axons of VIP-expressing neurons in the superficial layers extend vertically, covering all cortical layers without spreading horizontally (Vucurovic et al., 2010; Pronneke et al., 2015; Karnani et al., 2016b; Badrinarayanan et al., 2021). On the other hand, VIP-expressing neurons in deeper layers in the barrel cortex are mainly local, with some branches entering the white matter (Pronneke et al., 2015).

All VIP-expressing neurons have symmetric type II synapses, inhibitory, predominately located onto the dendrites, but a small percentage target spine and somata of the postsynaptic neurons (Zhou et al., 2017). VIP-expressing neurons do not contact the somata but only the dendrites of the layer 1 GABAergic neurons. Only layer 6 VIP-expressing neurons have a higher proportion contacting the somata of the postsynaptic neurons. Each VIP-expressing neuron of the S1 cortex makes one single bouton on the postsynaptic neuron. In contrast, only a small fraction of postsynaptic neurons is targeted with two or three synaptic boutons (Zhou et al., 2017). In layer 2/3, VIP-expressing neurons of the somatosensory cortex (S1) are homogeneously distributed within columns and septum, but in deeper layers are mainly present in the septal (Almasi et al., 2019). According to their electrophysiological properties, VIP-expressing neurons are characterized by heterogeneous firing properties along with the cortical layers with different proportions of the four firing types. The major firing patterns found in the VIP-expressing neurons are: (1) irregular spiking, (2) continuous adapting, (3) burst spiking, and (4) a low percentage high threshold non-adapting, especially in the deep layer (Pronneke et al., 2015, 2020). This wide heterogeneity of firing patterns suggests different biophysical membrane features within the subclass of VIP-expressing neurons. The irregular spiking VIP-expressing neurons show a non-homogeneous firing pattern during depolarizing current at the threshold. Particularly, Porter et al. (1998) suggested that in the rat motor cortex, the slowly inactivating $I_D$-like K current is involved in generating the irregular discharge pattern of the VIP-expressing neurons. Indeed, about 20% of the VIP-expressing neurons in the superficial layer of the barrel cortex display burst spiking activity due to the expression of T-type calcium and HCN channels (Bean, 2007). It was also shown that the burst spiking activity recorded at the resting membrane potential turns into a regular firing depending on the membrane potentials and the activation of nicotinic receptors (by the acetylcholine) and serotonin (5HT) ionotropic and metabotropic receptors. The latest firing pattern was not found in the deeper layers (4–6) (Pronneke et al., 2020). The most abundant firing pattern in the superficial and deep layer is the continuous adapting. The expression of calcium-activated (KCa; both BK and SK) potassium channels are the critical key mediators to control this spike frequency during the sustained suprathreshold depolarized current. These variabilities found in this subclass of GABAergic neurons suggest that the timing and modality of the release of the inhibitory neurotransmitter is layer and subtype-specific.

Moreover, the firing patterns show no correlation with neurons' morphological properties, making the classification more complex. In addition to the very heterogeneous properties of the firing patterns, the VIP-expressing neurons are also characterized by a large diversity of membrane properties in response to hyperpolarizing current and near rheobase (Pronneke et al., 2015). Different membrane properties are found both in the barrel cortex (Pronneke et al., 2015, 2020) and in the medial entorhinal cortex (MEC) between the supragranular and infragranular cortex (Badrinarayanan et al., 2021), suggesting distinct physiological roles of these neurons.

Interestingly a subclass of VIP-expressing neurons expresses choline acetyltransferase (ChAT) at the presynaptic terminal (Bayraktar et al., 1997; Porter et al., 1998) and showed undistinguished intrinsic properties with the ChAT negative VIP-expressing neurons, even though this subpopulation is less excitable and has lower input resistance (Obermayer et al., 2019; Dudai et al., 2020; Granger et al., 2020).

Although VIP-expressing neurons are a specific subclass of GABAergic neurons that do not overlap with the two major classes, VIP can be co-expressed with other markers, such as cholecystokinin (CCK) or calretinin (CR) (Xu et al., 2010; Kubota et al., 2011; Cauli et al., 2014; Zeisel et al., 2015).

Little is known about the GABAergic neurons that co-express VIP with CCK since this group represents a small percentage of neurons in the cortex. Further studies using transgenic mice to identify these neurons are still needed to resolve their role in cortical physiology. The expression of different neuronal

molecules and peptides within the same GABAergic neuron class might indicate that these neurons play multiple roles in cortical circuits.

## EXCITATORY AND INHIBITORY SYNAPSES ONTO CORTICAL VIP-EXPRESSING NEURONS

The anatomical presence of excitatory synapses (presynaptic boutons) onto cortical VIP-expressing neurons are preferentially studied from long-range projections originating in different brain areas. In this review, we consider "long-range" GABAergic projections when they connect brain areas associated with different sensory modalities and/or executive functions. For this reason, we do not consider lateral or interlaminar connectivity within one brain area and between subregions of a brain area as "long-range" GABAergic connectivity. Rather, we include projections that connect areas with different functions within the ipsilateral hemisphere, such as motor and somatosensory cortex, as well as projections that connect cortical regions with the same function *via* the corpus callous (interhemispheric projections).

Most studies on the presynaptic local connectivity between GABAergic and glutamatergic neurons onto VIP-expressing neurons are performed electrophysiologically. These studies unveil that, in layer 2/3 of the S1, the probability of connections between local excitatory neurons and the VIP-expressing neurons is very low (about 20%; Karnani et al., 2016b). These connections are also characterized as depressing short-term synaptic plasticity (Karnani et al., 2016b).

Specifically, it has been shown that, in S1, layer 2/3 bipolar VIP-expressing neurons receive significantly more excitatory input from layer 2/3 and significantly less from the other layers (Xu and Callaway, 2009). After immunohistochemical labeling of presynaptic boutons and postsynaptic structures of the layer 2/3 VIP-expressing neurons of the mouse S1, Sohn et al. (2016) described that both cortico-cortical and thalamic excitatory synapses contact the distal dendrites of the VIP-expressing neurons (**Figure 1A**).

Moreover, Ji et al. (2016) demonstrated that in the mouse auditory (A1) and visual cortex (V1) cortex layer 4, VIP-expressing neurons are innervated by thalamic axons, and the synaptic strength was much weaker compared with excitatory and PV-expressing neurons.

Taken together, these studies revealed that synaptic inputs onto VIP-expressing neurons had preferences for specific layers and somato-dendritic compartments. In addition, the revealed layer 4 cell-type specificity connectivity of thalamocortical innervation suggests that VIP-expressing neurons are unlikely to contribute to feedforward inhibition. At the same time, they might be better suited to provide feedback inhibition onto pyramidal neurons (Kapfer et al., 2007; Silberberg and Markram, 2007; Ma et al., 2010; Adesnik et al., 2012; Xu et al., 2013).

GABAergic postsynaptic inputs onto VIP-expressing neurons received more attention (Staiger et al., 1997, 2002; Olah et al., 2007). VIP-expressing neurons show a low number of inhibitory synapses along their somato-dendritic arborization. Specifically,

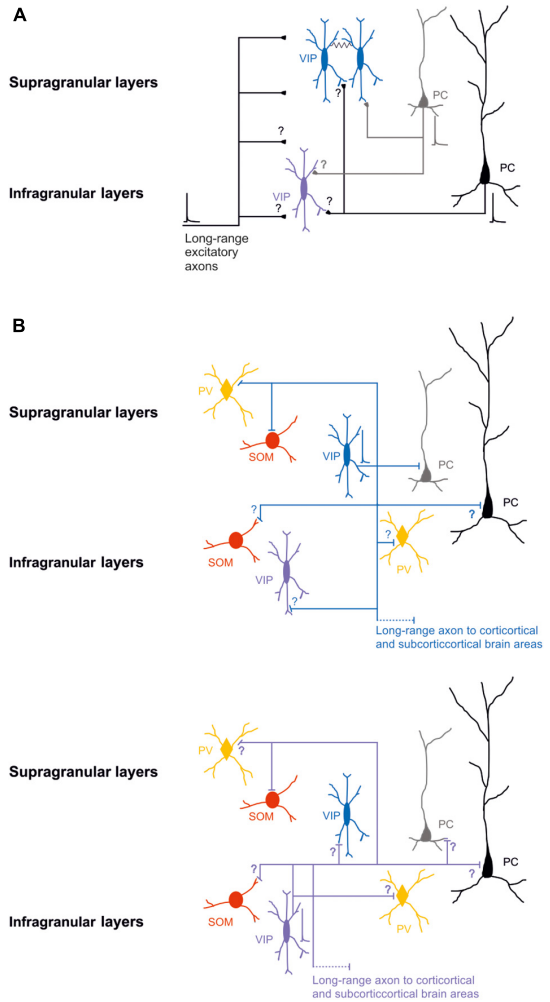


**FIGURE 1 |** Schematic wiring diagrams of neuronal circuits in the supragranular and infragranular cortical layers in which VIP-expressing neurons are involved. **(A)** Synaptic excitatory inputs from local and distal brain areas onto superficial and deep VIP-expressing neurons. **(B)** Synaptic outputs from supragranular VIP-expressing neurons (top) and infragranular VIP-expressing neurons (bottom) onto other types of neurons. Note that most of the connectivity between the different classes of neurons is still not known. VIP-expressing neurons are also electrically connected black line. Blue, VIP supragranular layer and purple VIP infragranular layer; Red SOM; orange PV; and gray superficial excitatory neurons and black deep excitatory neurons. Thick lines represent the axons that carries information and thin lines represent axons that are not active. Schematic action potentials are present depending on which neuronal circuit motive is recruited.

the synapses from PV-expressing neurons target the soma and the proximal dendrites of the VIP-expressing neurons. In contrast, the SOM-expressing neurons contact the VIP-expressing neurons' distal apical and basal dendrites. Reciprocal boutons between VIP-expressing neurons are found in all somato-dendritic compartments but are pretty sparse (**Figure 1B** top; Sohn et al., 2016).

It has also been demonstrated that VIP-expressing neurons, that express choline acetyltransferase (VIP-ChAT), can co-release acetylcholine with GABA onto other GABAergic neurons,

mainly in layer 1 and onto VIP-ChAT neurons. This suggests a possible microcircuit loop between these neurons that could be recruited within the subnetwork to amplify the incoming stream of information (Granger et al., 2020). In summary, at the microcircuit level, it has been suggested that VIP-expressing neurons receive different local and long-range glutamatergic/excitatory inputs (**Figure 1A**) and local synaptic inputs from other GABAergic neurons (**Figure 1B** top). It appears, at least in the superficial layer of the S1, that the density of excitatory input that arises from other cortical regions is larger compared to excitatory fibers from the thalamus, and the inhibitory synapses' density onto VIP expressing is similar to the PV-expressing and SOM-expressing neurons (Sohn et al., 2016). This shows a non-selective inhibition of VIP from the other two subclasses of GABAergic neurons, but the main excitatory inputs arise from other cortical areas. This could form a neuronal motif in which cortical VIP-expressing neurons are a key player in processing the incoming inputs (see next paragraph).

## LOCAL CIRCUIT ORGANIZATION OF VIP-EXPRESSING NEURONS

In recent years, numerous studies have been focused on the role of the superficial layer VIP-expressing neurons (Pronneke et al., 2015; Zhou et al., 2017; Almasi et al., 2019), while fewer have assessed the role of the deep layers VIP-expressing neurons (**Figure 1B** bottom; Xu and Callaway, 2009; Pronneke et al., 2015) due to the lower density of these neurons (Yu et al., 2019). For this reason, the organization of the underlying circuit of deeper layer VIP-expressing neurons and their role in cortical processing remains elusive. While the small numbers of these neurons poses a challenge, the use of opsins and transgenic Cre-mouse lines permits to pinpointing the direct and indirect inputs to VIP-expressing neurons as a population (He et al., 2016).

The strategy of driving the activity of channelrhodopsin-expressing VIP-expressing neurons has mainly been used to identify and compare the synaptic strength output onto different classes of neurons in layer 2/3 of the S1 and the primary visual cortex (V1; Lee et al., 2013; Pfeffer et al., 2013; Neske and Connors, 2016; Garcia-Junco-Clemente et al., 2017; Krabbe et al., 2019). Mainly, VIP-expressing neurons inhibit Martinotti neurons that express somatostatin in both cortices (Pfeffer et al., 2013; Walker et al., 2016).

In addition, Walker et al. (2016), using a paired recording technique in the S1, demonstrated that VIP-expressing input onto Martinotti-SOM-expressing neurons facilitated at high frequency. In contrast, PV-expressing input resulted in frequency independent depression. This suggests that differences in the connection properties among these neurons enable disinhibition with distinct temporal features.

The preferential inhibition of the SOM-expressing neurons in the S1 (most likely Martinotti neurons) might regulate and narrow the lateral inhibition after sustained GABA release from SOM-expressing to nearby pyramidal neurons (Karnani et al., 2016a). *In vitro* studies have also shown that during spontaneous network cortical activity, such as up and down cortical states, the selective photo-activation of VIP-expressing neurons does not affect the layer 2/3 pyramidal neurons firing, highlighting the crucial role in the neuronal plasticity properties and the network state at which the circuit is engaged (Neske and Connors, 2016).

VIP-expressing neurons at the microcircuit level in different brain structures such as V1, A1, and S1 are synaptically connected to other classes of GABAergic and non-GABAergic neurons. However, all the previous studies aimed to determine the role of the VIP-expressing neurons in cortical processing reached the same conclusion as "the general VIP-expressing neurons canonical circuit organization." These neurons are involved in a cortical disinhibitory (or inhibition of inhibition) motif (for review see: Kullander and Topolnik, 2021).

Notably, VIP-expressing neurons preferentially inhibit SOM-expressing neurons in superficial layers to break the inhibition on excitatory neurons (Lee et al., 2013; Pfeffer et al., 2013; Neske and Connors, 2016; Krabbe et al., 2019). An exciting aspect of the high connectivity found *in vitro* studies between VIP-expressing neurons and the SOM-expressing neurons is the inverse relationship of the number of neurons in the different layers. Mainly, the SOM-expressing neurons are present in deeper layers (Yavorska and Wehr, 2016), but VIP-expressing neurons are more present in the superficial layers (Pronneke et al., 2015, 2020). This intracortical connectivity, however, is still poorly studied (**Figure 1B**).

*In vivo* studies also have confirmed the functional role of the VIP→SOM disinhibitory motif. During selective photo-activation of the VIP-expressing neurons, the firing activity of the different neurons shifts to higher or lower rate/frequencies depending on the type of neurons (Pfeffer et al., 2013; Pi et al., 2013; Krabbe et al., 2019). More specifically, SOM-expressing neurons in the sensory and motor cortices are preferentially inhibited by photo-activation of VIP-expressing neurons, which leads to relief of excitatory neurons from suppression at least in the superficial layers of the cortex (Pfeffer et al., 2013; Pi et al., 2013; Garcia-Junco-Clemente et al., 2017; Keller et al., 2020).

In addition, it has been demonstrated that layer 2/3 pyramidal neurons innervate VIP- and SOM-expressing neurons with different inputs dynamics. Mainly, layer 2/3 pyramidal neurons in the sensory cortices formed depressing synapses onto VIP-expressing neurons and facilitating synapses onto SOM-expressing neurons (Karnani et al., 2016b). These results suggest that the VIP- and SOM-expressing neurons can be activated at different times during the excitation of the layer 2/3 circuits (Karnani et al., 2016b). Interestingly, Karnani et al. (2016b) also demonstrated that the VIP- and SOM-expressing neurons are excited by non-overlapping sets of nearby layer 2/3 pyramidal neurons. This indicates that VIP-expressing neurons are embedded in different local excitatory circuits (Karnani et al., 2016b), working as a single unit cooperating with other GABAergic neurons to control the firing selectively and specifically of pyramidal neurons (Hertag and Sprekeler, 2019).

One of the more exciting aspects is that none of the studies mentioned above took into consideration that the cortical and subcortical VIP-expressing neurons are highly electrically connected with each other and with different classes

of GABAergic neurons (**Figure 1A**; Karnani et al., 2016b; Francavilla et al., 2018). This leaves the question of what role this type of local connectivity has in controlling the activity of excitatory neurons during the synchronous network activity (Lee et al., 2013; Pfeffer et al., 2013; Krabbe et al., 2019). It has been shown that the activity of a single VIP-expressing neuron, through the electrical synapses, amplifies and synchronizes the response to control a broader range of local and distal target neurons (Karnani et al., 2016a,b; Hertag and Sprekeler, 2019).

In the medial prefrontal cortex (mPFC), a subclass of VIP-expressing neurons that co-expresses the choline acetyltransferase (ChAT) excites both GABAergic and glutamatergic neurons in different cortical layers (Obermayer et al., 2019). Even though the probability of finding these connections is low, the photo-activation of this circuit plays an essential role at the microcircuit level for behaviorally relevant tasks. The VIP-ChAT-expressing neurons do not provide inhibitory and/or disinhibitory control over the pyramidal neurons but exert direct excitation onto pyramidal neurons, showing a different mechanism of how VIP-ChAT-expressing neurons can regulate the activity of pyramidal neurons (von Engelhardt et al., 2007; Obermayer et al., 2019).

Another source of regulating cortical circuits is that VIP-expressing neurons release the peptide VIP, stored at the presynaptic level, into dense-core vesicles (Whittaker, 1989). In an initial study, Goadsby and Shelley (1990) demonstrated that high-frequency stimulation of the facial nerve results in the cortical release of VIP in the anesthetized cat. The vasoactive intestinal polypeptide (VIP) is not only a cell-type-specific molecular marker but is also a 28 amino-acid neuropeptide that has been shown to work as a neurotransmitter, neurotrophic or neuroprotective factor in the peripheral and central nervous system (Borbely et al., 2013; Deng and Jin, 2017). It has been shown that VIP acts through the $VPAC_1$ and $VPAC_2$ receptors that are part of the Group II receptor (GPCR) family (for review see Cunha-Reis and Caulino-Rocha, 2020). Mainly, in the hippocampus, the activation of the $VPAC_1$ receptors inhibits voltage-gated calcium channel-dependent GABA exocytosis through a $G_{i/o}$ and PKA-independent, and partially PKC-dependent, mechanism (Cunha-Reis et al., 2017). On the other hand, $VPAC_2$ receptors activation enhances voltage-gated calcium channel-dependent GABA exocytosis by a $G_s$/PKA/PKC-dependent mechanism. This suggests an additional way of modulating neuronal circuits during specific brain oscillations and possibly with the further activation of non-neuronal cells (Ashur-Fabian et al., 1997).

## FUNCTIONAL ORGANIZATION OF THE NEURONAL CIRCUITS INVOLVING VIP-EXPRESSING NEURONS

Every brain structure does not work in isolation. Each neuronal class is wired so that the activation of that class alters the activity of specific downstream neurons in ways that we are only starting to understand. Nonetheless, the role of any particular type of neuron at the local and distal network during specific behavior remains still unclear.

In recent years, it has been possible to develop new tools for characterizing and modulating the activity at the somato-dendritic and axon levels of different classes of neurons. These methods have revealed how individual classes of GABAergic and glutamatergic neurons are engaged in processing, at the microcircuit level, the incoming information from distal brain areas. Anatomical studies have shown that the major cortico-cortical inputs along the somato-dendritic compartments of GABAergic neurons in all layers of the S1 are from the primary motor cortex (M1), the secondary somatosensory cortex (S2), and contralateral S1 (S1; Wall et al., 2016).

Although all the classes of GABAergic neurons receive similar long-range excitatory inputs, VIP-expressing neurons localized in the deeper layers receive a higher density of excitatory inputs than the other inhibitory neuron classes (Wall et al., 2016). Immunofluorescence studies have also shown that VIP-expressing neurons in superficial layers of S1 receive most of the long-range excitatory synapses from cortico-cortical and thalamocortical input onto their distal dendrites (Sohn et al., 2016). Other long-distance excitatory inputs, from subcortical brain structure to GABAergic neurons in the S1, are from the ventral posterior nucleus (VPM) and the posteromedial complex (POm) of the thalamus (Staiger et al., 1996; Sohn et al., 2016; Wall et al., 2016; Guet-McCreight et al., 2020; **Figure 1A**).

From a functional point of view, physiological and anatomical studies confirmed that optogenetic stimulation of terminals arising from the POm increases the firing activity of VIP- and PV-expressing neurons. This effect induces disinhibitory control at the microcircuit level of the pyramidal neurons through the inhibition of SOM-expressing neurons. Moreover, the selective inhibition of the S1 VIP-expressing neurons is sufficient to induce LTP in layer 2/3 pyramidal neurons when POm inputs are photo-activated at specific frequencies. This suggests that VIP-expressing neurons are the key player in the disinhibitory circuit (Audette et al., 2018; Williams and Holtmaat, 2019).

Similar results have been demonstrated by Lee et al. (2019). In their study, the activity of VIP-expressing neurons increases in the open arms of an elevated plus maze in response to hippocampal inputs, leading to a disinhibitory effect onto layer 2/3 pyramidal neurons of the mouse prefrontal cortex. Thus, optogenetic inhibition of this subclass of neurons effectively controls how hippocampal input generates prefrontal representations, which drive avoidance behavior. Optogenetic activation of cortical VIP-expressing GABAergic neurons influences mouse behavior and sensory processing, depending on the cortical area and where the inputs originate (**Figure 2B**).

In addition, the selective activation of excitatory inputs from M1 or cingulate cortex mostly depolarize VIP-expressing neurons in superficial layers compared to the other classes of GABAergic neurons in S1 or V1, inducing a disinhibitory effect onto layer 2/3 pyramidal neurons through the SOM-expressing neurons (Lee et al., 2013; Zhang et al., 2014). Overall, these studies show a similar principle and possible connectivity pattern of the VIP-expressing neurons in the superficial layers of the cortex. However, they leave unanswered questions about the long-range

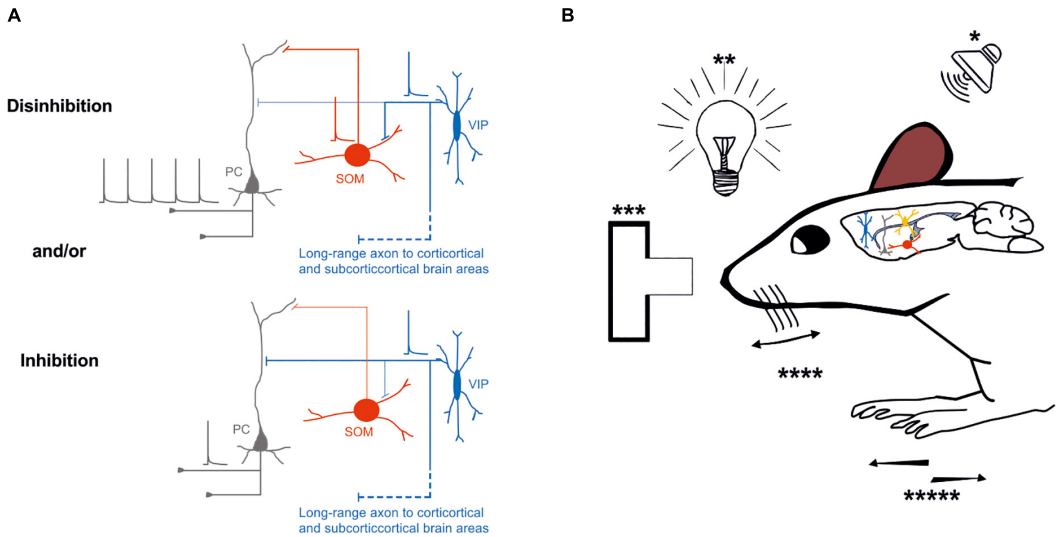


**FIGURE 2 |** Possible inhibitory and/or disinhibitory circuits are entrained during specific behavioral tasks. **(A)** Top left, Schematic representation of the disinhibitory circuit, in which the activity of an excitatory neuron (gray) is increased by the inhibitory effect of VIP-expressing neuron (blue) onto SOM–expressing neuron inhibition (red); bottom left, schematic representation of direct inhibition of the excitatory neuron (gray) by VIP-expressing neuron (blue). **(B)** External stimuli such as auditory (*), visual (**), decision making (***), whisking (****), or running (*****) entrain different circuits motive: inhibition or disinhibition of the excitatory neurons through the VIP-SOM microcircuit. Thick lines represent the axons that carries information and thin lines represent axons that are not active. Schematic action potentials are present depending on which neuronal circuit motive is recruited.

inputs onto VIP-expressing neurons in the infragranular layers, specifically their connectivity patterns and if there is a similar disinhibitory motif in these layers (**Figures 1A,B** bottom). These questions are important because in other cortical areas, such as the auditory and visual cortex, long-range excitatory inputs from the thalamus (MGB and dLGN) exert only weak depolarization onto VIP-expressing neurons, and these inputs are restricted to layer 4 (Kloc and Maffei, 2014; Ji et al., 2016).

More recent studies have shown that, depending on the input area, the excitatory responses of the three classes of GABAergic neurons in the superficial layers is region-dependent, suggesting that the same local circuit processes the information differently depending on the upstream information. More specifically, only long-range excitatory inputs arising from M1 induce a disinhibitory effect onto layer 2/3 pyramidal neurons *via* the VIP-expressing neurons in the barrel cortex (Lee et al., 2013). On the other hand, other sources of long-range excitatory inputs are not selective to a specific class of GABAergic neurons, indicating a different role of the VIP-expressing neurons in processing the information stream in the superficial layers (Naskar et al., 2021). Even though they were found using *in vitro* preparation, these exciting results suggest that, at least in the S1 barrel cortex, inputs from different brain structures recruit a specific class of GABAergic neurons preferentially. This indicates that the information flow from other brain areas is elaborated by the receiving brain region, depending on the activation of the upstream cortical input.

Still, most studies focus on the activation of GABAergic neurons in superficial layers, but how these neurons in the deep layers contribute to processing the incoming inputs from different brain areas is quite poorly studied (**Figure 1A**; Larkum et al., 2018). Notably, cortical VIP-expressing neurons also receive cholinergic inputs. The activation of these inputs selectively controls the spike activity of these neurons, increasing the complexity of regulation at the microcircuit level of this subclass of neurons (Dudai et al., 2020).

Overall, the recruitment of specific classes of neurons, such as VIP-expressing neurons, by long-range inputs might be determining either an inhibitory and/or disinhibitory effect at the microcircuit level that depends on different factors (**Figure 2A**). It is still unknown whether VIP-expressing neurons preferentially target different subclasses of glutamatergic neurons (Feldmeyer, 2012; Harris and Shepherd, 2015). Remarkably, the activation of VIP-expressing neurons could route the information processing to a specific pathway by inhibiting one subclass of pyramidal neurons while providing disinhibition to another subclass of pyramidal neurons (**Figure 2A**).

It is very well-established that cortical neurons regulate the activity of neurons across brain areas through long-range glutamatergic/excitatory projections, whereas inhibition is mediated by local feedforward and feedback circuits (for review, see Tremblay et al., 2016). It is, however, known that long-range GABAergic neurons are important circuit elements in many brain areas, such as the spiny projection neurons in the striatum and the Purkinje neurons in the cerebellum. Although the existence of cortical long-range GABAergic neurons has been proven anatomically (Ito and Yoshida, 1966; Seress and Ribak, 1983; Toth and Freund, 1992; Toth et al., 1993; Freund and Buzsaki, 1996; for review, see Caputi et al., 2013; Tremblay et al., 2016), previous studies have primarily focused on the local cortical circuit organization of GABAergic interneurons (Buzsaki, 1984; Ali et al., 1999;

Holmgren et al., 2003; Maccaferri and Lacaille, 2003; Pouille and Scanziani, 2004; Silberberg and Markram, 2007; Pouille et al., 2009, 2013; Stokes and Isaacson, 2010; Hayut et al., 2011; Pfeffer et al., 2013; Crandall and Connors, 2016), and inhibition is frequently described as being exclusively local.

However, more recent studies have shown that different classes of cortical GABAergic neurons project their axons to other cortices and subcortical brain areas, and their activation could influence the target region (Jinno and Kosaka, 2004; Tomioka et al., 2005; Higo et al., 2007, 2009; Tomioka and Rockland, 2007; McDonald et al., 2012; Melzer et al., 2012, 2017; Lee et al., 2014; Basu et al., 2016; Rock et al., 2016, 2018; Bertero et al., 2019, 2020, 2021; for review, see Tamamaki and Tomioka, 2010; Caputi et al., 2013; Melzer and Monyer, 2020). Specifically, for this review, VIP-expressing neurons in the auditory and motor cortex send long-range axons to different cortical and subcortical brain structures (Bertero et al., 2021), having the potential to exert their inhibition onto specific classes of neurons both locally and at the distal brain areas (**Figures 1B**, **2A**). Further characterization of VIP-expressing neurons at the local microcircuit along all cortical layers is needed to unveil the role of this subclass of GABAergic neurons during specific brain oscillation (coherence or power) and in shaping the incoming and outgoing flow of the information stream. The recruitment of this class of neurons and how they elaborate the information is still an open question.

## ROLE OF CORTICAL VIP-EXPRESSING NEURONS IN BEHAVING ANIMALS. DISINHIBITION VS. INHIBITION?

A key question for neuroscientists is to correlate how each class of neurons can promote the transformation of the sensory signals into reward-learning and action-selection behaviors in the brain and how these mechanisms are altered in pathological conditions.

Nowadays, the possibility to test the different hypotheses in behaving animals using an enormous number of different tools to identify and control specific classes of neurons is helping the neuroscience community to uncover and understand the contribution of each neuronal class during specific tasks in awake behaving animals.

So far, most of the studies have focused their attention on the role of PV- and SOM-expressing neurons in different brain structures during certain behavioral paradigms to link the behavioral results with the local connectivity that generates that behavior. Selective mouse transgenic Cre-lines are widely used to correlate the activity of GABAergic neurons by cell-type during cortical processing. Specifically, a well-characterized VIP-Cre line is currently used to study the role of VIP-expressing neurons in cortical information processing during relevant behavioral tasks (Pronneke et al., 2015). However, understanding the behaviorally relevant increase/decrease of activity in the cortical VIP-expressing neurons is still at the early stages of investigation.

To address the relevance of VIP-expressing neuron activity fluctuations, experimenters tried different behavioral conditions with optogenetic manipulations to control their activity (Yavorska and Wehr, 2016; Bigelow et al., 2019; Krabbe et al., 2019). Similar approaches were used in other rodents' brain areas, such as the A1 and the V1 cortex. These studies have shown that during animal movement, the VIP-expressing neurons are highly active, generating an overall disinhibitory effect onto local pyramidal neurons (Pi et al., 2013; Fu et al., 2014; Bigelow et al., 2019; Keller et al., 2020; Yavorska and Wehr, 2021; **Figure 2**).

Specifically, in both the primary auditory and visual cortex, the movement of the mouse affects both the local circuit activity and the information processing. Particularly, selective activation of VIP-expressing neurons in the A1 enhances only the local circuit activity during the auditory stimuli but not the information processing (Bigelow et al., 2019; **Figure 2B**). Interestingly, Yavorska and Wehr (2021) demonstrated how animal running behavior and optogenetic activation of VIP-expressing neurons differentially modulate sound-evoked activity across layers in the mouse auditory cortex. Mainly, they found that running increased spontaneous firing rates but decreased evoked firing rates, resulting in the reduced neuronal encoding of sound in all cortical layers. In contrast, the photo-activation of VIP-expressing neurons increased spontaneous and evoked firing rates and did not affect sound encoding. Overall, Yavorska and Wehr's (2021) results indicated that the VIP-expressing neurons circuits do not mediate the effects of locomotion in the auditory cortex (**Figure 2B**).

In addition, Pi et al. (2013) measured neurons' activity in the auditory cortex during a specific task in which a mouse was rewarded or punished depending on the tone presented. Remarkably, VIP-expressing neurons were strongly activated by reward and punishment signals (Pi et al., 2013). However, the strong recruitment of the VIP-expressing neurons did not correlate with an increased spiking of other nearby neurons, as can be expected by the identified canonical cortical disinhibitory circuit motif (for review, see Pfeffer, 2014; **Figure 2A**). One other important aspect of this disinhibitory circuit is that the VIP-expressing neurons strongly inhibit the SOM-expressing neurons, which in turn preferentially inhibit the pyramidal neurons' distal dendrites (Somogyi et al., 1998). This distal inhibition can open a window to increase synaptic integration or plasticity along the distal dendrites of the pyramidal neurons.

Are the long-range cortical VIP-expressing neurons (Bertero et al., 2021) part of a long-range disinhibitory circuit leading to integration and plasticity across cortical and subcortical areas? Future experiments will need to address these open questions on the role of the long-range VIP-expressing neurons that can dynamically affect the cortico-cortical processing (**Figure 2A**).

In the visual cortex, VIP-expressing neurons increase their firing rate mainly when the background and the stimulus are different. This increase in the firing rate reduces the activity of SOM-expressing neurons generating a disinhibitory effect onto local pyramidal neurons (Keller et al., 2020; **Figure 2A**). Moreover, during locomotion, the activity of VIP-expressing neurons is increased, and this effect is independent of the visual stimulus. However, this activation arises from nicotinic inputs from the nucleus of the diagonal bans of Broca, a cholinergic center in the basal forebrain (Fu et al., 2014; **Figure 2B**).

Interestingly, as shown by Fu et al. (2014), VIP-expressing neurons are more active in V1 during locomotion than other sensory cortices. The VIP-expressing neurons in the visual cortex are also the target of top-down inputs and mediate enhancement of local pyramidal cell activity in response to activation of those inputs (Zhang et al., 2014). It has been demonstrated that the mouse V1 is necessary to detect low contrast visual stimuli (Glickfeld et al., 2013). Selective optogenetic activation of either PV-, SOM-, or VIP-expressing of GABAergic neurons has a different effect on the contrast-detection observed in the mouse V1. The activation of VIP-expressing neurons lowers the thresholds of contrast detection while the activation of SOM- or PV-expressing neurons raises it (Cone et al., 2019). This suggests that the perception of low contrast stimuli is strongly enhanced by VIP neuron activity in V1.

Recently, Millman et al. (2020) have investigated the influence of stimulus contrast and locomotion on the visual responses of VIP-, SOM-expressing neurons, and pyramidal neurons in mouse V1. Particularly, they found that the SOM- and VIP-expressing neurons differentially responded to high and low contrast. Mainly, the SOM-expressing neurons responded exclusively at low contrast that is congruent with self-motion during locomotion. In this study, Millman et al. (2020) demonstrated that the VIP-driven disinhibition at low contrast could strongly increase the activity of pyramidal neurons, even though both pyramidal and SOM-expressing neurons are characterized by a lower activity during low contrast regime. Overall, the Millman et al. (2020) results indicated that the VIP-expressing neurons, *via* the VIP-disinhibitory circuit motif, can amplify the response of the pyramidal neurons to weak but behaviorally relevant stimuli such as low contrast front-to-back motion that can be fundamental for the detection of approaching obstacles during locomotion (**Figure 2B**).

It has also been demonstrated that the context can modulate the response of specific visual stimuli in the visual cortex. Lately, Keller et al. (2020) have identified a canonical VIP-driven disinhibitory circuit that, by inhibiting the SOM-expressing neurons, modulates the response in the mouse V1 accordingly to the similarity between the surround and the stimulus (**Figure 2B**).

In another sensory cortex, such as the S1 barrel cortex, it has been shown that layer 2/3 VIP-expressing neurons increase the firing rate during active whisking by disinhibiting the pyramidal neurons (Lee et al., 2013; **Figures 2A,B**). In addition, multiple studies have characterized different sub-classes of GABAergic neurons engaged during whisker-dependent behavior (Sachidhanandam et al., 2016; Yu et al., 2019). In their study, Sachidhanandam et al. (2016) trained mice to obtain a water reward in response to whisker deflection while recording the activity from genetically targeted GABAergic neurons in layer 2/3 of the mouse barrel cortex. They found that the SOM-expressing neurons fired at low rates, while both PV- and VIP-expressing neurons fired at high rates during whisker stimulation. Moreover, Yu et al. (2019) demonstrated that the VIP-expressing neurons during active tactile behavior are activated by non-sensory inputs that disinhibit both pyramidal and PV-expressing neurons. Overall, these studies indicate that the different class of GABAergic neurons is characterized by a specific firing dynamic that depends on the behavioral task execution (Sachidhanandam et al., 2016; Yu et al., 2019).

It has also been demonstrated that a subpopulation of VIP/ChAT positive neurons in the superficial layers are recruited during whisker movements and play a key role in encoding the external stimuli (Dudai et al., 2020). At this point, it is legitimate to ask: Is the activity of VIP-expressing neurons during locomotion applied only to sensory cortices?

The VIP-expressing neurons are also involved in motor skill learning (Adler et al., 2019). In their study, Adler et al. (2019) trained mice to run forward or backward at fixed speeds on a treadmill. During this motor learning task, GABAergic and pyramidal neurons exhibited different activation patterns. The layers 2/3 pyramidal neurons were characterized by sequential activation patterns (Adler et al., 2019), while the SOM-expressing neurons exhibited diverse responses. Their activity was enhanced, suppressed, or unchanged at the onset of forward and backward running, and their activation suppressed the sequential activation of pyramidal neurons. In addition, Adler et al. (2019) also revealed that VIP-expressing neurons could inhibit SOM-expressing GABAergic neurons, which leads to relief of pyramidal neurons from suppression (VIP-disinhibitory motif) permitting synaptic plasticity and learning to take place (**Figures 2A,B**).

Another study focused on the role of the VIP-expressing neurons in behavioral performance and neuronal action plan in the dorsomedial prefrontal cortex (Kamigaki and Dan, 2017). When VIP-expressing neurons were selectively photo-activated, through the disinhibitory circuit, performance on the go/no-go task was enhanced (**Figure 2**). This study highlights the role of this class of neurons in modulating behavioral performances and tasks.

Furthermore, medial prefrontal cortical inputs arising from the ventral hippocampus activate VIP-expressing neurons while animals are in the open arm of the elevated plus-maze. This has an overall disinhibitory effect at the prefrontal cortex microcircuit. Additionally, selective inactivation of VIP neurons during this task elicits an increase in avoidance behavior (Lee et al., 2019; **Figures 2A,B**). Overall, it is still intriguing to speculate about the role of layer 5 VIP-expressing neurons in cortical processing: are they establishing a disinhibitory local circuit motif (VIP→SOM→L5 Pyramidal neurons) mirroring their main organization in the layer 2/3 of the cortex? It is also possible to speculate that the layer 5 VIP-expressing neurons directly inhibit pyramidal neurons (VIP→L5 Pyramidal neurons).

Therefore, we think that the role of the layer 5 VIP-disinhibitory and VIP-inhibitory circuit motif still needs further elucidation (see **Figures 1B** bottom, **2A**).

## THE ROLE OF VIP-EXPRESSING NEURONS IN CORTICAL DYSFUNCTION

Alterations of GABAergic neurons, at the molecular and circuit level, have been proven to induce a dysfunctional effect leading

to several diseases such as epilepsy, autism, and anxiety (Yu et al., 2006; Marin, 2012; Lewis, 2014). Even though the GABAergic neurons represent only a small fraction of the entire cortical neuronal population, selective mutation of specific genes in diverse GABAergic neurons might induce several pathological conditions.

VIP-expressing neurons release the peptide VIP activating neuronal and non-neuronal cells (see Section "Local Circuit Organization of VIP-Expressing Neurons" above). The asymmetric activation of the two receptors (VPAC1 and VPAC2) suggests that different signaling pathways regulate neuronal circuits' activity. The alteration of VIP release and/or the VIP binding receptors could be potentially implicated in multiple pathophysiological conditions. It has been shown that the VIP peptide has a significant role in regulating neuronal activity, and the selective loss of this peptide is associated with several pathological disorders such as depression (Ivanova et al., 2012), Parkinson's disease, and epilepsy (Hill, 2007; White et al., 2010). Indeed, in human temporal lobe epilepsy brains, the receptors for the VIP peptide are increased in expression in the focus of the seizure. In the animal model of temporal lobe epilepsy, although there is a severe reduction of particular types of neurons, the number of VIP-expressing neurons seems not to be affected (King and LaMotte, 1988). VIP knock-out (KO) mice exhibit alterations in memory tasks and social behavior (Stack et al., 2008). However, the role of the VIP-expressing neurons at the neuronal level and their role in pathological conditions still need to be elucidated.

Al the circuit level, only recently, several groups have found that activity of dysfunctional VIP-expressing neurons is associated with neuronal disorders. Alteration of the specific gene or gene expression regulators, which control the transcription factors, specifically in VIP-expressing neurons, are implicated in pathophysiological conditions. These effects could alter the inhibitory/disinhibitory impact of the expressing neurons at the micro and long-range circuit level and alter the animal's behavior.

In the condition in which the gene ErbB4 that expresses the membrane-bound tyrosine kinase receptor is deleted, the V1 cortical circuits and neuronal synchrony between spike activity and brain oscillations in the gamma bands (40–60 Hz) are dysregulated, inducing an impairment in the information processing performed by neuronal circuits. This mutation reduces the activity of VIP-expressing neurons also witnessed with an increase excitatory neuronal activity, suggesting a direct inhibitory effect of the VIP (Batista-Brito et al., 2017). Other studies have found that the ablation of the gene that encodes for a gene expression regulator selectively reduced the cell vitality in adulthood and impaired intrinsic properties of VIP-expressing neurons. This lead to an increase in inhibitory inputs onto pyramidal neurons, indicating that a disinhibitory circuit is involved, and dysfunctional cortical oscillations. These effects induced a better spatial working memory and motor coordination in these mice but reduced their life span (Qiu et al., 2020).

In a complementary condition, the S1 VIP-expressing neurons lost their preferential abundance in the superficial layers. Moreover, the long-range inputs onto VIP-expressing neurons from ipsilateral and contralateral cortices were compromised, contributing to a dysfunctional elaboration of the incoming inputs (Hafner et al., 2021). In addition, Goff and Goldberg (2019) have shown that the neocortical VIP-expressing neurons in Scn1a$^{+/-}$ mice, a mouse model of Dravet syndrome, exhibited impaired excitability. Despite these two latest studies, it is still not known whether there is an inhibitory/disinhibitory alteration due to the mutation of the Scn1a gene.

Overall, these studies highlight how developmental dysregulation, gene expression ablation, and structural abnormalities specifically in VIP would lead to pathophysiological conditions, highlighting the crucial role of VIP-expressing, GABAergic neurons in neuronal circuit dysfunctions and neurological disorders.

## CONCLUSION AND PERSPECTIVES

In recent years, with the advanced technological tools, it has been possible to selectively control specific groups of neurons, including the VIP-expressing neurons, which represent a small percentage of the entire GABAergic population. This has allowed great strides in understanding the physiological role of a particular type of neurons, from the detailed anatomy of the neurons up to their activity during specific tasks.

The VIP-expressing neurons are mainly present in the superficial layers of the cortex (Pronneke et al., 2015, 2020; Zhou et al., 2017; Almasi et al., 2019; Badrinarayanan et al., 2021), where most of the studies are performed but leaving almost unexplored the physiology of VIP-expressing neurons in deeper cortical layers. The difficulty of *in vivo* studies for the infragranular VIP-expressing neurons is their low number (Yu et al., 2019). So far, only *in vitro* studies elucidate anatomical and electrophysiological differences between superficial and deep cortical VIP-expressing neurons. They mainly confirm some dissimilarity about these neurons and suggest a potential differential role at the circuit level and most likely during behavior.

*In vitro* and *in vivo* studies have previously revealed a preferential inhibition of the VIP-expressing neuron to SOM-expressing neurons labeling them as the main players of the disinhibitory role at the local circuit level (Lee et al., 2013; Pfeffer et al., 2013; Pi et al., 2013). However, recent studies have suggested that this subclass of GABAergic neurons can inhibit and disinhibit excitatory neurons (Garcia-Junco-Clemente et al., 2017; Zhou et al., 2017; see for review Kullander and Topolnik, 2021).

Further studies *in vitro* and *in vivo* done in different brain areas and during various behavioral tasks are still needed to resolve the functional role of the VIP-expressing GABAergic neurons. The peculiar local and distal circuit in which these neurons are embedded suggests a more complex function without limiting their role in the disinhibitory effect onto pyramidal neurons by inhibiting the SOM-expressing neurons (Naskar et al., 2021).

One example of an additional function of VIP-expressing neurons is their ability to inhibit other GABAergic and non-GABAergic neurons (Pfeffer et al., 2013), leading to a different scenario at the circuit level. Additionally, VIP-expressing neurons of the mouse auditory and motor cortices can also send long-range projections to cortical and subcortical areas. Particularly, VIP-expressing neurons of the auditory cortex can reach the contralateral auditory cortex and the ipsilateral striatum and amygdala, as shown for Somatostatin- and Parvalbumin-expressing long-range neurons. Moreover, these neurons also send long-range GABAergic projections to the medial geniculate body and both superior and inferior colliculus. In addition, Bertero et al. (2021; **Figures 1B**, **2A**) demonstrated that VIP-expressing neurons of the motor cortex also send long-range GABAergic projections to the dorsal striatum and contralateral cortex, suggesting that the long-range VIP projection is likely a general feature of the neocortex's network. Even though these studies suggest an unforeseen role of this subclass of neurons, more physiological data is still needed to frame and better understand their role in cortical circuits and behavior.

Another characteristic, which could shape the role of these neurons and give a better definition to their inhibitory/disinhibitory effect, is their synaptic plasticity. The dynamics in which these neurons release their neurotransmitters influence cortical circuits (Cirelli and Tononi, 2000). So far, *in vitro* experiments in the superficial layer of the S1 barrel showed short-term facilitation of these synapses onto SOM-expressing neurons but a short-term depression onto PV-expressing neurons (Walker et al., 2016). Nevertheless, data in deep neocortical layers and *in vivo* are still lacking. Different groups tested the long-distance cortico-cortical and cortico-thalamic excitatory inputs onto VIP-expressing neurons stimulating axon terminals in the recipient structure. Lee et al. (2013) found that M1 excitatory axons showed synaptic depression after paired-pulse stimuli. However, most of the protocols used were a single photo pulse, leaving the aspect of short-term dynamics still unexplored. Another crucial aspect that is still missing in the puzzle of the neocortical role of the VIP-expressing neurons is during brain oscillations. These results on temporal dynamics are still missing due to their low percentage of neurons, especially in the deep neocortical layers.

The present review shows the complexity of the neocortical VIP-expressing neurons' anatomical and electrophysiological properties and neurotransmitter release machinery. In addition, the characteristic input/output of the VIP-expressing neurons makes their collocation in the neocortical organization and function even more intriguing to resolve.

Many questions still need to be addressed concerning VIP-expressing neurons circuits in the neocortex and other brain areas. What role do the other subclasses of GABAergic neurons play in the disinhibitory circuit provided by the activation of VIP-expressing neurons? Do VIP-expressing neurons exert an inhibitory/disinhibitory effect in deeper neocortical layers? What is the role of this intracortical inhibition in the sensory integration of top-down and bottom-up information? What is the role of these neurons during specific neocortical activity in awake animals? Future experiments will provide further insight into the complexity of the local circuit's organization of the VIP-expressing neurons and their role in neocortical processing (for review see Larkum, 2013).

Overall, this review has highlighted the differential roles of the VIP-expressing neuron in cortical processing. However, future experiments are still necessary to determine the possible VIP-expressing neurons inhibitory and/or disinhibitory motifs across cortical layers and different brain structures.

## AUTHOR CONTRIBUTIONS

AjA and IM wrote and commented on the manuscript. Both authors contributed to the article and approved the submitted version.

## FUNDING

This research was supported by local funds of the University of Padua to IM, the National Institute of Mental Health (NIMH)—R01 MH123260, the National Institute of General Medical Sciences—SC1GM122645, and the National Science Foundation (NSF)—IOS-1565410 to AjA.

## REFERENCES

Acsady, L., Gorcs, T. J., and Freund, T. F. (1996). Different populations of vasoactive intestinal polypeptide-immunoreactive interneurons are specialized to control pyramidal cells or interneurons in the hippocampus. *Neuroscience* 73, 317–334. doi: 10.1016/0306-4522(95)00609-5

Adesnik, H., Bruns, W., Taniguchi, H., Huang, Z. J., and Scanziani, M. (2012). A neural circuit for spatial summation in visual cortex. *Nature* 490, 226–231. doi: 10.1038/nature11526

Adler, A., Zhao, R., Shin, M. E., Yasuda, R., and Gan, W. B. (2019). Somatostatin-expressing interneurons enable and maintain learning-dependent sequential activation of pyramidal neurons. *Neuron* 102, 202–216 e207. doi: 10.1016/j.neuron.2019.01.036

Ali, M., Jha, S. K., Kaur, S., and Mallick, B. N. (1999). Role of GABA-A receptor in the preoptic area in the regulation of sleep-wakefulness and rapid eye movement sleep. *Neurosci. Res.* 33, 245–250. doi: 10.1016/s0168-0102(99)00013-9

Almasi, Z., David, C., Witte, M., and Staiger, J. F. (2019). Distribution patterns of three molecularly defined classes of gabaergic neurons across columnar compartments in mouse barrel cortex. *Front. Neuroanat.* 13:45. doi: 10.3389/fnana.2019.00045

Ashur-Fabian, O., Giladi, E., Brenneman, D. E., and Gozes, I. (1997). Identification of VIP/PACAP receptors on rat astrocytes using antisense oligodeoxynucleotides. *J. Mol. Neurosci.* 9, 211–222. doi: 10.1007/BF02800503

Audette, N. J., Urban-Ciecko, J., Matsushita, M., and Barth, A. L. (2018). POm thalamocortical input drives layer-specific microcircuits in somatosensory cortex. *Cereb. Cortex* 28, 1312–1328. doi: 10.1093/cercor/bhx044

Badrinarayanan, S., Manseau, F., Williams, S., and Brandon, M. P. (2021). A characterization of the electrophysiological and morphological properties of vasoactive intestinal peptide (VIP) interneurons in the medial entorhinal cortex (MEC). *Front. Neural Circuits* 15:653116. doi: 10.3389/fncir.2021.653116

Basu, J., Zaremba, J. D., Cheung, S. K., Hitti, F. L., Zemelman, B. V., Losonczy, A., et al. (2016). Gating of hippocampal activity, plasticity, and memory by entorhinal cortex long-range inhibition. *Science* 351:aaa5694.

Batista-Brito, R., Vinck, M., Ferguson, K. A., Chang, J. T., Laubender, D., Lur, G., et al. (2017). Developmental dysfunction of VIP interneurons impairs cortical circuits. *Neuron* 95, 884–895 e889. doi: 10.1016/j.neuron.2017.07.034

Bayraktar, T., Staiger, J. F., Acsady, L., Cozzari, C., Freund, T. F., and Zilles, K. (1997). Co-localization of vasoactive intestinal polypeptide, gamma-aminobutyric acid and choline acetyltransferase in neocortical interneurons of the adult rat. *Brain Res.* 757, 209–217. doi: 10.1016/s0006-8993(97)00218-7

Bean, B. P. (2007). The action potential in mammalian central neurons. *Nat. Rev. Neurosci* .8, 451–465. doi: 10.1038/nrn2148

Bertero, A., Feyen, P. L. C., Zurita, H., and Apicella, A. J. (2019). A non-canonical cortico-amygdala inhibitory loop. *J. Neurosci.* 39, 8424–8438. doi: 10.1523/JNEUROSCI.1515-19.2019

Bertero, A., Garcia, C., and Apicella, A. J. (2021). Corticofugal VIP gabaergic projection neurons in the mouse auditory and motor cortex. *Front. Neural Circuits* 15:714780. doi: 10.3389/fncir.2021.714780

Bertero, A., Zurita, H., Normandin, M., and Apicella, A. J. (2020). Auditory long-range parvalbumin cortico-striatal neurons. *Front. Neural Circuits* 14:45. doi: 10.3389/fncir.2020.00045

Bigelow, J., Morrill, R. J., Dekloe, J., and Hasenstaub, A. R. (2019). Movement and VIP interneuron activation differentially modulate encoding in mouse auditory cortex. *eNeuro* 6:ENEURO.0164-19.2019. doi: 10.1523/ENEURO.0164-19.2019

Borbely, E., Scheich, B., and Helyes, Z. (2013). Neuropeptides in learning and memory. *Neuropeptides* 47, 439–450.

Buzsaki, G. (1984). Feed-forward inhibition in the hippocampal formation. *Prog. Neurobiol.* 22, 131–153. doi: 10.1016/0301-0082(84)90023-6

Caputi, A., Melzer, S., Michael, M., and Monyer, H. (2013). The long and short of GABAergic neurons. *Curr. Opin. Neurobiol.* 23, 179–186. doi: 10.1016/j.conb.2013.01.021

Cauli, B., Zhou, X., Tricoire, L., Toussay, X., and Staiger, J. F. (2014). Revisiting enigmatic cortical calretinin-expressing interneurons. *Front. Neuroanat.* 8:52. doi: 10.3389/fnana.2014.00052

Chamberland, S., Salesse, C., Topolnik, D., and Topolnik, L. (2010). Synapse-specific inhibitory control of hippocampal feedback inhibitory circuit. *Front. Cell Neurosci.* 4:130. doi: 10.3389/fncel.2010.00130

Cirelli, C., and Tononi, G. (2000). Differential expression of plasticity-related genes in waking and sleep and their regulation by the noradrenergic system. *J. Neurosci.* 20, 9187–9194. doi: 10.1523/JNEUROSCI.20-24-09187.2000

Cone, J. J., Scantlen, M. D., Histed, M. H., and Maunsell, J. H. R. (2019). Different inhibitory interneuron cell classes make distinct contributions to visual contrast perception. *eNeuro* 6:ENEURO.0337-18.2019. doi: 10.1523/ENEURO.0337-18.2019

Crandall, S. R., and Connors, B. W. (2016). Diverse ensembles of inhibitory interneurons. *Neuron* 90, 4–6. doi: 10.1016/j.neuron.2016.03.022

Cunha-Reis, D., and Caulino-Rocha, A. (2020). VIP modulation of hippocampal synaptic plasticity: a role for VIP receptors as therapeutic targets in cognitive decline and mesial temporal lobe epilepsy. *Front. Cell Neurosci.* 14:153. doi: 10.3389/fncel.2020.00153

Cunha-Reis, D., Ribeiro, J. A., De Almeida, R. F. M., and Sebastiao, A. M. (2017). VPAC1 and VPAC2 receptor activation on GABA release from hippocampal nerve terminals involve several different signalling pathways. *Br. J. Pharmacol.* 174, 4725–4737. doi: 10.1111/bph.14051

DeFelipe, J., Lopez-Cruz, P. L., Benavides-Piccione, R., Bielza, C., Larranaga, P., Anderson, S., et al. (2013). New insights into the classification and nomenclature of cortical GABAergic interneurons. *Nat. Rev. Neurosci.* 14, 202–216. doi: 10.1038/nrn3444

Deng, G., and Jin, L. (2017). The effects of vasoactive intestinal peptide in neurodegenerative disorders. *Neurol. Res.* 39, 65–72. doi: 10.1080/01616412.2016.1250458

Donato, F., Rompani, S. B., and Caroni, P. (2013). Parvalbumin-expressing basket-cell network plasticity induced by experience regulates adult learning. *Nature* 504, 272–276. doi: 10.1038/nature12866

Dudai, A., Yayon, N., Lerner, V., Tasaka, G. I., Deitcher, Y., Gorfine, K., et al. (2020). Barrel cortex VIP/ChAT interneurons suppress sensory responses in vivo. *PLoS Biol.* 18:e3000613. doi: 10.1371/journal.pbio.3000613

Emmenegger, V., Qi, G., Wang, H., and Feldmeyer, D. (2018). Morphological and functional characterization of non-fast-spiking GABAergic interneurons in layer 4 microcircuitry of rat barrel cortex. *Cereb. Cortex* 28, 1439–1457. doi: 10.1093/cercor/bhx352

Feldmeyer, D. (2012). Excitatory neuronal connectivity in the barrel cortex. *Front. Neuroanat.* 6:24. doi: 10.3389/fnana.2012.00024

Francavilla, R., Villette, V., Luo, X., Chamberland, S., Munoz-Pino, E., Camire, O., et al. (2018). Connectivity and network state-dependent recruitment of long-range VIP-GABAergic neurons in the mouse hippocampus. *Nat. Commun.* 9:5043. doi: 10.1038/s41467-018-07162-5

Freund, T. F., and Buzsaki, G. (1996). Interneurons of the hippocampus. *Hippocampus* 6, 347–470. doi: 10.1002/(sici)1098-1063(1996)6:4<347::aid-hipo1>3.0.co;2-i

Fu, Y., Tucciarone, J. M., Espinosa, J. S., Sheng, N., Darcy, D. P., Nicoll, R. A., et al. (2014). A cortical circuit for gain control by behavioral state. *Cell* 156, 1139–1152. doi: 10.1016/j.cell.2014.01.050

Garcia-Junco-Clemente, P., Ikrar, T., Tring, E., Xu, X., Ringach, D. L., and Trachtenberg, J. T. (2017). An inhibitory pull-push circuit in frontal cortex. *Nat. Neurosci.* 20, 389–392. doi: 10.1038/nn.4483

Glickfeld, L. L., Histed, M. H., and Maunsell, J. H. (2013). Mouse primary visual cortex is used to detect both orientation and contrast changes. *J. Neurosci.* 33, 19416–19422. doi: 10.1523/JNEUROSCI.3560-13.2013

Goadsby, P. J., and Shelley, S. (1990). High-frequency stimulation of the facial nerve results in local cortical release of vasoactive intestinal polypeptide in the anesthetised cat. *Neurosci. Lett.* 112, 282–289. doi: 10.1016/0304-3940(90)90217-w

Goff, K. M., and Goldberg, E. M. (2019). Vasoactive intestinal peptide-expressing interneurons are impaired in a mouse model of *Dravet syndrome*. *Elife* 8:e46846. doi: 10.7554/eLife.46846

Granger, A. J., Wang, W., Robertson, K., El-Rifai, M., Zanello, A. F., Bistrong, K., et al. (2020). Cortical ChAT(+) neurons co-transmit VIP-expressing neurons localized and GABA in a target- and brain-region-specific manner. *Elife* 9:e57749. doi: 10.7554/eLife.57749

Guet-McCreight, A., Skinner, F. K., and Topolnik, L. (2020). Common principles in functional organization of VIP/calretinin cell-driven disinhibitory circuits across cortical areas. *Front. Neural Circuits* 14:32. doi: 10.3389/fncir.2020.00032

Hafner, G., Guy, J., Witte, M., Truschow, P., Ruppel, A., Sirmpilatze, N., et al. (2021). Increased callosal connectivity in reeler mice revealed by brain-wide input mapping of VIP neurons in barrel cortex. *Cereb. Cortex* 31, 1427-1443. doi: 10.1093/cercor/bhaa280

Hajos, N., Acsady, L., and Freund, T. F. (1996). Target selectivity and neurochemical characteristics of VIP-immunoreactive interneurons in the rat dentate gyrus. *Eur. J. Neurosci.* 8, 1415–1431. doi: 10.1111/j.1460-9568.1996.tb01604.x

Harris, K. D., and Shepherd, G. M. (2015). The neocortical circuit: themes and variations. *Nat. Neurosci.* 18, 170–181. doi: 10.1038/nn.3917

Hayut, I., Fanselow, E. E., Connors, B. W., and Golomb, D. (2011). LTS and FS inhibitory interneurons, short-term synaptic plasticity, and cortical circuit dynamics. *PLoS Comput. Biol.* 7:e1002248. doi: 10.1371/journal.pcbi.1002248

He, M., Tucciarone, J., Lee, S., Nigro, M. J., Kim, Y., Levine, J. M., et al. (2016). Strategies and tools for combinatorial targeting of GABAergic neurons in mouse cerebral cortex. *Neuron* 92:555. doi: 10.1016/j.neuron.2016.10.009

Hertag, L., and Sprekeler, H. (2019). Amplifying the redistribution of somato-dendritic inhibition by the interplay of three interneuron types. *PLoS Comput. Biol.* 15:e1006999. doi: 10.1371/journal.pcbi.1006999

Higo, S., Akashi, K., Sakimura, K., and Tamamaki, N. (2009). Subtypes of GABAergic neurons project axons in the neocortex. *Front. Neuroanat.* 3:25. doi: 10.3389/neuro.05.025.2009

Higo, S., Udaka, N., and Tamamaki, N. (2007). Long-range GABAergic projection neurons in the cat neocortex. *J. Comp. Neurol.* 503, 421–431. doi: 10.1002/cne.21395

Hill, J. M. (2007). Vasoactive intestinal peptide in neurodevelopmental disorders: therapeutic potential. *Curr. Pharm. Des.* 13, 1079–1089. doi: 10.2174/138161207780618975

Holmgren, C., Harkany, T., Svennenfors, B., and Zilberter, Y. (2003). Pyramidal cell communication within local networks in layer 2/3 of rat neocortex. *J. Physiol.* 551, 139–153. doi: 10.1113/jphysiol.2003.044784

Huang, Z. J., and Paul, A. (2019). The diversity of GABAergic neurons and neural communication elements. *Nat. Rev. Neurosci.* 20, 563–572. doi: 10.1038/s41583-019-0195-4

Ito, M., and Yoshida, M. (1966). The origin of cerebral-induced inhibition of Deiters neurones. I. Monosynaptic initiation of the inhibitory postsynaptic potentials. *Exp. Brain Res.* 2, 330–349. doi: 10.1007/BF00234779

Ivanova, M., Belcheva, S., Belcheva, I., Negrev, N., and Tashev, R. (2012). Lateralized hippocampal effects of vasoactive intestinal peptide on learning and memory in rats in a model of depression. *Psychopharmacology (Berl)* 221, 561–574. doi: 10.1007/s00213-011-2600-1

Ji, X. Y., Zingg, B., Mesik, L., Xiao, Z., Zhang, L. I., and Tao, H. W. (2016). Thalamocortical innervation pattern in mouse auditory and visual cortex: laminar and cell-type specificity. *Cereb. Cortex* 26, 2612–2625. doi: 10.1093/cercor/bhv099

Jinno, S., and Kosaka, T. (2004). Parvalbumin is expressed in glutamatergic and GABAergic corticostriatal pathway in mice. *J. Comp. Neurol.* 477, 188–201. doi: 10.1002/cne.20246

Kamigaki, T., and Dan, Y. (2017). Delay activity of specific prefrontal interneuron subtypes modulates memory-guided behavior. *Nat. Neurosci.* 20, 854–863. doi: 10.1038/nn.4554

Kapfer, C., Glickfeld, L. L., Atallah, B. V., and Scanziani, M. (2007). Supralinear increase of recurrent inhibition during sparse activity in the somatosensory cortex. *Nat. Neurosci.* 10, 743–753. doi: 10.1038/nn1909

Karnani, M. M., Jackson, J., Ayzenshtat, I., Hamzehei Sichani, A., Manoocheri, K., Kim, S., et al. (2016a). Opening holes in the blanket of inhibition: localized lateral disinhibition by VIP interneurons. *J. Neurosci.* 36, 3471–3480. doi: 10.1523/JNEUROSCI.3646-15.2016

Karnani, M. M., Jackson, J., Ayzenshtat, I., Tucciarone, J., Manoocheri, K., Snider, W. G., et al. (2016b). Cooperative subnetworks of molecularly similar interneurons in mouse neocortex. *Neuron* 90, 86–100. doi: 10.1016/j.neuron.2016.02.037

Keller, A. J., Dipoppa, M., Roth, M. M., Caudill, M. S., Ingrosso, A., Miller, K. D., et al. (2020). A disinhibitory circuit for contextual modulation in primary visual cortex. *Neuron* 108, 1181–1193 e1188. doi: 10.1016/j.neuron.2020.11.013

King, J. T. Jr., and LaMotte, C. C. (1988). VIP-, SS-, and GABA-like immunoreactivity in the mid-hippocampal region of El (epileptic) and C57BL/6 mice. *Brain Res.* 475, 192–197. doi: 10.1016/0006-8993(88)90218-1

Kloc, M., and Maffei, A. (2014). Target-specific properties of thalamocortical synapses onto layer 4 of mouse primary visual cortex. *J. Neurosci.* 34, 15455–15465. doi: 10.1523/JNEUROSCI.2595-14.2014

Krabbe, S., Paradiso, E., D'aquin, S., Bitterman, Y., Courtin, J., Xu, C., et al. (2019). Adaptive disinhibitory gating by VIP interneurons permits associative learning. *Nat. Neurosci.* 22, 1834–1843. doi: 10.1038/s41593-019-0508-y

Kubota, Y., Shigematsu, N., Karube, F., Sekigawa, A., Kato, S., Yamaguchi, N., et al. (2011). Selective coexpression of multiple chemical markers defines discrete populations of neocortical GABAergic neurons. *Cereb. Cortex* 21, 1803–1817. doi: 10.1093/cercor/bhq252

Kullander, K., and Topolnik, L. (2021). Cortical disinhibitory circuits: cell types, connectivity and function. *Trends Neurosci.* 44, 643–657. doi: 10.1016/j.tins.2021.04.009

Larkum, M. (2013). A cellular mechanism for cortical associations: an organizing principle for the cerebral cortex. *Trends Neurosci.* 36, 141–151. doi: 10.1016/j.tins.2012.11.006

Larkum, M. E., Petro, L. S., Sachdev, R. N. S., and Muckli, L. (2018). A perspective on cortical layering and layer-spanning neuronal elements. *Front. Neuroanat.* 12:56. doi: 10.3389/fnana.2018.00056

Lee, A. T., Cunniff, M. M., See, J. Z., Wilke, S. A., Luongo, F. J., Ellwood, I. T., et al. (2019). VIP interneurons contribute to avoidance behavior by regulating information flow across hippocampal-prefrontal networks. *Neuron* 102, 1223–1234 e1224. doi: 10.1016/j.neuron.2019.04.001

Lee, A. T., Vogt, D., Rubenstein, J. L., and Sohal, V. S. (2014). A class of GABAergic neurons in the prefrontal cortex sends long-range projections to the nucleus accumbens and elicits acute avoidance behavior. *J. Neurosci.* 34, 11519–11525. doi: 10.1523/JNEUROSCI.1157-14.2014

Lee, S., Kruglikov, I., Huang, Z. J., Fishell, G., and Rudy, B. (2013). A disinhibitory circuit mediates motor integration in the somatosensory cortex. *Nat. Neurosci.* 16, 1662–1670. doi: 10.1038/nn.3544

Lewis, D. A. (2014). Inhibitory neurons in human cortical circuits: substrate for cognitive dysfunction in schizophrenia. *Curr. Opin. Neurobiol.* 26, 22–26. doi: 10.1016/j.conb.2013.11.003

Ma, W. P., Liu, B. H., Li, Y. T., Huang, Z. J., Zhang, L. I., and Tao, H. W. (2010). Visual representations by cortical somatostatin inhibitory neurons–selective but with weak and delayed responses. *J. Neurosci.* 30, 14371–14379. doi: 10.1523/JNEUROSCI.3248-10.2010

Maccaferri, G., and Lacaille, J. C. (2003). Interneuron diversity series: hippocampal interneuron classifications–making things as simple as possible, not simpler. *Trends Neurosci.* 26, 564–571. doi: 10.1016/j.tins.2003.08.002

Marin, O. (2012). Interneuron dysfunction in psychiatric disorders. *Nat. Rev. Neurosci.* 13, 107–120. doi: 10.1038/nrn3155

Markram, H., Muller, E., Ramaswamy, S., Reimann, M. W., Abdellah, M., Sanchez, C. A., et al. (2015). Reconstruction and simulation of neocortical microcircuitry. *Cell* 163, 456–492. doi: 10.1016/j.cell.2015.09.029

McDonald, A. J., Mascagni, F., and Zaric, V. (2012). Subpopulations of somatostatin-immunoreactive non-pyramidal neurons in the amygdala and adjacent external capsule project to the basal forebrain: evidence for the existence of GABAergic projection neurons in the cortical nuclei and basolateral nuclear complex. *Front. Neural Circuits* 6:46. doi: 10.3389/fncir.2012.00046

Melzer, S., and Monyer, H. (2020). Diversity and function of corticopetal and corticofugal GABAergic projection neurons. *Nat. Rev. Neurosci.* 21, 499–515. doi: 10.1038/s41583-020-0344-9

Melzer, S., Gil, M., Koser, D. E., Michael, M., Huang, K. W., and Monyer, H. (2017). Distinct corticostriatal GABAergic neurons modulate striatal output neurons and motor activity. *Cell Rep.* 19, 1045–1055. doi: 10.1016/j.celrep.2017.04.024

Melzer, S., Michael, M., Caputi, A., Eliava, M., Fuchs, E. C., Whittington, M. A., et al. (2012). Long-range-projecting GABAergic neurons modulate inhibition in hippocampus and entorhinal cortex. *Science* 335, 1506–1510. doi: 10.1126/science.1217139

Millman, D. J., Ocker, G. K., Caldejon, S., Kato, I., Larkin, J. D., Lee, E. K., et al. (2020). VIP interneurons in mouse primary visual cortex selectively enhance responses to weak but specific stimuli. *Elife* 9:e55130. doi: 10.7554/eLife.55130

Naskar, S., Qi, J., Pereira, F., Gerfen, C. R., and Lee, S. (2021). Cell-type-specific recruitment of GABAergic interneurons in the primary somatosensory cortex by long-range inputs. *Cell Rep.* 34:108774. doi: 10.1016/j.celrep.2021.108774

Neske, G. T., and Connors, B. W. (2016). Distinct roles of SOM and VIP interneurons during cortical up states. *Front. Neural Circuits* 10:52. doi: 10.3389/fncir.2016.00052

Obermayer, J., Luchicchi, A., Heistek, T. S., De Kloet, S. F., Terra, H., Bruinsma, B., et al. (2019). Prefrontal cortical ChAT-VIP interneurons provide local excitation by cholinergic synaptic transmission and control attention. *Nat. Commun.* 10:5280.

Olah, S., Komlosi, G., Szabadics, J., Varga, C., Toth, E., Barzo, P., et al. (2007). Output of neurogliaform cells to various neuron types in the human and rat cerebral cortex. *Front. Neural Circuits* 1:4. doi: 10.3389/neuro.04.004.2007

Petilla Interneuron Nomenclature Group, Ascoli, G. A., Alonso-Nanclares, L., Anderson, S. A., Barrionuevo, G., Benavides-Piccione, R., et al. (2008). Petilla terminology: nomenclature of features of GABAergic interneurons of the cerebral cortex. *Nat. Rev. Neurosci.* 9, 557–568. doi: 10.1038/nrn2402

Pfeffer, C. K. (2014). Inhibitory neurons: vip cells hit the brake on inhibition. *Curr. Biol.* 24, R18–R20. doi: 10.1016/j.cub.2013.11.001

Pfeffer, C. K., Xue, M., He, M., Huang, Z. J., and Scanziani, M. (2013). Inhibition of inhibition in visual cortex: the logic of connections between molecularly distinct interneurons. *Nat. Neurosci.* 16, 1068–1076. doi: 10.1038/nn.3446

Pi, H. J., Hangya, B., Kvitsiani, D., Sanders, J. I., Huang, Z. J., and Kepecs, A. (2013). Cortical interneurons that specialize in disinhibitory control. *Nature* 503, 521–524. doi: 10.1038/nature12676

Porter, J. T., Cauli, B., Staiger, J. F., Lambolez, B., Rossier, J., and Audinat, E. (1998). Properties of bipolar VIPergic interneurons and their excitation by pyramidal neurons in the rat neocortex. *Eur. J. Neurosci.* 10, 3617–3628. doi: 10.1046/j.1460-9568.1998.00367.x

Pouille, F., and Scanziani, M. (2004). Routing of spike series by dynamic circuits in the hippocampus. *Nature* 429, 717–723. doi: 10.1038/nature02615

Pouille, F., Marin-Burgin, A., Adesnik, H., Atallah, B. V., and Scanziani, M. (2009). Input normalization by global feedforward inhibition expands cortical dynamic range. *Nat. Neurosci.* 12, 1577–1585. doi: 10.1038/nn.2441

Pouille, F., Watkinson, O., Scanziani, M., and Trevelyan, A. J. (2013). The contribution of synaptic location to inhibitory gain control in pyramidal cells. *Physiol. Rep.* 1:e00067. doi: 10.1002/phy2.67

Pronneke, A., Scheuer, B., Wagener, R. J., Mock, M., Witte, M., and Staiger, J. F. (2015). Characterizing VIP neurons in the barrel cortex of VIPcre/tdTomato mice reveals layer-specific differences. *Cereb. Cortex* 25, 4854–4868. doi: 10.1093/cercor/bhv202

Pronneke, A., Witte, M., Mock, M., and Staiger, J. F. (2020). Neuromodulation leads to a burst-tonic switch in a subset of VIP neurons in mouse primary somatosensory (Barrel) Cortex. *Cereb. Cortex* 30, 488–504. doi: 10.1093/cercor/bhz102

Qiu, F., Mao, X., Liu, P., Wu, J., Zhang, Y., Sun, D., et al. (2020). microRNA deficiency in VIP+ Interneurons leads to cortical circuit dysfunction. *Cereb. Cortex* 30, 2229–2249. doi: 10.1093/cercor/bhz236

Rock, C., Zurita, H., Lebby, S., Wilson, C. J., and Apicella, A. J. (2018). Cortical circuits of callosal GABAergic neurons. *Cereb. Cortex* 28, 1154–1167. doi: 10.1093/cercor/bhx025

Rock, C., Zurita, H., Wilson, C., and Apicella, A. J. (2016). An inhibitory corticostriatal pathway. *Elife* 5:e15890. doi: 10.7554/eLife.15890

Rudy, B., Fishell, G., Lee, S., and Hjerling-Leffler, J. (2011). Three groups of interneurons account for nearly 100% of neocortical GABAergic neurons. *Dev. Neurobiol.* 71, 45–61. doi: 10.1002/dneu.20853

Sachidhanandam, S., Sermet, B. S., and Petersen, C. C. H. (2016). Parvalbumin-expressing GABAergic neurons in mouse barrel cortex contribute to gating a goal-directed sensorimotor transformation. *Cell Rep.* 15, 700–706. doi: 10.1016/j.celrep.2016.03.063

Seress, L., and Ribak, C. E. (1983). GABAergic cells in the dentate gyrus appear to be local circuit and projection neurons. *Exp. Brain Res.* 50, 173–182. doi: 10.1007/BF00239181

Silberberg, G., and Markram, H. (2007). Disynaptic inhibition between neocortical pyramidal cells mediated by Martinotti cells. *Neuron* 53, 735–746. doi: 10.1016/j.neuron.2007.02.012

Sohn, J., Okamoto, S., Kataoka, N., Kaneko, T., Nakamura, K., and Hioki, H. (2016). Differential inputs to the perisomatic and distal-dendritic compartments of VIP-positive neurons in layer 2/3 of the mouse barrel cortex. *Front. Neuroanat.* 10:124. doi: 10.3389/fnana.2016.00124

Somogyi, P., Tamas, G., Lujan, R., and Buhl, E. H. (1998). Salient features of synaptic organisation in the cerebral cortex. *Brain Res. Brain Res. Rev.* 26, 113–135. doi: 10.1016/s0165-0173(97)00061-1

Stack, C. M., Lim, M. A., Cuasay, K., Stone, M. M., Seibert, K. M., Spivak-Pohis, I., et al. (2008). Deficits in social behavior and reversal learning are more prevalent in male offspring of VIP deficient female mice. *Exp. Neurol.* 211, 67–84. doi: 10.1016/j.expneurol.2008.01.003

Staiger, J. F., Freund, T. F., and Zilles, K. (1997). Interneurons immunoreactive for vasoactive intestinal polypeptide (VIP) are extensively innervated by parvalbumin-containing boutons in rat primary somatosensory cortex. *Eur. J. Neurosci.* 9, 2259–2268. doi: 10.1111/j.1460-9568.1997.tb01644.x

Staiger, J. F., Schubert, D., Zuschratter, W., Kotter, R., Luhmann, H. J., and Zilles, K. (2002). Innervation of interneurons immunoreactive for VIP by intrinsically bursting pyramidal cells and fast-spiking interneurons in infragranular layers of juvenile rat neocortex. *Eur. J. Neurosci.* 16, 11–20. doi: 10.1046/j.1460-9568.2002.02048.x

Staiger, J. F., Zilles, K., and Freund, T. F. (1996). Recurrent axon collaterals of corticothalamic projection neurons in rat primary somatosensory cortex contribute to excitatory and inhibitory feedback-loops. *Anat. Embryol. (Berl)* 194, 533–543. doi: 10.1007/BF00187467

Stokes, C. C., and Isaacson, J. S. (2010). From dendrite to soma: dynamic routing of inhibition by complementary interneuron microcircuits in olfactory cortex. *Neuron* 67, 452–465. doi: 10.1016/j.neuron.2010.06.029

Tamamaki, N., and Tomioka, R. (2010). Long-range GABAergic connections distributed throughout the neocortex and their possible function. *Front. Neurosci.* 4:202. doi: 10.3389/fnins.2010.00202

Tasic, B. (2018). Single cell transcriptomics in neuroscience: cell classification and beyond. *Curr. Opin. Neurobiol.* 50, 242–249. doi: 10.1016/j.conb.2018.04.021

Tasic, B., Menon, V., Nguyen, T. N., Kim, T. K., Jarsky, T., Yao, Z., et al. (2016). Adult mouse cortical cell taxonomy revealed by single cell transcriptomics. *Nat. Neurosci.* 19, 335–346. doi: 10.1038/nn.4216

Thome, C., Kelly, T., Yanez, A., Schultz, C., Engelhardt, M., Cambridge, S. B., et al. (2014). Axon-carrying dendrites convey privileged synaptic input in hippocampal neurons. *Neuron* 83, 1418–1430. doi: 10.1016/j.neuron.2014.08.013

Tomioka, R., and Rockland, K. S. (2007). Long-distance corticocortical GABAergic neurons in the adult monkey white and gray matter. *J. Comp. Neurol.* 505, 526–538. doi: 10.1002/cne.21504

Tomioka, R., Okamoto, K., Furuta, T., Fujiyama, F., Iwasato, T., Yanagawa, Y., et al. (2005). Demonstration of long-range GABAergic connections distributed throughout the mouse neocortex. *Eur. J. Neurosci.* 21, 1587–1600. doi: 10.1111/j.1460-9568.2005.03989.x

Toth, K., and Freund, T. F. (1992). Calbindin D28k-containing nonpyramidal cells in the rat hippocampus: their immunoreactivity for GABA and projection to the medial septum. *Neuroscience* 49, 793–805. doi: 10.1016/0306-4522(92)90357-8

Toth, K., Borhegyi, Z., and Freund, T. F. (1993). Postsynaptic targets of GABAergic hippocampal neurons in the medial septum-diagonal band of broca complex. *J. Neurosci.* 13, 3712–3724. doi: 10.1523/JNEUROSCI.13-09-03712.1993

Tremblay, R., Lee, S., and Rudy, B. (2016). GABAergic Interneurons in the neocortex: from cellular properties to circuits. *Neuron* 91, 260–292. doi: 10.1016/j.neuron.2016.06.033

Tyan, L., Chamberland, S., Magnin, E., Camire, O., Francavilla, R., David, L. S., et al. (2014). Dendritic inhibition provided by interneuron-specific cells controls the firing rate and timing of the hippocampal feedback inhibitory circuitry. *J. Neurosci.* 34, 4534–4547. doi: 10.1523/JNEUROSCI.3813-13.2014

von Engelhardt, J., Eliava, M., Meyer, A. H., Rozov, A., and Monyer, H. (2007). Functional characterization of intrinsic cholinergic interneurons in the cortex. *J. Neurosci.* 27, 5633–5642. doi: 10.1523/JNEUROSCI.4647-06.2007

Vucurovic, K., Gallopin, T., Ferezou, I., Rancillac, A., Chameau, P., Van Hooft, J. A., et al. (2010). Serotonin 3A receptor subtype as an early and protracted marker of cortical interneuron subpopulations. *Cereb. Cortex* 20, 2333–2347. doi: 10.1093/cercor/bhp310

Walker, F., Mock, M., Feyerabend, M., Guy, J., Wagener, R. J., Schubert, D., et al. (2016). Parvalbumin- and vasoactive intestinal polypeptide-expressing neocortical interneurons impose differential inhibition on Martinotti cells. *Nat. Commun.* 7:13664. doi: 10.1038/ncomms13664

Wall, N. R., De La Parra, M., Sorokin, J. M., Taniguchi, H., Huang, Z. J., and Callaway, E. M. (2016). Brain-wide maps of synaptic input to cortical interneurons. *J. Neurosci.* 36, 4000–4009. doi: 10.1523/JNEUROSCI.3967-15.2016

White, C. M., Ji, S., Cai, H., Maudsley, S., and Martin, B. (2010). Therapeutic potential of vasoactive intestinal peptide and its receptors in neurological disorders. *CNS Neurol. Disord. Drug Targets* 9, 661–666. doi: 10.2174/187152710793361595

Whittaker, V. P. (1989). Vasoactive intestinal polypeptide (VIP) as a cholinergic co-transmitter: some recent results. *Cell Biol. Int. Rep.* 13, 1039–1051. doi: 10.1016/0309-1651(89)90018-0

Williams, L. E., and Holtmaat, A. (2019). Higher-order thalamocortical inputs gate synaptic long-term potentiation via disinhibition. *Neuron* 101, 91–102 e104. doi: 10.1016/j.neuron.2018.10.049

Xu, X., and Callaway, E. M. (2009). Laminar specificity of functional input to distinct types of inhibitory cortical neurons. *J. Neurosci.* 29, 70–85. doi: 10.1523/JNEUROSCI.4104-08.2009

Xu, H., Jeong, H. Y., Tremblay, R., and Rudy, B. (2013). Neocortical somatostatin-expressing GABAergic interneurons disinhibit the thalamorecipient layer 4. *Neuron* 77, 155–167. doi: 10.1016/j.neuron.2012.11.004

Xu, X., Roby, K. D., and Callaway, E. M. (2010). Immunochemical characterization of inhibitory mouse cortical neurons: three chemically distinct classes of inhibitory cells. *J. Comp. Neurol.* 518, 389–404. doi: 10.1002/cne.22229

Yavorska, I., and Wehr, M. (2016). Somatostatin-expressing inhibitory interneurons in cortical circuits. *Front. Neural Circuits* 10:76. doi: 10.3389/fncir.2016.00076

Yavorska, I., and Wehr, M. (2021). Effects of locomotion in auditory cortex are not mediated by the VIP network. *Front. Neural Circuits*. 15:618881. doi: 10.3389/fncir.2021.618881

Yu, F. H., Mantegazza, M., Westenbroek, R. E., Robbins, C. A., Kalume, F., Burton, K. A., et al. (2006). Reduced sodium current in GABAergic interneurons in a mouse model of severe myoclonic epilepsy in infancy. *Nat. Neurosci.* 9, 1142–1149. doi: 10.1038/nn1754

Yu, J., Hu, H., Agmon, A., and Svoboda, K. (2019). Recruitment of GABAergic interneurons in the barrel cortex during active tactile behavior. *Neuron* 104, 412–427 e414. doi: 10.1016/j.neuron.2019.07.027

Zeisel, A., Munoz-Manchado, A. B., Codeluppi, S., Lonnerberg, P., La Manno, G., Jureus, A., et al. (2015). Brain structure. Cell types in the mouse cortex and hippocampus revealed by single-cell RNA-seq. *Science* 347, 1138–1142. doi: 10.1126/science.aaa1934

Zhang, S., Xu, M., Kamigaki, T., Hoang Do, J. P., Chang, W. C., Jenvay, S., et al. (2014). Selective attention. Long-range and local circuits for top-down modulation of visual cortex processing. *Science* 345, 660–665. doi: 10.1126/science.1254126

Zhou, X., Rickmann, M., Hafner, G., and Staiger, J. F. (2017). Subcellular targeting of VIP boutons in mouse barrel cortex is layer-dependent and not restricted to interneurons. *Cereb. Cortex* 27, 5353–5368. doi: 10.1093/cercor/bhx220

**Conflict of Interest:** The authors declare that the research was conducted in the absence of any commercial or financial relationships that could be construed as a potential conflict of interest.

frontiers in Cellular Neuroscience

ORIGINAL RESEARCH
published: 23 March 2022
doi: 10.3389/fncel.2022.817198

# Electrophysiological Properties of Induced Pluripotent Stem Cell-Derived Midbrain Dopaminergic Neurons Correlate With Expression of Tyrosine Hydroxylase

*Aleksandar Rakovic[1†], Dorothea Voß[2†], Franca Vulinovic[1], Britta Meier[1], Ann-Katrin Hellberg[2], Carla Nau[2], Christine Klein[1] and Enrico Leipold[2*]*

[1] Institute of Neurogenetics, University of Lübeck, Lübeck, Germany, [2] Department of Anesthesiology and Intensive Care, Center of Brain, Behavior and Metabolism (CBBM), University of Lübeck, Lübeck, Germany

OPEN ACCESS

**Edited by:**
Srdjan D. Antic,
University of Connecticut Health Center, United States

**Reviewed by:**
Henner Koch,
University Hospital RWTH Aachen, Germany
Serge N. Schiffmann,
Université Libre de Bruxelles, Belgium
Joe Tauskela,
National Research Council Canada (NRC-CNRC), Canada
Patrick Michael McNutt,
Wake Forest School of Medicine, United States

***Correspondence:**
Enrico Leipold
enrico.leipold@uni-luebeck.de

[†] These authors have contributed equally to this work

**Specialty section:**
This article was submitted to Cellular Neurophysiology, a section of the journal Frontiers in Cellular Neuroscience

**Received:** 17 November 2021
**Accepted:** 28 February 2022
**Published:** 23 March 2022

**Citation:**
Rakovic A, Voß D, Vulinovic F, Meier B, Hellberg A-K, Nau C, Klein C and Leipold E (2022) Electrophysiological Properties of Induced Pluripotent Stem Cell-Derived Midbrain Dopaminergic Neurons Correlate With Expression of Tyrosine Hydroxylase. Front. Cell. Neurosci. 16:817198. doi: 10.3389/fncel.2022.817198

Induced pluripotent stem cell (iPSC)-based generation of tyrosine hydroxylase-positive ($TH^+$) dopaminergic neurons (DNs) is a powerful method for creating patient-specific *in vitro* models to elucidate mechanisms underlying Parkinson's disease (PD) at the cellular and molecular level and to perform drug screening. However, currently available differentiation paradigms result in highly heterogeneous cell populations, often yielding a disappointing fraction (<50%) of the PD-relevant $TH^+$ DNs. To facilitate the targeted analysis of this cell population and to characterize their electrophysiological properties, we employed CRISPR/Cas9 technology and generated an mCherry-based human TH reporter iPSC line. Subsequently, reporter iPSCs were subjected to dopaminergic differentiation using either a "floor plate protocol" generating DNs directly from iPSCs or an alternative method involving iPSC-derived neuronal precursors (NPC-derived DNs). To identify the strategy with the highest conversion efficiency to mature neurons, both cultures were examined for a period of 8 weeks after triggering neuronal differentiation by means of immunochemistry and single-cell electrophysiology. We confirmed that mCherry expression correlated with the expression of endogenous TH and that genetic editing did neither affect the differentiation process nor the endogenous TH expression in iPSC- and NPC-derived DNs. Although both cultures yielded identical proportions of $TH^+$ cells (≈30%), whole-cell patch-clamp experiments revealed that iPSC-derived DNs gave rise to larger currents mediated by voltage-gated sodium and potassium channels, showed a higher degree of synaptic activity, and fired trains of mature spontaneous action potentials more frequently compared to NPC-derived DNs already after 2 weeks in differentiation. Moreover, spontaneous action potential firing was more frequently detected in $TH^+$ neurons compared to the $TH^-$ cells, providing direct evidence that these two neuronal subpopulations exhibit different intrinsic electrophysiological

properties. In summary, the data reveal substantial differences in the electrophysiological properties of iPSC-derived $TH^+$ and $TH^-$ neuronal cell populations and that the "floor plate protocol" is particularly efficient in generating electrophysiologically mature $TH^+$ DNs, which are the most vulnerable neuronal subtype in PD.

**Keywords: dopaminergic neurons, tyrosine hydroxylase, differentiation, Parkinson's disease, patch-clamp, electrophysiology, iPSC**

## INTRODUCTION

Parkinson's disease (PD) is the second most common neurodegenerative disorder and characterized by a combination of motor and non-motor symptoms that are barely noticeable in early disease stages but gradually increase in intensity as the disease progresses (Bloem et al., 2021). At the cellular level, PD signs are linked to a progressive loss of dopaminergic neurons (DNs) in the *substantia nigra pars compacta* (SNpc), resulting in extensive alterations of the neurochemistry in the midbrain (Blaszczyk, 2016; Magrinelli et al., 2016; Bloem et al., 2021). The reasons for the selective vulnerability of SNpc DNs in PD conditions are not well understood.

The generation of induced pluripotent stem cells (iPSCs) from patient-derived blood cells or fibroblasts using cellular reprogramming techniques (Takahashi et al., 2007) enabled the generation of patient-specific *in vitro* disease models, including PD-relevant DN cultures, suitable for analyzing disease mechanisms at cellular and molecular levels (Shi et al., 2017) as well as drug screening (Garcia-Leon et al., 2019; Kouroupi et al., 2020). Among the various established differentiation procedures (Cooper et al., 2010; Kriks et al., 2011; Kirkeby et al., 2012; Sanchez-Danes et al., 2012), the "midbrain floor plate protocol" (Kriks et al., 2011), which is based on early patterning of differentiating cells toward a floor plate stage, is considered one of the most effective protocols for generating human DNs from iPSCs (Weykopf et al., 2019). An attractive alternative which bypasses the continuous and cumbersome generation of iPSCs and thus significantly reduces the time required to obtain DN cultures utilizes iPSC-derived neuronal precursor cells (NPCs) as starting material for subsequent differentiation steps (Reinhardt et al., 2013). In contrast to iPSCs, NPCs are easier to handle because they exhibit robust immortal expansion, and their cultivation involves less manual manipulation.

Despite these promising developments, only between 30 and 80% of the cells in iPSC-derived DN cultures express pan-neuronal markers such as βIII-tubulin, of which again only 8–85% also express TH, the rate-limiting enzyme of dopamine synthesis, corresponding to proportions of 3–30% $TH^+$ cells relative to all cells (Sundberg et al., 2013; Ishikawa et al., 2016; Awad et al., 2017; Beevers et al., 2017; Romero-Moya et al., 2017; Sheng et al., 2017). The most likely reasons for the variable yields of $TH^+$ neurons are considered to be differences in the iPSC lines used and non-standardized, laboratory-specific handling of the cells (Mahajani et al., 2019). In addition, studies assessing the electrical excitability of human iPSC-derived DN cultures demonstrated that the cells are also very heterogenous with respect to their electrophysiological properties (Belinsky et al., 2011; Hartfield et al., 2014; Pre et al., 2014), most likely due to high proportions of immature neurons. This intrinsic inhomogeneity of iPSC-derived DNs remains a challenge as it adds variability to datasets in downstream applications and limits their interpretation (Calatayud et al., 2019; Laperle et al., 2020).

Recently, a series of elegant studies demonstrated how some of these limitations can be circumvented. These studies described the generation of TH reporter iPSC lines engineered to express fluorescent proteins such as mOrange (Calatayud et al., 2019), GFP (Hong and Daadi, 2019; Uberbacher et al., 2019) or RFP (Xia et al., 2017) which were introduced into the endogenous TH locus, right before TH's stop codon using a CRISPR/Cas9-based editing strategy. Immunochemistry analysis and transcriptional assays confirmed the neuronal identity of TH-expressing ($TH^+$) cells, however, the electrophysiological properties of $TH^+$ and $TH^-$ subpopulations were not evaluated in these studies. To fill this gap, we employed CRISPR/Cas9 technology to generate a mCherry-based human TH reporter iPSC line and subjected the cells to dopaminergic differentiation using either a direct route for differentiation of iPSC into DNs (Kriks et al., 2011) (iPSC-derived DNs) or an indirect route involving NPCs (NPC-derived DNs) as an intermediate step (Reinhardt et al., 2013). Using single-cell patch-clamp electrophysiology, we assessed for the first time the development of the electrophysiological properties of $TH^+$ and $TH^-$ neurons in both reporter cultures over a period of 8 weeks and demonstrate that mature electrophysiological properties of iPSC-derived DNs is correlated with endogenous TH expression and depends on the applied differentiation strategy.

## MATERIALS AND METHODS

### Generation of a Tyrosine Hydroxylase Reporter Line

A human iPSC line (Zanon et al., 2017) generated from human foreskin fibroblasts (ATCC, CRL-2522) was used as starting material to engineer a TH-mCherry iPSC reporter line. To facilitate gene editing of CRL-2522 cells, we used plasmid pX330S-2 (a gift from Takashi Yamamoto; Addgene plasmid # 58778[1]; RRID:Addgene_58778) (Sakuma et al., 2014). Custom guide RNA (gRNA) targeting the sequence 5′-GTGCCATTGGCTAGGTGCA-3′ in exon 14 of the TH gene was cloned into the *Bbs*I sites as annealed oligonucleotides. The donor template for homology-directed repair (HDR) was generated

[1]http://n2t.net/addgene:58778

using Gibson cloning as described previously (Calatayud et al., 2019). In brief, for the TH donor template, 1 kb-long homology arms (HA) were amplified from genomic DNA extracted from unmodified iPSCs and verified by Sanger sequencing. HA were inserted into the pBS-SK (−) vector using *Kpn*I and *Apa*I restriction sites for the 5′ HA and *Spe*I and *Xba*I restriction sites for the 3′ HA sites of pBS-SK (−). A sequence encoding the T2A peptide was fused to the 5′ end of the mCherry open reading frame. Finally, the pRex1-Neo-SV40 cassette was inserted between the *Xho*I and *Spe*I restriction sites of the plasmid.

Next, iPSCs were transfected with the HDR template and the pX330S-2 plasmid expressing the gRNA mentioned above. In total, one million iPSCs were disaggregated into single cells using Accutase (Stemcell) on the day of transfection. Disaggregated iPSCs were diluted in 100 μl of human stem cell nucleofector Kit 2 solution (Lonza Group Ltd., Switzerland) supplemented with 2 μg of pX330S-2 plasmid and 2 μg HDR template and transfected using the 2b Nucleofector device (Lonza Group Ltd., Switzerland). Transfected cells were plated onto Matrigel (BD)-coated 6-well culture plates containing mTeSR1 medium (Stemcell), supplemented with ROCK inhibitor Y-27632 (EMD Biosciences). On the following day, the medium was replaced with fresh mTeSR1 containing 50 μg/mL G418 (Sigma) and cells were maintained for 2 weeks. At that time, one half of each resistant colony was manually picked, resuspended in 1x PCR buffer containing Proteinase K and incubated for 50 min at 56°C followed by 10 min incubation at 95°C. Integration of the resistance cassette into the TH locus was verified by PCR. Positive colonies were expanded and cryopreserved.

To excise the selection cassette, positive iPSCs were transfected with 2 μg of a Cre recombinase-expressing plasmid (pCAG-Cre was a gift from Connie Cepko; Addgene plasmid # 13775[2]; RRID:Addgene_13775) (Matsuda and Cepko, 2007) diluted in 100 μl of human stem cell nucleofector Kit 2 solution using the 2b Nucleofector device (both Lonza Group Ltd., Switzerland). Subsequently, transfected cells were plated onto Matrigel (BD)-coated dishes in mTeSR1 (Stemcell), supplemented with ROCK inhibitor Y-27632 (EMD Biosciences Ltd.). One week post transfection, one half of each resistant colony was manually picked, resuspended in 1x PCR buffer containing Proteinase K and incubated 50 min at 56°C followed by 10 min incubation at 95°C. The colonies were analyzed for complete excision of the resistance cassette using a PCR-based strategy. Clones with successfully excised resistance cassette were expanded, the iPSC lines were comprehensively characterized including expression analyses of pluripotency markers, and cryopreserved.

To yield DN-cultures, unedited and edited iPSCs were subjected to dopaminergic differentiation following either a "floor plate differentiation method" or an alternative strategy involving iPSC-derived NPCs. The associated procedures are detailed in the **Supplemental Material**.

## Immunocytochemistry

Cells were fixed with 4% paraformaldehyde for 15 min at room temperature (RT) and permeabilized for 15 min in 0.1% NP-40 in phosphate-buffered saline (PBS). Cells were blocked using 1% of normal goat serum for 1 h at RT. The following antibodies were used: rabbit anti-OCT4 (Abcam), mouse anti-TRA-1-60 (Millipore), rabbit anti-NANOG (Stemgent), mouse anti-SSEA-4 (Millipore), rabbit anti-TH (Calbiochem), mouse anti-SOX2 (R&D Systems), mouse anti-mouse anti-Nestin (Santa Cruz), mouse anti-Pax6 (Santa Cruz). Corresponding Alexa Fluor-conjugated secondary antibodies were from Thermo Fisher. To label nuclei, coverslips were mounted using DAPI Fluoromount-G (SouthernBiotech). Images were acquired using a confocal microscope (Zeiss LSM710) operated by the ZEN software package. ImageJ (Schneider et al., 2012) and Adobe Photoshop CS6 (Adobe, United States) software were used for final image processing.

## Fluorescence-Activated Cell Sorting

Dopaminergic neuronal cultures differentiated from parental and TH-mCherry reporter iPSCs were harvested 50 days after starting the differentiation regime. Briefly, cells were washed with 1x PBS, detached using Accutase (Stemcell Technologies) and singularized by filtering through a 37 μm reversible cell strainer (Stemcell Technologies). Subsequently, cells were pelleted, resuspended in 1 ml of 1x PBS, and sorted on a BD FACSAria™ III device (Becton, Dickinson and Company) to obtain mCherry-positive and mCherry-negative fractions.

## Western Blotting

Protein fractions from non-sorted, sorted mCherry-negative, and sorted mCherry-positive cells were isolated using RIPA buffer. Ten micrograms of protein from each fraction were separated on NuPAGE™ 4–12%, Bis-Tris, 1.0 mm gels (Thermo Fisher Scientific) by SDS polyacrylamide gel electrophoresis and blotted. The membrane was probed using antibodies raised against TH (Merckmillipore), GAPDH (Cell Signaling), or β-actin (Sigma). For densitometric analyses, TotalLab software (Non-linear Dynamics) was used.

## High-Performance Liquid Chromatography

Dopaminergic neuronal cultures differentiated from TH-mCherry reporter iPSCs were harvested 50 days after starting the differentiation regime and sorted into mCherry-positive ($TH^+$) and mCherry-negative ($TH^-$) cells using FACS as mentioned above. Two million cells were harvested, pelleted, washed in 1x PBS, and lysed in 200 μL of dopamine extraction buffer (100 mM perchloric acid, 0.2 mM EDTA) using sonification (2 × 5 s, 50% amplitude, Bandelin). The total amounts of dopamine (DA), 3,4-dihydroxyphenylacetic acid (DOPAC), and homovanillic acid (HVA) were measured by means of high-performance liquid chromatography using a C18 column (Eurospher RP 18, particle size 5 pm, column size 250 mm × 4.0 mm) combined with subsequent electrochemical detection. In addition, three standard solutions each for DA, DOPAC, and HVA were prepared and subsequently measured to establish corresponding standard curves. The mobile phase was a degassed solution of 0.15 M sodium acetate buffer (pH 4.0) containing 12% methanol,

[2]http://n2t.net/addgene:13775

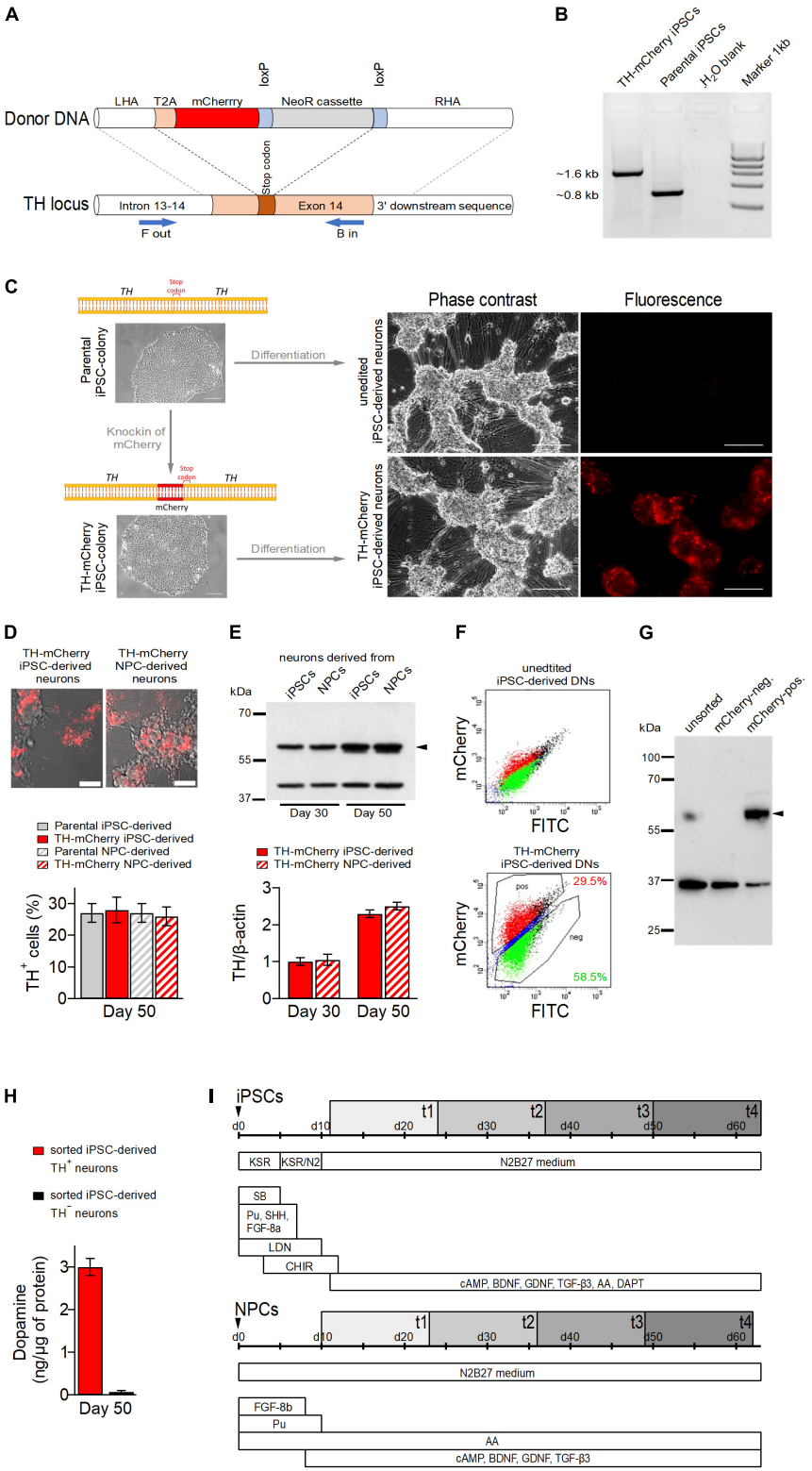


**FIGURE 1 |** Generation of TH-mCherry reporter iPSC and NPC lines and associated dopaminergic neuronal cultures. **(A)** Scheme illustrating the recombination strategy employed for genome editing. Blue arrows represent primers used for the PCR screening procedure. **(B)** PCR analysis of edited (TH-mCherry iPSCs) and unedited (Parental iPSCs) iPSC lines confirming correct integration of the T2A-mCherry sequence in the TH locus of the parental iPSC line. **(C)** Phase contrast and associated fluorescence images of representative clusters of undifferentiated iPSC colonies (*left*) and terminally differentiated DN cultures (*right*), obtained from

*(Continued)*

**FIGURE 1 |** unedited (unedited iPSC-derived neurons) or edited (TH-mCherry iPSC-derived neurons) iPSCs (*left*). Scale bars: 100 μm. **(D)** Live-cell images of TH-mCherry reporter DN cultures derived from iPSCs or NPCs (*top*, scale bars: 50 μm) and analysis (*bottom*) of the percentage of TH-positive cells present in unedited and edited iPSC- and NPC-derived neuronal cultures, obtained from fixed samples immunostained with a TH-specific antibody. For each condition, a total of six replicates from two independent differentiations were evaluated. **(E)** Representative Western blot image (*top*) and associated densiometric analysis (*bottom*) of TH protein levels in 30- and 50-day-old iPSC- and NPC-derived dopaminergic neuronal cultures. β−Actin (42 kDa, *top*) served as loading control, bands corresponding to TH (60 kDa, *top*) are marked with an arrowhead. Bars represent means ± s.e.m. obtained from two independent experiments each. **(F)** Representative two-component density plots for FACS sorting of terminally differentiated parental (*top*) and TH-mCherry reporter iPSC cultures (*bottom*) using FITC- and mCherry-specific detection channels. The unspecific autofluorescence of unedited iPSC-derived neurons served as template to set the sorting gate for mCherry-negative cells and to define the gate corresponding to mCherry-positive cells. **(G)** Western blot analysis to evaluate TH protein (arrowhead) in unsorted, FACS-sorted mCherry-negative and mCherry-positive cells. GAPDH (36 kDa) served as loading control. **(H)** Intracellular dopamine levels of $TH^+$ and $TH^-$ iPSC-derived neurons, normalized to total protein. Bars represent means ± s.e.m. obtained from two independent experiments. **(I)** Timelines summarizing the two differentiation strategies used for the creation of iPSC- (top) and NPC-derived DNs. Electrophysiological analysis of cells was performed during an 8-week period (gray rectangles), t1-t4 specify the four timing groups.

0.014 g/l EDTA and 0.1 mM sodium-1-octansulfonate pumped at a flow rate of 1 ml/min. All chromatography experiments were performed at 4°C and all solutions were kept on ice. The separations were achieved under isocratic conditions. The detector cell was operated at +0.8 V.

## Quantitative PCR

Total mRNA was extracted from neurons using the RNeasy Kit (Qiagen) followed by a reverse-transcription to obtain cDNA using the Maxima First Strand cDNA Synthesis Kit (Thermo scientific). Quantitative RT-PCR was performed with the Maxima SYBR® Green/fluorescein qPCR Master Mix kit (ThermoFisher) on a LightCycler 480 (Roche Diagnostics). Quantification was performed using the deltadelta-CP (ΔΔCP) method (Livak and Schmittgen, 2001). All oligonucleotides used are summarized in **Supplementary Table 1** along with the corresponding target genes.

## Quantification of TH-Positive Neurons

To determine the efficiency of differentiation into $TH^+$ neurons, Poly-L-Ornithine/Laminin/Fibronectin-coated coverslips containing terminally differentiated iPSC- or NPC-derived neurons were fixed and stained using an anti-TH antibody and mounted using DAPI-containing mounting medium, as mentioned above. On each coverslip, five randomly chosen sections were imaged using a confocal microscope (Zeiss LSM710) together with a 40x objective. Cell counting and evaluation of the differentiation efficiency were performed manually. Six coverslips obtained from two independently differentiated cultures were evaluated for each iPSC- or NPC-derived culture. The total number of cells analyzed exceeded 1,000 cells.

## Electrophysiology

Individual cells were subjected to whole-cell patch-clamp experiments 1–8 weeks after initiation of the neuronal differentiation process (**Figure 1G**). To analyze the time course of electrophysiological maturation of cells and to facilitate statistical analysis, data were clustered into 4 timing groups (t1-t4), each representing a period of 2 consecutive weeks (t1: weeks 1 and 2, t2: weeks 3 and 4, t3: weeks 5 and 6, t4: weeks 7 and 8). Voltage- and current-clamp data were acquired using an EPC-10 patch-clamp amplifier, operated by PatchMaster software (both HEKA Elektronik, Lambrecht, Germany). All recordings were performed at a constant temperature of 20 ± 0.5°C using a microincubation stage (ALA Scientific Instruments, Farmingdale, NY, United States), feedback-controlled by a PTC-10 temperature controller (NPI Electronic GmbH, Tamm, Germany). Recording pipettes with resistances of 2–4 MΩ were fabricated from borosilicate glass and coated with silicone elastomer (RTV 615, Momentive Performance Materials, Waterford, NY, United States) to reduce tip capacitance. Series resistance was corrected electronically up to 80% and all voltages were corrected off-line for the liquid junction potential (−7 mV). Only cells with an uncompensated series resistance < 20 MΩ were included in the analysis. Data were low-pass filtered at 2.87 kHz and digitized with a sampling interval of 50 μs. For voltage- and current-clamp recordings patch pipettes were filled with (in mM) 125 KCl, 8 NaCl, 1 $CaCl_2$, 1 $MgCl_2$, 0.4 $Na_2$-GTP, 4 Mg-ATP, 10 EGTA and 10 HEPES (pH 7.3 with KOH). The bath solution contained in all experimental conditions (in mM) 120 NaCl, 3 KCl, 2.5 $CaCl_2$, 1 $MgCl_2$, 30 HEPES, 15 glucose (pH 7.4 with NaOH).

### Voltage-Clamp Recordings

Sodium and potassium channel-specific currents were evoked from a holding potential of −107 mV with a two-step voltage protocol. Activation of mostly voltage-gated sodium channels was triggered with a series of 20 ms test depolarizations ranging from −87 to −7 mV in steps of 10 mV followed by a 140 ms recovery period at −107 mV. Subsequently, voltage-gated potassium channels were activated with a series of 80 ms test depolarizations ranging from −7 to 73 mV in steps of 10 mV. The repetition interval was 2 s. Leak and capacitive currents were recorded using a P/4 method with four leak pulses, each with 0.15 time the amplitude of the test pulse P. Summed and scaled leak traces were subtracted online using the leak pulse feature available in PatchMaster software. Sodium and potassium channel-specific peak current amplitudes were normalized to the cell membrane capacitance and are reported as current densities, $I(V)/C_m$, where $I(V)$ is the peak current amplitude and $C_m$ the cell membrane capacitance.

The membrane input resistance, $R_{in}$, was estimated from current responses to depolarizing voltage pulses to −87, −77, and −67 mV, from which leak currents were not subtracted. The holding potential was −107 mV. $R_{in}$ was obtained as

the inverse of the linear slope of the associated current-voltage relationship.

Inward post-synaptic currents (PSCs) were recorded at a holding potential of −77 mV for a period of 20 s. PSCs measured under these conditions are a superposition of spontaneous and network activity-driven events. Recordings were analyzed for the occurrence of PSCs using IgorPro software (WaveMetrics, Lake Oswego, OR, United States) and customized scripts. A threshold-crossing of the first derivative of the current responses was used as objective detection criterion for PSCs. The detection threshold was set to $-4 \times \sigma_{dI/dt}$ where $\sigma_{dI/dt}$ is the standard deviation of the first derivative of the current responses. Detected events were verified by visual inspection and further analyzed regarding their peak amplitudes and frequencies.

### Current-Clamp Recordings

Spontaneously fired action potentials were recorded for a period of 30 s at zero current injection. The detection threshold for action potentials was set to −20 mV. Individual action potentials fired during this period were further analyzed for their peak voltage.

To obtain evoked action potential responses, cells were clamped to −77 mV and repetitively stimulated with 2 s current injections ranging from 0 to 180 pA in steps of 20 pA, delivered at an interval of 3 s. Parameters characterizing evoked action potentials were obtained from the first action potential fired during the stimulation paradigm.

### Data Analysis and Statistics

Data analysis was performed using FitMaster software (HEKA Elektronik, Lambrecht, Germany) and Igor Pro (WaveMetrics, Lake Oswego, OR, United States). Data points are presented as means ± s.e.m. ($n$) with $n$ being the number of independent experimental replicates. Data sets were tested for statistical significance with an unpaired 2-tailed Mann–Whitney $U$-test for averaged data or Fisher's exact test for proportions when appropriate.

## RESULTS

### Generation of a TH-mCherry Reporter Induced Pluripotent Stem Cell Line Using CRISPR/Cas9-Mediated Genome Editing

To distinguish $TH^+$ from $TH^-$ cells in DN cultures and to facilitate the analysis of their specific electrophysiological properties, we generated TH reporter iPSCs by incorporating the open reading frame of the fluorescent protein mCherry into the TH locus of a human control iPSC line (Zanon et al., 2017) using a previously described strategy (Calatayud et al., 2019).

The iPSCs were co-transfected with a plasmid expressing guide RNA (gRNA), SpCas9, and a plasmid containing a T2A-mCherry fusion as donor (**Figure 1A**) followed by Neomycin selection for 7 days. Resistant clones were analyzed for correct integration of the donor DNA using a PCR-based assay (**Figure 1B**) and Sanger sequencing upon excision of the resistance cassette. The successfully edited iPSC line with correct biallelic integration of T2A-mCherry in the TH locus was expanded and analyzed for the presence of pluripotency markers. Control and edited iPSC lines showed positive expression of pluripotency markers OCT4, NANOG, TRA-1-60, and SSEA4 (**Supplementary Figure 1A**) and gene expression of NANOG, OCT4, GDF3, and SOX2 was elevated in both unedited and edited iPSCs compared to parental fibroblasts (**Supplementary Figure 1B**).

### Expression of mCherry Correlates With the Expression of TH in Differentiated Neuronal Cultures

To yield DN cultures, unedited and TH reporter iPSCs were differentiated toward dopaminergic SNpc neurons following two widely used protocols, i.e., the "midbrain floor plate protocol" (Kriks et al., 2011), and a protocol that utilizes iPSC-derived neuronal progenitor cells (NPCs) (Reinhardt et al., 2013). NPCs were obtained from both parental iPSCs and TH reporter iPSCs using small molecules (Reinhardt et al., 2013) and subsequently characterized by immunochemistry and qPCR. As shown in **Supplementary Figures 1C,D**, both unedited and TH reporter NPCs expressed comparable levels of NPC-specific markers Musashi 1, Nestin, and Pax6 which were also considerably higher compared to in iPSCs, demonstrating (a) the generation of NPCs was successful and (b) genetic editing did not affect the efficiency of conversion of iPSCs to NPCs.

Unedited and TH reporter iPSCs were differentiated for 50 days (**Figure 1C**) to yield DN cultures. Both cultures developed a comparable neuronal morphology. While red fluorescence was absent in DNs obtained from unedited iPSCs, it was observed in a subset of cells derived from TH-mCherry reporter iPSCs as early as 15 days after the differentiation process was triggered. Similar observations were made for NPC-derived TH reporter cultures. As revealed by live cell imaging after 50 days of differentiation, NPC-derived TH reporter cultures were also indistinguishable from iPSC-derived TH reporter cultures with respect to their morphological development (**Figure 1D**, *top*). Immunochemical analysis of fixed samples revealed comparable proportions of TH-immunoreactive cells in DN cultures obtained from both unedited and TH reporter iPSCs and NPCs (parental iPSC-derived neurons: 27 ± 3%, TH-mCherry iPSC-derived neurons: 28 ± 4%, parental NPC-derived neurons: 27 ± 3%, TH-mCherry NPC-derived neurons 26 ± 3%) further confirming that genetic editing did not interfere with the differentiation efficiency (**Figure 1D**, *bottom*). In addition, relative TH expression levels in TH-mCherry iPSC- and NSC-derived cultures were compared 30 and 50 days after the onset of differentiation using a Western blot assay. As shown in **Figure 1E**, both cultures expressed TH at comparable levels, which also increased equally in both cultures with increasing differentiation time.

To test whether mCherry expression overlaps with TH expression, DNs derived from TH reporter iPSCs using the "midbrain floor plate protocol" were sorted into mCherry-positive and mCherry-negative cell populations using fluorescence-activated cell sorting (FACS) (**Figure 1F**). DNs

obtained from unedited iPSCs were used to define the sorting gates. Subsequently, whole protein was isolated from unsorted cells and from sorted mCherry-positive and mCherry-negative cell populations. As shown in **Figure 1G**, western blot analysis with a TH-specific antibody confirmed the presence of TH in unsorted cells and in the mCherry-positive cell population, while TH expression was not detected in mCherry-negative cells. The sorted cell populations were also analyzed for their ability to synthesize dopamine by means of HPLC-coupled electrochemical detection. As shown in **Figure 1H**, dopamine could be detected exclusively in the lysates of $TH^+$ neurons, confirming the dopaminergic nature of this cell type. However, the dopamine metabolites DOPAC and HVA were not detected in the lysates, possibly because they were released from the cells during the separation procedure, or their amounts were below the detection limit of our HPLC system.

Taken together, this demonstrates that mCherry-mediated red fluorescence in TH reporter DNs is a reliable indicator of both endogenous TH expression and dopamine synthesis.

## Assessment of Ion Channel Function and Synaptic Activity in SNpc Neurons Derived From Neuronal Precursor Cells and Induced Pluripotent Stem Cells

Electrical excitability is a fundamental feature of mature neurons and requires the concerted activity of various types of ion channels. Especially voltage-gated ion channels, such as $Na_V$ and $K_V$ channels, are important in neurons because they trigger and shape action potentials. To assess the functional expression of these channels, we performed whole-cell voltage-clamp measurements on $TH^-$ and $TH^+$ NPC- and iPSC-derived neurons and analyzed $Na_V$- and $K_V$-specific current components in these cells at four different time points (t1-t4), each combining data from two consecutive weeks (t1: weeks 1–2, t2: weeks 3–4, t3: weeks 5–6, t4: weeks 7–8) after initiation of neuronal maturation (**Figure 1I**).

To obtain $Na_V-$ and $K_V$-specific current responses, we used a double-pulse protocol as shown in **Figure 2A**. $Na_V$-dependent inward currents were triggered with a first series of brief test pulses ranging from −87 to −7 mV followed by a second test pulse series, ranging from −7 to 73 mV, to activate $K_V$-dependent outward currents. Since the voltage dependencies of inward and outward currents largely overlapped (**Figures 2A,B** and **Supplementary Figure 2**), further analysis of $Na_V$-specific currents was restricted to a test pulse voltage of −27 mV where $Na_V$ channels but barely any $K_V$ channels are active. $K_V$-specific currents were further analyzed at a voltage of 73 mV, which is close to the calculated $Na^+$ reversal potential (68.4 mV) at which the contribution of $Na_V$-dependent currents is expected to be neglectable. Both, NPC- and iPSC-derived neurons generated inward and outward currents with kinetics typical for $Na_V$ and $K_V$ channels, respectively (**Figures 2A,B**). The associated peak current densities in NPC-derived neurons increased gradually during differentiation without apparent differences between $TH^-$ and $TH^+$ cells (**Figure 2C**). Both current components were consistently larger in iPSC-derived neurons than in NPC-derived neurons and exhibited a biphasic development characterized by an increase of current densities from t1 to t2, a plateau phase between t2 and t3 and a decrease to almost initial levels at t4. $K_V$-specific currents were not different between $TH^-$ and $TH^+$ iPSC-derived neurons, but $Na_V$ channel-mediated currents were larger in the $TH^+$ subpopulation at all-time points tested, being significant for groups at t1, t3 and t4 (**Figure 2C**). The cell membrane capacitance, a passive property that scales with the cell membrane surface area, increased significantly during differentiation in NPC- as well as in iPSC-derived neurons by factors of 4.0 and 4.6, respectively (both $P < 0.001$, **Figure 2**). As shown in **Supplementary Figure 3**, the membrane input resistance ($R_{in}$) of NPC-derived $TH^-$ neurons was independent of the time in differentiation but decreased by a factor of approximately 2 in corresponding $TH^+$ cells from 3.9 ± 0.5 GΩ at t1 to 2.0 ± 0.3 GΩ at t4 ($P < 0.05$). In contrast, $R_{in}$ of both iPSC-derived subpopulations decreased continuously from t1 to t3 before reaching a plateau at t4 ($TH^-$: from 2.5 ± 0.3 GΩ at t1 to 1.5 ± 0.2 GΩ at t4, $P < 0.01$; $TH^+$: from 3.5 ± 0.7 GΩ at t1 to 1.1 ± 0.2 GΩ at t4, $P < 0.001$). In neither cell line did $R_{in}$ correlate with the expression of TH.

To make an inference on the development of the synaptic apparatus in NPC- and iPSC-derived neuronal cultures, post-synaptic currents (PSCs) were recorded in the absence of specific inhibitors (**Figures 3A,B**). Post-synaptic events detected under these conditions reflect network activity driven by action potential-dependent and -independent mechanisms (Pinheiro and Mulle, 2008). Independent of the time in differentiation, PSCs were evident in less than 20% of NPC-derived $TH^-$ and $TH^+$ neurons, suggesting a low level of synaptic activity in this culture (**Figure 3C**). Mean frequencies and amplitudes of the events varied marginally during differentiation between 0.26 ± 0.05 Hz and 1.18 ± 0.76 Hz and between −5.5 ± 1.2 pA and −18.6 ± 6.5 pA for $TH^-$ and $TH^+$ cells, respectively, and were virtually independent of TH expression (**Figure 3D**). By contrast, the proportions of iPSC-derived neurons exhibiting PSCs varied between 28.6% and 55.9% during differentiation, demonstrating an overall higher degree of synaptic activity compared to neurons obtained from NPCs. Although variable, the percentage of iPSC-derived cells capable of generating PSCs was independent of both, TH expression and time in differentiation (**Figure 3C**). The mean frequencies of events were comparable to those observed in neurons obtained from NPCs and showed no obvious time-dependence, either. However, the mean amplitudes of the events increased gradually in both iPSC-derived subpopulations over time (**Figure 3D**): At an early phase of differentiation at time point t1, they were almost indistinguishable from the amplitudes measured in NPC-derived cells, but by time point t4 they had more than doubled (t1: −12.7 ± 2.6 pA and −13.8 ± 3.5 pA, t4: −34.7 ± 6.1 pA and −33.6 ± 3.5 pA for $TH^-$ and $TH^+$, respectively).

In summary, the direct differentiation of iPSCs to DNs yielded a neuronal population that contained more functional $Na_V$ and $K_V$ channels and displayed a higher degree of synaptic activity compared to DNs generated using an indirect differentiation strategy involving neural precursors.

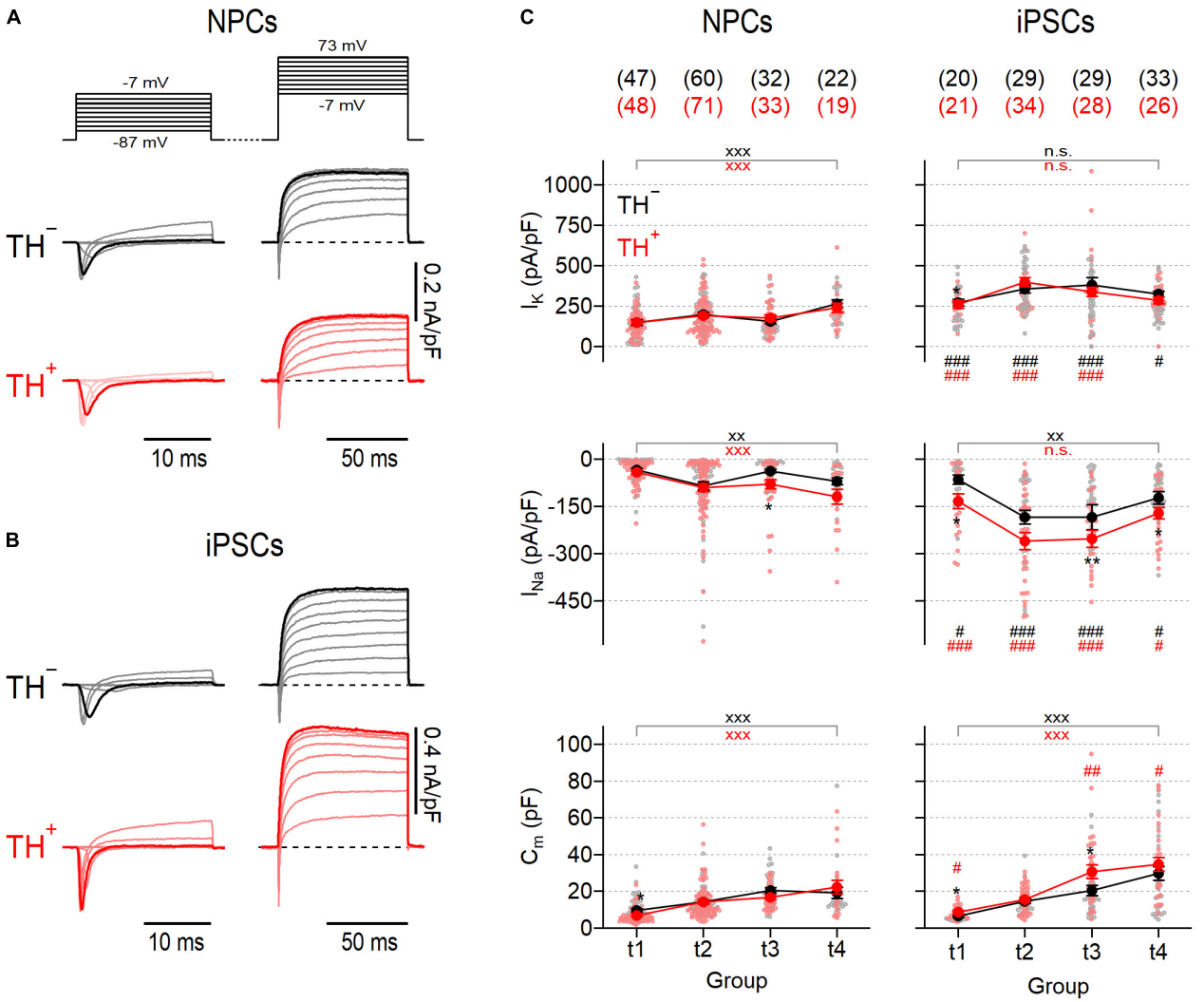


**FIGURE 2 |** Activity of voltage-gated $Na_V$ and $K_V$ channels in NPC- and iPSC-derived dopaminergic reporter lines. Families of representative current traces obtained from NPC-derived **(A)** or iPSC-derived **(B)** neurons either positive ($TH^+$, red) or negative ($TH^-$, black) for the expression of TH in response to various step depolarizations (*top,* **A**). 20-ms depolarizations ranging from –87 to –7 mV (*left*) were applied to elicit mostly $Na_V$-specific fast activating and inactivating inward currents, whereas slow activating outward currents reflecting the activity of $K_V$ channels were triggered with 80-ms depolarizations ranging from to –7 mV to 73 mV (*right*). Inward and outward current traces highlighted in bold correspond to test pulse voltages to –27 mV and 73 mV, respectively. Data in **(A,B)** were obtained at time point 2 (t2), i.e., 3–4 weeks after neuronal differentiation was initiated. **(C)** Mean peak current densities associated to $K_V$ (*top*) or $Na_V$ (*middle*) channels and mean cell membrane capacitances (*bottom*), obtained from current traces at 73 mV and –27 mV, respectively, as shown in **(A,B)** at the indicated time points (t1–4). Individual data points are shown as open circles, filled circles represent means ± s.e.m. with the number of experimental replicates, *n*, indicated in parentheses. Straight lines connect means for clarity. Significance between pairs of data was tested with a two-tailed Mann–Whitney *U*-test: $^{**}P < 0.01$, $^{*}P < 0.05$ for testing $TH^-$ against $TH^+$ neurons from the same line; $^{xxx}P < 0.01$, $^{xx}P < 0.01$ for testing data obtained at t1 against data obtained at t4; $^{###}P < 0.001$, $^{##}P < 0.01$, $^{#}P < 0.05$ for testing data obtained from NPCs against data obtained from iPSCs; n.s., not significant.

## Action Potential Characteristics in Neuronal Precursor Cell- and Induced Pluripotent Stem Cell-Derived TH Reporter Cultures

To further characterize functional maturation of NPC- and iPSC-derived neuronal DN cultures, we performed whole-cell current-clamp recordings on individual $TH^-$ and $TH^+$ neurons from both lines at different time points after triggering dopaminergic differentiation and analyzed the ability of the cells to generate action potentials. To evoke responses, cells were kept at −77 mV and stimulated with escalating current injections ranging from 0 pA to 180 pA. Using this stimulation protocol one or more action potentials were triggered in 56.8–84.4% of NPC-derived neurons and in 80–100% of iPSC-derived neurons (**Figures 4A–C**). Independent of the amplitude of current injected, the time point in differentiation, and the differentiation protocol used, $TH^-$ cells rarely fired more than one action potential in response to a current stimulus (**Supplementary Figure 4**). In contrast, in $TH^+$ cells, the firing of evoked action potentials evolved

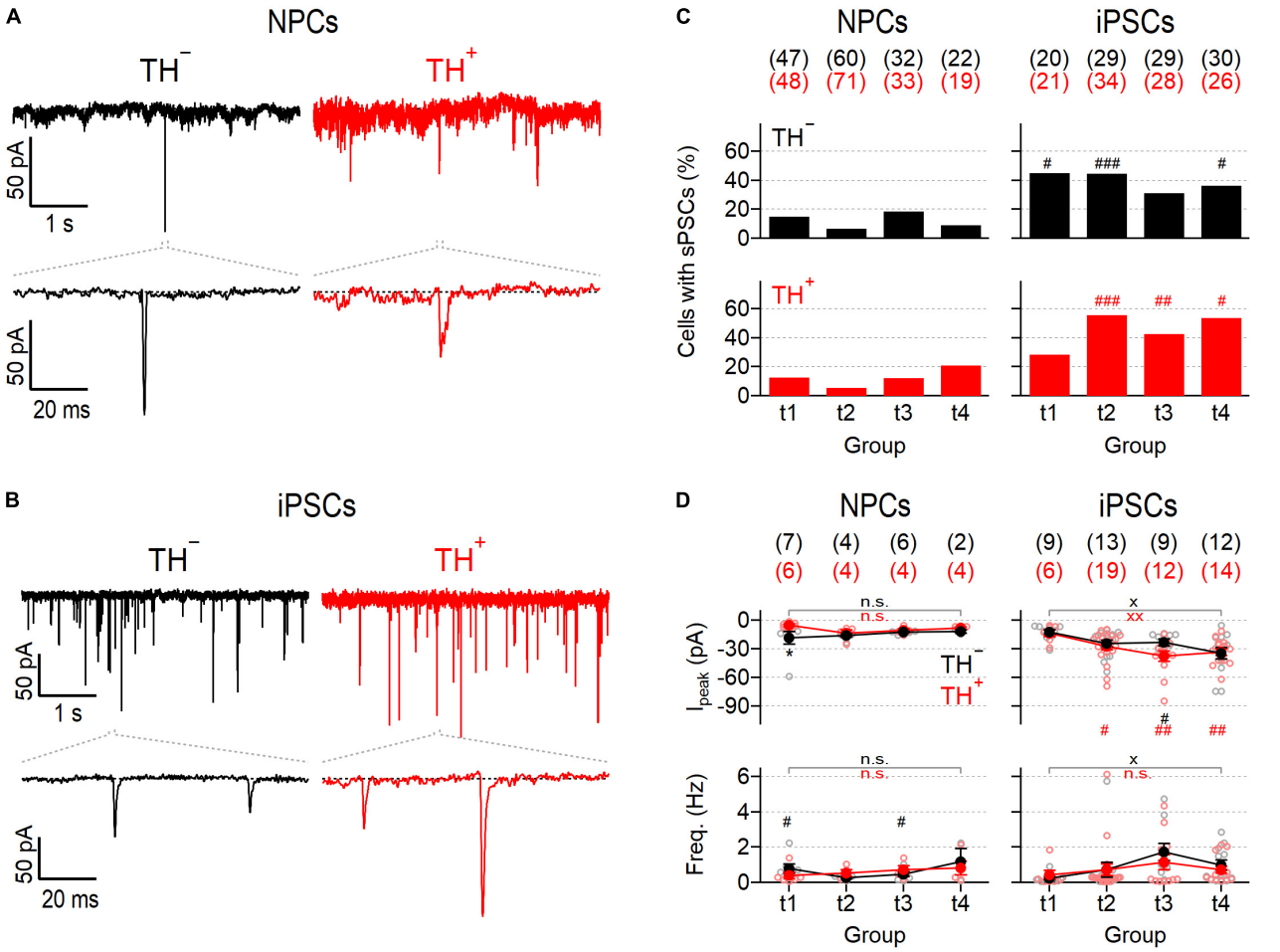


**FIGURE 3 |** Different synaptic activity in NPC- and iPSC-derived dopaminergic reporter cultures. **(A)** Representative post-synaptic current responses (PSCs) at time point 2 (t2) from TH$^-$ (*left*) and TH$^+$ (*right*) NPC-derived neurons at a membrane potential of –77 mV. Bottom traces are enlarged views (100 ms) of the regions specified with dashed lines. **(B)** Identical recordings as in **(A)**, obtained from TH$^-$ (*left*) and TH$^+$ (*right*) iPSC-derived neurons at t2. **(C)** Bar graphs showing percentages of NPC- (*left*) and iPSC-derived (*right*) TH$^-$ (*top,* black) and TH$^+$ (*bottom,* red) neurons that showed PSCs as shown in **(A,B)**, analyzed at the specified time points (t1–4). Statistic indicators refer to Fisher's exact test performed for each time point between data obtained from NPC- and iPSC-derived neurons:$^{###}P < 0.001$, $^{##}P < 0.01$, $^{#}P < 0.05$. **(D)** Mean peak current amplitudes (*top*) and frequencies (*bottom*) of PSCs, obtained from NPC- (*left*) or iPSC-derived (*right*) TH$^-$ or TH$^+$ neurons at different time points during maturation. Filled circles are means ± s.e.m. with the numbers of experimental replicates, *n*, indicated in parentheses. Straight lines connect means for clarity. Individual data points are shown as open circles. Statistical significance between data pairs was analyzed with a two-tailed Mann–Whitney *U*-test: $^{*}P < 0.05$ for testing TH$^-$ against TH$^+$ of the same line; $^{xx}P < 0.01$, $^{x}P < 0.05$ for comparing data obtained at t1 with data obtained at t4; $^{##}P < 0.01$, $^{#}P < 0.05$ for testing data derived from iPSCs against data derived from NPCs.

throughout the differentiation period and was dependent on the differentiation protocol applied. Whereas the mean firing frequencies of NPC-derived TH$^+$ cells increased above those of corresponding TH$^-$ cells particularly in the last phase of differentiation (t4), the firing rates of iPSC-derived TH$^+$ cells increased already from t2 and reached a maximum of 4.0 Hz at t3.

In both cultures the proportions of cells firing were independent of TH expression and varied only marginally between time points, except for the TH$^-$ subpopulation of NPC-derived neurons, which showed a small yet significant increase of the proportion of excitable cells from 56.8% at t1 to 81.8% at t4 ($P < 0.05$). The minimum current amplitude required to initiate an action potential response was virtually identical in NPC- and iPSC-derived cultures among the entire differentiation period and did also not correlate with TH expression (**Figure 4D**, bottom). Analysis of the peak voltage of the first action potential fired during the stimulation paradigm, $V_{peak}$, revealed significant differences between the two neuronal cell lines: While in both NPC-derived subpopulations $V_{peak}$ did not exceed 0 mV at all-time points tested, it reached values above 0 mV in both iPSC-derived subpopulations already from time point t2, indicating that neuronal maturation was more efficient in the iPSC-derived culture. Moreover, $V_{peak}$ was consistently higher in the TH$^+$ subpopulation of iPSC-derived neurons compared to their TH$^-$ counterparts, suggesting that electrophysiological maturation of TH$^+$ cells was preferred in this culture.

Since spontaneous activity is a hallmark feature of mature SNpc neurons (Guzman et al., 2009), we also analyzed the ability

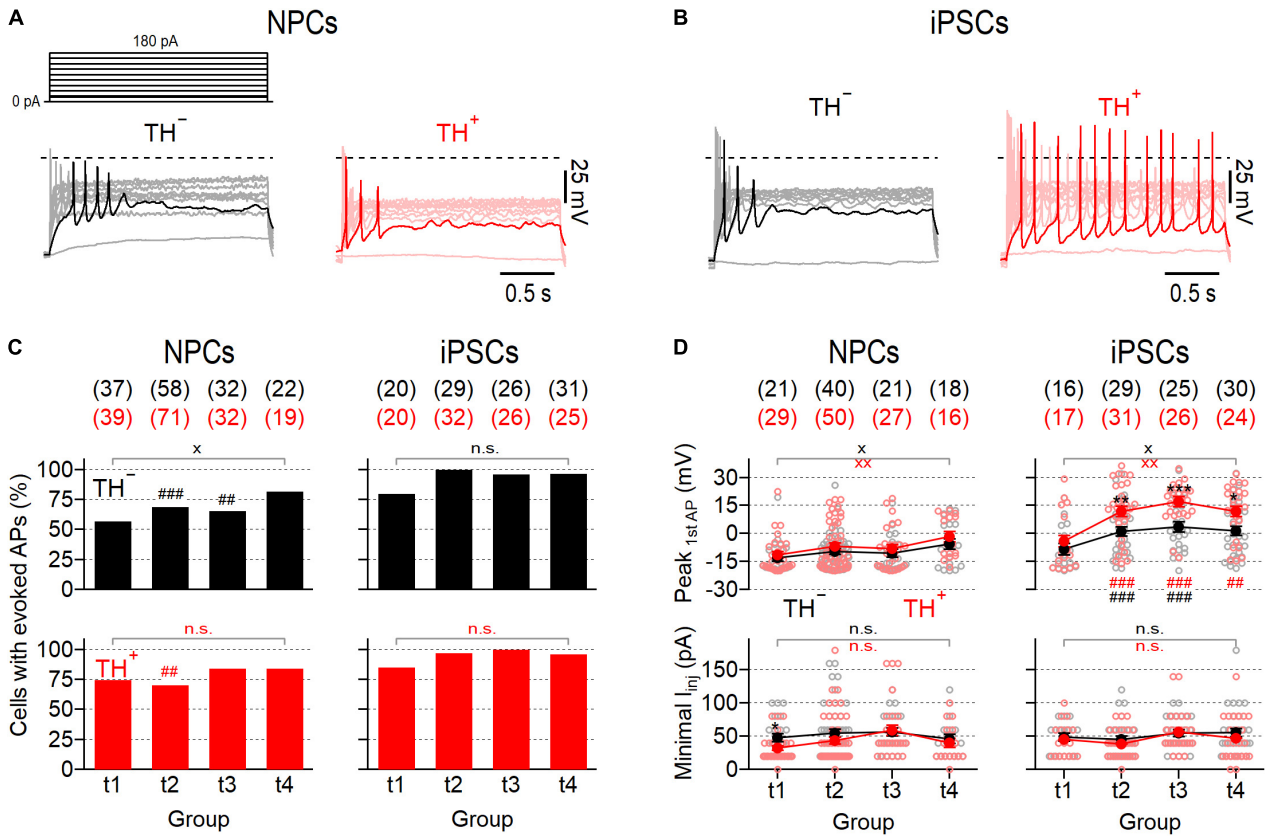


**FIGURE 4 |** Evolution of evoked action potential responses in NPC- and iPSC-derived dopaminergic cultures. **(A)** Representative voltage responses (*bottom*) of TH$^-$ (*left*) and TH$^+$ (*right*) NPC-derived neurons at time point 3 (t3) to 2 s current injections ranging from 0 to 180 pA (*top*). The 20 pA stimulation step is shown bold in the pulse protocol, corresponding voltage responses are highlighted in black (TH$^-$) and red (TH$^+$). **(B)** Identical recordings as in **(A)**, from TH$^-$ and TH$^+$ iPSC-derived neurons at t3. **(C)** Percentage of NPC- (*left*) and iPSC-derived (*right*) TH$^-$ (*top,* black) and TH$^+$ (*bottom,* red) neurons that responded to 2 s current injections of up to 180 pA with one or more APs, analyzed at specified time points. **(D)** Mean minimal current (*bottom*) required to evoke APs as shown in **(A,B)** and associated mean peak voltages (*top*) of the first AP fired, analyzed at indicated time points. Filled circles represent means ± s.e.m, connected with straight lines for clarity. Open circles indicate data obtained from individual cells. The numbers of cells analyzed in **(C,D)** are provided in parentheses. Statistical indicators in **(C,D)** refer to Fisher's exact test or a Mann–Whitney *U*-test, respectively: $^{***}P < 0.001$, $^{**}P < 0.01$, $^{*}P < 0.05$ for testing TH$^-$ against TH$^+$ neurons of the same line; $^{xx}P < 0.01$, $^{x}P < 0.05$, n.s. for comparing data obtained at t1 with data from t4; $^{###}P < 0.001$, $^{##}P < 0.01$ for testing data obtained with iPSC-derived neurons against data from NPC-derived neurons.

of the cells to generate action potentials in the absence of a current stimulus. Representative recordings obtained from both subpopulations of NPC- and iPSC-derived neurons are shown in **Figure 5A**. The proportions of spontaneously firing cells were generally low in NPC-derived neurons ranging from 4.0 to 13.6% and from 7.1 to 36.8% for TH$^-$ and TH$^+$ cells, respectively (**Figure 5B**). Although spontaneous firing was more frequently detected in TH$^+$ cells than in TH$^-$ cells at all-time points tested, these differences did not reach the level of significance. Independent of the time in differentiation and the expression of TH, the mean peak voltages of spontaneous action potentials did not exceed 0 mV, except for TH$^+$ cells at t2, which fired trains of action potentials with a mean peak voltage of 0.7 ± 5.2 mV (**Figure 5C**). As sown in **Figure 5B**, the proportions of spontaneously active cells increased in the iPSC-derived culture continuously over time and exhibited noticeable differences between the TH$^-$ and TH$^+$ subpopulations, particularly in late phases of differentiation: In TH$^-$ neurons, spontaneous firing occurred first at time point t2 (24.1%) and increased only slightly until t4 (33.3%). By contrast, the proportion of spontaneously active TH$^+$ cells increased more rapidly as the culture matured, reaching significantly higher levels at t3 (66,7%, $P < 0.001$ vs. TH$^-$) and t4 (65.4%, $P < 0.05$ vs. TH$^-$). In addition, the average peak voltages of spontaneous action potentials were consistently higher in the iPSC-derived TH$^+$ cell population compared to in the TH$^-$ subpopulation (**Figures 5A,C**): While TH$^-$ cells fired—at all-time points tested—trains of spontaneous action potentials with a mean peak voltage below 0 mV, the TH$^+$ cells generated action potentials with an average peak voltage above 0 mV, being significant for groups at t2 and t4 (both $P < 0.05$). To identify possible mechanisms underlying the different electrophysiological properties of TH$^+$ and TH$^-$ cells, both neuronal subpopulations were isolated from the iPSC-derived culture at day 50 of differentiation (corresponding to t4) by FACS and subsequently analyzed for the mRNA levels of the neuronal progenitor markers Pax6, SOX2, and ASCL1. As shown

in **Supplementary Figure 5**, TH$^-$ cells expressed Pax6 and SOX2 at higher levels than TH$^+$ neurons ($P < 0.05$), whereas ASCL1 was expressed almost equally in both subpopulations.

Thus, mature action potentials developed preferentially in TH$^+$ iPSC-derived cells, whereas the associated TH$^-$ cells as well as both NPC-derived subpopulations were characterized by electrophysiological features characteristic of premature neuronal precursors.

## DISCUSSION

Human iPSCs are widely used to model physiological and pathophysiological conditions because they can be differentiated into a variety of cell types (Takahashi et al., 2007; Yu et al., 2007; Dimos et al., 2008; Ebert et al., 2009; Soldner et al., 2009; Guimaraes et al., 2018) including SNpc-associated DNs, which play a major role in the pathogenesis of PD. Several procedures have been developed that enable the differentiation of DNs from iPSCs, all with specific advantages and disadvantages (Chambers et al., 2009; Kirkeby et al., 2012; Xi et al., 2012; Doi et al., 2014). However, all differentiation strategies available to date give rise to largely inhomogeneous DN cultures containing variable proportions of neurons capable of synthesizing dopamine (TH$^+$) and morphologically indistinguishable non-dopaminergic (TH$^-$) cells which lack TH expression. This variability makes the targeted analysis of the PD-relevant TH$^+$ subpopulation difficult, especially when functional assays are involved, which require living neurons (Calatayud et al., 2019; Laperle et al., 2020).

To overcome this issue, we adapted an established strategy (Xia et al., 2017; Calatayud et al., 2019; Hong and Daadi, 2019; Uberbacher et al., 2019) and engineered an mCherry-based TH reporter iPSC line, which enables visual identification of cells expressing TH, the rate-limiting enzyme in dopamine synthesis. The subsequent differentiation into DN cultures was performed according to two well-established procedures to evaluate if and how protocol-specific conditions affect the electrophysiological characteristics of DNs. First, we applied a protocol that converts iPSCs into expandable and easy-to-handle NPCs before differentiating them to DNs (Reinhardt et al., 2013). In a second set of experiments, we followed a "midbrain floor plate protocol" to yield DNs directly from iPSCs (Kriks et al., 2011).

Both NPC- and iPSC-derived DN cultures were morphologically indistinguishable and contained comparable proportions of TH$^+$ neurons, ranging between 26 and 28%, which is compatible with most previous studies reporting yields of between 3 and 30% TH$^+$ cells relative to all cells (Sundberg et al., 2013; Ishikawa et al., 2016; Awad et al., 2017; Beevers et al., 2017; Romero-Moya et al., 2017; Sheng et al., 2017). Variable yields of TH$^+$ cells at low levels are a known limitation of all differentiation strategies available to date, largely attributed to the asynchronous maturation of cells due to a stochastic component inherent in the differentiation process that ultimately leads to unequal responses of iPSCs to morphogens (Antonov and Novosadova, 2021). In addition, iPSCs may be epigenetically unique, such that their potential to differentiate into a specific

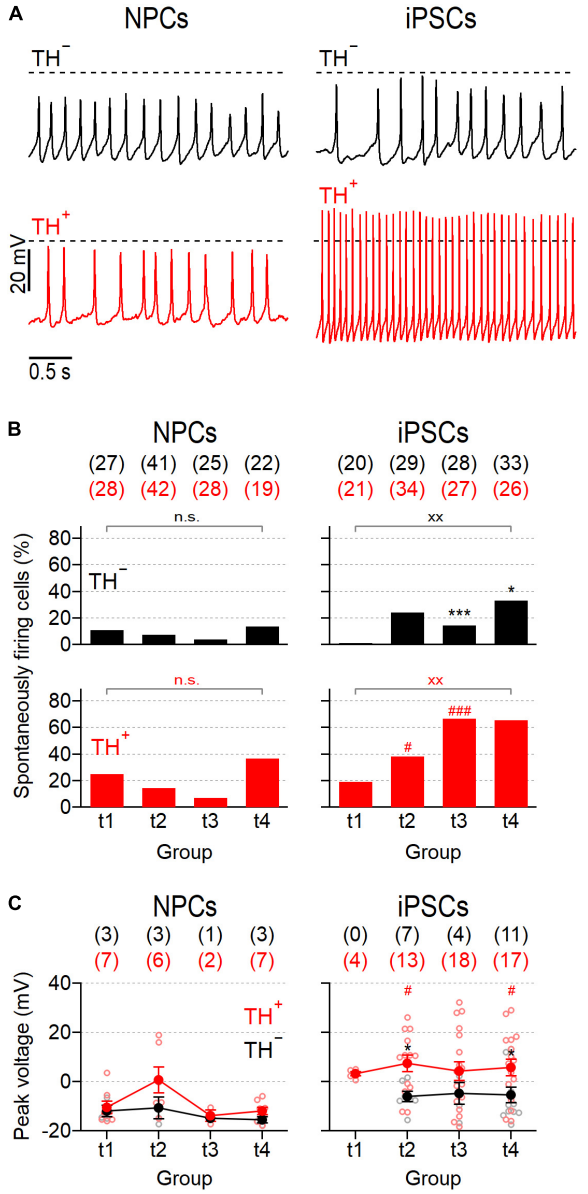


**FIGURE 5 |** NPC- and iPSC-derived dopaminergic cultures contain different proportions of spontaneously firing neurons. **(A)** Representative action potential recordings obtained at time point 2 (t2) from NPC- (*left*) and iPSC-derived (*right*) neurons that were negative (TH$^-$, *top*) or positive (TH$^+$, *bottom*) for the expression of TH, in response to zero current injection. Dashed lines indicate a membrane potential of 0 mV. **(B)** Percentage of NPC- and iPSC-derived TH$^-$ (*top*) and TH$^+$ (*bottom*) neurons that fired spontaneous action potentials as shown in **(A)**, analyzed at different time points during maturation. For each condition, the total number of cells analyzed, *n*, is provided in parentheses. **(C)** Average peak voltages (filled circles) of spontaneously fired action potentials as shown in **(A)**, analyzed at specified time points. Data points are means ± s.e.m. with the numbers of cells analyzed, *n*, given in parentheses. Straight lines connect data for clarity. Open circles represent data obtained from individual cells. Statistical indicators in **(B,C)** refer to a Fisher's exact test and a Mann–Whitney *U*-test, respectively: $^{***}P < 0.001$, $^{*}P < 0.05$ for testing TH$^-$ against TH$^+$ neurons of the same line;$^{xx}P < 0.01$ for comparing data obtained at t1 with data obtained at t4;$^{\#\#\#}P < 0.001$, $^{\#}P < 0.05$ for testing data obtained from NPC-derived neurons against data obtained from iPSC-derived neurons; n.s. not significant.

sublinage may be predetermined (Hu et al., 2010). Laboratory-specific handling of the cells is also considered to affect the conversion efficiency (Mahajani et al., 2019).

However, approximately 10 days after dopaminergic differentiation was initiated, cells from both cultures started to cluster and adopted a neuronal morphology. In both cultures, the morphological development was accompanied by a continuous increase of the cells' membrane capacitance, indicating that cell surface area and thus cell size increased during differentiation as it is expected for developing cultures (Golowasch et al., 2009). Moreover, the input resistance ($R_{in}$), a passive membrane property inversely correlated with cell size and open channel density, was in both cultures independent of TH expression but decreased with increasing differentiation time in both iPSC-derived subpopulations, which is consistent with previous studies focusing on developing human iPSC-derived DNs (Pre et al., 2014) or postnatal DNs obtained from rats (Dufour et al., 2014). Further evidence of morphological and functional maturation is that $R_{in}$ levels at late stages of differentiation (t3-t4) were comparable to those previously reported for terminally differentiated iPSC-derived cortical linage neurons including DNs (Stanslowsky et al., 2014; Gunhanlar et al., 2018).

$Na_V-$ and $K_V$-dependent current densities, both of which are essential for action potential formation, increased during differentiation in cells from both cultures (**Figure 2**) further confirming that both differentiation strategies yielded cells with developing neuronal characteristics. Furthermore, measured mean current densities, as well as their evolution during maturation, are consistent with previous studies examining the electrophysiological properties of human non-reporter NPC- and iPSC-derived DNs (Reinhardt et al., 2013; Pre et al., 2014; Stanslowsky et al., 2014). Although $Na^+$ and $K^+$ currents increased during maturation in cells from both cultures, they were always larger in iPSC-derived neurons compared to neurons obtained from NPCs. In addition, the $TH^+$ subpopulation of iPSC-derived neurons generated larger $Na_V$-dependent current amplitudes than the corresponding $TH^-$ neurons, a property that was not observed in the NPC-derived reporter culture (**Figure 2**).

The ability of neurons to communicate with each other *via* synaptic contacts is a fundamental property of mature neural networks that is continuously and dynamically regulated (Glasgow et al., 2019). Synaptogenesis requires the coordinated interplay of various cellular processes, including those that control neurotransmitter release and postsynaptic recognition, and is therefore considered one of the signature endpoints of neurogenesis (Bradford and McNutt, 2015). Here we used a single-cell patch-clamp approach to analyze PSCs which are triggered by both pre- and postsynaptic processes and thus allow to make inferences on the synaptic activity of individual cells. In both DN cultures, the proportions of PSC-positive neurons were independent of TH expression and varied only marginally during differentiation. However, the proportions of PSC-generating neurons, and thus the overall synaptic activity, were on average more than three times higher in the iPSC-derived culture compared to in the NPC-derived culture (**Figure 3C**). In addition, only iPSC-derived neurons showed a progressive increase of PSC amplitudes, suggesting that the synaptic apparatus of these cells matured over time. The frequencies of events varied only marginally between time points t1 and t4, ranging from 0.3 to 1.7 Hz in both cultures. Together, these results are both qualitatively and quantitatively comparable to previous reports on NPC- and iPSC-derived SNpc neurons (Reinhardt et al., 2013; Pre et al., 2014; Stanslowsky et al., 2014; Gunhanlar et al., 2018).

The action potential characteristics of NPC- and iPSC-derived DNs also developed differently. Already 3–4 weeks after the differentiation process was triggered (t2), evoked and spontaneous action potentials were more frequently detected in iPSC-derived neurons and displayed more mature characteristics compared to the responses obtained from NPC-derived neurons (**Figures 4**, **5**). Considering that the two differentiation protocols differ significantly in terms of the morphogens used and the timing of their application, and that both factors are crucially important for cell conversion, the different electrophysiological properties of NPC- and iPSC-derived neurons are not unexpected. For example, the combination of immediate specification of early neuronal progenitors by SHH/FGF8 and simultaneous activation of the Wnt signaling pathway by CHIR99021 as used in the "floor plate protocol" (**Figure 1I**) is considered to be particularly effective for obtaining DNs with a midbrain phenotype (Kriks et al., 2011; Weykopf et al., 2019; Antonov and Novosadova, 2021). Moreover, the presence of the Notch pathway antagonist DAPT may also have facilitated the electrophysiological maturation of iPSC-derived neurons, as it has been shown to promote the differentiation and maturation of derived neurons (Abranches et al., 2009; Borghese et al., 2010). In addition, the pluripotency of NPCs, and thus their ability to differentiate into mature neurons, appears to be negatively correlated with the number of cell passages they have experienced (Bardy et al., 2016).

However, the most striking observation was that the ability to generate action potentials with mature characteristics correlated in iPSC-derived neurons with the expression of TH while such a correlation was not seen in the NPC-derived DN culture: Throughout the 8-week differentiation period (t1–4), the action potential peak voltages of the iPSC-derived $TH^+$ subpopulation were above 0 mV and significantly higher compared to the responses of $TH^-$ cells. In addition, the proportions of spontaneously firing $TH^+$ cells increased faster over time and were significantly larger compared to the proportions of spontaneously active $TH^-$ neurons (**Figure 5**) particularly during late phases of differentiation. Together, these results demonstrate that of the two differentiation strategies evaluated in this work, the "midbrain floor plate protocol" (Kriks et al., 2011) yielded higher numbers of electrophysiologically mature neurons, most of which also expressed TH.

The reasons why $TH^-$ and $TH^+$ neurons matured differently in this culture cannot be inferred from the data shown here, but this finding is compatible with a previous study in which the transcriptome of $TH^-$ and $TH^+$ subpopulations of an iPSC-derived TH reporter line was analyzed (Xia et al., 2017). This work demonstrated that $TH^+$ cells expressed genes with neuron-specific functions at higher levels than $TH^-$ cells, which in contrast expressed elevated levels of cell cycle-associated genes

suggesting the fraction of mature neurons was higher in the $TH^+$ cell population whereas the $TH^-$ subpopulation consisted mainly of undifferentiated neural precursors. In line with this interpretation, they found floor plate neuronal markers such as TH, LMX1B, ERBB3, NR4A2, and DDC enriched in $TH^+$ cells, while $TH^-$ cells were positive for neural stem cell markers such as Pax6, SOX2, ASCL1, and ZIC5TH and the non-midbrain floor plate markers HOXB1 and GLI2. Consistent with these data, we also found Pax6 and SOX2 enriched in $TH^-$ cells. In another study it has been shown that $TH^+$ and $TH^-$ subpopulations of a TH reporter culture developed spontaneous calcium transients with distinguishable characteristics when analyzed in a Fluo-4AM-based imaging assay (Calatayud et al., 2019). This study demonstrated that amplitudes of spontaneous calcium signals were larger in $TH^-$ neurons compared to $TH^+$ cells, suggesting differences between the two neuronal subpopulations with respect to their electrical activity. However, although intracellular calcium signals are considered a proxy for spike activity (Kerr et al., 2005; Tian et al., 2009; Kwan and Dan, 2012; Chen et al., 2013), it is difficult to draw quantitative conclusions about cellular excitability solely based on calcium signals because elevated intracellular calcium levels can also be a consequence of suprathreshold depolarizations which do not trigger action potentials (Ali and Kwan, 2020).

In this study, we used single-cell electrophysiology as a direct measure of neuronal activity to compare for the first time the electrophysiological maturation of iPSC- and NPC-derived TH reporter DNs over a period of 8 weeks during differentiation. We demonstrated that although both differentiation strategies yielded basically identical proportions of $TH^+$ cells with neuronal morphology, the fraction of electrophysiologically mature $TH^+$ DNs was significantly larger in the iPSC-derived culture than in the NPC-derived culture suggesting that the direct differentiation of iPSCs to DNs using the "midbrain floor plate protocol" (Kriks et al., 2011) has the higher conversion efficiency to mature $TH^+$ DNs, which represent the most vulnerable cell type in PD. However, given that NPC- and iPSC-derived cultures contained identical proportions of $TH^+$ cells and expressed TH at comparable levels, it is evident that TH expression, although an important maturation marker for DNs, is not a sufficient indicator of the cells' electrophysiological phenotype. Because excitability is an important physiological feature of mature neurons, electrophysiological properties of DNs derived from iPSCs should consequently be considered to monitor and evaluate the maturation process. Furthermore, the data support the notion that TH reporter DNs are a valuable tool for basic and translational PD research as they provide a means to restrict the analysis of cellular excitability and their PD-associated modulation to $TH^+$ DNs, which is expected to reduce variability in associated data sets.

## DATA AVAILABILITY STATEMENT

The original contributions presented in the study are included in the article/**Supplementary Material**, further inquiries can be directed to the corresponding author/s.

## AUTHOR CONTRIBUTIONS

AR and EL designed the study. DV, FV, BM, and A-KH performed experiments. AR, DV, CN, CK, and EL analyzed and interpreted the data. AR, CN, CK, and EL wrote the manuscript with input from DV, FV, BM, and A-KH. All authors contributed to the article and approved the submitted version.

## FUNDING

This work was supported by grants from the German Research Foundation as part of the Research Unit ProtectMove (FOR 2488 to AR and CK).

## ACKNOWLEDGMENTS

We would like to thank the University Hospital Schleswig Holstein for supporting this work with intramural funds.

## SUPPLEMENTARY MATERIAL

The Supplementary Material for this article can be found online at: https://www.frontiersin.org/articles/10.3389/fncel.2022.817198/full#supplementary-material

## REFERENCES

Abranches, E., Silva, M., Pradier, L., Schulz, H., Hummel, O., Henrique, D., et al. (2009). Neural differentiation of embryonic stem cells in vitro: a road map to neurogenesis in the embryo. *PLoS One* 4:e6286. doi: 10.1371/journal.pone.0006286

Ali, F., and Kwan, A. C. (2020). Interpreting in vivo calcium signals from neuronal cell bodies, axons, and dendrites: a review. *Neurophotonics* 7:011402. doi: 10.1117/1.NPh.7.1.011402

Antonov, S. A., and Novosadova, E. V. (2021). Current State-of-the-Art and Unresolved Problems in Using Human Induced Pluripotent Stem Cell-Derived Dopamine Neurons for Parkinson's Disease Drug Development. *Int. J. Mol. Sci.* 22:3381. doi: 10.3390/ijms22073381

Awad, O., Panicker, L. M., Deranieh, R. M., Srikanth, M. P., Brown, R. A., Voit, A., et al. (2017). Altered Differentiation Potential of Gaucher's Disease iPSC Neuronal Progenitors due to Wnt/beta-Catenin Downregulation. *Stem Cell Rep.* 9, 1853–1867. doi: 10.1016/j.stemcr.2017.10.029

Bardy, C., van den Hurk, M., Kakaradov, B., Erwin, J. A., Jaeger, B. N., Hernandez, R. V., et al. (2016). Predicting the functional states of human iPSC-derived neurons with single-cell RNA-seq and electrophysiology. *Mol. Psychiatry* 21, 1573–1588. doi: 10.1038/mp.2016.158

Beevers, J. E., Lai, M. C., Collins, E., Booth, H. D. E., Zambon, F., Parkkinen, L., et al. (2017). MAPT Genetic Variation and Neuronal Maturity Alter Isoform Expression Affecting Axonal Transport in iPSC-Derived Dopamine Neurons. *Stem Cell Rep.* 9, 587–599. doi: 10.1016/j.stemcr.2017.06.005

Belinsky, G. S., Moore, A. R., Short, S. M., Rich, M. T., and Antic, S. D. (2011). Physiological properties of neurons derived from human embryonic stem cells using a dibutyryl cyclic AMP-based protocol. *Stem Cells Dev.* 20, 1733–1746. doi: 10.1089/scd.2010.0501

Blaszczyk, J. W. (2016). Parkinson's Disease and Neurodegeneration: GABA-Collapse Hypothesis. *Front. Neurosci.* 10:269. doi: 10.3389/fnins.2016.00269

Bloem, B. R., Okun, M. S., and Klein, C. (2021). Parkinson's disease. *Lancet* 397, 2284–2303.

Borghese, L., Dolezalova, D., Opitz, T., Haupt, S., Leinhaas, A., Steinfarz, B., et al. (2010). Inhibition of notch signaling in human embryonic stem cell-derived neural stem cells delays G1/S phase transition and accelerates neuronal differentiation in vitro and in vivo. *Stem Cells* 28, 955–964. doi: 10.1002/stem.408

Bradford, A. B., and McNutt, P. M. (2015). Importance of being Nernst: synaptic activity and functional relevance in stem cell-derived neurons. *World J. Stem Cells* 7, 899–921. doi: 10.4252/wjsc.v7.i6.899

Calatayud, C., Carola, G., Fernandez-Carasa, I., Valtorta, M., Jimenez-Delgado, S., Diaz, M., et al. (2019). CRISPR/Cas9-mediated generation of a tyrosine hydroxylase reporter iPSC line for live imaging and isolation of dopaminergic neurons. *Sci. Rep.* 9:6811. doi: 10.1038/s41598-019-43080-2

Chambers, S. M., Fasano, C. A., Papapetrou, E. P., Tomishima, M., Sadelain, M., and Studer, L. (2009). Highly efficient neural conversion of human ES and iPS cells by dual inhibition of SMAD signaling. *Nat. Biotechnol.* 27, 275–280. doi: 10.1038/nbt.1529

Chen, T. W., Wardill, T. J., Sun, Y., Pulver, S. R., Renninger, S. L., Baohan, A., et al. (2013). Ultrasensitive fluorescent proteins for imaging neuronal activity. *Nature* 499:295. doi: 10.1038/nature12354

Cooper, O., Hargus, G., Deleidi, M., Blak, A., Osborn, T., Marlow, E., et al. (2010). Differentiation of human ES and Parkinson's disease iPS cells into ventral midbrain dopaminergic neurons requires a high activity form of SHH, FGF8a and specific regionalization by retinoic acid. *Mol. Cell. Neurosci.* 45, 258–266. doi: 10.1016/j.mcn.2010.06.017

Dimos, J. T., Rodolfa, K. T., Niakan, K. K., Weisenthal, L. M., Mitsumoto, H., Chung, W., et al. (2008). Induced pluripotent stem cells generated from patients with ALS can be differentiated into motor neurons. *Science* 321, 1218–1221. doi: 10.1126/science.1158799

Doi, D., Samata, B., Katsukawa, M., Kikuchi, T., Morizane, A., Ono, Y., et al. (2014). Isolation of human induced pluripotent stem cell-derived dopaminergic progenitors by cell sorting for successful transplantation. *Stem Cell Rep.* 2, 337–350. doi: 10.1016/j.stemcr.2014.01.013

Dufour, M. A., Woodhouse, A., Amendola, J., and Goaillard, J. M. (2014). Non-linear developmental trajectory of electrical phenotype in rat substantia nigra pars compacta dopaminergic neurons. *Elife* 3:e04059. doi: 10.7554/eLife.04059

Ebert, A. D., Yu, J., Rose, F. F. Jr., Mattis, V. B., Lorson, C. L., Thomson, J. A., et al. (2009). Induced pluripotent stem cells from a spinal muscular atrophy patient. *Nature* 457, 277–280. doi: 10.1038/nature07677

Garcia-Leon, J. A., Vitorica, J., and Gutierrez, A. (2019). Use of human pluripotent stem cell-derived cells for neurodegenerative disease modeling and drug screening platform. *Future Med. Chem.* 11:1305. doi: 10.4155/fmc-2018-0520

Glasgow, S. D., McPhedrain, R., Madranges, J. F., Kennedy, T. E., and Ruthazer, E. S. (2019). Approaches and Limitations in the Investigation of Synaptic Transmission and Plasticity. *Front. Synaptic Neurosci.* 11:20. doi: 10.3389/fnsyn.2019.00020

Golowasch, J., Thomas, G., Taylor, A. L., Patel, A., Pineda, A., Khalil, C., et al. (2009). Membrane capacitance measurements revisited: dependence of capacitance value on measurement method in nonisopotential neurons. *J. Neurophysiol.* 102, 2161–2175. doi: 10.1152/jn.00160.2009

Guimaraes, M. Z. P., De Vecchi, R., Vitoria, G., Sochacki, J. K., Paulsen, B. S., Lima, I., et al. (2018). Generation of iPSC-Derived Human Peripheral Sensory Neurons Releasing Substance P Elicited by TRPV1 Agonists. *Front. Mol. Neurosci.* 11:277. doi: 10.3389/fnmol.2018.00277

Gunhanlar, N., Shpak, G., van der Kroeg, M., Gouty-Colomer, L. A., Munshi, S. T., Lendemeijer, B., et al. (2018). A simplified protocol for differentiation of electrophysiologically mature neuronal networks from human induced pluripotent stem cells. *Mol. Psychiatry* 23, 1336–1344. doi: 10.1038/mp.2017.56

Guzman, J. N., Sanchez-Padilla, J., Chan, C. S., and Surmeier, D. J. (2009). Robust pacemaking in substantia nigra dopaminergic neurons. *J. Neurosci.* 29, 11011–11019. doi: 10.1523/JNEUROSCI.2519-09.2009

Hartfield, E. M., Yamasaki-Mann, M., Ribeiro Fernandes, H. J., Vowles, J., James, W. S., Cowley, S. A., et al. (2014). Physiological characterisation of human iPS-derived dopaminergic neurons. *PLoS One* 9:e87388. doi: 10.1371/journal.pone.0087388

Hong, H., and Daadi, M. M. (2019). Generating Neural Stem Cells from iPSCs with Dopaminergic Neurons Reporter Gene. *Methods Mol. Biol.* 1919, 119–128. doi: 10.1007/978-1-4939-9007-8_9

Hu, B. Y., Weick, J. P., Yu, J., Ma, L. X., Zhang, X. Q., Thomson, J. A., et al. (2010). Neural differentiation of human induced pluripotent stem cells follows developmental principles but with variable potency. *Proc. Natl. Acad. Sci. U. S. A.* 107, 4335–4340. doi: 10.1073/pnas.0910012107

Ishikawa, T., Imamura, K., Kondo, T., Koshiba, Y., Hara, S., Ichinose, H., et al. (2016). Genetic and pharmacological correction of aberrant dopamine synthesis using patient iPSCs with BH4 metabolism disorders. *Hum. Mol. Genet.* 25, 5188–5197. doi: 10.1093/hmg/ddw339

Kerr, J. N., Greenberg, D., and Helmchen, F. (2005). Imaging input and output of neocortical networks in vivo. *Proc. Natl. Acad. Sci. U. S. A.* 102, 14063–14068. doi: 10.1073/pnas.0506029102

Kirkeby, A., Grealish, S., Wolf, D. A., Nelander, J., Wood, J., Lundblad, M., et al. (2012). Generation of regionally specified neural progenitors and functional neurons from human embryonic stem cells under defined conditions. *Cell Rep.* 1, 703–714. doi: 10.1016/j.celrep.2012.04.009

Kouroupi, G., Antoniou, N., Prodromidou, K., Taoufik, E., and Matsas, R. (2020). Patient-Derived Induced Pluripotent Stem Cell-Based Models in Parkinson's Disease for Drug Identification. *Int. J. Mol. Sci.* 21:7113. doi: 10.3390/ijms21197113

Kriks, S., Shim, J. W., Piao, J., Ganat, Y. M., Wakeman, D. R., Xie, Z., et al. (2011). Dopamine neurons derived from human ES cells efficiently engraft in animal models of Parkinson's disease. *Nature* 480, 547–551. doi: 10.1038/nature10648

Kwan, A. C., and Dan, Y. (2012). Dissection of cortical microcircuits by single-neuron stimulation in vivo. *Curr. Biol.* 22, 1459–1467. doi: 10.1016/j.cub.2012.06.007

Laperle, A. H., Sances, S., Yucer, N., Dardov, V. J., Garcia, V. J., Ho, R., et al. (2020). iPSC modeling of young-onset Parkinson's disease reveals a molecular signature of disease and novel therapeutic candidates. *Nat. Med.* 26, 289–299. doi: 10.1038/s41591-019-0739-1

Livak, K. J., and Schmittgen, T. D. (2001). Analysis of relative gene expression data using real-time quantitative PCR and the 2(-Delta Delta C(T)) Method. *Methods* 25, 402–408. doi: 10.1006/meth.2001.1262

Magrinelli, F., Picelli, A., Tocco, P., Federico, A., Roncari, L., Smania, N., et al. (2016). Pathophysiology of Motor Dysfunction in Parkinson's Disease as the Rationale for Drug Treatment and Rehabilitation. *Parkinsons Dis.* 2016:9832839. doi: 10.1155/2016/9832839

Mahajani, S., Raina, A., Fokken, C., Kugler, S., and Bahr, M. (2019). Homogenous generation of dopaminergic neurons from multiple hiPSC lines by transient expression of transcription factors. *Cell Death Dis.* 10:898. doi: 10.1038/s41419-019-2133-9

Matsuda, T., and Cepko, C. L. (2007). Controlled expression of transgenes introduced by in vivo electroporation. *Proc. Natl. Acad. Sci. U. S. A.* 104, 1027–1032. doi: 10.1073/pnas.0610155104

Pinheiro, P. S., and Mulle, C. (2008). Presynaptic glutamate receptors: physiological functions and mechanisms of action. *Nat. Rev. Neurosci.* 9, 423–436. doi: 10.1038/nrn2379

Pre, D., Nestor, M. W., Sproul, A. A., Jacob, S., Koppensteiner, P., Chinchalongporn, V., et al. (2014). A time course analysis of the electrophysiological properties of neurons differentiated from human induced pluripotent stem cells (iPSCs). *PLoS One* 9:e103418. doi: 10.1371/journal.pone.0103418

Reinhardt, P., Glatza, M., Hemmer, K., Tsytsyura, Y., Thiel, C. S., Hoing, S., et al. (2013). Derivation and expansion using only small molecules of human neural progenitors for neurodegenerative disease modeling. *PLoS One* 8:e59252. doi: 10.1371/journal.pone.0059252

Romero-Moya, D., Santos-Ocana, C., Castano, J., Garrabou, G., Rodriguez-Gomez, J. A., Ruiz-Bonilla, V., et al. (2017). Genetic Rescue of Mitochondrial and Skeletal Muscle Impairment in an Induced Pluripotent Stem Cells Model of Coenzyme Q(10) Deficiency. *Stem Cells* 35, 1687–1703. doi: 10.1002/stem.2634

Sakuma, T., Nishikawa, A., Kume, S., Chayama, K., and Yamamoto, T. (2014). Multiplex genome engineering in human cells using all-in-one CRISPR/Cas9 vector system. *Sci. Rep.* 4:5400. doi: 10.1038/srep05400

Sanchez-Danes, A., Consiglio, A., Richaud, Y., Rodriguez-Piza, I., Dehay, B., Edel, M., et al. (2012). Efficient Generation of A9 Midbrain Dopaminergic Neurons by Lentiviral Delivery of LMX1A in Human Embryonic Stem Cells and Induced Pluripotent Stem Cells. *Hum. Gene Ther.* 23, 56–69. doi: 10.1089/hum.2011.054

Schneider, C. A., Rasband, W. S., and Eliceiri, K. W. (2012). NIH Image to ImageJ: 25 years of image analysis. *Nat. Methods* 9, 671–675. doi: 10.1038/nmeth.2089

Sheng, Y., Preston, K. L., Phillips, K. A., Lin, Z., Tesar, P., Hoffer, B., et al. (2017). Using iPSC-Derived Human DA Neurons From Opioid-Dependent Subjects to Study Dopamine Dynamics. *Cell Transplant.* 26:724. doi: 10.1002/brb3.491

Shi, Y., Inoue, H., Wu, J. C., and Yamanaka, S. (2017). Induced pluripotent stem cell technology: a decade of progress. *Nat. Rev. Drug Discov.* 16, 115–130. doi: 10.1038/nrd.2016.245

Soldner, F., Hockemeyer, D., Beard, C., Gao, Q., Bell, G. W., Cook, E. G., et al. (2009). Parkinson's disease patient-derived induced pluripotent stem cells free of viral reprogramming factors. *Cell* 136, 964–977. doi: 10.1016/j.cell.2009.02.013

Stanslowsky, N., Haase, A., Martin, U., Naujock, M., Leffler, A., Dengler, R., et al. (2014). Functional differentiation of midbrain neurons from human cord blood-derived induced pluripotent stem cells. *Stem Cell Res. Ther.* 5:35. doi: 10.1186/scrt423

Sundberg, M., Bogetofte, H., Lawson, T., Jansson, J., Smith, G., Astradsson, A., et al. (2013). Improved Cell Therapy Protocols for Parkinson's Disease Based on Differentiation Efficiency and Safety of hESC-, hiPSC-, and Non-Human Primate iPSC-Derived Dopaminergic Neurons. *Stem Cells* 31, 1548–1562. doi: 10.1002/stem.1415

Takahashi, K., Tanabe, K., Ohnuki, M., Narita, M., Ichisaka, T., Tomoda, K., et al. (2007). Induction of pluripotent stem cells from adult human fibroblasts by defined factors. *Cell* 131, 861–872. doi: 10.1016/j.cell.2007.11.019

Tian, L., Hires, S. A., Mao, T., Huber, D., Chiappe, M. E., Chalasani, S. H., et al. (2009). Imaging neural activity in worms, flies and mice with improved GCaMP calcium indicators. *Nat. Methods* 6:875. doi: 10.1038/nmeth.1398

Uberbacher, C., Obergasteiger, J., Volta, M., Venezia, S., Muller, S., Pesce, I., et al. (2019). Application of CRISPR/Cas9 editing and digital droplet PCR in human iPSCs to generate novel knock-in reporter lines to visualize dopaminergic neurons. *Stem Cell Res.* 41:101656. doi: 10.1016/j.scr.2019.101656

Weykopf, B., Haupt, S., Jungverdorben, J., Flitsch, L. J., Hebisch, M., Liu, G. H., et al. (2019). Induced pluripotent stem cell-based modeling of mutant LRRK2-associated Parkinson's disease. *Eur. J. Neurosci.* 49, 561–589. doi: 10.1111/ejn.14345

Xi, J., Liu, Y., Liu, H., Chen, H., Emborg, M. E., and Zhang, S. C. (2012). Specification of midbrain dopamine neurons from primate pluripotent stem cells. *Stem Cells* 30:1655. doi: 10.1002/stem.1152

Xia, N., Fang, F., Zhang, P., Cui, J., Tep-Cullison, C., Hamerley, T., et al. (2017). A Knockin Reporter Allows Purification and Characterization of mDA Neurons from Heterogeneous Populations. *Cell Rep.* 18:2533. doi: 10.1016/j.celrep.2017.02.023

Yu, J., Vodyanik, M. A., Smuga-Otto, K., Antosiewicz-Bourget, J., Frane, J. L., Tian, S., et al. (2007). Induced pluripotent stem cell lines derived from human somatic cells. *Science* 318:1917.

Zanon, A., Kalvakuri, S., Rakovic, A., Foco, L., Guida, M., Schwienbacher, C., et al. (2017). SLP-2 interacts with Parkin in mitochondria and prevents mitochondrial dysfunction in Parkin-deficient human iPSC-derived neurons and Drosophila. *Hum. Mol. Genet.* 26, 2412–2425. doi: 10.1093/hmg/ddx132

**Conflict of Interest:** CK serves as medical advisor to Centogene for genetic testing reports in the fields of movement disorders and dementia, excluding Parkinson's disease.

The remaining authors declare that the research was conducted in the absence of any commercial or financial relationships that could be construed as a potential conflict of interest.

**Publisher's Note:** All claims expressed in this article are solely those of the authors and do not necessarily represent those of their affiliated organizations, or those of the publisher, the editors and the reviewers. Any product that may be evaluated in this article, or claim that may be made by its manufacturer, is not guaranteed or endorsed by the publisher.

frontiers | Frontiers in Cellular Neuroscience

ORIGINAL RESEARCH
published: 22 April 2022
doi: 10.3389/fncel.2022.872347

# Fragile X Mental Retardation Protein Mediates the Effects of Androgen on Hippocampal PSD95 Expression and Dendritic Spines Density/Morphology and Autism-Like Behaviors Through miR-125a

*Huan Chen[1,2†], Dan Qiao[1,2†], Chang Wang[1,2,3], Bohan Zhang[1,2], Zhao Wang[1,2], Longmei Tang[4], Yibo Wang[5], Ran Zhang[5], Yizhou Zhang[1,2,3], Leigang Song[1,2], Hongchun Zuo[1,2], Fangzhen Guo[1,2], Xia Wang[6], Sha Li[1,2,3]* and Huixian Cui[1,2,3]**

[1] Department of Anatomy, Hebei Medical University, Shijiazhuang, China, [2] Neuroscience Research Center, Hebei Medical University, Shijiazhuang, China, [3] Hebei Key Laboratory of Neurodegenerative Disease Mechanism, Shijiazhuang, China, [4] Department of Epidemiology and Statistics, Hebei Medical University, Shijiazhuang, China, [5] Clinical Medicine, Hebei Medical University, Shijiazhuang, China, [6] Department of Child Health (Psychological Behavior), Children's Hospital of Hebei Province, Shijiazhuang, China

Dysregulated synaptic plasticity is a key feature of neurodevelopmental disorders, including autism. This study investigated whether Fragile X mental retardation protein (FMRP), a selective RNA-binding protein that regulates synaptic protein expression by interacting with miRNAs, mediates the effects of androgens that play an important role in regulating the synaptic plasticity in the hippocampus. Experiments using mouse hippocampal neuron HT22 cells demonstrated that dihydrotestosterone (DHT) increased the expression of postsynaptic density protein 95 (PSD95) by inhibiting FMRP expression. Administration of miR-125a inhibitor upregulated the PSD95 expression and significantly increased the DHT-induced upregulation of PSD95. FMRP knockdown in HT22 cells reduced the expression of miR-125a. Moreover, miR-125a inhibitor upregulated the PSD95 expression in the DHT-treated HT22 cells with FMRP knockdown. Subsequently, the effects of androgen-mediated *via* FMRP in regulating neural behaviors and PSD95 expression and dendritic spines density/morphology were investigated using *Fmr1* knockout (KO) and wild-type littermate (WT) mice. The castration of WT mice reduced the androgen levels, aggravated anxiety and depression, and impaired learning and memory and sociability of mice. DHT supplementation post-castration reversed the alterations in density and maturity of dendritic spines of hippocampal neurons and behavioral disorders in WT mice; however, it did not reveal such effects in *Fmr1* KO mice. Further, immunohistochemical staining and western blotting analyses after knocking down miR-125a revealed similar effects of castration and post-castration DHT supplementation on PSD95 protein expression. These findings clarified that FMRP mediated the effects of DHT through miR-125a in regulating the

OPEN ACCESS

**Edited by:**
Andreas Frick,
Institut National de la Santé et de la Recherche Médicale (INSERM), France

**Reviewed by:**
Pierre Billuart,
Institut National de la Santé et de la Recherche Médicale (INSERM), France
Luca Murru,
National Research Council (CNR), Italy

***Correspondence:**
Huixian Cui
cuihx@hebmu.edu.cn
Sha Li
lisha@hebmu.edu.cn

[†] These authors have contributed equally to this work

**Specialty section:**
This article was submitted to Cellular Neuropathology, a section of the journal Frontiers in Cellular Neuroscience

**Received:** 09 February 2022
**Accepted:** 30 March 2022
**Published:** 22 April 2022

**Citation:**
Chen H, Qiao D, Wang C, Zhang B, Wang Z, Tang L, Wang Y, Zhang R, Zhang Y, Song L, Zuo H, Guo F, Wang X, Li S and Cui H (2022) Fragile X Mental Retardation Protein Mediates the Effects of Androgen on Hippocampal PSD95 Expression and Dendritic Spines Density/Morphology and Autism-Like Behaviors Through miR-125a. Front. Cell. Neurosci. 16:872347. doi: 10.3389/fncel.2022.872347

expression of hippocampal synaptic protein PSD95. This study provides evidence for the neuroprotective mechanism of androgen in PSD95 expression and dendritic spines density/morphology and suggests that treatment interventions with androgen could be helpful for the management of synaptic plasticity disorders.

**Keywords: androgen, FMRP, synaptic plasticity, PSD95, miR-125a**

## INTRODUCTION

Autism is a neurodevelopmental disorder characterized by deficits in social communication, language development, and the presence of narrow interest and repetitive behavior (Levy et al., 2009). The incidence of autism has increased markedly (Daniels et al., 2017); however, its etiology is still a mystery. Accumulating evidence suggests that genetic and environmental factors play important roles in its pathogenesis (Chaste and Leboyer, 2012; Bai et al., 2019). For instance, Fragile X Syndrome (FXS) is the most common genetic cause of autism caused by a single gene mutation of the fragile X mental retardation gene 1 (*Fmr1*) encoding the fragile X mental retardation protein (FMRP) (Mila et al., 2018). FMRP is a selective RNA-binding protein highly expressed in many tissues, especially neurons and testicular tissues (Zhang et al., 2014). FMRP can bind 4% mRNA in the mammalian brain (Ashley, Wilkinson et al., 1993) and regulate the translation and expression of target genes related to dendritic development in specific time and space (Banerjee et al., 2018). In many disease models, the loss of function of FMRP leads to an abundance of certain proteins, resulting in dendrite dysplasia and cognitive deficits. The characteristic neuropathological changes of FXS are related to the abnormal development of dendritic spines and synapses (Sokol et al., 2011), which hinders the transformation of filopodia to mature mushroom spines (Jawaid et al., 2018). In addition to *Fmr1*, several other genes at high risk for autism encode synaptic proteins and affect synapse formation, maturation, and synaptic connections (Sugathan et al., 2014; Nia et al., 2020). Therefore, autism is considered as a synaptic dysfunction. Moreover, the impaired synaptic development and function in autism indicate that the neurobiological study of abnormal development of dendritic spines could provide insights into the pathogenesis of autism.

The physiological effects of androgens, the steroid hormones synthesized in the brain, gonads, and adrenal glands in both sexes, play important roles in regulating synaptic plasticity (Tozzi et al., 2019). Our previous study demonstrated that androgens play an important role in maintaining normal hippocampal synaptic plasticity and affect neurobehaviors by changing synaptic density and dendritic spines morphology. Furthermore, the androgen level in autistic children has been reported to be significantly higher than the age-matched healthy children (Majewska et al., 2014; Needham et al., 2021). These studies suggest the neuroplastic effects of abnormal androgen levels on brain development and the incidence and progression of neurological disorders such as autism. However, the underlying mechanism of how these effects are mediated remains elusive.

miRNAs, a class of non-coding single-stranded RNA, play crucial roles in the post-transcriptional regulation of target gene expression (Baby et al., 2020). miRNAs are highly expressed in the nervous system and are involved in a series of physiological functions such as neurodevelopment, dendritic spines morphology, and synaptic plasticity (Hu and Li, 2017). Imbalance in miRNA expression can induce changes in brain circuits and synaptic functions, resulting in some neurological diseases such as autism (Lu et al., 2020) and Alzheimer's disease (Mai et al., 2019). Several miRNAs targeting the 3′ UTR of PSD95 mRNA have been predicted, including miR-1, miR-103, and miR-125a. miR-125a plays a crucial role in mGluR-mediated PSD95 mRNA translation activation in cultured primary cortical neurons. Further, it has been shown that in neuro2A cells, the transfection of miR-125a, not miR-1 and miR-103, significantly inhibited the expression of f-luciferase-PSD95 UTR (Muddashetty et al., 2011). The associative theory between FMRP and miRNA suggests that the interaction between FMRP and miRNA promotes RNA-induced silencing complex (RISC), which contains Argonaute, and mRNA binding and negatively regulates the translation and expression of synaptic protein mRNA in specific time and space (Muddashetty et al., 2011).

Therefore, in this study, we aimed to test the hypothesis that androgens can regulate the development of dendritic spines and PSD95 abnormalities mediated by FMRP defects through miR-125a. Furthermore, we investigated the pathogenesis of autism from the perspective of the association between FMRP and miRNA.

## MATERIALS AND METHODS

### Cell Culture

Mouse hippocampal neuron HT22 cells were cultured in Dulbecco's Modified Eagle Medium (DMEM, cat#: 11965092, Gibco, United States) containing 10% fetal bovine serum (FBS) and 1% penicillin/streptomycin under standard conditions (37°C, 5% $CO_2$) in a humidified atmosphere. The cells were digested with 0.25% trypsin at 85–90% confluency. Then, the cells were seeded into 10 cm culture dishes for RNA-binding protein immunoprecipitation. Subsequently, the cells were transferred to 6- or 24-well plates for western blotting, immunofluorescence cytochemical staining, and quantitative reverse transcription-polymerase chain reaction (qRT-PCR) analyses. The cells in the experimental groups were treated with 10 nM dihydrotestosterone (DHT; cat#: A0462, *Tokyo Chemical Industry*, *Japan)* for 36 h, and those in the control (Ctrl) group were treated with equal volume dimethyl sulfoxide (DMSO).

## Animal Castration and Dosing

Two-month-old healthy male *Fmr1* knockout (KO) mice purchased from Jackson Labs (stock # 003025, United States) and wild-type littermate (WT) mice were used. After *Fmr1* KO and WT mice were anesthetized, a small incision was made from the scrotum to remove the testis in the experimental group. The scrotum was cut open and sutured in the Ctrl group without hurting the testis. The experimental groups (DHT group and DHT + anta-125a group) were administered *via* an intraperitoneal (i.p.) injection with DHT (1 mg/kg body weight) after 3 days of castration, and the Ctrl group was injected with equal volume sesame oil for 30 consecutive days. Subsequently, neurobehaviors, PSD95 expression and dendritic spines density/morphology, and the associative regulation of FMRP and miR-125a were evaluated.

The animals were maintained in accordance with the Guide for the Care and Use of Laboratory Animals, and the study was approved by the Animal Experiment Ethics Committee of Hebei Medical University.

## Knockdown of *Fmr1* With RNA Interference

Short hairpin RNA (shRNA) targeting *Fmr1* (5′-CGCACCAAGTTGTCTCTTATA-3′) and negative control (NC) RNA were packaged into lentivirus (Genechem, China). At 30% confluency, the HT22 cells were infected with lentivirus. The culture medium was replaced with fresh medium after 8 h of infection and the cells were cultured for 48 h. Afterward, the stable clones were selected using 4.5 μg/mL puromycin. The knockdown efficiency of FMRP was about 85% by western blotting assay.

## Downregulation of miR-125a in HT22 Cells

Lipofectamine$^{TM}$ 2000 (cat#: 11668-019, Invitrogen, United States) was used to transfect 40 nM miR-125a-5p inhibitor (5′-UCACAGGUUAAAGGGUCUCAGGGA-3′) and NC inhibitor (5′-CAGUACUUUUGUGUAGUACAA-3′) (Genepharma, China) into HT22 cells, respectively. The culture medium was replaced with fresh medium after 4 h of transfection and the cells were cultured for 20 h.

## RNA Immunoprecipitation

The direct binding between FMRP and PSD95 mRNA was verified by RIP. HT22 cells were lysed on ice with a buffer (20 mM Tris–HCl PH 7.5, 150 mM NaCl, 1 mM EDTA, 0.5% NP-40) containing RNA enzyme inhibitors and protease inhibitors. The dynabeads$^{TM}$ Protein G beads (cat#: 10003D, Invitrogen, United States) with 3 μg primary anti-FMRP antibody (cat#: ab17722, Abcom, United States) or rabbit IgG (cat#: *A7016, Beyotime, China*) were incubated for 30 min and mixed with cell lysates for 12 h at 4°C by rotation. Afterward, the sample was washed. The TRIzol reagent containing protein kinase K was added and incubated at 55°C for 30 min to purify and extract RNA for the reverse transcription-polymerase chain reaction (RT-PCR) experiment.

## Reverse Transcription-Polymerase Chain Reaction

The mRNA (2 μg) of HT22 cells extracted by RIP was reverse transcribed into cDNA using the RevertAid First Strand cDNA Synthesis Kit (cat#: K1622, Thermo Scientific, United States). The conditions for reverse transcription were 42°C for 60 min and 70°C for 5 min. Subsequently, the cDNA was used for PCR using the 2 × Taq PCR MasterMix (cat#: KT201, Tiangen, China), and the following primers were used for RT-PCR: postsynaptic density protein 95 (PSD95) forward, 5′-TACCAAAGACCGTGCCAACG-3′ and PSD95 reverse, 5′-CGGCATTGGCTGAGACATCA-3′; GAPDH forward, 5′-CCGGTGCTGAGTATGTCGTG-3′ and GAPDH reverse, 5′-TGGTCATGAGCCCTTCCACA-3′. The cycling conditions were 94°C for 3 min; 38 cycles of 94°C for 30 s, 59°C for 30 s, and 72°C for 30 s; and a final extension at 72°C for 5 min. The RT-PCR products were resolved using agarose gel electrophoresis. Gel images were acquired using the Image Lab system (Bio-Rad, United States), and gray values were analyzed using the Image J software. The relative expression of PSD95 mRNA was calculated with the gray value of GAPDH mRNA as a reference.

## Western Blotting

Radioimmunoprecipitation assay (RIPA) lysis buffer containing phenylmethylsulfonyl fluoride (PMSF) was added to lyse samples, and the proteins were extracted for quantification. Proteins were separated using sodium dodecyl sulfate-polyacrylamide gel electrophoresis (SDS-PAGE) and transferred onto a polyvinylidene fluoride (PVDF) membrane. Then, the membrane was blocked using 5% milk for 2 h and incubated overnight at 4°C with the following primary antibodies: anti-PSD95 (cat#: ab18258, Abcam, United States), anti-FMRP (cat#: ab17722, Abcam, United States), and anti-β-actin (cat#: AC026, ABclonal, China). Subsequently, they were incubated with Dylight$^{TM}$ 800 goat anti-rabbit fluorescent secondary antibody (cat#: 611-145-002, Rockland, United States) at room temperature in the dark for 2 h. Finally, imaging analysis was performed using the Odyssey imaging system (LICOR, United States). The relative expression of the target protein was calculated with the gray value of β-actin as a reference.

## Quantitative Reverse Transcription-Polymerase Chain Reaction

Total miRNA of HT22 cells was extracted and isolated using the miRcute miRNA kit (cat#: DP501, Tiangen, China). cDNA was reverse transcribed using the miRcute enhanced miRNA first-strand cDNA synthesis kit (cat#: KR211, Tiangen, China). The conditions of reverse transcription were 42°C for 60 min and 95°C for 3 min. qRT-PCR was performed using miRcute enhanced miRNA fluorescence quantitation kit (SYBR Green, cat#: FP411, Tiangen, China) on a real-time PCR instrument (Thermo Fisher Scientific, United States). The $2^{-\Delta\Delta Ct}$ method was used for the qRT-PCR analysis. The expression of miR-125a was calculated with the expression of *U6* as an internal

reference. miR-125a and U6 primers were obtained from Tiangen Biotech, China.

## Immunofluorescence Cytochemistry

HT22 cells were fixed with 4% paraformaldehyde at room temperature for 15 min, blocked in 10% donkey serum at room temperature for 1 h, and incubated overnight at 4°C with the following primary antibodies: anti-PSD95 (cat#: ab18258, Abcam, United States), anti-FMRP (cat#: ab17722, Abcam, United States). Afterward, the cells were incubated with donkey anti-rabbit fluorescent secondary antibody (cat#: A21207, Invitrogen, United States) at room temperature in the dark for 2 h, counterstained with 4′,6-diamidino-2-phenylindole (DAPI) (cat#: C0065, Solarbio, China) for 10 min, and sealed with *anti*-fluorescence quenching *sealing* tablets (cat#: S2100, Solarbio, China). Images were photographed using a laser confocal microscope (Olympus, Japan), and the average optical density was analyzed using the Image J software (National Institutes of Health, United States).

## Open Field Test

Subsequently, we investigated the involvement of FMRP in androgen regulating neural behaviors using *Fmr1* KO and WT mice. The mice were put into the behavioral laboratory 1 day in advance to adapt to the test environment and reduce animal stress. SMART 3.0 software (Panlab, Spain) was used to divide the central region (25 cm × 25 cm) and the peripheral region of the open field box (50 cm × 50 cm) and record the movement distance and time of the mice in the central and peripheral region within 5 min.

## Morris Water Maze

The classic Morris water maze experiment principle is that rats or mice learn to find hidden platforms with fixed positions and form stable spatial position cognition during multiple training. This spatial cognition is formed by processing spatial information based on external cues (different marks at different positions on the inner wall of cylindrical pool). The circular pool (120 cm in diameter) was divided into four quadrants, and the platform (6 cm in diameter) was placed 1 cm underwater in either quadrant. After 2 days of adaptive training, an orientation *navigation* trial was conducted for five consecutive days. The mice were placed in the water from four quadrants facing the pool wall, and the time of finding the platform was recorded within 60 s, that is, the escape latency. If they did not find the platform within 60 s, the mice were guided to find it and stay for 1 min. On the sixth day, the spatial probe trial was conducted. The platform was removed, and the mice were put into water. The times taken by the mice crossing the position of the platform within 60 s were recorded.

## Forced Swim Test

Transparent glass cylinders (10 cm in diameter) were filled with water up to 20 cm deep. Then, the mice were put into the water-filled cylinder for 6 min, and the total floating time of the mice within 4 min was recorded. Floating time refers to when the mice have no movement other than a slight movement to maintain balance or keep their head above the water.

## Novel Object Recognition Test

Two identical objects were placed on the left and right ends of one sidewall of the open field box, and the mice were placed in a box with their backs to the objects, with the same distance from the two objects, and allowed to explore freely for 10 min. After 24 h, an original object was replaced with a new object of different color and shape. The exploration time of the mice to the two objects was recorded within 5 min, and the exploration distance was 2–3 cm from the objects. The exploration behavior refers to putting the front paw on the object, smelling the object with the nose, licking the object, etc. Holding a pose or climbing on the object without moving is not exploration of the object. The discrimination index, represented by the ratio of the exploration time of the mice to the total exploration time, was calculated.

## Three-Chamber Test

Rectangular open field boxes were separated into three chambers using transparent partitions. The partitions had a door (6 cm × 6 cm) for the free movement of the mice. The mice were habituated to the empty box before the test. To assess the sociability index, one chamber was kept empty and in the third chamber, a new mouse (Stranger) was put. The test mouse was put in the middle chamber and was allowed to explore the chambers freely for 10 min. The time to explore the two cages was recorded at 2–3 cm from the cages. The sociability index was calculated by the ratio of the time taken to explore the "Stranger" to the total time to explore the cages. Next, the social novelty preference index was estimated by putting another new mouse (Novel) in the empty cage, while the "Stranger" was renamed "Familiar." The time taken by the test mouse to explore the two cages in 10 min was recorded. Then, the social novelty preference index represented by the ratio of the time of exploring the "Novel" mouse to the total time of exploring the cages was calculated.

## Golgi Staining

After the behavioral study, mice were deeply anesthetized and transcardially perfused with 0.9% saline followed by 4% paraformaldehyde. Whole brains were extracted and postfixed in 4% paraformaldehyde for 24 h. The brains were cut from superior colliculus to optic chiasma, stained with Golgi staining kit (cat#: GMS80020.1, Genmed, China) with a fixative solution in the dark for 14 days. Subsequently, they were dehydrated in 30% sucrose solution at 4°Cfor 48 h under dark and sliced into *100* μm thick sections using oscillating tissue slicers. Brain slices were incubated with staining solution for 30 min at room temperature, followed by incubation in a chromogenic solution for 20 min at room temperature. The stained brain slices were protected from light, dehydrated, and sealed with neutral resin. Secondary and tertiary apical dendritic spines in the hippocampal CAl region were observed and imaged under a 100 × light microscope (Olympus, Japan). On the basis of morphology, spines were classified into the following

categories: (i) Thin: spines with a long neck and a visible small head; (ii) Mushroom: big spines with a well-defined neck and a very voluminous head; and (iii) Stubby: very short spines without a distinguishable neck and stubby appearance. After the dendritic spines were visually identified, Fiji software (National Institutes of Health, United States) was used to label them to prevent miscounting. Three brain slices were selected from each mouse and three neurons were selected from each brain slice.

## Immunohistochemical Staining

The mice were perfusion-fixed with PFA, and their brains were removed. The brains were cut from superior colliculus to optic chiasma, conventionally dehydrated, immersed by wax, embedded and sectioned into 5 μm thick slices. After dewaxing and hydration, the sections were subjected to high-pressure antigen repairing. Subsequently, they were blocked and incubated overnight at 4°C with anti-PSD95 antibody (cat#: ab18258, Abcam, United States). Afterward, the sections were incubated with goat anti-rabbit IgG secondary antibody (cat#: SP-9001, ZSGB-BIO, China) for 1 h, horseradish enzyme-labeled streptavidin for 1 h, followed by DAB staining and hematoxylin counterstaining. Images of hippocampal CA1 and CA3 were observed and collected under a 40 × light microscope (Leica, Germany), and the average optical density was analyzed using the Image J software (National Institutes of Health, United States).

## Silencing of miR-125a in Mice

After anesthetized, the mice were put on an electric StereoDrive (NeuroStar, Germany). Their anterior fontanelle and posterior fontanelle were fully exposed, and their lateral ventricles (left ML = −0.95 mm, AP = −0.22 mm, DV = 2.37 mm) were located by mouse brain atlas (Watson, 3rd edition) software. 5 μL of miR-125a antagomir or NC antagomir (20 μM) (miR-125a antagomir sequence: 5′-UCACAGGUUAAAGGGUCUCAGGGA-3′; NC Antagomir sequence: 5′ -CAGUACUUUUGUGUAGUACAA-3′; Genepharma, China) were injected by intracerebroventricular (icv.) injection per day for three consecutive days to knockdown the expression level of miR-125a in the hippocampus of mice. On day 7, the hippocampus or brains were collected for subsequent western blot and immunohistochemical staining.

## Statistical Analysis

All statistical analyses were performed using the SPSS 22.0 statistical software. The experimental results were expressed as mean ± standard deviation (SD). *Data were* subjected to *normality* testing using the Shapiro–Wilk *normality* test. For two-sample comparisons of normally distributed data ($p > 0.1$), Student's *t*-test was used. Data from multiple groups were subjected to the homogeneity of variances test using *Levene's test*. One-way analysis of variance (ANOVA) was performed for data with a normal distribution ($p > 0.1$) and homogeneity of variance ($p > 0.1$), and *post hoc* multiple comparisons were performed with the *SNK-q* test. Differences were considered statistically significant at $p < 0.05$.

# RESULTS

## Effects of DHT on PSD95 Protein and FMRP in HT22 Cells

Immunofluorescence cytochemical staining results showed that the fluorescence intensity of PSD95 in the DHT group was higher than that in the Ctrl group [$t_{(8)} = -9.739$, $p < 0.05$, Cohen's $d = 6.887$] (**Figures 1A,C**). On the contrary, the fluorescence intensity of FMRP in the DHT group was lower than that in the Ctrl group [$t_{(8)} = 5.080$, $p < 0.05$, Cohen's $d = 3.592$] (**Figures 1B,D**). These results were further validated using western blotting, which showed that the expression of PSD95 in the DHT group was higher than that in the Ctrl group [$t_{(8)}$ = -5.360, $p < 0.05$, Cohen's $d = 3.790$] (**Figures 1E,F**). Conversely, the expression of FMRP in the DHT group was lower than that in the Ctrl group [$t_{(8)} = 5.842$, $p < 0.05$, Cohen's $d = 4.131$] (**Figures 1G,H**). DHT upregulated the expression of synaptic protein PSD95 and downregulated the expression of FMRP, affecting both proteins, which laid a foundation for us to investigate whether FMRP mediates DHT upregulated PSD95.

## FMRP Regulates DHT Affecting the Expression of PSD95 Protein in HT22 Cells

RIP revealed that the input and FMRP groups demonstrated specific binding to the FMRP antibody, wherein only non-specific binding to the control IgG group was observed (**Figure 2A**). The enrichment of PSD95 mRNA in the FMRP group was higher than that in control IgG group [$t_{(8)} = 15.447$, $p < 0.05$, Cohen's $d = 10.923$] (**Figures 2B,C**). We also infected HT22 cells with sh-Fmr1 lentivirus to knockdown FMRP and detected its effect on PSD95. Immunofluorescence cytochemical staining showed that the fluorescence intensity of PSD95 in the sh-Fmr1 group was higher than that in the NC group [$t_{(8)} = -9.209$, $p < 0.05$, Cohen's $d = 6.512$] (**Figures 2D,F**). Western blotting results showed that the expression of PSD95 in the sh-Fmr1 group was higher than that in the NC group [$t_{(8)}$ = -5.543, $p < 0.05$, Cohen's $d = 3.919$] (**Figures 2E,G**). In addition, immunofluorescence cytochemical staining showed that fluorescence intensity of PSD95 was significantly different in all groups [$F_{(2,12)} = 1.517$, $p < 0.05$, $\eta^2 = 0.908$]. The fluorescence intensity of PSD95 in the DHT group was higher than that in the NC group but lower than that in the sh-Fmr1 + DHT group (**Figures 2H,J**). Consistent with these results, western blotting also demonstrated higher expression of PSD95 in the sh-Fmr1 + DHT group than that in the DHT and NC groups [$F_{(2,12)} = 2.159$, $p < 0.05$, $\eta^2 = 0.947$] (**Figures 2I,K**).

## FMRP and miR-125a Associatively Regulate the Effects of DHT on PSD95 Protein in HT22 Cells

FMRP knockdown enhances DHT to upregulate the expression of synaptic protein PSD95, which verifies our hypothesis. Then, to determine whether miR-125a is a downstream molecule of

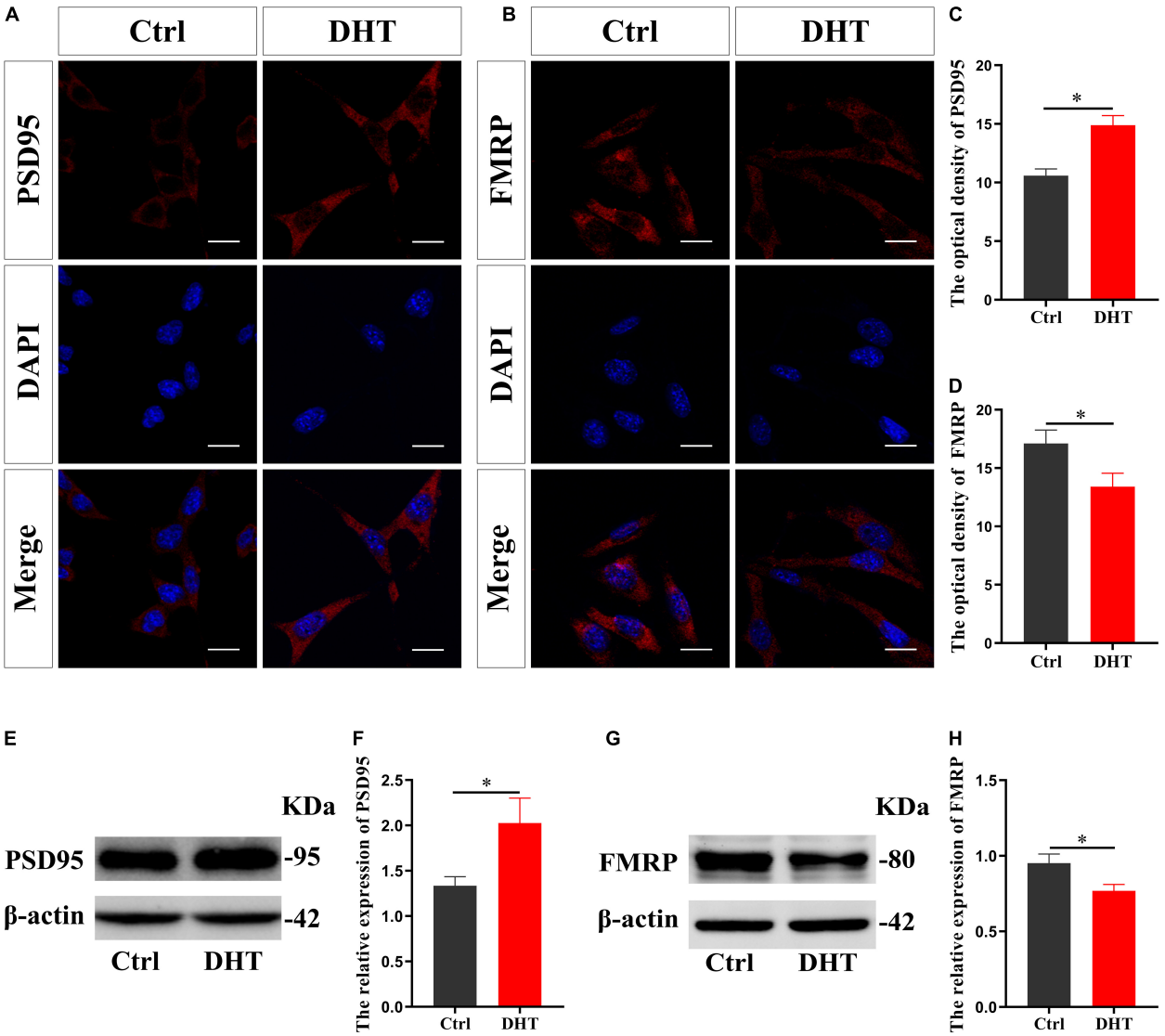


**FIGURE 1 |** Effects of DHT on PSD95 protein and FMRP in HT22 cells. **(A,C)** Immunofluorescence cytochemistry for PSD95 expression induced by DHT in HT22 cells. **(B,D)** Immunofluorescence cytochemistry for FMRP expression induced by DHT in HT22 cells. **(E,F)** Western blotting for PSD95 expression induced by DHT in HT22 cells. **(G,H)** Western blotting for FMRP expression induced by DHT in HT22 cells. Scale bars = 20 μm (*$p < 0.05$, $n = 5$).

FMRP and mediates the effects of DHT on PSD95 in HT22 cells, we conducted a series of analyses (administration process, **Figure 3A**). First, the effect of DHT on the expression of miR-125a was assessed using qRT-PCR. The expression of miR-125a in the DHT group was lower than that in the Ctrl group [$t_{(4)} = -7.133$, $p < 0.05$, Cohen's $d = 5.044$] (**Figure 3B**). Second, immunofluorescence cytochemical staining to estimate the effect of miR-125a on PSD95 revealed that the fluorescence intensity of PSD95 in the anti-miR 125a group was higher than that in the NC group [$t_{(8)} = -7.216$, $p < 0.05$, Cohen's $d = 5.102$] (**Figures 3C,D**). In addition, western blotting demonstrated higher expression of PSD95 in the anti-miR 125a group than in the NC group [$t_{(8)} = -6.455$, $p < 0.05$, Cohen's $d = 4.564$] (**Figures 3E,F**).

Next, we investigated whether miR-125a was involved in regulating the DHT-induced expression of PSD95. The fluorescence intensity of PSD95 was significantly different among all groups [$F_{(2,12)} = 0.090$, $p < 0.05$, $\eta^2 = 0.879$]. The fluorescence intensity of PSD95 in the DHT group was higher than that in the NC group. Meanwhile, the fluorescence intensity of PSD95 in the DHT + anti-miR 125a group was higher than that in the DHT group (**Figures 3G,I**). Western blotting [$F_{(2,12)} = 0.378$, $p < 0.05$, $\eta^2 = 0.887$] also revealed similar results of higher expression of PSD95 in the DHT + anti-miR 125a group than in the DHT and NC groups (**Figures 3H,J**).

Subsequently, the effect of FMRP knockdown on the expression of miR-125a was investigated. qRT-PCR showed a lower expression of miR-125a in the sh-Fmr1 group than in

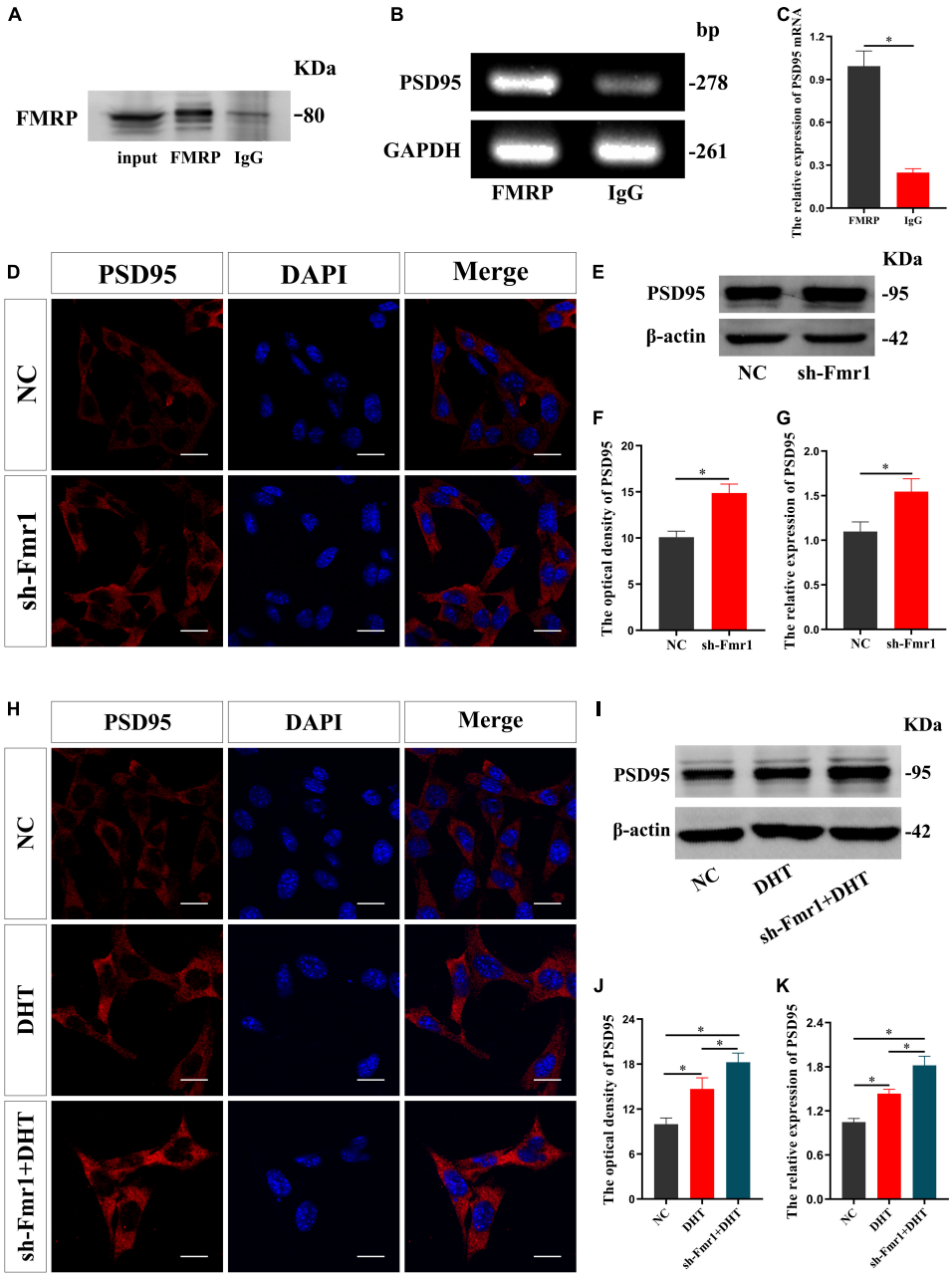


**FIGURE 2 |** FMRP regulates DHT-induced expression of PSD95 protein in HT22 cells. **(A–C)** RNA immunoprecipitation for the interaction between FMRP and PSD95 mRNA in HT22 cells. **(D,F)** Immunofluorescence cytochemistry for PSD95 expression in HT22 cells pre-treated with NC or sh-Fmr1. **(E,G)** Western blotting for PSD95 expression in HT22 cells pre-treated with NC or sh-Fmr1. **(H,J)** Immunofluorescence cytochemistry for PSD95 expression induced by DHT *via* FMRP in HT22 cells. **(I,K)** Western blotting for PSD95 expression induced by DHT *via* FMRP in HT22 cells. Scale bars = 20 μm (*$p < 0.05$, $n = 5$).

the NC group [$t_{(4)} = -7.481$, $p < 0.05$, Cohen's $d = 7.481$] (**Figure 4A**). Further, we investigated the involvement of miR-125a in regulating FMRP-mediated PSD95 expression. Immunofluorescence cytochemical staining demonstrated significantly different fluorescence intensity of PSD95 in all groups [$F_{(2,12)} = 0.476$, $p < 0.05$, $\eta^2 = 0.824$]. Particularly, the fluorescence intensity of PSD95 in the sh-Fmr1 + anti-miR 125a group was higher than that in the sh-Fmr1 and NC groups (**Figures 4B,C**). Furthermore, the results of western blotting [$F_{(2,12)} = 2.708$, $p < 0.05$, $\eta^2 = 0.816$] were consistent with the results of immunofluorescence cytochemical staining (**Figures 4D,E**).

Finally, we investigated whether FMRP and miR-125a associatively regulate the effects of DHT on PSD95 expression. Immunofluorescence cytochemical staining results showed that the fluorescence intensity of PSD95 was statistically different

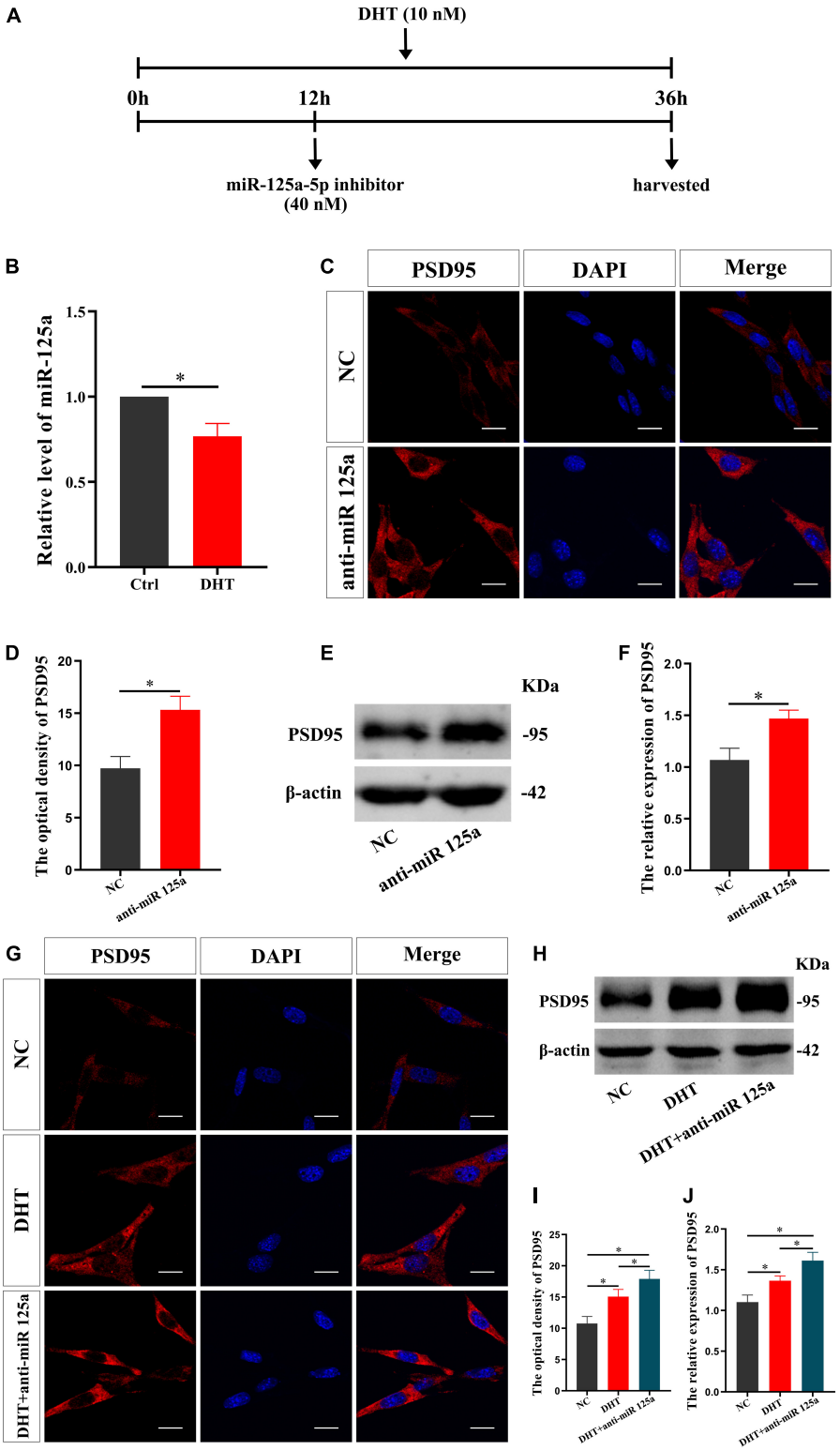


**FIGURE 3 |** miR-125a regulates DHT affecting the expression of PSD95 protein in HT22 cells. **(A)** Experimental procedure. HT22 cells were treated with DHT (10 nM) and miR-125a-5p inhibitor (40 nM). **(B)** qRT-PCR for miR-125a induced by DHT in HT22 cells. **(C,D)** Immunofluorescence cytochemistry for PSD95 expression in HT22 cells pre-treated with NC inhibitor or miR-125a-5p inhibitor. **(E,F)** Western blotting for PSD95 expression in HT22 cells pre-treated with NC or miR-125a-5p inhibitors. **(G,I)** Immunofluorescence cytochemistry for PSD95 expression induced by DHT *via* miR-125a in HT22 cells. **(H,J)** Western blotting for PSD95 expression induced by DHT *via* miR-125a in HT22 cells. Scale bars = 20 μm (*$p < 0.05$, $n = 5$).

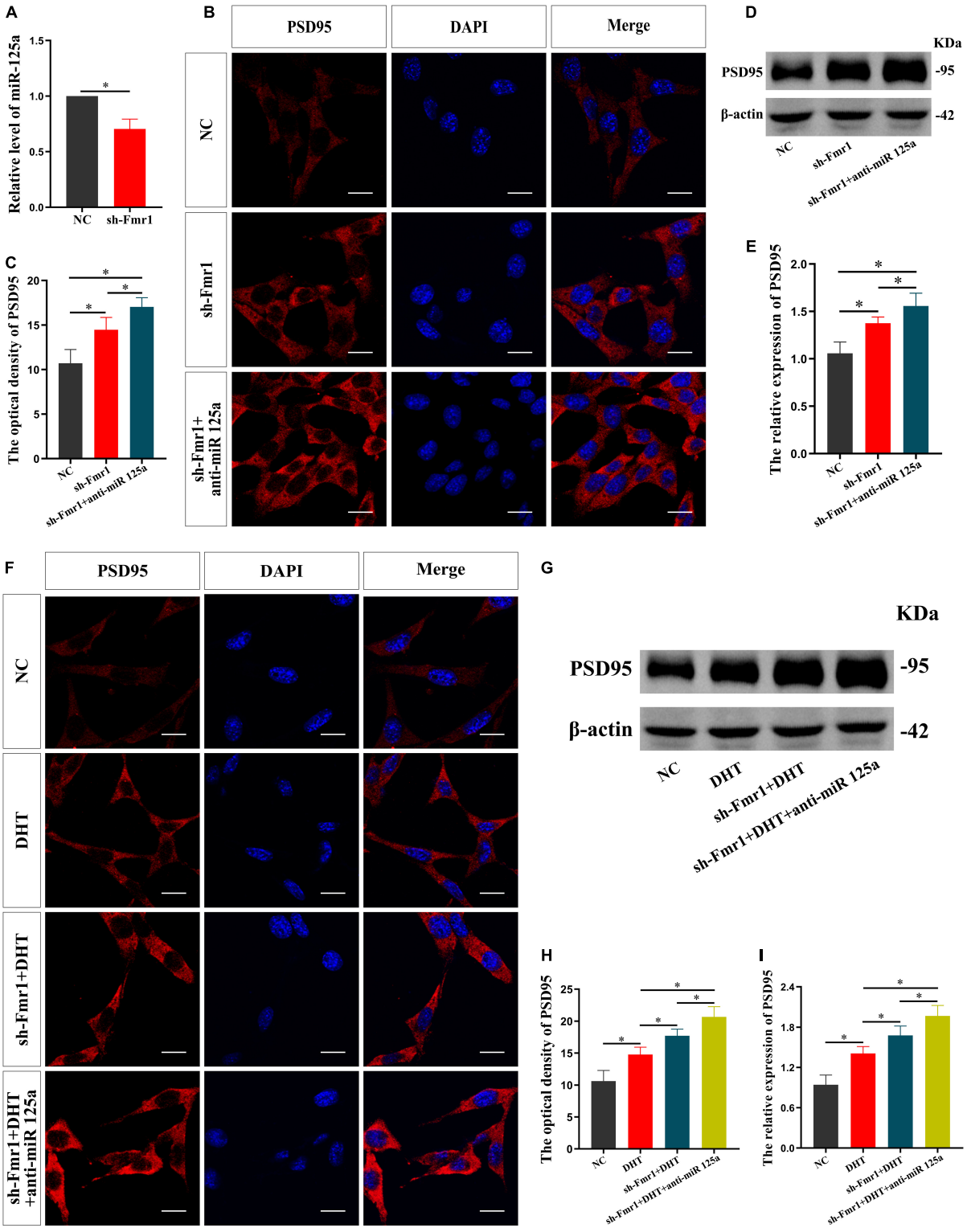


**FIGURE 4 |** FMRP mediates the effects of DHT on PSD95 through miR-125a in HT22 cells. **(A)** qRT-PCR for miR-125a induced by FMRP in HT22 cells. **(B,C)** Immunofluorescence cytochemistry for PSD95 expression in HT22 cells pre-treated with NC or sh-Fmr1 and with NC inhibitor or miR-125a-5p inhibitor. **(D,E)** Western blotting for PSD95 expression in HT22 cells pre-treated with NC or sh-Fmr1 and NC inhibitor or miR-125a-5p inhibitor. **(F,H)** Immunofluorescence cytochemistry for PSD95 expression induced by DHT in HT22 cells pre-treated with NC or sh-Fmr1 and with NC inhibitor or miR-125a-5p inhibitor. **(G,I)** Western blotting for PSD95 expression induced by DHT in HT22 cells pre-treated with NC or sh-Fmr1 and NC inhibitor or miR-125a-5p inhibitor. Scale bars = 20 μm (*$p < 0.05$, $n = 5$).

in all groups [$F_{(3,16)}$ = 0.329, $p < 0.05$, $\eta^2$ = 0.899]. The fluorescence intensity of PSD95 in the DHT group was higher than that in the NC group, whereas that in the sh-Fmr1 + DHT + anti-miR-125a group was higher than the sh-Fmr1 + DHT group (**Figures 4F,H**). Western blotting revealed similar results [$F_{(3,16)}$ = 0.608, $p < 0.05$, $\eta^2$ = 0.902] as those of immunofluorescence cytochemical staining (**Figures 4G,I**).

## Effects of Castration and DHT Supplementation on the Behaviors of *Fmr1* KO Mice

We then tested the effect of DHT on the behaviors in WT and *Fmr1* KO mice (**Figure 5A**). The OFT showed that there were statistical differences in the percentage of movement distance [$F_{(5,37)}$ = 1.702, $p < 0.05$, $\eta^2$ = 0.480] and the percentage of movement time [$F_{(5,37)}$ = 1.024, $p < 0.05$, $\eta^2$ = 0.447] in central region in all groups. The percentage of movement distance and time of the *Fmr1* KO Ctrl and WT castration group in the central region was lower than that in the WT Ctrl group. DHT supplementation increased the movement distance and time of WT mice in the central region. However, neither castration nor DHT supplementation significantly affected the movement distance and time of the *Fmr1* KO mice in the central region (**Figures 5B–D**).

The NOR test revealed significant differences in discrimination index in all groups [$F_{(5,38)}$ = 1.485, $p < 0.05$, $\eta^2$ = 0.586]. The discrimination index of mice in the *Fmr1* KO Ctrl and WT castration groups was lower than that in the WT Ctrl group. DHT supplementation increased the discrimination index of WT mice. However, neither castration nor DHT supplementation affected the discrimination index of *Fmr1* KO mice (**Figures 5E,F**).

The TCT also showed significant differences in sociability [$F_{(5,37)}$ = 0.777, $p < 0.05$, $\eta^2$ = 0.229] and social novelty preference indices [$F_{(5,37)}$ = 1.033, $p < 0.05$, $\eta^2$ = 0.674] in all groups. The sociability index of the WT castration group and the social novelty preference indices of the *Fmr1* KO Ctrl and WT castration groups were lower than that of the WT Ctrl group. DHT supplementation restored sociability and social novelty preference in WT mice. However, neither castration nor DHT supplementation affected sociability and social novelty preference in *Fmr1* KO mice (**Figures 5G–I**).

The MWM test demonstrated significant differences in escape latency on day 5 [$F_{(5,36)}$ = 0.882, $p < 0.05$, $\eta^2$ = 0.815] and number of platform crossing [$F_{(5,36)} = 0.206$, $p < 0.05$, $\eta^2 = 0.484$] in all groups. Compared with the mice in the WT Ctrl group, the escape latency of mice in the *Fmr1* KO Ctrl and WT castration groups was increased, whereas the number of platform crossings was decreased. DHT supplementation restored the learning and memory ability of the WT mice but not those in the *Fmr1* KO mice (**Figures 5J–L**).

The floating time in all groups differed significantly [$F_{(5,37)} = 1.032$, $p < 0.05$, $\eta^2 = 0.761$]. The FST test demonstrated that the floating time of mice in the *Fmr1* Ctrl and WT castration groups was higher than that in the WT Ctrl group. Although DHT supplementation reduced floating time in WT mice, neither castration nor DHT supplementation affected the floating time in *Fmr1* KO mice (**Figure 5M**).

## Effects of Castration and DHT Supplementation on Dendritic Spines of *Fmr1* KO Mice

We studied the effect of DHT on dendritic spines of hippocampal neurons in *Fmr1* KO and WT mice using Golgi staining after the behavioral experiments. The density of dendritic spines of the hippocampus was significantly different among all groups [$F_{(5,24)}$ = 0.550, $p < 0.05$, $\eta^2$ = 0.948]. The Golgi staining revealed a higher density of dendritic spines in the *Fmr1* KO Ctrl and WT castration groups than in the WT Ctrl group (**Figures 6A,B**). DHT supplementation increased the density of dendritic spines in WT mice. However, neither castration nor DHT supplementation affected the density of dendritic spines in *Fmr1* KO mice (**Figures 6A,B**).

The density of mushroom dendritic spines [$F_{(5,24)}$ = 1.413, $p < 0.05$, $\eta^2$ = 0.973] and the density of thin dendritic spines [$F_{(5,24)}$ = 0.638, $p < 0.05$, $\eta^2$ = 0.992] differed significantly in all groups; whereas no significant difference in the density of stubby dendritic spines was observed [$F_{(5,24)}$ = 2.254, $p < 0.05$, $\eta^2$ = 0.079]. Compared with the WT Ctrl group, the density of mushroom dendritic spines in the *Fmr1* KO Ctrl group decreased, and that of the thin dendritic spines increased. The density of mushroom and thin dendritic spines in the WT castration group was lower than that in the WT Ctrl group. DHT supplementation increased the density of mushroom and thin dendritic spines in WT mice; however, no changes were observed in *Fmr1* KO mice either after castration or after DHT supplementation (**Figures 6A,C**).

## FMRP and miR-125a Associatively Regulate the Effects of DHT on PSD95 Protein in *Fmr1* KO Mice

We then verified whether FMRP mediates the effects of DHT on synaptic protein PSD95 in *Fmr1* KO and WT mice through miR-125a, and whether the results were consistent with cells (**Figure 7A**). Immunohistochemical staining demonstrated significant differences in the expression of PSD95 in hippocampal CA1 region [$F_{(7,32)}$ = 1.494, $p < 0.05$, $\eta^2$ = 0.926] and CA3 region [$F_{(7,32)}$ = 0.414, $p < 0.05$, $\eta^2$ = 0.914] in all groups. PSD95 expression in hippocampal CA1 and CA3 regions of the WT castration group was decreased compared with that in the hippocampal CA1 and CA3 regions of the WT Ctrl group. However, DHT supplementation recovered the PSD95 expression of WT mice, its expression in *Fmr1* KO mice did not change after castration or DHT supplementation. Notably, antagomir treatment considerably increased the expression of PSD95 in hippocampal CA1 and CA3 regions of WT DHT + anta-125a and *Fmr1* KO DHT + anta-125a groups than in the hippocampal CA1 and CA3 regions of the WT Ctrl and WT DHT groups (**Figures 7B–E**).

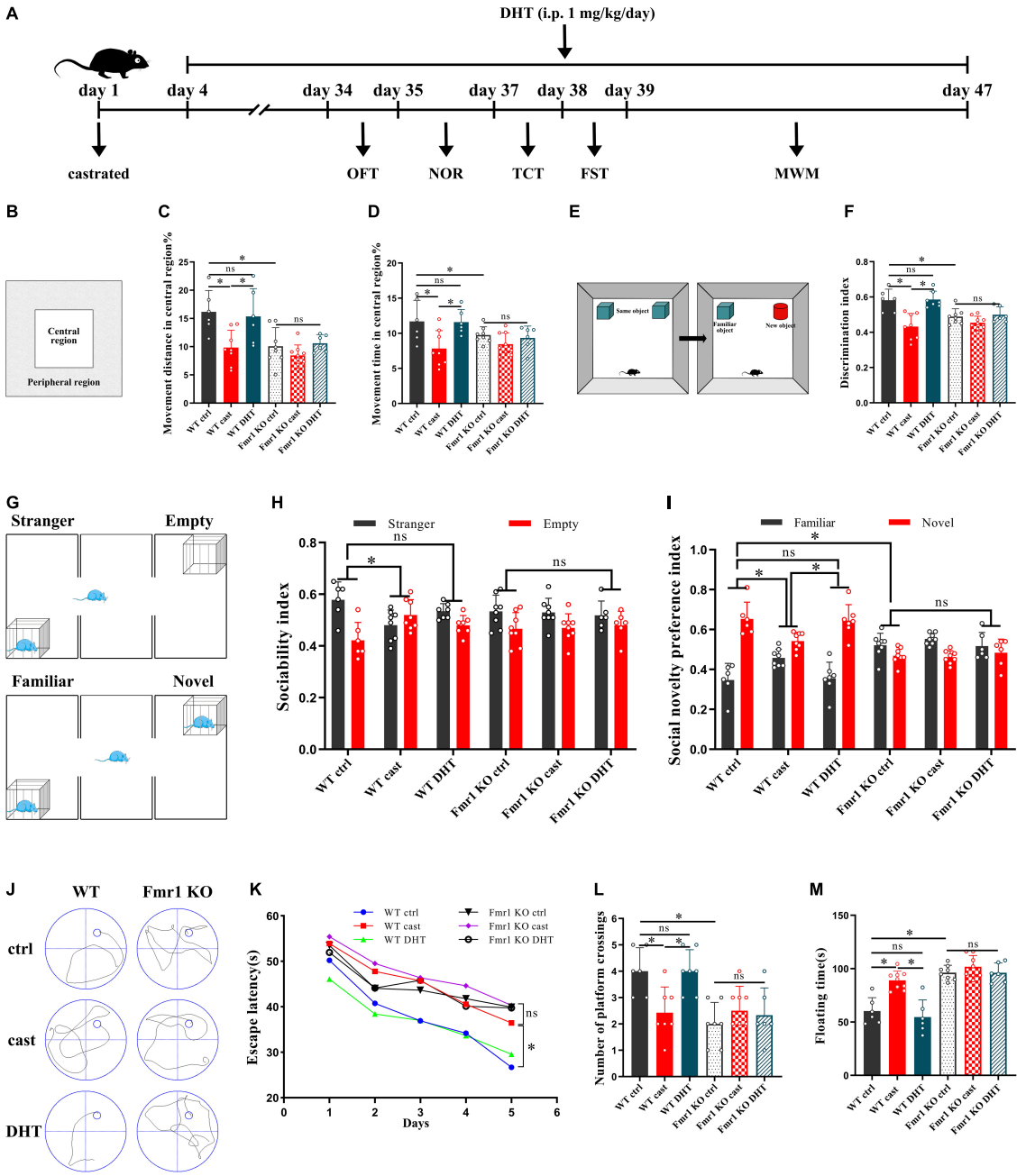


**FIGURE 5 |** Effects of castration and DHT supplementation on the behaviors of *Fmr1* KO mice. **(A)** Experimental procedure. Mice were treated with castration, DHT (i.p., 1 mg/kg/day), and behavioral tests. **(B)** Schematic diagram of the OFT. **(C,D)** OFT was performed to assess exploratory behavior. **(E)** Schematic diagram of the NOR. **(F)** NOR was performed to assess memory retention. **(G)** Schematic diagram of the TCT. **(H,I)** TCT was performed to test for sociability and social novelty preference. **(J)** Trajectories of the MWM (the 5th day). **(K,L)** MWM was performed to test for learning and memory. **(M)** FST was performed to assess depressive-like behavior (*$p < 0.05$).

These results were further confirmed by western blotting. The expression of PSD95 in hippocampus was significantly different in all groups [$F_{(7,32)} = 1.172$, $p < 0.05$, $\eta^2 = 0.947$]. The expression of PSD95 in the hippocampus of the WT castration group was lower than that in the hippocampus of the WT Ctrl group. DHT supplementation recovered the PSD95 expression in WT mice; however, there was no effect of castration or DHT supplementation on the expression of PSD95 in *Fmr1* KO mice. Moreover, antagomir treatment increased the expression of PSD95 in the hippocampus of WT DHT + anta-125a and *Fmr1* KO DHT + anta-125a groups compared with that in the hippocampus of WT Ctrl and WT DHT groups (**Figures 7F,G**).

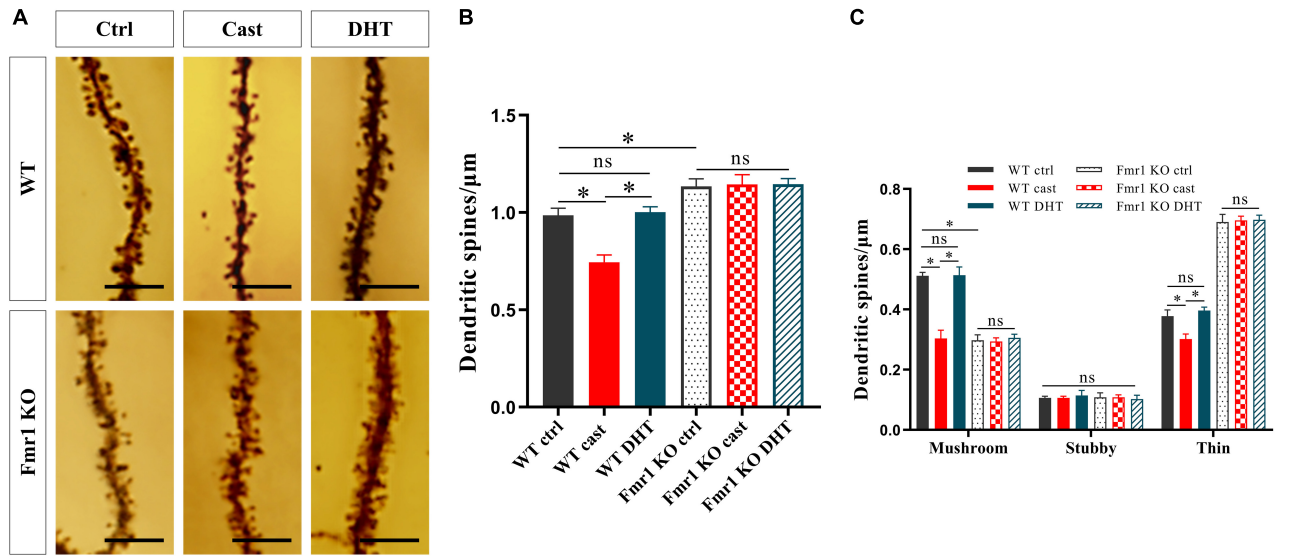


**FIGURE 6 |** Effects of castration and DHT supplementation on dendritic spines of *Fmr1* KO mice. **(A)** Golgi staining of hippocampal CA1 pyramidal neurons for dendritic spine counting after behaviors. Scale bars = 5 μm. **(B)** Quantification of dendritic spine density in hippocampal CA1 pyramidal neurons calculated as the number of spines per 1 μm of dendrite. **(C)** Quantification of mushroom, stubby, and thin dendritic spine density in hippocampal CA1 pyramidal neurons calculated as the number of spines per 1 μm of the dendrite (*$p < 0.05$, $n = 5$).

According to the result, we draw the integration diagram of FMRP and miR-125a associatively regulating the effects of DHT on PSD95 expression and dendritic spines density/morphology and autism-like behaviors (**Figure 8**).

## DISCUSSION

Autism is a complex neurodevelopmental disorder commonly seen in children (Silverman et al., 2010). Since its first recognition and naming in 1943 (Kanner, 1943), the understanding of the etiology of autism has been deepened with extensive research conducted, starting from the initial biology to psychology and then to the present genetics. Accumulating evidence shows that FXS is the most common genetic intellectual disorder and the most major single-gene genetic disorder causing autism (Mila et al., 2018). It is caused by the abnormal methylation of CpG island upstream caused by unstable amplification of CGG repeats in the 5′ untranslated region (UTR) of *Fmr1* gene on the X chromosome, resulting in *Fmr1* transcriptional silencing and loss of protein product FMRP (Sutcliffe et al., 1992). FMRP is highly expressed in the mammalian central nervous system and is located in the cell body and dendrites of neurons (Zhang et al., 2015). As an RNA-binding protein, FMRP directly binds to the mRNAs of a large number of genes related to neural development and remodeling in a variety of ways and regulates protein synthesis and function, thus affecting the development of neuronal dendrites and dendritic spines, and synaptic plasticity (Jin and Warren, 2003; Vita et al., 2021). Zhang et al. (Reeve et al., 2008; Yao et al., 2011) found that dFMRP encoded by Drosophila *dfmr1* gene (homologous gene of human *Fmr1* gene) can regulate synaptic development. The studies on cadaveric brain tissues of FXS patients found abnormal development of dendritic spines, and an increase of dendritic spines on the apical and basal dendrites of neurons was observed in multiple cortical regions (Hinton et al., 1991). Loss of FMRP may result in dysplasia or impaired elimination of dendritic spines, providing important information to unravel the molecular mechanism of abnormal development of dendritic spines and synaptic dysfunction.

Sex hormones play an important role in brain structural (Hara et al., 2015; Hyer et al., 2018) and functional development (Okamoto et al., 2012) and sexual dimorphism (Marrocco and McEwen, 2016). Androgen levels were higher in autistic people than non-autistic (Majewska et al., 2014; Needham et al., 2021). But there is a great difference in behavior between males and females with autism. Males with autism show more explicit behavioral problems, such as aggressive behavior (Neuhaus et al., 2022), excessive activity, stereotypical behavior, and narrow interests (Knutsen et al., 2019). Women with autism had more severe internalized symptoms, such as anxiety, depression (Werling and Geschwind, 2013), social problems, attention problems, and thought problems (Holtmann et al., 2007), but there were no gender differences in core autism symptoms in childhood, suggesting that abnormal sex hormone levels may be responsible for differences in behavior and brain structure.

Androgens play a role in regulating synaptic plasticity (Tozzi et al., 2019). The density of dendritic spines in the CA1 region of the hippocampus decreased significantly after castration in mice. Androgen supplementation increased the density of dendritic spines to the same level as that of animals with intact gonads (Li et al., 2015). Further, the effect of androgens on hippocampal synaptic plasticity does not depend on estrogen conversion because aromatase inhibitors do not affect androgens. In contrast, androgen antagonists attenuated the effect of androgen on

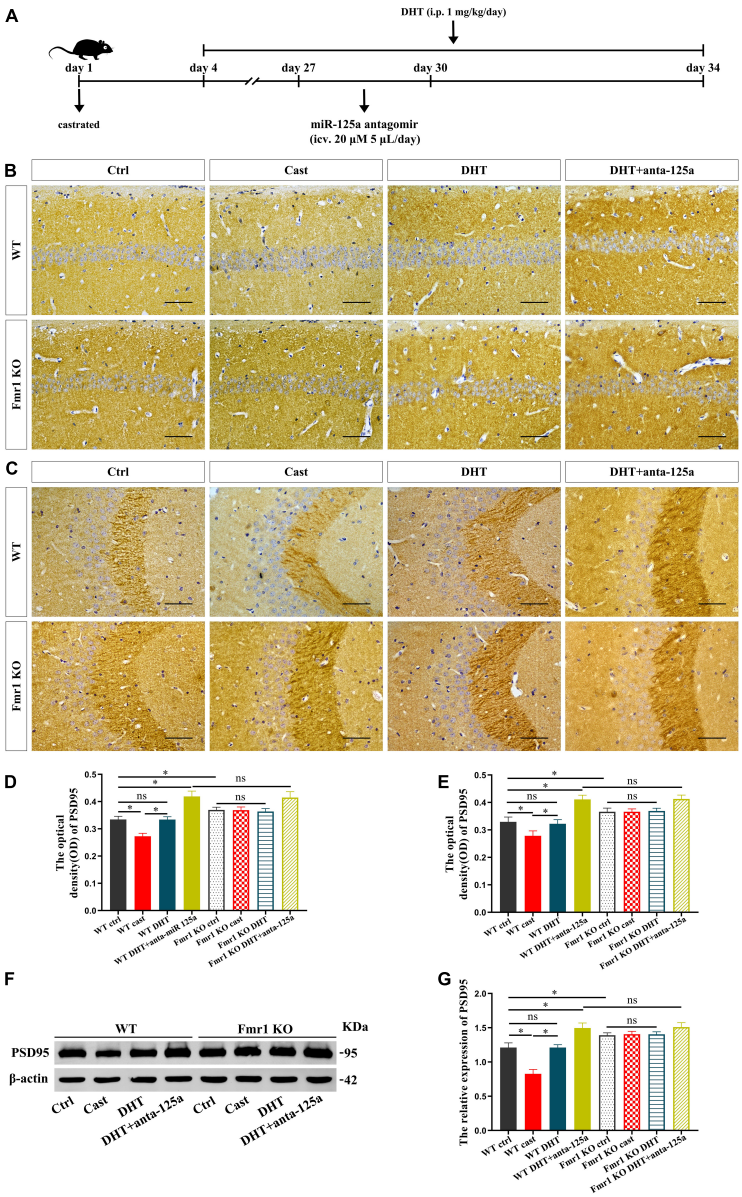


**FIGURE 7 |** FMRP and miR-125a associatively regulate the effects of DHT on PSD95 protein in *Fmr1* KO mice. **(A)** Experimental procedure. Mice were treated with castration and DHT (i.p. 1 mg/kg/day), and miR-125a antagomir (icv. 20 μm, 5 μL/day). **(B,C)** Immunohistochemical staining for PSD95 of hippocampal CA1 and CA3 pyramidal neurons induced by DHT pre-treated with miR-125a antagomir or NC antagomir. **(D,E)** Graphs show the average optical density values of PSD95 protein of hippocampal CA1 and CA3 pyramidal neurons. **(F)** Western blotting for PSD95 of hippocampus induced by DHT pre-treated with miR-125a antagomir or NC antagomir. **(G)** Graphs show the relative expression of PSD95 protein of the hippocampus. Scale bars = 50 μm (*$p < 0.05$, $n = 5$).

dendritic spines. These findings suggest that androgens play an important role in maintaining the normal density of dendritic spines in the male hippocampus. However, the effects of androgens on synaptic plasticity are different in different animal models and different types of synapses (Moser et al., 1994; Skucas et al., 2013; Li et al., 2015). To explore the regulatory role and importance of androgens in the development of dendritic spines and abnormal behaviors in the brain of autistic individuals, in this study, a non-aromatizable androgen DHT was used as an intervening drug.

PSD95 is one of the most important proteins in the postsynaptic density (PSD) family. Its main function is to maintain the balance between excitatory and inhibitory synapses (Smith et al., 2017) and to participate in synapse development (Lambert et al., 2017) and synaptic plasticity (Zeng et al., 2016; Wang et al., 2021) through signal transduction and integration (Tulodziecka et al., 2016; Ren et al., 2019). Neurobiological studies have shown that autism is not a localized injury to a specific brain region but a structural abnormality of the entire brain during early development (Courchesne et al., 2005).

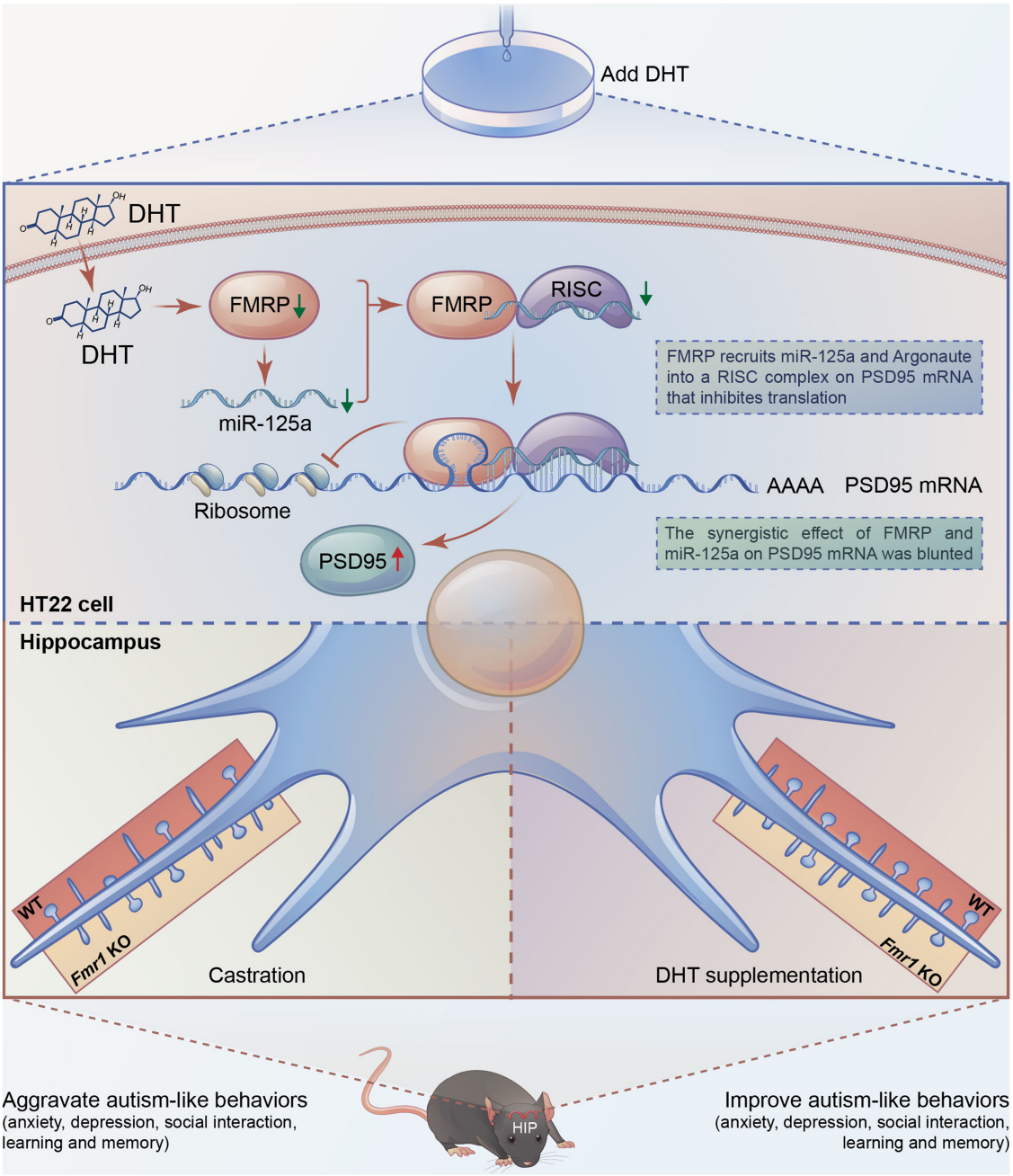


**FIGURE 8 |** Integration of FMRP and miR-125a associatively regulating the effects of DHT on synaptic plasticity and autism-like behaviors.

The most common neuroanatomical feature of autism is the excessive growth and accelerated brain volume development in early childhood, leading to neural network connections changes (Courchesne et al., 2003). Studies have also demonstrated an imbalance of excitatory/inhibitory synapses in the central nervous system of autism patients (Jeckel et al., 2021). For example, Tsai et al. (2012) have shown that multiple autism-related genes can promote the elimination of excitatory synapses by regulating proteasome degradation of PSD95, which is conducive to improving synaptic plasticity in autism. Further, it has also been shown that the downregulation of postsynaptic FMRP leads to increased inhibitory synapses and decreased excitatory synapses. These results in abnormal synaptogenesis, the imbalance of the ratio of excitatory and inhibitory neurons, and alteration in the development of neural network connections (Yang et al., 2021).

In this study, we found that DHT increased PSD95 expression and decreased FMRP expression. After *Fmr1* knockdown in HT22 cells, the expression of PSD95 protein was elevated. However, when the HT22 cells with *Fmr1* knockdown were

treated with DHT intervention, the expression of PSD95 protein was higher than that of the DHT alone intervention group, suggesting that FMRP was involved in regulating DHT affecting the expression of PSD95 in HT22 cells. Experimental results of mice demonstrated that castration decreased the androgen level, expression of PSD95, the density of dendritic spines, altered the maturity of dendritic spines, aggravated anxiety and depression, impaired learning memory function, and social ability in WT mice. However, these effects were recovered with DHT supplementation in WT mice. On the contrary, in *Fmr1* KO mice, neither castration nor DHT supplementation affected PSD95 protein expression, density, maturity of dendritic spines, and neurobehaviors.

In this study, we demonstrated that DHT decreased the expression of miR-125a in HT22 cells, and the expression of PSD95 protein increased after inhibition of miR-125a. In addition, DHT significantly upregulated the expression of PSD95 protein in the hippocampus of WT mice silenced miR-125a by antagomir injected into the lateral ventricle compared with the groups without miR-125a intervention. These results demonstrated that both FMRP and miR-125a are involved in DHT-induced PSD95 protein expression. These findings indicated that a mechanism of interaction between FMRP and miR-125a might be important for understanding the neurodevelopmental disorders such as autism caused by the imbalance of the post-transcriptional translation process due to abnormal androgen levels.

The study provided further insights into such interactions. We showed that *Fmr1* knockdown reduced the expression of miR-125a in HT22 cells, and the expression of PSD95 protein in the *Fmr1* and miR-125a knockdown group was significantly higher than that in the *Fmr1* knockdown group. These results suggest that miR-125a is involved in the process of FMRP regulating PSD95 protein translation. However, these results could not precisely clarify the interaction mechanism between FMRP and miR-125a. It has been reported that FMRP affects the rapid and reversible regulation of the miR-125a-mediated translation process, and FMRP phosphorylation promotes the formation of miR-125a-AGO2 translation repressor complex on PSD95 mRNA. Conversely, FMRP dephosphorylation activates the translation process (Muddashetty et al., 2011). Based on the associative theory between FMRP and miRNA, we studied the effect of DHT on PSD95 protein expression. It is noteworthy that our study showed that DHT significantly upregulated the expression of PSD95 in *Fmr1* and miR-125a knockdown group in HT22 cells compared with the *Fmr1* knockdown group. These observations could be explained by the fact that although *Fmr1* knockdown significantly downregulated the expression of FMRP in HT22 cells (knockdown efficiency was about 85%), it was partially expressed. Conversely, in *Fmr1* KO mice, FMRP was completely downregulated; therefore, DHT-induced upregulation in PSD95 protein expression, density and maturity of dendritic spines, and neurobehaviors mediated *via* FMRP was inhibited. These results indicate that FMRP mediated the effects of DHT on the expression of PSD95 protein and dendritic spines density/morphology through miR-125a.

## CONCLUSION

In conclusion, a series of analyses were conducted to understand the effects of androgens regulating the expression of PSD95 and the maturity of dendritic spines and autism-like behaviors. The analyses revealed that FMRP targeting PSD95 mRNA inhibits the translation of PSD95 protein through miR-125a. This study provides a basis for further studies to understand the interaction between miRNA and FMRP and its role in the dynamic and bidirectional control of excitatory postsynaptic protein translation and synthesis that affects the structure and function of synapses, which has broad significance for neurodevelopmental disorders such as autism, including FXS with abnormal androgen levels. Collectively, we suggest that androgen intervention strategies can be considered to prevent and treat neurodevelopmental disorders; however, further studies should ascertain the effects.

## DATA AVAILABILITY STATEMENT

The original contributions presented in the study are included in the article/supplementary material, further inquiries can be directed to the corresponding author/s.

## ETHICS STATEMENT

The animal study was reviewed and approved by Hebei Medical University Laboratory Animal Welfare and Ethics Committee.

## AUTHOR CONTRIBUTIONS

HC and DQ performed the experimental phase, methodology, data curation, and writing-original draft. CW, BZ, ZW, YW, and RZ performed the experimental phase. YZ, LS, HZ, FG, and XW contributed to the investigation and visualization. LT contributed to the statistical support. SL and HC designed the study, writing-review, editing, project administration, and funding acquisition. All authors contributed to the article and approved the submitted.

## FUNDING

This work was supported by the National Natural Science Foundation of China (82171582 and 91849134), Natural Science Foundation of Hebei Province (C2020206044 and H2018206361), and Science and Technology Research Foundation for Universities in Hebei Province (ZD2020105).

## REFERENCES


Ashley, C. T. Jr., Wilkinson, K. D., Reines, D., and Warren, S. T. (1993). FMR1 protein: conserved RNP family domains and selective RNA binding. *Science* 262, 563–566. doi: 10.1126/science.7692601

Baby, N., Alagappan, N., Dheen, S. T., and Sajikumar, S. (2020). MicroRNA-134-5p inhibition rescues long-term plasticity and synaptic tagging/capture in an Abeta(1-42)-induced model of Alzheimer's disease. *Aging Cell* 19:e13046. doi: 10.1111/acel.13046

Bai, D., Yip, B. H. K., Windham, G. C., Sourander, A., Francis, R., Yoffe, R., et al. (2019). Association of genetic and environmental factors with autism in a 5-country cohort. *JAMA Psychiatry* 76, 1035–1043. doi: 10.1001/jamapsychiatry.2019.1411

Banerjee, A., Ifrim, M. F., Valdez, A. N., Raj, N., and Bassell, G. J. (2018). Aberrant RNA translation in fragile X syndrome: from FMRP mechanisms to emerging therapeutic strategies. *Brain Res.* 1693, 24–36. doi: 10.1016/j.brainres.2018.04.008

Chaste, P., and Leboyer, M. (2012). Autism risk factors: genes, environment, and gene-environment interactions. *Dialogues Clin. Neurosci.* 14, 281–292. doi: 10.31887/DCNS.2012.14.3/pchaste

Courchesne, E., Carper, R., and Akshoomoff, N. (2003). Evidence of brain overgrowth in the first year of life in autism. *JAMA* 290, 337–344. doi: 10.1001/jama.290.3.337

Courchesne, E., Redcay, E., Morgan, J. T., and Kennedy, D. P. (2005). Autism at the beginning: microstructural and growth abnormalities underlying the cognitive and behavioral phenotype of autism. *Dev. Psychopathol.* 17, 577–597. doi: 10.1017/S0954579405050285

Daniels, J., Schwartz, J., Albert, N., Du, M., and Wall, D. P. (2017). The GapMap project: a mobile surveillance system to map diagnosed autism cases and gaps in autism services globally. *Mol. Autism* 8:55. doi: 10.1186/s13229-017-0163-7

Hara, Y., Waters, E. M., McEwen, B. S., and Morrison, J. H. (2015). Estrogen effects on cognitive and synaptic health over the lifecourse. *Physiol. Rev.* 95, 785–807. doi: 10.1152/physrev.00036.2014

Hinton, V. J., Brown, W. T., Wisniewski, K., and Rudelli, R. D. (1991). Analysis of neocortex in three males with the fragile X syndrome. *Am. J. Med. Genet.* 41, 289–294. doi: 10.1002/ajmg.1320410306

Holtmann, M., Bölte, S., and Poustka, F. (2007). Autism spectrum disorders: sex differences in autistic behaviour domains and coexisting psychopathology. *Dev. Med. Child Neurol.* 49, 361–366. doi: 10.1111/j.1469-8749.2007.00361.x

Hu, Z., and Li, Z. (2017). miRNAs in synapse development and synaptic plasticity. *Curr. Opin. Neurobiol.* 45, 24–31. doi: 10.1016/j.conb.2017.02.014

Hyer, M. M., Phillips, L. L., and Neigh, G. N. (2018). Sex Differences in Synaptic Plasticity: Hormones and Beyond. *Front. Mol. Neurosci.* 11:266. doi: 10.3389/fnmol.2018.00266

Jawaid, S., Kidd, G. J., Wang, J., Swetlik, C., Dutta, R., and Trapp, B. D. (2018). Alterations in CA1 hippocampal synapses in a mouse model of fragile X syndrome. *Glia* 66, 789–800. doi: 10.1002/glia.23284

Jeckel, P., Kriebel, M., and Volkmer, H. (2021). Autism spectrum disorder risk factor met regulates the organization of inhibitory synapses. *Front. Mol. Neurosci.* 14:659856. doi: 10.3389/fnmol.2021.659856

Jin, P., and Warren, S. T. (2003). New insights into fragile X syndrome: from molecules to neurobehaviors. *Trends Biochem. Sci.* 28, 152–158. doi: 10.1016/S0968-0004(03)00033-1

Kanner, L. (1943). Autistic disturbances of affective contact. *Nerv. Child* 2, 217–250.

Knutsen, J., Crossman, M., Perrin, J., Shui, A., and Kuhlthau, K. (2019). Sex differences in restricted repetitive behaviors and interests in children with autism spectrum disorder: an autism treatment network study. *Autism* 23, 858–868. doi: 10.1177/1362361318786490

Lambert, J. T., Hill, T. C., Park, D. K., Culp, J. H., and Zito, K. (2017). Protracted and asynchronous accumulation of PSD95-family MAGUKs during maturation of nascent dendritic spines. *Dev. Neurobiol.* 77, 1161–1174. doi: 10.1002/dneu.22503

Levy, S. E., Mandell, D. S., and Schultz, R. T. (2009). Autism. *Lancet* 374, 1627–1638. doi: 10.1016/S0140-6736(09)61376-3

Li, S., Kang, L., Zhang, Y., Feng, B., Du, J., and Cui, H. (2015). Detecting the presence of hippocampus membrane androgen receptors in male SAMP8 mice and their induced synaptic plasticity. *Mol. Cell. Endocrinol.* 414, 82–90. doi: 10.1016/j.mce.2015.07.005

Lu, J., Zhu, Y., Williams, S., Watts, M., Tonta, M. A., Coleman, H. A., et al. (2020). Autism-associated miR-873 regulates ARID1B, SHANK3 and NRXN2 involved in neurodevelopment. *Transl. Psychiatry* 10:418. doi: 10.1038/s41398-020-01106-8

Mai, H., Fan, W., Wang, Y., Cai, Y., Li, X., Chen, F., et al. (2019). Intranasal administration of miR-146a agomir rescued the pathological process and cognitive impairment in an AD mouse model. *Mol. Ther. Nucleic Acids* 18, 681–695. doi: 10.1016/j.omtn.2019.10.002

Majewska, M. D., Hill, M., Urbanowicz, E., Rok-Bujko, E. P., Bieńkowski, P., Namysłowska, I., et al. (2014). Marked elevation of adrenal steroids, especially androgens, in saliva of prepubertal autistic children. *Eur. Child Adolesc. Psychiatry* 23, 485–498. doi: 10.1007/s00787-013-0472-0

Marrocco, J., and McEwen, B. S. (2016). Sex in the brain: hormones and sex differences. *Dialogues Clin. Neurosci.* 18, 373–383. doi: 10.31887/DCNS.2016.18.4/jmarrocco

Mila, M., Alvarez-Mora, M. I., Madrigal, I., and Rodriguez-Revenga, L. (2018). Fragile X syndrome: an overview and update of the FMR1 gene. *Clin. Genet.* 93, 197–205. doi: 10.1111/cge.13075

Moser, M. B., Trommald, M., and Andersen, P. (1994). An increase in dendritic spine density on hippocampal CA1 pyramidal cells following spatial learning in adult rats suggests the formation of new synapses. *Proc. Natl. Acad. Sci. U. S. A.* 91, 12673–12675. doi: 10.1073/pnas.91.26.12673

Muddashetty, R. S., Nalavadi, V. C., Gross, C., Yao, X., Xing, L., Laur, O., et al. (2011). Reversible inhibition of PSD-95 mRNA translation by miR-125a, FMRP phosphorylation, and mGluR signaling. *Mol. Cell* 42, 673–688. doi: 10.1016/j.molcel.2011.05.006

Needham, B. D., Adame, M. D., Serena, G., Rose, D. R., Preston, G. M., Conrad, M. C., et al. (2021). Plasma and fecal metabolite profiles in autism spectrum disorder. *Biol. Psychiatry* 89, 451–462. doi: 10.1016/j.biopsych.2020.09.025

Neuhaus, E., Kang, V. Y., Kresse, A., Corrigan, S., Aylward, E., Bernier, R., et al. (2022). Language and aggressive behaviors in male and female youth with autism spectrum disorder. *J. Autism Dev. Disord.* 52, 454–462. doi: 10.1007/s10803-020-04773-0

Nia, F. H., Woike, D., Martens, V., Klussendorf, M., Honck, H. H., Harder, S., et al. (2020). Targeting of delta-catenin to postsynaptic sites through interaction with the Shank3 N-terminus. *Mol. Autism* 11:85. doi: 10.1186/s13229-020-00385-8

Okamoto, M., Hojo, Y., Inoue, K., Matsui, T., Kawato, S., McEwen, B. S., et al. (2012). Mild exercise increases dihydrotestosterone in hippocampus providing evidence for androgenic mediation of neurogenesis. *Proc. Natl. Acad. Sci. U. S. A.* 109, 13100–13105. doi: 10.1073/pnas.1210023109

Reeve, S. P., Lin, X., Sahin, B. H., Jiang, F., Yao, A., Liu, Z., et al. (2008). Mutational analysis establishes a critical role for the N terminus of fragile X mental retardation protein FMRP. *J. Neurosci.* 28, 3221–3226. doi: 10.1523/JNEUROSCI.5528-07.2008

Ren, E., Roncace, V., Trazzi, S., Fuchs, C., Medici, G., Gennaccaro, L., et al. (2019). Functional and structural impairments in the perirhinal cortex of a mouse model of CDKL5 deficiency disorder are rescued by a TrkB agonist. *Front. Cell. Neurosci.* 13:169. doi: 10.3389/fncel.2019.00169

Silverman, J. L., Yang, M., Turner, S. M., Katz, A. M., Bell, D. B., Koenig, J. I., et al. (2010). Low stress reactivity and neuroendocrine factors in the BTBR T+tf/J mouse model of autism. *Neuroscience* 171, 1197–1208. doi: 10.1016/j.neuroscience.2010.09.059

Skucas, V. A., Duffy, A. M., Harte-Hargrove, L. C., Magagna-Poveda, A., Radman, T., Chakraborty, G., et al. (2013). Testosterone depletion in adult male rats increases mossy fiber transmission, LTP, and sprouting in area CA3 of hippocampus. *J. Neurosci.* 33, 2338–2355. doi: 10.1523/JNEUROSCI.3857-12.2013

Smith, K. R., Jones, K. A., Kopeikina, K. J., Burette, A. C., Copits, B. A., Yoon, S., et al. (2017). Cadherin-10 maintains excitatory/inhibitory ratio through interactions with synaptic proteins. *J. Neurosci.* 37, 11127–11139. doi: 10.1523/JNEUROSCI.1153-17.2017

Sokol, D. K., Maloney, B., Long, J. M., Ray, B., and Lahiri, D. K. (2011). Autism, Alzheimer disease, and fragile X: APP, FMRP, and mGluR5 are molecular links. *Neurology* 76, 1344–1352. doi: 10.1212/WNL.0b013e3182166dc7

Sugathan, A., Biagioli, M., Golzio, C., Erdin, S., Blumenthal, I., Manavalan, P., et al. (2014). CHD8 regulates neurodevelopmental pathways associated with autism spectrum disorder in neural progenitors. *Proc. Natl. Acad. Sci. U. S. A.* 111, E4468–E4477. doi: 10.1073/pnas.1405266111

Sutcliffe, J. S., Nelson, D. L., Zhang, F., Pieretti, M., Caskey, C. T., Saxe, D., et al. (1992). DNA methylation represses FMR-1 transcription in fragile X syndrome. *Hum. Mol. Genet.* 1, 397–400. doi: 10.1093/hmg/1.6.397

Tozzi, A., Durante, V., Manca, P., Mauro, M. D., Blasi, J., Grassi, S., et al. (2019). Bidirectional synaptic plasticity is driven by sex neurosteroids targeting estrogen and androgen receptors in hippocampal CA1 pyramidal neurons. *Front. Cell. Neurosci.* 13:534. doi: 10.3389/fncel.2019.00534

Tsai, N. P., Wilkerson, J. R., Guo, W., Maksimova, M. A., DeMartino, G. N., Cowan, C. W., et al. (2012). Multiple autism-linked genes mediate synapse elimination via proteasomal degradation of a synaptic scaffold PSD-95. *Cell* 151, 1581–1594. doi: 10.1016/j.cell.2012.11.040

Tulodziecka, K., Diaz-Rohrer, B. B., Farley, M. M., Chan, R. B., Paolo, G. D., Levental, K. R., et al. (2016). Remodeling of the postsynaptic plasma membrane during neural development. *Mol. Biol. Cell* 27, 3480–3489. doi: 10.1091/mbc.E16-06-0420

Vita, D. J., Meier, C. J., and Broadie, K. (2021). Neuronal fragile X mental retardation protein activates glial insulin receptor mediated PDF-Tri neuron developmental clearance. *Nat. Commun.* 12:1160. doi: 10.1038/s41467-021-21429-4

Wang, Y., Fu, W. Y., Cheung, K., Hung, K. W., Chen, C., Geng, H., et al. (2021). Astrocyte-secreted IL-33 mediates homeostatic synaptic plasticity in the adult hippocampus. *Proc. Natl. Acad. Sci. U. S. A.* 118:e2020810118. doi: 10.1073/pnas.2020810118

Werling, D. M., and Geschwind, D. H. (2013). Sex differences in autism spectrum disorders. *Curr. Opin. Neurol.* 26, 146–153. doi: 10.1097/WCO.0b013e32835ee548

Yang, K., Shi, Y., Du, X., Wang, J., Zhang, Y., Shan, S., et al. (2021). SENP1 in the retrosplenial agranular cortex regulates core autistic-like symptoms in mice. *Cell Rep.* 37:109939. doi: 10.1016/j.celrep.2021.109939

Yao, A., Jin, S., Li, X., Liu, Z., Ma, X., Tang, J., et al. (2011). Drosophila FMRP regulates microtubule network formation and axonal transport of mitochondria. *Hum. Mol. Genet.* 20, 51–63. doi: 10.1093/hmg/ddq431

Zeng, M., Shang, Y., Araki, Y., Guo, T., Huganir, R. L., and Zhang, M. (2016). Phase transition in postsynaptic densities underlies formation of synaptic complexes and synaptic plasticity. *Cell* 166, 1163–1175.e12. doi: 10.1016/j.cell.2016.07.008

Zhang, P., Abdelmohsen, K., Liu, Y., Tominaga-Yamanaka, K., Yoon, J. H., Ioannis, G., et al. (2015). Novel RNA- and FMRP-binding protein TRF2-S regulates axonal mRNA transport and presynaptic plasticity. *Nat. Commun.* 6:8888. doi: 10.1038/ncomms9888

Zhang, Y., Gaetano, C. M., Williams, K. R., Bassell, G. J., and Mihailescu, M. R. (2014). FMRP interacts with G-quadruplex structures in the 3'-UTR of its dendritic target Shank1 mRNA. *RNA Biol.* 11, 1364–1374. doi: 10.1080/15476286.2014.996464

**Conflict of Interest:** The authors declare that the research was conducted in the absence of any commercial or financial relationships that could be construed as a potential conflict of interest.

**Publisher's Note:** All claims expressed in this article are solely those of the authors and do not necessarily represent those of their affiliated organizations, or those of the publisher, the editors and the reviewers. Any product that may be evaluated in this article, or claim that may be made by its manufacturer, is not guaranteed or endorsed by the publisher.

frontiers | Frontiers in Cellular Neuroscience

ORIGINAL RESEARCH
published: 22 July 2022
doi: 10.3389/fncel.2022.906313

# Voltage-Gated Ion Channels and the Variability in Information Transfer

*Rahul Kumar Rathour and Hanoch Kaphzan**

*Sagol Department of Neurobiology, University of Haifa, Haifa, Israel*

The prerequisites for neurons to function within a circuit and be able to contain and transfer information efficiently and reliably are that they need to be homeostatically stable and fire within a reasonable range, characteristics that are governed, among others, by voltage-gated ion channels (VGICs). Nonetheless, neurons entail large variability in the expression levels of VGICs and their corresponding intrinsic properties, but the role of this variability in information transfer is not fully known. In this study, we aimed to investigate how this variability of VGICs affects information transfer. For this, we used a previously derived population of neuronal model neurons, each with the variable expression of five types of VGICs, fast $Na^+$, delayed rectifier $K^+$, A-type $K^+$, T-type $Ca^{++}$, and HCN channels. These analyses showed that the model neurons displayed variability in mutual information transfer, measured as the capability of neurons to successfully encode incoming synaptic information in output firing frequencies. Likewise, variability in the expression of VGICs caused variability in EPSPs and IPSPs amplitudes, reflected in the variability of output firing frequencies. Finally, using the virtual knockout methodology, we show that among the ion channels tested, the A-type $K^+$ channel is the major regulator of information processing and transfer.

**Keywords: active dendrites, information transfer, global sensitivity analysis, variability, voltage-gated ion channels**

OPEN ACCESS

***Edited by:***
*Michele Migliore,*
*National Research Council (CNR), Italy*

***Reviewed by:***
*Sonal Kedia,*
*Brandeis University, United States*
*Sam Neymotin,*
*Nathan Kline Institute for Psychiatric Research, United States*

****Correspondence:***
*Hanoch Kaphzan*
*hkaphzan@univ.haifa.ac.il*

***Specialty section:***
*This article was submitted to Cellular Neurophysiology, a section of the journal Frontiers in Cellular Neuroscience*

***Received:*** *28 March 2022*
***Accepted:*** *24 June 2022*
***Published:*** *22 July 2022*

***Citation:***
*Rathour RK and Kaphzan H (2022) Voltage-Gated Ion Channels and the Variability in Information Transfer. Front. Cell. Neurosci. 16:906313. doi: 10.3389/fncel.2022.906313*

## INTRODUCTION

One of the important features of neurons within a homogenous population is that they express variability in their various physiological parameters, both intrinsic and extrinsic (Marder, 2011; Marder et al., 2014; Rathour and Narayanan, 2019; Goaillard and Marder, 2021). While there are multiple studies concerning homeostasis that accounted for this variability (Goldman et al., 2001; Taylor et al., 2009; Marder and Taylor, 2011; Rathour and Narayanan, 2012, 2014), studies on information encoding/transfer in face of variability are few (Padmanabhan and Urban, 2010, 2014; Tripathy et al., 2013). The general theme that has emerged from studies on homeostasis and variability is that variability of physiological parameters between neurons is critical for maintaining the homeostasis on multiple levels, both the single neuron and circuit functioning, serving the aim of information encoding (Goldman et al., 2001; Prinz et al., 2003, 2004; Taylor et al., 2009; Padmanabhan and Urban, 2010; Marder, 2011; Marder and Taylor, 2011; Tripathy et al., 2013; Padmanabhan and Urban, 2014; Rathour and Narayanan, 2014; Anirudhan and Narayanan, 2015; Srikanth and Narayanan, 2015; Rathour et al., 2016; Mittal and Narayanan, 2018; Mishra and Narayanan, 2019; Basak and Narayanan, 2020; Jain and Narayanan, 2020; Goaillard and Marder, 2021; Roy and Narayanan, 2021).

The role of variable expression of voltage-gated ion channels in maintaining homeostasis in neuronal physiology is well established, but how this variable expression of voltage-gated ion channels and homeostasis affect information encoding/transfer is not fully understood. Variability in voltage-gated ion channels is crucial for information encoding by enabling variability in input and output processing, thereby reducing spike train correlations and redundancy in the population of neurons (Padmanabhan and Urban, 2010, 2014). Hence, understanding the effects of intrinsic variability on neuronal responses and neuronal coding is essential. Furthermore, it raises the question of whether maintaining homeostasis occurs at the expense of robust information transfer or homeostasis itself brings about robust information transfer, which has not been answered.

In this study, we aimed to investigate the relations between the variability of intrinsic properties between neurons and their ability to encode information while maintaining the intrinsic homeostasis of their functional maps—a graded progression of physiologically relevant measurement along the spatial axis of the neuron. Specifically, we asked whether maintaining homeostasis occurs at the expense of robust information transfer or homeostasis itself brings about robust information transfer.

For this, we utilized previously derived CA1 neuronal models, which showed homeostasis of six coexistent functional maps and expressed variability in five voltage-gated ion channels (Rathour and Narayanan, 2014). We found that neurons in the model population displayed variability in mutual information transfer. Likewise, we found that the input of EPSPs and IPSPs showed huge variability in their amplitudes, due to the variability in the expression of voltage-gated ion channels, which was also reflected in output processing, as firing frequencies of model neurons similarly displayed huge variability. Finally, using virtual knockout models we show that the *A*-type $K^+$ channel is the major regulator of these effects.

# RESULTS

We utilized a previously derived base model neuron and valid neuronal population ($n = 228$) (Rathour and Narayanan, 2014) to test how variability in voltage-gated ion channels (VGICs) expression in neurons affects robust information transfer. To this end, we first computed information encoding capabilities of a base model neuron (**Figure 1**), in which we employed a 3D reconstructed neuronal morphology (**Figure 1A**) expressing experimentally constrained six coexistent functional maps (Rathour and Narayanan, 2014), and included AMPA and $GABA_A$ receptor-type excitatory and inhibitory synapses (**Figure 1A**). To reduce the computational cost, we uniformly distributed an excitatory synapse only on the apical side within a distance of 303 μm from the soma, while inhibitory synapses were placed in the perisomatic region within a distance of 50 μm from soma (**Figure 1A**). This led to a total of 327 excitatory synapses and 50 inhibitory synapses. We activated these synapses in a Poisson manner at different frequencies. This led to variability in inputs.

This variability in inputs led to variable output (**Figures 1B,C**). We also generated an input–output curve for the base model (**Figure 1D**). From the input–output curve, we noted that firing frequencies were exponentially distributed (**Figure 1E**). Under rate coding schema, mutual information was computed as the ability of the model neuron to successfully encode incoming information (different stimulus frequencies) in distinct neuronal outputs (firing frequencies). To do this, we computed response and noise entropy from neuronal inputs and outputs (**Figures 1F,G**). Then, we subtracted noise entropy from response entropy to obtain mutual information (**Figure 1G**). We found that a base model neuron had good information encoding capabilities (**Figure 1G**).

## Validation of Model Population Using *F–I* Relationship

The previously derived model population was validated with respect to the experimental data of six functional maps (Rathour and Narayanan, 2014). Here, we intended to test the information encoding capabilities of the model population neurons under the rate coding schema. At first, we aimed to show that the model population is truly representative of real-world neurons. To show this, we tested the *F–I* relationship of the model population to that of the experimental counterpart. For that, we generated the *F–I* relationship of the model population by injecting current from 0 to 250 pA in steps of 50 pA for 1 s and counted the number of spikes elicited, which provided us with various firing rate profiles of the neurons. Comparisons of these firing rates against the experimental data demonstrated that firing rates were largely within the experimentally observed ranges (**Supplementary Figure S1**) [experimental data taken from Narayanan and Johnston (2007), Narayanan et al. (2010), Rathour et al. (2016)], with no statistically significant differences. It is noteworthy that these models were never optimized for firing rate profiles, further proving the validity of our model population.

## Variability in Voltage-Gated Ion Channel Expression Causes Variable Input Processing

In order to study the role of variable VGIC expression in input processing, we first hand-tuned synaptic permeability values in the base model so that each excitatory synapse had unitary EPSP (uEPSP) amplitude at the soma of about 0.2 mV, irrespective of the synapse location (**Supplementary Figure S2A**). This ensured that a dendritic democracy (Magee and Cook, 2000) was maintained. Similarly, inhibitory synapses were fixed for uIPSP amplitude at the soma of about −1 mV (**Supplementary Figure S2B**).

Next, in order to examine how variability in VGICs expression affects the variable input processing, we placed the same synapses with the same permeability values on a valid neuronal population, which generated somatic uEPSP and uIPSP amplitude maps (**Figures 2A,B**) for the entire valid neuronal population. As expected, we found that variability in VGICs expression and passive membrane properties induced variability in somatic uEPSP and uIPSP amplitude maps (**Figure 2**). Following, we examined whether somatic uEPSP and uIPSP amplitude maps of a valid neuronal population are significantly different from the base model neuron. KS tests between each pair of base

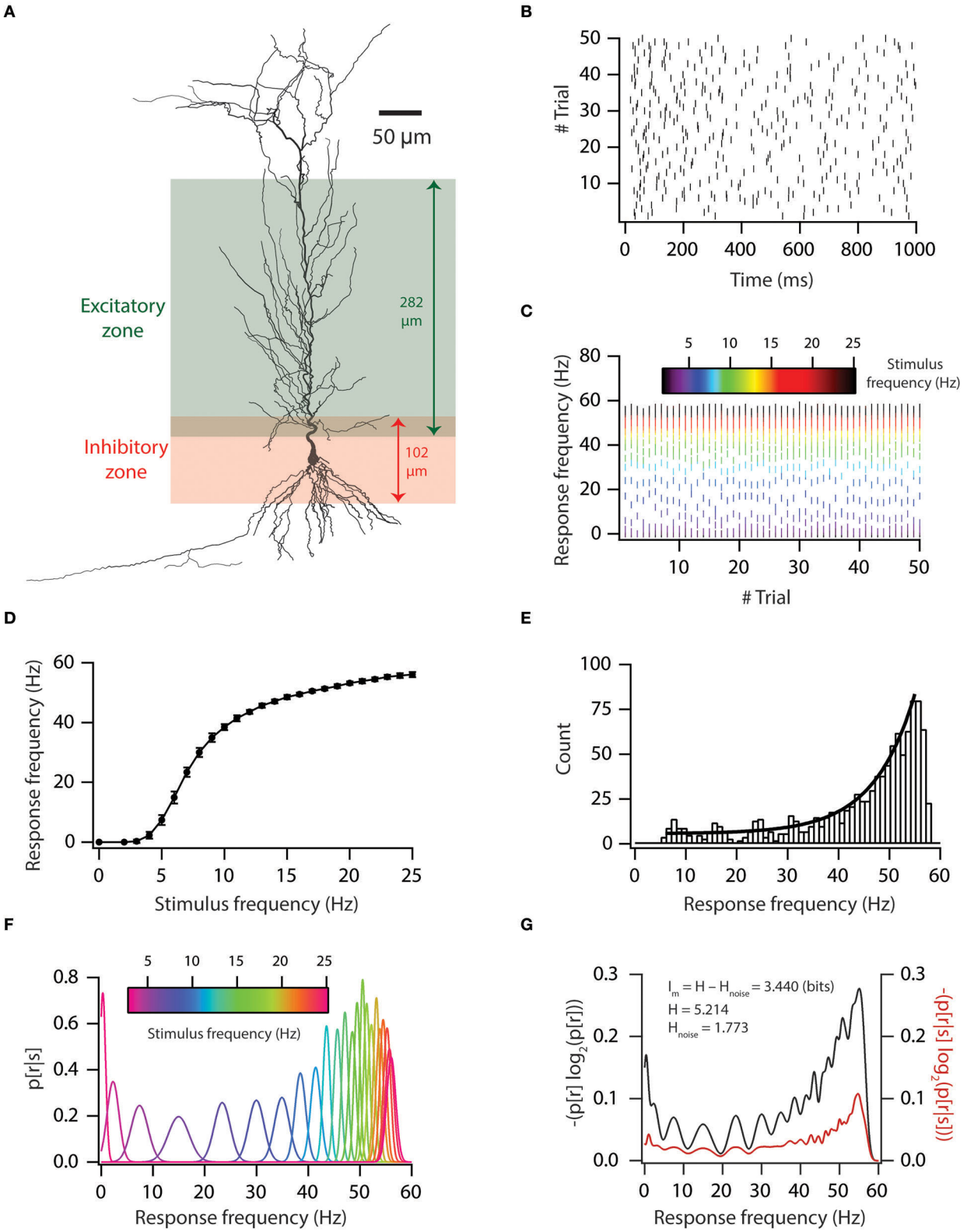


**FIGURE 1 |** Input–output relationship and mutual information of base model. **(A)** A morphological reconstruction of CA1 pyramidal neuron used as a substrate for all simulations. **(B)** Trial-to-trial variability in spike times for 5-Hz Poisson-distributed inputs. **(C)** Trial-to-trial variability in firing frequency for different stimulus frequencies. **(D)** Input–output relationship in the base model. **(E)** Firing frequency distribution in the base model. Solid black line denotes the exponential fit. **(F)** Probability distribution of firing frequency, given stimulus frequency. **(G)** Graph showing the computation of mutual information from total response entropy and noise entropy for the base model.

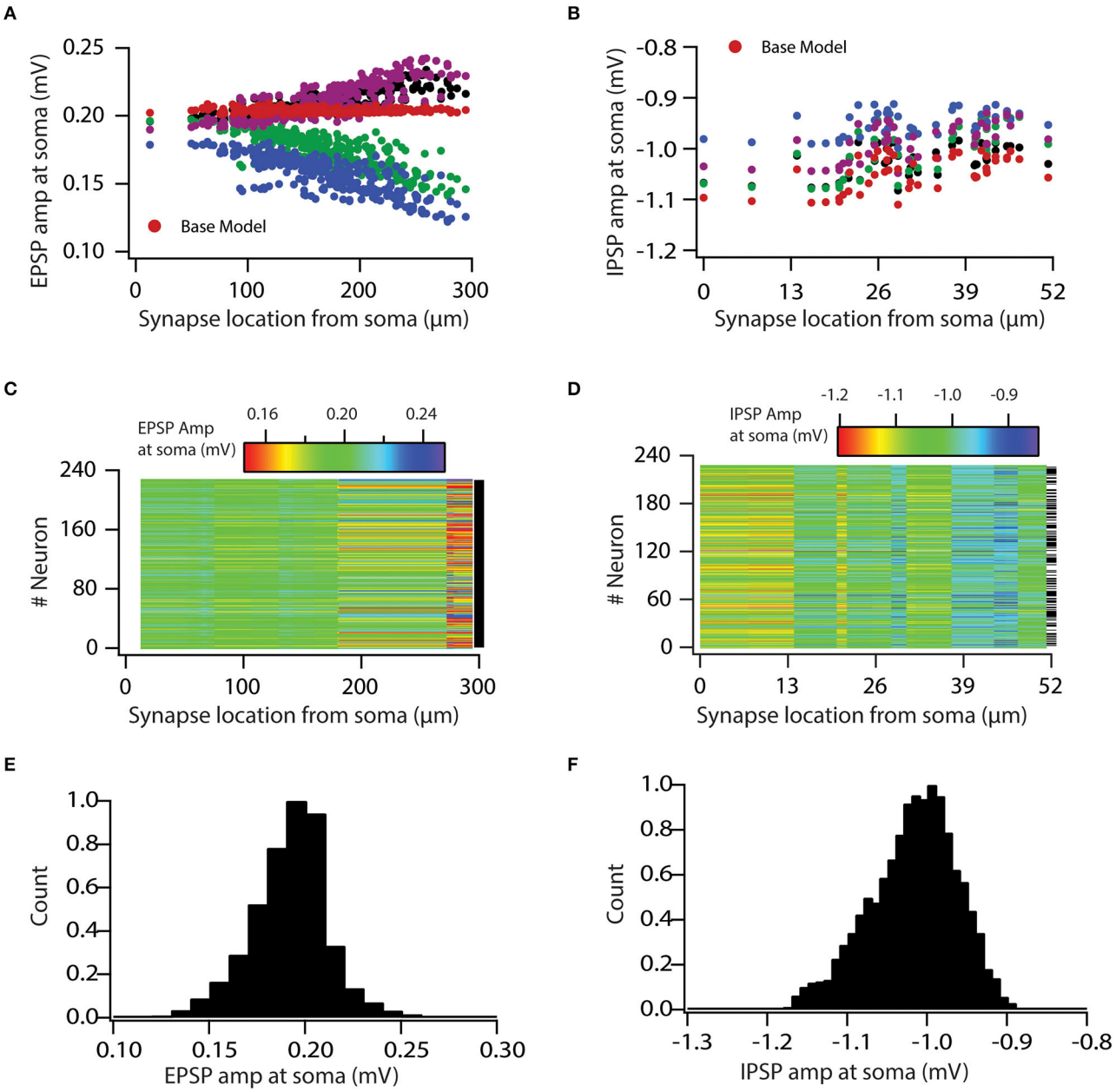


**FIGURE 2 |** Variability in expression of functional maps leads to variable input processing in neuronal population. **(A,B)** uEPSP **(A)** and uIPSP **(B)** amplitudes at the soma as a function of synapse location for four valid model neurons and the base model neuron. **(C,D)** Color-coded uEPSP **(C)** and uIPSP **(D)** amplitudes at the soma as a function of synapse location for all the valid neurons. **(E,F)** Distribution of all uEPSPs **(E)** and uIPSPs **(F)** amplitudes in valid neuronal population. Note that conductance values of the given type of synapse are same for all the model neurons.

model neuron and neuron of the valid neuronal population (total 228 pairs) showed that somatic uEPSP amplitude maps of the valid neuronal population were significantly different from those of the base model neuron for all pairs (**Figure 2C**; black dash against color-coded uEPSP amplitude maps denotes significance). Similarly, for somatic uIPSP amplitude maps of the valid neuronal population, we found that out of 228 pairs of neurons 122 pairs were significantly different from uIPSP amplitude map of the base model neuron (**Figure 2D**; black dash against color-coded uIPSP amplitude maps denotes significance). The *p*-value for performing the KS test was set at 0.001.

Following, we aimed to determine the boundaries for this variability and whether it is in a physiological range. For that, we generated histograms of all somatic uEPSP and uIPSP amplitudes in response to a single-synapse activation. This simulation yielded a rather large variability in the somatic uEPSP and uIPSP amplitudes (**Figures 2E,F**). Specifically, somatic uEPSP amplitude exhibited about ±25% variability in their

amplitudes from the mean value of 0.19 mV, whereas somatic uIPSP amplitude exhibited about +12 and −10% variability in their amplitudes from the mean value of −1.01 mV. Nonetheless, somatic uEPSP and uIPSP amplitudes were still within physiological ranges. Taken together, these analyses clearly demonstrated the role of VGICs in input processing and showed that variability in VGICs expression leads to variable input processing.

## Variability in Neuronal Outputs Leads to Decorrelation in Firing Frequencies

Afterward, we assessed the role of variability in VGICs expression and passive membrane properties in modulating the variability of neuronal output. Specifically, we aimed to investigate whether variability in neuronal input processing is translated to variability in neuronal output. For this aim, we first generated a raster plot of spike times for all neurons for a given stimulus frequency of 8 Hz (**Figure 3A**). For this, all synapses were activated in a Poisson manner at once. The controlled input of a spatio-temporal activation pattern of synaptic inputs was kept constant for all neurons. As visible from the graph, the simulation shows that different neurons emit different numbers of spikes for this given stimulus frequency, which suggests that the firing frequency of neurons is variable. Similarly, it is demonstrated that apart from firing frequency, spike timings also show variability (**Figure 3A**).

Thereafter, we examined the variability in response to the entire physiological range of stimulus frequencies. For that, we computed firing frequencies for all neurons for all stimulus frequencies. Again, a spatio-temporal activation pattern of synaptic inputs was kept constant for all neurons and was trail matched. Thus, any variability incurred in firing frequencies across neurons would be due to variability in VGICs expression and passive membrane properties. Plotting the firing frequencies for all neurons against stimulus frequencies showed that firing frequencies exhibit huge variability across all neurons (**Figure 3B**). To get a deeper understanding of this variability, we plotted minimum and maximum firing frequencies for all neurons (**Figure 3C**). From this, we noted that minimum firing frequencies did not show huge variability as most of the neurons did not fire action potentials at minimum stimulus frequency (5 Hz). However, in contrast to minimum firing frequencies, maximum firing frequencies displayed huge variability across neurons, from 2 to 100 Hz (**Figures 3C,D**). These analyses showed that variability in VGICs expression and passive membrane properties cause large variability in neuronal firing frequencies.

Next, given that correlation among firing frequencies between neuronal pairs could have a profound effect on information encoding (Panzeri et al., 1999), we investigated how variability in VGICs expression and passive membrane properties would affect this correlation of firing frequencies across the neuronal pairs. When we generated average correlation coefficient values among all possible pairs of neurons across the range of stimulus frequencies, we found that the average correlation coefficient values were generally small (**Figures 3E,F**) in the range of −0.2 to 0.5. Only a subset of neuronal pairs had average correlation coefficient values >0.5. This analysis demonstrates that variability in VGICs expression and passive membrane properties enables the decorrelation in firing frequencies among the neuronal pairs.

## Variability in Voltage-Gated ion Channel Expression Causes Variable Information Encoding Capabilities

Next, we determined whether the variability in input and output processing impacts the information encoding capabilities of neurons. For that, we employed a rate coding schema, and by using a well-established Shannon entropy principle, we computed mutual information of individual neurons. In this scenario, a synaptic activation at different stimulus frequencies forms the incoming information which is subsequently encoded by neurons' output firing frequencies. In this system, mutual information is defined as the capability of the neuron to successfully encode or represent different stimulus frequencies by the variability of the neuron's output firing frequencies. In such a system, a synaptic activation pattern was Poisson-distributed spike trains at different stimulus frequencies.

First, we computed response entropy for the given range of stimulus frequencies (5 to 25 Hz) for individual neurons. With this, we found that response entropies of individual neurons displayed large variability (**Figures 4A,B**). Similarly, the noise entropy of individual neurons also showed variability (**Figures 4C,D**). Mutual information was then calculated by subtracting noise entropy from response entropy. We found that the mutual information of individual neurons showed huge variability across the neuronal population (**Figures 4E,F**). This neuronal population spanned the spectrum of mutual information from as low as 0.1761 bits to as high as 4.02 bits. These analyses demonstrated that variability in VGICs expression and passive membrane properties causes the variability in information encoding capabilities of neurons.

Following, we explore the underlying principle that determines the parameters that enable the high and low information encoding capabilities of neurons. Specifically, we asked whether neurons with high mutual information transfer capabilities have any kind of preference toward any distinct parametric space for each parameter. To do this, we selected neurons whose mutual information was in the range of >3 bits, which yielded 80 neuronal models. Next, we generated histograms of all 32 parameters of the 80 neuronal models (**Figure 5A**, bottom-most row). This analysis showed that all the parameters were spanning through their entire range. To conclude, we observed no restriction on the parametric space of the 32 tested parameters that cause high mutual information, at least for the tested range.

Because a previous study showed that morphology and connected nature of compartments were insufficient for inducing a high correlation among the parameters when the population was sampled based upon intrinsic properties, we tested whether high mutual information capabilities enforce a significant correlation between parameters. For that, we took the aforementioned 80 neuronal models

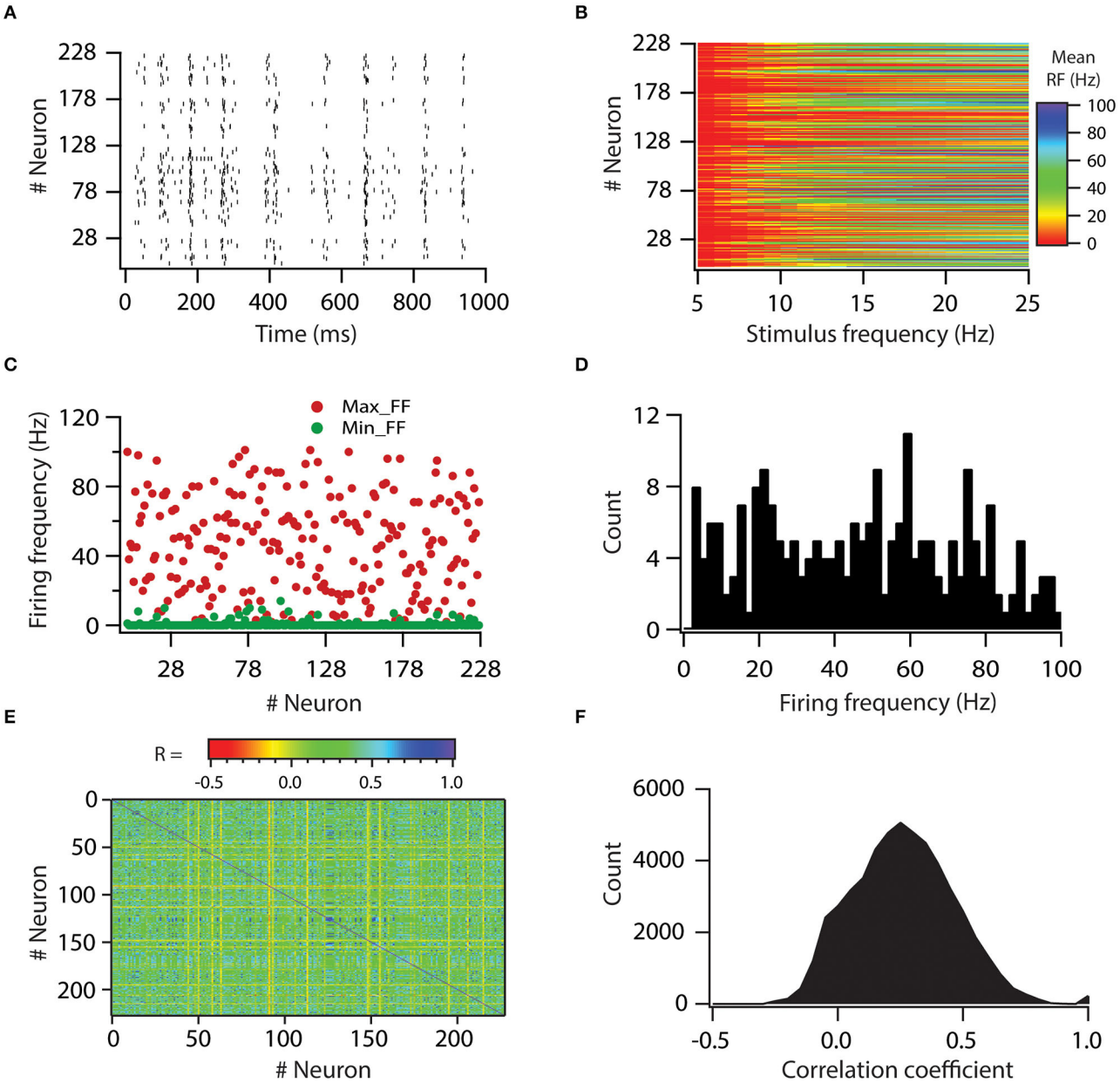


**FIGURE 3 |** Variability in expression of functional maps leads to decorrelation in firing rates of the neuronal population. **(A)** Spike raster for all the valid model neurons in response to 8-Hz Poisson-distributed synapse activation. A spatio-temporal activation pattern of synapses was same across the neuronal population. **(B)** Color-coded mean firing frequency, averaged over 50 trials, as a function of stimulus frequency. **(C)** Distribution of minimum and maximum firing frequencies in model neurons. **(D)** Histogram of maximum firing frequencies in model neuron population. **(E)** Color-coded matrix of correlation coefficient values for firing frequencies. **(F)** Histogram of correlation coefficient values for firing frequencies in model neuron population. Note that for a given stimulus frequency, a spatio-temporal activation pattern of synapses was trial-matched across the neuronal population.

and performed linear correlations among their parameters (**Figure 5A**). We found that the correlation coefficient values were relatively low (>-0.3 and <0.4) among all of the possible pairs of parameters (**Figures 5B,C**), suggesting that collective channelostasis is the mechanism underlying robust information transfer.

## Virtual Knockout Models Suggest KA Channels Are Major Regulators

Within the framework of the herein modeling, we examined whether one of the channels is a major contributor in determining the effects on mutual information. To answer this, we utilized a previously derived virtual knockout methodology

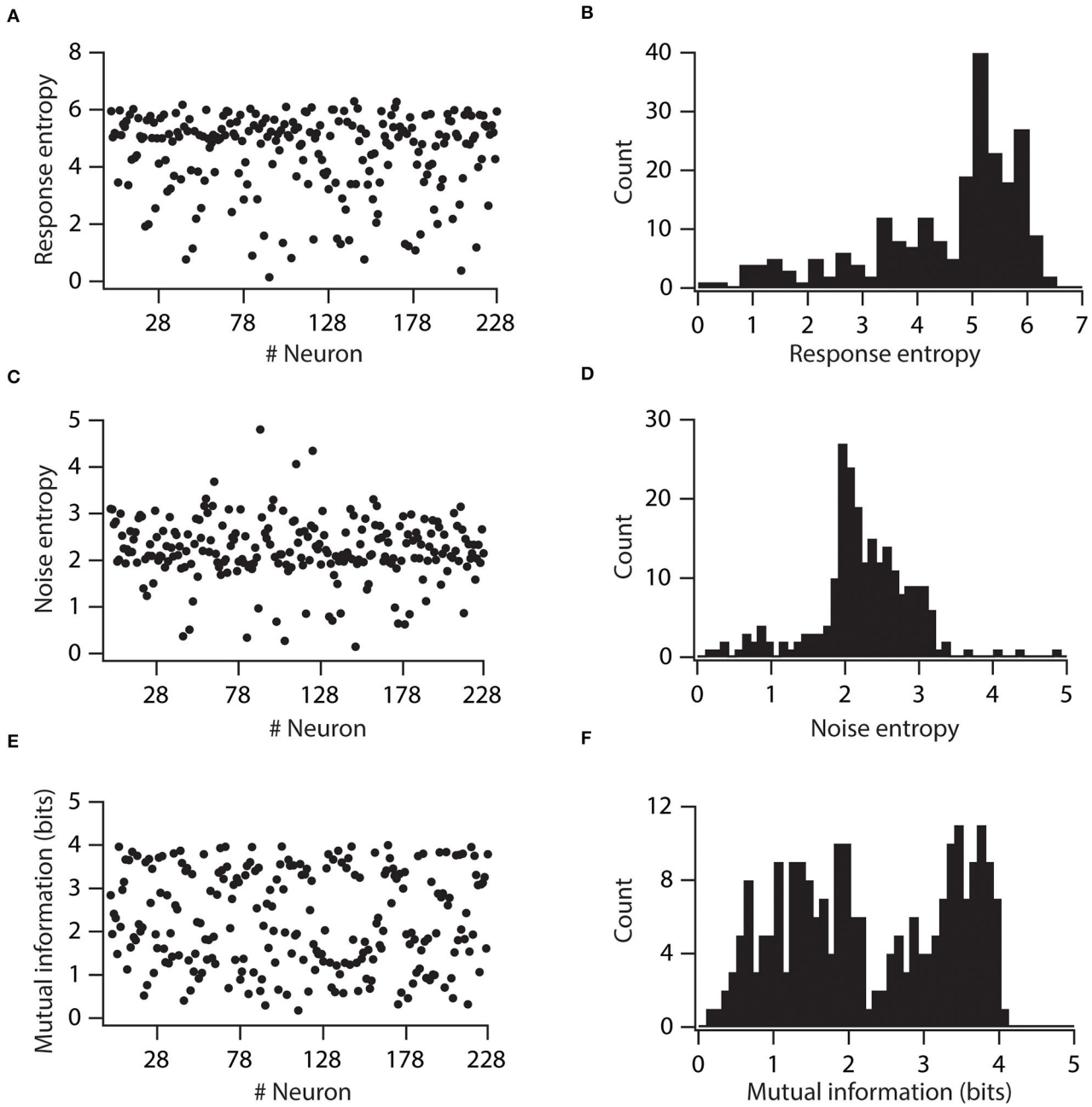


**FIGURE 4 |** Variability in expression of functional maps leads to distributed mutual information in the neuronal population. **(A)** Total response entropy for all the valid neurons. **(B)** Distribution of total response entropy in the population of valid neurons. **(C)** Noise entropy for all the valid neurons. **(D)** Distribution of noise entropy in the population of valid neurons. **(E)** Mutual information for all the valid neurons. **(F)** Distribution of mutual information in the population of valid neurons.

(VKM) technique on our model neurons. Specifically, we removed a specific conductance from each of the 228 valid models and repeated our simulations on uEPSP, uIPSP, firing frequency, and mutual information. Given that fast $Na^+$ channels and delayed rectifier K+ channels are basic requirements for action potential generation, we used virtual knockout models (VKMs) of only three types of channels: *A*-type $K^+$, *T*-type $Ca^{++}$, and HCN channels. These analyses demonstrated the impact of knocking out the specific conductance of either *A*-type $K^+$, *T*-type $Ca^{++}$, or HCN channels on information processing and transfer (**Figure 6**, **Supplementary Figures S3, S4**).

At first, we looked at the role of *A*-type $K^+$, *T*-type $Ca^{++}$, and HCN channels in affecting input processing. In accordance with the VKM, we removed each time the specific conductance

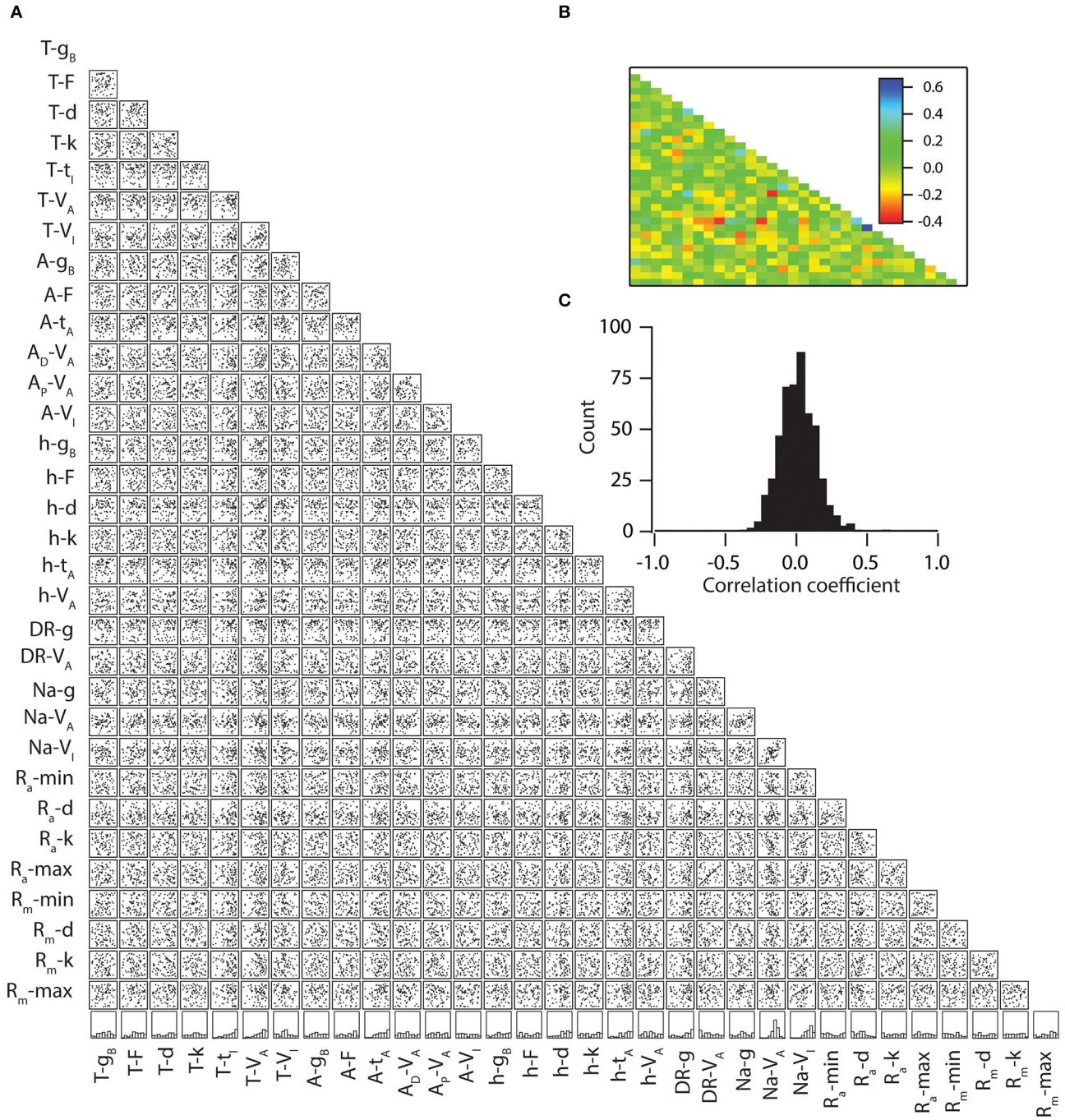


**FIGURE 5 |** Weak pair-wise correlations between parameters for the models with similar mutual information. **(A)** Lower diagonal of a matrix depicting interactions among the 32 parameters derived from all valid models ($n = 80$). Each subpanel depicts a scatter plot of the values of two parameters (labeled below and left) derived from all valid models. Correlation coefficients were computed for each of the scatter plots. The bottom-most row denotes the normalized histograms of individual parameters in the models with similar mutual information. **(B)** Lower diagonal of a color-coded matrix of correlation coefficients corresponding to the scatter plots in **(A)**. **(C)** Distribution of correlation coefficients for the 496 pairs corresponding to the scatter plots in **(A)**.

related to either *A*-type $K^+$ or *T*-type $Ca^{++}$ or HCN channels and simulated the uEPSP and uIPSP responses from each of the three VKMs. Next, we generated histograms of uEPSPs and uIPSPs and compared the histograms of the VKMs responses to the responses histograms of the baseline valid (BLV) neurons (**Supplementary Figure S2**). These comparisons show that the removal of *A*-type $K^+$ channels led to an increase in uEPSP and uIPSP amplitude (**Supplementary Figure S3**). Specifically,

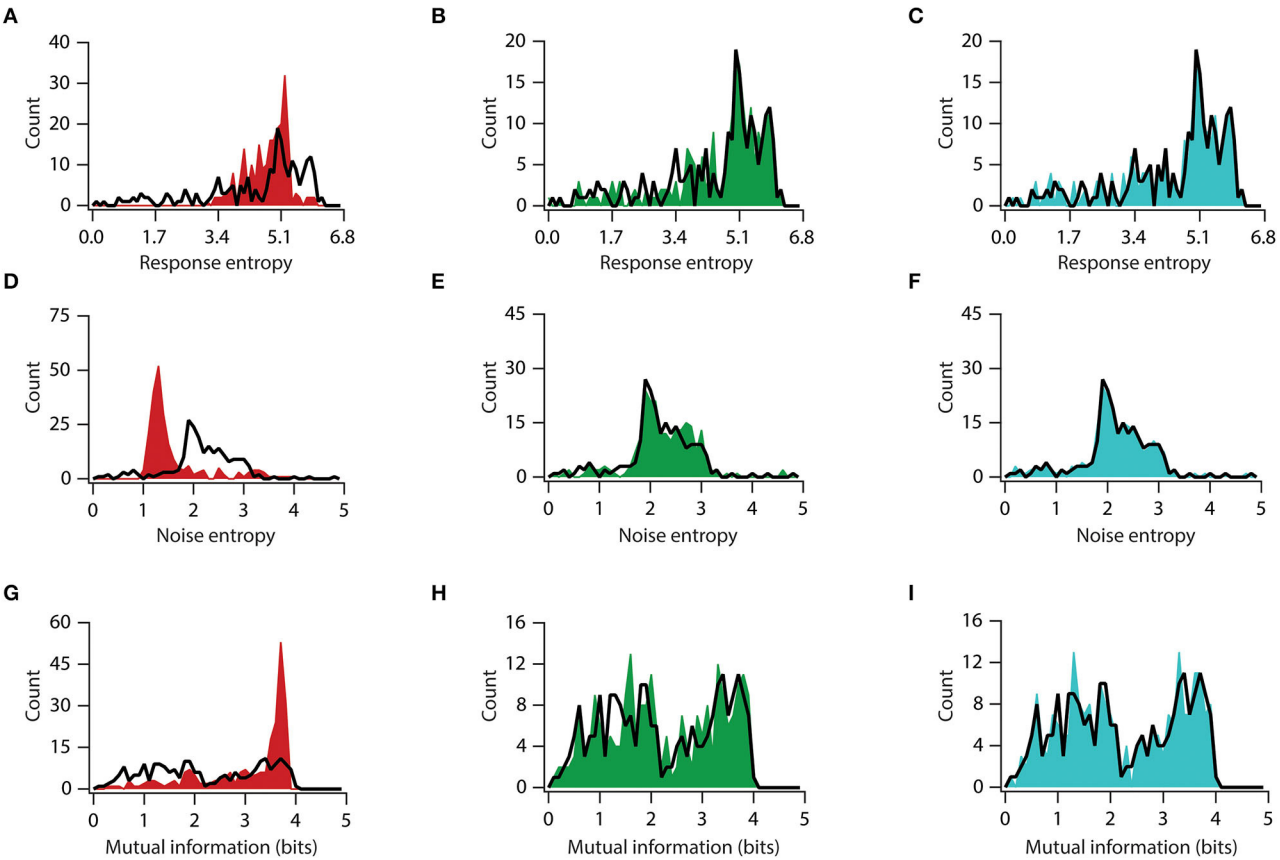


**FIGURE 6 |** Knocking out conductance has variable impact on mutual information. **(A–C)** Distribution of total response entropy in valid neuronal population (black trace) and virtual knockout model population of KA **(A)**, HCN **(B)**, and CaT **(C)**. **(D–F)** Distribution of noise entropy in valid neuronal population (black trace) and virtual knockout model population of KA **(D)**, HCN **(E)**, and CaT **(F)**. **(G–I)** Distribution of mutual information in valid neuronal population (black trace) and virtual knockout model population of KA **(G)**, HCN **(H)**, and CaT **(I)**.

removing *A*-type $K^+$ channels increased the mean uEPSP response from 0.192 to 0.357 mV (D = 0.55, $p < 0.0001$, in Kolmogorov–Smirnov [K–S] between *A*-type $K^+$-KO and BLV neuron) and the response of the uIPSP increased from a mean value of −1.01−−1.19 mV (D = 0.46, $p < 0.0001$, in K–S between *A*-type $K^+$ KO and BLV neuron). Removing HCN channels did not alter the uEPSP response (0.192–0.201 mV) (D = 0.20, $p = 0.34$, in K–S between HCN-KO and BLV neuron) and the uIPSP response (−1.01−−1.05 mV) (D = 0.09, $p > 0.99$, in K–S between HCN-KO and BLV neuron). Similarly, removing *T*-type $Ca^{++}$ channels did not change the uEPSP (0.192 mV to 0.1.85 mV) (D = 0.10, $p > 0.99$, in K–S between *T-type* $Ca^{2+}$-KO and BLV neuron) and the uIPSP amplitude (−1.01−−1.00 mV) (D = 0.09, $p > 0.99$, in K–S between *T-type* $Ca^{2+}$-KO and BLV neuron). These analyses showed that only the removal of *A*-type $K^+$ channel-specific conductance had an impact on input processing in the neuronal population.

Next, we analyzed the role of *A*-type $K^+$, *T*-type $Ca^{++}$, and HCN channels in affecting output processing. To this end, we generated the input/output relationship of all valid models after removing the specific conductance of either *A*-type $K^+$, *T*-type $Ca^{++}$, or HCN channels and compared the resultant firing frequency to that of the baseline valid model population. These analyses showed that the removal of *A*-type $K^+$ channels results in an increased firing frequency (**Figure 4SA**), from a mean firing frequency of neurons of 26.78 Hz in the baseline model to 49.57 Hz after removing *A*-type $K^+$ conductance (D = 0.31, $p = 0.0001$, in K–S between *A*-type $K^+$ KO and BLV neuron). In contrast, the removal of either HCN or *T*-type $Ca^{2+}$ channels did not change the firing frequency outputs distribution and mean frequencies (28.59 and 26.76 Hz for HCN-KO and *T*-type $Ca^{2+}$-KO, respectively; D = 0.12, $p = 0.47$, and D = 0.04, $p > 0.99$, in K–S between HCN-KO and BLV neurons and between *T*-type $Ca^{2+}$-KO and BLV neurons, respectively) (**Figures 4SB,C**). In conclusion, among the channels we examined, only *A*-type $K^+$ conductance is a significant contributor toward constraining neuronal firing frequency.

Next, we examined each channel's contribution to information transfer. For this, we used a similar approach of analyzing elements of information transfer after removing each specific conductance. An analysis of response entropy in model neurons showed that the removal of the *A*-type $K^+$ channels significantly

altered the distribution of response entropy, with a significant increase in mean response entropy from 4.5 to 4.8 bits ($t_{(454)} = 2.93$, $p < 0.01$, for unpaired *t*-test; D = 0.40, $p < 0.0001$, in K–S between *A*-type $K^+$ KO and BLV neurons) (**Figure 6A**), while the removal of the HCN or *T*-type $Ca^{2+}$ conductance did not affect the response entropy distribution or their means ($t_{(454)} = 0.87$, $p = 0.38$, for unpaired *t*-test and D = 0.05, $p > 0.99$; $t_{(454)} = 0.15$, $p = 0.89$, for unpaired *t*-test and D = 0.08, $p = 0.99$, in K–S between HCN-KO and BLV neurons and between *T*-type $Ca^{2+}$-KO and BLV neurons, respectively) (**Figures 6B,C**). On the other hand, when we looked into noise entropy, we found that removing *A*-type $K^+$ channels decreased the noise entropy in model neurons, with a mean noise entropy reduction from 2.20 to 1.68 ($t_{(454)} = 7.97$, $p < 0.0001$, for unpaired *t*-test), although the distribution was not significantly altered (D = 0.31, $p = 0.17$, in K–S) (**Figure 6D**). However, the removal of HCN and *T*-type $Ca^{2+}$ channels did neither alter the means nor the distributions of noise entropy ($t_{(454)} = 1.13$, $p = 0.26$, and $t_{(454)} = 0.22$, $p = 0.83$, in unpaired *t*-tests; D = 0.11, $p > 0.99$, and D = 0.04, $p > 0.99$, in K–S, between HCN-KO and BLV neurons and between *T*-type $Ca^{2+}$-KO and BLV neurons, respectively, for each test) (**Figures 6E,F**). Next, we analyzed mutual information and found that removing *A*-type $K^+$ channels improved the mutual information, with mean mutual information increasing from 2.28 bits to 3.10 bits ($t_{(454)} = 8.63$, $p < 0.0001$, for unpaired *t*-test; D = 0.35, $p < 0.05$, in K–S between *A*-type $K^+$-KO and BLV neurons) (**Figure 6G**). In contrast, removing *T*-type $Ca^{++}$ and HCN channels did not affect mutual information ($t_{(454)} = 0.37$, $p = 0.71$, for unpaired *t*-test and D = 0.08, $p > 0.99$; $t_{(454)} = 0.05$, $p = 0.96$, for unpaired *t*-test and D = 0.05, $p > 0.99$, in K–S between HCN-KO and BLV neurons and between *T*-type $Ca^{2+}$-KO and BLV neurons, respectively) (**Figures 6H,I**). Taken together, these analyses showed that the *A*-type $K^+$ channel is the major regulator of information transfer at least within the framework of our analyses.

## DISCUSSION

Intricate regulation of information encoding/transfer capabilities is extremely important for the individual neurons, their circuits, and the brain as a whole. Hence, it is essential to elucidate how neurons achieve this regulation, given the fact that they express a rich and differential repertoire of voltage-gated ion channels (VGICs) across the dendrite–soma–axon continuum. The presence of these VGICs has a tremendous influence on the input, integration, and output module of the neuron.

Furthermore, neurons are affected by additional multiple factors, which are given as follows:

1. Intracellular biochemical milieu, upon which cellular processes are heavily dependent and receive continuous perturbations (Marder and Thirumalai, 2002; Desai, 2003; Frick et al., 2004; Turrigiano and Nelson, 2004; Fan et al., 2005).
2. Various ion channels, which define basic neuronal properties undergo continuous trafficking at the plasma membrane (Lai and Jan, 2006; Shepherd and Huganir, 2007; Vacher et al., 2008; Shah et al., 2010; Nusser, 2012).
3. Properties of ion channels are susceptible to change by various factors including phosphorylation/dephosphorylation, interaction with intracellular messengers, and lipid composition of the plasma membrane (Levitan, 1994; Ismailov and Benos, 1995).
4. Continuous rewiring of synaptic connectivity (Chen et al., 2014; Attardo et al., 2015).
5. Changes in dendritic arborization at microscopic (spines) and macroscopic (dendritic branches) levels (Ikegaya et al., 2001; Yuste and Bonhoeffer, 2001; Attardo et al., 2015).
6. Dynamics related to various functions brought about by astrocytes, oligodendrocytes, and microglial cells (Baumann and Pham-Dinh, 2001; Haydon and Carmignoto, 2006; Sierra et al., 2014). Yet, despite all of these ongoing dynamics of perturbations, neurons maintain their stability and functionality and perform robust functions.

In this study, by performing global sensitivity analyses on neuronal information encoding/transfer capabilities, we show that neurons can achieve similar information encoding/transfer capabilities in several non-unique ways (**Figure 5**). This implies that neural mechanisms, involved in information encoding, e.g., VGICs, need not maintain the density and properties of individual channels at particular specific values (Rathour and Narayanan, 2014). This brings a tremendous opportunity for neurons to encode novel information through several non-unique combinations of ion channels. Therefore, collective channelostasis presents an important answer to the aforementioned question.

In addition, we have demonstrated that the contribution of the various VGICs is highly differential. In our simulations, we showed that between the three VGICs, namely, *A*-type $K^+$, HCN, and *T-type* $Ca^{2+}$, the major contribution was of the *A*-type $K^+$ channel, and its knockout completely altered the information processing, resulting in a significantly aberrant output (**Figure 6**, **Supplementary Figures 3S, 4S**). Investigating the differential contribution of each channel to information encoding has the potential to contribute to a more comprehensive understanding of the effects of various genetic mutations on brain functioning, leading to cognitive and behavioral deficits. Our finding suggests that genetic variations in some VGICs are less lenient, and will cause a much more severe impact on brain functioning than others.

Variability in VGICs and passive membrane properties could be crucial where inputs are highly correlated in a homogeneous neuronal population, which eventually leads to the correlated output spiking (Panzeri et al., 1999). Output correlation could have a severe effect on the information. There are a number of factors that could contribute toward a decrease in correlation. One such factor is variability in VGICs and passive membrane properties. Our analysis with firing rate correlation showed that correlation values among their firing frequencies were generally low (**Figure 4**), while inputs that were introduced by us were perfectly correlated. Therefore, variability in VGICs and passive membrane properties helps in inducing decorrelation of the

output activity. Although we did not explicitly analyze spike times correlation, analyses of the raster plots for all neurons for a given input frequency and trial showed that the neurons firing patterns were phase shifted to each other (**Figure 3A**). This gave us a glimpse that variability in VGICs and passive membrane properties could help in causing decorrelation in spike times.

Although our model neurons were homeostatically stable with a reference to six coexistent functional maps, the model neurons did not show high mutual information (**Figure 4**). How do we reconcile this? A possible explanation can be that each neuron is tuned to different optimal variabilities to encode incoming stimuli (Tripathy et al., 2013). Therefore, it stands to reason that during learning these neurons could adjust their level of variability such that they could encode incoming stimuli more efficiently. Further studies should focus on how a different degree of variability affects mutual information and homeostasis.

# METHODS

## Model and Valid Neuronal Population

A 3D reconstructed CA1 neuronal morphology was used as a substrate for all the simulations. The base model and valid neuronal population were taken from the previous study (Rathour and Narayanan, 2014). In brief, our model neurons expressed five voltage-gated ion channels (VGICs): fast $Na^+$, delayed rectifier $K^+$, A-type $K^+$, T-type $Ca^{++}$, and HCN channels. A valid neuronal population was generated by performing a global sensitivity analysis on a hand-tuned base model. The base model was hand-tuned in such a way that six coexistent functional maps matched their experimental counterparts. After having the experimentally constrained base model, we randomized 32 parameters, associated with five voltage-gated ion channels and passive membrane properties, within a large neighborhood of its default values, and followed an independent uniform distribution within that range. We generated a population of 20,420 models, with each model built by assigning independently random values for each of the 32 parameters in the base model. After having the model population, we tested the model properties corresponding to an experimental counterpart. Specifically, from the experimental data, we assigned a range for six measurements at three different locations along the somato-apical trunk. Each model neuron's properties were tested against these experimental ranges, and if a model neuron satisfies all the 18 constrains (six measurements at three different locations), it is called a valid neuron. Performing this validation procedure on each model resulted in 228 valid neurons. Owing to the validation procedure, this valid neuronal population of 228 neurons was heavily constrained by the experimental data and expressed variability in well-defined six coexistent functional maps. This valid neuronal population of 228 neurons was used throughout the study.

## Synaptic Inputs

Excitatory synapses were modeled as only AMPA receptor-type conductance as modeled previously (Narayanan and Johnston, 2010). Inhibitory synapses were modeled as only GABA-$_A$ receptor-type conductance as modeled previously (Sinha and Narayanan, 2015). Each model neuron was endowed with 327 excitatory and 50 inhibitory synapses. Excitatory synapses were distributed uniformly only on an apical dendrite and in the distance from 12 to 294 μm from the soma. Inhibitory synapses were distributed uniformly only in a perisomatic region. As the model population was generated by randomly assigning the values of 32 parameters, related to five VGICs and passive membrane properties, the number of compartments for neurons in the valid neuronal population was highly variable. Thus, in order to match the synaptic locations across the neurons, all neurons were recompartmentalized such that for a given section, a number of compartments were counted across all the neurons of the population, and then the section was recompartmentalized with the higher most count value, thus insuring the uniformity of numbers of compartments for a given section across all the neurons of valid population. Doing this recompartmentalization on each section yielded a total of 909 compartments for a given neuron of the valid population. A synaptic activation pattern was Poisson-distributed. Excitatory synapses were activated at different frequencies ranging from 5 to 25 Hz in steps of 1 Hz, and each stimulus frequency had 50 trials. Inhibitory synapses were activated only at 5 Hz irrespective of the excitatory synaptic stimulus frequency and were used throughout the study. A spatio-temporal activation pattern of excitatory and inhibitory synapses was trial-matched across the neurons of the valid population.

## Mutual Information

Mutual information between response frequency and stimulus frequency was computed as described previously (Honnuraiah and Narayanan, 2013). Specifically, mutual information was taken to be the difference between total response entropy and noise entropy:

$$I_m = H - H_{noise}$$

where $I_{\mathrm{m}}$ is the mutual information, $H$ is the total response entropy, and $H_{\mathrm{noise}}$ is the noise entropy. The total response entropy, $H$, was computed as follows:

$$H = -\sum_r p[r]\ \log_2(\mathrm{p[r]})$$

where p[r] denotes the response probability distribution of response frequency, r, over the entire range of stimulus frequencies (see synaptic inputs section). The response probability distribution of response frequency was computed as follows:

$$p[r] = \sum_s p[s]\ \ \mathrm{p[r|s]}$$

where p[r|s] denotes the response probability distribution of response frequency, r, for a given stimulus frequency, s. p[s] was

assumed to be uniformly distributed as the presentation of any stimulus frequency was equally probable. p[r|s] was computed from the array containing response frequency values for 50 trials for a given stimulus frequency. The first- and second-order statistics of an array containing response frequency values for 50 trials for a given stimulus frequency were used to generate p[r|s] with an implicit assumption of a normal distribution for p[r|s].

In order to compute noise entropy, the entropy of the responses for a given stimulus, s, was computed:

$$H_s = -\sum_r p[r \mid s] \ \log_2(p[r \mid s])$$

and then, noise entropy was computed as follows:

$$H_{noise} = \sum_s p[s]\, H_s$$

.

## COMPUTATIONAL DETAILS

All simulations were performed using the NEURON simulation environment (Carnevale and Hines, 2006) at −65 mV, and a temperature was set at 34° C, which accounted for ion channel kinetics relative to their q10 values. For solving various differential equations, an integration time step was set at 25 μs. All analyses were performed using custom-built software written with IGOR Pro (WaveMetrics Inc., USA). A correlation analysis was performed using the statistical computing package *R* (http://www.R-project.org).

## DATA AVAILABILITY STATEMENT

Publicly available datasets were analyzed in this study. This data can be found here: http://neuromorpho.org/.

## AUTHOR CONTRIBUTIONS

RKR and HK designed the research, analyzed the data, and wrote the paper. RKR performed the research. HK supervision and funding acquisition. Both authors contributed to the article and approved the submitted version.

## FUNDING

This work was supported by the Israel Science Foundation, Grant Number 248/20 (HK).

## ACKNOWLEDGMENTS

The authors thank Rishikesh Narayanan for his valuable discussion throughout the study.

## SUPPLEMENTARY MATERIAL

The Supplementary Material for this article can be found online at: https://www.frontiersin.org/articles/10.3389/fncel.2022.906313/full#supplementary-material

**Figure S1 |** Validation of model population using firing rate profiles. (A) Firing rate profiles of model neurons (red dots) and neurons from experiments (black dots) for different current injections. (B) Same as A. But data is presented as mean ± SEM.

**Figure S2 |** Synaptic permeability values and corresponding somatic PSP potentials in base models. (A-D) Somatic EPSP (A) and IPSP (C) amplitudes and their corresponding synaptic permeability values for excitatory (B) and inhibitory (D) synapses.

**Figure S3 |** Effects of removing a specific voltage gated ion channels on PSP potentials in a population of valid model neurons. (A & D) Removal of A-type $K^+$ channels causes an increase in EPSP (A) and IPSP (D) amplitudes. (B & E) Removal of h channels causes a non-significant trend for an increase increase in EPSP (B) and IPSP (E) amplitude. (C & F) Removal of T-type $Ca^+$ channels does not affect EPSP (C) and IPSP (F) amplitude.

**Figure S4 |** Effects of removing a specific voltage gated ion channels on firing frequency in a population of valid model neurons. (A) Removal of A-type $K^+$ channels causes an increase in firing frequency. Removal of either h channels (B) or T-type $Ca^+$ channels (C) does not affect firing frequency.

**Figure S5 |** Effect of removing a specific voltage gated ion channels on firing frequency correlation in a population of valid model neurons. (A-B) Removal of A-type $K^+$ channels causes an increase in firing frequency correlation. Removal of either h channels (C-D) or A-type $K^+$ channels (E-F) does not affect firing frequency correlation.

## REFERENCES

Anirudhan, A., and Narayanan, R. (2015). Analogous synaptic plasticity profiles emerge from disparate channel combinations. *J. Neurosci.* 35, 4691–4705. doi: 10.1523/JNEUROSCI.4223-14.2015

Attardo, A., Fitzgerald, J. E., and Schnitzer, M. J. (2015). Impermanence of dendritic spines in live adult CA1 hippocampus. *Nature* 523, 592–596. doi: 10.1038/nature14467

Basak, R., and Narayanan, R. (2020). Robust emergence of sharply tuned place-cell responses in hippocampal neurons with structural and biophysical heterogeneities. *Brain Struct. Funct.* 225, 567–590. doi: 10.1007/s00429-019-02018-0

Baumann, N., and Pham-Dinh, D. (2001). Biology of oligodendrocyte and myelin in the mammalian central nervous system. *Physiol. Rev.* 81, 871–927. doi: 10.1152/physrev.2001.81.2.871

Carnevale, N. T., and Hines, M. L. (2006). *The NEURON Book*. Cambridge, UK: Cambridge University Press. doi: 10.1017/CBO9780511541612

Chen, C. C., Lu, J, and Zuo, Y. (2014). Spatiotemporal dynamics of dendritic spines in the living brain. *Front. Neuroanat.* 8, 28. doi: 10.3389/fnana.2014.00028

Desai, N. S. (2003). Homeostatic plasticity in the CNS: synaptic and intrinsic forms. *J. Physiol. Paris* 97, 391–402. doi: 10.1016/j.jphysparis.2004.01.005

Fan, Y., Fricker, D., Brager, D. H., Chen, X., Lu, H. C., Chitwood, R. A., et al. (2005). Activity-dependent decrease of excitability in rat hippocampal neurons through increases in I(h). *Nat. Neurosci.* 8, 1542–1551. doi: 10.1038/nn1568

Frick, A., Magee, J., and Johnston, D. (2004). LTP is accompanied by an enhanced local excitability of pyramidal neuron dendrites. *Nat. Neurosci.* 7, 126–135. doi: 10.1038/nn1178

Goaillard, J. M., and Marder, E. (2021). Ion Channel Degeneracy, Variability, and Covariation in Neuron and Circuit Resilience. *Annu. Rev. Neurosci.* 44, 335–357. doi: 10.1146/annurev-neuro-092920-121538

Goldman, M. S., Golowasch, J., Marder, E., and Abbott, L. F. (2001). Global structure, robustness, and modulation of neuronal models. *J. Neurosci.* 21, 5229–5238. doi: 10.1523/JNEUROSCI.21-14-05229.2001

Haydon, P. G., and Carmignoto, G. (2006). Astrocyte control of synaptic transmission and neurovascular coupling. *Physiol. Rev.* 86, 1009–1031. doi: 10.1152/physrev.00049.2005

Honnuraiah, S., and Narayanan, R. (2013). A calcium-dependent plasticity rule for HCN channels maintains activity homeostasis and stable synaptic learning. *PLoS ONE* 8, e55590. doi: 10.1371/journal.pone.0055590

Ikegaya, Y., Kim, J. A., Baba, M., Iwatsubo, T., Nishiyama, N., and Matsuki, N. (2001). Rapid and reversible changes in dendrite morphology and synaptic efficacy following NMDA receptor activation: implication for a cellular defense against excitotoxicity. *J. Cell Sci.* 114, 4083–4093. doi: 10.1242/jcs.114.22.4083

Ismailov, I. I., and Benos, D. J. (1995). Effects of phosphorylation on ion channel function. *Kidney Int.* 48, 1167–1179. doi: 10.1038/ki.1995.400

Jain, A., and Narayanan, R. (2020). Degeneracy in the emergence of spike-triggered average of hippocampal pyramidal neurons. *Sci. Rep.* 10, 374. doi: 10.1038/s41598-019-57243-8

Lai, H. C., and Jan, L. Y. (2006). The distribution and targeting of neuronal voltage-gated ion channels. *Nat. Rev. Neurosci.* 7, 548–562. doi: 10.1038/nrn1938

Levitan, I. B. (1994). Modulation of ion channels by protein phosphorylation and dephosphorylation. *Annu. Rev. Physiol.* 56, 193–212. doi: 10.1146/annurev.ph.56.030194.001205

Magee, J. C., and Cook, E. P. (2000). Somatic EPSP amplitude is independent of synapse location in hippocampal pyramidal neurons. *Nat. Neurosci.* 3, 895–903. doi: 10.1038/78800

Marder, E. (2011). Variability, compensation, and modulation in neurons and circuits. *Proc. Natl. Acad. Sci. U. S. A.* 108, 15542–15548. doi: 10.1073/pnas.1010674108

Marder, E., O'Leary, T., and Shruti, S. (2014). Neuromodulation of circuits with variable parameters: single neurons and small circuits reveal principles of state-dependent and robust neuromodulation. *Annu. Rev. Neurosci.* 37, 329–346. doi: 10.1146/annurev-neuro-071013-013958

Marder, E., and Taylor, A. L. (2011). Multiple models to capture the variability in biological neurons and networks. *Nat. Neurosci.* 14, 133–138. doi: 10.1038/nn.2735

Marder, E., and Thirumalai, V. (2002). Cellular, synaptic and network effects of neuromodulation. *Neural. Netw.* 15, 479–493. doi: 10.1016/S0893-6080(02)00043-6

Mishra, P., and Narayanan, R. (2019). Disparate forms of heterogeneities and interactions among them drive channel decorrelation in the dentate gyrus: degeneracy and dominance. *Hippocampus* 29, 378–403. doi: 10.1002/hipo.23035

Mittal, D., and Narayanan, R. (2018). Degeneracy in the robust expression of spectral selectivity, subthreshold oscillations, and intrinsic excitability of entorhinal stellate cells. *J. Neurophysiol.* 120, 576–600. doi: 10.1152/jn.00136.2018

Narayanan, R., Dougherty, K. J., and Johnston, D. (2010). Calcium store depletion induces persistent perisomatic increases in the functional density of h channels in hippocampal pyramidal neurons. *Neuron* 68, 921–935. doi: 10.1016/j.neuron.2010.11.033

Narayanan, R., and Johnston, D. (2007). Long-term potentiation in rat hippocampal neurons is accompanied by spatially widespread changes in intrinsic oscillatory dynamics and excitability. *Neuron* 56, 1061–1075. doi: 10.1016/j.neuron.2007.10.033

Narayanan, R., and Johnston, D. (2010). The h current is a candidate mechanism for regulating the sliding modification threshold in a BCM-like synaptic learning rule. *J. Neurophysiol.* 104, 1020–1033. doi: 10.1152/jn.01129.2009

Nusser, Z. (2012). Differential subcellular distribution of ion channels and the diversity of neuronal function. *Curr. Opin. Neurobiol.* 22, 366–371. doi: 10.1016/j.conb.2011.10.006

Padmanabhan, K., and Urban, N. N. (2010). Intrinsic biophysical diversity decorrelates neuronal firing while increasing information content. *Nat. Neurosci.* 13, 1276–1282. doi: 10.1038/nn.2630

Padmanabhan, K., and Urban, N. N. (2014). Disrupting information coding via block of 4-AP-sensitive potassium channels. *J. Neurophysiol.* 112, 1054–1066. doi: 10.1152/jn.00823.2013

Panzeri, S., Schultz, S. R, Treves, A., and Rolls, E. T. (1999). Correlations and the encoding of information in the nervous system. *Proc. Biol. Sci.* 266, 1001–1012. doi: 10.1098/rspb.1999.0736

Prinz, A. A, Billimoria, C. P., and Marder, E. (2003). Alternative to hand-tuning conductance-based models: construction and analysis of databases of model neurons. *J. Neurophysiol.* 90, 3998–4015. doi: 10.1152/jn.00641.2003

Prinz, A. A, Bucher, D., and Marder, E. (2004). Similar network activity from disparate circuit parameters. *Nat. Neurosci.* 7, 1345–1352. doi: 10.1038/nn1352

Rathour, R. K, Malik, R., and Narayanan, R. (2016). Transient potassium channels augment degeneracy in hippocampal active dendritic spectral tuning. *Sci. Rep.* 6, 24678. doi: 10.1038/srep24678

Rathour, R. K, and Narayanan, R. (2012). Inactivating ion channels augment robustness of subthreshold intrinsic response dynamics to parametric variability in hippocampal model neurons. *J. Physiol.* 590, 5629–5652. doi: 10.1113/jphysiol.2012.239418

Rathour, R. K, and Narayanan, R. (2014). Homeostasis of functional maps in active dendrites emerges in the absence of individual channelostasis. *Proc. Natl. Acad. Sci. U. S. A.* 111, E1787–E1796. doi: 10.1073/pnas.1316599111

Rathour, R. K, and Narayanan, R. (2019). Degeneracy in hippocampal physiology and plasticity. *Hippocampus* 29, 980–1022. doi: 10.1002/hipo.23139

Roy, A., and Narayanan, R. (2021). Spatial information transfer in hippocampal place cells depends on trial-to-trial variability, symmetry of place-field firing, and biophysical heterogeneities. *Neural Netw.* 142, 636–660. doi: 10.1016/j.neunet.2021.07.026

Shah, M. M., Hammond, R. S., and Hoffman, D. A. (2010). Dendritic ion channel trafficking and plasticity. *Trends Neurosci.* 33, 307–316. doi: 10.1016/j.tins.2010.03.002

Shepherd, J. D., and Huganir, R. L. (2007). The cell biology of synaptic plasticity: AMPA receptor trafficking. *Annu. Rev. Cell Dev. Biol.* 23, 613–643. doi: 10.1146/annurev.cellbio.23.090506.123516

Sierra, A., Tremblay, M. È., and Wake, H. (2014). Never-resting microglia: physiological roles in the healthy brain and pathological implications. *Front. Cell Neurosci.* 8, 240. doi: 10.3389/fncel.2014.00240

Sinha, M., and Narayanan, R. (2015). HCN channels enhance spike phase coherence and regulate the phase of spikes and LFPs in the theta-frequency range. *Proc. Natl. Acad. Sci. U. S. A.* 112, E2207–E2216. doi: 10.1073/pnas.1419017112

Srikanth, S., and Narayanan, R. (2015). Variability in State-Dependent Plasticity of Intrinsic Properties during Cell-Autonomous Self-Regulation of Calcium Homeostasis in Hippocampal Model Neurons. *eNeuro*. 2:ENEURO.0053-15.2015. doi: 10.1523/ENEURO.0053-15.2015

Taylor, A. L., Goaillard, J. M., and Marder, E. (2009). How multiple conductances determine electrophysiological properties in a multicompartment model. *J. Neurosci.* 29, 5573–5586. doi: 10.1523/JNEUROSCI.4438-08.2009

Tripathy, S. J., Padmanabhan, K, Gerkin, R. C., and Urban, N. N. (2013). Intermediate intrinsic diversity enhances neural population coding. *Proc. Natl. Acad. Sci. U. S. A.* 110, 8248–8253. doi: 10.1073/pnas.1221214110

Turrigiano, G. G., and Nelson, S. B. (2004). Homeostatic plasticity in the developing nervous system. *Nat. Rev. Neurosci.* 5, 97–107. doi: 10.1038/nrn1327

Vacher, H., Mohapatra, D. P., and Trimmer, J. S. (2008). Localization and targeting of voltage-dependent ion channels in mammalian central neurons. *Physiol. Rev.* 88, 1407–1447. doi: 10.1152/physrev.00002.2008

Yuste, R., and Bonhoeffer, T. (2001). Morphological changes in dendritic spines associated with long-term synaptic plasticity. *Annu. Rev. Neurosci.* 24, 1071–1089. doi: 10.1146/annurev.neuro.24.1.1071

**Conflict of Interest:** The authors declare that the research was conducted in the absence of any commercial or financial relationships that could be construed as a potential conflict of interest.

frontiers | Frontiers in Cellular Neuroscience

TYPE Original Research
PUBLISHED 22 August 2022
DOI 10.3389/fncel.2022.957232



OPEN ACCESS

EDITED BY
Dion Dickman,
University of Southern California,
United States

REVIEWED BY
Yulia Akbergenova,
Massachusetts Institute of Technology,
United States
C. Andrew Frank,
The University of Iowa, United States

*CORRESPONDENCE
Faith L. W. Liebl
fliebl@siue.edu

SPECIALTY SECTION
This article was submitted to
Cellular Neurophysiology,
a section of the journal
Frontiers in Cellular Neuroscience

RECEIVED 30 May 2022
ACCEPTED 04 August 2022
PUBLISHED 22 August 2022

CITATION
Hendricks EL, Smith IR, Prates B, Barmaleki F and Liebl FLW (2022) The CD63 homologs, Tsp42Ee and Tsp42Eg, restrict endocytosis and promote neurotransmission through differential regulation of synaptic vesicle pools.
*Front. Cell. Neurosci.* 16:957232.
doi: 10.3389/fncel.2022.957232



# The CD63 homologs, Tsp42Ee and Tsp42Eg, restrict endocytosis and promote neurotransmission through differential regulation of synaptic vesicle pools

Emily L. Hendricks, Ireland R. Smith, Bruna Prates, Fatemeh Barmaleki and Faith L. W. Liebl*

Department of Biological Sciences, Southern Illinois University Edwardsville, Edwardsville, IL, United States

The Tetraspanin (Tsp), CD63, is a transmembrane component of late endosomes and facilitates vesicular trafficking through endosomal pathways. Despite being widely expressed in the human brain and localized to late endosomes, CD63's role in regulating endo- and exocytic cycling at the synapse has not been investigated. Synaptic vesicle pools are highly dynamic and disruptions in the mobilization and replenishment of these vesicle pools have adverse neuronal effects. We find that the CD63 homologs, Tsp42Ee and Tsp42Eg, are expressed at the *Drosophila* neuromuscular junction to regulate synaptic vesicle pools through both shared and unique mechanisms. Tsp42Ee and Tsp42Eg negatively regulate endocytosis and positively regulate neurotransmitter release. Both *tsp* mutants show impaired locomotion, reduced miniature endplate junctional current frequencies, and increased endocytosis. Expression of human CD63 in *Drosophila* neurons leads to impaired endocytosis suggesting the role of Tsps in endocytosis is conserved. We further show that Tsps influence the synaptic cytoskeleton and membrane composition by regulating Futsch loop formation and synaptic levels of SCAR and $PI(4,5)P_2$. Finally, Tsp42Ee and Tsp42Eg influence the synaptic localization of several vesicle-associated proteins including Synapsin, Synaptotagmin, and Cysteine String Protein. Together, our results present a novel function for Tsps in the regulation of vesicle pools and provide insight into the molecular mechanisms of Tsp-related synaptic dysfunction.

KEYWORDS

**tetraspanins, CD63, endocytosis, glutamate, neuromuscular junction**

## Introduction

The Tetraspanin (Tsp) family of transmembrane proteins populate cell membranes and organize characteristic membrane landscapes known as Tsp-enriched microdomains (Stipp et al., 2003). At these sites, Tsps exert regulatory control over the spatiotemporal distribution of their binding partners (Charrin et al., 2014). Tsps mediate these interactions through well-conserved structural motifs, most notably the EC2 extracellular loop, which contains the characteristic CCG motif (Seigneuret et al., 2001; Kovalenko et al., 2005). Analyses of Tsp-binding proteins reveal interactions between Tsps and other transmembrane proteins, cell surface receptors, adhesion molecules, and intracellular signaling proteins (Hemler, 2005; Termini and Gillette, 2017). Therefore, Tsps act as orchestrators of cell signaling and extracellular interactions by maintaining structural organization of the cell membrane.

Tsps are expressed in diverse cell types and have wide-ranging physiological functions. For example, they contribute to immune function, reproduction, gastric cell regulation, and astrocyte differentiation (Kelić et al., 2001; Duffield et al., 2003; Stipp et al., 2003; Termini and Gillette, 2017; Zou et al., 2018; Jankovičová et al., 2020). Several Tsps are widely expressed in the central nervous system (Murru et al., 2018) but their neuronal functions are largely limited to descriptions of the organizational control that Tsps exert on cell membranes. For example, Tspan5, whose expression is enriched in the mammalian brain, facilitates dendritic spine maturation through regulation of transsynaptic cell adhesion molecule clustering (Moretto et al., 2019). Tspan7 interacts with protein interacting with C kinase 1 (PICK1) thereby regulating AMPA receptor trafficking (Bassani et al., 2012).

In addition to their role at the cell membrane, some Tsps function intracellularly. Specifically, the Tsp, CD63, is important for targeting KFERQ-containing peptides to exosomes in an ESCRT-independent manner (Ferreira et al., 2022). Furthermore, CD63 is highly enriched in exosomes (Escola et al., 1998) and late endosomal vesicles (Pols and Klumperman, 2009) and regulates the trafficking of synaptic proteins, including Synaptotagmin VII (Flannery et al., 2010) and the neurotrophin receptor p75 (Escudero et al., 2014) through endosomal pathways. Although vesicular trafficking is fundamental for basal cell function, it has extensive physiological implications at specialized sites like neuronal synapses with high rates of vesicle turnover (Saheki and De Camilli, 2012).

Disruptions in CD63 function are associated with a number of diseases and disorders impacting the brain like neuroblastoma progression (Chivet et al., 2014; Marimpietri et al., 2021), Herpes Simplex Virus 1 neuronal infection (Dogrammatzis et al., 2019), and neuronal dysfunction in Down syndrome (Gauthier et al., 2017). Additionally, CD63 is used as a platelet biomarker for advancing cognitive decline in Alzheimer's disease (Yu et al., 2021). Together, these clinical findings highlight the importance of CD63 in neurons. A better understanding of CD63's synaptic function would enhance our understanding of how Tsps are implicated in human health and disease.

To study the role of CD63 at the synapse, we used the glutamatergic *Drosophila* neuromuscular junction (NMJ), which, both structurally and functionally, resembles mammalian glutamatergic synapses (Chou et al., 2020). Human *CD63* gives rise to eight unique mRNA transcripts due to exon skipping and/or the use of an alternative start codon in exon 7. These alternative splice variants produce three human CD63 (hCD63) isoforms whose expression may confer tissue-specific functions (Hochheimer et al., 2019). In *Drosophila,* however, hCD63 orthologs are encoded by separate *tsp* genes that have diverse tissue expression profiles. Of the 37 *tsps* encoded by the *Drosophila* genome (Todres et al., 2000), we show that two CD63 orthologs, *tsp42Ee* and *tsp42Eg*, are expressed transsynaptically at the NMJ to functionally regulate locomotion and neurotransmitter release. We find that Tsps modulate these synaptic processes by influencing the localization of synaptic vesicle-associated proteins, including Synaptotagmin (Syt), Cysteine String Protein (CSP), and Synapsin (Syn), and by regulating cytoskeletal and membrane structure through the microtubule associated protein 1B (MAP1B)/Futsch, SCAR, and $PI(4,5)P_2$. Our findings establish distinct roles for Tsp42Ee and Tsp42Eg in the maintenance of synaptic vesicle pools and negative regulation of endocytosis. Overall, these results uncover a novel role for the CD63 orthologs, *tsp42Ee* and *tsp42Eg*, in the regulation of neurotransmission and synaptic organization.

## Materials and methods

### Fly rearing and stocks

All fly stocks were reared at 25°C on Jazz Mix fly food (Fischer Scientific) in a Percival DR-36NL *Drosophila* incubator with an alternating 12 h light-dark cycle. Male and female third instar larvae or adult flies were used for all experiments. The following stocks were obtained from Bloomington *Drosophila* Stock Center: $w^{1118}$ (RRID:BDSC_5905), $tsp42Ee^{G2619}$ (RRID:BDSC_28119), $tsp42Ee^{CC01420}$/*tsp42Ee-GFP* (RRID:BDSC_51558), $tsp42Eg^{MB08050}$ (RRID:BDSC_25658), *UAS-hCD63* (RRID:BDSC_82215), *24B-Gal4* (RRID:BDSC_1767), and $elav^{C155}$*-Gal4* (RRID:BDSC_458). The $tsp42Ee^{G2619}$ and $tsp42Eg^{MB08050}$ loss of function mutants were originally described in Bellen et al. (2011).

### Protein sequence accession and alignment

Tsp42Ee (NP_001260753.1), Tsp42Eg (NP_523633.1), and hCD63 (NP_001244318.1) reference protein sequences were

obtained from NCBI and multiple sequence alignment was performed using EMBL-EBI Clustal Omega (v1.2.4) (Madeira et al., 2019). Aligned sequences were analyzed for residue similarity using the Sequence Manipulation Suite (written by Paul Stothard; bioinformatics.org/sms). References to similar amino acid residues use the following categorizations based on biochemical properties: ILV, FWY, KRH, DE, GAS, P, C, TNQM, with commas separating each group.

## Immunohistochemistry

Third instar larvae were filet dissected on 60 mm Sylgard-coated (World Precision Instruments) dishes in Roger's Ringer solution (pH = 7.15, 135 mM NaCl, 5 mM KCl, 4 mM $MgCl_2^*6H_2O$, 1.8 mM $CaCl_2^*2H_2O$, 5 mM TES, 72 mM sucrose, and 2 mM glutamate). Filet dissected larvae were fixed either in Bouin's fixative or 3.7% paraformaldehyde (PFA) for 30 min. Fixed larvae were placed in 1.5 mL centrifuge tubes containing PTX (PBS + 0.1% Triton X-100, Accuris Life Science Reagents; Integra Chemical) and washed in PTX for three 10-min intervals. Larvae were next washed in PBTX (PTX + 1% Bovine Serum Albumin, Fisher BioReagents) twice for 30 min. Primary antibodies included rabbit α-GFP (1:100, Torrey Pines Biolabs; RRID: AB_2313770), rabbit α-GluRIIC [1:5000, generated by Genscript using the sequence found in Marrus et al. (2004)], rabbit α-vGLUT [1:10,000, a gift from the Aaron DiAntonio lab (Daniels et al., 2004)], mouse α-Brp (1:50, Developmental Studies Hybridoma Bank; RRID: AB_2314866), mouse α-Syt1 (1:100, Developmental Studies Hybridoma Bank; RRID: AB_528483), mouse α-CSP (1:200, Developmental Studies Hybridoma Bank; RRID: AB_528183), mouse α-Syn (1:50, Developmental Studies Hybridoma Bank; RRID: AB_528479), mouse α-Futsch (1:100, Developmental Studies Hybridoma Bank; RRID: AB_528403), mouse α-SCAR (1:50, Developmental Studies Hybridoma Bank; RRID: AB_2618386), mouse α-WASp (1:10, Developmental Studies Hybridoma Bank; RRID: AB_2618392), rabbit α-Nwk (1:1000, a gift from the Kate O'Connor-Giles lab), and mouse α-$PI(4,5)P_2$ (1:250, Echelon Biosciences, RRID: AB_427225). Primary antibodies were diluted in PBTX and incubated with larval tissues overnight at 4°C. Larvae then underwent three 10-min and two 30-min washes in PBTX. Secondary antibodies included α-mouse FITC (Jackson ImmunoResearch; RRID: AB_233558), α-rabbit FITC (Jackson ImmunoResearch; RRID: AB_2337972), and α-mouse TRITC (Jackson ImmunoResearch; RRID: AB_2340767) and were diluted 1:400 in PBTX and co-applied with Cy3- (RRID: AB_2338959) or A647-conjugated HRP (1:125, Jackson ImmunoResearch; RRID: AB_2338967 for 2 h at room temperature. Larvae were next washed with PBTX for three times for 10 min and two times for 30 min and placed on microscope slides and covered with Vectashield mounting medium (Vector Laboratories).

## FM 1-43FX labeling

FM 1-43FX labeling was performed as described (Verstreken et al., 2008). Briefly, third instar larvae were filet dissected in HL-3 without $Ca^{2+}$ (pH = 7.2; 100 mM NaCl, 5 mM KCl, 10 mM $NaHCO_3$, 5 mM HEPES, 30 mM Sucrose, 5 mM Trehelose, 10 mM $MgCl_2$). Larvae were rinsed with HL-3 to remove debris, central nervous systems were carefully removed by cutting the innervating motor neurons, and the HL-3 without $Ca^{2+}$ solution was replaced with 4μM FM 1-43FX in HL-3 containing 1 mM $Ca^{2+}$ and 90 mM KCl. After 1 min, the FM 1-43FX was removed and larvae were washed five times over 5–10 min with HL-3 without $Ca^{2+}$. Larvae were then fixed for 5 min with 3.7% PFA diluted in HL-3 without $Ca^{2+}$. The fixative was washed off through a series of five washes over 15 min with HL-3 without $Ca^{2+}$ containing 2.5% normal goat serum (Thermo Fisher Scientific). Dissected larvae were unpinned and placed in 1.5 mL centrifuge tubes containing HL-3 without $Ca^{2+}$. Larvae were washed five times with HL-3 without $Ca^{2+}$ over a 10 min period and then incubated with A647 HRP (1:100, diluted in HL-3 without $Ca^{2+}$) for 30 min. Finally, the A647 HRP solution was removed and five washes using HL-3 without $Ca^{2+}$ were performed. Samples were placed on microscope slides, covered with Vectashield mounting medium, and imaged the same day.

## Image acquisition and analysis

6/7 NMJs of body wall segments 3 or 4 were imaged using the 60x oil immersion objective on an Olympus Fluoview 1,000 laser scanning confocal microscope. For each experimental replicate, all genotypes were immunostained using the same reagents. Confocal acquisition settings were obtained for all controls, averaged, and then used for experimental animals. Approximately equal numbers of controls and experimental animals were imaged each day. Each experiment included at least two biological replicates.

Image z-stacks were processed in Fiji (NIH Image J) (Schindelin et al., 2012). Using max projection confocal images, NMJs were outlined and relative fluorescence was calculated by subtracting the background fluorescence from the synaptic fluorescence. All values reported from immunohistochemistry experiments were normalized to the average relative fluorescence of control animals. Bruchpilot (Brp) densities were calculated by manually counting the number of NMJ Brp puncta and dividing by the area of the NMJ. The distance between Brp and GluRIIC was determined by drawing lines through boutons perpendicular to the NMJ

branch on z-projected images, generating red-green intensity profiles, and calculating the distance between the maximum peaks for Brp and GluRIIC. Peak distances were calculated for five terminal boutons per NMJ and the mean was used to represent each NMJ.

To measure FM 1-43FX signal intensity, NMJ region of interests were obtained from max projection confocal images. For each z-stack slice, relative fluorescence was calculated by subtracting background fluorescence from synaptic fluorescence. The relative fluorescence value of each slice was averaged and reported as mean NMJ fluorescence intensity.

## RNA isolation and RT-qPCR

Central nervous systems and muscle pelts were dissected from third instar larvae in Roger's Ringer solution and placed into nuclease-free 1.5 mL centrifuge tubes containing 200 $\mu$L of RNAlater (Thermo Fisher Scientific). Dissected tissues were stored at −20°C until RNA isolation was performed using the Ambion PureLink RNA Mini Kit (Thermo Fisher Scientific). RNA concentrations were determined using an Implen NanoPhotometer N50. Reverse transcription quantitative polymerase chain reaction (RT-qPCR) was performed using the iTaq Universal SYBR Green One-Step Kit (BioRad). 100 ng of RNA and 50 pmol/µl of cDNA-specific primers were added to each reaction. RT-qPCR was performed using a CFX Connect thermal cycler (BioRad) to obtain cycle threshold or C(t) values. Heat maps were generated using GraphPad Prism (v. 9.3.0) from $2^{-(\Delta\Delta Ct)}$, which was calculated by first subtracting the C(t) value of the target transcript reaction from the C(t) value for GAPDH to obtain $\Delta$C(t) for each transcript. Next, the difference between control and *tsp* mutant $\Delta$C(t)s was calculated to obtain the $\Delta\Delta$C(t), which was subsequently log transformed. At least three biological replicates including three technical replicates were used for data analysis.

## Electrophysiology

Third instar larvae were dissected on Sylgard-coated coverslips (World Precision Instruments) in ice cold HL-3 containing 0.25 mM $Ca^{2+}$, which was replaced with room temperature HL-3 containing 1.0 mM $Ca^{2+}$ for recordings. Two electrode voltage clamp was performed on muscle six of body wall segments 3 or 4 using electrodes with resistances of 10–30 M$\Omega$ filled with 3 M KCl. Muscles were clamped at −60 mV using an Axoclamp 900A amplifier (Molecular Devices). Recordings were collected in pClamp (v. 11.1) and only obtained from muscles if the input resistance was <5 M$\Omega$. Suprathreshold stimuli were delivered to segmental nerves using a suction electrode filled with bath saline and a Grass S88 stimulator with a SIU5 isolation unit (Grass Technologies). Quantal content was calculated by dividing the integrated area of evoked currents by the integrated area of spontaneous currents (eEJC nA * ms/mEJC nA * ms) as previously described (Bykhovskaia, 2008). The high frequency stimulation protocol consisted of stimuli administered at 0.2 Hz for 50 s, 20 Hz for 60 s, and 0.2 Hz for 50 s. Paired pulse amplitudes were measured after delivering two each of 10, 20, 50, and 100 Hz pulses with each pair separated by a 20 s intertrial interval. To measure the size of the vesicle pools, dissected larvae were incubated at room temperature for 20 min in freshly prepared 2 $\mu$M Bafilomycin in HL-3 containing 1 mM $Ca^{2+}$. After mEJCs were recorded, the segmental nerve was stimulated at 3 Hz for 10 min or at 10 Hz for 5 min. Recordings were digitized with a Digidata 1443 digitizer (Molecular Devices). An approximately equal number of recordings from controls and experimental animals were obtained each day. Data were analyzed in Clampfit (v 11.1, Molecular Devices) and GraphPad Prism (v. 9.3.0).

## Behavior

Third instar larvae were placed onto 1.6% agar plates and allowed to wander for 1 min to remove excess food debris and acclimate to the agar crawling surface. Larvae were then transferred to a 1.6% agar-coated behavioral arena and video recorded for 30 s at 29.97 frames per second with a Canon EOS M50 camera. Each recording was performed on a group of five larvae. Video recordings were analyzed in Fiji with the wrMTrck plugin by Jesper S. Pedersen. Values for distance crawled, average and maximum velocities, and body lengths traveled per second (to normalize for variation in larval body size) were recorded.

## Longevity

Newly enclosed (Day 0) adult flies were collected, separated by sex, and put into vials containing Jazz Mix fly food (Fisher Scientific). Each vial contained 10 adults of the same genotype and sex. Vials were checked daily and deaths were recorded along with the number of days survived. One sample represents one individual ($w^{1118}$, $n = 74$; $tsp42Ee^{G2619}$, $n = 76$; $tsp42Eg^{MB08050}$, $n = 64$). Survival curves were generated and analyzed in GraphPad Prism (v. 9.3.0).

## Experimental design and statistical analyses

All experiments included at least two biological replicates. Each replicate included an approximately equal number of control and experimental animals. Sample sizes are indicated by data points on graphs. All statistical analyses were performed using GraphPad Prism (v 9.3.0). Unpaired *t* tests were used

when comparing one control group to one experimental group. Log-rank (Mantel-Cox) tests were used for survival curve comparison. One-way ANOVAs followed by *post hoc* Tukey's multiple comparisons tests were used for statistical analyses across genotypes for immunocytochemistry experiments when there was more than one control group. *P*-values were adjusted for multiple comparisons. Two-way ANOVAs followed by Dunnett's multiple comparison tests were used to determine if there were differences in evoked currents during high frequency, 3 and 10 Hz stimulation protocols. Statistical significance is denoted on graphs: * = <0.05, ** = <0.01, *** = <0.001, with error bars representing standard error of the mean (SEM).

# Results

## *Tsp42Ee* and *Tsp42Eg* are CD63 orthologs expressed at the *Drosophila* NMJ

Tsps are transmembrane proteins that form homophilic and heterophilic complexes to organize membrane microdomains (Termini and Gillette, 2017). There are 33 Tsps in humans (Murru et al., 2018) and 37 in *Drosophila* (Todres et al., 2000) but little is known about their roles at the synapse. Three Tsps are expressed in the motor neuron (Fradkin et al., 2002) and three are expressed in the muscle (flybase.org; Gramates et al., 2022) of the glutamatergic *Drosophila* larval NMJ. To better understand the function of synaptic Tsps, we focused on two previously unexamined Tsps, Tsp42Ee and Tsp42Eg. Both are homologs of CD63, which is best characterized for its interactions with β1-integrin and its roles in cell migration and adhesion (Justo and Jasiulionis, 2021). Tsp42Ee is 24% identical and 49% similar as human CD63 while Tsp42Eg is 26% identical and 41% similar as human CD63 (Figure 1A). Importantly, both Tsp42Ee and Tsp42Eg demonstrate conservation of the canonical CCG motif and two cysteine residues (Figure 1A, arrowheads) located in the EC2 extracellular loop (Seigneuret et al., 2001). The CCG motif and cysteine residues participate in the formation of stabilizing disulfide bridges and thus, are critical for Tsp structure (Kitadokoro et al., 2001). Regions devoid of sequence conservation, especially those in the EC2 extracellular loop, mediate interactions between Tsps and other membrane proteins (Kovalenko et al., 2005).

We used the loss of function mutants, $tsp42Ee^{G2619}$ and $tsp42Eg^{MB08050}$, to examine their roles at the synapse. Both alleles result from transposon insertions in the genes (Figure 1B) (Bellen et al., 2011). Using RT-qPCR, we found $tsp42Ee^{G2619}$ expresses 43.8% of control *tsp42Ee* while $tsp42Eg^{MB08050}$ expresses 45.5% of *tsp42Eg*. Both mutants are homozygous viable with mean lifespans similar as controls ($w^{1118}$ = 73.72 ± 3.35 days, $n$ = 74; $tsp42Ee^{G2619}$ = 70.03 ± 2.94 days, $n$ = 76, $p$ = 0.41; $tsp42Eg^{MB08050}$ = 79.59 ± 1.45 days, $n$ = 64, $p$ = 0.13). However, both *tsp* mutants show significant differences in survival curves relative to controls ($tsp42Ee^{G2619}$, $p$ = 0.0003; $tsp42Eg^{MB08050}$, $p$ = 0.0222; Supplementary Figure 1) indicating that their median survival differs from controls. Therefore, while Tsp42Ee and Tsp42Eg are important for overall survival, Tsps may have functionally redundant physiological roles over the lifespan as previously suggested (Fradkin et al., 2002).

*tsp42Ee* and *tsp42Eg* are expressed in the central nervous system (CNS) and postsynaptic muscle cells in $w^{1118}$ controls (Figure 1C). *tsp42Ee* is highly expressed in both CNS and muscle tissue relative to *bruchpilot* (*brp*) and *dynamin* (*dyn*) (Figure 1C), which encode an active zone scaffold protein (Wagh et al., 2006) and a GTPase required for endocytosis (McMahon and Boucrot, 2011), respectively. Tsp42Ee is found in synaptic boutons at the NMJ as indicated by expression of $tsp42Ee^{CC01420}$, which encodes a Tsp42Ee GFP fusion protein (Figure 1D). *tsp42Eg* is more highly expressed in postsynaptic muscle than CNS in $w^{1118}$ controls (Figure 1C). It is expressed in muscle cells at slightly higher levels than *rab11*, which encodes a GTPase that facilitates vesicle trafficking from recycling endosomes to the plasma membrane (Ng and Tang, 2008). *brp*, *dyn*, and *rab11* transcripts were expressed similarly in $w^{1118}$ controls and *tsp* mutants (Supplementary Figure 2).

*tsp42Ee* and *tsp42Eg* are found within a cluster of 18 *tsp* genes, *tsp42Ea-tsp42Er*, on the second chromosome (Figure 1B). Given their proximity in the genome, we used RT-qPCR to assess the transcripts encoded by the *tsps* adjacent to *tsp42Ee* and *tsp42Eg* in $tsp42Ee^{G2619}$ and $tsp42Eg^{MB08050}$ mutants (Figure 1E). We used whole larvae for these analyses because there are no reports of *tsp42Ed* or *tsp42Ef* expression in the CNS or postsynaptic muscle. While *tsp42Ed*, *tsp42Ee*, *tsp42Ef*, and *tsp42Eh* were similar as controls in $tsp42Eg^{MB08050}$ mutants, *tsp42Ed* and *tsp42Eh* were slightly lower than controls in $tsp42Ee^{G2619}$ mutants. *tsp42Ed* is expressed in the circulatory and digestive systems and *tsp42Eh* is expressed in the integumentary system and more highly in adult than larval muscles (flybase.org). Therefore, we began by investigating the function of Tsps at $tsp42Ee^{G2619}$ and $tsp42Eg^{MB08050}$ mutant synapses.

## Tsp42Ee and Tsp42Eg promote neurotransmission by facilitating neurotransmitter release

Synaptic function in *tsp* mutants was assessed by examining larval crawling behavior and recording miniature and evoked endplate junctional currents (mEJCs and eEJCs, respectively). Larval locomotor behavior relies on both central nervous system central pattern generators and peripheral motor neurons (Heckscher et al., 2012; Gjorgjieva et al., 2013). Although there is not always a correlation between NMJ function and movement, there is a positive correlation between the frequency

10.3389/fncel.2022.957232

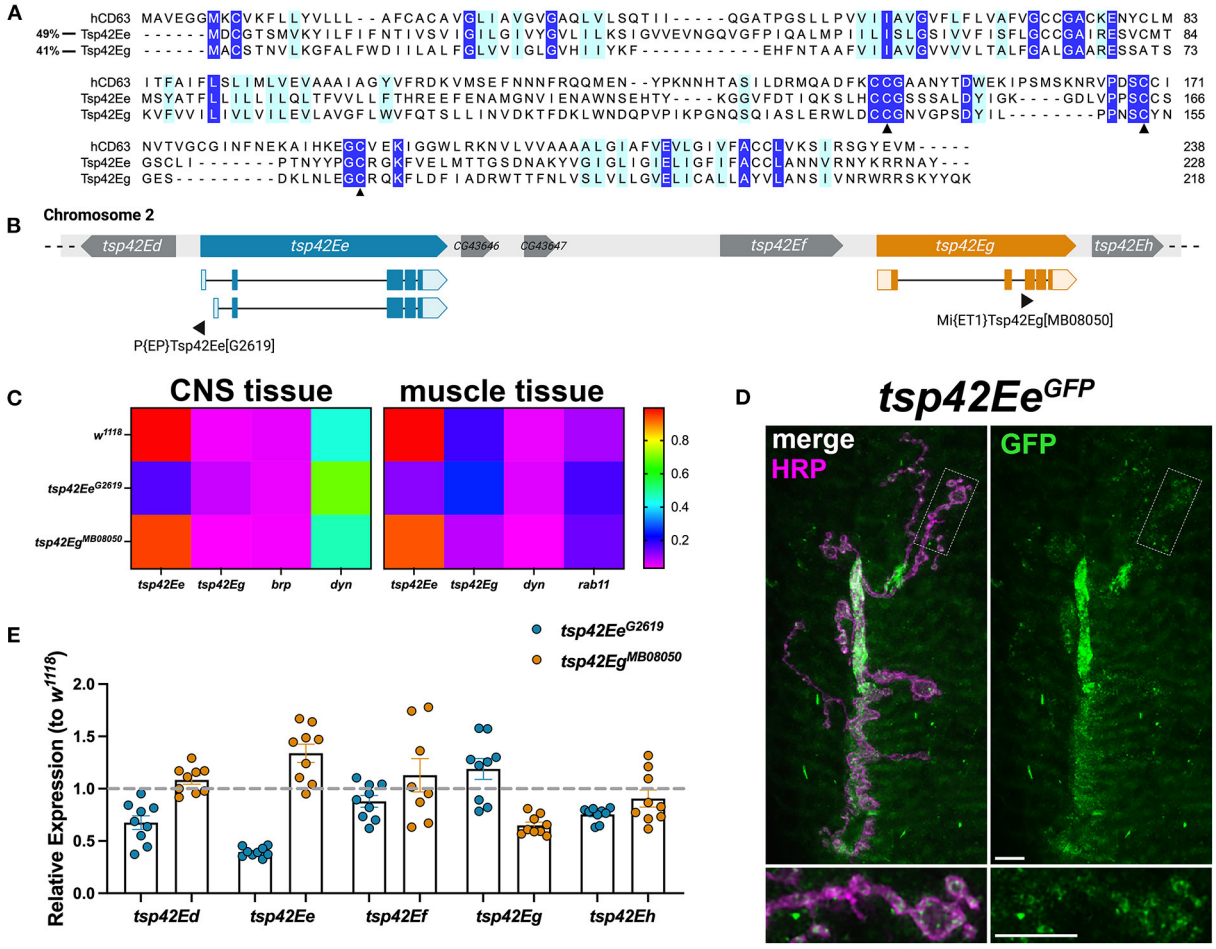


FIGURE 1
Tsp42Ee and Tsp42Eg are CD63 homologs expressed at the *Drosophila* NMJ. **(A)** Multiple sequence alignment (Clustal Omega) of hCD63, Tsp42Ee, and Tsp42Eg. Identical residues (dark blue) and similar residues as determined by biochemical properties (light blue) are indicated. Arrowheads denote regions of critical motif conservation. **(B)** Arrangement of *tsp* genes (*tsp42Ed–tsp42Eh*) on *Drosophila* chromosome 2. Exonic regions of *tsp42Ee* and *tsp42Eg* are mapped with lighter shaded regions denoting 5′ and 3′ untranslated regions. Sites of transposon insertion for each *tsp* mutant construct are indicated below. **(C)** Heat maps of relative transcript expression in $tsp42Ee^{G2619}$ and $tsp42Eg^{MB08050}$ CNS and muscle tissue relative to controls ($w^{1118}$). **(D)** Representative confocal image of the 6/7 NMJ showing the localization of GFP-tagged Tsp42Ee (green) in presynaptic terminal boutons (magenta, HRP). Scale bar = 5 $\mu$M. **(E)** Histograms of *tsp* transcript expression in $tsp42Ee^{G2619}$ and $tsp42Eg^{MB08050}$ whole larvae relative to controls ($w^{1118}$; dashed line). Each point represents one technical replicate. Error bars represent SEM.

and duration of motor neuron activity and contractile force of postsynaptic muscles (Ormerod et al., 2022). $tsp42Ee^{G2619}$ and $tsp42Eg^{MB08050}$ mutants showed impaired movement as evidenced by reductions in maximum and average larval crawling velocity. These resulted in decreased total distance traveled (Figure 2A). To determine whether the observed movement deficits correlated with synaptic function, we recorded mEJCs and eEJCs from muscle six of third instar larva using two electrode voltage clamp. $tsp42Eg^{MB08050}$ but not $tsp42Ee^{G2619}$ mutants exhibited reduced eEJC amplitudes compared to $w^{1118}$ controls (Figure 2C) producing reduced quantal content compared with controls (Figure 2B). Both *tsp* mutants showed reductions in mEJC frequency compared to controls but there were no differences in mEJC amplitudes (Figure 2D; $w^{1118} = 1.23$ nA, $n = 14$; $tsp42Ee^{G2619} = 1.16$ nA, $n = 14$, $p = 0.70$; $tsp42Eg^{MB08050} = 1.16$ nA, $n = 12$, $p = 0.66$). The reduction in mEJC frequency indicates that both *tsp* mutants may possess fewer functional active zones.

Each synaptic bouton contains several active zones, which include the scaffold protein Brp (Wagh et al., 2006). We quantified the density of active zones as indicated by Brp and found that both *tsp* mutants showed an increase in density of active zones compared with controls (Figures 3A,A′). Active zones are closely apposed to postsynaptic glutamate receptors and this apposition is important for the efficiency of neurotransmission. There were no differences in apposition as indicated by the distances between Brp and the essential postsynaptic glutamate receptor subunit, GluRIIC, in either

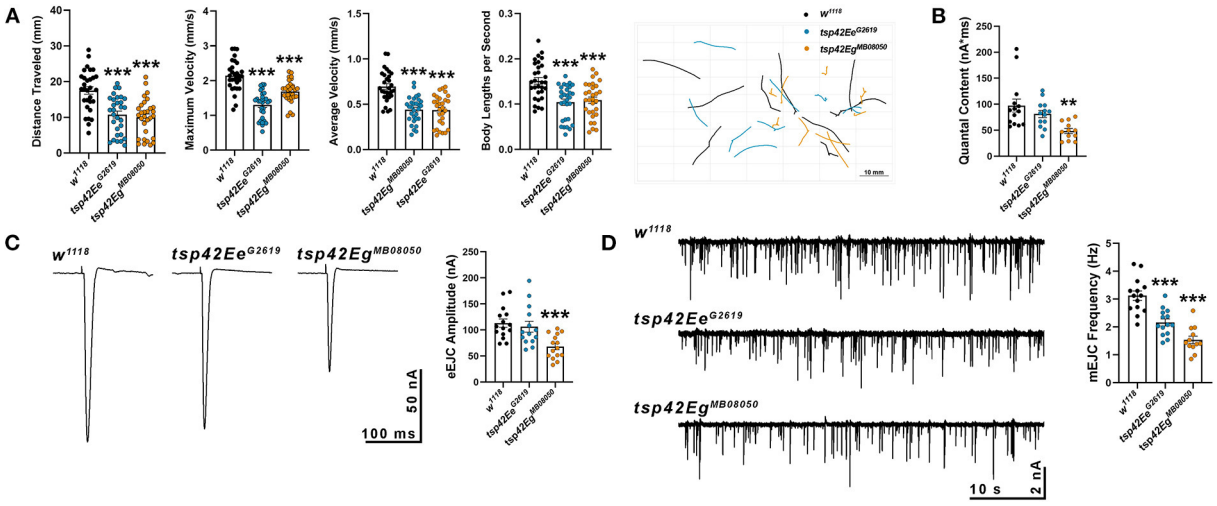


FIGURE 2
Tetraspanin function is important for proper vesicle release and locomotion. **(A)** wrMTrck quantification of larval crawling behavior on an agar arena for 30 s. Distance traveled, maximum velocity, average velocity, and crawling velocity normalized to body size (body lengths per second) were significantly reduced in both *tsp42Ee* ($p < 0.0001$) and *tsp42Eg* mutants ($p < 0.0001$). **(B)** Quantal content is significantly reduced in $tsp42Eg^{MB08050}$ ($p = 0.0022$) but not $tsp42Ee^{G2619}$ ($p = 0.28$) mutants. **(C)** Representative traces (left) and quantification (right) show reduced eEJC amplitudes in $tsp42Eg^{MB08050}$ ($p < 0.0001$) but not $tsp42Ee^{G2619}$ ($p = 0.60$) mutants. **(D)** Representative mEJC traces (left) from larval body wall muscle 6. Quantification (right) of mEJC frequency indicates both $tsp42Ee^{G2619}$ ($p = 0.0001$) and $tsp42Eg^{MB08050}$ ($p < 0.0001$) mutants exhibit significant reductions in mEJC frequency. Error bars represent SEM. Unpaired *t* tests were used for all statistical comparisons.

*tsp* mutant (data not shown). There was, however, a decrease in GluRIIC fluorescence intensity in $tsp42Ee^{G2619}$ mutants compared to controls (Figures 3A,A').

The reduction in mEJC frequency in *tsp* mutants also led us to examine synaptic morphology and synaptic proteins important for vesicle release. We examined gross morphology of motor neurons using α-Horseradish peroxidase (HRP), which recognizes neuronal N-glycans (Parkinson et al., 2013), to label neuronal membranes. Motor neurons contain presynaptic boutons arranged within branched arbors (Menon et al., 2013). While $tsp42Eg^{MB08050}$ mutants were morphologically similar as controls, $tsp42Ee^{G2619}$ mutants exhibited overgrown motor neurons characterized by increased numbers of branches and boutons (Figure 3B).

We next examined several additional presynaptic proteins. Syt binds $Ca^{2+}$ to enable SNARE complex formation thereby facilitating exocytosis of presynaptic vesicles (Hackett and Ueda, 2015) and CSP is a vesicle-associated protein chaperone (Gundersen, 2020). Synaptic levels of both Syt and CSP were reduced in *tsp* mutants compared with $w^{1118}$ controls (Figures 3C,C',D,D'). Similarly, Syn, a protein that tethers the reserve pool of vesicles to the actin cytoskeleton (Hackett and Ueda, 2015), was reduced in $tsp42Ee^{G2619}$ mutants but increased in $tsp42Eg^{MB08050}$ mutants (Figures 3E,E'). The vesicular glutamate transporter, vGLUT, however, was similar in mutants and controls (Supplementary Figure 3). These data indicate that the impaired synaptic function in *tsp* mutants may be due to a reduction in the release probability of vesicles. We investigated this possibility by performing paired pulse recordings at *tsp* mutant NMJs. Increases in paired pulse ratios are correlated with a decrease in release probability (Regehr, 2012). There were no significant differences in paired pulse ratios in *tsp* mutants at interstimulus intervals of 10, 20, 50, or 100 ms (Supplementary Figure 4) indicating that intracellular $Ca^{2+}$ dynamics at *tsp* mutant active zones are unaffected.

## Tsp42Ee and Tsp42Eg differentially regulate synaptic vesicle pools to restrict endocytosis

Altered endocytosis may contribute to reductions in evoked and spontaneous neurotransmission in *tsp* mutants. Therefore, we assessed endocytosis using the lipophilic dye, FM 1–43FX, to label newly endocytosed synaptic vesicles (Verstreken et al., 2008) after 1 min stimulation with 1.0 mM $Ca^{2+}$ and 90 mM KCl. Surprisingly, both *tsp* mutants exhibited an increase in endocytosis compared with controls (Figure 4A). To ensure mutations in *tsps* do not affect the affinity of FM 1-43FX for the membrane, we examined FM 1-43FX intensities in the absence of stimulation and found no differences between controls and *tsp* mutants (Supplementary Figure 5).

Endocytosis requires Endophilin A (EndoA) to facilitate membrane invagination and recruit Dyn (Kjaerulff et al.,

10.3389/fncel.2022.957232

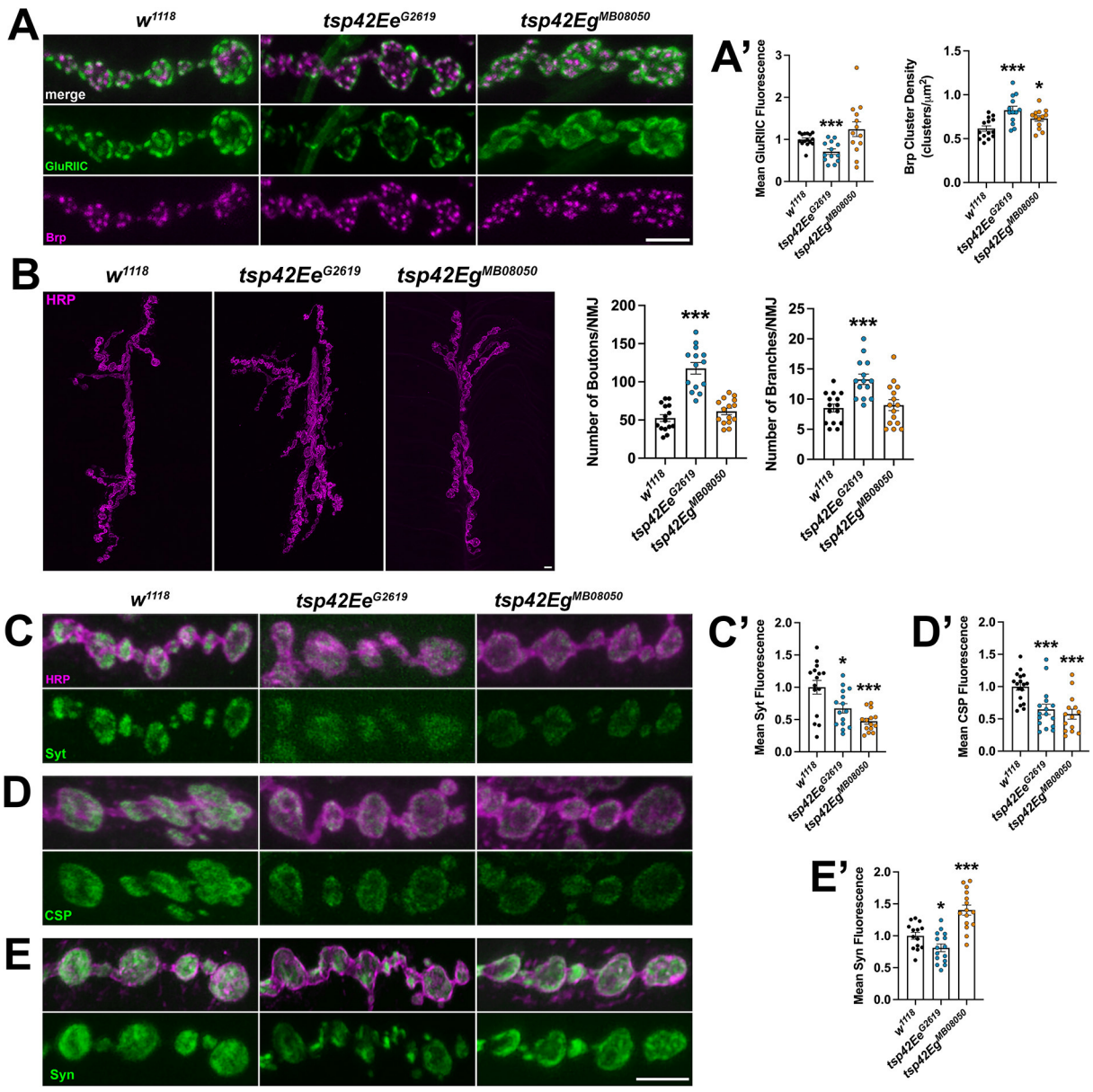


FIGURE 3
Tsp42Ee and Tsp42Eg are important for active zone organization and vesicle-associated protein localization. **(A)** Panels show representative images of control ($w^{1118}$) and *tsp* mutant boutons immunolabeled for the active zone marker, Brp (magenta), and postsynaptic glutamate receptor subunit, GluRIIC (green). **(A')** Quantification of mean Brp puncta density and fluorescence intensity of GluRIIC. Brp density is significantly increased in both $tsp42Ee^{G2619}$ ($p = 0.0006$) and $tsp42Eg^{MB08050}$ ($p = 0.0142$) mutants. GluRIIC fluorescence is significantly reduced in $tsp42Ee^{G2619}$ mutants ($p = 0.0005$). **(B)** Confocal images of HRP-labeled 6/7 NMJ's (left) and quantification of bouton and branch number (right). Boutons ($p < 0.0001$) and branch numbers ($p = 0.0001$) were significantly increased in $tsp42Ee^{G2619}$ mutants. **(C–E)** Representative confocal images showing HRP-labeled neurons (magenta) and the localization of Syt **(C)**, CSP **(D)**, or Syn **(E)** (green). Right bar graphs show quantification of immunofluorescence normalized to $w^{1118}$ controls. Mean Syt fluorescence **(C')** is significantly reduced in $tsp42Ee^{G2619}$ ($p = 0.0168$) and $tsp42Eg^{MB08050}$ ($p = 0.0001$) mutants. Mean CSP fluorescence **(D')** is significantly reduced in $tsp42Ee^{G2619}$ ($p = 0.0010$) and $tsp42Eg^{MB08050}$ ($p < 0.0001$) mutants. Mean Syn fluorescence **(E')** is significantly reduced in $tsp42Ee^{G2619}$ mutants ($p = 0.0295$) but increased in $tsp42Eg^{MB08050}$ mutants ($p = 0.0003$). Scale bars = 5 $\mu$M. Errors bars represent SEM. Unpaired *t* tests were used for all statistical comparisons.

2011). EndoA is recruited to perisynaptic membranes by the endocytic scaffold, Dap160/Intersectin, which directly interacts with Eps15 (Koh et al., 2007). EndoA was increased in both *tsp* mutants compared to controls while Dyn was increased in $tsp42Ee^{G2619}$ but not $tsp42Eg^{MB08050}$ mutants (Figure 4B). Conversely, there were no differences in synaptic levels of Dap160 or Eps15 in *tsp* mutants (data not shown). Thus, the increase in endocytosis in *tsp* mutants may be partly explained by increases in synaptic EndoA and/or Dyn.

10.3389/fncel.2022.957232

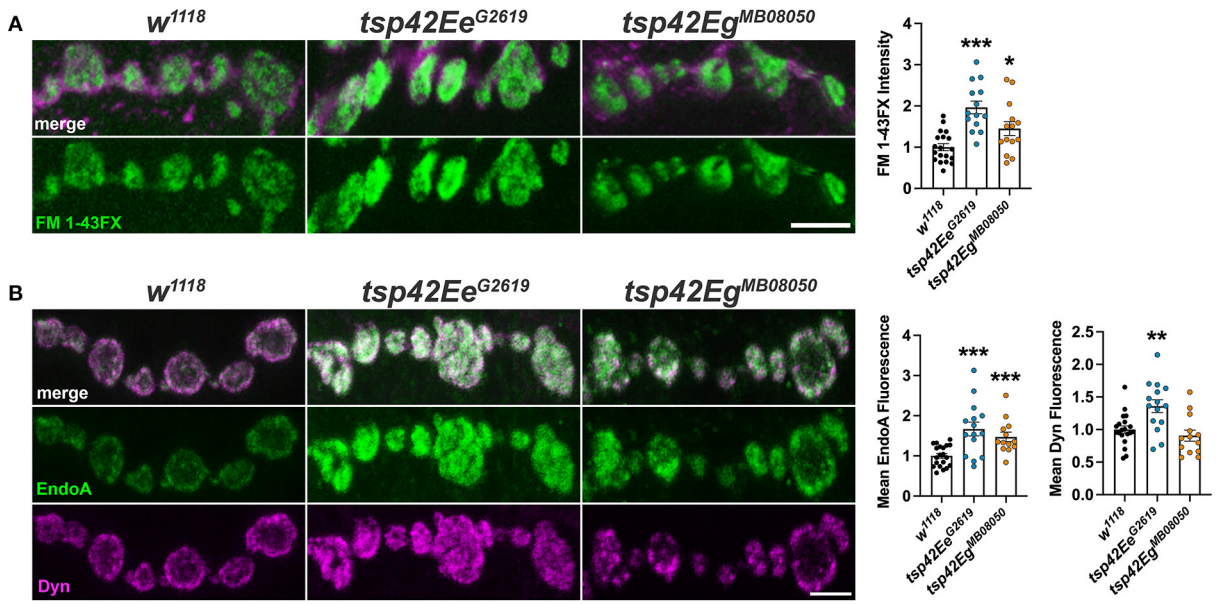


FIGURE 4
Tsps negatively regulate endocytosis and endocytic protein localization. **(A)** Representative confocal images showing relative rates of endocytosis in HL-3 + 1.0 mM $Ca^{2+}$ as measured by FM 1-43FX immunofluorescence at 6/7 terminal boutons (left). Quantification of FM 1-43FX fluorescence intensity relative to $w^{1118}$ controls (right). Both $tsp42Ee^{G2619}$ and $tsp42Eg^{MB08050}$ mutants show significantly higher endocytosis ($p < 0.0001$ and $p = 0.0144$, respectively). **(B)** Representative images of terminal boutons (left) immunolabeled for EndoA (green) and Dyn (magenta) and quantification of mean immunofluorescence (right). EndoA fluorescence is significantly increased in both $tsp42Ee^{G2619}$ ($p = 0.0002$) and $tsp42Eg^{MB08050}$ mutants ($p = 0.0004$). Mean Dyn fluorescence is significantly increased in $tsp42Ee^{G2619}$ mutants ($p = 0.0018$). Scale bars = 5 $\mu$M. Errors bars represent SEM. Unpaired *t* tests were used for all statistical comparisons.

In addition to the proper localization of endocytic proteins, neurotransmission relies on the coordinated mobilization and trafficking of vesicles from the reserve (RP), readily releasable (RRP), and recycling pools (Augustine et al., 1999; Alabi and Tsien, 2012). Vesicles in the RRP are docked at presynaptic active zone release sites and, therefore, are the first to be released upon stimulation (Rosenmund and Stevens, 1996; Hoopmann et al., 2010). The RP, however, is mobilized upon high frequency stimulation to replenish the RRP (Pieribone et al., 1995; Zhang and Augustine, 2021). To sustain rapid vesicle release at the synapse, recycling of synaptic vesicles through the endocytic and endosomal sorting pathways must occur (Hoopmann et al., 2010; Saheki and De Camilli, 2012). Thus, disruptions in vesicle trafficking through endosomal pathways and synaptic vesicle pools may alter endocytosis and compromise neurotransmitter release.

To determine if *tsp* mutants exhibited altered vesicle pool dynamics, we assessed evoked responses induced by several stimulation paradigms. First, we examined both clathrin-mediated and activity-dependent bulk endocytosis by recording eEJCs in 1.0 mM $Ca^{2+}$ during and after high frequency stimulation. This stimulation first utilizes the RRP of vesicles, then mobilizes the RP of vesicles, and measures recycling of newly endocytosed synaptic vesicles (Delgado et al., 2000; Long et al., 2010; Müller et al., 2012). eEJC amplitudes were assessed at 20 Hz stimulation for 60 s followed by a recovery period of 0.2 Hz stimulation for a 50 s (Long et al., 2010). During high frequency stimulation, controls show a rapid reduction in eEJC amplitudes followed by increased eEJC amplitudes during the post-stimulation recovery period when the RRP of vesicles is replenished. $tsp42Ee^{G2619}$ mutant eEJCs were similar as $w^{1118}$ controls at all time points (Figures 5A,B). $tsp42Eg^{MB08050}$ mutants, however, exhibited potentiated eEJCs for the first 30 s of high frequency stimulation followed by a gradual decline in eEJCs. The increase in eEJC amplitudes during high frequency stimulation in $tsp42Eg^{MB08050}$ mutants is consistent with the increase in FM 1-43FX uptake (Figure 4A). During the recovery period, however, eEJCs were reduced in $tsp42Eg^{MB08050}$ mutants indicating vesicle recycling is impaired. Therefore, even though there is increased endocytosis in $tsp42Eg^{MB08050}$ mutants, the endocytosed vesicles are recycled slower than controls.

To assess whether the increase in endocytosis occurs in *tsp* mutants because of increased vesicle pool sizes, we used Bafilomycin A1, which inhibits vesicular $H^+$ pumps to block glutamate uptake into vesicles (Cavelier and Attwell, 2007). In the presence of Bafilomycin, newly endocytosed vesicles will not be refilled with glutamate and eEJC amplitudes will diminish over time as vesicles that lack glutamate are

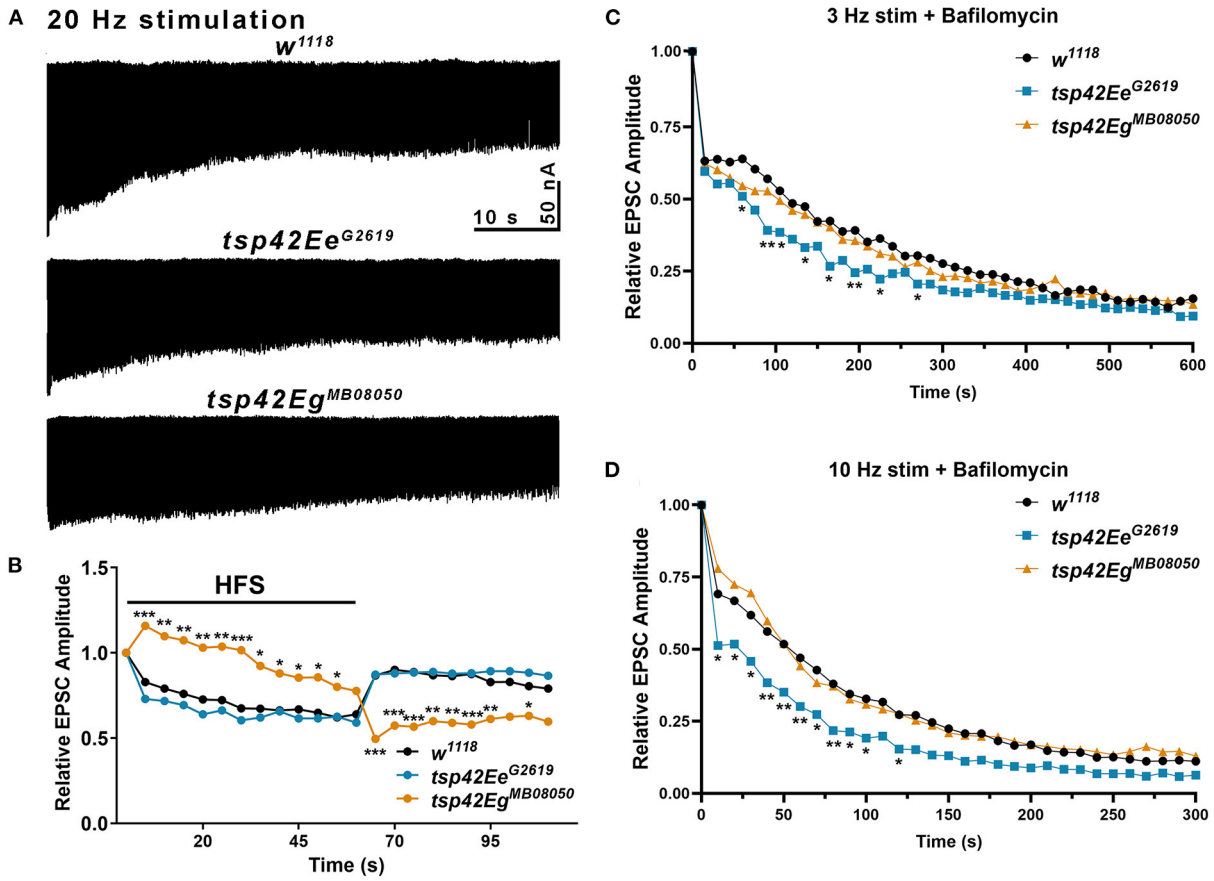


FIGURE 5
Tsp42Ee and Tsp42Eg differentially affect evoked responses to high frequency stimulation and synaptic vesicle pools. **(A)** Representative recordings from animals during 20 Hz stimulation in HL-3 + 1.0 mM $Ca^{2+}$. **(B)** Relative EPSC amplitudes (to the first stimulus) over time during both 20 Hz stimulation (first 60 s) and the recovery period (final 50 s). *Tsp42Eg*$^{MB08050}$ mutants showed increased EPSC amplitudes during the first 55 s of 20 Hz stimulation but decreased amplitudes during the recovery period as determined by a two-way ANOVA ($F_{(39,858)} = 15.27$, $p < 0.0001$) followed by *post hoc* Dunnett's multiple comparisons tests. **(C)** Relative EPSC amplitudes over time during 3 Hz stimulation in HL-3 containing 2 $\mu$m Bafilomycin and 1.0 mM $Ca^{2+}$. *Tsp42Ee*$^{G2619}$ mutants showed significant reductions in EPSC amplitudes at 60, 90, 105, 135, 165, 195, 225, and 270 s as determined by a two-way ANOVA ($F_{(29,1160)} = 71.38$, $p < 0.0001$) followed by *post hoc* Dunnett's multiple comparisons tests. **(D)** Relative EPSC amplitudes over time during 10 Hz stimulation in HL-3 containing 2 $\mu$m Bafilomycin and 1.0 mM $Ca^{2+}$. *Tsp42Ee*$^{G2619}$ mutants showed significant reductions in EPSC amplitudes at 10–100 and 120 s as determined by a two-way ANOVA ($F_{(28,840)} = 86.10$, $p < 0.0001$) followed by *post hoc* Dunnett's multiple comparisons tests.

released. Low frequency, 3 Hz stimulation relies on the RRP and recycling pools of vesicles. Higher frequency, 10 Hz stimulation mobilizes the RP of vesicles (Delgado et al., 2000). We examined eEJC amplitudes after 20 min incubation with Bafilomycin in 1.0 mM $Ca^{2+}$ during 3 or 10 Hz stimulation. The initial decline in eEJC amplitudes at both 3 and 10 Hz was more pronounced in *tsp42Ee*$^{G2619}$ mutants compared with controls (Figures 5C,D) suggesting these animals possess smaller vesicle pools. There were no differences in *tsp42Eg*$^{MB08050}$ mutants at any time point during either 3 or 10 Hz stimulation. Collectively, these data suggest that the increase in endocytosis at *tsp* mutant synapses occurs through different mechanisms.

## Tsps regulate synaptic cytoskeleton structure and membrane lipid composition

The recruitment and assembly of endocytic machinery is influenced by membrane lipid composition (Sun et al., 2007). Specifically, phosphatidylinositol-4,5-bisphosphate [PI(4,5)$P_2$] organizes into microdomains and regulates endocytosis, vesicle trafficking, and NMJ growth by interacting with cytoskeleton-binding and synaptic vesicle-associated proteins (Cremona et al., 1999; Khuong et al., 2010; Mandal, 2020). Thus, Tsps may negatively regulate endocytosis (Figure 4A) and endocytic protein localization (Figure 4B) by regulating synaptic

$PI(4,5)P_2$ distribution. Notably, CD63 directly interacts with Syntenin-1, a high affinity $PI(4,5)P_2$ binding protein (Mortier et al., 2005; Latysheva et al., 2006). There was a marked reduction in $PI(4,5)P_2$ at *tsp42Eg*$^{MB08050}$ mutant synapses while *tsp42Ee*$^{G2619}$ mutants showed no change in synaptic $PI(4,5)P_2$ levels (Figures 6A,A'). These results, however, do not explain why endocytosis is increased in *tsp* mutants as $PI(4,5)P_2$ is important for both clathrin-mediated and activity-dependent bulk endocytosis (Sun et al., 2007; Li et al., 2020). One possibility is that Tsps recruit cytoskeletal proteins to sites of endocytosis and regulate vesicle trafficking independent of $PI(4,5)P_2$ microdomains.

Microtubules and F-actin are foundational building blocks of the synaptic cytoskeleton. Their dynamics regulate active zone organization, neurotransmission, and vesicle transport (Roos et al., 2000; Lepicard et al., 2014; Piriya Ananda Babu et al., 2020). Furthermore, actin assembly at sites of endocytosis facilitates the mechanics of membrane invagination and endocytic vesicle trafficking (Smythe and Ayscough, 2006; Liu et al., 2009). The highly dynamic microtubule cytoskeleton is regulated by covalent modifications such as tubulin acetylation, polyglutamylation, and detyrosination that either promote microtubule polymerization or depolymerization. Specifically, $\alpha$-tubulin acetylation at Lys-40 confers stability to microtubule polymers (Li and Yang, 2015) and disruptions in synaptic microtubule integrity lead to defective synaptic vesicle anchoring and neurotransmitter release (Piriya Ananda Babu et al., 2020). No significant differences in synaptic acetylated tubulin levels were observed in *tsp* mutants compared with $w^{1118}$ controls (data not shown). Thus, alterations in microtubule stability cannot explain the endo/exocytic dysregulation observed at *tsp* mutant NMJs.

The microtubule-binding protein, Futsch, which is the MAP1B homolog, colocalizes with the microtubule cytoskeleton and is required for normal glutamate release at the *Drosophila* NMJ (Lepicard et al., 2014). During periods of synaptic growth, microtubules adopt looped structures that are stabilized by association with Futsch. In contrast, Futsch does not associate with unbundled microtubules found in static boutons (Roos et al., 2000; Ruiz-Canada et al., 2004; Miech et al., 2008). The presence of Futsch loops in synaptic boutons can be used to indicate sites of active growth and cytoskeletal rearrangement (Sarthi and Elefant, 2011). We immunostained for Futsch at 6/7 NMJs and found that both *tsp* mutant synapses have increased Futsch-positive loops (Figures 6B,B') indicating that *tsp* mutant synapses have more dynamic microtubule rearrangements than controls. This result is consistent with the increase in active zone density in *tsp* mutants (Figures 3A,A') as previous findings directly implicate Futsch in the anchoring of active zone components to the microtubule cytoskeleton (Lepicard et al., 2014). These results, however, fail to explain our finding that, while *tsp* mutants have more active zones, some active zones don't function properly during spontaneous or evoked neurotransmission.

We next examined the synaptic localization of two F-actin regulators, Wiskott-Aldrich syndrome protein (WASp) and SCAR. WASp and the WASp family verprolin-homologous (WAVE) protein homolog, SCAR, regulate Arp2/3-dependent actin branching by integrating intracellular signaling inputs in *Drosophila* (Machesky et al., 1999; Ben-Yaacov et al., 2001; Zallen et al., 2002; Stradal et al., 2004). Actin branching is important for maintaining both overall synaptic morphology and the local formation of synaptic actin patches at sites of endocytosis. WASp, through interactions with Dap160, is a regulator of active zone assembly and endocytic function at the *Drosophila* NMJ (Del Signore et al., 2021). We examined WASp at *tsp* mutant synapses and observed no differences in the synaptic levels of WASp in either *tsp42Ee*$^{G2619}$ or *tsp42Eg*$^{MB08050}$ mutants compared to controls (data not shown). Similarly, the WASp-dependent actin regulator, Nervous Wreck (Nwk) (Coyle et al., 2004) was unchanged at either *tsp* mutant synapse (data not shown). Both *tsp* mutants, however, exhibited decreased levels of SCAR at the synapse (Figures 6C,C'). Upon Rac1 signaling, SCAR induces Arp2/3 activity and subsequent remodeling of the actin cytoskeleton during synaptic development and plasticity (Zallen et al., 2002; Schenck et al., 2004). These results suggest that Tsp42Ee and Tsp42Eg influence synaptic levels of SCAR, but not WASp, to regulate actin branching. These results also suggest that, despite reduced $PI(4,5)P_2$ and SCAR in *tsp42Eg*$^{MB08050}$ mutants and reduced SCAR in *tsp42Ee*$^{G2619}$ mutants, there may be sufficient WASp at the synapse to promote Arp2/3-dependent branching that facilitates increased endocytosis in these animals.

## Expression of human CD63 at the *Drosophila* NMJ attenuates endocytosis

Tsp42Ee and Tsp42Eg are homologs of human CD63 (Figure 1A). CD63 was the first characterized Tsp and is expressed in all cell types. It is localized to the plasma membrane but is enriched on internal membranes including late endosomes and lysosomes (Pols and Klumperman, 2009). The described function of CD63 in neurons is largely limited to its role in the trafficking and biogenesis of exosomes (Andreu and Yanez-Mo, 2014). To investigate the contribution of CD63 to the synaptic vesicle cycle, we expressed human CD63 (hCD63) in neurons using the *elav-Gal4* driver or in postsynaptic muscle using the *24B-Gal4* driver. Expression of hCD63 in either neurons or muscle decreased endocytosis as evidenced by reduced internalization of FM 1-43FX dye (Figures 7A,B). Similarly, there were reductions in EPSC amplitudes at 10 and 50 s after administering 20 Hz high frequency stimulation when hCD63 was expressed in neurons but not in postsynaptic muscle cells

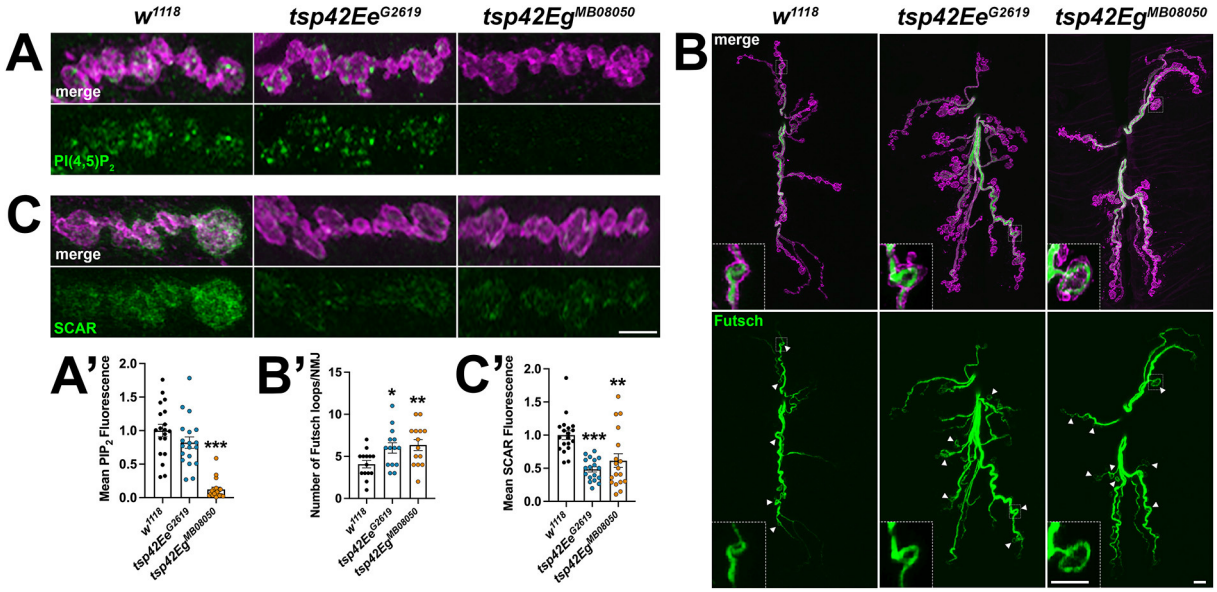


FIGURE 6
Tsp42Ee and Tsp42Eg regulate synaptic membrane lipids and cytoskeletal structures. **(A,C)** Panels showing terminal boutons (HRP, magenta) immunolabeled for $PI(4,5)P_2$ (A, green) or SCAR (C, green). **(A')** Quantification of mean $PI(4,5)P_2$ fluorescence intensity relative to $w^{1118}$ controls. $PI(4,5)P_2$ fluorescence is decreased at $tsp42Eg^{MB08050}$ mutant synapses ($p < 0.0001$). **(B)** Confocal images of 6/7 NMJs (HRP, magenta) immunolabeled for Futsch (green), a microtubule-binding protein. Arrowheads indicate Futsch-labeled looped microtubules with inset panels showing details of a representative Futsch loop. **(B')** Histograms display numbers of Futsch-positive loops void of punctate signal at control and *tsp* mutant NMJs. Futsch loops are significantly increased in $tsp42Ee^{G2619}$ ($p = 0.0174$) and $tsp42Eg^{MB08050}$ mutants ($p = 0.0073$). **(C')** Quantification of mean SCAR fluorescence intensity relative to $w^{1118}$ controls. SCAR fluorescence intensity is significantly decreased in both $tsp42Ee^{G2619}$ and $tsp42Eg^{MB08050}$ mutants ($p < 0.0001$ and $p = 0.0032$, respectively). Scale bars = 5 μM. Errors bars represent SEM. Unpaired *t* tests were used for all statistical comparisons.

(Figures 7C,D). There were no differences in EPSC amplitudes during the recovery period. There were also no differences in eEJC amplitudes, quantal content, mEJC amplitudes, or mEJC frequencies in animals expressing hCD63 in neurons or muscle (data not shown). These data indicate that hCD63, like Tsp42Ee and Tsp42Eg (Figure 4A), restricts endocytosis and may be functionally redundant with Tsp42Ee and Tsp42Eg.

## Discussion

Our findings uncover novel synaptic roles for the *Drosophila* CD63 orthologs, Tsp42Ee and Tsp42Eg, and highlight their shared and unique functions. Both Tsps facilitate basal neurotransmitter release and locomotor output (Figure 2) by regulating synaptic vesicle pool dynamics (Figure 5). Tsp42Ee and Tsp42Eg also promote synaptic localization of the vesicle-associated proteins Syt and CSP (Figures 3C,D) but restrict the cytoskeletal proteins Futsch and SCAR (Figures 6B,C). Finally, we find that Tsp42Ee and Tsp42Eg both negatively regulate endocytosis (Figure 4A). Given that Tsps are organizational hubs (Stipp et al., 2003; Charrin et al., 2014), loss of *tsp42Ee* or *tsp42Eg* function likely affects the synaptic and membrane-specific localization of additional neuronal proteins. Thus, the unique combination of synaptic perturbations in $tsp42Ee^{G2619}$ and $tsp42Eg^{MB08050}$ mutants may produce some of the unique phenotypes we observed.

Both $tsp42Ee^{G2619}$ and $tsp42Eg^{MB08050}$ mutants exhibited enhanced synaptic endocytosis (Figure 4A) and, in support of functionally redundant roles for Tsps (Fradkin et al., 2002), both *tsp42Ee* and *tsp42Eg* are expressed in presynaptic motor neurons and postsynaptic muscles (Figure 1C) of the NMJ. $tsp42Ee^{G2619}$ and $tsp42Eg^{MB08050}$ mutants differed, however, in their evoked responses and in synaptic levels of GluRIIC, Syn, Dyn, and $PI(4,5)P_2$ (Figures 3A,E, 4B, 6A). Our findings are consistent with previous studies establishing distinct roles for Tsps as the mammalian Tsps, TSPAN5, TSPAN6, and TSPAN7 also perform different hippocampal functions. While knock down of TSPAN5 does not affect mEPSC amplitude, mEPSC frequency, or evoked amplitudes (Moretto et al., 2019), knock down of postsynaptic TSPAN7 attenuates each of these (Bassani et al., 2012). The AMPA receptor subunits GluA1 and GluA2/3 are significantly reduced in TSPAN7 knock down hippocampal pyramidal neuron cultures (Moretto et al., 2019) but unchanged in *Tspan6* knock out synaptosomes (Salas et al., 2017). Similarly, we observed a significant decrease in GluRIIC and Syn in $tsp42Ee^{G2619}$ but $tsp42Eg^{MB08050}$ mutants exhibited no change in GluRIIC and increased Syn (Figures 3A,E). The loss of Syn could account for the reduction in total vesicles in $tsp42Ee^{G2619}$ mutant NMJs (Figures 5C,D). Mouse Syn triple

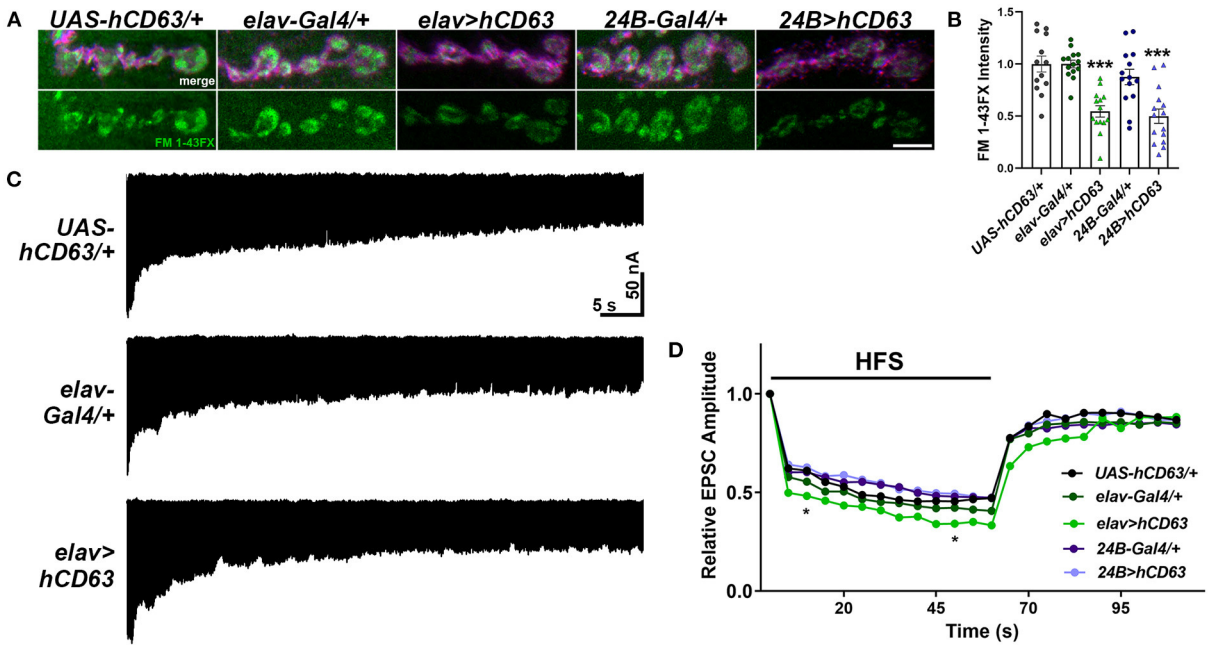


FIGURE 7
Expression of human CD63 in *Drosophila* larval neurons impairs endocytosis. **(A)** Representative confocal images showing relative rates of endocytosis in HL-3 + 1.0 mM $Ca^{2+}$ as measured by FM 1-43FX immunofluorescence in 6/7 terminal boutons of genotypes as indicated. **(B)** Quantification of FM 1-43FX fluorescence intensity relative to the *UAS-hCD63/+* outcrossed controls. FM 1-43FX fluorescence is significantly reduced when hCD63 is expressed in neurons (*elav>hCD63*; $F_{(2,38)} = 21.18$, $p < 0.0001$, one-way ANOVA) and in muscle (*24B>hCD63*; $F_{(2,39)} = 12.97$, $p < 0.0001$, one-way ANOVA). **(C)** Representative recordings from animals during 20 Hz stimulation in HL-3 + 1.0 mM $Ca^{2+}$. **(D)** Relative EPSC amplitudes over time during both 20 Hz stimulation (first 60s) and the recovery period (final 50s). Expressing human CD63 (hCD63) in neurons using the *elav-Gal4* driver resulted in a significant decrease in EPSC amplitudes at 10 and 50 s as determined by a two-way ANOVA ($F_{(53,1166)} = 25.37$, $p < 0.0001$) followed by *post hoc* Dunnett's multiple comparisons tests.

knock outs (Fornasiero et al., 2012) and *Drosophila syn* knock outs (Akbergenova and Bykhovskaia, 2010) exhibit reductions in the total number of synaptic vesicles. Indeed, *tsp42Ee*$^{G2619}$ mutant responses to 10 Hz stimulation in the presence of Bafilomycin mirror that of *syn* knock outs (Akbergenova and Bykhovskaia, 2010). The RRP is unaffected in Syn triple knock outs (Fornasiero et al., 2012) and this may be why, similar as *tsp42Ee*$^{G2619}$ mutants, there are no changes in single evoked currents in Syn triple knock outs (Gitler et al., 2008).

Presynaptic exo- and endocytosis are thought to be coupled to maintain appropriate protein localization, preserve the structure of the synapse, and enable continued exocytosis (Maritzen and Haucke, 2018). Loss of function mutations in both *tsp42Ee* and *tsp42Eg* lead to reduced mEJC frequencies (Figure 2D) and evoked EJCs and quantal content in *tsp42Eg*$^{MB08050}$ but not *tsp42Ee*$^{G2619}$ mutants (Figures 2B,C). Both *tsp* mutants also exhibited increased endocytosis (Figure 4A) suggesting an uncoupling of exo- and endocytosis. Further, *tsp42Eg* mutants showed potentiated evoked responses during 20 Hz high frequency stimulation. Reduced evoked responses from a single stimulus but increased evoked responses during high frequency stimulation could occur because of altered $Ca^{2+}$ and/or $K^{+}$ dynamics.

Presynaptic exocytosis requires $Ca^{2+}$ influx through voltage-gated $Ca^{2+}$ channels thereby increasing intracellular $Ca^{2+}$ at the AZ. $Ca^{2+}$ binding to Syt enables the fusion and exocytosis of vesicles (Hackett and Ueda, 2015). Similarly, endocytosis also requires $Ca^{2+}$ influx (Augustine et al., 2003), which occurs at AZs and periactive zones by $Ca_V2$ and $Ca_V1$ channels, respectively (Krick et al., 2021). The loss of Syt in both *tsp42Ee*$^{G2619}$ and *tsp42Eg*$^{MB08050}$ mutants (Figure 3C) may result in fewer functional release sites, despite an increase in Brp-positive puncta (Figure 3A), leading to reductions in mEJC frequency and evoked responses to a single suprathreshold stimulus in *tsp42Eg*$^{MB08050}$ mutants. Because paired pulse ratios in both *tsp* mutants were similar as controls (Supplementary Figure 4), $Ca^{2+}$ entry through properly localized AZ voltage-gated $Ca^{2+}$ channels and $Ca^{2+}$ sensitivity are probably unaffected in *tsp* mutants. Impaired $Ca^{2+}$ buffering and/or extrusion, however, could potentially overcome the loss of Syt and result in increased $Ca^{2+}$ accumulation during high frequency stimulation, enhanced evoked currents during high frequency stimulation, and enhanced endocytosis as observed in *tsp42Eg*$^{MB08050}$ mutants (Figures 4A, 5A,B). Cbp53E is the sole $Ca^{2+}$ buffer at *Drosophila* neuronal synapses including the NMJ (Hagel et al., 2015). In addition to $Ca^{2+}$ buffers, synaptic $Ca^{2+}$

10.3389/fncel.2022.957232

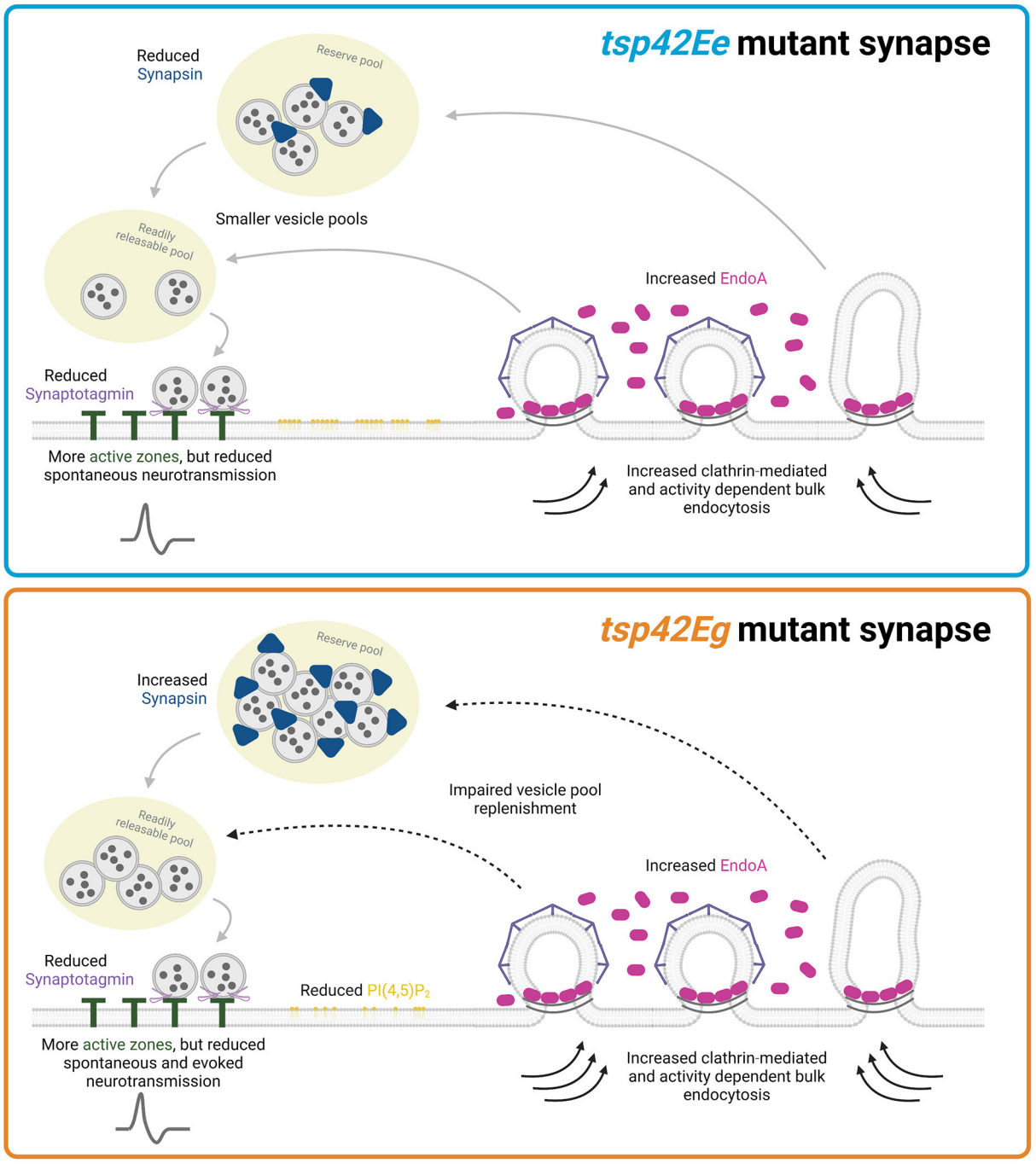


FIGURE 8
Tsp42Ee and Tsp42Eg regulate synaptic function through shared and distinct mechanisms. Both Tsp42Ee and Tsp42Eg negatively regulate endocytosis and synaptic localization of the endocytic protein, EndoA. However, Tsp42Ee and Tsp42Eg differentially affect Synapsin and vesicle pool dynamics. Tsp42Ee promotes synaptic localization of Synapsin and is implicated in the maintenance of vesicle pool size and mobilization of vesicles from the reserve pool to the readily releasable pool. Tsp42Eg, however, restricts Synapsin and is necessary for vesicle recycling. Tsp42Eg also distinctly regulates $PI(4,5)P_2$ localization. Finally, both Tsp42Ee and Tsp42Eg facilitate active zone organization and promote Synaptotagmin localization to active zones. The combined synaptic functions of Tsp42Ee and Tsp42Eg allow for proper neurotransmission as *tsp42Ee*$^{G2619}$ mutants have reduced spontaneous neurotransmission and *tsp42Eg*$^{MB08050}$ mutants have reduced spontaneous and evoked release. Figure created with BioRender.com.

is taken up by mitochondria and extruded by plasma membrane $Ca^{2+}$ ATPases (PMCA). The latter is primarily responsible for $Ca^{2+}$ clearance in *Drosophila* NMJ boutons after both single and trains of action potentials (Lnenicka et al., 2006). Thus, Cbp53E and/or PMCA may be deficient or mislocalized at *tsp* mutant synapses resulting in enhanced evoked responses during HFS and endocytosis.

Increased intracellular $Ca^{2+}$ accumulation could also occur because of increased EndoA in *tsp* mutant NMJs (Figure 4B). Mammalian EndoAs are involved in multiple steps of endocytosis including the invagination of coated pits, the recruitment of Dyn to the neck, and the recruitment of Synaptojanin (Kjaerulff et al., 2011), which initiates uncoating of the vesicle. EndoA also interacts with Intersectin/Dap160 to facilitate vesicle priming and fusion in chromaffin neurosecretory cells (Gowrisankaran et al., 2020) and promotes $Ca^{2+}$ channel clustering and $Ca^{2+}$ influx in inner hair cell ribbon synapses (Kroll et al., 2019). In mouse hippocampal cells, overexpression of Endophilin A1 increases the release probability of vesicles (Weston et al., 2011).

Alternatively, reduced evoked responses from a single stimulus but increased evoked responses during high frequency stimulation could occur because of the loss of $PI(4,5)P_2$ in $tsp42Eg^{MB08050}$ mutants (Figure 6A). $PI(4,5)P_2$ associates with synaptic proteins that include PDZ and pleckstrin homology (PH) domains and, through ionic interactions, receptors, ion channels, and cytoskeletal proteins (Katan and Cockcroft, 2020). $PI(4,5)P_2$-rich regions of the membrane are bound by Syt1 (Park et al., 2015) and $PI(4,5)P_2$ promotes, even in the absence of $Ca^{2+}$, the membrane insertion of Syt1 (Bradberry et al., 2019). Notably, depletion of $PI(4,5)P_2$ reduces inward $K^+$ currents through $K_V7.2$ channels in HEK cells (Gomis-Perez et al., 2017). $K_V7.2$ and $K_V7.3$ are subunits of voltage-gated $K^+$ channel that progressively open during membrane depolarization to enable repolarization resulting in reduced excitability (Brown et al., 2007). Loss of function mutations in the genes encoding $K_V7.2$ and $K_V7.3$, *KCNQ2* and *KCNQ3*, respectively, are associated with hyperexcitability and seizure activity in animal models and humans (Nappi et al., 2020). Thus, the loss of $PI(4,5)P_2$ in $tsp42Eg^{MB08050}$ mutants may increase evoked responses during high frequency stimulation without affecting the size of vesicle pools due to a reduction in inward $K^+$ currents.

The actin and microtubule cytoskeletons influence synaptic structure, neurotransmission, and endocytosis (Wu et al., 2016; Maritzen and Haucke, 2018; Piriya Ananda Babu et al., 2020). Actin polymers are enriched near both AZs and periactive zones (Kudryashova, 2021) and promote vesicle exocytosis (Guzman et al., 2019) and recycling (Dason et al., 2014). Our data suggest that actin polymerization is impaired at *tsp* mutant NMJs. Consistent with this, decreased $PI(4,5)P_2$ levels, as we observed in $tsp42Eg^{MB08050}$ mutants (Figure 6A), are correlated with decreased actin stability (Katan and Cockcroft, 2020). SCAR, which promotes actin nucleation and branching by activating Arp 2/3 (Zallen et al., 2002; Schenck et al., 2004), is reduced in both *tsp* mutants (Figure 6C). Actin associates with Syn (Bloom et al., 2003), which plays a role in maintaining (Zhang and Augustine, 2021) and releasing the RP vesicles to replenish the RRP during exocytosis (Akbergenova and Bykhovskaia, 2007; Shupliakov et al., 2011; Vasileva et al., 2012). Thus, altered actin dynamics in $tsp42Eg^{MB08050}$ mutants may promote neurotransmitter release during high frequency stimulation. Inhibition of actin polymerization in cultured rat hippocampal neurons increases the amplitude of EPSCs (Morales et al., 2000). Similarly, the microtubule interacting protein Futsch/MAP1B is localized between microtubules and AZs where it is associated with $Ca_V1$/Cacophony channels and Brp (Lepicard et al., 2014). Increased Futsch (Figure 6B) and Syn (Figure 3E) coupled with decreased actin stability at $tsp42Eg^{MB08050}$ mutant NMJs may allow for more vesicles to be released upon intense stimulation.

Collectively, our data suggest that Tsp42Eg restricts endocytosis, EndoA, Syn, and evoked release during HFS. Tsp42Eg may influence these synaptic characteristics by regulating synaptic $PI(4,5)P_2$, and polymerization of the actin and microtubule cytoskeletons. Alternatively, Tsp42Ee restricts endocytosis and EndoA but promotes the synaptic localization of Syn thereby maintaining the total vesicle pool (Figure 8). Thus, our findings highlight both shared and distinct mechanisms through which Tsp42Ee and Tsp42Eg regulate synaptic function.

## Data availability statement

The raw data supporting the conclusions of this article will be made available by the authors, without undue reservation.

## Author contributions

EH and FL designed and performed experiments, analyzed data, prepared figures, and wrote and edited the manuscript. IS, BP, and FB performed experiments, analyzed data, and collaborated on writing the methods. All authors contributed to this manuscript and approved of the submitted version.

## Funding

This work was supported by the National Institution of Health Grant, NINDS 1R15NS101608-01A1, to FL and the Southern Illinois University Graduate School Competitive Graduate Award to EH.

## Acknowledgments

We thank the Bloomington *Drosophila* Stock Center for fly stocks (NIH P40OD018537), the Developmental Studies Hybridoma Bank for antibodies, the Aaron DiAntonio lab

(Washington University, St. Louis, MO) for the VGLUT antibody, Kate O-Connor-Giles lab (Brown University, Providence, RI) for the Nwk antibody, and Dave Featherstone for his mentorship.

## Conflict of interest

The authors declare that the research was conducted in the absence of any commercial or financial relationships that could be construed as a potential conflict of interest.

## Publisher's note

All claims expressed in this article are solely those of the authors and do not necessarily represent those of their affiliated organizations, or those of the publisher, the editors and the reviewers. Any product that may be evaluated in this article, or claim that may be made by its manufacturer, is not guaranteed or endorsed by the publisher.

## Supplementary material

The Supplementary Material for this article can be found online at: https://www.frontiersin.org/articles/10.3389/fncel.2022.957232/full#supplementary-material

SUPPLEMENTARY FIGURE 1
Survival curves of *tsp* mutants are significantly different from control ($w^{1118}$) animals ($tsp42Ee^{G2619}$, $p = 0.0003$ and $tsp42Eg^{MB08050}$, $p = 0.0222$). Log-rank (Mantel-Cox) tests were used for survival curve comparison. Shaded regions indicate 95% confidence intervals.

SUPPLEMENTARY FIGURE 2
Expression of the reference transcripts, *brp*, *dyn*, and *rab11*, do not differ in $tsp42Ee^{G2619}$ or $tsp42Eg^{MB08050}$ mutants. Reference transcripts were assessed in CNS, muscle (*dyn* and *rab11* only), and all tissues of *tsp* mutants. There were no differences in expression of *brp*, *dyn*, and *rab11* in *tsp* mutants in any tissue type. Expression is shown in all tissues relative to controls ($w^{1118}$).

SUPPLEMENTARY FIGURE 3
Synaptic levels of vGLUT are similar in *tsp* mutants and controls. High resolution confocal images of $w^{1118}$ (control), $tsp42Ee^{G2619}$ mutant, or $tsp42Eg^{MB08050}$ mutant NMJs. Synaptic vGLUT (green, bottom left panels) does not differ between controls and *tsp* mutants (right bar graph). Scale bar = 5 $\mu$M.

SUPPLEMENTARY FIGURE 4
Paired pulse ratios are similar in $tsp42Ee^{G2619}$ and $tsp42Eg^{MB08050}$ mutants compared with controls ($w^{1118}$). Paired pulse ratios were obtained in a bath solution containing 1.0 mM $Ca^{2+}$ and calculated by dividing the amplitude of the first evoked response by the amplitude of the second evoked response.

SUPPLEMENTARY FIGURE 5
FM 1-43FX does not preferentially adhere to *tsp* mutant membranes. Genotypes were dissected in HL-3 without $Ca^{2+}$. Subsequently animals were either stimulated with 90 mM KCl for 1 min (bottom panels) or the HL-3 was replaced (top panels) in the presence of 4 $\mu$M FM 1-43FX and 1.0 mM $Ca^{2+}$. Scale bar = 5 $\mu$M.

## References


Akbergenova, Y., and Bykhovskaia, M. (2007). Synapsin maintains the reserve vesicle pool and spatial segregation of the recycling pool in Drosophila presynaptic boutons. *Brain Res.* 1178, 52–64. doi: 10.1016/j.brainres.2007.08.042

Akbergenova, Y., and Bykhovskaia, M. (2010). Synapsin regulates vesicle organization and activity-dependent recycling at Drosophila motor boutons. *Neuroscience* 170, 441–452. doi: 10.1016/j.neuroscience.2010.07.021

Alabi, A. A., and Tsien, R. W. (2012). Synaptic vesicle pools and dynamics. *Cold Spring Harb. Perspect. Biol.* 4, a013680–a013680. doi: 10.1101/cshperspect.a013680

Andreu, Z., and Yanez-Mo, M. (2014). Tetraspanins in extracellular vesicle formation and function. *Front. Immunol.* 5:442. doi: 10.3389/fimmu.2014.00442

Augustine, G. J., Burns, M. E., DeBello, W. M., Hilfiker, S., Morgan, J. R., Schweizer, F. E., et al. (1999). Proteins involved in synaptic vesicle trafficking. *J. Physiol.* 520, 33–41. doi: 10.1111/j.1469-7793.1999.00033.x

Augustine, G. J., Santamaria, F., and Tanaka, K. (2003). Local calcium signaling in neurons. *Neuron* 40, 331–346. doi: 10.1016/S0896-6273(03)00639-1

Bassani, S., Cingolani, L. A., Valnegri, P., Folci, A., Zapata, J., Gianfelice, A., et al. (2012). The X-linked intellectual disability protein TSPAN7 regulates excitatory synapse development and AMPAR trafficking. *Neuron* 73, 1143–1158. doi: 10.1016/j.neuron.2012.01.021

Bellen, H. J., Levis, R. W., He, Y., Carlson, J. W., Evans-Holm, M., Bae, E., et al. (2011). The Drosophila gene disruption project: progress using Transposons with distinctive site specificities. *Genetics* 188, 731–743. doi: 10.1534/genetics.111.126995

Ben-Yaacov, S., Le Borgne, R., Abramson, I., Schweisguth, F., and Schejter, E. D. (2001). Wasp, the Drosophila Wiskott-Aldrich syndrome gene homologue, is required for cell fate decisions mediated by Notch signaling. *J. Cell Biol.* 152, 1–13. doi: 10.1083/jcb.152.1.1

Bloom, O., Evergren, E., Tomilin, N., Kjaerulff, O., Low, P., Brodin, L., et al. (2003). Colocalization of synapsin and actin during synaptic vesicle recycling. *J. Cell Biol.* 161, 737–747. doi: 10.1083/jcb.200212140

Bradberry, M. M., Bao, H., Lou, X., and Chapman, E. R. (2019). Phosphatidylinositol 4,5-bisphosphate drives Ca(2+)-independent membrane penetration by the tandem C2 domain proteins synaptotagmin-1 and Doc2β. *J. Biol. Chem.* 294, 10942–10953. doi: 10.1074/jbc.RA119.007929

Brown, D. A., Hughes, S. A., Marsh, S. J., and Tinker, A. (2007). Regulation of M(Kv7.2/7.3) channels in neurons by PIP(2) and products of PIP(2) hydrolysis: significance for receptor-mediated inhibition. *J. Physiol.* 582, 917–925. doi: 10.1113/jphysiol.2007.132498

Bykhovskaia, M. (2008). Making quantal analysis more convenient, fast, and accurate: user-friendly software QUANTAN. *J. Neurosci. Methods* 168, 500–513. doi: 10.1016/j.jneumeth.2007.10.006

Cavelier, P., and Attwell, D. (2007). Neurotransmitter depletion by bafilomycin is promoted by vesicle turnover. *Neurosci. Lett.* 412, 95–100. doi: 10.1016/j.neulet.2006.10.040

Charrin, S., Jouannet, S., Boucheix, C., and Rubinstein, E. (2014). Tetraspanins at a glance. *J. Cell Sci.* 127, 3641–3648. doi: 10.1242/jcs.154906

Chivet, M., Javalet, C., Laulagnier, K., Blot, B., Hemming, F. J., and Sadoul, R. (2014). Exosomes secreted by cortical neurons upon glutamatergic synapse activation specifically interact with neurons. *J. Extracell. Vesicles* 3, 24722–24722. doi: 10.3402/jev.v3.24722

Chou, V. T., Johnson, S. A., and Van Vactor, D. (2020). Synapse development and maturation at the Drosophila neuromuscular junction. *Neural Dev.* 15:11. doi: 10.1186/s13064-020-00147-5

Coyle, I. P., Koh, Y.-H., Lee, W.-C. M., Slind, J., Fergestad, T., Littleton, J. T., et al. (2004). Nervous wreck, an SH3 adaptor protein that interacts with Wsp, regulates synaptic growth in Drosophila. *Neuron* 41, 521–534. doi: 10.1016/S0896-6273(04)00016-9

Cremona, O., Di Paolo, G., Wenk, M. R., Lüthi, A., Kim, W. T., Takei, K., et al. (1999). Essential role of phosphoinositide metabolism in synaptic vesicle recycling. *Cell* 99, 179–188. doi: 10.1016/S0092-8674(00)81649-9

Daniels, R. W., Collins, C. A., Gelfand, M. V., Dant, J., Brooks, E. S., Krantz, D. E., et al. (2004). Increased expression of the Drosophila vesicular glutamate transporter leads to excess glutamate release and a compensatory decrease in quantal content. *J. Neurosci.* 24, 10466–10474. doi: 10.1523/JNEUROSCI.3001-04.2004

Dason, J. S., Smith, A. J., Marin, L., and Charlton, M. P. (2014). Cholesterol and F-actin are required for clustering of recycling synaptic vesicle proteins in the presynaptic plasma membrane. *J. Physiol.* 592, 621–633. doi: 10.1113/jphysiol.2013.265447

Del Signore, S. J., Kelley, C. F., Messelaar, E. M., Lemos, T., Marchan, M. F., Ermanoska, B., et al. (2021). An autoinhibitory clamp of actin assembly constrains and directs synaptic endocytosis. *eLife* 10:69597. doi: 10.7554/eLife.69597

Delgado, R., Maureira, C., Oliva, C., Kidokoro, Y., and Labarca, P. (2000). Size of vesicle pools, rates of mobilization, and recycling at neuromuscular synapses of a Drosophila mutant, shibire. *Neuron* 28, 941–953. doi: 10.1016/S0896-6273(00)00165-3

Dogrammatzis, C., Deschamps, T., and Kalamvoki, M. (2019). Biogenesis of extracellular vesicles during herpes simplex virus 1 infection: role of the CD63 tetraspanin. *J. Virol.* 93:e01850-18. doi: 10.1128/JVI.01850-18

Duffield, A., Kamsteeg, E.-J., Brown, A. N., Pagel, P., and Caplan, M. J. (2003). The tetraspanin CD63 enhances the internalization of the H,K-ATPase β-subunit. *Proc. Natl. Acad. Sci. U. S. A.* 100, 15560–15565. doi: 10.1073/pnas.2536699100

Escola, J.-M., Kleijmeer, M. J., Stoorvogel, W., Griffith, J. M., Yoshie, O., and Geuze, H. J. (1998). Selective enrichment of tetraspan Proteins on the internal vesicles of multivesicular endosomes and on exosomes secreted by human B-lymphocytes. *J. Biol. Chem.* 273, 20121–20127. doi: 10.1074/jbc.273.32.20121

Escudero, C. A., Lazo, O. M., Galleguillos, C., Parraguez, J. I., Lopez-Verrilli, M. A., Cabeza, C., et al. (2014). The p75 neurotrophin receptor evades the endolysosomal route in neuronal cells, favouring multivesicular bodies specialised for exosomal release. *J. Cell Sci.* 127, 1966–1979. doi: 10.1242/jcs.141754

Ferreira, J. V., Soares, A., d,.R., Ramalho, J., Carvalho, C. M., Cardoso, M. H., et al. (2022). LAMP2A regulates the loading of proteins into exosomes. *Sci. Adv.* 8:eabm1140. doi: 10.1126/sciadv.abm1140

Flannery, A. R., Czibener, C., and Andrews, N. W. (2010). Palmitoylation-dependent association with CD63 targets the Ca2+ sensor synaptotagmin VII to lysosomes. *J. Cell Biol.* 191, 599–613. doi: 10.1083/jcb.201003021

Fornasiero, E. F., Raimondi, A., Guarnieri, F. C., Orlando, M., Fesce, R., Benfenati, F., et al. (2012). Synapsins contribute to the dynamic spatial organization of synaptic vesicles in an activity-dependent manner. *J. Neurosci.* 32, 12214–12227. doi: 10.1523/JNEUROSCI.1554-12.2012

Fradkin, L. G., Kamphorst, J. T., DiAntonio, A., Goodman, C. S., and Noordermeer, J. N. (2002). Genomewide analysis of the Drosophila tetraspanins reveals a subset with similar function in the formation of the embryonic synapse. *Proc. Natl. Acad. Sci. U. S.A.* 99, 13663–13668. doi: 10.1073/pnas.212511099

Gauthier, S. A., Pérez-González, R., Sharma, A., Huang, F.-K., Alldred, M. J., Pawlik, M., et al. (2017). Enhanced exosome secretion in Down syndrome brain - a protective mechanism to alleviate neuronal endosomal abnormalities. *Acta Neuropathol. Commun.* 5:65. doi: 10.1186/s40478-017-0466-0

Gitler, D., Cheng, Q., Greengard, P., and Augustine, G. J. (2008). Synapsin IIa controls the reserve pool of glutamatergic synaptic vesicles. *J. Neurosci.* 28, 10835–10843. doi: 10.1523/JNEUROSCI.0924-08.2008

Gjorgjieva, J., Berni, J., Evers, J. F., and Eglen, S. J. (2013). Neural circuits for peristaltic wave propagation in crawling Drosophila larvae: analysis and modeling. *Front. Comput. Neurosci.* 7:24. doi: 10.3389/fncom.2013.00024

Gomis-Perez, C., Soldovieri, M. V., Malo, C., Ambrosino, P., Taglialatela, M., Areso, P., et al. (2017). Differential regulation of PI(4,5)P2 sensitivity of Kv7.2 and Kv7.3 channels by calmodulin. *Front. Mol. Neurosci.* 10:117. doi: 10.3389/fnmol.2017.00117

Gowrisankaran, S., Houy, S., Del Castillo, J. G. P., Steubler, V., Gelker, M., Kroll, J., et al. (2020). Endophilin-A coordinates priming and fusion of neurosecretory vesicles *via* intersectin. *Nat. Commun.* 11:1266. doi: 10.1038/s41467-020-14993-8

Gramates, L. S., Agapite, J., Attrill, H., Calvi, B. R., Crosby, M. A., Dos Santos, G., et al. (2022). FlyBase: a guided tour of highlighted features. *Genetics* 220:iyac035. doi: 10.1093/genetics/iyac035

Gundersen, C. B. (2020). Cysteine string proteins. *Prog. Neurobiol.* 188:101758. doi: 10.1016/j.pneurobio.2020.101758

Guzman, G. A., Guzman, R. E., Jordan, N., and Hidalgo, P. (2019). A tripartite interaction among the calcium channel alpha1- and beta-subunits and F-actin increases the readily releasable pool of vesicles and its recovery after depletion. *Front. Cell. Neurosci.* 13:125. doi: 10.3389/fncel.2019.00125

Hackett, J. T., and Ueda, T. (2015). Glutamate release. *Neurochem. Res.* 40, 2443–2460. doi: 10.1007/s11064-015-1622-1

Hagel, K. R., Beriont, J., and Tessier, C. R. (2015). Drosophila Cbp53E regulates axon growth at the neuromuscular junction. *PLoS ONE* 10:e0132636. doi: 10.1371/journal.pone.0132636

Heckscher, E. S., Lockery, S. R., and Doe, C. Q. (2012). Characterization of Drosophila larval crawling at the level of organism, segment, and somatic body wall musculature. *J. Neurosci.* 32, 12460–12471. doi: 10.1523/JNEUROSCI.0222-12.2012

Hemler, M. E. (2005). Tetraspanin functions and associated microdomains. *Nat. Rev. Mol. Cell Biol.* 6, 801–811. doi: 10.1038/nrm1736

Hochheimer, N., Sies, R., Aschenbrenner, A. C., Schneider, D., and Lang, T. (2019). Classes of non-conventional tetraspanins defined by alternative splicing. *Sci. Rep.* 9:14075. doi: 10.1038/s41598-019-50267-0

Hoopmann, P., Punge, A., Barysch, S. V., Westphal, V., Bückers, J., Opazo, F., et al. (2010). Endosomal sorting of readily releasable synaptic vesicles. *Proc. Natl. Acad. Sci. U. S. A.* 107, 19055–19060. doi: 10.1073/pnas.1007037107

Jankovičová, J., Sečová, P., Michalková, K., and Antalíková, J. (2020). Tetraspanins, more than markers of extracellular vesicles in reproduction. *Int. J. Mol. Sci.* 21:7568. doi: 10.3390/ijms21207568

Justo, B. L., and Jasiulionis, M. G. (2021). Characteristics of TIMP1, CD63, and Beta1-Integrin and the functional impact of their interaction in cancer. *Int. J. Mol. Sci.* 22:9319. doi: 10.3390/ijms22179319

Katan, M., and Cockcroft, S. (2020). Phosphatidylinositol(4,5)bisphosphate: diverse functions at the plasma membrane. *Essays Biochem.* 64, 513–531. doi: 10.1042/EBC20200041

Kelić, S., Levy, S., Suarez, C., and Weinstein, D. E. (2001). CD81 regulates neuron-induced astrocyte cell-cycle exit. *Mol. Cell. Neurosci.* 17, 551–560. doi: 10.1006/mcne.2000.0955

Khuong, T. M., Habets, R. L. P., Slabbaert, J. R., and Verstreken, P. (2010). WASP is activated by phosphatidylinositol-4,5-bisphosphate to restrict synapse growth in a pathway parallel to bone morphogenetic protein signaling. *Proc. Natl. Acad. Sci. U. S. A.* 107, 17379–17384. doi: 10.1073/pnas.1001794107

Kitadokoro, K., Bordo, D., Galli, G., Petracca, R., Falugi, F., Abrignani, S., et al. (2001). CD81 extracellular domain 3D structure: insight into the tetraspanin superfamily structural motifs. *EMBO J.* 20, 12–18. doi: 10.1093/emboj/20.1.12

Kjaerulff, O., Brodin, L., and Jung, A. (2011). The structure and function of endophilin proteins. *Cell Biochem. Biophys.* 60, 137–154. doi: 10.1007/s12013-010-9137-5

Koh, T. W., Korolchuk, V. I., Wairkar, Y. P., Jiao, W., Evergren, E., Pan, H., et al. (2007). Eps15 and Dap160 control synaptic vesicle membrane retrieval and synapse development. *J. Cell Biol.* 178, 309–322. doi: 10.1083/jcb.200701030

Kovalenko, O. V., Metcalf, D. G., DeGrado, W. F., and Hemler, M. E. (2005). Structural organization and interactions of transmembrane domains in tetraspanin proteins. *BMC Struct. Biol.* 5:11. doi: 10.1186/1472-6807-5-11

Krick, N., Ryglewski, S., Pichler, A., Bikbaev, A., Gotz, T., Kobler, O., et al. (2021). Separation of presynaptic Cav2 and Cav1 channel function in synaptic vesicle exo- and endocytosis by the membrane anchored Ca(2+) pump PMCA. *Proc. Natl. Acad. Sci. U. S. A.* 118:e2106621118. doi: 10.1073/pnas.2106621118

Kroll, J., Jaime Tobon, L. M., Vogl, C., Neef, J., Kondratiuk, I., Konig, M., et al. (2019). Endophilin-A regulates presynaptic Ca(2+) influx and synaptic vesicle recycling in auditory hair cells. *EMBO J.* 38:e100116. doi: 10.15252/embj.2018100116

Kudryashova, I. V. (2021). The reorganization of the actin matrix as a factor of presynaptic plasticity. *Neurochem. J.* 15, 217–225. doi: 10.1134/S1819712421030089

Latysheva, N., Muratov, G., Rajesh, S., Padgett, M., Hotchin, N. A., Overduin, M., et al. (2006). Syntenin-1 is a new component of tetraspanin-enriched microdomains: mechanisms and consequences of the interaction of syntenin-1 with CD63. *Mol. Cell. Biol.* 26, 7707–7718. doi: 10.1128/MCB.00849-06

Lepicard, S., Franco, B., de Bock, F., and Parmentier, M.-L. (2014). A presynaptic role of microtubule-associated protein 1/futsch in Drosophila: regulation of active zone number and neurotransmitter release. *J. Neurosci.* 34, 6759–6771. doi: 10.1523/JNEUROSCI.4282-13.2014

Li, L., and Yang, X.-J. (2015). Tubulin acetylation: responsible enzymes, biological functions and human diseases. *Cell. Mol. Life Sci.* 72, 4237–4255. doi: 10.1007/s00018-015-2000-5

Li, T.-N., Chen, Y.-J., Lu, T.-Y., Wang, Y.-T., Lin, H.-C., and Yao, C.-K. (2020). A positive feedback loop between Flower and PI(4,5)P2 at periactive zones controls bulk endocytosis in Drosophila. *eLife* 9:e60125. doi: 10.7554/eLife.60125.sa2

Liu, J., Sun, Y., Drubin, D. G., and Oster, G. F. (2009). The mechanochemistry of endocytosis. *PLoS Biol.* 7:e1000204. doi: 10.1371/journal.pbio.1000204

Lnenicka, G. A., Grizzaffi, J., Lee, B., and Rumpal, N. (2006). Ca2+ dynamics along identified synaptic terminals in Drosophila larvae. *J. Neurosci.* 26, 12283–12293. doi: 10.1523/JNEUROSCI.2665-06.2006

Long, A. A., Mahapatra, C. T., Woodruff, E. A. 3rd, Rohrbough, J., Leung, H. T., Shino, S., et al. (2010). The nonsense-mediated decay pathway maintains synapse architecture and synaptic vesicle cycle efficacy. *J. Cell Sci.* 123, 3303–3315. doi: 10.1242/jcs.069468

Machesky, L. M., Mullins, R. D., Higgs, H. N., Kaiser, D. A., Blanchoin, L., May, R. C., et al. (1999). Scar, a WASp-related protein, activates nucleation of actin filaments by the Arp2/3 complex. *Proc. Natl. Acad. Sci. U. S. A.* 96, 3739–3744. doi: 10.1073/pnas.96.7.3739

Madeira, F., Park, Y. M., Lee, J., Buso, N., Gur, T., Madhusoodanan, N., et al. (2019). The EMBL-EBI search and sequence analysis tools APIs in 2019. *Nucleic Acids Res.* 47, W636–W641. doi: 10.1093/nar/gkz268

Mandal, K. (2020). Review of PIP2 in cellular signaling, functions and diseases. *Int. J. Mol. Sci.* 21:8342. doi: 10.3390/ijms21218342

Marimpietri, D., Airoldi, I., Faini, A. C., Malavasi, F., and Morandi, F. (2021). The role of extracellular vesicles in the progression of human neuroblastoma. *Int. J. Mol. Sci.* 22:3964. doi: 10.3390/ijms22083964

Maritzen, T., and Haucke, V. (2018). Coupling of exocytosis and endocytosis at the presynaptic active zone. *Neurosci. Res.* 127, 45–52. doi: 10.1016/j.neures.2017.09.013

Marrus, S. B., Portman, S. L., Allen, M. J., Moffat, K. G., and DiAntonio, A. (2004). Differential localization of glutamate receptor subunits at the Drosophila neuromuscular junction. *J. Neurosci.* 24, 1406–1415. doi: 10.1523/JNEUROSCI.1575-03.2004

McMahon, H. T., and Boucrot, E. (2011). Molecular mechanism and physiological functions of clathrin-mediated endocytosis. *Nat. Rev. Mol. Cell Biol.* 12, 517–533. doi: 10.1038/nrm3151

Menon, K. P., Carrillo, R. A., and Zinn, K. (2013). Development and plasticity of the Drosophila larval neuromuscular junction. *Wiley Interdiscip. Rev. Dev. Biol.* 2, 647–670. doi: 10.1002/wdev.108

Miech, C., Pauer, H.-U., He, X., and Schwarz, T. L. (2008). Presynaptic local signaling by a canonical wingless pathway regulates development of the Drosophila neuromuscular junction. *J. Neurosci.* 28, 10875–10884. doi: 10.1523/JNEUROSCI.0164-08.2008

Morales, M., Colicos, M. A., and Goda, Y. (2000). Actin-dependent regulation of neurotransmitter release at central synapses. *Neuron* 27, 539–550. doi: 10.1016/S0896-6273(00)00064-7

Moretto, E., Longatti, A., Murru, L., Chamma, I., Sessa, A., Zapata, J., et al. (2019). TSPAN5 enriched microdomains provide a platform for dendritic spine maturation through neuroligin-1 clustering. *Cell Rep.* 29, 1130–1146.e1138. doi: 10.1016/j.celrep.2019.09.051

Mortier, E., Wuytens, G., Leenaerts, I., Hannes, F., Heung, M. Y., Degeest, G., et al. (2005). Nuclear speckles and nucleoli targeting by PIP2-PDZ domain interactions. *EMBO J.* 24, 2556–2565. doi: 10.1038/sj.emboj.7600722

Müller, M., Liu, K. S. Y., Sigrist, S. J., and Davis, G. W. (2012). RIM controls homeostatic plasticity through modulation of the readily-releasable vesicle pool. *J. Neurosci.* 32, 16574–16585. doi: 10.1523/JNEUROSCI.0981-12.2012

Murru, L., Moretto, E., Martano, G., and Passafaro, M. (2018). Tetraspanins shape the synapse. *Mol. Cell. Neurosci.* 91, 76–81. doi: 10.1016/j.mcn.2018.04.001

Nappi, P., Miceli, F., Soldovieri, M. V., Ambrosino, P., Barrese, V., and Taglialatela, M. (2020). Epileptic channelopathies caused by neuronal Kv7 (KCNQ) channel dysfunction. *Pflügers Arch. Eur. J. Physiol.* 472, 881–898. doi: 10.1007/s00424-020-02404-2

Ng, E. L., and Tang, B. L. (2008). Rab GTPases and their roles in brain neurons and glia. *Brain Res. Rev.* 58, 236–246. doi: 10.1016/j.brainresrev.2008.04.006

Ormerod, K. G., Scibelli, A. E., and Littleton, J. T. (2022). Regulation of excitation-contraction coupling at the Drosophila neuromuscular junction. *J. Physiol.* 600, 349–372. doi: 10.1113/JP282092

Park, Y., Seo, J. B., Fraind, A., Pérez-Lara, A., Yavuz, H., Han, K., et al. (2015). Synaptotagmin-1 binds to PIP2-containing membrane but not to SNAREs at physiological ionic strength. *Nat. Struct. Mol. Biol.* 22, 815–823. doi: 10.1038/nsmb.3097

Parkinson, W., Dear, M. L., Rushton, E., and Broadie, K. (2013). N-glycosylation requirements in neuromuscular synaptogenesis. *Development* 140, 4970–4981. doi: 10.1242/dev.099192

Pieribone, V. A., Shupliakov, O., Brodin, L., Hilfiker-Rothenfluh, S., Czernik, A. J., and Greengard, P. (1995). Distinct pools of synaptic vesicles in neurotransmitter release. *Nature* 375, 493–497. doi: 10.1038/375493a0

Piriya Ananda Babu, L., Wang, H.-Y., Eguchi, K., Guillaud, L., and Takahashi, T. (2020). Microtubule and actin differentially regulate synaptic vesicle cycling to maintain high-frequency neurotransmission. *J. Neurosci.* 40, 131–142. doi: 10.1523/JNEUROSCI.1571-19.2019

Pols, M. S., and Klumperman, J. (2009). Trafficking and function of the tetraspanin CD63. *Exp. Cell Res.* 315, 1584–1592. doi: 10.1016/j.yexcr.2008.09.020

Regehr, W. G. (2012). Short-term presynaptic plasticity. *Cold Spring Harb. Perspect. Biol.* 4:a005702. doi: 10.1101/cshperspect.a005702

Roos, J., Hummel, T., Ng, N., Klämbt, C., and Davis, G. W. (2000). Drosophila futsch regulates synaptic microtubule organization and is necessary for synaptic growth. *Neuron* 26, 371–382. doi: 10.1016/S0896-6273(00)81170-8

Rosenmund, C., and Stevens, C. F. (1996). Definition of the readily releasable pool of vesicles at hippocampal synapses. *Neuron* 16, 1197–1207. doi: 10.1016/S0896-6273(00)80146-4

Ruiz-Canada, C., Ashley, J., Moeckel-Cole, S., Drier, E., Yin, J., and Budnik, V. (2004). New synaptic bouton formation is disrupted by misregulation of microtubule stability in aPKC mutants. *Neuron* 42, 567–580. doi: 10.1016/S0896-6273(04)00255-7

Saheki, Y., and De Camilli, P. (2012). Synaptic vesicle endocytosis. *Cold Spring Harb. Perspect. Biol.* 4:a005645. doi: 10.1101/cshperspect.a005645

Salas, I. H., Callaerts-Vegh, Z., Arranz, A. M., Guix, F. X., D'Hooge, R., Esteban, J. A., et al. (2017). Tetraspanin 6: a novel regulator of hippocampal synaptic transmission and long term plasticity. *PLoS ONE* 12:e0171968. doi: 10.1371/journal.pone.0187179

Sarthi, J., and Elefant, F. (2011). dTip60 HAT activity controls synaptic bouton expansion at the Drosophila neuromuscular junction. *PLoS ONE* 6:e26202. doi: 10.1371/journal.pone.0026202

Schenck, A., Qurashi, A., Carrera, P., Bardoni, B., Diebold, C., Schejter, E., et al. (2004). WAVE/SCAR, a multifunctional complex coordinating different aspects of neuronal connectivity. *Dev. Biol.* 274, 260–270. doi: 10.1016/j.ydbio.2004.07.009

Schindelin, J., Arganda-Carreras, I., Frise, E., Kaynig, V., Longair, M., Pietzsch, T., et al. (2012). Fiji: an open-source platform for biological-image analysis. *Nat. Methods* 9, 676–682. doi: 10.1038/nmeth.2019

Seigneuret, M., Delaguillaumie, A., Lagaudrière-Gesbert, C., and Conjeaud, H. (2001). Structure of the tetraspanin main extracellular domain: a partially conserved fold with a structurally variable domain insertion. *J. Biol. Chem.* 276, 40055–40064. doi: 10.1074/jbc.M105557200

Shupliakov, O., Haucke, V., and Pechstein, A. (2011). How synapsin I may cluster synaptic vesicles. *Semin. Cell Dev. Biol.* 22, 393–399. doi: 10.1016/j.semcdb.2011.07.006

Smythe, E., and Ayscough, K. R. (2006). Actin regulation in endocytosis. *J. Cell Sci.* 119, 4589–4598. doi: 10.1242/jcs.03247

Stipp, C. S., Kolesnikova, T. V., and Hemler, M. E. (2003). Functional domains in tetraspanin proteins. *Trends Biochem. Sci.* 28, 106–112. doi: 10.1016/S0968-0004(02)00014-2

Stradal, T. E. B., Rottner, K., Disanza, A., Confalonieri, S., Innocenti, M., and Scita, G. (2004). Regulation of actin dynamics by WASP and WAVE family proteins. *Trends Cell Biol.* 14, 303–311. doi: 10.1016/j.tcb.2004.04.007

Sun, Y., Carroll, S., Kaksonen, M., Toshima, J. Y., and Drubin, D. G. (2007). PtdIns(4,5)P2 turnover is required for multiple stages during clathrin- and actin-dependent endocytic internalization. *J. Cell Biol.* 177, 355–367. doi: 10.1083/jcb.200611011

Termini, C. M., and Gillette, J. M. (2017). Tetraspanins function as regulators of cellular signaling. *Front. Cell Dev. Biol.* 5:34. doi: 10.3389/fcell.2017.00034

Todres, E., Nardi, J. B., and Robertson, H. M. (2000). The tetraspanin superfamily in insects. *Insect Mol. Biol.* 9, 581–590. doi: 10.1046/j.1365-2583.2000.00222.x

Vasileva, M., Horstmann, H., Geumann, C., Gitler, D., and Kuner, T. (2012). Synapsin-dependent reserve pool of synaptic vesicles supports replenishment of the readily releasable pool under intense synaptic transmission. *Eur. J. Neurosci.* 36, 3005–3020. doi: 10.1111/j.1460-9568.2012.08225.x

Verstreken, P., Ohyama, T., and Bellen, H. J. (2008). FM 1-43 labeling of synaptic vesicle pools at the Drosophila neuromuscular junction. *Methods Mol. Biol.* 440, 349–369. doi: 10.1007/978-1-59745-178-9_26

Wagh, D. A., Rasse, T. M., Asan, E., Hofbauer, A., Schwenkert, I., Durrbeck, H., et al. (2006). Bruchpilot, a protein with homology to ELKS/CAST, is required for structural integrity and function of synaptic active zones in Drosophila. *Neuron* 49, 833–844. doi: 10.1016/j.neuron.2006.02.008

Weston, M. C., Nehring, R. B., Wojcik, S. M., and Rosenmund, C. (2011). Interplay between VGLUT isoforms and endophilin A1 regulates neurotransmitter release and short-term plasticity. *Neuron* 69, 1147–1159. doi: 10.1016/j.neuron.2011.02.002

Wu, X. S., Lee, S. H., Sheng, J., Zhang, Z., Zhao, W. D., Wang, D., et al. (2016). Actin is crucial for all kinetically distinguishable forms of endocytosis at synapses. *Neuron* 92, 1020–1035. doi: 10.1016/j.neuron.2016.10.014

Yu, H., Liu, Y., He, B., He, T., Chen, C., He, J., et al. (2021). Platelet biomarkers for a descending cognitive function: a proteomic approach. *Aging Cell* 20:e13358. doi: 10.1111/acel.13358

Zallen, J. A., Cohen, Y., Hudson, A. M., Cooley, L., Wieschaus, E., and Schejter, E. D. (2002). SCAR is a primary regulator of Arp2/3-dependent morphological events in Drosophila. *J. Cell Biol.* 156, 689–701. doi: 10.1083/jcb.200109057

Zhang, M., and Augustine, G. J. (2021). Synapsins and the synaptic vesicle reserve pool: floats or anchors? *Cells* 10:658. doi: 10.3390/cells10030658

Zou, F., Wang, X., Han, X., Rothschild, G., Zheng, S. G., Basu, U., et al. (2018). Expression and function of tetraspanins and their interacting partners in B cells. *Front. Immunol.* 9, 1606–1606. doi: 10.3389/fimmu.2018.01606

frontiers | Frontiers in Cellular Neuroscience

TYPE Review
PUBLISHED 20 September 2022
DOI 10.3389/fncel.2022.979856



OPEN ACCESS

EDITED BY
Ulises Gomez-Pinedo,
Health Research Institute of Hospital Clínico San Carlos, Spain

REVIEWED BY
Edwin Estefan Reza,
Instituto de Tecnología y Educación Superior de Monterrey (ITESM), Mexico
Doddy Denise Ojeda-Hernández,
Universidad Complutense de Madrid, Spain

*CORRESPONDENCE
Tianyu Zhong
zhongtianyu@gmail.com
Zhigang Jiao
jiaozhigang8043@163.com

SPECIALTY SECTION
This article was submitted to Cellular Neuropathology, a section of the journal Frontiers in Cellular Neuroscience

RECEIVED 28 June 2022
ACCEPTED 10 August 2022
PUBLISHED 20 September 2022

CITATION
Jiao Z, He Z, Liu N, Lai Y and Zhong T (2022) Multiple roles of neuronal extracellular vesicles in neurological disorders.
*Front. Cell. Neurosci.* 16:979856.
doi: 10.3389/fncel.2022.979856



# Multiple roles of neuronal extracellular vesicles in neurological disorders

Zhigang Jiao[1,2,3,4]*, Zhengyi He[5], Nanhai Liu[6], Yanwei Lai[6] and Tianyu Zhong[1,3]*

[1]Laboratory Medicine, First Affiliated Hospital of Gannan Medical University, Ganzhou, China, [2]Key Laboratory of Prevention and Treatment of Cardiovascular and Cerebrovascular Diseases, Ministry of Education, Gannan Medical University, Ganzhou, China, [3]Precision Medicine Center, First Affiliated Hospital of Gannan Medical University, Ganzhou, China, [4]Gannan Branch of National Geriatric Center, First Affiliated Hospital of Gannan Medical University, Ganzhou, China, [5]Department of Clinical Research Center, The First Affiliated Hospital of Gannan Medical University, Ganzhou, China, [6]Department of Neurology, First Affiliated Hospital of Gannan Medical University, Ganzhou, China

Neuropathy is a growing public health problem in the aging, adolescent, and sport-playing populations, and the number of individuals at risk of neuropathy is growing; its risks include aging, violence, and conflicts between players. The signal pathways underlying neuronal aging and damage remain incompletely understood and evidence-based treatment for patients with neuropathy is insufficiently delivered; these are two of the reasons that explain why neuropathy is still not completely curable and why the progression of the disease cannot be inhibited. Extracellular vesicles (EVs) shuttling is an important pathway in disease progression. Previous studies have focused on the EVs of cells that support and protect neurons, such as astrocytes and microglia. This review aims to address the role of neuronal EVs by delineating updated mechanisms of neuronal damage and summarizing recent findings on the function of neuronal EVs. Challenges and obstacles in isolating and analyzing neuronal EVs are discussed, with an emphasis on neuron as research object and modification of EVs on translational medicine.

KEYWORDS

**neuron, extracellular vesicles, neuropathy, biomarker, neurodegeneration**

## Introduction

Neurons are the cells that make up the brain and the nervous system. They are the fundamental units that send and receive signals, allowing us to move our muscles, feel the external world, think, form memories, and much more. A great number of studies have shown that neurons are more vulnerable to various stresses, including oxidative stress, hypoxia, ischemia, inflammation, or neurotoxin than other neural cells and are considered less capable of regeneration and self-repair (Gonzalez et al., 2016). The disease burden resulting from neuronal damage induced by pollution, violence, and other factors is a growing health problem. Examples include Alzheimer's disease

(AD), Parkinson's disease (PD), multiple sclerosis, amyotrophic lateral sclerosis (ALS), cerebral ischemia, cerebral hemorrhage, and traumatic brain injury, among others. The etiology and mechanism of neuron impairment are complex and remain to be elucidated. Numerous studies have shown that the dysregulation of cellular function underlying the process of neurodegeneration results from both abnormal cellular communication and misfolded proteins that cannot be effectively degraded or cleaned up. The exact mechanisms leading to these defects remain to be investigated (Peng et al., 2020), but studies have shown that major contributors are the classical pathway, including diffusion, phagocytosis, and exocytosis (Asai et al., 2015), and the unconventional secretion pathway, such as pore-mediated translocation, ATP-binding cassette transporter-based secretion, membrane-bound organelle-based secretion, the Golgi bypass pathway, and extracellular vesicles (EVs) secretion.

EVs have recently caught more attention due to their physicochemical characteristics and biological function. EVs are one type of small lipid bilayer vesicles, including large vesicles (in the size range of ∼50 nm to 1 μm) and exosomes [in the size range of ∼40–160 nm (average ∼100 nm in diameter)] and have an important role in the therapy and development of neurodegenerative diseases. Although many research approaches on EVs have been established and applied, it is challenging to study alone the large vesicles or exosomes due to the resemblance of their biogenesis pathway and regulatory mechanisms. Therefore, in this manuscript we favor the term EVs.

EVs were first observed and termed "platelet dust" 50 years ago (Wolf, 1967). EVs contain many cell components, depending on the original cell, including nucleic acid, lipids, metabolites, cytosolic and cell-surface proteins, and can be found in all biological fluids and tissues, including the central nervous system (CNS). However, the physiological purpose of generating EVs remains largely unknown and needs to be investigated. One speculated role is that EVs remove excess and/or unnecessary constituents from cells to maintain cellular homeostasis, a process that would be similar to autophagy, which was discovered earlier and is also considered to eliminate the cellular garbage (Mizushima and Komatsu, 2011; Babuta et al., 2019). Meanwhile, studies in these years found that both processes play a vital role in cellular homeostasis and intercellular communication (Pan and Johnstone, 1983; Harding et al., 1984) and affect each other through common elements (Babuta et al., 2019; Zhang X. W. et al., 2020). Notably, studies indicated a negative correlation between the ratio of the release of EVs with the ratio of formation of autophagosome—the intermediate material of the autophagy process (Zhang X. W. et al., 2020), and the EVs biogenesis and release are closely related to the formation of the multivesicular body (MVB), which is also involved in autophagy (Baixauli et al., 2014). These studies supported the conclusion that EVs may play a role in the process of cellular homeostasis.

Recent studies reviewed here also indicate a functional, targeted, and active accumulation of specific cellular components in EVs, suggesting that they may play an important role in regulating intercellular communication and trigger phenotypic changes in the recipient cells (Pegtel and Gould, 2019). For instance, EVs from nicotine-stimulated macrophages promote the migration and proliferation of vascular smooth muscle cells (VSMC), whereas neuron-derived EVs promote the polarization of M1 microglia in culture (Zhu et al., 2019; Yin et al., 2020). In addition, several lines of evidence showed that EVs from CNS might directly alter the function of the nearby cell *via* the paracrine pathway or leave the brain and betray the state of CNS as potential biomarkers released into the biological fluids, including cerebrospinal fluid (CSF), plasma, serum, saliva, urine, semen, breast milk, amniotic fluid, and ascites fluid (Wang and Zhang, 2020; Yu et al., 2020). In the meantime, many studies revealed that EVs derived from neurons and/or glial cells might be involved in the initial development of neurodegeneration. However, the culprit of neurodegenerative diseases remains to be investigated (Singh and Muqit, 2020; Yin et al., 2020; You et al., 2020). This review focuses on the regulation mechanism of biogenesis, the release of the neuronal EVs, and its effects on the receptor cells in the pathogenesis, diagnosis, treatment, and prognosis of neurodegeneration. Glia-derived EVs and their effects in neurons have been the focus of several studies and will not be addressed in this review (Lemaire et al., 2019; Upadhya et al., 2020).

## Biogenesis and release of neuronal extracellular vesicles

The biogenesis and release of neuronal EVs are partially similar to other cells (**Figure 1**). For example, the biogenesis of neuronal EVs also begins with the endosome system and is released into the extracellular space through fusion with the plasma membrane (Hessvik and Llorente, 2018). However, this mode is not the only pathway due to multiple lines of evidence showing that EVs also directly bud from the plasma membrane (Nabhan et al., 2012; Bianchi et al., 2014; Nager et al., 2017). The general process of EVs biogenesis and release mainly include three steps: the first step, the formation of early endosome mediated by endocytosis; the second step, the production of intracellular MVBs regulated by endosomal sorting complexes required for transport (ESCRT) machinery, including ESCRT-0, ESCRT-I, ESCRT-II, and ESCRT-III (Hessvik and Llorente, 2018) or ESCRT-I, ESCRT-II, and ESCRT-III (Vietri et al., 2020), with their accessory proteins and then the intraluminal vesicles (ILVs) formed by inward budding from the limiting membrane of MVBs; and the last step, in which ILVs are secreted through the MVBs containing ILVs fused with the plasma membrane and exocytosis.

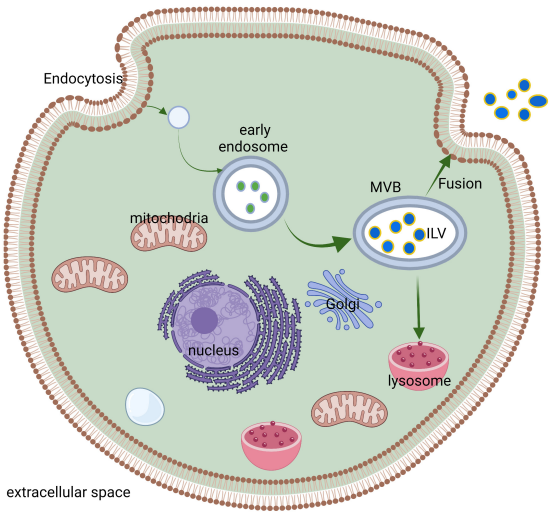


FIGURE 1
A common process for EVs synthesis and release. Cells internalized the cellular components/extracellular ligands and then formed the early endosome. Subsequently, the early endosome matured into MVB, and the inward budding of early endosomes formed ILVs. In the last step, MVB either digests and degrades after fusion with lysosomes or releases exosomes through fusion with cell membranes.

In general, the ESCRT machinery is considered to play a vital role during the assembled MVBs and the budding of ILV (Colombo et al., 2013; Vietri et al., 2020). However, the pathway of independent-ESCRT is also uncovered, such as the interaction of RAB31 with the epidermal growth factor receptor (EGFR) (Wei et al., 2021) or the tetraspanin pathway (Kenific et al., 2021). Indeed, loss of VPS4 function, an essential factor for the ESCRT function (Vietri et al., 2020), did not affect the secretion of EVs marker proteins such as CD63 (Fang et al., 2007; Trajkovic et al., 2008; Colombo et al., 2013). These studies demonstrated that other molecules might regulate EVs biogenesis beyond the ESCRT machinery. In addition, evidence collected during the last 20 years also indicated that the dynamics of protein trafficking are also involved in the process of EVs biogenesis and release. However, the regulatory mechanisms of these processes remain to be elucidated due to its high precision and complexity (Pegtel and Gould, 2019). For instance, a vast number of studies found that the Ras-related protein GTPase Rab (Ostrowski et al., 2010), Sytenin-1, tumor susceptibility gene 101 (TSG101), apoptosis-linked gene 2-interacting protein X (ALIX), syndecan-1 (Baietti et al., 2012), ESCRT proteins (Colombo et al., 2013), tetraspanins (Escola et al., 1998), ceramides, sphingomyelinases, and soluble N-ethylmaleimide–sensitive factor attachment protein receptor (SNARE) complex proteins (Vilcaes et al., 2021) are involved in the origin and biogenesis process of EVs (D'Souza-Schorey and Schorey, 2018; Pegtel and Gould, 2019). However, their precise rate-limiting actions and functions in EVs biogenesis require further in-depth exploration, especially *in vivo*.

The Rab protein family has received more attention due to their roles in regulating vesicle trafficking between different compartments along the endo-lysosomal and secretory pathways (Pfeffer, 2017). For example, studies found that Rab27, Rab35, or Rab11 cooperation with their effectors Slp4, Slac2b and Munc13-4, and regulator TBC1D10B play important roles in MVB biogenesis and positioning. The loss of Rab27 or Rab35 function results in a ∼50–75% drop or little effect on EVs biogenesis upon differentiation of a cell line (Hsu et al., 2010; Ostrowski et al., 2010), overexpressing Rab11 within RAW macrophages elevated the amounts of EVs by about 50% through promoting homotypic fusion/maturation of MVBs (Savina et al., 2002). It is worth noting that there is controversy about how Rab proteins regulate EVs biogenesis. For instance, studies have shown that Rab27/Rab11 proteins promote MVB maturation and deliver MVB to the plasma membrane (Savina et al., 2002; Ostrowski et al., 2010). Others revealed that Rab27a is also required for assembling plasma membrane microdomains (Booth et al., 2006). Thus, it appears that Rab27 proteins control exosome biogenesis at both endosome and plasma membranes. In addition, Ostrowski et al. (2010) found that inhibition of Rab11a did not significantly modify EVs secretion in the HeLa B6H4 cell line. These results indicated that EVs biogenesis and secretion, which do not have to comply with the canonical regulations, were regulated by multiple pathways.

Although most of our knowledge is about the mechanism of EVs biogenesis and secretion in cancer (non-neuronal) cells, many of these mechanisms also function in neurons. However, it is known that the regulatory mechanism of EVs biogenesis and secretion depends on the cell type and state. Therefore, both processes of neuronal EVs have a different pathway compared to cancer cells due to the differential expression of genes and their extreme morphologies. For example, previous research found that endocannabinoid 2-arachadonoylglycerol (2-AG) containing EVs derived from midbrain dopaminergic (DA) neurons can be released in the Arf6-myosin light chain kinase (MLCK) pathway (Nakamura et al., 2019). However, the Arf6-MLCK pathway is specifically attributed to microvesicle (MV) release in tumor cells (Muralidharan-Chari et al., 2009). Moreover, neuronal EVs are released in response to stimulation or depolarization. Furthermore, a positive correlation was observed between the concentration of neuronal EVs and the degree of neuronal depolarization (Faure et al., 2006; Blanchette and Rodal, 2020). Meanwhile, previous studies suggest that neuronal somatodendritic compartments or axons may be the release site of neuronal EVs (Coulter et al., 2018; Polanco et al., 2018). However, the above-mentioned correlation or similar bioconstructors remain to be explored in cancer cells. The same genes may even play different roles in regulating the biogenesis or release of EVs depending in different types of cells. For instance, knockdown of the autophagy-related

gene 5 (*ATG5*) in the MDA-MB-231 cells (a human breast cancer cell line) not only inhibited the autophagy but also induced a severely decreased EVs production (Guo et al., 2017). In contrast, knockout of *ATG5* in neuronal cells greatly increases the release of EVs and EV-associated prions from neuronal cells (Abdulrahman et al., 2018). This result showed that the regulatory mechanism of EVs biogenesis and release is not common.

Due to above reasons, studies about EVs derived from neurons need to have neurons as their research object rather than other cell lines such as HEK293 (Zheng et al., 2017, 2018). The exciting news is that some experiments using neurons as research objects have been implemented and acquired some achievements in healthy or disease models. For example, a study in hippocampus neurons found that brain fibroblast growth factors-2 (bFGF2) can greatly improve the fusion of MVB with the plasma membrane and the release of neuronal exosome by promoting the v-SNARE vesicle-associated membrane protein 3 (VAMP3) translocation to the exosome rather than VAMP2 (Kumar et al., 2020). Moreover, the bFGF2 system regulates neuronal calcium homeostasis and plasticity and promotes neuroprotection and repair in response to neural tissue damage (Guillemot and Zimmer, 2011). Blocked Drp1 in N27 or SH-SY5Y cells treated with PFF (Human α-synuclein preformed fibrils) can enhance the autophagy flux, inhibit the release of EVs, and prevent the transmission of aggregative or misfolded α-synuclein (α-syn) protein between neurons *via* EVs (Fan et al., 2019). KIBRA regulates the secretion of EVs derived from the mouse hippocampal and cortex neuron rather than the liver or muscle tissue *via* inhibiting the proteasomal degradation of Rab27a (Song et al., 2019c). Although the function of these proteins or genes may also be involved with other disorders and needs to be investigated, it has been confirmed that the disorder of these proteins or their gene expression is involved in the progress or development of neurodegeneration such as major depressive disorder, bipolar disorder (BPD), PD, or AD (Evans et al., 2004; Gaughran et al., 2006; Song et al., 2019b; Zhang W. et al., 2019). Therefore, based on the above results, we suggested that disorders in the neuronal EVs biogenesis or release contribute to the neurological disorder. More interestingly, Pastuzyn et al. (2018) found that neuronal Arc protein self-assembles into virus-like capsids that encapsulated *Arc* mRNA and mediated the transmission of Arc protein and *Arc* mRNA between neurons in EVs, where it can undergo activity-dependent translation to regulate the synaptic plasticity of recipient neurons. This finding provides new insight into EVs biogenesis or release mechanism. Moreover, the secretion of neuron-derived EVs was also modulated by the activities of sphingolipid metabolizing enzymes, including neutral sphingomyelinase 2 (nSMase2) and sphingomyelin synthase 2 (SMS2) (Yuyama et al., 2012); however, nSMase2 or SMS2 expression can be detected in other cells (Hitomi et al., 2020), the regulated biogenesis or secrete mechanism of EVs by nSMase2 or SMS2 in other cells are few.

## Neuronal extracellular vesicles affected the function of glial cells and other cells

EVs derived from neurons are continuously secreted into the extracellular space and are up taken by the glia cells and nearby neurons or other cells through neuronal junctions (Faure et al., 2006). The cargo of EVs, like non-coding RNAs (ncRNAs) or proteins and other molecules, influences the function of recipient cells by binding their target molecules. Although how and why neuronal EVs are delivered into other cells are being investigated, some studies have shown that the neuronal EVs containing ncRNA or proteins may modulate the neuronal survival or activity, neural circuits, and the function of other organs by regulating the specific gene expression of receptor cells. For example, Morel et al. (2013) found that exosome-containing *miRNA-124a* derived from a cortical neuron can be engulfed by astrocytes and indirectly regulate glutamate transporter-1(GLT-1). Furthermore, they confirmed that the translational regulation of GLT-1 protein in astrocytes is dependent on neuronal exosome-containing *miRNA-124a* (Morel et al., 2013). However, they did not identify the target genes of *miRNA-124a* that regulate the translation of the GLT-1 protein in astrocytes. Men et al. also confirmed that secreted neuronal exosome-containing miRNAs could be shuttled into astrocytes and influence the function of astrocytes (Men et al., 2019). Furthermore, overexpressed *miRNA-124-3p* in exosomes can strongly upregulate the expression of GLT-1 *via* the abolition of the inhibitory effects of *miR-132* or *miR-128* on GLT-1 in astrocytes (Men et al., 2019). Our previous studies indicated that downregulation of GLT-1 expression in astrocytes results in the drastic increase of glutamate concentration in the dopaminergic (DA) neuronal synaptic cleft and then induces DA degeneration *via* glutamate excitatory toxicity (Zhang Y. et al., 2020). There is also evidence indicating that *miRNA-124-3p* is involved in the perioperative neurocognitive disorders in patients after cardiac surgery (Xiao Q. X. et al., 2020). Furthermore, neuron axonal exosome-containing *miRNA-124-3p* can suppress the activation of M1 microglia and A1 astrocyte *via* inhibiting MYH9 by directly targeting its 3′-UTR and thereby modulating the PI3K/Akt/NF-κB pathway improving over the motor function of spinal cord injury (SCI) mice (Jiang D. et al., 2020). However, the exact role of *miRNA-124-3p* in neurodegenerative diseases remains to be investigated.

The effects of EVs on recipient cells depend on the state of neuron. EVs derived from the neurons with physiological status or drug treatment may protect other cells. For instance, healthy cortical neurons released the *miRNA-181-3p*-containing

exosome, which suppressed the neuroinflammation by targeting the CXCL1 gene in astrocytes. However, the expression of neuronal and exosomal *miRNA-181-3p* is significantly elevated in the ischemic brain injury (IBI) (Song et al., 2019a). CD2019 improved the deficiency of locomotor and sensory *via* promoting the regeneration of neuronal axonal and decreasing the glial scar formation in SCI rats. The underlying mechanism of the protective effect may be the induction of the translocation of PTEN and promotion of the secretion of enriched PTEN-containing exosome *via* activating the retinoic acid receptor β (RARβ). These PTEN-containing exosomes are then delivered to astrocytes, inhibiting the proliferation and activation of the cells (Goncalves et al., 2015). In contrast, the gene expression in damaged neurons causes the dysregulation of the cargo that is packaged into EVs. Subsequently, these cargo molecules are delivered to other cells and then disrupt the function of recipient cells. For example, Yin and his colleagues found that the expression of *miRNA-21-5p* is significantly elevated in PC12 cells and exosomes from PC12 cells after scratch injury. These EV-containing *miRNA-21-5p* shuttle into the BV2 cells, inducing the polarization of cells, and then the polarized BV2 cells cause chronic neuro-inflammation *via* secreting pro-inflammation factors like IL-1β, IL-6, and TNF-α (Yin et al., 2020). Irreversible neuro-inflammation is considered to play an important role in the onset and development of neurodegenerative disease (Calsolaro and Edison, 2016; Han X. et al., 2019; Jiao et al., 2019; Passamonti et al., 2019). SH-SY5Y cells transfected with wild-type human *SNCA* gene secreted exosomes with a higher expression of *miRNA-19a-3p*. The *miRNA-19a-3p*-containing exosomes elevated the expression of *miRNA-19a-3p* in microglia *via* delivering *miRNA-19a-3p* into the microglia, and then the miRNA inhibited the autophagy of microglia by targeting the PTEN/AKT/mTOR signal pathway (Zhou T. et al., 2019). However, a healthy autophagy-lysosome pathway of microglia plays a crucial role in the process that cleans up toxic molecules such as misfolded α-syn (Nash et al., 2017; Choi et al., 2020), abnormal tau, amyloid-β (Aβ) protein (Cho et al., 2014; Heckmann et al., 2019; Houtman et al., 2019), and cellular debris (Pluvinage et al., 2019). On the contrary, the dysregulated autophagy of microglia impacted the degradation of phagocytized cargo and induced an accumulation of misfolded proteins or cellular debris in the microglia or extracellular space, which ultimately contributes to the pathophysiology of neurodegeneration (Qin et al., 2021).

Neuronal EVs in CNS may be absorbed by glial cells; however, neuronal EVs of the peripheral nervous system (PNS) regulated the function of other cells by shuttling to other organ cells and neurites (**Figure 2**). For instance, the impaired sensory neuron in dorsal root ganglia secreted exosomes with a high *miRNA-21* expression that macrophages may engulf by phagocytosis, inducing their activation and release of pro-inflammation cytokines (Simeoli et al., 2017). These cytokines recruit more macrophages, which infiltrate into the site of injury, amplifying and deteriorating the immunity response, ultimately causing neuro-inflammation and neurodegeneration (Harland et al., 2020; Zhang Y. et al., 2020). Xu et al. (2017) also found that neurons transfer *miR-132 via* secreting exosomes to endothelial cells (ECs) and then regulate the expression

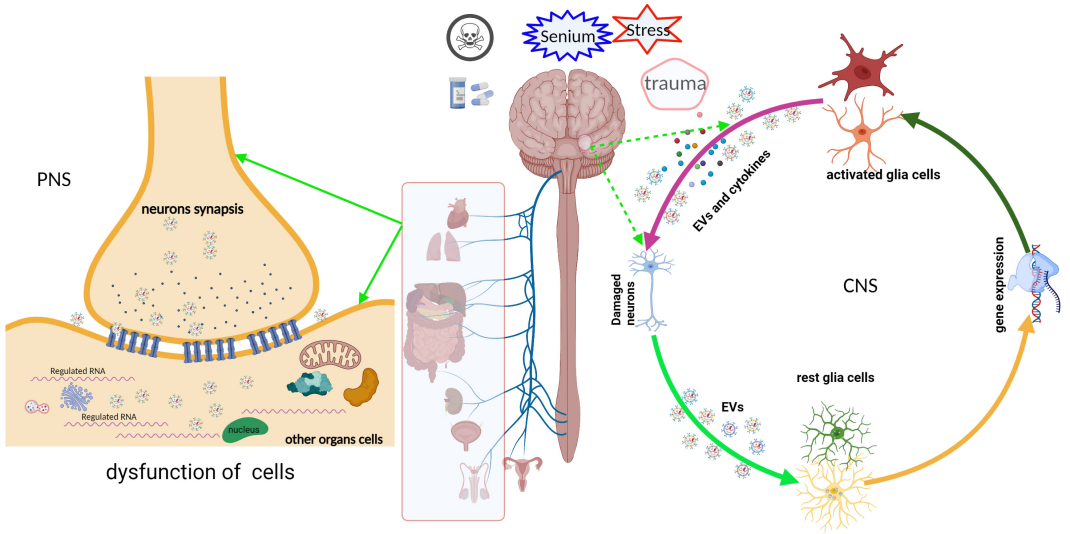


FIGURE 2
Schematic representation of the neuronal EVs that regulated the function of receptor cells. EVs derived from neurons undergoing various stress deliver their cargoes, such as ncRNA, mRNA, or misfold proteins, into other cells in CNS or PNS *via* paracrine or active transport. These cargoes are abnormal expressions and are packaged into EVs, which disturb the gene expression or signal pathway of the recipient cells, ultimately leading to cell dysfunction. Meanwhile, dysfunctional recipient cells secrete "detrimental molecules" and then damage the neurons or nearby cells, and vice versa.

of vascular endothelial cadherin (VE-cadherin), an important adherens junction protein, by directly targeting the eukaryotic elongation factor 2 kinase (eef2k) to maintain brain vascular integrity. However, an adequate supply of blood and structural and functional integrity of blood vessels are key to normal brain functioning. In contrast, cerebral blood flow shortfalls and blood-brain barrier dysfunction can be earlier discovered in neurodegenerative disorders in humans and animal models (Iturria-Medina et al., 2016; Sweeney et al., 2018; Zhang C. et al., 2020). The abnormal structure and function of blood vessels result in the destruction of blood-brain barrier integrity, and peripheral immune cells like T cells infiltrated into CNS and evoked neuro-inflammation. For instance, evidence from postmortem or animal models of neurodegenerative disorder showed that T cells are abundantly present in the impaired region of the brain (Machado-Santos et al., 2018; Liu et al., 2019; Lodygin et al., 2019; Haque et al., 2020). Meanwhile, we reported that the expression of *miRNA-132* is significantly reduced in primary hippocampus neurons treated by soluble Aβ oligomers, a classical cell model of AD (Wei et al., 2020). Furthermore, oxidative stress after SCI injured neurons and altered the release of the neuronal exosome; secreted exosomes promoted the apoptosis of transplanted bone marrow-derived stem cells with oxidative stress (Luo et al., 2019).

In addition to ncRNA, proteins such as Tau and α-syn within EVs also regulate the function of recipient cells and even disturb the cellular homeostasis (Meng et al., 2020). For example, NSC-34 cell, a kind of motor neuron-like cell, mutated superoxide dismutase 1 (mSOD1, G93A) as donor cells released exosome-containing mSOD1, which are phagocytosed by N9-microglial cells. Internalized exosome-containing mSOD1 upregulated the expression of IL-1β, TNF-α, MHC-II, and iNOS gene *via* activating the NF-κB pathway in N9 cells and reducing the phagocytic ability of N9 cells (Pinto et al., 2017). Meanwhile, neuronal PTEN can be transferred to astrocytes by EVs and inhibit the information of glia scar (Goncalves et al., 2015). The formatted glial scar is considered an obstacle to the regeneration of neuronal axons (Anderson et al., 2016). Tau pathology or misfolded α-syn protein spreading is also achieved by direct transmission of exosomes between neurons and then induced Tau protein aggregation or misfolded endogenous α-syn in the receptor neurons (Wang et al., 2017; Sardar Sinha et al., 2018); ultimately, these abnormal proteins induced neurodegenerative diseases.

Based on the above results, we proposed that the expressed dysregulation encapsulated in neuronal EVs containing ncRNAs or pathological proteins induced by diverse factors, such as neurotoxic or mild traumatic brain injury, may result in neurodegeneration. It is noteworthy that almost all studies supposed that the level of cargo in EVs depends on the parental cells. However, Men et al. (2019) found that secreted neuronal exosomes contain a subset of microRNAs that is drastically different from the miRNA profile of neurons. This result is significantly distinct from previous reports (Morel et al., 2013; Xu et al., 2017; Ying et al., 2017; Zhu et al., 2019). Therefore, the sorting mechanism of exosomal cargo remains to be investigated.

## Neuronal extracellular vesicles modulated the function of other neurons

The postmortem studies identified that the stereotypical and temporal distribution of pathology is limited due to a lack of longitudinal data and therefore do not provide direct evidence of the sequential evolvement of different brain regions during disease progression. Nevertheless, numerous studies from cell and animal models have shown that pathological proteins such as α-syn and Tau, or the abnormal regulator such as miRNA, lncRNA, and rRNA undergo neuron-to-neuron transmission and partially contribute to the progress of neurodegenerative diseases (Emmanouilidou et al., 2010; Zhou W. et al., 2019; Ruan et al., 2021; Vilcaes et al., 2021). Although the modes of interplay with neurons are various, EV-based secretion and uptake, one of the unconventional secretion pathways, is the most extensively studied pathway for the transmission of excessive regulators of pathological proteins. EVs containing an excessive level of regulators or misfolded proteins are engulfed into the nearby or distal neurons. The former induced a dysfunction in neurons by disturbing the expression of a specific gene in the recipient neurons. The latter work as "pathological seeds" that damage the function of neurons *via* inducing their normal endogenous counterpart protein to misfold, leading to the amplification of the pathological protein conformation in the receptor cell (Wang et al., 2017; **Figure 3**). Previous research has revealed that EVs derived from dysfunctional neurons may contain the "misfolded proteins" such as α-syn oligomer in PD (Niu et al., 2020), Aβ and tau aggregates in AD (Guix et al., 2018; Sardar Sinha et al., 2018), TAR DNA-binding protein 43(TDP43) and mSOD1 pathology in ALS (Neumann et al., 2006; Iguchi et al., 2016; Silverman et al., 2019), and mutated huntingtin (HTT) (DiFiglia et al., 1997; Jeon et al., 2016). These "unusual EVs" are taken up by other neurons and disturb cellular homeostasis by perturbing the gene expression or protein folding. For example, Han et al. found that the intravenous or intrastriatal treatment of mice with exosomes derived from patients with PD containing α-syn, IL-1β, and TNF-α could trigger dopamine neuron degeneration *via* inducing α-syn, ubiquitin, and p62 aggregation in recipient cells (Han C. et al., 2019). Sinha et al. also found that tau-containing exosomes derived from SH-SY5Y cells when treated with Aβ shuttled to the normal SH-SY5Y cells and increased the LDH level of normal SH-SY5Y cells; dynasore, which is an inhibitor of endocytosis, can inhibit this cytotoxicity effect (Sardar Sinha et al., 2018). Furthermore, Park et al. also

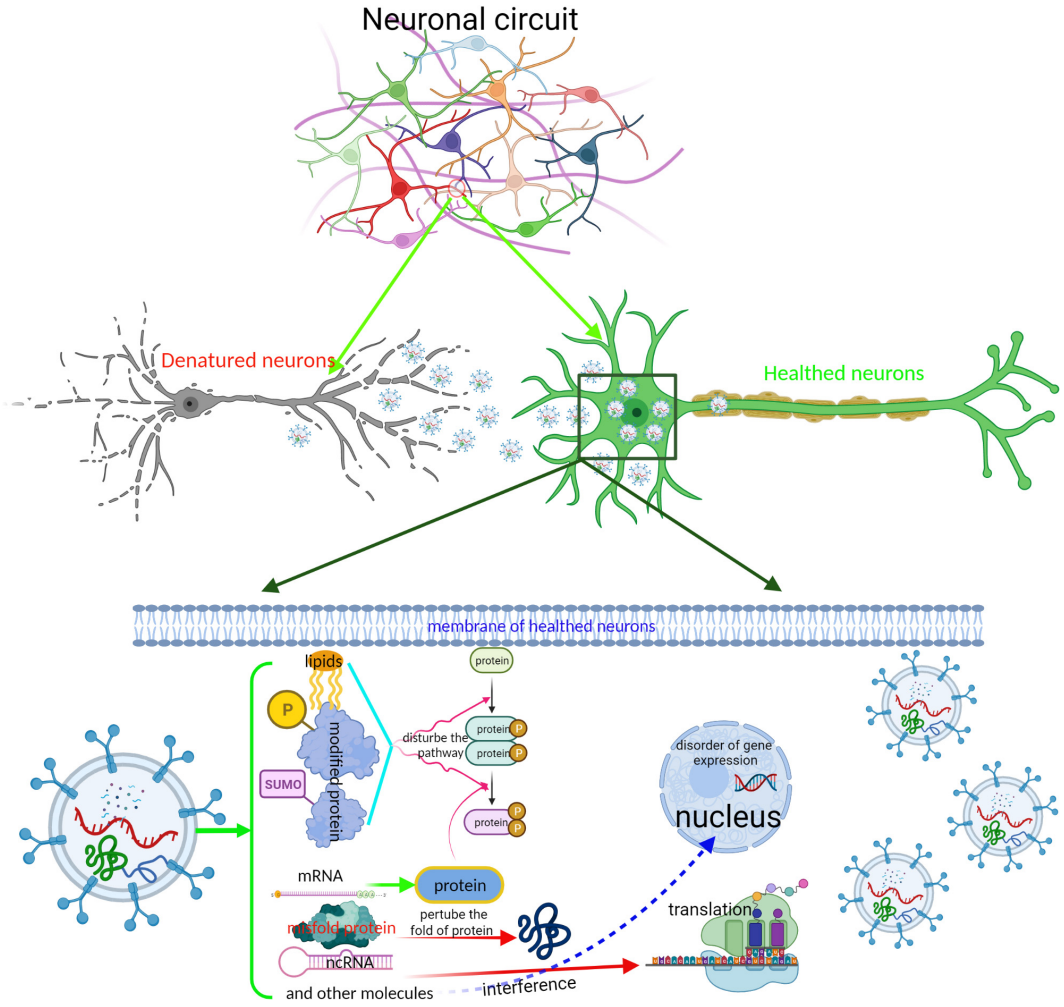


FIGURE 3
Schematic representation of the interplay between neurons by EVs. EVs is an important tool for maintaining the completion of neuronal circuit and the delivery of neurotransmitters. EVs derived from impaired neurons containing abnormal regulators or neurotransmitters are absorbed into healthy neurons, perturbing the neuronal function. The completion of neuronal circuit depends on the neuronal function. Especially, those EVs containing misfold proteins, such as Tau, α-syn, and TDP43, spread to other neurons; these misfold proteins acting as "pathological seeds" induce misfolding of endogenous protein, cause a dissemination from local brain region to others, and accelerate disease progression.

confirmed that the Fas-associated factor 1 (FAF1) of SY5Y cells was secreted and transmitted to neighboring cells *via* exocytosis as well as an exosomal pathway, where it induced cell death through apoptotic and necrotic pathways (Park et al., 2020).

The dysfunction of a neuron may cause the disorder of package and release of the exosome. For example, studies have shown that the release of cortex neuronal exosome is regulated upon the calcium homeostasis in the cytoplasm and glutamatergic synaptic activity (Faure et al., 2006; Lachenal et al., 2011); however, both contribute to neuronal impairment (Cheng et al., 2016; Malik and Willnow, 2019; Alvarez et al., 2020). In contrast, the cargo of normal neuronal EVs contribute to the homeostasis of neuronal function and circuit. For example, Sharma et al. found that exosomes derived from hiPSC-derived neurons increased neurogenesis by promoting cultured primary neuronal proliferation and differentiation and rescued the aberrant neural circuit development mediated by X-linked *Methyl-CpG-binding protein 2* (*MECP2*) gene mutation, which is involved with Rett syndrome (Sharma et al., 2019). Although their study did not reveal the effector within the exosome, these results confirmed the protected role of exosomal cargo in neurons. Subsequently, studies indicate that miRNA-containing exosomes derived from normal cells play a protective role in maintaining the function of other cells (de Rivero Vaccari et al., 2016; Mead and Tomarev, 2017). For instance, HT-22 secreted *miRNA-21-5p*-containing exosomes exert a protection effect by targeting the Rab11a to inhibit the autophagy flux of injured HT-22 (Li et al., 2019). Furthermore, *miRNA-126-3p*-enriched EVs from hypoxia-preconditioned VSC 4.1 neurons attenuate ischemia-reperfusion-induced pain

hypersensitivity by regulating the PIK3R2-mediated pathway (Wang et al., 2021). Together, these papers uncovered the partial underlying mechanism of the gradual progress of neurodegeneration and confirmed the role of neuronal EVs in the disease process. Meanwhile, they also verified that the interplay between neurons is vital for maintaining neuronal homeostasis except for the glial cells which deliver nerve trophic factor into neurons (Upadhya et al., 2020) or maintain the synaptic plasticity of neurons using EVs (Wilton et al., 2019).

## The implication of neuronal extracellular vesicles in the diagnosis and therapy of neuropathy

EVs are released into various body fluids or across the various biological membranes into the cells due to their physicochemical characteristics, such as the small size and similar composition with the cellular membrane. Meanwhile, EV contents are cellular-specific due to the existence of different donor cells. Furthermore, EVs secretion is a constitutive phenomenon involved in both physiological and pathological processes. Hence, many studies focused on the EVs and their carried cargo as biomarkers, vaccines, and drug carriers, and have modified them rationally for therapeutic interventions (**Figure 4**). In particular, the development of EVs for cancer is exploding (Rayamajhi et al., 2019; Zhang W. et al., 2019; Guo et al., 2020; Nie et al., 2020; Xiao Y. et al., 2020; Liu et al., 2021; Yang et al., 2021; Zhao et al., 2021). It is worth mentioning that the development of exosome-containing GPC-1(GPC-$1^+$ crExos) for pancreatic ductal adenocarcinoma (PDAC) is inspiring. For example, Melo et al. (2015) found that GPC-$1^+$ crExos derived from PDAC and breast cancer patients' serum is significantly elevated. They found that GPC-$1^+$ crExos strongly correlates with the PDAC rather than breast cancer. The most impressive finding was that the GPC-$1^+$ crExos distinguished patients with PDAC and pancreatic cancer precursor lesions (PCPL) from healthy donors and BPD patients; the sensitivity and specificity of GPC-$1^+$ crExos prediction are 100% compared with CA19-9 (the clinical standard tumor biomarker for patients with PDAC). These findings are outstanding because no biomarker performs with 100% sensitivity and specificity in the history of cancer biomarker identification and validation, especially for an early stage of the disease. These findings remain to be validated before being applied in clinical settings because the GPC-$1^+$ cross is also higher in others cancer such as breast cancer (Su et al., 2006). Studies about EVs have made great progress. However, there are still huge challenges concerning nerve diseases, especially in CNS diseases, due to the insufficiency of samples and contradictory conclusions. For instance, Winston et al. (2018) found that plasma exosomes containing neurogranin were highly diagnostic (sensitivity = 86.1 ± 0.037, confidence interval = 63.4–100) in distinguishing mild cognitive impairment patients from cognitively normal controls. However, a great number of published studies indicated that L1 cell adhesion molecule (L1CAM, CD147) positive exosome-containing Aβ42, T-tau, P-T181-tau, α-syn, and other proteins or ncRNA had higher

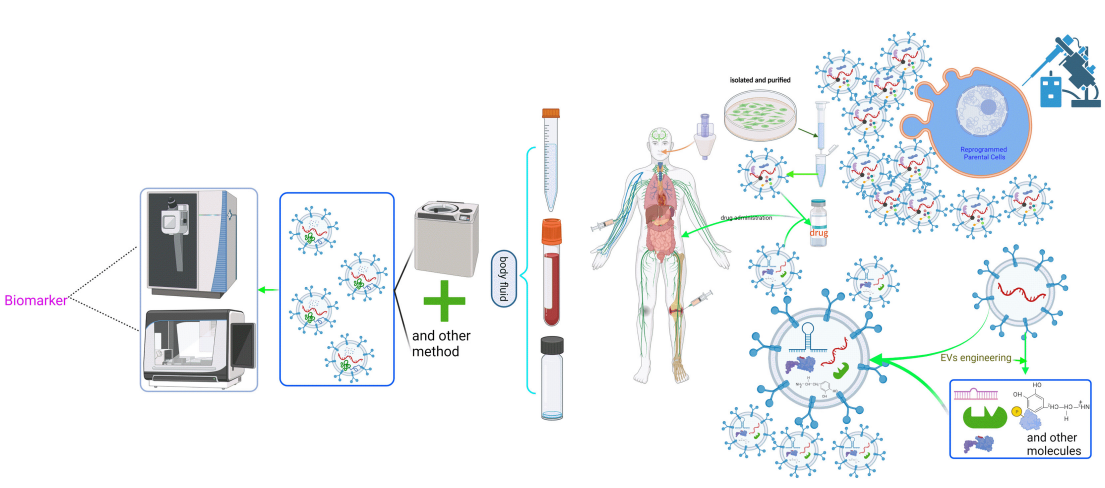


FIGURE 4
Schematic representation of the clinical application of neuronal EVs. The cargoes in EVs are derived from the parental cells, which partly reflect the physiological or pathological state of the donor cells. Moreover, EVs can effectively protect their contents from being degraded by various enzymes in body fluids, prolonging the half-life of various biomarkers. Therefore, isolating and purifying EVs from body fluids using various methods, including ultracentrifugation, and then analyzing and studying them are of great significance for predicting the state of cells. However, clinical application of EVs is still quite difficult because there is no effective method to purify EVs from a defined cell. Additionally, based on the physical and chemical characteristics of EVs, such as the ability to pass the blood-brain barrier, EVs can package some targeted drugs *via* genetic manipulation to deal with neuropathy.

diagnostic power for neurodegenerative diseases (Shi et al., 2014; Fiandaca et al., 2015; Yang et al., 2018; Jia et al., 2019; Jiang C. et al., 2020; Wang and Zhang, 2020). That said, the conclusions remain to be confirmed in longitudinal studies due to the small sample size. In addition, the enriched method of neuronal exosomes in immunoprecipitation with anti-L1CAM antibody further needs to be validated because the L1CAM protein is not only expressed in the nervous system but also expressed in other tissues or cells, such as soft tissue, fallopian tube, kidney cells, and epithelial cells (according to the Human Protein Atlas)[1] (Pace et al., 2019; Asano et al., 2020), which may mean that the EVs pulled down with anti-L1CAM antibodies are not solely derived from neural tissues. Meanwhile, EVs derived from CSF are valuable for diagnosing CNS diseases (Jia et al., 2019; Muraoka et al., 2020). However, CSF samples are commonly obtained by lumbar puncture, which is an invasive test that can cause headaches and other side effects (Doherty and Forbes, 2014). Thus, it is challenging to recruit patients and healthy volunteers who agree to undergo lumbar puncture. Moreover, most research on the neuronal EVs as a biomarker has relied on the patient's serum or plasma. Although serum or plasma is easily collected compared to CSF, the EVs in the serum or plasma is pool of EVs that come from various cells and organs. This factor may compromise the repeatability and accuracy of the results.

## Conclusion and future directions

During the past 5 years, EVs research has confirmed the transmission of EVs cargo between cells. Given the important role and therapeutic significance of EVs in neurological diseases, this topic is likely to continue under the spotlight.

One challenge for the field is that most studies were performed using a patient's serum plasma or animal model. The limited availability of brain tissue currently constrains these studies. However, accumulating evidence demonstrates that isolating and purifying unmixed neuronal EVs from these samples is extremely difficult. Moreover, results from cultured primary neurons or cell lines as research objects *in vitro* are inconsistent due to the difference between protocols, operators, and devices. More importantly, *in vitro* studies cannot replicate exactly the state of physiology or pathology *in vivo*, which precludes a direct clinical translation. In the future, developing improved methods to isolate and purify EVs from neuropathological patients' humor will be extremely beneficial for this field.

Another major challenge is understanding the underlying molecular mechanisms of packaging and transmission of neuronal EVs cargo. Analyzing the interaction of different trafficking proteins involved with both processes is extremely challenging. Although several studies found that many trafficking proteins and complexes contribute to the packaging and transmission of EVs cargo, both processes are unclear. Many proteins are associated with various cellular functions and participate in multiple pathways; the regulated mechanism remains to be investigated.

Despite the progress made, there are several key gaps in our knowledge. First, we do not yet know the physiological purpose of the generated EVs. Second, whether EVs maintain an essential cellular function is not known. Finally, although the different sizes of EVs have now been identified, how these different EVs are generated is unclear. The development of new technologies to track, isolate, and analyze EVs will be essential in addressing these important questions.

## Author contributions

ZJ and TZ designed the structure of the manuscript and finalized the manuscript. ZJ drafted the manuscript. ZH, NL, and YL provided critical revisions and improvements to the manuscript. All authors approved the final version of the manuscript.

## Funding

This work was supported by the Key Laboratory of Prevention and Treatment of Cardiovascular and Cerebrovascular Diseases, Ministry of Education (XN202014).

## Acknowledgments

We thank everyone who contributed to this manuscript.

## Conflict of interest

The authors declare that the research was conducted in the absence of any commercial or financial relationships that could be construed as a potential conflict of interest.

## Publisher's note



1 www.proteinatlas.org

# References


Abdulrahman, B. A., Abdelaziz, D. H., and Schatzl, H. M. (2018). Autophagy regulates exosomal release of prions in neuronal cells. *J. Biol. Chem.* 293, 8956–8968.

Alvarez, J., Alvarez-Illera, P., Garcia-Casas, P., Fonteriz, R. I., and Montero, M. (2020). The Role of Ca(2+) Signaling in Aging and Neurodegeneration: Insights from Caenorhabditis elegans Models. *Cells* 9:204. doi: 10.3390/cells9010204

Anderson, M. A., Burda, J. E., Ren, Y., Ao, Y., O'Shea, T. M., Kawaguchi, R., et al. (2016). Astrocyte scar formation aids central nervous system axon regeneration. *Nature* 532, 195–200. doi: 10.1038/nature17623

Asai, H., Ikezu, S., Tsunoda, S., Medalla, M., Luebke, J., Haydar, T., et al. (2015). Depletion of microglia and inhibition of exosome synthesis halt tau propagation. *Nat. Neurosci.* 18, 1584–1593. doi: 10.1038/nn.4132

Asano, H., Hatanaka, K. C., Matsuoka, R., Dong, P., Mitamura, T., Konno, Y., et al. (2020). L1CAM Predicts Adverse Outcomes in Patients with Endometrial Cancer Undergoing Full Lymphadenectomy and Adjuvant Chemotherapy. *Ann. Surg. Oncol.* 27, 2159–2168. doi: 10.1245/s10434-019-08103-2

Babuta, M., Furi, I., Bala, S., Bukong, T. N., Lowe, P., Catalano, D., et al. (2019). Dysregulated autophagy and lysosome function are linked to exosome production by micro-rna 155 in alcoholic liver disease. *Hepatology* 70, 2123–2141. doi: 10.1002/hep.30766

Baietti, M. F., Zhang, Z., Mortier, E., Melchior, A., Degeest, G., Geeraerts, A., et al. (2012). Syndecan-syntenin-ALIX regulates the biogenesis of exosomes. *Nat. Cell Biol.* 14, 677–685.

Baixauli, F., Lopez-Otin, C., and Mittelbrunn, M. (2014). Exosomes and autophagy: Coordinated mechanisms for the maintenance of cellular fitness. *Front. Immunol.* 5:403. doi: 10.3389/fimmu.2014.00403

Bianchi, E., Doe, B., Goulding, D., and Wright, G. J. (2014). Juno is the egg Izumo receptor and is essential for mammalian fertilization. *Nature* 508, 483–487.

Blanchette, C. R., and Rodal, A. A. (2020). Mechanisms for biogenesis and release of neuronal extracellular vesicles. *Curr. Opin. Neurobiol.* 63, 104–110.

Booth, A. M., Fang, Y., Fallon, J. K., Yang, J. M., Hildreth, J. E., and Gould, S. J. (2006). Exosomes and HIV Gag bud from endosome-like domains of the T cell plasma membrane. *J. Cell Biol.* 172, 923–935. doi: 10.1083/jcb.200508014

Calsolaro, V., and Edison, P. (2016). Neuroinflammation in Alzheimer's disease: Current evidence and future directions. *Alzheimers Dement* 12, 719–732.

Cheng, A., Yang, Y., Zhou, Y., Maharana, C., Lu, D., Peng, W., et al. (2016). Mitochondrial SIRT3 Mediates Adaptive Responses of Neurons to Exercise and Metabolic and Excitatory Challenges. *Cell Metab.* 23, 128–142. doi: 10.1016/j.cmet.2015.10.013

Cho, M. H., Cho, K., Kang, H. J., Jeon, E. Y., Kim, H. S., Kwon, H. J., et al. (2014). Autophagy in microglia degrades extracellular beta-amyloid fibrils and regulates the NLRP3 inflammasome. *Autophagy* 10, 1761–1775. doi: 10.4161/auto.29647

Choi, I., Zhang, Y., Seegobin, S. P., Pruvost, M., Wang, Q., Purtell, K., et al. (2020). Microglia clear neuron-released alpha-synuclein via selective autophagy and prevent neurodegeneration. *Nat. Commun.* 11:1386. doi: 10.1038/s41467-020-15119-w

Colombo, M., Moita, C., van Niel, G., Kowal, J., Vigneron, J., Benaroch, P., et al. (2013). Analysis of ESCRT functions in exosome biogenesis, composition and secretion highlights the heterogeneity of extracellular vesicles. *J. Cell Sci.* 126, 5553–5565. doi: 10.1242/jcs.128868

Coulter, M. E., Dorobantu, C. M., Lodewijk, G. A., Delalande, F., Cianferani, S., Ganesh, V. S., et al. (2018). The ESCRT-III Protein CHMP1A Mediates Secretion of Sonic Hedgehog on a Distinctive Subtype of Extracellular Vesicles. *Cell Rep.* 24, 973–986e8. doi: 10.1016/j.celrep.2018.06.100

de Rivero Vaccari, J. P., Brand, F., Adamczak, S., Lee, S. W., Perez-Barcena, J., and Wang, M. Y. (2016). Exosome-mediated inflammasome signaling after central nervous system injury. *J. Neurochem.* 136, 39–48. doi: 10.1111/jnc.13036

DiFiglia, M., Sapp, E., Chase, K. O., Davies, S. W., Bates, G. P., Vonsattel, J. P., et al. (1997). Aggregation of huntingtin in neuronal intranuclear inclusions and dystrophic neurites in brain. *Science* 277, 1990–1993. doi: 10.1126/science.277.5334.1990

Doherty, C. M., and Forbes, R. B. (2014). Diagnostic Lumbar Puncture. *Ulster Med. J.* 83, 93–102.

D'Souza-Schorey, C., and Schorey, J. S. (2018). Regulation and mechanisms of extracellular vesicle biogenesis and secretion. *Essays Biochem.* 62, 125–133.

Emmanouilidou, E., Melachroinou, K., Roumeliotis, T., Garbis, S. D., Ntzouni, M., and Margaritis, L. H. (2010). Cell-produced alpha-synuclein is secreted in a calcium-dependent manner by exosomes and impacts neuronal survival. *J. Neurosci.* 30, 6838–6851. doi: 10.1523/JNEUROSCI.5699-09.2010

Escola, J. M., Kleijmeer, M. J., Stoorvogel, W., Griffith, J. M., Yoshie, O., and Geuze, H. J. (1998). Selective enrichment of tetraspan proteins on the internal vesicles of multivesicular endosomes and on exosomes secreted by human B-lymphocytes. *J. Biol. Chem.* 273, 20121–20127. doi: 10.1074/jbc.273.32.20121

Evans, S. J., Choudary, P. V., Neal, C. R., Li, J. Z., Vawter, M. P., Tomita, H., et al. (2004). Dysregulation of the fibroblast growth factor system in major depression. *Proc. Natl. Acad. Sci. U.S.A.* 101, 15506–15511.

Fan, R. Z., Guo, M., Luo, S., Cui, M., and Tieu, K. (2019). Exosome release and neuropathology induced by alpha-synuclein: New insights into protective mechanisms of Drp1 inhibition. *Acta Neuropathol. Commun.* 7:184. doi: 10.1186/s40478-019-0821-4

Fang, Y., Wu, N., Gan, X., Yan, W., Morrell, J. C., and Gould, S. J. (2007). Higher-order oligomerization targets plasma membrane proteins and HIV gag to exosomes. *PLoS Biol.* 5:e158. doi: 10.1371/journal.pbio.0050158

Faure, J., Lachenal, G., Court, M., Hirrlinger, J., Chatellard-Causse, C., Blot, B., et al. (2006). Exosomes are released by cultured cortical neurones. *Mol. Cell Neurosci.* 31, 642–648.

Fiandaca, M. S., Kapogiannis, D., Mapstone, M., Boxer, A., Eitan, E., Schwartz, J. B., et al. (2015). Identification. *Alzheimers Dement* 11, 600–7e1.

Gaughran, F., Payne, J., Sedgwick, P. M., Cotter, D., and Berry, M. (2006). Hippocampal FGF-2 and FGFR1 mRNA expression in major depression, schizophrenia and bipolar disorder. *Brain Res. Bull.* 70, 221–227. doi: 10.1016/j.brainresbull.2006.04.008

Goncalves, M. B., Malmqvist, T., Clarke, E., Hubens, C. J., Grist, J., Hobbs, C., et al. (2015). Neuronal RARbeta Signaling Modulates PTEN Activity Directly in Neurons and via Exosome Transfer in Astrocytes to Prevent Glial Scar Formation and Induce Spinal Cord Regeneration. *J. Neurosci.* 35, 15731–15745. doi: 10.1523/JNEUROSCI.1339-15.2015

Gonzalez, R., Hamblin, M. H., and Lee, J. P. (2016). Neural Stem Cell Transplantation and CNS Diseases. *CNS Neurol. Disord. Drug Targets* 15, 881–886.

Guillemot, F., and Zimmer, C. (2011). From cradle to grave: The multiple roles of fibroblast growth factors in neural development. *Neuron* 71, 574–588. doi: 10.1016/j.neuron.2011.08.002

Guix, F. X., Corbett, G. T., Cha, D. J., Mustapic, M., Liu, W., Mengel, D., et al. (2018). Detection of Aggregation-Competent Tau in Neuron-Derived Extracellular Vesicles. *Int. J. Mol. Sci.* 19:663. doi: 10.3390/ijms19030663

Guo, C., Liu, J., Zhou, Q., Song, J., Zhang, Z., Li, Z., et al. (2020). Exosomal Noncoding RNAs and Tumor Drug Resistance. *Cancer Res.* 80, 4307–4313.

Guo, H., Chitiprolu, M., Roncevic, L., Javalet, C., Hemming, F. J., Trung, M. T., et al. (2017). Atg5 disassociates the v1v0-atpase to promote exosome production and tumor metastasis independent of canonical macroautophagy. *Dev. Cell* 43, 716–730.e7. doi: 10.1016/j.devcel.2017.11.018

Han, C., Xiong, N., Guo, X., Huang, J., Ma, K., Liu, L., et al. (2019). Exosomes from patients with Parkinson's disease are pathological in mice. *J. Mol. Med.* 97, 1329–1344.

Han, X., Sun, S., Sun, Y., Song, Q., Zhu, J., Song, N., et al. (2019). Small molecule-driven NLRP3 inflammation inhibition via interplay between ubiquitination and autophagy: Implications for Parkinson disease. *Autophagy* 15, 1860–1881. doi: 10.1080/15548627.2019.1596481

Haque, A., Samantaray, S., Knaryan, V. H., Capone, M., Hossain, A., Matzelle, D., et al. (2020). Calpain mediated expansion of CD4+ cytotoxic T cells in rodent models of Parkinson's disease. *Exp. Neurol.* 330:113315. doi: 10.1016/j.expneurol.2020.113315

Harding, C., Heuser, J., and Stahl, P. (1984). Endocytosis and intracellular processing of transferrin and colloidal gold-transferrin in rat reticulocytes: Demonstration of a pathway for receptor shedding. *Eur. J. Cell Biol.* 35, 256–263.

Harland, M., Torres, S., Liu, J., and Wang, X. (2020). Neuronal Mitochondria Modulation of LPS-Induced Neuroinflammation. *J. Neurosci.* 40, 1756–1765.

Heckmann, B. L., Teubner, B. J. W., Tummers, B., Boada-Romero, E., Harris, L., Yang, M., et al. (2019). LC3-Associated Endocytosis Facilitates beta-Amyloid Clearance and Mitigates Neurodegeneration in Murine Alzheimer's Disease. *Cell* 178, 536–551.e14.

Hessvik, N. P., and Llorente, A. (2018). Current knowledge on exosome biogenesis and release. *Cell. Mol. Life Sci.* 75, 193–208.

Hitomi, K., Okada, R., Loo, T. M., Miyata, K., Nakamura, A. J., and Takahashi, A. (2020). DNA Damage Regulates Senescence-Associated Extracellular Vesicle

Release via the Ceramide Pathway to Prevent Excessive Inflammatory Responses. *Int. J. Mol. Sci.* 21:3720. doi: 10.3390/ijms21103720

Houtman, J., Freitag, K., Gimber, N., Schmoranzer, J., Heppner, F. L., and Jendrach, M. (2019). Beclin1-driven autophagy modulates the inflammatory response of microglia via NLRP3. *EMBO J.* 38:e99430. doi: 10.15252/embj.201899430

Hsu, C., Morohashi, Y., Yoshimura, S., Manrique-Hoyos, N., Jung, S., Lauterbach, M. A., et al. (2010). Regulation of exosome secretion by Rab35 and its GTPase-activating proteins TBC1D10A-C. *J. Cell Biol.* 189, 223–232. doi: 10.1083/jcb.200911018

Iguchi, Y., Eid, L., Parent, M., Soucy, G., Bareil, C., Riku, Y., et al. (2016). Exosome secretion is a key pathway for clearance of pathological TDP-43. *Brain* 139, 3187–3201. doi: 10.1093/brain/aww237

Iturria-Medina, Y., Sotero, R. C., Toussaint, P. J., Mateos-Perez, J. M., Evans, A. C., and Alzheimer's Disease Neuroimaging, I. (2016). Early role of vascular dysregulation on late-onset Alzheimer's disease based on multifactorial data-driven analysis. *Nat. Commun.* 7:11934. doi: 10.1038/ncomms11934

Jeon, I., Cicchetti, F., Cisbani, G., Lee, S., Li, E., Bae, J., et al. (2016). Human-to-mouse prion-like propagation of mutant huntingtin protein. *Acta Neuropathol.* 132, 577–592. doi: 10.1007/s00401-016-1582-9

Jia, L., Qiu, Q., Zhang, H., Chu, L., Du, Y., Zhang, J., et al. (2019). Concordance between the assessment of Abeta42, T-tau, and P-T181-tau in peripheral blood neuronal-derived exosomes and cerebrospinal fluid. *Alzheimers Dement* 15, 1071–1080. doi: 10.1016/j.jalz.2019.05.002

Jiang, C., Hopfner, F., Katsikoudi, A., Hein, R., Catli, C., Evetts, S., et al. (2020). Serum neuronal exosomes predict and differentiate Parkinson's disease from atypical parkinsonism. *J. Neurol. Neurosurg. Psychiatry* 91, 720–729. doi: 10.1136/jnnp-2019-322588

Jiang, D., Gong, F., Ge, X., Lv, C., Huang, C., Feng, S., et al. (2020). Neuron-derived exosomes-transmitted miR-124-3p protect traumatically injured spinal cord by suppressing the activation of neurotoxic microglia and astrocytes. *J. Nanobiotechnol.* 18:105. doi: 10.1186/s12951-020-00665-8

Jiao, Z., Zhang, W., Chen, C., Zhu, X., Chen, X., Zhou, M., et al. (2019). Gene Dysfunction Mediates Immune Response to Dopaminergic Degeneration in Parkinson's Disease. *ACS Chem. Neurosci.* 10, 803–811.

Kenific, C. M., Zhang, H., and Lyden, D. (2021). An exosome pathway without an ESCRT. *Cell Res.* 31, 105–106.

Kumar, R., Tang, Q., Muller, S. A., Gao, P., Mahlstedt, D., Zampagni, S., et al. (2020). Fibroblast Growth Factor 2-Mediated Regulation of Neuronal Exosome Release Depends on VAMP3/Cellubrevin in Hippocampal Neurons. *Adv. Sci.* 7:1902372. doi: 10.1002/advs.201902372

Lachenal, G., Pernet-Gallay, K., Chivet, M., Hemming, F. J., Belly, A., Bodon, G., et al. (2011). Release of exosomes from differentiated neurons and its regulation by synaptic glutamatergic activity. *Mol. Cell Neurosci.* 46, 409–418.

Lemaire, Q., Raffo-Romero, A., Arab, T., Van Camp, C., Drago, F., Forte, S., et al. (2019). Isolation of microglia-derived extracellular vesicles: Towards miRNA signatures and neuroprotection. *J. Nanobiotechnol.* 17:119. doi: 10.1186/s12951-019-0551-6

Li, D., Huang, S., Zhu, J., Hu, T., Han, Z., Zhang, S., et al. (2019). Exosomes from MiR-21-5p-increased neurons play a role in neuroprotection by suppressing RAB11A-mediated neuronal autophagy *in vitro* after traumatic brain injury. *Med. Sci. Monit.* 25, 1871–1885. doi: 10.12659/MSM.915727

Liu, X. N., Zhang, C. B., Lin, H., Tang, X. Y., Zhou, R., Wen, H. L., et al. (2021). microRNA-204 shuttled by mesenchymal stem cell-derived exosomes inhibits the migration and invasion of non-small-cell lung cancer cells via the KLF7/AKT/HIF-1alpha axis. *Neoplasma* 68, 719–731. doi: 10.4149/neo_2021_201208N1328

Liu, Z., Qiu, A. W., Huang, Y., Yang, Y., Chen, J. N., Gu, T. T., et al. (2019). IL-17A exacerbates neuroinflammation and neurodegeneration by activating microglia in rodent models of Parkinson's disease. *Brain Behav. Immun.* 81, 630–645. doi: 10.1016/j.bbi.2019.07.026

Lodygin, D., Hermann, M., Schweingruber, N., Flugel-Koch, C., Watanabe, T., Schlosser, C., et al. (2019). beta-Synuclein-reactive T cells induce autoimmune CNS grey matter degeneration. *Nature* 566, 503–508.

Luo, Z., Wu, F., Xue, E., Huang, L., Yan, P., Pan, X., et al. (2019). Hypoxia preconditioning promotes bone marrow mesenchymal stem cells survival by inducing HIF-1alpha in injured neuronal cells derived exosomes culture system. *Cell Death Dis.* 10:134. doi: 10.1038/s41419-019-1410-y

Machado-Santos, J., Saji, E., Troscher, A. R., Paunovic, M., Liblau, R., Gabriely, G., et al. (2018). The compartmentalized inflammatory response in the multiple sclerosis brain is composed of tissue-resident CD8+ T lymphocytes and B cells. *Brain* 141, 2066–2082. doi: 10.1093/brain/awy151

Malik, A. R., and Willnow, T. E. (2019). Excitatory Amino Acid Transporters in Physiology and Disorders of the Central Nervous System. *Int. J. Mol. Sci.* 20:5671.

Mead, B., and Tomarev, S. (2017). Bone Marrow-Derived Mesenchymal Stem Cells-Derived Exosomes Promote Survival of Retinal Ganglion Cells Through miRNA-Dependent Mechanisms. *Stem Cells Transl. Med.* 6, 1273–1285. doi: 10.1002/sctm.16-0428

Melo, S. A., Luecke, L. B., Kahlert, C., Fernandez, A. F., Gammon, S. T., Kaye, J., et al. (2015). Glypican-1 identifies cancer exosomes and detects early pancreatic cancer. *Nature* 523, 177–182.

Men, Y., Yelick, J., Jin, S., Tian, Y., Chiang, M. S. R., Higashimori, H., et al. (2019). Exosome reporter mice reveal the involvement of exosomes in mediating neuron to astroglia communication in the CNS. *Nat. Commun.* 10:4136. doi: 10.1038/s41467-019-11534-w

Meng, Y., Ding, J., Li, C., Fan, H., He, Y., and Qiu, P. (2020). Transfer of pathological alpha-synuclein from neurons to astrocytes via exosomes causes inflammatory responses after METH exposure. *Toxicol. Lett.* 331, 188–199. doi: 10.1016/j.toxlet.2020.06.016

Mizushima, N., and Komatsu, M. (2011). Autophagy: Renovation of cells and tissues. *Cell* 147, 728–741.

Morel, L., Regan, M., Higashimori, H., Ng, S. K., Esau, C., Vidensky, S., et al. (2013). Neuronal exosomal miRNA-dependent translational regulation of astroglial glutamate transporter GLT1. *J. Biol. Chem.* 288, 7105–7116. doi: 10.1074/jbc.M112.410944

Muralidharan-Chari, V., Clancy, J., Plou, C., Romao, M., Chavrier, P., Raposo, G., et al. (2009). ARF6-regulated shedding of tumor cell-derived plasma membrane microvesicles. *Curr. Biol.* 19, 1875–1885. doi: 10.1016/j.cub.2009.09.059

Muraoka, S., Jedrychowski, M. P., Yanamandra, K., Ikezu, S., Gygi, S. P., and Ikezu, T. (2020). Proteomic Profiling of Extracellular Vesicles Derived from Cerebrospinal Fluid of Alzheimer's Disease Patients: A Pilot Study. *Cells* 9:1959. doi: 10.3390/cells9091959

Nabhan, J. F., Hu, R., Oh, R. S., Cohen, S. N., and Lu, Q. (2012). Formation and release of arrestin domain-containing protein 1-mediated microvesicles (ARMMs) at plasma membrane by recruitment of TSG101 protein. *Proc. Natl. Acad. Sci. U.S.A.* 109, 4146–4151. doi: 10.1073/pnas.1200448109

Nager, A. R., Goldstein, J. S., Herranz-Perez, V., Portran, D., Ye, F., Garcia-Verdugo, J. M., et al. (2017). An Actin Network Dispatches Ciliary GPCRs into Extracellular Vesicles to Modulate Signaling. *Cell* 168, 252–263.e14. doi: 10.1016/j.cell.2016.11.036

Nakamura, Y., Dryanovski, D. I., Kimura, Y., Jackson, S. N., Woods, A. S., Yasui, Y., et al. (2019). Cocaine-induced endocannabinoid signaling mediated by sigma-1 receptors and extracellular vesicle secretion. *elife* 8:e47209. doi: 10.7554/eLife.47209

Nash, Y., Schmukler, E., Trudler, D., Pinkas-Kramarski, R., and Frenkel, D. (2017). DJ-1 deficiency impairs autophagy and reduces alpha-synuclein phagocytosis by microglia. *J. Neurochem.* 143, 584–594. doi: 10.1111/jnc.14222

Neumann, M., Sampathu, D. M., Kwong, L. K., Truax, A. C., Micsenyi, M. C., Chou, T. T., et al. (2006). Ubiquitinated TDP-43 in frontotemporal lobar degeneration and amyotrophic lateral sclerosis. *Science* 314, 130–133.

Nie, W., Wu, G., Zhang, J., Huang, L. L., Ding, J., Jiang, A., et al. (2020). Responsive Exosome Nano-bioconjugates for Synergistic Cancer Therapy. *Angew. Chem. Int. Ed. Engl.* 59, 2018–2022. doi: 10.1002/anie.201912524

Niu, M., Li, Y., Li, G., Zhou, L., Luo, N., Yao, M., et al. (2020). A longitudinal study on alpha-synuclein in plasma neuronal exosomes as a biomarker for Parkinson's disease development and progression. *Eur. J. Neurol.* 27, 967–974. doi: 10.1111/ene.14208

Ostrowski, M., Carmo, N. B., Krumeich, S., Fanget, I., Raposo, G., Savina, A., et al. (2010). Rab27a and Rab27b control different steps of the exosome secretion pathway. *Nat. Cell Biol.* 12, 19–30.

Pace, K. R., Dutt, R., and Galileo, D. S. (2019). Exosomal L1CAM Stimulates Glioblastoma Cell Motility, Proliferation, and Invasiveness. *Int. J. Mol. Sci.* 20:3982.

Pan, B. T., and Johnstone, R. M. (1983). Fate of the transferrin receptor during maturation of sheep reticulocytes *in vitro*: Selective externalization of the receptor. *Cell* 33, 967–978.

Park, G., Kim, B. S., and Kim, E. (2020). A novel function of FAF1, which induces dopaminergic neuronal death through cell-to-cell transmission. *Cell Commun. Signal.* 18:133. doi: 10.1186/s12964-020-00632-8

Passamonti, L., Tsvetanov, K. A., Jones, P. S., Bevan-Jones, W. R., Arnold, R., Borchert, R. J., et al. (2019). Neuroinflammation and functional connectivity in alzheimer's disease: Interactive influences on cognitive performance. *J. Neurosci.* 39, 7218–7226.

Pastuzyn, E. D., Day, C. E., Kearns, R. B., Kyrke-Smith, M., Taibi, A. V., McCormick, J., et al. (2018). The Neuronal Gene Arc Encodes a Repurposed Retrotransposon Gag Protein that Mediates Intercellular RNA Transfer. *Cell* 172, 275–288.e18.

Pegtel, D. M., and Gould, S. J. (2019). Exosomes. *Annu. Rev. Biochem.* 88, 487–514.

Peng, C., Trojanowski, J. Q., and Lee, V. M. (2020). Protein transmission in neurodegenerative disease. *Nat. Rev. Neurol.* 16, 199–212.

Pfeffer, S. R. (2017). Rab GTPases: Master regulators that establish the secretory and endocytic pathways. *Mol. Biol. Cell* 28, 712–715.

Pinto, S., Cunha, C., Barbosa, M., Vaz, A. R., and Brites, D. (2017). Exosomes from nsc-34 cells transfected with hsod1-g93a are enriched in mir-124 and drive alterations in microglia phenotype. *Front. Neurosci.* 11:273. doi: 10.3389/fnins.2017.00273

Pluvinage, J. V., Haney, M. S., Smith, B. A. H., Sun, J., Iram, T., Bonanno, L., et al. (2019). CD22 blockade restores homeostatic microglial phagocytosis in ageing brains. *Nature* 568, 187–192.

Polanco, J. C., Li, C., Durisic, N., Sullivan, R., and Gotz, J. (2018). Exosomes taken up by neurons hijack the endosomal pathway to spread to interconnected neurons. *Acta Neuropathol. Commun.* 6:10. doi: 10.1186/s40478-018-0514-4

Qin, Y., Qiu, J., Wang, P., Liu, J., Zhao, Y., Jiang, F., et al. (2021). Impaired autophagy in microglia aggravates dopaminergic neurodegeneration by regulating NLRP3 inflammasome activation in experimental models of Parkinson's disease. *Brain Behav. Immun.* 91, 324–338. doi: 10.1016/j.bbi.2020.10.010

Rayamajhi, S., Nguyen, T. D. T., Marasini, R., and Aryal, S. (2019). Macrophage-derived exosome-mimetic hybrid vesicles for tumor targeted drug delivery. *Acta Biomater.* 94, 482–494. doi: 10.1016/j.actbio.2019.05.054

Ruan, Z., Pathak, D., Venkatesan Kalavai, S., Yoshii-Kitahara, A., Muraoka, S., and Bhatt, N. (2021). Alzheimer's disease brain-derived extracellular vesicles spread tau pathology in interneurons. *Brain* 144, 288–309.

Sardar Sinha, M., Ansell-Schultz, A., Civitelli, L., Hildesjo, C., Larsson, M., Lannfelt, L., et al. (2018). Alzheimer's disease pathology propagation by exosomes containing toxic amyloid-beta oligomers. *Acta Neuropathol.* 136, 41–56. doi: 10.1007/s00401-018-1868-1

Savina, A., Vidal, M., and Colombo, M. I. (2002). The exosome pathway in K562 cells is regulated by Rab11. *J. Cell Sci.* 115, 2505–2515. doi: 10.1242/jcs.115.12.2505

Sharma, P., Mesci, P., Carromeu, C., McClatchy, D. R., Schiapparelli, L., Yates, J. R. III, et al. (2019). Exosomes regulate neurogenesis and circuit assembly. *Proc. Natl. Acad. Sci. U.S.A.* 116, 16086–16094. doi: 10.1073/pnas.1902513116

Shi, M., Liu, C., Cook, T. J., Bullock, K. M., Zhao, Y., Ginghina, C., et al. (2014). Plasma exosomal alpha-synuclein is likely CNS-derived and increased in Parkinson's disease. *Acta Neuropathol.* 128, 639–650.

Silverman, J. M., Christy, D., Shyu, C. C., Moon, K. M., Fernando, S., Gidden, Z., et al. (2019). CNS-derived extracellular vesicles from superoxide dismutase 1 (SOD1)(G93A) ALS mice originate from astrocytes and neurons and carry misfolded SOD1. *J. Biol. Chem.* 294, 3744–3759. doi: 10.1074/jbc.RA118.004825

Simeoli, R., Montague, K., Jones, H. R., Castaldi, L., Chambers, D., Kelleher, J. H., et al. (2017). Exosomal cargo including microRNA regulates sensory neuron to macrophage communication after nerve trauma. *Nat. Commun.* 8:1778. doi: 10.1038/s41467-017-01841-5

Singh, P. K., and Muqit, M. M. K. (2020). Parkinson's: A disease of aberrant vesicle trafficking. *Annu. Rev. Cell Dev. Biol.* 36, 237–264. doi: 10.1146/annurev-cellbio-100818-125512

Song, L., Tang, S., Han, X., Jiang, Z., Dong, L., Liu, C., et al. (2019c). KIBRA controls exosome secretion via inhibiting the proteasomal degradation of Rab27a. *Nat. Commun.* 10:1639. doi: 10.1038/s41467-019-09720-x

Song, L., Tang, S., Dong, L., Han, X., Cong, L., Dong, J., et al. (2019b). The Neuroprotection of KIBRA in Promoting Neuron Survival and Against Amyloid beta-Induced Apoptosis. *Front. Cell Neurosci.* 13:137. doi: 10.3389/fncel.2019.00137

Song, H., Zhang, X., Chen, R., Miao, J., Wang, L., Cui, L., et al. (2019a). Cortical neuron-derived exosomal microrna-181c-3p inhibits neuroinflammation by downregulating cxcl1 in astrocytes of a rat model with ischemic brain injury. *Neuroimmunomodulation* 26, 217–233. doi: 10.1159/000502694

Su, G., Meyer, K., Nandini, C. D., Qiao, D., Salamat, S., and Friedl, A. (2006). Glypican-1 is frequently overexpressed in human gliomas and enhances FGF-2 signaling in glioma cells. *Am. J. Pathol.* 168, 2014–2026. doi: 10.2353/ajpath.2006.050800

Sweeney, M. D., Sagare, A. P., and Zlokovic, B. V. (2018). Blood-brain barrier breakdown in Alzheimer disease and other neurodegenerative disorders. *Nat. Rev. Neurol.* 14, 133–150.

Trajkovic, K., Hsu, C., Chiantia, S., Rajendran, L., Wenzel, D., Wieland, F., et al. (2008). Ceramide triggers budding of exosome vesicles into multivesicular endosomes. *Science* 319, 1244–1247. doi: 10.1126/science.1153124

Upadhya, R., Zingg, W., Shetty, S., and Shetty, A. K. (2020). Astrocyte-derived extracellular vesicles: Neuroreparative properties and role in the pathogenesis of neurodegenerative disorders. *J. Control Release* 323, 225–239. doi: 10.1016/j.jconrel.2020.04.017

Vietri, M., Radulovic, M., and Stenmark, H. (2020). The many functions of ESCRTs. *Nat. Rev. Mol. Cell Biol.* 21, 25–42.

Vilcaes, A. A., Chanaday, N. L., and Kavalali, E. T. (2021). Interneuronal exchange and functional integration of synaptobrevin via extracellular vesicles. *Neuron* 109, 971–983.e5. doi: 10.1016/j.neuron.2021.01.007

Wang, H., Chen, F. S., Zhang, Z. L., Zhou, H. X., Ma, H., and Li, X. Q. (2021). MiR-126-3p-enriched extracellular vesicles from hypoxia-preconditioned VSC 4.1 neurons attenuate ischaemia-reperfusion-induced pain hypersensitivity by regulating the PIK3R2-mediated pathway. *Mol. Neurobiol.* 58, 821–834. doi: 10.1007/s12035-020-02159-y

Wang, L., and Zhang, L. (2020). Circulating Exosomal miRNA as Diagnostic Biomarkers of Neurodegenerative Diseases. *Front. Mol. Neurosci.* 13:53. doi: 10.3389/fnmol.2020.00053

Wang, Y., Balaji, V., Kaniyappan, S., Kruger, L., Irsen, S., Tepper, K., et al. (2017). The release and trans-synaptic transmission of Tau via exosomes. *Mol. Neurodegener.* 12:5. doi: 10.1186/s13024-016-0143-y

Wei, D., Zhan, W., Gao, Y., Huang, L., Gong, R., Wang, W., et al. (2021). RAB31 marks and controls an ESCRT-independent exosome pathway. *Cell Res.* 31, 157–177. doi: 10.1038/s41422-020-00409-1

Wei, Z., Meng, X., El Fatimy, R., Sun, B., Mai, D., Zhang, J., et al. (2020). Environmental enrichment prevents Abeta oligomer-induced synaptic dysfunction through mirna-132 and hdac3 signaling pathways. *Neurobiol. Dis.* 134:104617. doi: 10.1016/j.nbd.2019.104617

Wilton, D. K., Dissing-Olesen, L., and Stevens, B. (2019). Neuron-Glia Signaling in Synapse Elimination. *Annu. Rev. Neurosci.* 42, 107–127.

Winston, C. N., Goetzl, E. J., Baker, L. D., Vitiello, M. V., and Rissman, R. A. (2018). Growth Hormone-Releasing Hormone Modulation of Neuronal Exosome Biomarkers in Mild Cognitive Impairment. *J. Alzheimers Dis.* 66, 971–981. doi: 10.3233/JAD-180302

Wolf, P. (1967). The nature and significance of platelet products in human plasma. *Br. J. Haematol.* 13, 269–288.

Xiao, Q. X., Cheng, C. X., Deng, R., Liu, Q., Ren, Y. B., He, L., et al. (2020). LncRNA-MYL2-2 and miR-124-3p Are Associated with Perioperative Neurocognitive Disorders in Patients after Cardiac Surgery. *J. Invest. Surg.* 34, 1297–1303. doi: 10.1080/08941939.2020.1797949

Xiao, Y., Zhong, J., Zhong, B., Huang, J., Jiang, L., Jiang, Y., et al. (2020). Exosomes as potential sources of biomarkers in colorectal cancer. *Cancer Lett.* 476, 13–22.

Xu, B., Zhang, Y., Du, X. F., Li, J., Zi, H. X., Bu, J. W., et al. (2017). Neurons secrete miR-132-containing exosomes to regulate brain vascular integrity. *Cell Res.* 27, 882–897. doi: 10.1038/cr.2017.62

Yang, K. S., Ciprani, D., O'Shea, A., Liss, A. S., Yang, R., Fletcher-Mercaldo, S., et al. (2021). Extracellular Vesicle Analysis Allows for Identification of Invasive IPMN. *Gastroenterology* 160, 1345–1358.e11. doi: 10.1053/j.gastro.2020.11.046

Yang, T. T., Liu, C. G., Gao, S. C., Zhang, Y., and Wang, P. C. (2018). The Serum Exosome Derived MicroRNA-135a, -193b, and -384 Were Potential Alzheimer's Disease Biomarkers. *Biomed. Environ. Sci.* 31, 87–96. doi: 10.3967/bes2018.011

Yin, Z., Han, Z., Hu, T., Zhang, S., Ge, X., Huang, S., et al. (2020). Neuron-derived exosomes with high miR-21-5p expression promoted polarization of M1 microglia in culture. *Brain Behav. Immun.* 83, 270–282.

Ying, W., Riopel, M., Bandyopadhyay, G., Dong, Y., Birmingham, A., Seo, J. B., et al. (2017). Adipose Tissue Macrophage-Derived Exosomal miRNAs Can Modulate *In Vivo* and *In Vitro* Insulin Sensitivity. *Cell* 171, 372–384.e12. doi: 10.1016/j.cell.2017.08.035

You, Y., Borgmann, K., Edara, V. V., Stacy, S., Ghorpade, A., and Ikezu, T. (2020). Activated human astrocyte-derived extracellular vesicles modulate neuronal uptake, differentiation and firing. *J. Extracell. Vesicles* 9:1706801. doi: 10.1080/20013078.2019.1706801

Yu, H., Sun, T., An, J., Wen, L., Liu, F., Bu, Z., et al. (2020). Potential roles of exosomes in parkinson's disease: From pathogenesis, diagnosis, and treatment to prognosis. *Front. Cell Dev. Biol.* 8:86. doi: 10.3389/fcell.2020.00086

Yuyama, K., Sun, H., Mitsutake, S., and Igarashi, Y. (2012). Sphingolipid-modulated exosome secretion promotes clearance of amyloid-beta by microglia. *J. Biol. Chem.* 287, 10977–10989. doi: 10.1074/jbc.M111.324616

Zhang, X. W., Zhou, J. C., Peng, D., Hua, F., Li, K., Yu, J. J., et al. (2020). Disrupting the TRIB3-SQSTM1 interaction reduces liver fibrosis by restoring autophagy and suppressing exosome-mediated HSC activation. *Autophagy* 16, 782–796. doi: 10.1080/15548627.2019.1635383

Zhang, C., Wu, B., Wang, X., Chen, C., Zhao, R., Lu, H., et al. (2020). Vascular, flow and perfusion abnormalities in Parkinson's disease. *Parkinsonism Relat. Disord.* 73, 8–13.

Zhang, Y., Meng, X., Jiao, Z., Liu, Y., Zhang, X., and Qu, S. (2020). Generation of a Novel Mouse Model of Parkinson's Disease via Targeted Knockdown of Glutamate Transporter GLT-1 in the Substantia Nigra. *ACS Chem. Neurosci.* 11, 406–417. doi: 10.1021/acschemneuro.9b00609

Zhang, Q., Hu, C., Huang, J., Liu, W., Lai, W., Leng, F., et al. (2019). ROCK1 induces dopaminergic nerve cell apoptosis via the activation of Drp1-mediated aberrant mitochondrial fission in Parkinson's disease. *Exp. Mol. Med.* 51, 1–13. doi: 10.1038/s12276-019-0318-z

Zhang, W., Zhu, J., He, X., Liu, X., Li, J., Li, W., et al. (2019). Exosome complex genes mediate RNA degradation and predict survival in mantle cell lymphoma. *Oncol. Lett.* 18, 5119–5128. doi: 10.3892/ol.2019.10850

Zhao, S., Mi, Y., Guan, B., Zheng, B., Wei, P., Gu, Y., et al. (2021). Correction to: Tumor-derived exosomal miR-934 induces macrophage M2 polarization to promote liver metastasis of colorectal cancer. *J. Hematol. Oncol.* 14:33. doi: 10.1186/s13045-021-01042-0

Zheng, T., Pu, J., Chen, Y., Guo, Z., Pan, H., Zhang, L., et al. (2017). Exosomes Secreted from HEK293-APP Swe/Ind Cells Impair the Hippocampal Neurogenesis. *Neurotox. Res.* 32, 82–93. doi: 10.1007/s12640-017-9713-1

Zheng, T., Wu, X., Wei, X., Wang, M., and Zhang, B. (2018). The release and transmission of amyloid precursor protein via exosomes. *Neurochem. Int.* 114, 18–25. doi: 10.1016/j.neuint.2017.12.009

Zhou, T., Lin, D., Chen, Y., Peng, S., Jing, X., Lei, M., et al. (2019). alpha-synuclein accumulation in SH-SY5Y cell impairs autophagy in microglia by exosomes overloading miR-19a-3p. *Epigenomics* 11, 1661–1677. doi: 10.2217/epi-2019-0222

Zhou, W., Woodson, M., Sherman, M. B., Neelakanta, G., and Sultana, H. (2019). Exosomes mediate Zika virus transmission through SMPD3 neutral Sphingomyelinase in cortical neurons. *Emerg. Microbes Infect.* 8, 307–326. doi: 10.1080/22221751.2019.1578188

Zhu, J., Liu, B., Wang, Z., Wang, D., Ni, H., Zhang, L., et al. (2019). Exosomes from nicotine-stimulated macrophages accelerate atherosclerosis through miR-21-3p/PTEN-mediated VSMC migration and proliferation. *Theranostics* 9, 6901–6919. doi: 10.7150/thno.37357

frontiers | Frontiers in Cellular Neuroscience

TYPE Original Research
PUBLISHED 08 November 2022
DOI 10.3389/fncel.2022.1006797



OPEN ACCESS

EDITED BY
Ji Chen,
Zhejiang University, China

REVIEWED BY
Yuchao Jiang,
University of Electronic Science and Technology of China, China
Tumbwene Mwansisya,
Aga Khan University, Tanzania

*CORRESPONDENCE
Zhening Liu
zhening.liu@csu.edu.cn
Zebin Fan
1209565379@qq.com
Jie Yang
yang0826@csu.edu.cn

SPECIALTY SECTION
This article was submitted to Cellular Neuropathology, a section of the journal Frontiers in Cellular Neuroscience

RECEIVED 29 July 2022
ACCEPTED 18 October 2022
PUBLISHED 08 November 2022

CITATION
Cheng P, Liu Z, Yang J, Sun F, Fan Z and Yang J (2022) Decreased integration of default-mode network during a working memory task in schizophrenia with severe attention deficits.
*Front. Cell. Neurosci.* 16:1006797.
doi: 10.3389/fncel.2022.1006797



# Decreased integration of default-mode network during a working memory task in schizophrenia with severe attention deficits

Peng Cheng[1,2], Zhening Liu[1,2]*, Jun Yang[1,2], Fuping Sun[1,2], Zebin Fan[1,2]* and Jie Yang[1,2]*

[1]Department of Psychiatry, The Second Xiangya Hospital of Central South University, Changsha, China, [2]National Clinical Research Center for Mental Disorders, Changsha, China

**Background:** Working memory (WM) and attention deficits are both important features of schizophrenia. WM is closely related to attention, for it acted as an important characteristic in activating and manipulating WM. However, the knowledge of neural mechanisms underlying the relationship between WM and attention deficits in schizophrenia is poorly investigated.

**Methods:** Graph theory was used to examine the network topology at the whole-brain and large-scale network levels among 125 schizophrenia patients with different severity of attention deficits (65 mild attention deficits; 46 moderate attention deficits; and 14 severe attention deficits) and 53 healthy controls (HCs) during an N-back WM task. These analyses were repeated in the same participants during the resting state.

**Results:** In the WM task, there were omnibus differences in small-worldness and normalized clustering coefficient at a whole-brain level and normalized characterized path length of the default-mode network (DMN) among all groups. *Post hoc* analysis further indicated that all patient groups showed increased small-worldness and normalized clustering coefficient of the whole brain compared with HCs, and schizophrenia with severe attention deficits showed increased normalized characterized path length of the DMN compared with schizophrenia with mild attention deficits and HCs. However, these observations were not persisted under the resting state. Further correlation analyses indicated that the increased normalized characterized path length of the DMN was correlated with more severe attentional deficits and poorer accuracy of the WM task.

**Conclusion:** Our research demonstrated that, compared with the schizophrenia patients with less attention deficits, disrupted integration of the DMN may more particularly underlie the WM deficits in schizophrenia patients with severe attention deficits.

KEYWORDS

**working memory, attention deficits, brain networks, graph theory, N-back task**

## Introduction

Working memory (WM) is a complex cognitive process involved in encoding, storing, and retrieving information steps (Baddeley, 1986). It is closely related to attention, which is a crucial cognitive ability that enables humans to select goal-relevant information from external sensory stimuli in the environment. Previous studies have reported that impairments in attentional selection can have detrimental effects on WM encoding, specifically when top-down processes are involved (Baddeley, 1996). Meanwhile, the ability to resist interference is also crucial for maintaining the stability of memory representation over time and extracting information from WM (Berti and Schröger, 2003; Lorenc et al., 2021). Thus, attention deficits are likely to affect WM at different processing.

Both attention and WM deficits are common neurocognitive impairments of schizophrenia. They are persisted in schizophrenia even after systematic treatment, which would contribute to frequent relapses (Hui et al., 2016) and companied prolonged illness burden (Park et al., 1999). However, current treatments are mainly aimed at addressing the positive symptoms, with minor effects on neurocognitive deficits. Therefore, understanding the neural mechanism of attention and WM impairments is vitally important for developing new treatments that can impact the long-term functional outcome of schizophrenia.

Extensive previous studies have investigated the neural mechanism of WM dysfunction in patients with schizophrenia and revealed that the hyperactivity (i.e., failure to deactivate) within the default-mode network (DMN) (Pomarol-Clotet et al., 2008; Whitfield-Gabrieli et al., 2009) was companied with hypoactivity of the task-positive network (TPN) (Meyer-Lindenberg et al., 2001) during the WM task. Reduced suppression of the DMN in schizophrenia can be interpreted as a failure to allocate attentional resources to the current task, with consequent impairment in task performance (Whitfield-Gabrieli and Ford, 2012). The anticorrelation could be regarded as an alternating balance of attention to internal thoughts (associated with DMN) and external feelings (associated with TPN). This greater anticorrelation, associated with superior cognitive task performance, seemed to be reduced in schizophrenia patients (Kelly et al., 2008; Hampson et al., 2010; Liu et al., 2012). Especially, Whitfield-Gabrieli et al. (2009) have demonstrated that compared with healthy controls (HCs), patients with schizophrenia showed reduced anticorrelation between the medial prefrontal cortex (MPFC), a crucial component of DMN, and the dorsolateral prefrontal cortex (DLPFC), a well-known important region for TPN.

Previous studies have also explored the neural mechanisms of attention deficits in patients with schizophrenia. It was reported a significant uncoupling between attention performance and mean regional homogeneity in the left middle frontal gyrus, right superior/inferior parietal lobe (IPL), and right angular gyrus (AG) in patients with schizophrenia compared with HCs (Hong et al., 2019). The decreased integrity of the bilateral cingulum and splenium may underlie the impaired attention in schizophrenia (Abdolalizadeh et al., 2020).

Although these studies have investigated the neural mechanisms of the WM and attention deficits in schizophrenia and obtained some progress these years, however, the potential mechanism of attention deficits affecting WM performance in schizophrenia is still unclear. The WM can be defined as a certain subset of the process encompassed by the attention, which is composed of multiple neuropsychological and/or clinical processes (Fan et al., 2003; Pessoa et al., 2003), and the attention deficits in schizophrenia can have effects on their WM performance (Dickinson et al., 2007; Luck and Gold, 2008). It is meaningful to investigate the possible connection between WM and attention deficits among schizophrenias.

Mathematical graph theory employed in neuroimaging data can represent the topological structure of the brain connectome and infer its neural efficiency (Bullmore and Sporns, 2009; Rubinov and Sporns, 2010; Fornito et al., 2011). Compared with the traditional functional connectivity analysis that mainly investigates the synchrony between different brain regions (Pomarol-Clotet et al., 2008; Whitfield-Gabrieli et al., 2009), the graph theory could further indicate the efficiency of information processing at either the subnetwork level or the whole-brain level (van den Heuvel and Fornito, 2014). Moreover, previous related studies have suggested that human brain networks are organized in an efficient small-world manner (i.e., a highly clustered/segregated neighborhood of brain regions, with occasional integrative long-distance connections) (Tononi et al., 1994; Bullmore and Sporns, 2009). Some studies have explored the brain connectome topology in patients with schizophrenia during resting state and reported less efficient organization in patients compared with HCs (Fornito et al., 2012; Hadley et al., 2016; Yu et al., 2017; Jiang et al., 2022). Some studies go further to investigate the brain connectome topology of schizophrenias during tasks. For example, our previous work (Yang et al., 2020) demonstrated a putative mechanistic link between whole-brain connectome topology and impaired performance in schizophrenia during the WM task. It suggested that the task-dependent increased small-worldness relates to, but remains inefficient in, improving the performance above par in patients with severe negative symptoms. However, to our knowledge, no studies have investigated the brain connectome topology in schizophrenia with attention deficits under the WM task.

This study aimed to use the graph theory method to investigate the topology properties of the functional connectome at different granularity (i.e., whole brain and subnetworks) of schizophrenia patients with different attention deficit severity during the WM task. Based on the results of our prior

work (Yang et al., 2020), we speculated that all patients with schizophrenia, despite of their different attentional deficit severity, would show increased small-worldness of the whole-brain functional connectome, and this increment is induced by the elevation of the clustering coefficient. Meanwhile, based on the abnormal activation of DMN and TPN among schizophrenias during the WM task claimed by previous studies (Moraschi et al., 2020; Yuan et al., 2021), we also speculated that the topology property of subnetworks in patients with schizophrenia might also change when processing the WM task. In addition, based on the close association between WM and attention deficits, we further hypothesized that schizophrenia patients with more severe attention deficits were more likely to their special topology alterations of their brain connectome than other patients.

# Materials and methods

## Participants

Participants in the current study were enrolled in the Second Xiangya Hospital, Central South University, during 2009–2014. A total of 142 patients with schizophrenia and 59 HCs were enrolled. All the participants were right-handed native Chinese speakers. Written informed consent was obtained from participants at the beginning of the study. The Medical Ethics Committee of the Second Xiangya Hospital, Central South University, approved this study. Raw data in the current research have been reported by previous work of our research team (Yang et al., 2020; Wang et al., 2022; Wu et al., 2022).

Patients were confirmed to meet the DSM-IV (Diagnostic and Statistical Manual of Mental Disorders, 4th edition) criteria for schizophrenia (First and Gibbon, 2004). Exclusion criteria included (1) age less than 16 or greater than 45 years; (2) any contraindications for MRI; (3) history of receiving electroconvulsive therapy; (4) history of alcohol or substance dependence except nicotine; (5) serious physical ailments, organic brain disease (e.g., former stroke, cerebral vascular malformations, and epilepsy), formerly recorded brain injury, chronic neurological illness, or debilitating physical illness; and (6) alcohol use or benzodiazepine treatment, if any, stopped for at least 24 h before scanning.

Clinical symptoms of schizophrenia patients were assessed by the scale for assessment of positive symptoms (SAPS) and the scale for assessment of negative symptoms (SANS) (Phillips et al., 1991). Both patients and HCs were assessed for cognitive functions with the information and digit symbol subscales of the Wechsler Adult Intelligence Scale–Chinese Revised (WAIS-CR) (Gong, 1983) to measure verbal comprehension and processing speed, respectively.

We further divided qualified patients with schizophrenia into three subgroups according to their attention deficit severity, which was measured by the No. 24 item of SANS. The content of the No. 24 item of SANS was "comprehensive severity evaluation of attention" conducted by the interviewer on patients, which mainly included the following aspects: social contact inattention, being absent-minded during the interview, and any other presentation possibly associated with attention deficits (Andreasen, 1989). The score range of this item was 0–5. Thus, we classified the patients based on the score of No. 24 item according to the hierarchy of clinical symptom descriptions (Andreasen, 1989; Phillips et al., 1991). Patients whose No. 24 item score equals 0 or 1 were identified as the mild attention deficit group, patients whose No. 24 item score equals 2 or 3 were identified as the moderate attention deficit group, and patients whose No. 24 item score equals 4 or 5 were identified as the severe attention deficit group.

HCs were recruited and assessed using the Structured Clinical Interview for DSM-IV Axis I Disorders, Research Version, Non-patient Edition (SCID-I/NP). It was confirmed that HCs did not meet any criteria for mental disorders, and their first-degree relatives had no history of any known psychiatric disorders.

## Magnetic resonance imaging data acquisition and preprocessing

The fMRI data were acquired on a Philips Gyroscan Achieva 3.0 T scanner, which had an eight-channel head coil with gradient-recalled echo-planar imaging (EPI) pulse sequence. Participants were asked to perform an N-back WM task during the task-fMRI scanning. Detailed parameter information of the task-fMRI was listed as follows: repetition time (TR) = 2,000 ms, echo time (TE) = 30 ms, flip angle = 90°, field of view (FOV) = 240 × 240 $mm^2$, matrix = 64 × 64, slices = 36, slice thickness = 4 mm, gap = 0 mm, and total volumes = 250.

The fMRI data were preprocessed by using the DPABI toolbox (Yan et al., 2016). It consisted of the following steps: discarded several images to reach magnetic saturation, slice timing correction, head motion realignment, spatial normalization to the brain template of Montreal Neurological Institute (MNI) space, smoothing, and linear detrending. Details are seen in **Supplementary material 1**.

As for the data filtration, the preliminary exclusion criteria of data for preprocessing steps were (1) head motions larger than a 2.5-mm translation or 2.5° rotation in any direction; (2) failure of fMRI data normalization and registration to MNI space due to acquisition errors. Moreover, a number of patients were removed to control the demographic variance (age and gender) among all patient groups. After data quality control, a total of 143 participants, consisting of 92 schizophrenia patients,

were grouped by the severity of attention deficits into mild ($n$ = 49), moderate ($n$ = 29), and severe ($n$ = 14), and 51 HCs were enrolled in the subsequent analyses. No statistically significant difference in the total number of displaced volumes for interpolation existed across all groups ($p$ = 0.472).

## Working memory task paradigm

The adopted n-back WM task consists of "0-back" and "2-back" loads. Under the "0-back" load, participants were required to press the specific button when they saw the letter "X," whereas under the "2-back" load, participants were asked to press the specific button when they recognized that the letter shown was identical to the two letters before. The duration of presentation for each letter was 500 ms with an interstimulus interval of 1,500 ms. The stimulation period consisted of "0-back" load and "2-back" load, followed by a resting period during which participants were required to relax and focus on a cross in the screen for 20 s. Stimulation periods and resting periods were shown alternatively. There were four blocks for either "2-back" or "0-back" in this WM task paradigm, and each block included a 2 s guidance and 20 stimulations containing seven targets. The task paradigm is shown in **Figure 1**. As the "0-back" load is not considered as a qualified WM task, only the volumes during the four blocks of "2-back" load were extracted and concatenated for the construction of the whole-brain functional connectome. We also considered that the BOLD signal has a certain delay, about 5 s (Poldrock et al., 2011), and then shift the extraction window to backward about two volumes when conducting the extracting step. The mean time series was extracted from each of the 264 nodes using 6-mm spheres defined by the Power atlas (Power et al., 2011). A 264 × 264 symmetric matrix was generated for each participant by computing the Pearson correlation coefficients between the time series for each pair of regions of interest (ROIs) and then normalized by the Fisher's z transformation. We also controlled the variance caused by the effects of age, gender, and education years to derive a corrected matrix.

## Network construction

Network measures at each density (sparsity) were calculated on the Power atlas 264 × 264 weighted adjacency matrices, which were acquired by thresholding the symmetric matrices at a series of network densities, ranging from top 10 to 50% of all connections, with 2% increments, in line with previous studies (Yu et al., 2017; Yang et al., 2020; Tan et al., 2021; Deng et al., 2022). This range density was chosen in the current study for its lower risk of non-biological artifacts and noise (Kaiser and Hilgetag, 2006), and negative correlations were set to zero (Rubinov and Sporns, 2010, 2011). As binarization is arbitrary without widely recognized criteria, which might result in the loss of important illness-related biological features, hence weighted network approaches were applied in our research to avoid this drawback (van den Heuvel et al., 2017; Váša et al., 2018). The Brain Connectivity Toolbox (Rubinov et al., 2009) and the Graph Analysis Toolbox (Hosseini et al., 2012) were applied to quantify network measures and compare the functional networks across all groups, respectively.

## Network properties

Three common network properties of the functional connectome underlying the WM task were subsequently calculated, including the small-worldness, normalized clustering coefficient, and normalized characterized path length. Small-worldness (represented by sigma) was the ratio of normalized clustering coefficient (represented by gamma) to normalized characterized path length (represented by lambda) (i.e., sigma = $\frac{gamma}{lambda}$), as normalized topological properties were supposed to be benchmarked against corresponding mean values of null random graphs (i.e., normalized clustering coefficient (gamma) = $\frac{C}{C_{null}}$; normalized characterized path length (lambda) = $\frac{L}{L_{null}}$). Thus, we generated 20 null random networks with the same number of nodes, degree, and degree distribution as the network of interest (Palaniyappan et al., 2015; Das et al., 2018). Based on the network theory, the clustering coefficient (C) of a network was defined as the average of ratio between the actual number of edges between all neighboring nodes and the maximum possible number of edges. The characterized path length (L) of a certain network was defined as the mean value of the shortest path among all pairs of nodes in this network (Achard and Bullmore, 2007; He et al., 2007).

Considering the widely acknowledged hypotheses of function segregation and a growing number of studies focused on relationships between cognition and subnetworks rather than the whole brain (Sheffield et al., 2017; Fransson et al., 2018), we, therefore, further parcellated the whole brain into subnetworks based on the Power atlas to explore the association of WM deficits with subnetworks in schizophrenia with different attention deficits severity. Nodes of each subnetwork were isolated, and topological characteristics of subnetworks were analyzed individually (details of subnetworks are shown in **Supplementary material 2**).

## Statistical analysis

Group-related differences among demographic, clinical characteristics, and WM task performances were analyzed using a one-way analysis of variance (one-way ANOVA) and chi-square ($\chi^2$) analysis. *Post hoc* analyses were applied to compare

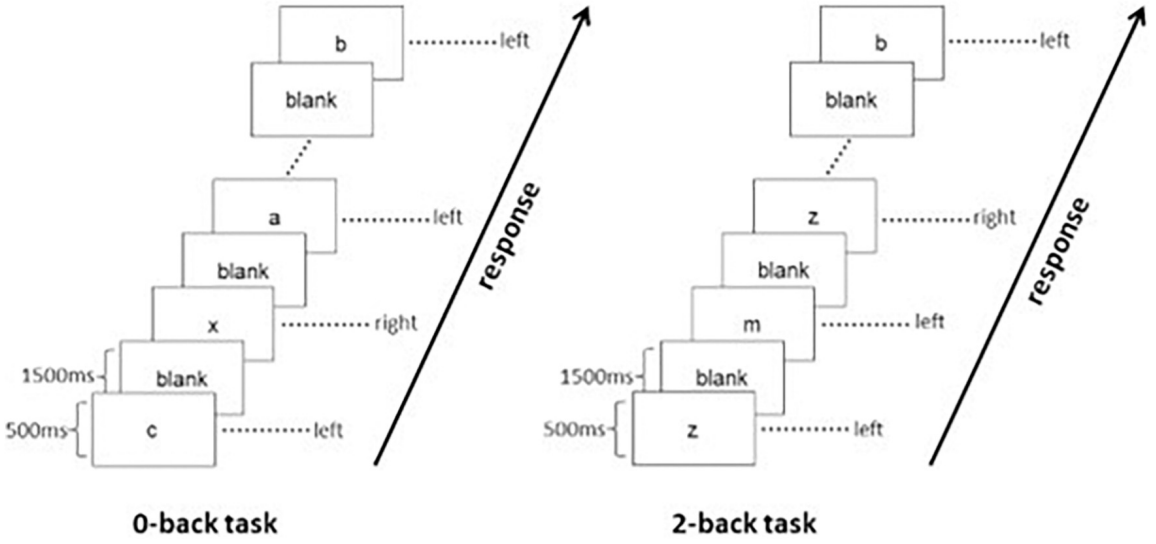


FIGURE 1
Paradigm of working memory tasks.

subgroups (patient and HCs groups) alternatively to figure out where difference specifically existed based on the results of the ANOVA test. As network properties were calculated across densities, we first used functional data analysis (FDA) (Bassett et al., 2012) to synthesize values across densities. In the FDA, each network metric curve is treated as a function [$y = f(x)$], and the sum of differences in y-values is calculated across densities. It is necessary to mention that network metrics calculated on all large-scale networks in our study were generated after the correction of multiple-comparison analysis [false discovery rate (FDR) corrected using the Benjamin–Hochberg method with $p < 0.05$]. Correlation analyses were conducted to further investigate the relationships between the WM task performance, the clinical symptoms severity, and topology properties.

# Results

## Participant characteristics and working memory performance

Demographic, clinical, and WM performance data of all groups are shown in Table 1. Except the education received years ($F = 11.938$, $p < 0.001$), other demographic variables did not differ significantly among all groups. As for the WM task performance, the "2-back" accuracy of the HCs group ($84.37 \pm 12.63\%$) was better than all patient groups ($F = 12.177$, $p < 0.001$), and the "2-back" accuracy of schizophrenia patients with mild attention deficits was higher than that of schizophrenia patients with severe attention deficits ($p = 0.027$).

There are omnibus differences in clinical symptoms among all patient groups [SAPS: $F = 4.755$, $p = 0.011$; SANS-adapted (SANS scale without attention items): $F = 89.268$, $p < 0.001$]. Patients with mild attention deficit have lower SAPS scores than patients with moderate ($p < 0.001$) or severe ($p = 0.024$) attention deficit. As for the negative symptoms except attention deficits, there was a "ladder" pattern of the SANS-adapted among all patient groups (severe > moderate, $p < 0.001$; moderate > mild, $p < 0.001$). Detailed information is presented in Table 1.

## Network properties

At the whole-brain level, one-way ANOVA detected omnibus differences in small-worldness [patients: mild = 1.414 (0.167), moderate = 1.407 (0.210), severe = 1.455 (0.138); HCs = 1.306 (0.148); *p-corrected* = 0.018] and in normalized clustering coefficient [patients: mild = 1.539 (0.173), moderate = 1.541 (0.219), severe = 1.596 (0.132); HCs = 1.426 (0.146); *p-corrected* = 0.014]. The *post hoc* analysis indicated that compared with HCs, patients with mild (small-worldness, $p = 0.0023$; normalized clustering coefficient, $p = 0.0017$), moderate (small-worldness, $p = 0.0005$; normalized clustering coefficient, $p = 0.0002$), and severe (small-worldness, $p = 0.0154$; normalized clustering coefficient, $p = 0.0061$) attention deficit showed aberrantly increased small-worldness and normalized clustering coefficient. Details are presented in Table 2 and Figure 2.

At the subnetwork level, one-way ANOVA detected omnibus differences in normalized characterized path length of the DMN [patients, mild = 1.108 (0.029), moderate = 1.114

TABLE 1 Demographic, clinical, and neurocognitive information.

| Variables | Schizophrenia patients ($N$ = 92) | | | HCs ($N$ = 51) | $F/\chi^2$ | $P$ | *Post hoc* Tukey significance |
|---|---|---|---|---|---|---|---|
| | Mild ($n$ = 49) | Moderate ($n$ = 29) | Severe ($n$ = 14) | | | | |
| Age | 23.96 ± 5.37 | 24.14 ± 7.11 | 23.07 ± 5.23 | 23.08 ± 4.65 | 0.356 | 0.785 | N/A |
| Gender (M/F) | 29/20 | 15/14 | 11/3 | 28/23 | 3.131 | 0.372 | N/A |
| Education (years) | 11.76 ± 2.75 | 11.40 ± 2.19 | 12.61 ± 2.69 | 14.14 ± 1.87 | 11.938 | **<0.001*** | HCs > mild: $p < 0.001$; HCs > moderate: $p < 0.001$ |
| SAPS total score | 18.67 ± 12.81 | 26.62 ± 18.78 | 30.86 ± 13.82 | N/A | 4.755 | **0.011*** | Severe > mild: $P = 0.024$ |
| SANS total score | 22.06 ± 13.04 | 58.31 ± 17.09 | 81.50 ± 12.09 | N/A | 89.283 | **<0.001*** | Moderate > mild: $p < 0.001$; severe > mild: $p < 0.001$; severe > moderate: $p < 0.001$ |
| SANS-adapted | 20.16 ± 12.53 | 50.41 ± 16.56 | 69.50 ± 11.67 | N/A | 88.825 | **<0.001*** | Moderate > mild: $p < 0.001$; severe > mild: $p < 0.001$; severe > moderate: $p < 0.001$ |
| Attention deficit score | 0.41 ± 0.50 | 2.76 ± 0.44 | 4.21 ± 0.43 | N/A | 462.477 | **<0.001*** | Moderate > mild: $p < 0.001$; severe > mild: $p < 0.001$; severe > moderate: $p < 0.001$ |
| Total dosage (mg/d) | 153.85 ± 512.692 | 96.56 ± 313.04 | 1526.73 ± 4275.33 | N/A | 3.686 | **0.03*** | Severe > mild: $p < 0.001$; severe > moderate: $p < 0.001$ |
| Illness duration (M) | 23.59 ± 29.32 | 23.44 ± 30.08 | 41.71 ± 40.12 | N/A | 1.994 | 0.142 | N/A |
| WAIS-information | 17.26 ± 4.81 | 14.80 ± 4.14 | 14.25 ± 4.57 | N/A | 1.513 | 0.233 | N/A |
| WAIS-Digit symbol | 63.24 ± 14.01 | 61.10 ± 11.93 | 53.00 ± 9.93 | N/A | 1.06 | 0.356 | N/A |
| ACC of 2-back (%) | 72.44 ± 14.90 | 64.69 ± 18.27 | 61.16 ± 22.41 | 84.37 ± 12.63 | 12.177 | **<0.001*** | HCs > mild: $p = 0.002$; HCs > moderate: $p < 0.001$; HCs > severe: $p < 0.001$; mild > severe: $p = 0.027$ |
| RTC of 2-back (ms) | 679.42 ± 127.97 | 660.21 ± 165.49 | 592.74 ± 202.87 | 659.83 ± 134.51 | 1.148 | 0.333 | N/A |

*$p < 0.05$; n, number; HCs, healthy controls; SAPS, Scale for Assessment of Positive Symptoms; SANS, Scale for Assessment of Negative Symptoms; SANS-adapted, SANS total score without attention items; WAIS_information, information subscale of Wechsler Adult Intelligence Scale-Chinese Revised; WAIS_Digit_Symbol, digit symbol subscale of Wechsler Adult Intelligence Scale-Chinese Revised; N/A, not available; antipsychotic dosage refers to the dose equivalents for chlorpromazine. Bold values indicate statistically significant values.

(0.035), severe = 1.143 (0.049); HCs = 1.104 (0.026); *p-corrected* = 0.014]. The *post hoc* analysis indicated that patients with severe attention deficits showed increased normalized characterized path length of the DMN compared with HCs ($p < 0.001$), patients with mild attention deficits ($p = 0.0021$), and patients with moderate attention deficits ($p = 0.029$). Details are presented in Table 2 and Figure 3.

We further explored whether the detected network properties of the whole-brain functional connectome and DMN subnetwork showed omnibus across all groups during the resting state. Detailed scanning parameters, data preprocessing, and network construction information of resting fMRI are shown in Supplementary material 3. However, we did not observe any omnibus differences in the network properties of the whole-brain functional connectome and DMN subnetwork under the resting state (see Table 3).

## Correlation analyses

We observed the decreased accuracy of the WM task was correlated with increased clinical symptoms (SANS-adapted, $r = -0.230$, $p = 0.041$; SAPS, $r = -0.246$, $p = 0.029$; attention deficit level, $r = -0.472$, $p < 0.001$), increased topology properties (small-worldness, $r = -0.195$, $p = 0.03$; normalized clustering coefficient, $r = -0.237$, $p = 0.008$) of the whole brain, and increased normalized characterized path length of the DMN network ($r = -0.237$, $p = 0.008$). The topology properties significantly related to the attention deficit level were whole-brain small-worldness ($r = 0.275$, $p = 0.001$), whole-brain normalized clustering coefficient ($r = 0.305$, $p < 0.001$), and DMN normalized characterized path length ($r = 0.292$, $p < 0.001$). Details are presented in Figure 4 and Supplementary material 4.

# Discussion

To our best knowledge, this is the first study to investigate the topology of the functional connectome during the WM task in schizophrenia with different attention deficit severity. We reported three key findings. First, all patient groups showed increased small-worldness and local clustering of the whole-brain functional connectome compared with HCs, despite their

TABLE 2 Network properties of functional connectome during WM task.

| Measures | Schizophrenia patients | | | HCs | *F* | *p* | *p*-corrected | *Post hoc* Tukey significance |
|---|---|---|---|---|---|---|---|---|
| | Mild | Moderate | Severe | | | | | |
| **Whole-brain** | | | | | | | | |
| Sigma | 1.417 (0.167) | 1.407 (0.210) | 1.455 (0.138) | 1.306 (0.148) | 5.329 | **0.002*** | **0.018*** | HCs < mild: $p = 0.002$<br>HCs < moderate: $p < 0.001$<br>HCs < severe: $p = 0.015$ |
| Gamma | 1.539 (0.173) | 1.541 (0.219) | 1.596 (0.132) | 1.426 (0.146) | 6.022 | **0.001*** | **0.011*** | HCs < mild: $p = 0.002$<br>HCs < moderate: $p < 0.001$<br>HCs < severe: $p = 0.006$ |
| Lambda | 1.077 (0.030) | 1.086 (0.025) | 1.088 (0.036) | 1.086 (0.026) | 1.125 | 0.341 | 0.614 | N/A |
| **VAN** | | | | | | | | |
| Sigma | 1.494 (1.301) | 1.455 (0.788) | 1.788 (1.329) | 1.389 (0.638) | 0.580 | 0.629 | 0.830 | N/A |
| Gamma | 1.304 (0.599) | 1.325 (0.482) | 1.408 (0.600) | 1.264 (0.389) | 0.316 | 0.814 | 0.907 | N/A |
| Lambda | 0.985 (0.067) | 0.967 (0.073) | 0.933 (0.130) | 0.972 (0.074) | 1.661 | 0.178 | 0.486 | N/A |
| **SBN** | | | | | | | | |
| Sigma | 1.815 (0.976) | 1.858 (0.785) | 1.884 (0.761) | Null | 0.044 | 0.957 | 0.957 | N/A |
| Gamma | 1.631 (0.482) | 1.666 (0.482) | 1.750 (0.469) | Null | 0.339 | 0.714 | 0.838 | N/A |
| Lambda | 0.948 (0.073) | 0.949 (0.086) | 0.977 (0.054) | 0.978 (0.062) | 2.064 | 0.108 | 0.486 | N/A |
| **SSHN** | | | | | | | | |
| Sigma | 1.489 (0.232) | 1.515 (0.295) | 1.579 (0.198) | 1.468 (0.257) | 0.774 | 0.511 | 0.812 | N/A |
| Gamma | 1.642 (0.288) | 1.659 (0.290) | 1.793 (0.276) | 1.616 (0.324) | 1.284 | 0.282 | 0.614 | N/A |
| Lambda | 1.103 (0.047) | 1.121 (0.051) | 1.127 (0.036) | 1.109 (0.051) | 1.455 | 0.230 | 0.565 | N/A |
| **SN** | | | | | | | | |
| Sigma | 1.612 (0.739) | 1.437 (0.428) | 1.638 (0.511) | 1.447 (0.377) | 1.190 | 0.316 | 0.614 | N/A |
| Gamma | 1.523 (0.389) | 1.426 (0.360) | 1.626 (0.359) | 1.423 (0.309) | 1.701 | 0.170 | 0.486 | N/A |
| Lambda | 1.029 (0.076) | 1.031 (0.060) | 1.052 (0.031) | 1.025 (0.057) | 0.656 | 0.581 | 0.830 | N/A |
| **FPN** | | | | | | | | |
| Sigma | 1.314 (0.282) | 1.356 (0.301) | 1.392 (0.269) | 1.408 (0.216) | 1.141 | 0.335 | 0.614 | N/A |
| Gamma | 1.378 (0.294) | 1.444 (0.318) | 1.530 (0.354) | 1.501 (0.242) | 1.914 | 0.130 | 0.486 | N/A |
| Lambda | 1.066 (0.054) | 1.078 (0.052) | 1.100 (0.062) | 1.077 (0.045) | 1.653 | 0.180 | 0.486 | N/A |
| **DAN** | | | | | | | | |
| Sigma | 1.439 (0.541) | 1.322 (0.366) | 1.374 (0.457) | 1.341 (0.367) | 0.579 | 0.630 | 0.830 | N/A |
| Gamma | 1.344 (0.361) | 1.274 (0.270) | 1.290 (0.319) | 1.268 (0.294) | 0.552 | 0.647 | 0.830 | N/A |
| Lambda | 0.964 (0.082) | 0.967 (0.061) | 0.969 (0.062) | 0.974 (0.075) | 0.149 | 0.930 | 0.957 | N/A |
| **DMN** | | | | | | | | |
| Sigma | 1.266 (0.172) | 1.321 (0.186) | 1.392 (0.152) | 1.321 (0.193) | 2.026 | 0.113 | 0.486 | N/A |
| Gamma | 1.411 (0.196) | 1.481 (0.213) | 1.607 (0.186) | 1.470 (0.221) | 3.371 | **0.020*** | 0.135 | N/A |
| Lambda | 1.108 (0.029) | 1.114 (0.035) | 1.143 (0.049) | 1.104 (0.026) | 5.863 | **0.001*** | **0.011*** | HCs < severe: $p < 0.001$<br>Mild < severe: $p = 0.002$<br>Moderate < severe: $p = 0.029$ |
| **CON** | | | | | | | | |
| Sigma | 1.558 (0.488) | 1.621 (0.481) | 1.473 (0.343) | 1.719 (0.855) | 0.815 | 0.488 | 0.812 | N/A |
| Gamma | 1.480 (0.323) | 1.523 (0.372) | 1.441 (0.310) | 1.577 (0.631) | 0.510 | 0.676 | 0.830 | N/A |
| Lambda | 0.988 (0.077) | 0.985 (0.065) | 0.993 (0.057) | 0.978 (0.055) | 0.279 | 0.840 | 0.907 | N/A |

*$p < 0.05$. VAN, ventral attention network; SBN, subcortical network; SSHN, sensory somatomotor hand network; SN, salience network; FPN, frontoparietal network; DAN, dorsal attention network; DMN, default-mode network; CON, cingulo-opercular network; sigma, small-worldness; gamma, clustering coefficient; lambda, characterized path length. Bold values indicate statistically significant values.

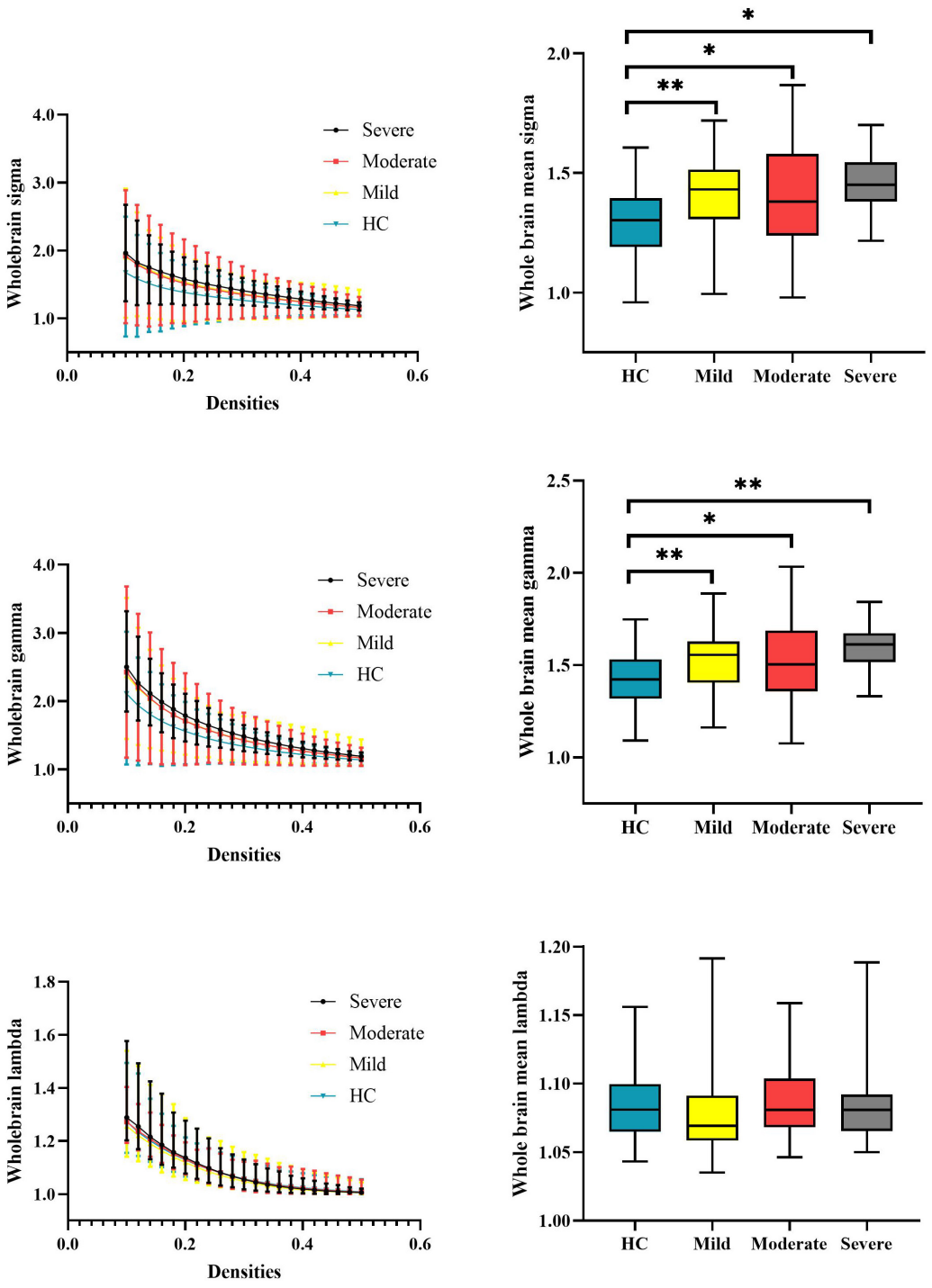


FIGURE 2
Global properties of the whole-brain functional connectome calculated on the Power atlas of schizophrenia patients with different severities of attention deficits and HCs and comparisons of mean topology properties (sigma, gamma, and lambda) across densities between patients with different severities of attention deficits and HCs. The range of densities is 0.1: 0.02: 0.5, symbol "*" represents $p < 0.05$, and symbol "**" represents $p < 0.01$. HCs, healthy controls; sigma, small-worldness; gamma, clustering coefficient; lambda, characterized path length.

varied attention deficit severity. Second, patients with severe attention deficits showed decreased global integration of the DMN network compared with HCs and patients with less severe attention deficits. Third, the abovementioned findings in patients with schizophrenia under the WM task were not manifested under the resting state.

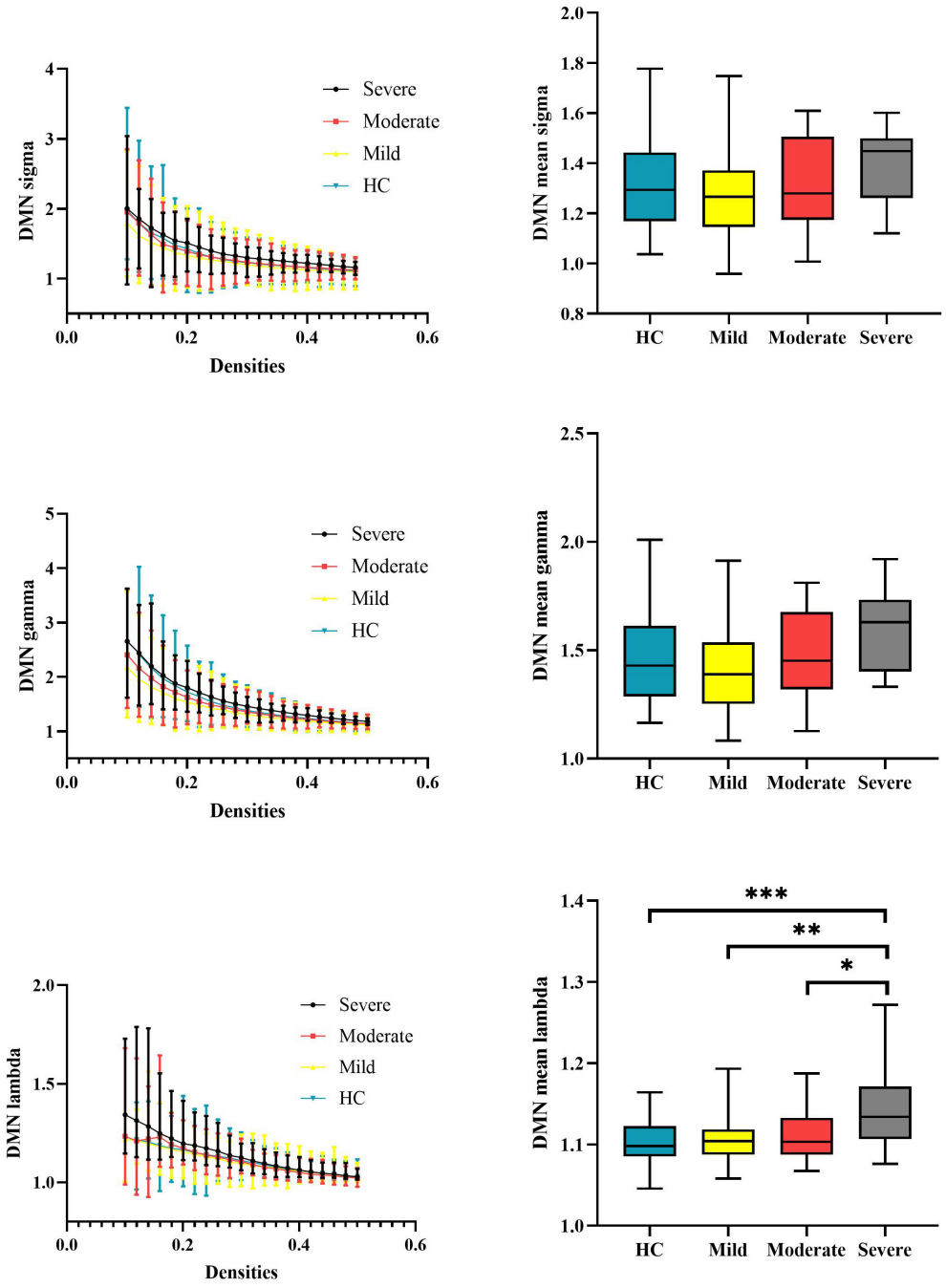


FIGURE 3
Global properties of the DMN functional connectome calculated on Power atlas of schizophrenia patients and HCs and comparisons of mean topology properties (sigma, gamma, and lambda) across densities between schizophrenia patients with different severities of attention deficits and HCs. The range of densities is 0.1: 0.02: 0.5, symbol "*" represents $p < 0.05$, and symbol "**" represents $p < 0.01$. DMN, default-mode network; HCs, healthy controls; sigma, small-worldness; gamma, clustering coefficient; lambda, characterized path length. ***$P < 0.001$.

In line with our prior work (Yang et al., 2020), this study reported that all patients with different attention deficit severity showed increased small-worldness and normalized clustering coefficient of their whole-brain functional connectome during the WM task. In patient groups, the increased small-worldness is driven by higher local clustering but not the global integration. This topology alteration was similar to the ketamine-induced alteration of the functional connectome (Dawson et al., 2014), which was commonly seen among the pharmacological models of the behavioral deficits similar to schizophrenia in both

TABLE 3 Network properties of functional connectome during resting state.

| Measures | Schizophrenia patients | | | HCs | *F* | *p* |
|---|---|---|---|---|---|---|
| | Mild | Moderate | Severe | | | |
| **Whole-brain** | | | | | | |
| Sigma | 1.468 (0.206) | 1.460 (0.182) | 1.420 (0.129) | 1.415 (0.242) | 0.529 | 0.663 |
| Gamma | 1.584 (0.213) | 1.585 (0.184) | 1.550 (0.118) | 1.540 (0.242) | 0.397 | 0.756 |
| Lambda | 1.072 (0.035) | 1.076 (0.027) | 1.083 (0.048) | 1.083 (0.045) | 0.728 | 0.538 |
| **DMN** | | | | | | |
| Sigma | 1.265 (0.162) | 1.312 (0.171) | 1.371 (0.136) | 1.305 (0.173) | 1.157 | 0.329 |
| Gamma | 1.408 (0.193) | 1.477 (0.224) | 1.528 (0.127) | 1.455 (0.203) | 1.151 | 0.331 |
| Lambda | 1.106 (0.028) | 1.117 (0.029) | 1.115 (0.064) | 1.098 (0.024) | 2.157 | 0.097 |

DMN, default-mode network; sigma, small-worldness; gamma, clustering coefficient; lambda, characterized path length.

humans (Morgan et al., 2004; D'Souza et al., 2012) and animals (Roberts et al., 2010; Skoblenick and Everling, 2012). The local clustering is essential for motor execution, whereas the global integration is vitally important for WM (Sakreida et al., 2018; Bhattacharjee and Schwarz, 2022). It is an inefficient way for patients with schizophrenia to promote their WM performance by improving their local clustering (Yang et al., 2020). Furthermore, we did not observe any differences in the topology properties of the whole-brain functional connectome among all patient groups. This finding may collaborate with our prior study and demonstrate that the increased local clustering under the WM task is more likely a "trait" marker of patients with schizophrenia, but irrelevant to their clinical symptoms.

Patients with severe attention deficits showed an increased normalized characterized path length of the DMN network compared with HCs and patients with mild attention deficits. Our results suggested that the efficiency of DMN might be positively meaningful when the demands on WM capacity increased (Spreng, 2012; Sormaz et al., 2018; Buckner and DiNicola, 2019). From the perspective of topology structure, the increase in normalized characterized path length indicated the worse global efficiency of DMN. Patients with severe attention deficits need to devote more neural resources to achieve the global transition of information in DMN. The increase in normalized characterized path length in DMN was correlated with the increase in the attention deficit degree among patients. This result could be attributed to the patients with severe attention deficits cannot timely respond to support the flexible topology reconfiguration when facing the demand of WM task (Moraschi et al., 2020). Thus, we speculated that the inefficiency of DMN among patients with severe attention deficits affects the processing of WM in these certain phases and then causes worse WM task performance than that of HCs.

The decreased integration of the DMN was only observed in schizophrenia with severe attention deficits, which may demonstrate that the DMN can be a potential target for clinical intervention. This speculation was also supported by previous research on attention-deficit/hyperactivity disorder (ADHD), a mental disorder that mainly includes attention deficits and an overload of cognitive process (Klingberg, 2009). Bachmann et al. (2018) have demonstrated that short-term mindfulness could significantly improve WM task performance in ADHD patients. Mindfulness is a widely approved psychological intervention for ADHD. It has been considered closely associated with DMN, and DMN has been recognized as a potential biomarker for monitoring the treatment effects of mindfulness (Simon and Engström, 2015).

It should be noted that there were no omnibus significant brain connectome topology alterations among all groups under resting state. Indeed, previous studies have reported significant differences of brain network topology between patients with schizophrenia and HCs. For example, Yu et al. (2017) and Jiang et al. (2022) have reported a lower clustering coefficient and small-worldness in schizophrenia compared with HCs. However, some studies reported inconsistent findings. For instance, Hadley et al. (2016) have reported the increased clustering coefficient but deceased global efficiency in the unmediated schizophrenias during resting state compared with HCs, and this pattern of aberrant functional network integration and segregation in responders can be modulated with 6-week risperidone treatment. We speculated this inconsistency may be due to the heterogeneity of the enrolled participants. However, it should be noted that the omnibus differences in network properties across all groups were detected during the WM task. It may suggest that the alteration of network properties was context-dependent. During the resting state, participants were only asked to keep their eyes open and not fall asleep. In contrast, during the WM task, attention resources need to be sufficiently devoted to accomplishing this task. Concerned about the dynamic switch of topological configurations of the DMN observed during the WM task (Duan et al., 2019; Moraschi et al., 2020), we speculated that the process of attention mobilization acted as an external inducement for the functional connectome topology alteration. This finding may be consistent with previous studies conducted in HCs, which indicated that the dynamic topology reorganization of DMN is associated with the WM task (Tommasin et al., 2018; Moraschi et al., 2020).

10.3389/fncel.2022.1006797

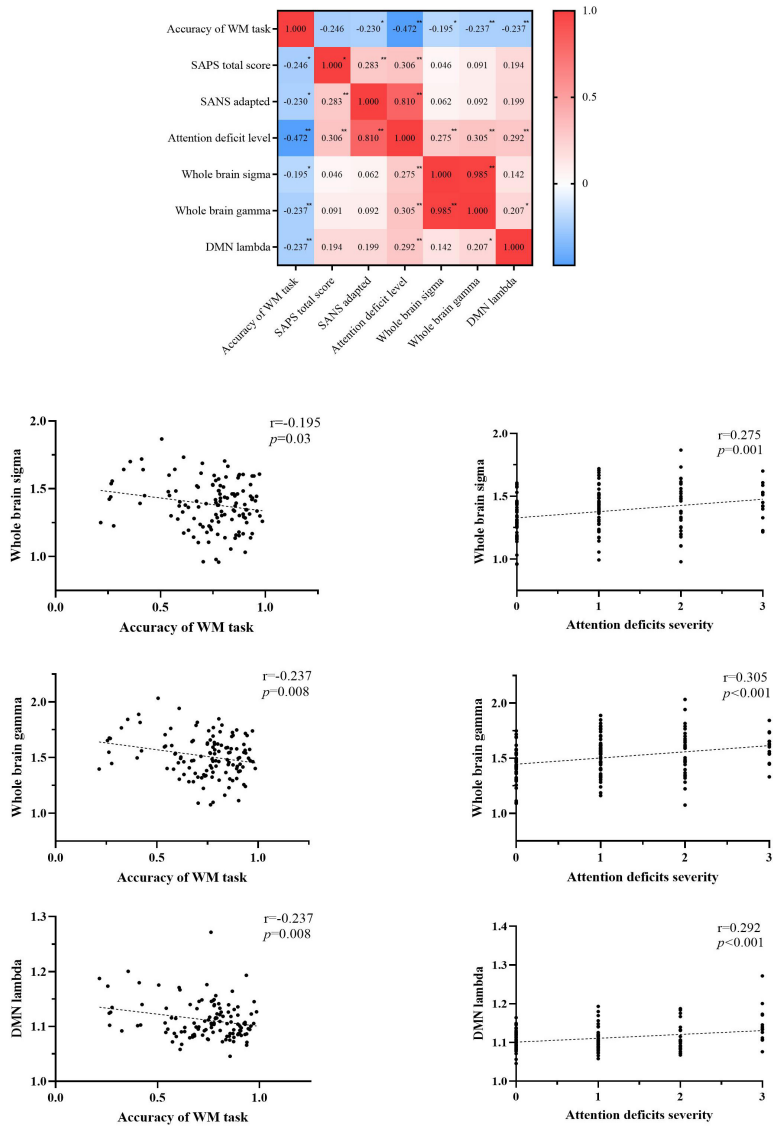


FIGURE 4
Correlations among the accuracy of the WM task, clinical symptoms, and topology properties. WM, working memory; SAPS, scale for assessing positive symptoms; SANS, scale for assessment of negative symptoms; SANS-adapted, SANS total score without attention items; DMN, default-mode network; sigma, small-worldness; gamma, clustering coefficient; lambda, characterized path length. *$P < 0.05$, **$P < 0.01$, ***$P < 0.001$.

## Limitation

There are some limitations in the current study. First, the proportion of schizophrenia patients with different severity of attention deficits is varied, especially the limited sample size of schizophrenia patients with severe attention deficits. We, therefore, suggest that these preliminary results of the current study need to be validated in a future big dataset. Second, the discrepancy in SANS total score among the schizophrenia patients with severe attention deficits and the other two patient groups was apparent. Concerned that the criterion of attention deficits applied in our research was a part of the SANS scale, which was associated with other negative symptoms like avolition or blunted effect, we considered that it was reasonable that other negative symptoms decrease the efficiency of attention allocation. So, it is hard to exclude the effect of the negative symptoms on the normalized characterized path length of DMN. Thus, we conducted the correlation analyses among SANS-adapted (SANS total score without attention items) and topology properties, which were related to the attention deficits. However, there were no significant relationships among these variables. Third, the adopted N-back paradigm lacked various WM loads, and we were not able

to further explore the differences in functional connectome topology of schizophrenia patients with diverse attention deficits and HCs under varied WM loads.

## Conclusion

This is the first study to investigate the topology of the functional connectome during a WM task in schizophrenia with different attention deficit severity. All patients with schizophrenia showed higher small-worldness that was induced by increased clustering compared with HCs. The decreased integration of DMN is associated with severe attention deficits in patients with schizophrenia, while these topology alterations were absent in schizophrenia patients with severe attention deficits during resting state. The current study suggested that the mobilization of attention resources might be an external inducement of the topology reorganization of the DMN during the N-back WM task among schizophrenia patients with severe attention deficits.

## Data availability statement

The raw data supporting the conclusions of this article will be made available by the authors, without undue reservation.

## Ethics statement

The studies involving human participants were reviewed and approved by the Medical Ethics Committee of the Second Xiangya Hospital, Central South University. Written informed consent to participate in this study was provided by the participants' legal guardian/next of kin.

## Author contributions

ZL and JiY designed the study. JuY, FS, ZF, and PC acquired the data. PC, JiY, and ZF analyzed the data. PC and JiY wrote the manuscript. All authors contributed to the article and approved the submitted version.

## Funding

This work was supported by grants from the National Natural Science Foundation of China (Grant Nos. 82071506 to ZL and 82201663 to JiY) and the Natural Science Foundation of Hunan Province, China (Grant No. 2021JJ40884 to JiY).

## Acknowledgments

We thank all participants for their time and patience in this study and thank everyone of the study team for their dedicated effort in collecting the data.

## Conflict of interest

The authors declare that the research was conducted in the absence of any commercial or financial relationships that could be construed as a potential conflict of interest.

The reviewer TM declared a past co-authorship with the author ZL to the handling editor.

## Publisher's note

All claims expressed in this article are solely those of the authors and do not necessarily represent those of their affiliated organizations, or those of the publisher, the editors and the reviewers. Any product that may be evaluated in this article, or claim that may be made by its manufacturer, is not guaranteed or endorsed by the publisher.

## Supplementary material

The Supplementary Material for this article can be found online at: https://www.frontiersin.org/articles/10.3389/fncel.2022.1006797/full#supplementary-material

## References

Abdolalizadeh, A., Ostadrahimi, H., Mohajer, B., Darvishi, A., Sattarian, M., Bayani Ershadi, A. S., et al. (2020). White matter microstructural properties associated with impaired attention in chronic schizophrenia: A multi-center study. *Psychiatry Res. Neuroimaging* 302:111105. doi: 10.1016/j.pscychresns.2020.111105

Achard, S., and Bullmore, E. (2007). Efficiency and cost of economical brain functional networks. *PLoS Comput. Biol.* 3:e17. doi: 10.1371/journal.pcbi.0030017

Andreasen, N. C. (1989). The Scale for the Assessment of Negative Symptoms (SANS): Conceptual and theoretical foundations. *Br. J. Psychiatry* 155, 49–52.

Bachmann, K., Lam, A. P., Sörös, P., Kanat, M., Hoxhaj, E., Matthies, S., et al. (2018). Effects of mindfulness and psychoeducation on working memory in adult ADHD: A randomised, controlled fMRI study. *Behav. Res. Ther.* 106, 47–56. doi: 10.1016/j.brat.2018.05.002

Baddeley, A. (1986). *Working memory*. Oxford: Clarendon Press.

Baddeley, A. (1996). The fractionation of working memory. *Proc. Natl. Acad. Sci. U.S.A.* 93, 13468–13472. doi: 10.1073/pnas.93.24.13468

Bassett, D. S., Nelson, B. G., Mueller, B. A., Camchong, J., and Lim, K. O. (2012). Altered resting state complexity in schizophrenia. *Neuroimage* 59, 2196–2207. doi: 10.1016/j.neuroimage.2011.10.002

Berti, S., and Schröger, E. (2003). Working memory controls involuntary attention switching: Evidence from an auditory distraction paradigm. *Eur. J. Neurosci.* 17, 1119–1122. doi: 10.1046/j.1460-9568.2003.02527.x

Bhattacharjee, A., and Schwarz, C. (2022). Temporally local tactile codes can be stored in working memory. *Front. Hum. Neurosci.* 16:840108. doi: 10.3389/fnhum.2022.840108

Buckner, R. L., and DiNicola, L. M. (2019). The brain's default network: Updated anatomy, physiology and evolving insights. *Nat. Rev. Neurosci.* 20, 593–608. doi: 10.1038/s41583-019-0212-7

Bullmore, E., and Sporns, O. (2009). Complex brain networks: Graph theoretical analysis of structural and functional systems. *Nat. Rev. Neurosci.* 10, 186–198. doi: 10.1038/nrn2575

Das, T., Borgwardt, S., Hauke, D. J., Harrisberger, F., Lang, U. E., Riecher-Rössler, A., et al. (2018). Disorganized gyrification network properties during the transition to psychosis. *JAMA Psychiatry* 75, 613–622. doi: 10.1001/jamapsychiatry.2018.0391

Dawson, N., McDonald, M., Higham, D. J., Morris, B. J., and Pratt, J. A. (2014). Subanesthetic ketamine treatment promotes abnormal interactions between neural subsystems and alters the properties of functional brain networks. *Neuropsychopharmacology* 39, 1786–1798. doi: 10.1038/npp.2014.26

Deng, M., Liu, Z., Zhang, W., Wu, Z., Cao, H., Yang, J., et al. (2022). Associations between polygenic risk, negative symptoms, and functional connectome topology during a working memory task in early-onset schizophrenia. *Schizophrenia* 8:54. doi: 10.1038/s41537-022-00260-w

Dickinson, D., Ramsey, M. E., and Gold, J. M. (2007). Overlooking the obvious: A meta-analytic comparison of digit symbol coding tasks and other cognitive measures in schizophrenia. *Arch. Gen. Psychiatry* 64, 532–542. doi: 10.1001/archpsyc.64.5.532

D'Souza, D. C., Ahn, K., Bhakta, S., Elander, J., Singh, N., Nadim, H., et al. (2012). Nicotine fails to attenuate ketamine-induced cognitive deficits and negative and positive symptoms in humans: Implications for schizophrenia. *Biol. Psychiatry* 72, 785–794. doi: 10.1016/j.biopsych.2012.05.009

Duan, J., Xia, M., Womer, F. Y., Chang, M., Yin, Z., Zhou, Q., et al. (2019). Dynamic changes of functional segregation and integration in vulnerability and resilience to schizophrenia. *Hum. Brain Mapp.* 40, 2200–2211. doi: 10.1002/hbm.24518

Fan, J., Fossella, J., Sommer, T., Wu, Y., and Posner, M. I. (2003). Mapping the genetic variation of executive attention onto brain activity. *Proc. Natl. Acad. Sci. U.S.A.* 100, 7406–7411. doi: 10.1073/pnas.0732088100

First, M. B., and Gibbon, M. (2004). "The structured clinical interview for DSM-IV axis I disorders (SCID-I) and the structured clinical interview for DSM-IV axis II disorders (SCID-II)," in *Comprehensive handbook of psychological assessment: Vol. 2. Personality assessment*, eds M. Hilsenroth and D. L. Segalaniel (Hoboken, NJ: Wiley), 134–143.

Fornito, A., Yoon, J., Zalesky, A., Bullmore, E. T., and Carter, C. S. (2011). General and specific functional connectivity disturbances in first-episode schizophrenia during cognitive control performance. *Biol. Psychiatry* 70, 64–72. doi: 10.1016/j.biopsych.2011.02.019

Fornito, A., Zalesky, A., Pantelis, C., and Bullmore, E. T. (2012). Schizophrenia, neuroimaging and connectomics. *Neuroimage* 62, 2296–2314. doi: 10.1016/j.neuroimage.2011.12.090

Fransson, P., Schiffler, B. C., and Thompson, W. H. (2018). Brain network segregation and integration during an epoch-related working memory fMRI experiment. *Neuroimage* 178, 147–161. doi: 10.1016/j.neuroimage.2018.05.040

Gong, Y. X. (1983). Revision of wechsler's adult intelligence scale in China. *Acta Psychol. Sin.* 15, 362–370.

Hadley, J. A., Kraguljac, N. V., White, D. M., Ver Hoef, L., Tabora, J., and Lahti, A. C. (2016). Change in brain network topology as a function of treatment response in schizophrenia: A longitudinal resting-state fMRI study using graph theory. *NPJ Schizophr.* 2:16014. doi: 10.1038/npjschz.2016.14

Hampson, M., Driesen, N., Roth, J. K., Gore, J. C., and Constable, R. T. (2010). Functional connectivity between task-positive and task-negative brain areas and its relation to working memory performance. *Magn. Reson. Imaging* 28, 1051–1057. doi: 10.1016/j.mri.2010.03.021

He, Y., Chen, Z. J., and Evans, A. C. (2007). Small-world anatomical networks in the human brain revealed by cortical thickness from MRI. *Cereb. Cortex* 17, 2407–2419. doi: 10.1093/cercor/bhl149

Hong, W., Zhao, Z., Shen, Z., Sun, B., Li, S., Mekbib, D. B., et al. (2019). Uncoupled relationship in the brain between regional homogeneity and attention function in first-episode, drug-naïve schizophrenia. *Psychiatry Res. Neuroimaging* 294:110990. doi: 10.1016/j.pscychresns.2019.110990

Hosseini, S. H., Hoeft, F., and Kesler, S. R. (2012). GAT: A graph-theoretical analysis toolbox for analyzing between-group differences in large-scale structural and functional brain networks. *PLoS One* 7:e40709. doi: 10.1371/journal.pone.0040709

Hui, C. L., Li, Y. K., Li, A. W., Lee, E. H., Chang, W. C., Chan, S. K., et al. (2016). Visual working memory deterioration preceding relapse in psychosis. *Psychol. Med.* 46, 2435–2444. doi: 10.1017/s0033291716000751

Jiang, Y., Yao, D., Zhou, J., Tan, Y., Huang, H., Wang, M., et al. (2022). Characteristics of disrupted topological organization in white matter functional connectome in schizophrenia. *Psychol. Med.* 52, 1333–1343. doi: 10.1017/s0033291720003141

Kaiser, M., and Hilgetag, C. C. (2006). Nonoptimal component placement, but short processing paths, due to long-distance projections in neural systems. *PLoS Comput. Biol.* 2:e95. doi: 10.1371/journal.pcbi.0020095

Kelly, A. M., Uddin, L. Q., Biswal, B. B., Castellanos, F. X., and Milham, M. P. (2008). Competition between functional brain networks mediates behavioral variability. *Neuroimage* 39, 527–537. doi: 10.1016/j.neuroimage.2007.08.008

Klingberg, T. (2009). *The overflowing brain: Information overload and the limits of working memory*. New York, NY: Oxford University Press.

Liu, H., Kaneko, Y., Ouyang, X., Li, L., Hao, Y., Chen, E. Y., et al. (2012). Schizophrenic patients and their unaffected siblings share increased resting-state connectivity in the task-negative network but not its anticorrelated task-positive network. *Schizophr. Bull.* 38, 285–294. doi: 10.1093/schbul/sbq074

Lorenc, E. S., Mallett, R., and Lewis-Peacock, J. A. (2021). Distraction in visual working memory: Resistance is not futile. *Trends Cogn. Sci.* 25, 228–239. doi: 10.1016/j.tics.2020.12.004

Luck, S. J., and Gold, J. M. (2008). The construct of attention in schizophrenia. *Biol. Psychiatry* 64, 34–39. doi: 10.1016/j.biopsych.2008.02.014

Meyer-Lindenberg, A., Poline, J. B., Kohn, P. D., Holt, J. L., Egan, M. F., Weinberger, D. R., et al. (2001). Evidence for abnormal cortical functional connectivity during working memory in schizophrenia. *Am. J. Psychiatry* 158, 1809–1817. doi: 10.1176/appi.ajp.158.11.1809

Moraschi, M., Mascali, D., Tommasin, S., Gili, T., Hassan, I. E., Fratini, M., et al. (2020). Brain network modularity during a sustained working-memory task. *Front. Physiol.* 11:422. doi: 10.3389/fphys.2020.00422

Morgan, C. J., Mofeez, A., Brandner, B., Bromley, L., and Curran, H. V. (2004). Acute effects of ketamine on memory systems and psychotic symptoms in healthy volunteers. *Neuropsychopharmacology* 29, 208–218. doi: 10.1038/sj.npp.1300342

Palaniyappan, L., Park, B., Balain, V., Dangi, R., and Liddle, P. (2015). Abnormalities in structural covariance of cortical gyrification in schizophrenia. *Brain Struct. Funct.* 220, 2059–2071. doi: 10.1007/s00429-014-0772-2

Park, S., Püschel, J., Sauter, B. H., Rentsch, M., and Hell, D. (1999). Spatial working memory deficits and clinical symptoms in schizophrenia: A 4-month follow-up study. *Biol. Psychiatry* 46, 392–400. doi: 10.1016/s0006-3223(98)00370-9

Pessoa, L., Kastner, S., and Ungerleider, L. G. (2003). Neuroimaging studies of attention: From modulation of sensory processing to top-down control. *J. Neurosci.* 23, 3990–3998. doi: 10.1523/jneurosci.23-10-03990.2003

Phillips, M. R., Xiong, W., Wang, R. W., Gao, Y. H., Wang, X. Q., and Zhang, N. P. (1991). Reliability and validity of the Chinese versions of the scales for assessment of positive and negative symptoms. *Acta Psychiatr. Scand.* 84, 364–370.

Poldrock, R. A., Mumford, J. A., and Nichols, T. E. (2011). *Handbook of functional MRI data analysis*. New York, NY: Cambridge University Press.

Pomarol-Clotet, E., Salvador, R., Sarró, S., Gomar, J., Vila, F., Martínez, A., et al. (2008). Failure to deactivate in the prefrontal cortex in schizophrenia: Dysfunction of the default mode network? *Psychol. Med.* 38, 1185–1193. doi: 10.1017/s0033291708003565

Power, J. D., Cohen, A. L., Nelson, S. M., Wig, G. S., Barnes, K. A., Church, J. A., et al. (2011). Functional network organization of the human brain. *Neuron* 72, 665–678. doi: 10.1016/j.neuron.2011.09.006

Roberts, B. M., Holden, D. E., Shaffer, C. L., Seymour, P. A., Menniti, F. S., Schmidt, C. J., et al. (2010). Prevention of ketamine-induced working

memory impairments by AMPA potentiators in a nonhuman primate model of cognitive dysfunction. *Behav. Brain Res.* 212, 41–48. doi: 10.1016/j.bbr.2010.03.039

Rubinov, M., and Sporns, O. (2010). Complex network measures of brain connectivity: Uses and interpretations. *Neuroimage* 52, 1059–1069.

Rubinov, M., and Sporns, O. (2011). Weight-conserving characterization of complex functional brain networks. *Neuroimage* 56, 2068–2079. doi: 10.1016/j.neuroimage.2011.03.069

Rubinov, M., Kötter, R., Hagmann, P., and Sporns, O. (2009). Brain connectivity toolbox: A collection of complex network measurements and brain connectivity datasets. *Neuroimage* 47:S169. doi: 10.1016/j.neuroimage.2009.10.003

Sakreida, K., Higuchi, S., Di Dio, C., Ziessler, M., Turgeon, M., Roberts, N., et al. (2018). Cognitive control structures in the imitation learning of spatial sequences and rhythms-an fMRI study. *Cereb. Cortex* 28, 907–923. doi: 10.1093/cercor/bhw414

Sheffield, J. M., Kandala, S., Tamminga, C. A., Pearlson, G. D., Keshavan, M. S., Sweeney, J. A., et al. (2017). Transdiagnostic associations between functional brain network integrity and cognition. *JAMA Psychiatry* 74, 605–613. doi: 10.1001/jamapsychiatry.2017.0669

Simon, R., and Engström, M. (2015). The default mode network as a biomarker for monitoring the therapeutic effects of meditation. *Front. Psychol.* 6:776. doi: 10.3389/fpsyg.2015.00776

Skoblenick, K., and Everling, S. (2012). NMDA antagonist ketamine reduces task selectivity in macaque dorsolateral prefrontal neurons and impairs performance of randomly interleaved prosaccades and antisaccades. *J. Neurosci.* 32, 12018–12027. doi: 10.1523/jneurosci.1510-12.2012

Sormaz, M., Murphy, C., Wang, H. T., Hymers, M., Karapanagiotidis, T., Poerio, G., et al. (2018). Default mode network can support the level of detail in experience during active task states. *Proc. Natl. Acad. Sci. U.S.A.* 115, 9318–9323. doi: 10.1073/pnas.1721259115

Spreng, R. N. (2012). The fallacy of a "task-negative" network. *Front. Psychol.* 3:145. doi: 10.3389/fpsyg.2012.00145

Tan, W., Liu, Z., Xi, C., Deng, M., Long, Y., Palaniyappan, L., et al. (2021). Decreased integration of the frontoparietal network during a working memory task in major depressive disorder. *Aust. N. Z. J. Psychiatry* 55, 577–587. doi: 10.1177/0004867420978284

Tommasin, S., Mascali, D., Moraschi, M., Gili, T., Hassan, I. E., Fratini, M., et al. (2018). Scale-invariant rearrangement of resting state networks in the human brain under sustained stimulation. *Neuroimage* 179, 570–581. doi: 10.1016/j.neuroimage.2018.06.006

Tononi, G., Sporns, O., and Edelman, G. M. (1994). A measure for brain complexity: Relating functional segregation and integration in the nervous system. *Proc. Natl. Acad. Sci. U.S.A.* 91, 5033–5037. doi: 10.1073/pnas.91.11.5033

van den Heuvel, M. P., and Fornito, A. (2014). Brain networks in schizophrenia. *Neuropsychol. Rev.* 24, 32–48. doi: 10.1007/s11065-014-9248-7

van den Heuvel, M. P., de Lange, S. C., Zalesky, A., Seguin, C., Yeo, B. T. T., and Schmidt, R. (2017). Proportional thresholding in resting-state fMRI functional connectivity networks and consequences for patient-control connectome studies: Issues and recommendations. *Neuroimage* 152, 437–449. doi: 10.1016/j.neuroimage.2017.02.005

Váša, F., Bullmore, E. T., and Patel, A. X. (2018). Probabilistic thresholding of functional connectomes: Application to schizophrenia. *Neuroimage* 172, 326–340. doi: 10.1016/j.neuroimage.2017.12.043

Wang, F., Xi, C., Liu, Z., Deng, M., Zhang, W., Cao, H., et al. (2022). Load-dependent inverted U–shaped connectivity of the default mode network in schizophrenia during a working-memory task: Evidence from a replication functional MRI study. *J. Psychiatry Neurosci.* 47:E341. doi: 10.1503/jpn.220053

Whitfield-Gabrieli, S., and Ford, J. M. (2012). Default mode network activity and connectivity in psychopathology. *Annu. Rev. Clin. Psychol.* 8, 49–76. doi: 10.1146/annurev-clinpsy-032511-143049

Whitfield-Gabrieli, S., Thermenos, H. W., Milanovic, S., Tsuang, M. T., Faraone, S. V., McCarley, R. W., et al. (2009). Hyperactivity and hyperconnectivity of the default network in schizophrenia and in first-degree relatives of persons with schizophrenia. *Proc. Natl. Acad. Sci. U.S.A.* 106, 1279–1284. doi: 10.1073/pnas.0809141106

Wu, G., Palaniyappan, L., Zhang, M., Yang, J., Xi, C., Liu, Z., et al. (2022). Imbalance between prefronto-thalamic and sensorimotor-thalamic circuitries associated with working memory deficit in schizophrenia. *Schizophr. Bull.* 48, 251–261. doi: 10.1093/schbul/sbab086

Yan, C. G., Wang, X. D., Zuo, X. N., and Zang, Y. F. D. P. A. B. I. (2016). Data processing & analysis for (resting-state) brain imaging. *Neuroinformatics* 14, 339–351. doi: 10.1007/s12021-016-9299-4

Yang, J., Pu, W., Wu, G., Chen, E., Lee, E., Liu, Z., et al. (2020). Connectomic underpinnings of working memory deficits in schizophrenia: Evidence from a replication fMRI study. *Schizophr. Bull.* 46, 916–926. doi: 10.1093/schbul/sbz137

Yu, M., Dai, Z., Tang, X., Wang, X., Zhang, X., Sha, W., et al. (2017). Convergence and divergence of brain network dysfunction in deficit and non-deficit schizophrenia. *Schizophr. Bull.* 43, 1315–1328. doi: 10.1093/schbul/sbx014

Yuan, Y., Pan, X., and Wang, R. (2021). Biophysical mechanism of the interaction between default mode network and working memory network. *Cogn. Neurodyn.* 15, 1101–1124. doi: 10.1007/s11571-021-09674-1

frontiers | Frontiers in Cellular Neuroscience

TYPE Original Research
PUBLISHED 10 November 2022
DOI 10.3389/fncel.2022.1036813



OPEN ACCESS

EDITED BY
Luigi Catacuzzeno,
University of Perugia, Italy

REVIEWED BY
Gary Richard Mirams,
University of Nottingham,
United Kingdom
David Kelly Jones,
University of Michigan, United States

*CORRESPONDENCE
Kees McGahan
mcgahan@math.utah.edu

SPECIALTY SECTION
This article was submitted to Cellular Neurophysiology, a section of the journal Frontiers in Cellular Neuroscience

RECEIVED 05 September 2022
ACCEPTED 24 October 2022
PUBLISHED 10 November 2022

CITATION
McGahan K and Keener J (2022) Modeling the kinetics of heteromeric potassium channels. *Front. Cell. Neurosci.* 16:1036813. doi: 10.3389/fncel.2022.1036813



# Modeling the kinetics of heteromeric potassium channels

Kees McGahan* and James Keener

Math Department, University of Utah, Salt Lake City, UT, United States

Mechanistic mathematical modeling has long been used as a tool for answering questions in cellular physiology. To mathematically describe cellular processes such as cell excitability, volume regulation, neurotransmitter release, and hormone secretion requires accurate descriptions of ion channel kinetics. One class of ion channels currently lacking a physiological model framework is the class of channels built with multiple different potassium protein subunits called heteromeric voltage gated potassium channels. Here we present a novel mathematical model for heteromeric potassium channels that captures both the number and type of protein subunits present in each channel. Key model assumptions are validated by showing our model is the reduction of a Markov model and through observations about voltage clamp data. We then show our model's success in replicating kinetic properties of concatemeric channels with different numbers of $K_V1.1$ and $K_V1.2$ subunits. Finally, through comparisons with multiple expression experiments across multiple voltage gated potassium families, we use the model to make predictions about the importance and effect of genetic mutations in heteromeric channel formation.

KEYWORDS

**heteromeric potassium ion channels, $K_V1$ channels, $K_V7$ channels, mathematical modeling, ion channel kinetics**

## 1. Introduction

Potassium channels are membrane spanning proteins that are responsible for the transport of potassium ions into and out of cells. Found in virtually all species, these channels regulate a whole host of cellular processes (MacKinnon, 2003). In addition to their importance in regulating neuron, cardiac cell, and pancreatic $\beta$-cell excitability, potassium channels have been found to aid in other physiological functions such as volume regulation, neurotransmitter release, and hormone secretion (Barfield et al., 2005; Ghatta et al., 2006). Working to account for all these function are upwards of 80 genes coding for different potassium channel protein $\alpha$-subunits (Harding et al., 2022). These are categorized into three broad groups based on their number of transmembrane domains (TMDs): inward rectifier channels (two TMDs), leak or $K_{2p}$ channels (four TMDs), and voltage gated or $K_V$ channels (six TMDs) (Coetzee et al., 1999).

The most well-studied of these groups, accounting for about half of the total genes, is the collection of voltage gated potassium channel subunits. Broken up into 12 subfamilies according to physiological characteristics, four $K_V$ $\alpha$-subunits are required to form a functional, pore forming channel. Each of the four $\alpha$-subunits can be encoded for by one

gene forming a homotetramer (homomer), or by multiple genes from either the same, or in rare cases, different subfamilies thereby forming heterotetramers (heteromers). As a result of all the different possible numbers and arrangements of each subunit type, formation of these heteromeric potassium channels drastically increases $K_V$ channel diversity. With such a large collection of possible channels, researchers have begun asking which subunit combinations are physiologically relevant and how do their kinetics compare to their homomeric counterparts?

Attempts at answering these questions have taken a variety of forms including using pharmacological and electrophysiological techniques, and studying properties of concatenated subunit genes and expression systems. Work by Cordeiro et al. (2019) concatenated different ratios of $K_V1$ subunits together and examined the concatemers' different levels of binding affinity to $\kappa$M-conotoxin RIIIJ. It was found that $\kappa$M-conotoxin RIIIJ not only had preference for channels with $K_V1.1$, $K_V1.2$, and $K_V1.6$ subunits, but had the highest binding affinity for heteromers in the particular configuration of three $K_V1.2$ subunits and 1 $K_V1.1$ or $K_V1.6$ subunit. Al-Sabi et al. (2013) combined electrophysiology tools with $K_V1.1/K_V1.2$ concatemers and determined distinct activation kinetics and TEA sensitivity distinguishing each of the heteromeric and homomeric concatemers. While looking at epilepsy associated mutations in $K_V7.2$ genes, Miceli et al. (2013, 2015) showed that wildtype and mutant $K_V7.2$ subunits likely form heteromeric channels whose kinetic properties are intermediate between those of the associated homomeric channels. Similar conclusions were reached about the heteromers formed from $K_V1.1$, $K_V1.2$, and $K_V1.1$ mutant subunits thought to be responsible for ataxia and epilepsy (Hasan et al., 2017; Miceli et al., 2022).

One of the current problems faced in this field of work is connecting the results of these concatenation experiments with experiments involving natural expression systems. Determining which heteromeric ratio of subunits is present in a natural expressed system has remained elusive for experimentalists. The straightforward technique of gene knockouts renders all functioning, present heteromers useless thereby preventing further analysis. One possible avenue of approach to this issue is mathematical modeling. Since the groundbreaking work of Hodgkin and Huxley on modeling action potentials in the squid giant axon, mechanistic math modeling has become a staple in furthering understanding of homomeric ion channels and their role in cellular processes (Hodgkin and Huxley, 1952; Miura, 2002; Moreno et al., 2016; McGahan and Keener, 2020). Two types of general model frameworks are typically considered to describe homomeric ion channel function: those in the spirit of Hodgkin and Huxley, and Markov models that explicitly detail each conformational protein change between channel states (Nekouzadeh et al., 2008; Keener, 2009, 2010). Increases in data availability and advancements in experimental techniques have led to more detailed models capable of answering and asking questions about drug-channel interactions, complex experimental protocols, different activating stimuli, and even channel structure (Cheng et al., 2007; Perissinotti et al., 2015; Moreno et al., 2016).

Successful modeling results, across multiple ion channel types, hints at modeling as a natural next step for connecting the different types of existing heteromeric $K_V$ channel experimental results. Models of heteromeric channels, especially biophysical ones reflecting protein composition and structure, are currently scarce relative to the available data and experimental interest. Work by Cheng et al. (2007) coupled spectroscopy-based fluorescence resonance energy transfer and computational modeling to indicate that heat-sensitive transient receptor potential channels prefer heteromeric configurations. Looking at heteromeric cyclic nucleotide–gated channels, Benndorf et al. (2022) analyzed the ability to determine model parameters using concatemeric experimental data. Modeling work with heteromeric $K_V$ channels has primarily consisted of fitting Boltzmann-like equations, or in rare cases Markov Models, for channel gating to voltage clamp data of either concatemeric heteromers or cells with two or more coexpressed cDNA types (Sale et al., 2008; Miceli et al., 2013, 2015). Although these fitted heteromeric $K_V$ models can be used to simulate generic heteromeric behavior, they do not encode knowledge about the $\alpha$-subunit ratios. This limitation implies they cannot be generalized to heteromers of different ratios let alone heteromeric channels with completely different subunits.

Using a Hodgkin-Huxley type gating model, which we show has a parallel Markov structure, we present a novel heteromeric $K_V$ channel modeling framework. This framework is both generalizable to multiple $K_V$ families and captures $\alpha$-subunit type and stoichiometry. We outline the applicability of our model and justify specific model assumptions. With $K_V1.1/K_V1.2$ concatemeric results from Al-Sabi et al. (2013) we analyze the model's ability to replicate heteromeric channels' steady state open probability curves for each of the possible subunit combinations. We then apply our framework to look at multiple different experiments where two cDNAs for $K_V$ subunits are expressed together but the subunit ratios and relative percentages of the resulting channels is unknown. By comparing these known experimental results with model outputs we make predictions about which subunit ratios are important and when $\alpha$-subunits may be assembling randomly.

# 2. Methods

## 2.1. Hodgkin Huxley model framework

Our model is based on the work of Hodgkin and Huxley (1952). Their model tracks the membrane voltage $V$, which changes based on the sum of the individual ionic currents. The model for each current is composed of three parts: a maximal conductance $g_i$, an open probability consisting of some

number of activating or inactivating gates, and a driving force term $(V - E_i)$ describing the direction and magnitude of the current, for $i = Na, K$. The gating variables, $n, m$, and $h$, are each probabilities between 0 and 1, that change over time in response to changes in $V$. It is assumed that the gates operate independently and that all gates must be open for current flow. The numbers of each gate for each channel type were derived by Hodgkin and Huxley based on best fits to data. The differential equations for membrane voltage $V$, the sodium gates $m, h$, and the potassium gates $k$ are given here:

$$\frac{dV}{dt} = \frac{1}{Cm}(-I_{Na} - I_K - I_l) \tag{1}$$

$$\frac{dj}{dt} = [a_j(V)(1 - j) - b_j(V)j], j = m, n, h. \tag{2}$$

With the Hodgkin-Huxley current equations having the form:

$$I_{Na} = g_{Na}m^3h(V - E_{Na}) \tag{3}$$

$$I_K = g_K n^4(V - E_K) \tag{4}$$

$$I_l = g_l(V - E_l). \tag{5}$$

Rate constants $a_j, b_j$, and parameters, including the maximal conductances $g_{K/Na/L}$, reversal potentials $E_{K/Na/L}$, and membrane capacitance $Cm$ were all experimentally fit and are available in the literature (Hodgkin and Huxley, 1952; Keener and Sneyd, 2009; McGahan and Keener, 2020).

## 2.2. Heteromeric potassium channels (activating only)

Here we formalize our model structure proposed for heteromeric $K_V$ channels. This paper focuses on the set of heteromeric channels whose $\alpha$-subunits, when in homomeric configurations, confer minimal, or irrelevant inactivating kinetics. Each homomeric channel is modeled identically to the Hodgkin Huxley potassium channel, with the necessary rate constants. Each heteromeric channel is also mathematically described with three components as outlined above in Section 2. While the density and driving force are modeled identically to a homomeric potassium channel (Equation 4), the channel gating of a heteromer is modeled to reflect the specific number and type of $\alpha$-subunits present.

Since each $K_V$ channel, homomeric and heteromeric, is composed of four protein subunits, we assume that each heteromer has 4 gates, with number and type equal to that of the subunits present (Coetzee et al., 1999; Cordeiro et al., 2019). The gating variables and corresponding differential equations used in any heteromeric model are taken directly from their respective homomeric models. This guarantees that a heteromer's properties are derived mechanistically and are completely determined from subunit composition once the homomeric kinetics are known. As an example, to model a 1.1/1.2 K-channel heteromer, notated by either $K_V1.1/1.2$ or $K_{1.1/1.2}$, we first need $K_V1.1$ and $K_V1.2$ homomer models that are built with four independent and identical gates, $n_{1.1}$ and $n_{1.2}$. These homomeric models are referred to as the 4:0 and 0:4 models, denoting their subunit, and thus gate, number, and type. To then construct a $K_V1.1/1.2$ heteromer consisting of $x$ 1.1 subunits and $y$ 1.2 subunits, the model is referred to as an $x:y$ model and is built using $x$ 1.1 gates and $y$ 1.2 gates.

The representation for a heteromeric channel current made up of three 1.1 subunits and one 1.2 subunit is given below:

$$I_{1.1} = g_{1.1}n_{1.1}^4(V - E_K) \tag{6}$$

$$I_{1.2} = g_{1.2}n_{1.2}^4(V - E_K) \tag{7}$$

$$I_{1.1/1.2}^{3:1} = g_{1.1/1.2}n_{1.1}^3n_{1.2}^1(V - E_K). \tag{8}$$

As stated above, it is assumed $x + y = 4$ with $x$ and $y$ taking integer values between 0 and 4. This is to adhere to the 1 subunit for 1 gate hypothesis. We emphasize that setting either $x$ or $y$ to 0 returns a homomeric channel. Note that loosening the integer value restriction does not break the resulting analysis below, it simply carries a different set of biological assumptions with it.

## 2.3. Addressing the four gate and integer power assumptions

The primary model assumptions to address are that the sum of the number of gates must be 4 and that the gates take integer power values. These assumptions inherently dictate that each homomeric K-Channel is modeled with four gates. While Hodgkin and Huxley's original model utilized four gates to fit the data, since then there have been many activating only, homomeric, potassium channel models in the literature fit with only one activating gate (Hodgkin and Huxley, 1952; Miceli et al., 2013, 2015; Ranjan et al., 2019). There are two arguments outlined here to defend these two critical model assumptions. The first is that this model framework is actually a reduction of a well described Markov model for four interacting independent protein subunits of two (or more) types. The second argument involves looking at the outputs of voltage clamp recordings of cells containing $K_v1.1$ channels and seeing which number of gates best fits the time dependent data.

### 2.3.1. Markov model reduction

Work by Keener takes Markov models of ion channels and finds globally attracting invariant manifolds of reduced dimensions (Keener, 2009, 2010). The first important result of

these papers is for a potassium channel with four identical, independent subunits that can only transition between an open or closed state. If the conducting state is when all four subunits are open, then the Markov model's invariant manifold has exactly Hodgkin and Huxley's open probability of $P_o = n^4$, with $n$ governed by Equation (2). This Markov model and the invariant manifold's open probability are precisely what we have postulated for all homomeric potassium channel models under our outlined framework.

The second important result by Keener is for a sodium channel (Keener, 2009, 2010). The given Markov model has three activating subunits and 1 inactivating subunit, with all subunits independent. The model is shown to have an invariant manifold with open probability $P_o = m^3h$ for $m$ and $h$ governed by Equation (2). As seen with Equation (8), the open probability for the reduced sodium model $P_o = m^3h$, is equivalent to the open probability for a 3:1 or 1:3 heteromer. In both cases, there are three subunits of 1 type, 1 subunit of a different type, and all subunits must open to be conducting. Therefore, this result by Keener implies our 3:1 and 1:3 heteromeric models can be thought of as an invariant manifold of a Markov model for 3 subunits of one K-channel subunit type and 1 subunit of a second type, all independent. Finally, although not explicitly detailed, the manuscript posits that a Markov model with two independent subunits of type $K_v1.1$ and $K_v1.2$, would have an invariant manifold with open probability $P_o = n_{1.1}^2 n_{1.2}^2$, again what our framework predicts. One important observation is that this is the predicted open probability for a 2:2 heteromer regardless of if subunits of the same type are across from or next to each other.

### 2.3.2. Fitting to voltage clamp data

The second justification for our model assumptions is done by looking at voltage clamp data for $K_v1.1$ channels. Assuming that our homomeric potassium currents can be accurately modeled with a maximal conductance $g_k$, an open probability determined by some unknown number $p$ of gates of type $n$, and a driving force term $(V - E_k)$; we have the current equation:

$$I_K = g_K n(t)^p (V - E_K). \tag{9}$$

Using voltage clamp data for cells with $K_v1.1$ channels we ask which power $p$ best describes the channel gating. The first step in answering this question is to normalize any endogenous or capacitive currents that may be present in the data. This is done by subtracting the current value that is present at the very start of the voltage clamp protocol since before the channels have had time to activate there should be no noticeable current. This is all to say that the current traces at the initial engagement of the protocol should start with a current reading of 0 with some given noise. Next, since voltage is fixed, we can divide out the driving force term $(V - E_K)$ if $E_K$ is known. Then, assuming the voltage clamp has been performed at a high enough voltage to open all gates giving $n(t)^p = 1$, we can divide by the maximum value attained over the entire experiment. This step corresponds to dividing out $g_K$. The resulting transformed data is a function of time whose output is the open probability of the present $K_v$ channels. This data will be fit with the function for the open probability $P_o(t)$:

$$P_o(t) = n(t)^p. \tag{10}$$

which is what is left from Equation (9) after dividing by the maximal conductance $g_K$ and driving force term $(V - E_K)$.

To fit Equation (10) to the transformed data we also must know the form $n(t)$ takes at any fixed voltage. Recall that the differential equation governing a single gate's dynamics is described as follows:

$$\frac{dn}{dt} = [a_n(V)(1 - j) - b_n(V)n] = \frac{n_\infty - n(V)}{\tau_n} \tag{11}$$

where $n_\infty(V) = \frac{a_n}{a_n + b_n}$ and $\tau_n(V) = \frac{1}{a_n + b_n}$. Under this formulation $n_\infty$ describes the steady state open probability attained by the gate as a function of voltage, and $\tau_n$ is the voltage dependent time constant. If the channel behavior is analyzed under a voltage clamp protocol with voltage kept constant, then the resulting ODE is dependent only on $n$. Therefore, Equation (11) can be solved analytically to yield the following expression in $n$:

$$n(t) = n_\infty(1 - Ae^{\frac{-t}{\tau_n}}) \tag{12}$$

Here we have an integration constant $A$ with $n_\infty$ and $\tau_n$ both fixed parameters for the given fixed value of voltage $V$. If $n(0) = 0$, a reasonable assumption, given that in the voltage clamp protocols looked at, the initial holding voltage prior to the step is near −90 mV implying the channels are essentially closed, this simplifies to:

$$n(t) = n_\infty(1 - e^{\frac{-t}{\tau_n}}). \tag{13}$$

Equation (13) gives the time dependent open probability value for a single gate at a fixed voltage. Combining the results of Equations (10) and (13) yields the following complete description for $P_o(t)$:

$$P_o(t) = (n_\infty(1 - e^{\frac{-t}{\tau_n}}))^p. \tag{14}$$

Finally, using MATLAB's built in nonlinear least squares fitting method, we fit Equation 14, with different chosen values of $p$, to the transformed voltage clamp data (MATLAB, 2018). By setting bounds on the possible parameter values for $n_\infty$ (between 0 and 1) and $\tau_n$ (>0), the MATLAB function performs a parameter search that solves: $\min[\Sigma(P_o(t) - \text{data}(t))^2]$. In Figure 1, we see an example of how these curves fit a $K_V1.1$ voltage clamp experiment with $V = 20$ mV (channels close to fully open) and

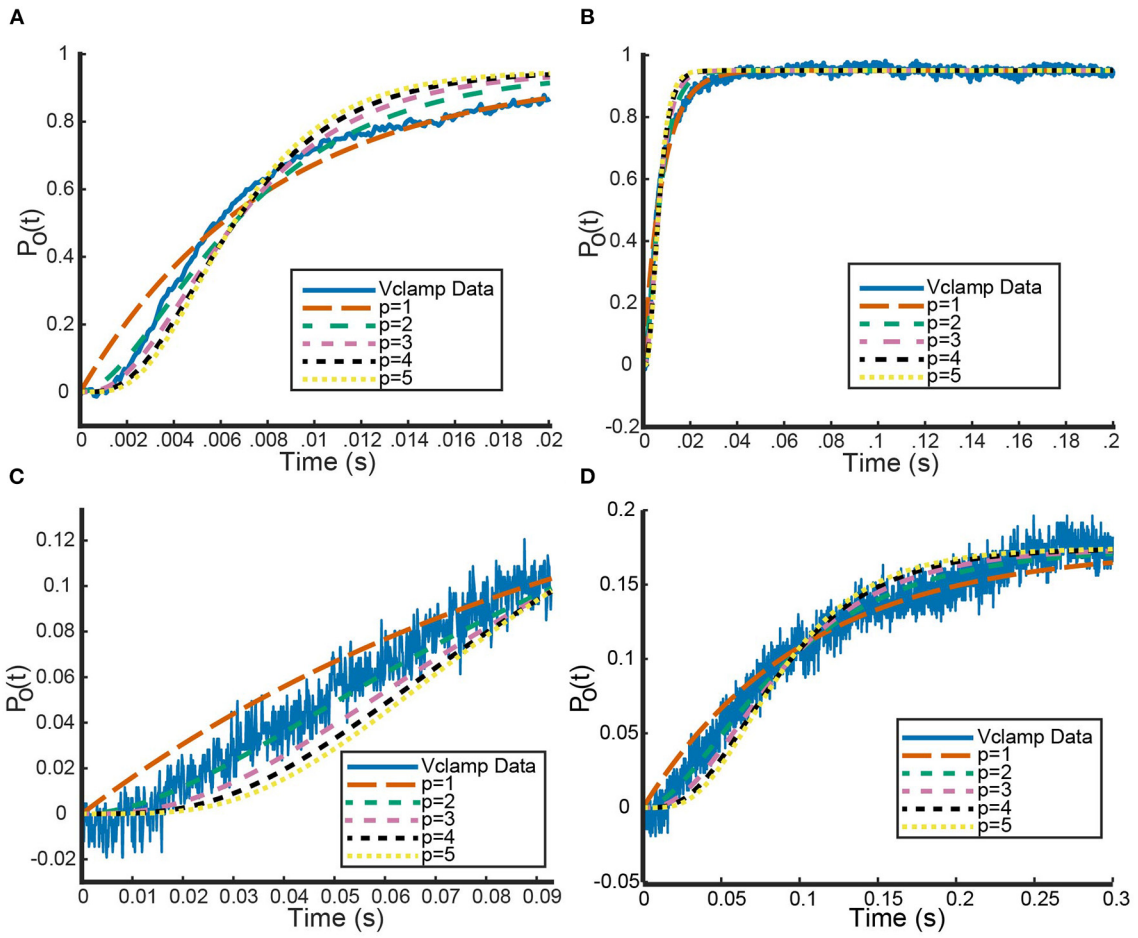


FIGURE 1
Sample fits of five curves of the form seen in Equation (14) to voltage clamp data (shown in blue) from Channelpedia (Ranjan et al., 2011, 2019). Each curve corresponds to a different value of $p$, the number of gates being used to fit the data. **(A,C)** A zoomed in version to make clear the performance of each model on capturing the sigmoid shape of the beginning portion of the data. **(B,D)** The whole timescale with each of the five fits. Curve colors are as follows: $p = 1$ (orange), $p = 2$ (green), $p = 3$ (pink), $p = 4$ (black), $p = 5$ (yellow). Curve dash sizing and spacing is given in figure legend. **(A,B)** correspond to a voltage step from −90 up to 20 mV while panels **(C,D)** correspond to a voltage step from −90 up to −30 mV.

$V = -30mV$ (channels beginning to open) for different values of $p$ from 1 to 5.

At initial glance, Figures 1B,D indicate that all powers of $p$ generate roughly identical fits to the data with $p = 1$ performing marginally better. We compared the fits of the different power $p$ curves across the entire data set using mean squared error (MSE) as our metric. Using voltage clamp recordings for six different cells, looking at data for six different value of $V$, we averaged the MSEs for all powers of $p$. This revealed that $p = 1$ generated the smallest MSE of 0.0006 and $p = 5$ the largest value of 0.0021 (Table 1).

However, zooming in on the data and the fits across a smaller range of time values shows an important detail to make note of Figures 1A,B clearly show clearly shows the shape of the data cannot be fit best with the simple exponential function that would result from setting $p = 1$. For each of the six cells, the voltage clamp data across all values of $V$, is seen to take on a sigmoid shape. This data, and the representative fits, suggests that modeling activation only $K_V$ channels with the Hodgkin Huxley gating kinetics seen in Equation (11) will require more than 1 gate to correctly model all aspects of the known data.

To quantify this hypothesis, we looked at two other error metrics: a MSE over a shorter time interval and a weighted error. Looking at the MSE over the shorter time interval, defined to be the component of the data seen before channel opening, every power $p > 1$ performed an order of magnitude (differing by a factor of 10) better than when $p = 1$ (Table 1). Although this analysis cannot distinguish between models with two or more gates, it does confirm that one gate is not sufficient for the shape of the data. This observation is recapitulated by the weighted error we computed. The weighted error is computed over the entire time interval by weighting the MSE over the short time

TABLE 1 Different error metrics comparing homomeric $K_v$ channel models with different gate numbers.

| p | Full | Short | Weighted |
|---|---|---|---|
| 1 | 0.0006 | 0.0028 | 0.28 |
| 2 | 0.0009 | 0.0006 | 0.06 |
| 3 | 0.0015 | 0.0004 | 0.04 |
| 4 | 0.0018 | 0.0004 | 0.04 |
| 5 | 0.0021 | 0.0004 | 0.04 |

The first column $p$ is the number of gates and thus power used to fit the data. The Full column gives the MSE between each fit model and the entire dataset. The Short column gives the MSE between model and the data over the time interval where the channel has not yet opened. The Weighted column gives a weighted MSE over the whole time interval where the time component corresponding to when the channel is closed is weighted 100 times heavier.

interval 100 times more than the remainder of the time. The idea behind this weighted error is to see how well the model adheres to the sigmoid shape while still accounting for error over the remaining time. As with the short time interval error, $p = 1$ was an order of magnitude worse than every other power.

# 3. Results

## 3.1. $K_v$1.1 and $K_v$1.2 heteromers

Here we show the model's ability to reproduce certain 2013 results by the Al-Sabi group (Al-Sabi et al., 2013). In their work, they were able to concatenate subunits of $K_v$1.1 and $K_v$1.2 channels together into functional homomers and heteromers of every possible ratio. Then by way of voltage clamp experiments, they found each heteromer's and homomer's steady state open probability as a function of voltage. Their data points were then fit with the following open probability equation:

$$P_{open}(V) = \frac{1}{1 + e^{(-(V - V_{.5})/k)}} \tag{15}$$

with different parameter values $V_{.5}$ and $k$ for each heteromer and homomer. Note that while Equation (15) is a function for the steady state probability of a given channel, it was fit assuming only one activating gate. Using the $V_{.5}$ and $k$ values for the $K_v$1.1 and $K_v$1.2 homomers from Al-Sabi et al. (2013), we calibrated the activating kinetics for the $K_v$1.1 and $K_v$1.2 gates to fulfill our four gate assumption. This was done by taking Equation (15) with parameters from Al-Sabi et al. (2013), and using the MATLAB nonlinear least squares fitting function to find the best fitting function of the form $P_{open}(V)^4$. The data points used in minimizing the least squares error were a discretized range of voltage values from −100 to 100 of step size 0.01. We arrived at the following steady state probabilities for $K_v$1.1 and $K_v$1.2 gates:

$$n_{1.1}(V) = \frac{1}{1 + e^{(-(V + V_{1.1})/k_{1.1})}} \tag{16}$$

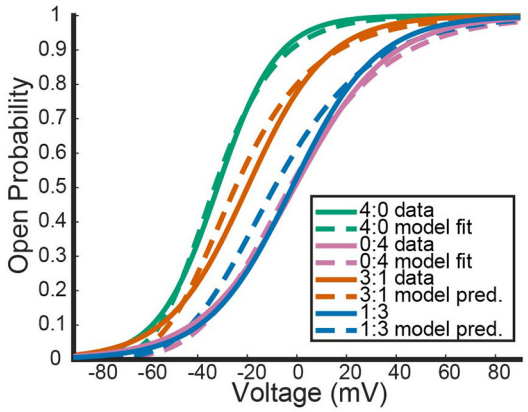


FIGURE 2
Comparisons between our mathematical framework predictions for $K_V$1.1/1.2 heteromers and data from Al-Sabi et al. (2013). The solid curves are the plotted fits from Al-Sabi and the dashed curves are the results of the mathematical model. The green and pink curves correspond to the two different homomers with the dashed curve model outputs having been fit directly to Al-Sabi parameters as described above. The mean squared error (MSE) between 4:0 curves is 0.00022 and between 0:4 curves is 0.00033. The orange and blue curves are model prediction outputs for 3:1 and 1:3 $K_v$1.1/1.2 heteromers using Equations (16) and (17) for the gating kinetics. The MSE for the 3:1 curve is 0.00091 and the MSE for 1:3 curves is 0.0018.

$$n_{1.2}(V) = \frac{1}{1 + e^{(-(V + V_{1.2})/k_{1.2})}} \tag{17}$$

where $V_{1.1} = 59.18$, $k_{1.1} = 15.61$, $V_{1.2} = 44.08$, and $k_{1.2} = 24.75$. The parameter values for Equations (16) and (17) were found by using the described fitting method and the steady state probability curves for the $K_v$1.1 and $K_v$1.2 homomers from Al-Sabi et al. (2013). Note that variations in the values for the parameters $V_{1.1}$, $k_{1.1}$, $V_{1.2}$, and $k_{1.2}$ could possibly yield better fits to the Al-Sabi data as we were only able to fit to the available functional forms of their steady state curves. For clarity, this original set of parameters will be referred hereafter as the optimal, or best fitting, parameter set.

Recall that under the framework outlined above, a 3:1 $K_V$1.1/1.2 heteromer will have steady state open probability $n_{1.1}^3 n_{1.2}$ and a 1:3 heteromer will have open probability $n_{1.1} n_{1.2}^3$. While the 2:2 heteromer's probability curve could be generated in a similar manner, the data recorded in Al-Sabi et al. (2013) for the 2:2 heteromer was from a separate experiment and is therefore left out. Utilizing our fit curves, we compared the model predictions for the 3:1 and 1:3 heteromer's open probability against the fit summary curves from the Al-Sabi study. This is shown in Figure 2.

Figure 2 shows the model's attempt at replicating $K_V$1.1/1.2 heteromeric steady state open probabilities. Most notably, the model does well at capturing the 3:1 heteromer steady state probability. This is highlighted by the mean squared error (MSE)

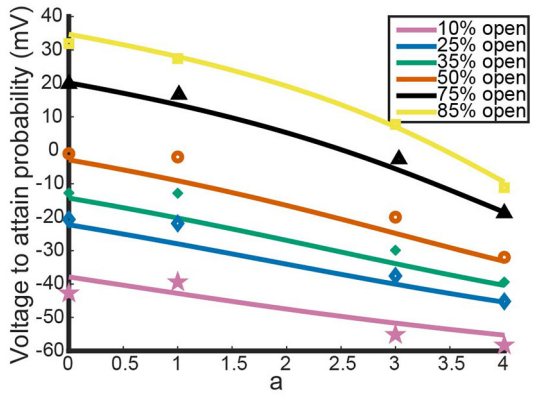


FIGURE 3
Model outputs showing the voltage at which a particular probability of opening is achieved. The x-axis denotes the proportion of subunits/gates that are $K_V1.1$ vs. $K_V1.2$ with $a = 4$ corresponding to a $K_V1.1$ homomer with four subunits/gates. Each curve color corresponds to a different probability of opening from the model output. The data points are the Al-Sabi data points of each channel type for any given probability of opening and are colored accordingly. Although the non-integer values of $a$ are irrelevant under the model framework, the curves are left for clarity of the trends moving from $a = 4$ to $a = 0$.

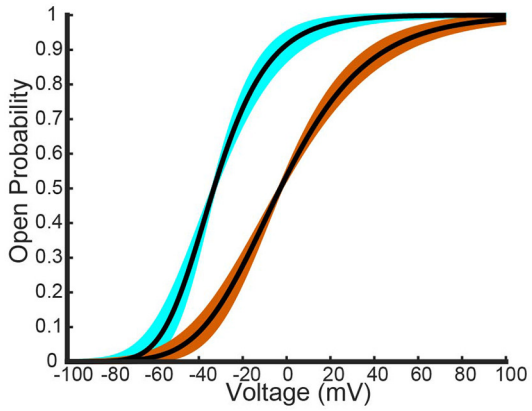


FIGURE 4
Different fits of a four gate model for $K_v1.1$ and $K_v1.2$ homomers to the Al-Sabi one gate model data. The best fit model generated from a nonlinear least squares fitting method is shown as a black curve for both channel types. The light blue curves are the other seven overlapping fit $K_v1.1$ models that have the same order of magnitude as the best fit $K_v1.1$ curve. The orange curves are the other overlapping eight fit $K_v1.2$ models that have the same order of magnitude as the best fit $K_v1.2$ curve.

for the 3:1 heteromer having the same order of magnitude as the 4:0 and 0:4 homomers. Additionally, we can see the model predicts some amount of nonlinearity in the shifts of probability curves moving from left to right. In Al-Sabi et al. (2013), they observed a much larger jump between the 4:0 and 3:1 curves compared with the difference in 1:3 and 0:4 curves. To explore this observation more concretely, we asked at what voltage do each of the different channel types (4:0, 3:1, 1:3, 0:4) achieve certain probabilities of being open. This was done by setting $n_{1.1}^{a} n_{1.2}^{4-a}$ equal to one of 10, 25, 35, 50, 75, or 80% and solving for $V$ at all values of $a$ between 0 and 4. This can be thought of as drawing horizontal lines through Figure 2 at a given probability and then plotting the intersection points with the steady state probability curves as a continuous function.

Figure 3 shows the voltage at which a specific probability of being open is reached as a function of $a$, the number of $K_V1.1$ subunits. For instance, the red curve corresponds directly to the $V_{.5}$ or 50% open probability of each channel type, with $a = 4$ giving the $V_{.5}$ of $K_V1.1$ homomers and $a = 0$ the $V_{.5}$ of $K_V1.2$ homomers. In Figure 3, we can clearly see the Al-Sabi data points showing the behavior that we hope the model replicates. The data points for each probability of opening show a much steeper increase going from four $K_V1.1$ subunits to 3 in comparison with the minimal change going from 1 $K_V1.1$ subunit to none. We see with this parameter set for $n_{1.1}(V)$ and $n_{1.2}(V)$ the model has this sharper change moving from $a = 4$ to $a = 3$ than moving from $a = 1$ to $a = 0$. However, this behavior is only present for the 50% and higher probability of opening curves, with the curves becoming more linear as the probability of opening is lowered.

Having noted above that this parameter set may not actually fit the data best, we perturbed $V_{1.1}$, $k_{1.1}$, $V_{1.2}$, and $k_{1.2}$ and examined the resulting model output. To perturb the parameters, we start with the original fit parameter set from above, increase or decrease $k_{1.x}$, and then refit $n_{1.x}(V)$ to get a new $V_{1.x}$, for $x = 1, 2$. Each $k_{1.x}$ was both increased and decreased until the newly fit homomeric open probability curves produced a mean squared error with the Al-Sabi curves that was of a higher order magnitude (differencing by a factor of ten) than our original best fit model curves. This procedure yielded 8 different $K_V1.1$ curves and 9 $K_V1.2$ curves that had the same MSE as the optimal fit curves. These curves are shown below in Figure 4.

These different parameter fits yield 72 different model combinations to test. Here we present the model results using the two most insightful combinations: when the slope factors $k_{1.x}$ are the closest and furthest apart.

Figures 5A,B show the model results using homomeric open probability curves with the closest possible $k_{1.x}$ values. This combination of parameter values resulted in heteromeric steady state probability curves that had more similar MSEs with the Al-Sabi data than those from the optimal parameter set. Additionally, Figure 5B shows a much better adherence to the observation that there are larger changes going from a 4:0 channel to a 3:1 channel than going from a 1:3 channel to a 0:4 channel. Whereas, the optimal parameter set generated curves that had the proper behavior only at higher

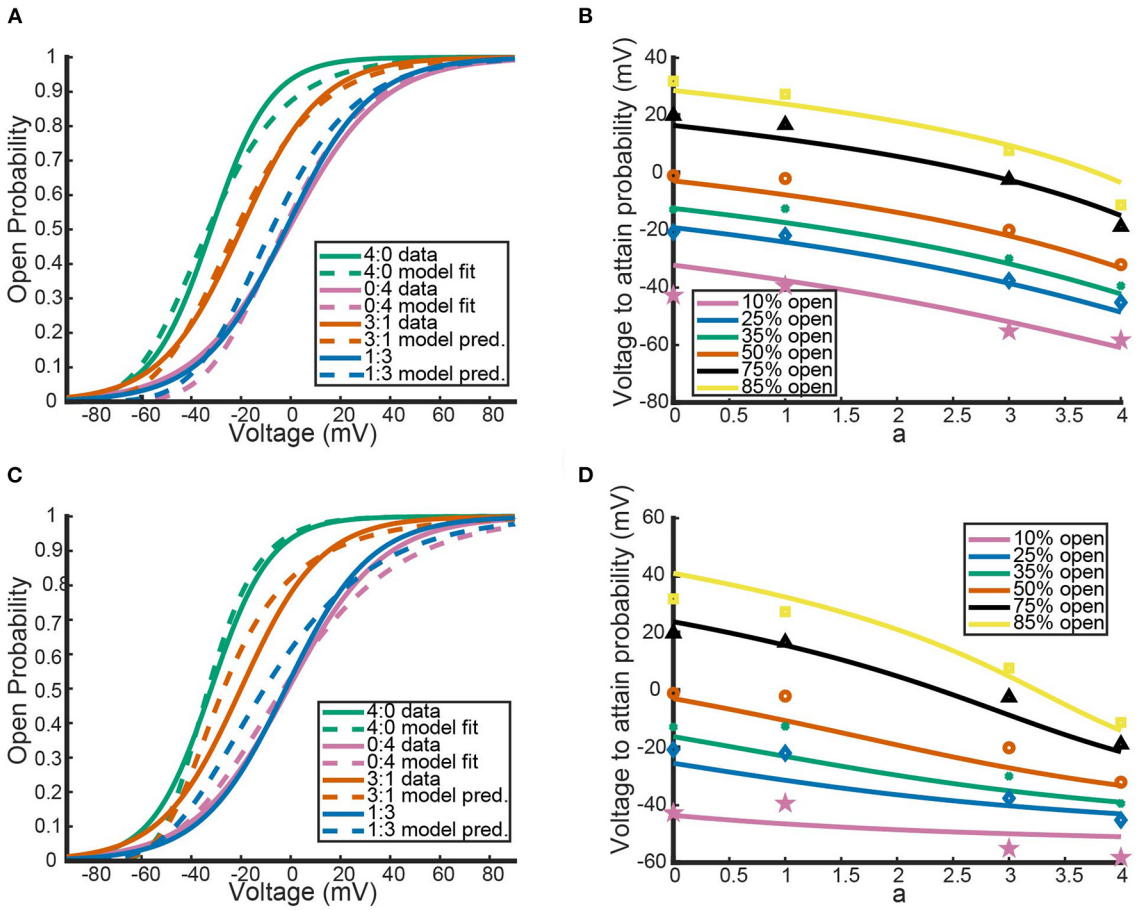


FIGURE 5
The model's performance relative to the Al-Sabi data using the $K_v$1.1 and $K_v$1.2 fit models with slope factors that are closest **(A,B)** and furthest **(C,D)** apart. Curve color and descriptions for **(A,C)** are identical to those given in Figure 2. Curve color and descriptions for **(B,D)** are identical to those given in Figure 3.

probabilities of being open, the closest possible $k_{1.x}$ parameter set had the correct curve concavity at all probabilities of being open.

In contrast, the outputs of the furthest apart possible $k_{1.x}$ parameter set, shown in Figures 5C,D, do worse than the optimal parameter set. Not only are the 3:1 and 1:3 steady state open probability curves farther from the data than those of the optimal parameter set, the spacing of the steady state probability curves as seen in Figure 5D also performs worse than the optimal parameter set. At the highest probability of being open there is still a larger change from a 4:0 to a 3:1 channel than from a 1:3 to a 4:0 channel. This feature is reversed at lower probabilities of being open, which conflicts with the known shape of the data points. The two different parameter sets looked at here, found *via* our parameter search methodology, yield the possible extreme model outcomes in comparison to the data. We do not rule out the possibility of better or worse performing parameter sets, but with only the summary data curves available this analysis must suffice.

## 3.2. Model predictions: Three examples

With our heteromeric model, we can begin to answer questions surrounding experiments involving heteromeric activation-only K-channels. One such question regarding these channel types involves understanding the differences between cells expressing heteromeric channels and cells expressing only the homomeric counterparts. Are these two cell types noticeably different? More specifically, if a cell expresses DNA for two different K-Channel proteins, is it possible to discern in which ratios the subunits form channels? Examples of this experimental setup includes work with $K_v$1.1, $K_v$1.2, and $K_v$1.1 mutant subunits, work with $K_v$7.4 and $K_v$7.5

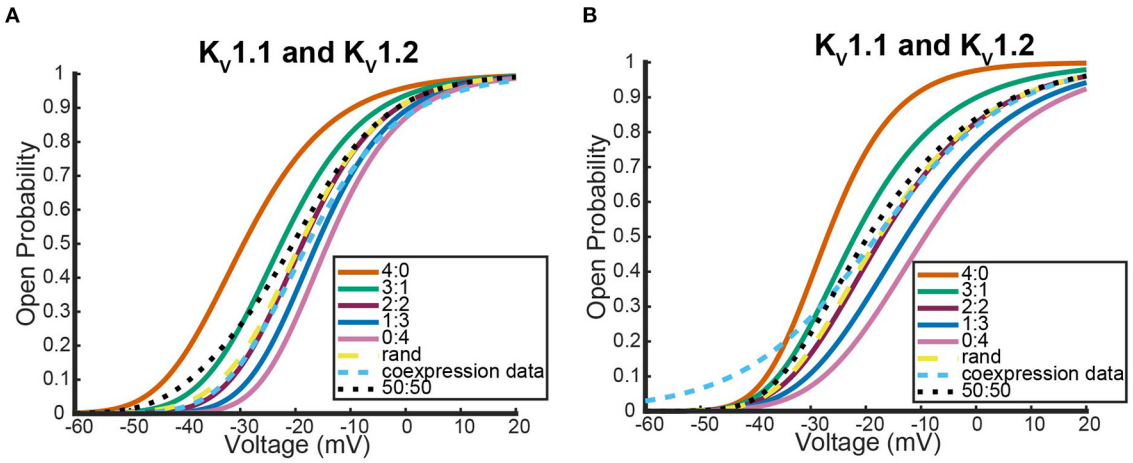


FIGURE 6
Steady state probability curves as a function of voltage for cells containing various channel types in two different experiments. The coexpression data and homomeric data for model fitting was taken from D'Adamo et al. (1999) **(A)** and Imbrici et al. (2008) **(B)**. The steady state probability curves presented here are for homomeric $K_V$1.1 (4:0) and $K_V$1.2 (0:4) channels, heteromeric $K_V$1.1/1.2 channels (3:1, 2:2, 1:3), the model output of a random assembly of $K_V$1.1 and $K_V$1.2 subunits expressed in 50:50 ratio (rand), the data output of a 50:50 expression of $K_V$1.1 and $K_V$1.2 cDNAs (coexpression data), and a model output of an equal split between only homomeric channels (50:50). Curve color and type are shown in the legends. Homomeric channels and their related heteromers being looked at are also detailed in figure titles.

subunits and work in $K_V$7.2, $K_V$7.3, and $K_V$7.2 mutant systems (D'Adamo et al., 1999; Imbrici et al., 2008; Miceli et al., 2013, 2015, 2022; Mani et al., 2016; Hasan et al., 2017). In each system, the different subunit types were expressed either alone or together in a cell, and the resulting steady state open probability curves were found. It was shown that the coexpressed subunit cell's probability curves always lie between those of the homomeric probability curves. However, for each scenario, it was not clear if the coexpressed subunits are coming together randomly, assembling in a preferred heteromeric ratio, or assembling together preferring the homomeric configurations.

For each experiment, we computed the steady state open probability that satisfies the power 4 model assumption for each homomeric channel type. This was done using the experimentally derived $V_{.5}$ and $k$ values in the manner as described above in Section 3.1. With the fit equations for the different gate types, we could plot the steady state probability curves for the homomeric expression data, the coexpression data, and what the model predicts would be generated for subunits assembling only in certain heteromeric ratios or completely randomly. Probability curves for channels expressing only a specific heteromeric ratio are calculated directly according to the mathematical framework outlined above. To generate the predicted steady state probability curve stemming from a random assembly of the two subunits, we make two assumptions. First, we assume that the transcription and translation of the expressed DNAs occur with the same effectiveness for all DNA types. Since experimentally the two distinct DNA types are expressed at 50:50 ratios, this assumption implies there is an equal amount of each protein subunit type. The second assumption is that we define random assembly as a binomial process for choosing four subunits with 50% probability of choosing either type. Combining the model's steady state probability curves for all the heteromeric and homomeric channel types with this binomial distribution results in the following prediction for a steady state probability curve generated from random subunit assembly:

$$P_{rand}(V) = \frac{1}{16}P_{4:0}(V) + \frac{1}{4}P_{3:1}(V) + \frac{3}{8}P_{2:2}(V) + \frac{1}{4}P_{1:3}(V) + \frac{1}{16}P_{0:4}(V). \quad (18)$$

Here $P_{x:y}$ denotes the probability curve for a channel with $x$ subunits of the first type and $y$ subunits of the second type. Note that a cell expressing only 2:2 heteromers will typically have an open probability curve that significantly overlaps with the random assembly curve, simply as a result of coefficients seen in Equation 18. The next subsections are the results of this analysis applied to multiple different experiments on $K_V$1.1, $K_V$1.2 heteromers, a $K_V$7.4 and $K_V$7.5 heteromeric experiment and multiple $K_V$7.2 and $K_V$7.3 heteromeric experiments. These results include looking at expression systems involving the wildtype subunits and different mutant types responsible for a multitude of neurological disorders.

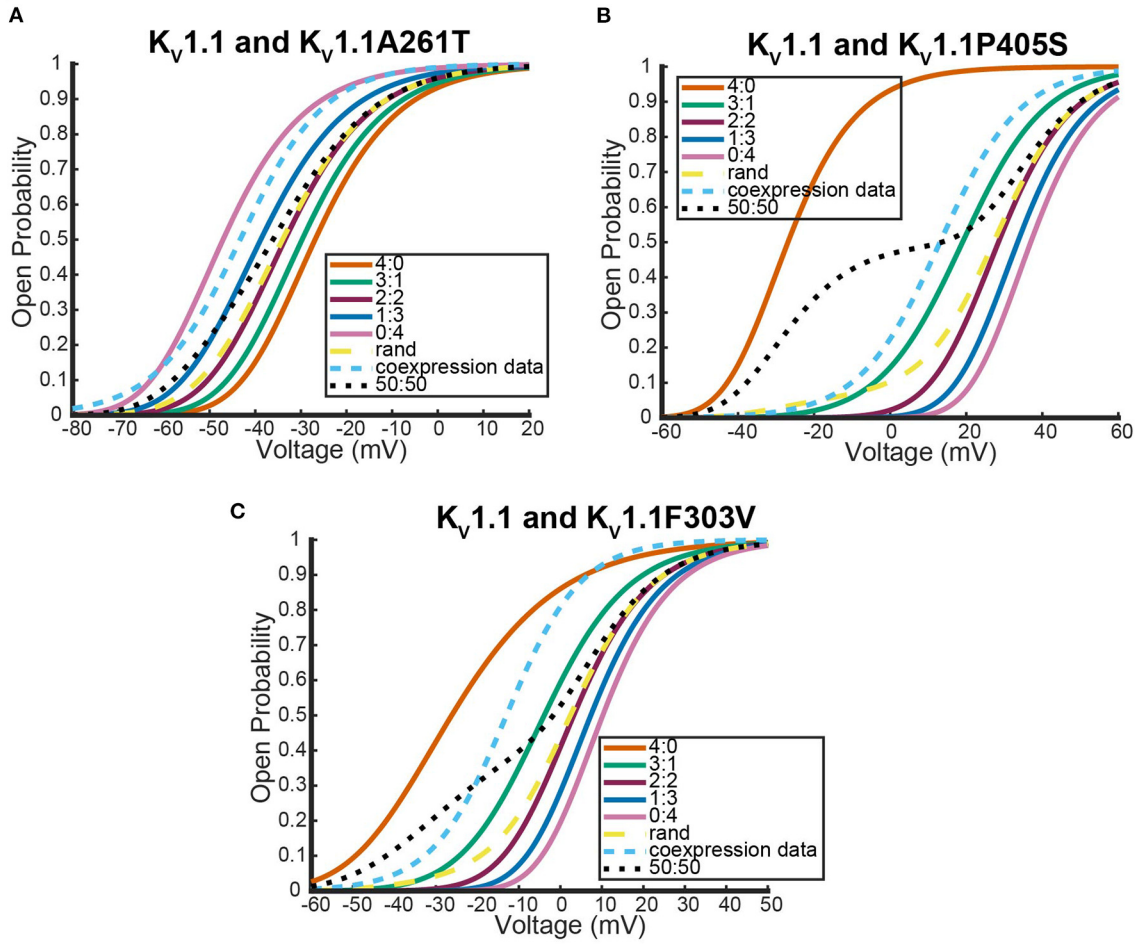


FIGURE 7
Steady state probability curves as a function of voltage for cells containing various channel types in three different experiments. The coexpression data and homomeric data for model fitting was taken from Miceli et al. (2022) **(A,B)** and Hasan et al. (2017) **(C)**. The steady state probability curves presented here are for homomeric $K_v$1.1 (4:0) and $K_v$1.1 mutant (0:4) channels, heteromeric assembly of $K_v$1.1 and $K_v$1.1 mutant subunits (3:1, 2:2, 1:3), the model output of a random assembly of $K_v$1.1 and $K_v$1.1 mutant subunits expressed in 50:50 ratio (rand), the data output of a 50:50 expression of $K_v$1.1 and mutant $K_v$1.1 subunits (coexpression data), and a model output of an equal split between only homomeric channels (50:50). Curve color and type are shown in the legends. Homomeric channels and their related heteromers being looked at are also detailed in figure titles.

### 3.2.1. $K_v$1.1, $K_v$1.2, and $K_v$1.1 mutant experiments

The first two experiments we looked at contain data for coexpression experiments with $K_v$1.1 and $K_v$1.2 wildtype DNA (D'Adamo et al., 1999; Imbrici et al., 2008).

Figure 6 shows where the coexpression probability curves lie in relation to model predictions for two different $K_v$1.1 and $K_v$1.2 experiments. In both experiments, we see the coexpression curve overlapping with the 2:2 heteromeric model prediction and the random assembly model prediction curves for a wide range of voltages. Although more data would be necessary to distinguish which curve the coexpression data most resembled, we show the model predicts that $K_v$1.1 and $K_v$1.2 subunits prefer to assemble in a 2:2 conformation or completely randomly. This result is in stark contrast to what happens when $K_v$1.1 subunits are coexpressed with a variety of different $K_v$1.1 mutant types. We looked at the following three neurological disease associated $K_v$1.1 mutants: F303V, A261T, and P405S (Hasan et al., 2017; Miceli et al., 2022).

Unlike the $K_v$1.1 and $K_v$1.2 wildtype coexpression experiments shown in Figure 6, we see in Figure 7 that each coexpression data curve does not overlap with the random assembly curves. In fact, for each mutant, the coexpression probability curves appear to have a preference for a conformation containing three subunits of one type and one of the other. It is important to observe that this preferred ratio is not always with three wildtype subunits as might be initially assumed. In the case of the $K_v$1.1 and

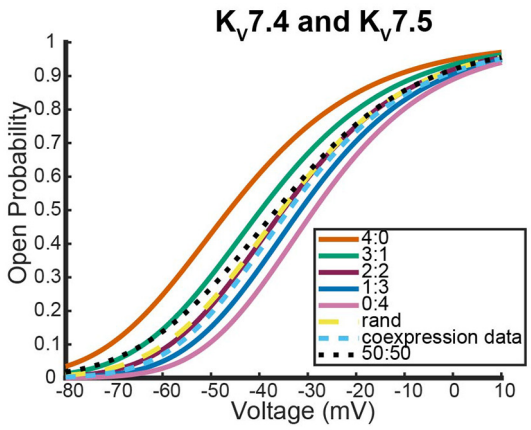


FIGURE 8
Steady state probability curves as a function of voltage for cells containing various channel types. The coexpression data and homomeric data for model fitting was taken from Mani et al. (2016). The steady state probability curves presented here are for homomeric $K_v$7.4 (4:0) and $K_v$7.5 (0:4) channels, heteromeric $K_v$7.4/7.5 channels (3:1, 2:2, 1:3), the model output of a random assembly of $K_v$7.4 and $K_v$7.5 subunits expressed in 50:50 ratio (rand), the data output of a 50:50 expression of $K_v$7.4 and $K_v$7.5 subunits (coexpression data), and a model output of an equal split between only homomeric channels (50:50). Curve color and type are shown in the legend. Homomeric channels and their related heteromers being looked at are also detailed in figure title.

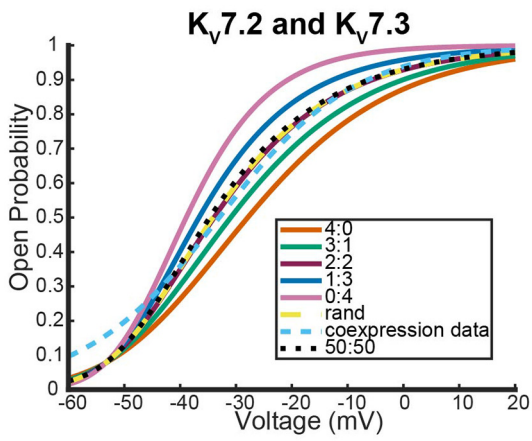


FIGURE 9
Steady state probability curves as a function of voltage for cells containing various channel types. The coexpression data and homomeric data for model fitting was taken from Miceli et al. (2015). The steady state probability curves presented here are for homomeric $K_v$7.2 (4:0) and $K_v$7.3 (0:4) channels, heteromeric $K_v$7.2/7.3 channels (3:1, 2:2,1:3), the model output of a random assembly of $K_v$7.2 and $K_v$7.3 subunits expressed in 50:50 ratio (rand), the data output of a 50:50 expression of $K_v$7.2 and $K_v$7.3 subunits (coexpression data), and a model output of an equal split between only homomeric channels (50:50). Curve color and type are shown in the legend. Homomeric channels and their related heteromers being looked at are also detailed in figure title.

$K_v$1.1*A261T* mutant coexpression data, the curve lies between the 0:4 mutant homomeric curve and the 1:3 heteromeric curve (Figure 7A). Meanwhile, the other mutant experiments both had coexpression data curves that were between the 4:0 wildtype homomeric and the 3:1 heteromeric curves (Figures 7C,D). While it is unclear why certain mutations would cause preferences for a 3:1 conformation and other mutations would prefer a 1:3 heteromic configuration; we highlight that in all cases the coexpression data lies between the heteromer and homomer curves that activate at the earliest voltages.

### 3.2.2. $K_v$7.4 and $K_v$7.5 experiments

Here we address the application of our model to a coexpression experiment by Mani et al. (2016) involving $K_v$7.4 and $K_v$7.5 DNA. Currently, there is no experiment similar to the work by Al-Sabi et al. (2013) for us to validate the heteromeric framework against for $K_v$7.4 and $K_v$7.5 heteromeric channels. However, both $K_v$7.4 and $K_v$7.5 form homomeric tetramers lacking noticeable inactivation thereby satisfying the necessary assumptions to be modeled identically to the $K_v$1.1 and $K_v$1.2 system (Lipinsky et al., 2020; Harding et al., 2022). Under the assumption that this framework is a reasonable approximation for $K_v$7.4 and $K_v$7.5 heteromers, we look at a coexpression experiment of $K_v$7.4 and $K_v$7.5 DNA done by Mani et al. (2016) with the results shown in Figure 8.

As was seen with the $K_v$1.1 and $K_v$1.2 wildtype experiments, the coexpression data overlaps with the 2:2 heteromer and the random assembly curves (Figure 8). This result is especially striking since it has been shown experimentally that unique characteristics of M-currents can be replicated with 2:2 $K_v$7.4 and $K_v$7.5 heteromers (Brueggemann et al., 2020).

### 3.2.3. $K_v$7.2, $K_v$7.3, and $K_v$7.2 mutant experiments

The final system we looked at that had similar coexpression experiments with wildtype heteromers that are not known to possess meaningful inactivation kinetics involved $K_v$7.2, $K_v$7.3, and $K_v$7.2 mutants (Lipinsky et al., 2020; Harding et al., 2022). The first data looked at were from a coexpression experiment between wildtype $K_v$7.2 and $K_v$7.3 to see how $K_v$7.2 heteromerizes (Miceli et al., 2015).

As was seen with the other two systems we looked at, expression of the two different wildtype DNAs results in a steady state probability curve that overlaps with the 2:2 and random assembly steady state probability curves for a large range of voltages (Figure 9). Once again, when we switched to coexpression experiments involving mutant subunit DNA the

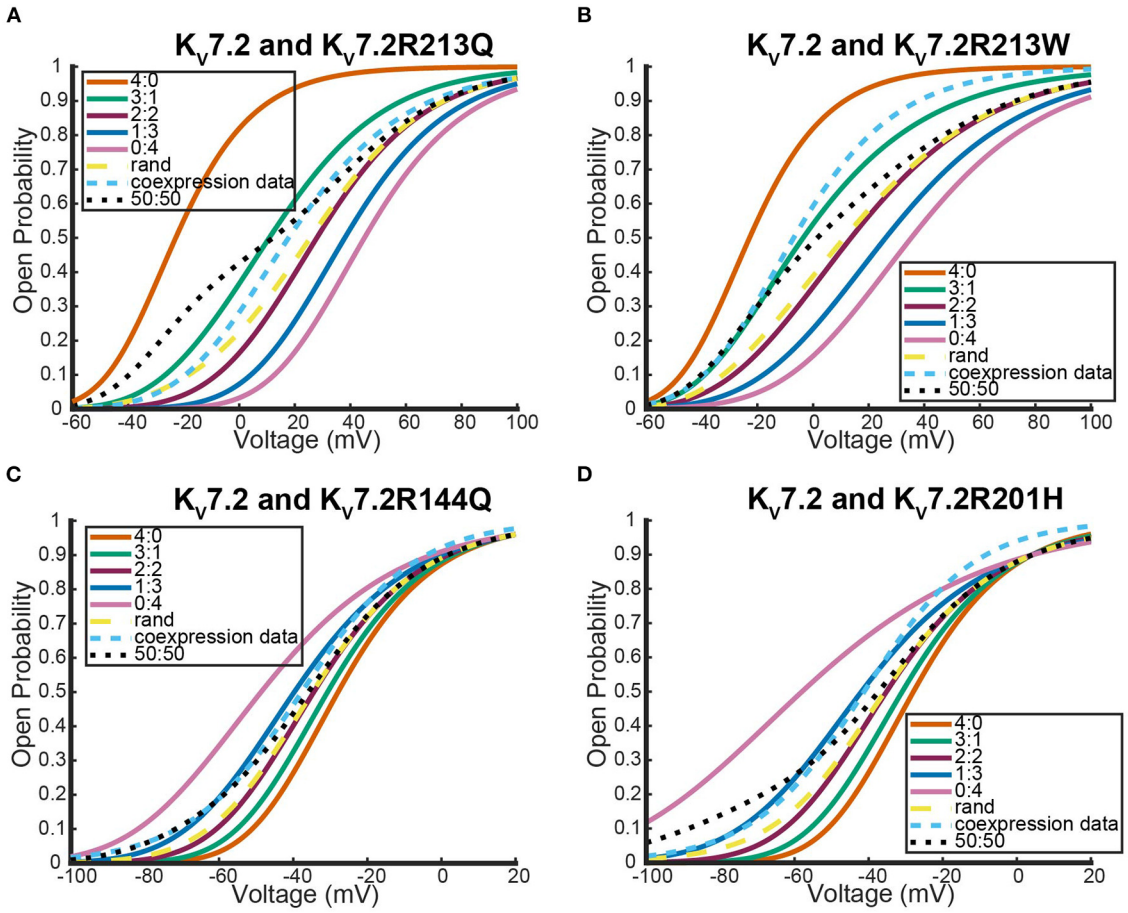


FIGURE 10
Steady state probability curves as a function of voltage for cells containing various channel types in four different experiments. The coexpression data and homomeric data for model fitting was taken from **(A,B)** Miceli et al. (2013) and **(C,D)** Miceli et al. (2015). The steady state probability curves presented here are for homomeric $K_V$7.2 (4:0) and $K_V$7.2 mutant (0:4) channels, heteromeric assembly of $K_V$7.2 and $K_V$7.2 mutant subunits (3:1, 2:2, 1:3), the model output of a random assembly of $K_V$7.2 and $K_V$7.2 mutant subunits expressed in 50:50 ratio (rand), the data output of a 50:50 expression of $K_V$7.2 and mutant $K_V$7.2 subunits (coexpression data), and a model output of an equal split between only homomeric channels (50:50). Curve color and type are shown in the legends. Homomeric channels and their related heteromers being looked at are also detailed in figure titles.

results were noticeably different. We looked at the coexpression of $K_V$7.2 and four different $K_V$7.2 mutants: R201H, R144Q, R213Q, and R213W (Miceli et al., 2013, 2015).

Interestingly, as was seen with $K_V$1.1 and its mutants, each $K_V$7.2 and $K_V$7.2 mutant coexpression experiment generated a steady state probability curve near or overlapping a curve corresponding to a 3 to 1 ratio of subunits. As before, this stoichiometric ratio of subunits is not a result of preference for wildtype subunits, but a preference toward activating at earlier or at more negative voltages. This is observable in Figures 10A,B by seeing that when the mutant subunit has a $V_{.5}$ to the right of the $V_{.5}$ of $K_V$7.2, the data lies near the 3:1 heteromer. On the other hand, if the mutant subunit has a more negative $V_{.5}$ than the $K_V$7.2 wildtype subunit, the data overlaps with the 1:3 heteromer (Figures 10C,D).

## 4. Discussion

Heteromeric $K_V$ channels have garnered significant attention in recent years. Some heteromers have been shown to be the specific target of conotoxins while other heteromers are hypothesized to be the primary cause of certain currents (Cordeiro et al., 2019; Brueggemann et al., 2020). This uptick in discoveries has resulted in an abundance of new questions about heteromers' importance, how their kinetic properties relate to homomeric channels, the subunit ratios in which they form, and if they are present in natural systems. Despite mechanistic differential equation modeling being a common technique for answering tough experimental neuroscience questions, little modeling of heteromeric $K_V$ channels has been done. Current modeling work for heteromeric experiments either

looks at different channel families or lacks the necessary known biological specificity (Cheng et al., 2007; Miceli et al., 2013, 2015; Benndorf et al., 2022).

Here we presented a novel heteromeric $K_V$ channel model framework that captures both $\alpha$-subunit number and type. We began by outlining and defending key model assumptions. We then examined the framework's effectiveness and ability to reproduce key observations using a $K_V1.1/1.2$ concatemer experiment. Finally, using results of various cDNA coexpression experiments, we used the model to make unique observations about the assembly of K-Channel $\alpha$-subunits and their preferences toward certain stoichiometries.

## 4.1. Model and assumptions

We have proposed a new model framework for heteromeric K-channels with little to no inactivation kinetics. The model stipulates that each $\alpha$-subunit present in the heteromer contributes one mathematical gate to the overall open probability. Equations for each gate type are derived from voltage clamp experiments performed on homomeric channels. With this model structure, once two homomers' steady state open probabilities are known, we can predict the kinetics for a heteromer with any ratio of these two homomers' subunits.

Key model assumptions were investigated and subsequently justified by comparing the framework to a Markov model and by analyzing time dependent voltage clamp data. To address our assumption that each subunit contributes one gate's worth of kinetics, we compared the Hodgkin-Huxley model with known ion channel Markov models. This analysis showed that for each ratio of subunits, our heteromeric model has a Markov model analog of four independently activating protein subunits that can switch between an open and closed state. Although the work here was done assuming each homomer is adequately modeled by four independent subunits that each have only two states, the only necessary condition for the model framework is subunit independence. For example, Markov models for homomeric potassium channels where each independent subunit has multiple closed states are given as possible models for $I_{Ks}$, the slow delayed rectifier $K^+$ current (Silva and Rudy, 2005; Keener, 2009). If a model of this type was required for one, or both, of the homomeric channels, it is possible to write a Markov model for 3:1, 2:2, and 1:3 heteromeric channels that still adhere to the one subunit to one "gate" hypothesis. In this case, the term "gate" is slightly misleading as the full Markov model no longer reduces to the Hodgkin and Huxley equations but something more complex. The derivation of the invariant manifold for the homomeric channel with subunits containing multiple closed states can be found in Keener (2009, 2010). Channels whose subunits undergo conformational changes in a cooperative manner break the independence assumption and therefore are not within the scope of the hypothesized model.

Continued exploration of the hypothesis that four gates are necessary and sufficient was done by using a publicly available database of voltage clamp experiments on $K_V1.1$ channels (Ranjan et al., 2011, 2019). Looking at multiple different cell voltage clamp recordings, each at multiple voltage steps, we showed that more than one gate is required to replicate the sigmoid shape of the time dependent data (Ranjan et al., 2011, 2019). We were unable to show that four gates provided the best overall fit to the data, but we did show that a single Hodgkin-Huxley like gating equation results in an exponential shape that cannot account for the delay of activation seen in the data (Figure 1). This observation is in agreement with previous work on $K_V1.4$ and $K_V11.1$ (hERG) channels that detailed the importance of including more than one gate, and in some cases more than one activating gate type (Wang et al., 1997; Bett et al., 2011). This question regarding the cause of the sigmoidicity of the data remains open and warrants future examination; but for future researchers using Hodgkin-Huxley like gating equations to model channel kinetics, we stress that the full time dependent data from voltage clamp experiments should be used to fit kinetic properties as this provides critical insight into the number of activating steps occurring.

## 4.2. $K_V1.1/1.2$ concatemeric experiment

To test the accuracy of our model, we used results from a study that looked at the open probability curves and TEA sensitivity of $K_V1.1/1.2$ concatemers (Al-Sabi et al., 2013). Using gating equations generated from the study's homomeric $K_V1.1$ and $K_V1.2$ steady state probability curves, we generated probability curves for each heteromic channel type (3:1, 2:2, and 1:3). The model outputs aligned well with the data, although the model predicts activation at earlier voltages than the data suggests. This result hints at either external factors influencing channel opening or a dependence between subunits. To verify this hypothesis, future studies should perform similar concatemeric experiments with other activating only heteromers to see if this behavior is standard across K-channel families.

The second result from comparisons to this experiment was how the model captured shifts in steady state probability curves as more $K_V1.2$ subunits were added. In the study it was observed there is a noticeably larger shift to activating later when transitioning from a $K^{4:0}_{1.1/1.2}$ homomer to a $K^{3:1}_{1.1/1.2}$ heteromer than when shifting from $K^{1:3}_{1.1/1.2}$ heteromer to a $K^{0:4}_{1.1/1.2}$ homomer (Al-Sabi et al., 2013). Our model shared this phenomenon, although it was more pronounced for the larger probabilities of opening.

A primary limitation for this particular analysis was data availability. Only summary parameters that generated the steady

state data curves were available and not the actual data itself. To combat this issue, we generated a few different fits to the homomeric steady state curve data and explored the newly fit models' performances. Here we presented two model extremes: one where the $K_V1.1$ and $K_V1.2$ homomeric model steady state curves were as close in slope factor ($k_{1.1}, k_{1.2}$) as possible, and the other where the slope factors were as far apart as possible. Only at the extreme where the homomeric slopes were fit to be far apart did the model framework begin to lose accuracy in both the steady state probability curves it generated and the spacing between said curves. In fact, heading toward the other extreme, slopes closer together, there was improvement in both heteromeric curve accuracy and the curve spacing accuracy. Thus, for a wide range of fitted homomeric model curves, our framework was able to mimic the steady state probability curves and the key observations about the relationship between them from Al-Sabi et al. (2013).

The second issue arising from a lack of data availability involved investigation of the time component of activation for these heteromeric concatemeric channels. In the work by Al-Sabi et al. (2013), time constants at a few select voltage values for all stoichiometric ratios are given. While this information could be used to fit a function of $\tau_n(V)$, the voltage dependent time constant, for the homomeric $K_v1.1$ and $K_V1.2$ models, there are issues drawing comparisons between the heteromeric time constants recorded in their work and model outputs. Under the proposed model, the heteromeric channels have two time components associated with their activation, one for each subunit type. This hypothesizes that the time course is the result of a double exponential and not the single exponential that was used to fit the heteromeric data. Therefore, there is no way to make direct comparisons between the model's prediction of the time constants of activation to the published time constant data. The limitations with the steady state analysis and with performing time constant analysis can both be resolved if the full time dependent voltage clamp data of the heteromeric channels is known. This then allows for direct comparisons between raw data and model outputs by simulating the heteromeric models through identical experimental protocols.

### 4.3. Coexpression experiments

We looked at three different systems of voltage gated potassium channels where DNA's for two different subunits, known to form heteromeric tetramers, were expressed in the same cell. By taking the steady state probability curves generated by the experiments and comparing them to our model's predictive outputs, we examined if certain subunits have preferred configurations and if so, what they are. With each of the different systems we studied, our model consistently predicted only two preferred configurations. The outcome was completely dependent on if the coexpression experiment was between two wildtype DNAs or if one DNA was for a mutant subunit responsible for certain neurological disorders.

If both cDNA's being expressed were wildtype, then the resulting coexpressed steady state probability curve overlapped the 2:2 heteromer and random assembly curves. As noted earlier, the inability to distinguish the coexpression curve from either of these curves is not surprising due to the coefficients in Equation (18). The model therefore predicts wildtype subunits assemble either with a preference toward the 2:2 configuration or, as has been suggested by some, random assembly with no stoichiometric preference (Miceli et al., 2013, 2015). More data and refined experimental techniques would be required to distinguish both mathematically and experimentally how precisely these wildtype subunits are assembling.

For each of the mutant coexpression experiments, the model indicates a clear preference away from the random assembly curve. In all cases the coexpression curve is found to be near a three to one subunit ratio curve where the three subunits correspond to whichever homomeric channel activates earlier. Critically, this predicts in some cases there is a preference toward channels assembling with more mutant subunits, while other mutations skew the assembly toward having one or fewer mutant subunits. This prediction could be the result of multiple different mechanisms. One possible mechanism is that upon 50–50 expression, the DNA is translated and transcribed equally, but not all subunit ratios form functional channels thereby weighting the steady state probability curve toward one side. A second option is the two DNA types are again translated and transcribed equally, but the proteins have a preferred ratio that they assemble in due to structure or compatibility. A third hypothesis for this outcome could be that the "translated and transcribed equally" assumption does not hold. Regardless of the mechanisms at play here, the model predicts that mutant and wildtype subunits for $K_v$ channels lacking inactivation kinetics assemble in a non-Bernoulli manner.

## 5. Conclusion

We have constructed a new mechanistic model framework for heteromeric voltage gated potassium channels. Based on justification of assumptions, model validation against known experimental results, and exploration of the possible questions the model can address; we claim this model is an excellent starting point for heteromeric $K_V$ channel models moving forward.

## Data availability statement

The datasets presented in this study can be found in online repositories. The names of the repository/repositories and accession number(s) can be found at: https://github.com/keesmcgahan/Heteromeric-K-Channels.

## Author contributions

KM: manuscript writing, model creation, model analysis, and coding. JK: manuscript editing, supervision, and guidance with model creation and analysis. All authors contributed to the article and approved the submitted version.

## Conflict of interest

The authors declare that the research was conducted in the absence of any commercial or financial relationships that could be construed as a potential conflict of interest.

## Publisher's note

All claims expressed in this article are solely those of the authors and do not necessarily represent those of their affiliated organizations, or those of the publisher, the editors and the reviewers. Any product that may be evaluated in this article, or claim that may be made by its manufacturer, is not guaranteed or endorsed by the publisher.

## References


Al-Sabi, A., Kaza, S. K., Dolly, J. O., and Wang, J. (2013). Pharmacological characteristics of Kv1. 1-and Kv1. 2-containing channels are influenced by the stoichiometry and positioning of their $\alpha$ subunits. *Biochem. J.* 454, 101–108. doi: 10.1042/BJ20130297

Barfield, J., Yeung, C., and Cooper, T. (2005). Characterization of potassium channels involved in volume regulation of human spermatozoa. *Mol. Hum. Reprod.* 11, 891–897. doi: 10.1093/molehr/gah208

Benndorf, K., Eick, T., Sattler, C., Schmauder, R., and Schulz, E. (2022). A strategy for determining the equilibrium constants for heteromeric ion channels in a complex model. *J. Gen. Physiol.* 154:e202113041. doi: 10.1085/jgp.202113041

Bett, G. C., Dinga-Madou, I., Zhou, Q., Bondarenko, V. E., and Rasmusson, R. L. (2011). A model of the interaction between N-type and C-type inactivation in Kv1. 4 channels. *Biophys. J.* 100, 11–21. doi: 10.1016/j.bpj.2010.11.011

Brueggemann, L. I., Cribbs, L. L., and Byron, K. L. (2020). Heteromeric channels formed from alternating Kv7. 4 and Kv7. 5 $\alpha$-subunits display biophysical, regulatory, and pharmacological characteristics of smooth muscle m-currents. *Front. Physiol.* 11:992. doi: 10.3389/fphys.2020.00992

Cheng, W., Yang, F., Takanishi, C. L., and Zheng, J. (2007). Thermosensitive trpv channel subunits coassemble into heteromeric channels with intermediate conductance and gating properties. *J. Gen. Physiol.* 129, 191–207. doi: 10.1085/jgp.200709731

Coetzee, W. A., Amarillo, Y., Chiu, J., Chow, A., Lau, D., McCormack, T., et al. (1999). Molecular diversity of K+ channels. *Ann. N.Y. Acad. Sci.* 868, 233–255. doi: 10.1111/j.1749-6632.1999.tb11293.x

Cordeiro, S., Finol-Urdaneta, R. K., Köpfer, D., Markushina, A., Song, J., French, R. J., et al. (2019). Conotoxin $\kappa$M-RIIIJ, a tool targeting asymmetric heteromeric Kv1 channels. *Proc. Natl. Acad. Sci. U.S.A.* 116, 1059–1064. doi: 10.1073/pnas.1813161116

D'Adamo, M. C., Imbrici, P., Sponcichetti, F., and Pessia, M. (1999). Mutations in the KCNA1 gene associated with episodic ataxia type-1 syndrome impair heteromeric voltage-gated K+ channel function. *FASEB J.* 13, 1335–1345. doi: 10.1096/fasebj.13.11.1335

Ghatta, S., Nimmagadda, D., Xu, X., and O'Rourke, S. T. (2006). Large-conductance, calcium-activated potassium channels: structural and functional implications. *Pharmacol. Therap.* 110, 103–116. doi: 10.1016/j.pharmthera.2005.10.007

Harding, S. D., Armstrong, J. F., Faccenda, E., Southan, C., Alexander, S. P., Davenport, A. P., et al. (2022). The IUPHAR/BPS guide to pharmacology in 2022: curating pharmacology for COVID-19, malaria and antibacterials. *Nucleic Acids Res.* 50, D1282-ŰD1294. doi: 10.1093/nar/gkab1010

Hasan, S., Bove, C., Silvestri, G., Mantuano, E., Modoni, A., Veneziano, L., et al. (2017). A channelopathy mutation in the voltage-sensor discloses contributions of a conserved phenylalanine to gating properties of Kv1. 1 channels and ataxia. *Sci. Rep.* 7, 1–13. doi: 10.1038/s41598-017-03041-z

Hodgkin, A. L., and Huxley, A. F. (1952). A quantitative description of membrane current and its application to conduction and excitation in nerve. *J. Physiol.* 117:500. doi: 10.1113/jphysiol.1952.sp004764

Imbrici, P., Gualandi, F., D'Adamo, M. C., Masieri, M. T., Cudia, P., De Grandis, D., et al. (2008). A novel KCNA1 mutation identified in an Italian family affected by episodic ataxia type 1. *Neuroscience* 157, 577–587. doi: 10.1016/j.neuroscience.2008.09.022

Keener, J., and Sneyd, J. (2009). *Mathematical Physiology 1: Cellular Physiology, Vol. 2*. New York, NY: Springer. doi: 10.1007/978-0-387-75847-3_1

Keener, J. P. (2009). Invariant manifold reductions for Markovian ion channel dynamics. *J. Math. Biol.* 58, 447–457. doi: 10.1007/s00285-008-0199-6

Keener, J. P. (2010). Exact reductions of markovian dynamics for ion channels with a single permissive state. *J. Math. Biol.* 60, 473–479. doi: 10.1007/s00285-009-0271-x

Lipinsky, M., Tobelaim, W. S., Peretz, A., Simhaev, L., Yeheskel, A., Yakubovich, D., et al. (2020). A unique mechanism of inactivation gating of the KV channel family member KV7. 1 and its modulation by PIP2 and calmodulin. *Sci. Adv.* 6:eabd6922. doi: 10.1126/sciadv.abd6922

MacKinnon, R. (2003). Potassium channels. *FEBS Lett.* 555, 62–65. doi: 10.1016/S0014-5793(03)01104-9

Mani, B. K., Robakowski, C., Brueggemann, L. I., Cribbs, L. L., Tripathi, A., Majetschak, M., et al. (2016). Kv7. 5 potassium channel subunits are the primary targets for PKA-dependent enhancement of vascular smooth muscle Kv7 currents. *Mol. Pharmacol.* 89, 323–334. doi: 10.1124/mol.115.101758

MATLAB (2018). *9.7.0.1190202 (R2019b)*. Natick, MA: The MathWorks Inc..

McGahan, K., and Keener, J. (2020). A mathematical model analyzing temperature threshold dependence in cold sensitive neurons. *PLoS ONE* 15:e0237347. doi: 10.1371/journal.pone.0237347

Miceli, F., Guerrini, R., Nappi, M., Soldovieri, M. V., Cellini, E., Gurnett, C. A., et al. (2022). Distinct epilepsy phenotypes and response to drugs in KCNA1 gain-and loss-of function variants. *Epilepsia* 63, e7Űe14. doi: 10.1111/epi.17118

Miceli, F., Soldovieri, M. V., Ambrosino, P., Barrese, V., Migliore, M., Cilio, M. R., et al. (2013). Genotype-phenotype correlations in neonatal epilepsies caused by mutations in the voltage sensor of Kv7. 2 potassium channel subunits. *Proc. Natl. Acad. Sci. U.S.A.* 110, 4386–4391. doi: 10.1073/pnas.1216867110

Miceli, F., Soldovieri, M. V., Ambrosino, P., De Maria, M., Migliore, M., Migliore, R., et al. (2015). Early-onset epileptic encephalopathy caused by gain-of-function mutations in the voltage sensor of Kv7. 2 and Kv7. 3 potassium channel subunits. *J. Neurosci.* 35, 3782–3793. doi: 10.1523/JNEUROSCI.4423-14.2015

Miura, R. M. (2002). Analysis of excitable cell models. *J. Comput. Appl. Math.* 144, 29–47. doi: 10.1016/S0377-0427(01)00550-7

Moreno, J. D., Lewis, T. J., and Clancy, C. E. (2016). Parameterization for *in-silico* modeling of ion channel interactions with drugs. *PLoS ONE* 11:e0150761. doi: 10.1371/journal.pone.0150761

Nekouzadeh, A., Silva, J. R., and Rudy, Y. (2008). Modeling subunit cooperativity in opening of tetrameric ion channels. *Biophys. J.* 95, 3510–3520. doi: 10.1529/biophysj.108.136721

Perissinotti, L. L., Guo, J., De Biase, P. M., Clancy, C. E., Duff, H. J., and Noskov, S. Y. (2015). Kinetic model for NS1643 drug activation of WT and L529I variants of Kv11. 1 (HERG1) potassium channel. *Biophys. J.* 108, 1414–1424. doi: 10.1016/j.bpj.2014.12.056

Ranjan, R., Khazen, G., Gambazzi, L., Ramaswamy, S., Hill, S. L., Schürmann, F., et al. (2011). Channelpedia: an integrative and interactive database for ion channels. *Front. Neuroinform*. 5:36. doi: 10.3389/fninf.2011.00036

Ranjan, R., Logette, E., Marani, M., Herzog, M., Tâche, V., Scantamburlo, E., et al. (2019). A kinetic map of the homomeric voltage-gated potassium channel (Kv) family. *Front. Cell. Neurosci*. 13:358. doi: 10.3389/fncel.2019.00358

Sale, H., Wang, J., O'Hara, T. J., Tester, D. J., Phartiyal, P., He, J.-Q., et al. (2008). Physiological properties of hERG 1a/1b heteromeric currents and a hERG 1b-specific mutation associated with long-QT syndrome. *Circul. Res*. 103, e81–e95. doi: 10.1161/CIRCRESAHA.108.185249

Silva, J., and Rudy, Y. (2005). Subunit interaction determines I KS participation in cardiac repolarization and repolarization reserve. *Circulation* 112, 1384–1391. doi: 10.1161/CIRCULATIONAHA.105.543306

Wang, S., Liu, S., Morales, M. J., Strauss, H. C., and Rasmusson, R. L. (1997). A quantitative analysis of the activation and inactivation kinetics of hERG expressed in xenopus oocytes. *J. Physiol*. 502(Pt 1):45. doi: 10.1111/j.1469-7793.1997.045bl.x

frontiers | Frontiers in Cellular Neuroscience

TYPE Original Research
PUBLISHED 23 February 2023
DOI 10.3389/fncel.2023.1126577



OPEN ACCESS

EDITED BY
Junhui Wang,
University of Toronto, Canada

REVIEWED BY
Maryam Ardalan,
University of Gothenburg, Sweden
Kazuhiko Yamamuro,
Nara Medical University, Japan

*CORRESPONDENCE
Bradley S. Peterson
✉ bpeterson@chla.usc.edu

SPECIALTY SECTION
This article was submitted to Cellular Neuropathology, a section of the journal Frontiers in Cellular Neuroscience

RECEIVED 18 December 2022
ACCEPTED 06 February 2023
PUBLISHED 23 February 2023

CITATION
Peterson BS, Kaur T, Sawardekar S, Colibazzi T, Hao X, Wexler BE and Bansal R (2023) Aberrant hippocampus and amygdala morphology associated with cognitive deficits in schizophrenia.
*Front. Cell. Neurosci.* 17:1126577.
doi: 10.3389/fncel.2023.1126577



# Aberrant hippocampus and amygdala morphology associated with cognitive deficits in schizophrenia

Bradley S. Peterson[1]*, Tejal Kaur[2], Siddhant Sawardekar[1], Tiziano Colibazzi[2], Xuejun Hao[2], Bruce E. Wexler[3] and Ravi Bansal[1]

[1]Children's Hospital Los Angeles, Department of Psychiatry at the Keck School of Medicine, University of Southern California, Los Angeles, CA, United States, [2]Department of Psychiatry, Columbia College of Physicians and Surgeons, New York, NY, United States, [3]Department of Psychiatry, Yale University School of Medicine, New Haven, CT, United States

**Background:** Working memory deficits are thought to be a primary disturbance in schizophrenia. We aimed to identify differences in morphology of the hippocampus and amygdala in patients with schizophrenia compared with healthy controls (HCs), and in patients who were either neuropsychologically near normal (NPNN) or neuropsychologically impaired (NPI). Morphological disturbances in the same subfields of the hippocampus and amygdala, but of greater magnitude in those with NPI, would strengthen evidence for the centrality of these limbic regions and working memory deficits in the pathogenesis of schizophrenia.

**Methods:** We acquired anatomical MRIs in 69 patients with schizophrenia (18 NPNN, 46 NPI) and 63 age-matched HC participants. We compared groups in hippocampus and amygdala surface morphologies and correlated morphological measures with clinical symptoms and working memory scores.

**Results:** Schizophrenia was associated with inward deformations of the head and tail of the hippocampus, protrusion of the hippocampal body, and widespread inward deformations of the amygdala. In the same regions where we detected the effects of schizophrenia, morphological measures correlated positively with the severity of symptoms and inversely with working memory performance. Patients with NPI displayed a similar pattern of anatomical abnormality compared to patients with NPNN.

**Conclusion:** Our findings indicate that anatomical abnormalities of the hippocampus relate to working memory performance and clinical symptoms in persons with schizophrenia. Moreover, NPNN and NPI patients may lie on a continuum of severity, both in terms of working memory abilities and altered brain structure, with NPI patients being more severe than NPNN patients in both domains.

KEYWORDS

**amygdala, schizophrenia, MRI, biomarker, endophenotype, working memory, hippocampus**

## 1. Introduction

Symptoms of psychosis and cognitive deficits are the hallmarks of schizophrenia. Cognitive deficits in particular contribute to enduring functional impairments in persons with this illness (Green et al., 2004; Leifker et al., 2009). Working memory, one of the cognitive domains most affected in schizophrenia, involves the temporary storage of information within temporoparietal regions and the manipulation of that information by the dorsolateral prefrontal cortex (Baddeley, 1992; Barch, 2006; Lett et al., 2014). Evidence from animal (Yoon et al., 2008; Colgin, 2011; Gordon, 2011), fMRI (Karlsgodt et al., 2005; Anticevic et al., 2012), and electrophysiological (Benchenane et al., 2011) studies demonstrate that the maintenance and manipulation of information in working memory tasks relies on the integration of activity within the prefrontal cortex and hippocampus.

We previously reported that individuals with schizophrenia, compared to healthy control (HC) participants, have smaller volumes of white matter in regions underlying temporal, parietal, and sensorimotor cortices, and that these abnormalities increase in proportion to the degree of working memory deficits (Palmer et al., 1997; Colibazzi et al., 2013). Because 20–25% of patients across multiple studies display normal or near normal scores on tests of cognition that include working memory (Palmer et al., 1997; Weickert et al., 2000; Seaton et al., 2001), we further divided our patient group into those who were neuropsychologically near normal (NPNN) and those who were neuropsychologically impaired (NPI). We found that white matter abnormalities in NPI individuals were similar to, but more extensive than, those in the NPNN group, suggesting that NPI and NPNN test performance may represent a continuum of illness severity rather than differing neurobiological subtypes of illness.

Because corticolimbic circuits support working memory abilities (Karlsgodt et al., 2005; Benchenane et al., 2011; Colgin, 2011; Gordon, 2011; Anticevic et al., 2012), we now assess morphological characteristics of the hippocampus and amygdala in NPI and NPNN individuals relative to HC participants. NPNN persons could differ from NPI persons in either the magnitude or in the location of anatomical abnormalities within limbic regions of working memory circuits. Differing anatomical locations of disturbance would suggest differing underlying pathogenic mechanisms across groups. Similar anatomical locations in both NPI and NPNN individuals, but with differing magnitudes of anatomical disturbance, would suggest either similarities in pathogenic mechanism for these individuals or similarities in a common final pathway that contributes to working memory deficits.

Working memory deficits are prevalent in multiple neuropsychiatric disorders, but they are thought to be a primary disturbance in schizophrenia. Few studies (Colibazzi et al., 2013), however, have correlated working memory performance with disturbances in the same brain regions where we detect the effect of schizophrenia diagnosis, and therefore scant evidence directly supports the centrality of working memory in the pathogenesis of schizophrenia. However, if the degree of anatomical abnormalities identified in patients compared to HC participants are also associated with the severity of working memory deficits, that finding would support the centrality of working memory in the pathogenesis of schizophrenia.

Limbic regions, particularly the hippocampus, are thought to play a critical role in the pathogenesis of schizophrenia. Neuroimaging studies have detected abnormalities of the hippocampus in individuals with schizophrenia (Csernansky et al., 2002; Velakoulis et al., 2006; Vita et al., 2006; Mattai et al., 2011; Prestia et al., 2014), their unaffected family members (Tepest et al., 2003; Ho and Magnotta, 2010), and in persons at clinical high risk for schizophrenia (Velakoulis et al., 2006; Schobel et al., 2009), suggesting that these abnormalities predate illness and are not simply a consequence of being ill. They are therefore strong candidates for an endophenotype in schizophrenia (Gottesman and Gould, 2003). Abnormalities of the anterior hippocampus have been associated with positive symptoms and may predict the development of schizophrenia in putatively prodromal individuals (Schobel et al., 2009). Animal models support the theory that abnormal activity of the anterior hippocampus, with aberrant modulation from the basolateral amygdala, could contribute to abnormalities downstream within a circuit that includes the striatum and cortex (Sah et al., 2003; Lodge and Grace, 2008, 2011). In an animal model, these circuit-based abnormalities correlate with working memory performance (Li et al., 2011). However, to our knowledge, no prior studies in humans have reported correlations between structural abnormality of subregions of the hippocampus or amygdala with measures of working memory.

A previous study in our cohort of persons with schizophrenia reported differences between patient and HC groups in overall volumes of the hippocampus and amygdala. Deformation-based surface measures can detect variation within subregions of brain structures, however, and they therefore have greater sensitivity and regional specificity when assessing group differences in brain structure than total volume measures (Peterson, 2010). We therefore have applied these deformation-based methods to assess group differences within the hippocampus and amygdala and their correlations with working memory abilities. We hypothesized that we would detect significant morphological abnormalities of the hippocampus and amygdala in individuals with schizophrenia relative to HC participants, that these abnormalities in NPI participants would be similar to, but more extensive than, abnormalities in the NPNN participants, and that the magnitude of these abnormalities would correlate significantly with deficits of working memory and clinical symptoms of psychosis.

## 2. Methods and materials

We included 69 patients with schizophrenia (18 NPNN and 46 NPI) and 63 healthy age-matched control participants. Patients with schizophrenia were recruited from the Clinic at the Yale in New Haven, Connecticut. Control participants were randomly recruited from a list of 10,000 names purchased from a telemarketing company who were in the age range and lived in the same zip code area as patients with schizophrenia. Written informed consent was obtained for all the participants. Approval for the study was provided by the Human Investigation Committee of the Yale School of Medicine (New Haven) and by the institutional review board of the New York State Psychiatric Institute

(New York). All patients met The Diagnostic and Statistical Manual of Mental Disorders (DSM)-IV criteria for a diagnosis of schizophrenia. Exclusion criteria for healthy participants included a history of axis I disorders, heavy substance use within the last 5 years, or neurological illness. Additional exclusion criteria for both groups included any previous seizure, head trauma with loss of consciousness, current or previous substance abuse, or intelligence quotient (IQ) below 70. Diagnoses were established through evaluation using the Schedule for Affective Disorders and Schizophrenia (Endicott and Spitzer, 1978) and a best-estimate consensus procedure that considered all available study materials and medical records. Symptom severities at the time of the study were assessed by doctoral level psychologists with established interrater reliability using the Positive and Negative Symptom Scale for Schizophrenia (Kay, 1990). All but three patients had been in treatment for over 5 years, most had been hospitalized more than three times (but none had been hospitalized within the 3 months preceding the study). None had abused substances for at least 60 days, and all had been taking their current medications for at least 30 days.

## 2.1. Definition of subgroups

As in our previous study, the patient group was divided into two subgroups based on neuropsychological performance on four serial position tasks (SPT), which assessed verbal and non-verbal working memory using four types of stimuli: words; easily named sounds, such as a ringing telephone; birdsongs; and snowflake designs (French et al., 2003). One group was considered NPI on the basis of overall scores on all four tests that were more than 1.0 SD below the mean of HC (NPI, $n = 46$). The second group was considered NPNN on the basis of overall working memory scores within 0.5 SD of the HC mean (NPNN, $n = 18$). These tests were selected for subgroup definition because patients with schizophrenia have been shown in previous studies to perform particularly poorly on these tasks, and because deficits in working memory in general, and verbal memory in particular, are among the most consistent and robust cognitive deficits in schizophrenia (Kay, 1990; French et al., 2003). We have previously validated the subgroups by comparing them to each other and to HC participants on the California Verbal Learning Test and a degraded stimulus continuous performance test, two tests widely used to demonstrate cognitive deficits in people with schizophrenia (LeDoux, 2007). In our sample of 76 patients, five were not classified as either NPNN or NPI because neuropsychological data were not available.

## 2.2. Clinical measures

Length of illness was a best-estimate judgment based on the patient's report of the first appearance of symptoms or functional compromise related to the clinical features of schizophrenia (e.g., hallucinations, delusional thinking, paranoid fears, social withdrawal, decline in school, or work performance), first hospitalization, and history of illness as documented in reports related to initial hospitalizations. When insufficient information was available, no duration was assigned. Severity of illness was measured using the Positive and Negative Syndrome Scale (PANSS) (Lee et al., 2004). PANSS scores were available for 46 of the 69 patients in our sample. The two patient subgroups did not differ substantially in clinical symptoms (**Table 1**) or medication status (**Table 2**) (French et al., 2003).

## 2.3. MRI scanning and image pre-processing

MRI scans were obtained using a Siemens Sonata 1.5 Tesla scanner (Siemens, AG, Erlangen, Germany). Head positioning was standardized using canthomeatal landmarks. Anatomical images were acquired using a 3D MP-RAGE sequence (repetition time, 24 msec; echo time, 2.96 msec; 45° flip angle; 256 × 192 matrix; field of view, 30 cm; 2 excitations, slice thickness 1.2 mm; 124 contiguous slices encoded for sagittal slice reconstruction with voxel dimensions of 1.17 mm × 1.17 mm × 1.2 mm).

We corrected large-scale variations in image intensity using a validated algorithm developed at the Montreal Neurological Institute (Sled et al., 1998). We removed extracerebral tissues using an automated tool for extracting the brain (Shattuck and Leahy, 2002). Connecting dura was then removed manually on each slice in the sagittal view and checked in the orthogonal views. The brainstem was transected at the pontomedullary junction. We measured whole brain volume (WBV) for use as a covariate to control for global scaling effects in statistical analyses of conventional volumes. This measure included not only gray and white matter but also cerebrospinal fluid within the ventricles and cortical sulci to ensure the exclusion of any possible confound of age-related effects of tissue atrophy with this general measure of body scaling (Skullerud, 1985).

## 2.4. Hippocampus and amygdala morphology

Methods for defining the hippocampus and the amygdala followed previously published algorithms (Kates et al., 1997). The hippocampus and amygdala were traced manually on Sun Ultra 10 workstations using ANALYZE 8.0 software (Biomedical Imaging Resource, Mayo Foundation, Rochester, MN, USA), together with software developed in-house, while blind to participant characteristics and hemisphere (images were randomly flipped in the transverse plane before pre-processing and then reversed prior to statistical analysis) (Plessen et al., 2006). The rostral extent of the amygdala coincided with the most anterior section in which the anterior commissure crossed the midline. We determined the transition between the amygdala and hippocampus by a line connecting the inferior horn of the lateral ventricle with the amygdaloid sulcus or, when the sulcus was not obvious, with a straight horizontal line connecting the inferior horn of the lateral ventricle with the surface on the uncus (Watson et al., 1992). The most posterior section was the last section in which the crus of the fornix and the fimbria of the hippocampal formation could be delineated.

Our previously validated procedures for surface analysis (Bansal et al., 2007) were customized to accommodate independent

TABLE 1 Demographic and clinical characteristics of study participants.

| Characteristic | Patients ($N$ = 69) | Healthy controls ($N$ = 63) | df | $F/T$ or $\chi^2$ | $P$-value | NPI ($N$ = 46) | NPNN ($N$ = 18) | df | $F/T$ or $\chi^2$ | $P$-value |
|---|---|---|---|---|---|---|---|---|---|---|
| Age | 42.3 (8.6) | 32.9 (11.1) | 131 | 29.4 | **<0.001** | 43.3 (8.9) | 35.6 (8.2) | 63 | 2.3 | 0.138 |
| Sex (M:F) | (45:24) | (31:32) | 1 | 3.46 | 0.063 | 28:18 | 15:3 | 1 | 2.96 | 0.085 |
| Education | 13.0 (2.4) | 15.9 (4.7) | 103 | 17.0 | **0.001** | 12.7 (2.3) | 13.7 (2.3) | 58 | 2.56 | 0.115 |
| Minority/Caucasian ($N$) | 27:42 | 11:52 | 1 | 7.54 | **0.006** | 17:29 | 7:11 | 1 | 0.021 | 0.886 |
| Duration of illness (years) | | | | | | 18.4 (8.4) | 18.0 (8.7) | 59 | 0.025 | 0.874 |
| Chlorpromazine equivalents (mg) | | | | | | 692.3 (626.5) | 676.0 (471.6) | 46 | 0.008 | 0.928 |
| PANSS scores | | | | | | | | | | |
| Positive | | | | | | 14.8 (5.7) | 15.23 (6.0) | 40 | 0.039 | 0.845 |
| Negative | | | | | | 16.4 (6.6) | 15.2 (5.1) | 40 | 0.35 | 0.558 |
| midrule General | | | | | | 31.7 (11.4) | 31.97 (8.7) | 40 | 0.005 | 0.943 |
| Total | | | | | | 62.9 (20.9) | 62.4 (16.4) | 40 | 0.007 | 0.935 |
| Working memory index | | | | | | 72.7 (3.8) | 51.3 (10.2) | 61 | 74.7 | **<0.001** |

*P*-values that are statistically significant at a significance level of 0.05 are indicated in bold.

TABLE 2 Psychotropic medication at the time of MRI scan.

| Antipsychotic medication | NPI ($n$ = 46) | NPNN ($n$ = 18) |
|---|---|---|
| Any antipsychotic medication | 43 | 16 |
| Typical | 17 | 3 |
| Atypical | 32 | 15 |
| Typical + atypical | 6 | 2 |
| Missing data | 2 | 0 |

analysis of the right and left hippocampus and amygdala. Briefly, a rigid-body similarity transformation with global scaling was used to register the entire brain of each participant with the template brain, thereby inherently controlling for WBV in all subsequent measurements. Each region (right and left hippocampus and amygdala) was then rigidly coregistered to the corresponding template region. This second transformation created a refined registration by which to compare surfaces of isolated regions. Each region was warped to the corresponding region of the template using a high-dimensional, non-rigid warping algorithm based on the principles of fluid-flow dynamics. Warping permitted point-to-point matching of the surfaces of the regions for each participant with the surfaces of the corresponding regions in the template brain. The high-dimensionally warped images were then unwarped to the refined affine registration, while maintaining the point-to-point correspondences established by the non-linear warping. These point correspondences permitted calculation of the signed Euclidean distance of each surface point from the corresponding point on the surface of the template region. Euclidean distances were compared statistically across groups to identify areas of protrusion or indention, from which we infer underlying increases or decreases in volume, respectively, along the surface of each amygdala and hippocampus.

Boundaries of subfields of the hippocampus and nuclei of the amygdala of the template brain were estimated using a modified version of a digital brain atlas (Chakravarty et al., 2006) with a widely used parcellation scheme and nomenclature (Hirai and Jones, 1989). The atlas was registered to the four template structures (right and left hippocampus and amygdala) using a 3-dimensional non-linear transformation based on voxel intensity. After smoothing this image manually, a simplified outline of the hippocampal subfields and amygdala nuclei, respectively, were overlaid on the respective template structures to aid localization of findings to individual subfields or nuclei.

## 2.5. Selection of the template brain

As we have done previously, we used a single representative brain as a template rather than an averaged brain from many participants, because a single brain has sharp borders at the cerebrospinal fluid (CSF)-gray matter or gray matter-white matter interface that improve the accuracy of registration (Plessen et al., 2006; Bansal et al., 2007; Amat et al., 2008). Averaging images for a template blurs these boundaries and increases registration errors that are important when distinguishing subtle effects across

populations. In addition, precise surface morphometry requires a brain with smooth gray and white matter surfaces that are devoid of topological defects, which cannot be reconstructed by averaging brains from many individuals. This technique produces group differences that are independent of the specific template chosen.

To select the most appropriate, representative template brain for surface morphometry, we first selected as a preliminary template brain the HC participant whose age and overall brain size were nearest the average of all participants. The brains of the remaining participants were coregistered to this preliminary template, the point correspondences across their surfaces were identified as detailed above, and the distances of those points from the corresponding points on the preliminary template surface were calculated. The brain for which all points across its surface were closest, in the least squares sense, to the average of the distances across those points for the entire sample was selected as the final template because it was morphologically most representative of all brains in the cohort.

## 2.6. Statistical analyses

Analyses of conventional volumes were performed using SPSS version 17.0. We used a repeated measures analysis of variance over a spatial domain (the amygdala and hippocampus). The model included the within-participant factors of hemisphere with two levels (left and right) and region with two levels (amygdala and hippocampus). Diagnosis was a between-participants factor. Covariates included sex, age, and WBV. Similar analyses were repeated using only the patient group with diagnosis defined instead as NPI or NPNN. The model was determined through a procedure in which all main effects were forced into the model and higher-order terms were removed *via* backward stepwise selection with the constraint that the model was hierarchically well-formulated at each step.

For analyses of surface morphological features, we used linear regression at each voxel on the surface of each structure to compare across groups the signed Euclidean distances from points on the surfaces of the amygdala and hippocampus in each participant to the corresponding points on the surface of the respective reference structure. We applied a false discovery rate (FDR) correction threshold of $P < 0.05$ and color-coded probability values at each voxel across the surface of the reference structures. In all statistical analyses we covaried for age, age$^2$, sex, and minority status (Caucasian or anything other than Caucasian).

# 3. Results

Socio-demographic and clinical characteristics of the groups are provided in Table 1. Patients compared with HCs were on average older, had fewer years of education, and were more likely to be an ethnic minority. We therefore included minority status and age, as well as age$^2$ and sex, as covariates in all statistical analyses. We did not include years of education as a covariate, however, because the fewer year of education in patients with schizophrenia was a consequence of their illness, and therefore co-varying for it would risk eliminating the primary effect of interest, group differences in regional morphology between HC participants and patients with schizophrenia. The NPI and NPNN groups were similar in age, sex, education, and minority status, as well as in the severity of clinical symptoms, length of illness, and chlorpromazine equivalents of medication use (Table 2).

## 3.1. Conventional volumes

After adjusting for age, sex, minority status, and WBV, overall volumes of the hippocampus, and amygdala differed significantly between the patient and HC groups ($F_{127} = 56.2$; $p = 0.0001$) (Table 3). Overall volumes did not significantly differ between NPI and NPNN. We did not detect a significant interaction between either region (amygdala or hippocampus) and diagnosis, or between hemisphere and diagnosis. The mean ± SD WBV did not differ appreciably across diagnostic group (patients: 4,898 ± 53.5 cm$^3$; controls: 4,821 ± 56.3 cm$^3$; $F_{131} = 0.87$; $p = 0.35$), but did differ between NPI and NPNN participants (NPI: 4,908 ± 45.7 cm$^3$; NPNN: 5,107 ± 74.3 cm$^3$; $F_{63} = 5.04$; $p = 0.029$). Neither the severity of clinical symptoms nor the working memory index correlated with overall volumes.

## 3.2. Surface analyses

We detected significant diagnosis effects as inward deformations in the head and tail of the hippocampus, protrusion of the hippocampal body, and diffuse inward deformations of the amygdala (Figure 1A). We detected similar patterns of group differences when we compared NPI and NPNN separately to HC participants (Figures 1B, C). However, the NPI compared to NPNN group had greater inward deformations of the head and tail, as well as greater protrusion of the body of the hippocampus

TABLE 3 Overall volumes of the hippocampus and amygdala.

| Conventional volumes | Patients ($n$ = 69) vs. Controls ($n$ = 63)* | | NPI ($n$ = 46) vs. NPNN ($n$ = 18) | |
|---|---|---|---|---|
| Whole brain[a] (cc) | 4,898 ± 53.5 | 4,821 ± 56.3 | 4,908 ± 45.7 | 5,107 ± 74.3 |
| Right hippocampus[b] (mm$^3$) | 2,929.5 ± 47.8 | 3,212.5 ± 50.3 | 3,098.0 ± 102.5 | 2,943.4 ± 61.9 |
| Left hippocampus[b] (mm$^3$) | 2,945.3 ± 50.8 | 3,201.4 ± 53.5 | 3,068.9 ± 99.5 | 2,978.5 ± 60.1 |
| Right amygdala[b] (mm$^3$) | 1,561.0 ± 41.1 | 1,961.8 ± 43.2 | 1,564.5 ± 52.3 | 1,595.3 ± 31.6 |
| Left amygdala[b] (mm$^3$) | 1,553.0 ± 39.7 | 2,025.1 ± 41.9 | 1,562.6 ± 48.2 | 1,600.1 ± 29.1 |

[a]Mean value is corrected for age and sex.
[b]All mean values are corrected for age, sex, and whole brain volume (WBV). *Overall volumes of the hippocampus and amygdala differed significantly between the patient and HC groups ($F_{127} = 56.2$; $P < 0.0001$).

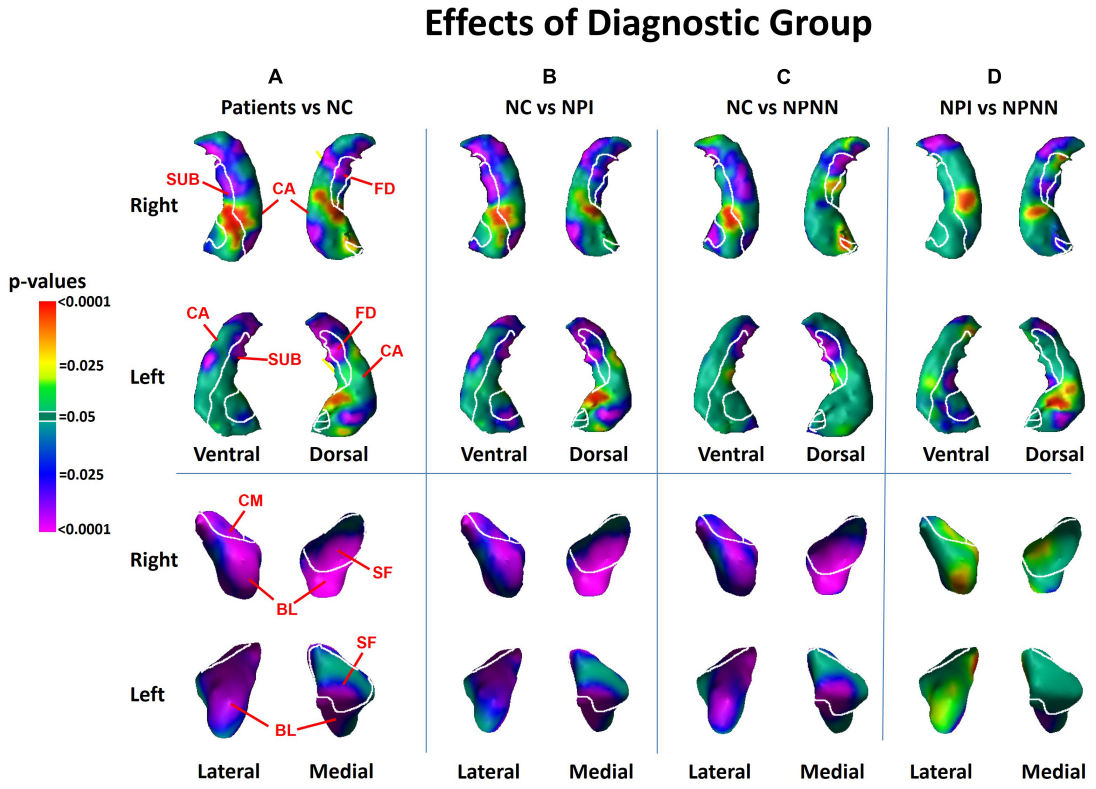


FIGURE 1
Main effects of diagnostic group on surface morphologic features. The right and left hippocampus are shown in their dorsal and ventral perspectives. The right and left amygdala are shown in their lateral and medical perspectives. The cytoarchitectonic map overlies the structures. At each point on the hippocampal amygdala surface, the statistical significance (probability values) of differences in surface morphology across risk-groups are color coded. The color bar indicates the color coding for *P*-values associated with the main effect of diagnostic group, with warmer colors (yellow and red) indicating protruding surfaces, presumably from larger underlying volumes, and cooler colors (blue and purple) indicating indented surfaces and presumably smaller underlying volumes in those regions. *P*-values are thresholded at $P < 0.05$ after correction for multiple comparisons using false discovery rate (FDR). The statistical model included the main effect of diagnostic group, and the covariates of age, age$^2$, sex, and minority status. Statistical maps for the differences in surface morphology of the hippocampus and amygdala are shown for **(A)** individuals with schizophrenia vs. healthy control (HC); **(B)** neuropsychologically impaired (NPI) vs. HC; **(C)** neuropsychologically near normal (NPNN) vs. HC; and **(D)** NPI vs. NPNN. CA, cornu ammonis; FD, fascia dentata; SUB, subiculum; SF, superficial nucleus; CM, centromedial nucleus; BL, basolateral nucleus.

(Figure 1D). The NPI compared to NPNN group also had a greater indentation in the ventral aspect of the left amygdala, but an attenuated indentation in the ventral posterior aspect of the left amygdala (Figure 1D). We detected several significant correlations of surface measures with symptom severity and working memory performance within the schizophrenia patients. Worse performance on working memory tasks accompanied inward deformation of the head and tail, and protrusion of the body, of the hippocampus (Figure 2A) in similar regions where we detected the effects of diagnosis (patient group compared to HC).

More severe positive symptoms accompanied inward deformation of the head and tail and protrusion of the body of the hippocampus, and more severe negative symptoms accompanied inward deformation of the tail (Figure 2B), all in regions close to those where we detected the effects of diagnosis. We detected an inverse association of both positive symptoms with surface measures at the lateral aspect of the basolateral nucleus (BL) of the amygdala (Figure 2B), and of negative symptoms with surface measures at the medial aspect of the superficial nucleus (Figure 2C), such that greater severity of positive and negative symptoms accompanied larger inward deformations. We also detected a positive association of working memory performance with surface measures of the medial aspect of the superficial nucleus. None of the cognitive or clinical associations with the surface of the amygdala overlapped with regions where we detected the effect of diagnosis.

The effects of medication use (chlorpromazine equivalents of antipsychotic medication at time of MRI scan) and length of illness both consisted of predominant inward deformations of the head, body and tail of the hippocampus bilaterally and of the left lateral amygdala (Figure 3). The effect of medication and chronicity of illness overlapped with the regions where we detected diagnosis effects. However, the effect of diagnosis on the surface measures of the hippocampus and amygdala remained similar even after including medication and chronicity of illness as covariates in our statistical analyses. Furthermore, within the hippocampus, the pattern of group differences when we compared NPI to NPNN was similar to the main effect of diagnosis (patients vs. HC) (Figure 1D), even though NPI and NPNN did not differ in length of illness or chlorpromazine equivalents (Tables 1, 2).

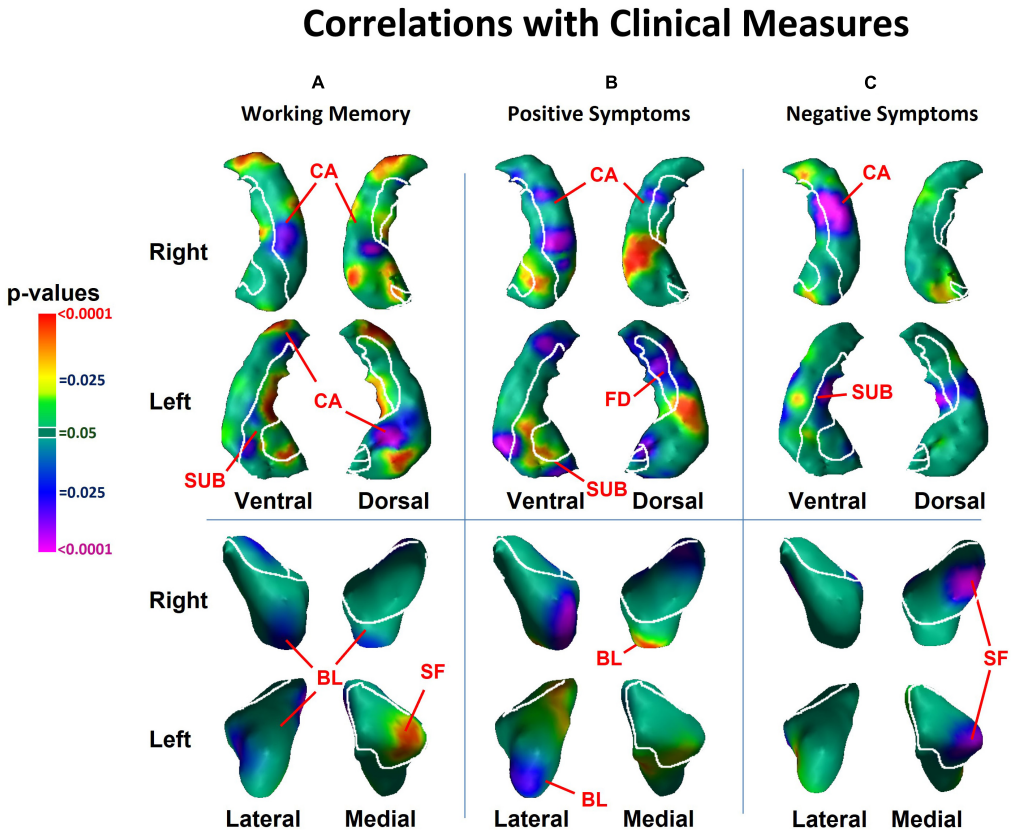


FIGURE 2
Associations with surface morphology of the hippocampus and amygdala for clinical measures of **(A)** working memory performance, **(B)** positive psychosis symptom severity, and **(C)** negative psychosis symptom severity. Here, working memory scores are inverted so that higher scores indicate greater deficits in working memory. Higher values of positive and negative symptoms indicate greater clinical symptoms. The cytoarchitectonic map overlies the structures. CA, cornu ammonis; FD, fascia dentata; SUB, subiculum; SF, superficial nucleus; CM, centromedial nucleus; BL, basolateral nucleus.

## 4. Discussion

This is, to our knowledge, the first study to assess the associations of morphological abnormalities in hippocampus and amygdala subfields with working memory deficits in persons who have schizophrenia. Our findings collectively and strongly suggest that both the morphological disturbances and working memory deficits are tightly linked and are central to the pathogenesis of schizophrenia. We demonstrated that individuals with schizophrenia compared to HCs had inward deformations in the head and tail of the hippocampus, protrusion of the hippocampal body, and diffuse inward deformations of the amygdala. The locations of abnormalities were similar in NPNN and NPI participants, despite the NPNN participants having relatively normal cognitive abilities. However, the NPI participants had a greater magnitude of morphological abnormalities compared to NPNN participants. We previously reported that the NPI and NPNN groups displayed a similar pattern of white matter abnormalities within the cortex, but with NPI participants showing greater magnitude of structural abnormality as well as greater degree of working memory deficits (Colibazzi et al., 2013). Taken together with these previous findings, our current findings suggest that NPI and NPNN participants lie on a continuum of severity in terms of both the magnitude of neuroanatomical disturbance and cognitive ability, with those who are NPI being more severe in both domains.

We also found that the magnitude of clinical symptoms and working memory deficits associated positively with surface deformations in similar locations within the hippocampus where we identified group differences between patients and HC. Worse working memory performance accompanied inward deformations of the head and tail, and outward deformation of the body, of the hippocampus. Similarly, more severe positive symptoms accompanied inward deformation of the head and tail and protrusion of the body of the hippocampus, and more severe negative symptoms accompanied inward deformation of the tail. Most of the associations of symptom measures and working memory performance with surface measures of the hippocampus occurred in regions where we detected group differences between patients and HCs. Within the amygdala, greater severity of positive symptoms accompanied larger inward deformations of the lateral aspect of the BL, and negative symptoms accompanied larger inward deformations of the medial aspect of the superficial nucleus. Because the associations of clinical and neurocognitive measures with surface measures of the hippocampus were located in similar portions of the hippocampus where we detected differences between patients and HC, our findings suggest that an increasing magnitude of neuroanatomical abnormalities within the

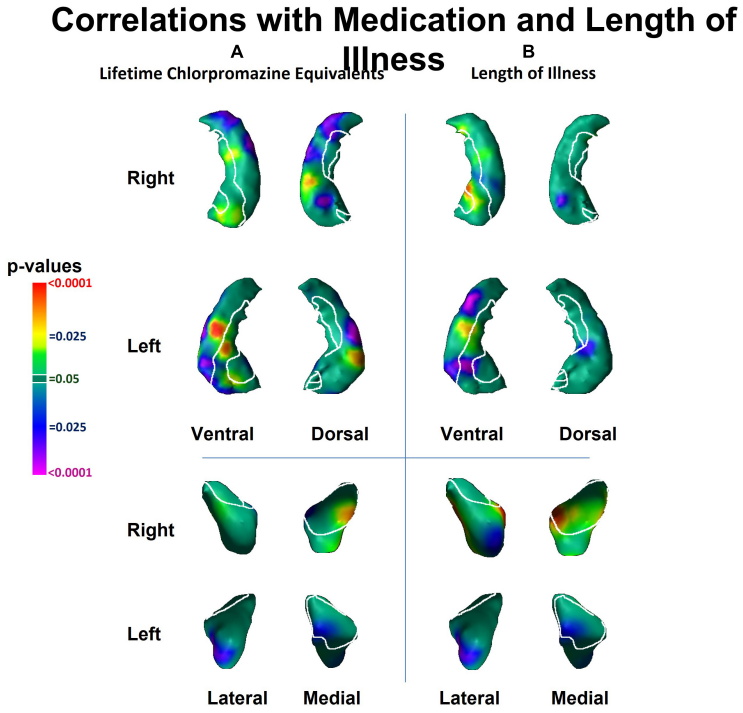


FIGURE 3
Associations of lifetime chlorpromazine equivalents and of length of illness with surface morphology of the hippocampus and amygdala. Statistical maps for the association of panel **(A)** lifetime chlorpromazine equivalents and **(B)** length of illness with surface morphological measures (Euclidian distances) of the hippocampus and amygdala. The effects of medication and lifetime illness on surface measures overlapped with the regions of the hippocampus and the amygdala where we detected diagnosis effects (**Figure 1**).

hippocampus may contribute to the cognitive deficits and clinical symptoms of schizophrenia. However, future studies that include individuals at high-risk for psychosis are necessary to test whether these neuroanatomical abnormalities precede and likely contribute to the genesis of frank psychosis, or whether they are a consequence of psychotic illness or its treatment. Furthermore, even if NPI and NPNN share similar structural abnormalities, it is possible that these abnormalities are the common downstream consequences of differing etiologic pathways.

## 4.1. Hippocampus subfields

We detected inward deformations in the head and tail, and protrusion in the body, of the hippocampus in persons with schizophrenia compared to HCs. The magnitude of positive symptoms and working memory deficits associated significantly with the structural abnormalities we detected along the head, body and tail of the hippocampus in the cornu ammonis (CA), fascia dentata (FD), and subiculum (SUB) subfields, whereas the magnitude of negative symptoms associated significantly with the structural abnormalities along the body and tail of the hippocampus in the CA and FD subfields.

Each hippocampus subfield participates in a distinct component of learning and memory, with the SUB supporting memory retrieval, the FD and CA3 classifying those memories into patterns ("pattern separation"), the CA3 completing the recognition of those patterns in relation to stored memories ("pattern completion"), and the CA1 integrating these inputs within the hippocampus (Small et al., 2011). Disturbances in these components of learning and memory could lead to errors when categorizing stimuli, thereby generating delusional or hallucinatory symptoms (Corlett et al., 2009; Tamminga et al., 2010). Whereas positive symptoms and working memory performance accompanied anatomical abnormalities of the FD, CA, and SUB, the specificity of negative symptoms to FD and CA, but not to the SUB, could suggest that negative symptoms relate more to difficulties in recognizing and completing patterns than to disturbances in memory retrieval.

Our finding that negative and positive symptoms and working memory performance were associated with distinct subregions of the hippocampus likely also reflects the regional distinctions in function along the longitudinal axis of the hippocampus. The anterior portion projects prominently to medial prefrontal and orbitofrontal cortices, as well as to the amygdala, and is thought to support the emotional content of cognitive processes (Fanselow and Dong, 2010). The posterior portion of the hippocampus projects to the anterior cingulate, posterior cingulate, and retrosplenial cortices, which together support primarily the non-emotional components of memory (Bast and Feldon, 2003; Fanselow and Dong, 2010). Our findings that working memory performance and positive symptoms accompany surface abnormalities of both the head and tail, suggest that emotional and cognitive processes likely contribute to both working memory performance and positive symptoms, a conclusion supported by prior studies (Yang et al., 2013). In contrast, negative symptoms correlated with

surface measures in the tail and body, perhaps because negative symptoms may associate with primarily cognitive, rather than emotional components of information processing. These and other interpretations are testable hypotheses for future studies that are informed by our neuroanatomical findings.

Our finding that hippocampus dysfunction accompanies symptoms of psychosis and neurocognitive deficits is consistent with prior studies. Both animal models and human research suggest that hypermetabolism of the anterior hippocampus may drive downstream disturbances in dopamine release in the striatum (Lodge and Grace, 2008, 2011) that are thought to generate symptoms of psychosis and contribute to cognitive deficits (Seaton et al., 2001; Howes et al., 2011). Increased cerebral blood volume (CBV) in the anterior hippocampus in CA1 reportedly associates with positive symptoms in both individuals with schizophrenia and those prodromal for psychosis (Schobel et al., 2009). Human studies and animal models suggest that the initial increase in CBV in CA1 spreads to the SUB during the onset of psychosis and appears to predate hippocampal atrophy (Schobel et al., 2013). Studies using surface measures have also detected inward deformations of the hippocampal head (Csernansky et al., 2002; Tepest et al., 2003; Narr et al., 2004; Ho and Magnotta, 2010; Johnson et al., 2013) and tail (Lee et al., 2004; Styner et al., 2004), as well as protrusion of the CA regions (Mamah et al., 2012) in individuals with schizophrenia, and one of these studies has correlated these findings with the severity of positive symptoms (Zierhut et al., 2013). Our study extends prior findings because we detected associations of working memory and clinical symptoms with surface measures in similar regions of the hippocampus where we detected group differences between patients and HC, suggesting that the neural correlates in the hippocampus of working memory, and of positive and negative symptoms, likely contribute to the pathogenesis of schizophrenia.

## 4.2. Amygdala subfields

We detected indentations throughout the amygdala in individuals with schizophrenia, in regions overlying all the major nuclei. The locations of abnormalities were similar in NPNN and NPI participants, but the NPI, compared to NPNN, group had larger indentations in the ventral aspect of the left amygdala, and attenuated indentation in the ventral posterior aspect of the left amygdala. In contrast to the diffuse abnormalities detected as group differences, we also detected associations with symptom measures in specific subregions. Surface measures of the basolateral nuclei associated significantly with positive symptoms, and the superficial nuclei associated significantly with negative symptoms, such that greater symptom severity accompanied greater magnitude of inward deformation.

Together, the basolateral and superficial nuclei subserve the comprehension of social context and the modulation of affective states with goal-directed actions. The basolateral nuclei project reciprocally to widespread cortical and subcortical regions that receive sensory input for social cues and that govern behaviors guided by these sensory stimuli (Amaral, 2002; Sah et al., 2003; LeDoux, 2007; Amaral et al., 2008). The basolateral nuclei of the amygdala and CA at the head of the hippocampus project reciprocally to one another (French et al., 2003). Dysfunction of the basolateral nuclei has been theorized to contribute to GABAergic dysfunction of the hippocampus (French et al., 2003; Sesack and Grace, 2010) and could modulate the emergence of positive symptoms. The superficial nuclei selectively extracts the social from non-social value of incoming sensory cues, particularly in the processing of facial expressions (Bzdok et al., 2012), abnormalities in which could lead to negative psychotic symptoms. Impairments in these capacities could produce social and functional deficits that contribute to the clinical symptoms that often characterize schizophrenia. Surface measures of subregions of the amygdala associated significantly with clinical symptoms and cognitive deficits, even though these same regions did not overlap with the subregions where we detected differences between patient and control groups, suggesting perhaps that these morphological features may modulate the severity of clinical symptoms and cognitive deficits but are unlikely to be central in causing schizophrenia.

## 4.3. Limitations and future directions

The primary limitation of our study is that we cannot distinguish the causes from consequences of illness in a sample of already ill individuals (Horga et al., 2014). Moreover, the effects of length of illness and lifetime medication on surface measures overlapped with the regions in which we detected the effect of diagnosis, suggesting that the effects of chronic illness and medication could contribute to our findings. However, because we continue to detect an effect of diagnosis when co-varying for medication and illness chronicity, our findings likely are present above and beyond simply the effects of chronic illness or stress. Moreover, we detected similar group differences between NPNN and NPI participants as we did between patients and HC, even though length of illness and chlorpromazine equivalents did not differ between NPNN and NPI. Therefore, our findings suggest that the pattern of inward deformation in the head and tail and protrusion in the body that we detected as an effect of diagnosis is not simply a consequence of illness. Furthermore, studies using surface analyses that include unaffected siblings of persons with schizophrenia also detect inward deformations of the anterior hippocampus (Tepest et al., 2003; Ho and Magnotta, 2010; Johnson et al., 2013), suggesting that surface deformations are not simply due to illness chronicity or medication exposure, but could be a vulnerability marker or endophenotype for schizophrenia. Subsequent longitudinal studies correlating surface measures with clinical and cognitive domains in unaffected individuals who are at high-risk for schizophrenia are necessary to distinguish whether our findings predate illness and contribute to generation of symptoms or whether they represent the consequence of illness. Future studies are also necessary to understand whether the cognitive deficits of NPNN and NPI participants precede illness or arise during illness or its treatment, and whether those cognitive deficits correspond longitudinally to anatomical changes in the brain.

# Data availability statement

The raw data supporting the conclusions of this article will be made available by the authors, without undue reservation.

## Ethics statement

The studies involving human participants were reviewed and approved by the Yale School of Medicine and the New York State Psychiatric Institute. The patients/participants provided their written informed consent to participate in this study.

## Author contributions

BP, BW, and RB: conceptualization and methodology. RB and XH: software. BP, SS, XH, and RB: image processing. BP, TK, TC, BW, and RB: statistical analysis. BP and BW: assessments and funding acquisition. BP, TK, BW, and RB: writing – original draft preparation. BP, TK, TC, BW, XH, and RB: writing – review and editing. All authors contributed to the article and approved the submitted version.

## Funding

This work was supported in part by the NIMH grants 5R01MH056642, 5R01MH068318-04, K02MH074677, and T32-16434, the Suzanne Crosby Murphy Endowment at Columbia University, and by an anonymous donor to Children's Hospital Los Angeles, Patrice and Mike Harmon, and the Robert Coury family. None of the funding sources were involved in the design and conduct of the study; collection, management, analysis, and interpretation of the data; and preparation, review, or approval of the manuscript.

## Acknowledgments

This research was made possible by the provision of data by the New York State Psychiatric Institute and Columbia University.

## Conflict of interest

The authors declare that the research was conducted in the absence of any commercial or financial relationships that could be construed as a potential conflict of interest.

## Publisher's note



## References

Amaral, D. G. (2002). The primate amygdala and the neurobiology of social behavior: Implications for understanding social anxiety. *Biol. Psychiatry* 51, 11–17.

Amaral, D. G., Schumann, C. M., and Nordahl, C. W. (2008). Neuroanatomy of autism. *Trends Neurosci.* 31, 137–145. doi: 10.1016/j.tins.2007.12.005

Amat, J. A., Bansal, R., Whiteman, R., Haggerty, R., Royal, J., and Peterson, B. S. (2008). Correlates of intellectual ability with morphology of the hippocampus and amygdala in healthy adults. *Brain Cogn.* 66, 105–114. doi: 10.1016/j.bandc.2007.05.009

Anticevic, A., Repovs, G., Krystal, J. H., and Barch, D. M. (2012). A broken filter: Prefrontal functional connectivity abnormalities in schizophrenia during working memory interference. *Schizophr. Res.* 141, 8–14. doi: 10.1016/j.schres.2012.07.007

Baddeley, A. (1992). Working memory. *Science* 255, 556–559.

Bansal, R., Staib, L. H., Xu, D., Zhu, H., and Peterson, B. S. (2007). Statistical analyses of brain surfaces using Gaussian random fields on 2-D manifolds. *IEEE Trans. Med. Imaging* 26, 46–57. doi: 10.1109/TMI.2006.884187

Barch, D. M. (2006). What can research on schizophrenia tell us about the cognitive neuroscience of working memory? *Neuroscience* 139, 73–84. doi: 10.1016/j.neuroscience.2005.09.013

Bast, T., and Feldon, J. (2003). Hippocampal modulation of sensorimotor processes. *Prog. Neurobiol.* 70, 319–345.

Benchenane, K., Tiesinga, P. H., and Battaglia, F. P. (2011). Oscillations in the prefrontal cortex: A gateway to memory and attention. *Curr. Opin. Neurobiol.* 21, 475–485. doi: 10.1016/j.conb.2011.01.004

Bzdok, D., Laird, A. R., Zilles, K., Fox, P. T., and Eickhoff, S. B. (2012). An investigation of the structural, connectional, and functional subspecialization in the human amygdala. *Hum. Brain Mapp.* 34, 3247–3266. doi: 10.1002/hbm.22138

Chakravarty, M. M., Bertrand, G., Hodge, C. P., Sadikot, A. F., and Collins, D. L. (2006). The creation of a brain atlas for image guided neurosurgery using serial histological data. *Neuroimage* 30, 359–376. doi: 10.1016/j.neuroimage.2005.09.041

Colgin, L. L. (2011). Oscillations and hippocampal-prefrontal synchrony. *Curr. Opin. Neurobiol.* 21, 467–474. doi: 10.1016/j.conb.2011.04.006

Colibazzi, T., Wexler, B. E., Bansal, R., Hao, X., Liu, J., Sanchez-Pena, J., et al. (2013). Anatomical abnormalities in gray and white matter of the cortical surface in persons with schizophrenia. *PLoS One* 8:e55783. doi: 10.1371/journal.pone.0055783

Corlett, P. R., Krystal, J. H., Taylor, J. R., and Fletcher, P. C. (2009). Why do delusions persist? *Front. Hum. Neurosci.* 3:12. doi: 10.3389/neuro.09.012.2009

Csernansky, J. G., Wang, L., Jones, D., Rastogi-Cruz, D., Posener, J. A., Heydebrand, G., et al. (2002). Hippocampal deformities in schizophrenia characterized by high dimensional brain mapping. *Am. J. Psychiatry* 159, 2000–2006.

Endicott, J., and Spitzer, R. L. (1978). A diagnostic interview: The schedule for affective disorders and schizophrenia. *Arch. Gen. Psychiatry* 35, 837–844.

Fanselow, M. S., and Dong, H. W. (2010). Are the dorsal and ventral hippocampus functionally distinct structures? *Neuron* 65, 7–19. doi: 10.1016/j.neuron.2009.11.031

French, S. J., Hailstone, J. C., and Totterdell, S. (2003). Basolateral amygdala efferents to the ventral subiculum preferentially innervate pyramidal cell dendritic spines. *Brain Res.* 981, 160–167. doi: 10.1016/s0006-8993(03)03017-8

Gordon, J. A. (2011). Oscillations and hippocampal-prefrontal synchrony. *Curr. Opin. Neurobiol.* 21, 486–491. doi: 10.1016/j.conb.2011.02.012

Gottesman, I. I., and Gould, T. D. (2003). The endophenotype concept in psychiatry: Etymology and strategic intentions. *Am. J. Psychiatry* 160, 636–645.

Green, M. F., Kern, R. S., and Heaton, R. K. (2004). Longitudinal studies of cognition and functional outcome in schizophrenia: Implications for MATRICS. *Schizophr. Res.* 72, 41–51. doi: 10.1016/j.schres.2004.09.009

Hirai, T., and Jones, E. G. (1989). A new parcellation of the human thalamus on the basis of histochemical staining. *Brain Res. Brain Res. Rev.* 14, 1–34. doi: 10.1016/0165-0173(89)90007-6

Ho, B. C., and Magnotta, V. (2010). Hippocampal volume deficits and shape deformities in young biological relatives of schizophrenia probands. *Neuroimage* 49, 3385–3393. doi: 10.1016/j.neuroimage.2009.11.033

Horga, G., Kaur, T., and Peterson, B. S. (2014). Annual research review: Current limitations and future directions in MRI studies of child- and adult-onset developmental psychopathologies. *J. Child Psychol. Psychiatry* 55, 659–680. doi: 10.1111/jcpp.12185

Howes, O., Bose, S., Turkheimer, F., Valli, I., Egerton, A., Stahl, D., et al. (2011). Progressive increase in striatal dopamine synthesis capacity as patients develop psychosis: A PET study. *Mol. Psychiatry* 16, 885–886. doi: 10.1038/mp.2011.20

Johnson, S. L., Wang, L., Alpert, K. I., Greenstein, D., Clasen, L., Lalonde, F., et al. (2013). Hippocampal shape abnormalities of patients with childhood-onset schizophrenia and their unaffected siblings. *J. Am. Acad. Child Adolesc. Psychiatry* 52, 527–536.e2. doi: 10.1016/j.jaac.2013.02.003

Karlsgodt, K. H., Shirinyan, D., van Erp, T. G., Cohen, M. S., and Cannon, T. D. (2005). Hippocampal activations during encoding and retrieval in a verbal working memory paradigm. *Neuroimage* 25, 1224–1231. doi: 10.1016/j.neuroimage.2005.01.038

Kates, W. R., Abrams, M. T., Kaufmann, W. E., Breiter, S. N., and Reiss, A. L. (1997). Reliability and validity of MRI measurement of the amygdala and Hippocampus in children with fragile X syndrome. *Psychiatry Res.* 75, 31–48. doi: 10.1016/s0925-4927(97)00019-x

Kay, S. R. (1990). Positive-negative symptom assessment in schizophrenia: Psychometric issues and scale comparison. *Psychiatr. Q.* 61, 163–178. doi: 10.1007/BF01064966

LeDoux, J. (2007). The amygdala. *Curr. Biol.* 17, R868–R874. doi: 10.1016/j.cub.2007.08.005

Lee, J. M., Kim, S. H., Jang, D. P., Ha, T. H., Kim, J. J., Kim, I. Y., et al. (2004). Deformable model with surface registration for hippocampal shape deformity analysis in schizophrenia. *Neuroimage* 22, 831–840. doi: 10.1016/j.neuroimage.2004.02.004

Leifker, F. R., Bowie, C. R., and Harvey, P. D. (2009). Determinants of everyday outcomes in schizophrenia: The influences of cognitive impairment, functional capacity, and symptoms. *Schizophr. Res.* 115, 82–87. doi: 10.1016/j.schres.2009.09.004

Lett, T. A., Voineskos, A. N., Kennedy, J. L., Levine, B., and Daskalakis, Z. J. (2014). Treating working memory deficits in schizophrenia: A review of the neurobiology. *Biol. Psychiatry* 75, 361–370. doi: 10.1016/j.biopsych.2013.07.026

Li, Y. C., Kellendonk, C., Simpson, E. H., Kandel, E. R., and Gao, W. J. (2011). D2 receptor overexpression in the striatum leads to a deficit in inhibitory transmission and dopamine sensitivity in mouse prefrontal cortex. *Proc. Natl. Acad. Sci. U.S.A.* 108, 12107–12112. doi: 10.1073/pnas.1109718108

Lodge, D. J., and Grace, A. A. (2008). Hippocampal dysfunction and disruption of dopamine system regulation in an animal model of schizophrenia. *Neurotox. Res.* 14, 97–104. doi: 10.1007/BF03033801

Lodge, D. J., and Grace, A. A. (2011). Hippocampal dysregulation of dopamine system function and the pathophysiology of schizophrenia. *Trends Pharmacol. Sci.* 32, 507–513. doi: 10.1016/j.tips.2011.05.001

Mamah, D., Harms, M. P., Barch, D., Styner, M., Lieberman, J. A., and Wang, L. (2012). Hippocampal shape and volume changes with antipsychotics in early stage psychotic illness. *Front. Psychiatry* 3:96. doi: 10.3389/fpsyt.2012.00096

Mattai, A., Hosanagar, A., Weisinger, B., Greenstein, D., Stidd, R., Clasen, L., et al. (2011). Hippocampal volume development in healthy siblings of childhood-onset schizophrenia patients. *Am. J. Psychiatry* 168, 427–435. doi: 10.1176/appi.ajp.2010.10050681

Narr, K. L., Thompson, P. M., Szeszko, P., Robinson, D., Jang, S., Woods, R. P., et al. (2004). Regional specificity of hippocampal volume reductions in first-episode schizophrenia. *Neuroimage* 21, 1563–1575. doi: 10.1016/j.neuroimage.2003.11.011

Palmer, B. W., Heaton, R. K., Paulsen, J. S., Kuck, J., Braff, D., Harris, M. J., et al. (1997). Is it possible to be schizophrenic yet neuropsychologically normal? *Neuropsychology* 11, 437–446.

Peterson, B. S. (2010). Form determines function: New methods for identifying the neuroanatomical loci of circuit-based disturbances in childhood disorders. *J. Am. Acad. Child Adolesc. Psychiatry* 49, 533–538. doi: 10.1016/j.jaac.2010.03.010

Plessen, K. J., Bansal, R., Zhu, H., Whiteman, R., Amat, J., Quackenbush, G. A., et al. (2006). Hippocampus and amygdala morphology in attention-deficit/hyperactivity disorder. *Arch. Gen. Psychiatry* 63, 795–807.

Prestia, A., Cavedo, E., Boccardi, M., Muscio, C., Adorni, A., Geroldi, C., et al. (2014). Hippocampal and amygdalar local structural differences in elderly patients with schizophrenia. *Am. J. Geriatr. Psychiatry* 23, 47–58. doi: 10.1016/j.jagp.2014.01.006

Sah, P., Faber, E. S., Lopez De Armentia, M., and Power, J. (2003). The amygdaloid complex: Anatomy and physiology. *Physiol. Rev.* 83, 803–834. doi: 10.1152/physrev.00002.2003

Schobel, S. A., Chaudhury, N. H., Khan, U. A., Paniagua, B., Styner, M. A., Asllani, I., et al. (2013). Imaging patients with psychosis and a mouse model establishes a spreading pattern of hippocampal dysfunction and implicates glutamate as a driver. *Neuron* 78, 81–93. doi: 10.1016/j.neuron.2013.02.011

Schobel, S. A., Lewandowski, N. M., Corcoran, C. M., Moore, H., Brown, T., Malaspina, D., et al. (2009). Differential targeting of the CA1 subfield of the hippocampal formation by schizophrenia and related psychotic disorders. *Arch. Gen. Psychiatry* 66, 938–946. doi: 10.1001/archgenpsychiatry.2009.115

Seaton, B. E., Goldstein, G., and Allen, D. N. (2001). Sources of heterogeneity in schizophrenia: The role of neuropsychological functioning. *Neuropsychol. Rev.* 11, 45–67.

Sesack, S. R., and Grace, A. A. (2010). Cortico-Basal Ganglia reward network: Microcircuitry. *Neuropsychopharmacology* 35, 27–47. doi: 10.1038/npp.2009.93

Shattuck, D. W., and Leahy, R. M. (2002). BrainSuite: An automated cortical surface identification tool. *Med. Image Anal.* 6, 129–142. doi: 10.1016/s1361-8415(02)00054-3

Skullerud, K. (1985). Variations in the size of the human brain. Influence of age, sex, body length, body mass index, alcoholism, Alzheimer changes, and cerebral atherosclerosis. *Acta Neurol. Scand. Suppl.* 102, 1–94.

Sled, J. G., Zijdenbos, A. P., and Evans, A. C. (1998). A nonparametric method for automatic correction of intensity nonuniformity in MRI data. *IEEE Trans. Med. Imaging* 17, 87–97.

Small, S. A., Schobel, S. A., Buxton, R. B., Witter, M. P., and Barnes, C. A. (2011). A pathophysiological framework of hippocampal dysfunction in ageing and disease. *Nat. Rev. Neurosci.* 12, 585–601. doi: 10.1038/nrn3085

Styner, M., Lieberman, J. A., Pantazis, D., and Gerig, G. (2004). Boundary and medial shape analysis of the hippocampus in schizophrenia. *Med. Image Anal.* 8, 197–203. doi: 10.1016/j.media.2004.06.004

Tamminga, C. A., Stan, A. D., and Wagner, A. D. (2010). The hippocampal formation in schizophrenia. *Am. J. Psychiatry* 167, 1178–1193. doi: 10.1176/appi.ajp.2010.09081187

Tepest, R., Wang, L., Miller, M. I., Falkai, P., and Csernansky, J. G. (2003). Hippocampal deformities in the unaffected siblings of schizophrenia subjects. *Biol. Psychiatry* 54, 1234–1240.

Velakoulis, D., Wood, S. J., Wong, M. T., McGorry, P. D., Yung, A., Phillips, L., et al. (2006). Hippocampal and amygdala volumes according to psychosis stage and diagnosis: A magnetic resonance imaging study of chronic schizophrenia, first-episode psychosis, and ultra-high-risk individuals. *Arch. Gen. Psychiatry* 63, 139–149. doi: 10.1001/archpsyc.63.2.139

Vita, A., De Peri, L., Silenzi, C., and Dieci, M. (2006). Brain morphology in first-episode schizophrenia: A meta-analysis of quantitative magnetic resonance imaging studies. *Schizophr. Res.* 82, 75–88. doi: 10.1016/j.schres.2005.11.004

Watson, C., Andermann, F., Gloor, P., Jones-Gotman, M., Peters, T., Evans, A., et al. (1992). Anatomic basis of amygdaloid and hippocampal volume measurement by magnetic resonance imaging. *Neurology* 42, 1743–1750. doi: 10.1212/wnl.42.9.1743

Weickert, T. W., Goldberg, T. E., Gold, J. M., Bigelow, L. B., Egan, M. F., and Weinberger, D. R. (2000). Cognitive impairments in patients with schizophrenia displaying preserved and compromised intellect. *Arch. Gen. Psychiatry* 57, 907–913. doi: 10.1001/archpsyc.57.9.907

Yang, H., Yang, S., and Isen, A. M. (2013). Positive affect improves working memory: Implications for controlled cognitive processing. *Cogn. Emot.* 27, 474–482. doi: 10.1080/02699931.2012.713325

Yoon, T., Okada, J., Jung, M. W., and Kim, J. J. (2008). Prefrontal cortex and hippocampus subserve different components of working memory in rats. *Learn. Mem.* 15, 97–105. doi: 10.1101/lm.850808

Zierhut, K. C., Grassmann, R., Kaufmann, J., Steiner, J., Bogerts, B., and Schiltz, K. (2013). Hippocampal CA1 deformity is related to symptom severity and antipsychotic dosage in schizophrenia. *Brain* 136(Pt 3), 804–814. doi: 10.1093/brain/aws335

frontiers | Frontiers in Cellular Neuroscience

TYPE Original Research
PUBLISHED 31 March 2023
DOI 10.3389/fncel.2023.1152248



OPEN ACCESS

EDITED BY
Yuh-Man Sun,
Retired, London, United Kingdom

REVIEWED BY
Torfi Sigurdsson,
Goethe University Frankfurt, Germany
Dennis Kätzel,
University of Ulm, Germany

*CORRESPONDENCE
M. Victoria Puig
✉ vickypuig.bcn@gmail.com

SPECIALTY SECTION
This article was submitted to Cellular Neurophysiology, a section of the journal Frontiers in Cellular Neuroscience

RECEIVED 27 January 2023
ACCEPTED 10 March 2023
PUBLISHED 31 March 2023

CITATION
Delgado-Sallent C, Gener T, Nebot P, López-Cabezón C and Puig MV (2023) Neural substrates of cognitive impairment in a NMDAR hypofunction mouse model of schizophrenia and partial rescue by risperidone.
*Front. Cell. Neurosci.* 17:1152248.
doi: 10.3389/fncel.2023.1152248



# Neural substrates of cognitive impairment in a NMDAR hypofunction mouse model of schizophrenia and partial rescue by risperidone

Cristina Delgado-Sallent[1], Thomas Gener[1,2,3], Pau Nebot[1], Cristina López-Cabezón[2,3] and M. Victoria Puig[1,2,3]*

[1]Hospital del Mar Medical Research Institute (IMIM), Barcelona Biomedical Research Park, Barcelona, Spain, [2]Catalan Institute of Nanoscience and Nanotechnology, CSIC and BIST, Barcelona, Spain, [3]Institut de Neurociències, Universitat Autònoma de Barcelona, Barcelona, Spain

N-methyl D-aspartate receptor (NMDAR) hypofunction is a pathophysiological mechanism relevant for schizophrenia. Acute administration of the NMDAR antagonist phencyclidine (PCP) induces psychosis in patients and animals while subchronic PCP (sPCP) produces cognitive dysfunction for weeks. We investigated the neural correlates of memory and auditory impairments in mice treated with sPCP and the rescuing abilities of the atypical antipsychotic drug risperidone administered daily for two weeks. We recorded neural activities in the medial prefrontal cortex (mPFC) and the dorsal hippocampus (dHPC) during memory acquisition, short-term, and long-term memory in the novel object recognition test and during auditory processing and mismatch negativity (MMN) and examined the effects of sPCP and sPCP followed by risperidone. We found that the information about the familiar object and its short-term storage were associated with mPFC→dHPC high gamma connectivity (phase slope index) whereas long-term memory retrieval depended on dHPC→mPFC theta connectivity. sPCP impaired short-term and long-term memories, which were associated with increased theta power in the mPFC, decreased gamma power and theta-gamma coupling in the dHPC, and disrupted mPFC-dHPC connectivity. Risperidone rescued the memory deficits and partly restored hippocampal desynchronization but did not ameliorate mPFC and circuit connectivity alterations. sPCP also impaired auditory processing and its neural correlates (evoked potentials and MMN) in the mPFC, which were also partly rescued by risperidone. Our study suggests that the mPFC and the dHPC disconnect during NMDAR hypofunction, possibly underlying cognitive impairment in schizophrenia, and that risperidone targets this circuit to ameliorate cognitive abilities in patients.

KEYWORDS

**phencyclidine, atypical antipsychotic drugs, theta and gamma oscillations, neural synchrony, novel object recognition, auditory evoked potentials, prefrontal cortex, hippocampus**

## Introduction

N-methyl D-aspartate receptor (NMDAR) hypofunction is a pathophysiological mechanism found in schizophrenia patients that can be replicated in rodent models by using pharmacological agents that block NMDAR, for example phencyclidine or ketamine (Lee and Zhou, 2019). Sub-chronic administration of phencyclidine (sPCP, also known as angel dust) to rodents mimics cognitive symptoms in schizophrenia for several months. That is, it impairs executive functions such as recognition memory, cognitive flexibility, and sensorimotor gating, including mismatch negativity (MMN; Rajagopal et al., 2014; Hamilton et al., 2018b; Lee and Zhou, 2019). Moreover, exposure to PCP reduces the density of PV-expressing GABAergic interneurons ($PV^+$) in the prefrontal cortex (PFC) and the hippocampus (HPC; Abdul-Monim et al., 2007) of the animals. This is similar to what is observed in *post mortem* tissue from patients with schizophrenia (Lewis et al., 2005; Konradi et al., 2011; Kaar et al., 2019), further validating subchronic PCP (sPCP) as a suitable animal model. The reduction in $PV^+$ neuron populations impair perisomatic inhibition of pyramidal neurons that likely contributes to a diminished gamma synchronization that is required for most cognitive functions (Lewis et al., 2005). However, a comprehensive neurophysiological characterization of prefrontal-hippocampal circuits following sPCP treatment is missing.

Atypical antipsychotic drugs are effective in reducing the positive symptoms of schizophrenia patients while showing modest amelioration of the negative and cognitive symptoms. The neural substrates underlying these complex behavioral effects are poorly understood, which makes the development of better treatments a difficult endeavor. In rodents, atypical antipsychotic drugs attenuate some of the behavioral effects induced by NMDAR antagonists, including sPCP-induced cognitive dysfunction (Grayson et al., 2007). They enhance dopamine efflux in the cortex and the HPC, affecting less the limbic system, whereas classical neuroleptics show the opposite effect. These actions are mediated by the affinity of atypical antipsychotic drugs for serotonin receptors, especially the 1A ($5\text{-}HT_{1A}R$) and the 2A ($5\text{-}HT_{2A}R$) subtypes, which have a widespread expression in the brain and modulate the dopaminergic, serotonergic, glutamatergic, and GABAergic systems. Risperidone is one of the most prescribed atypical antipsychotic drugs. It targets mainly D2R and $5\text{-}HT_{2A}R$ and is effective at treating the positive symptoms while also ameliorating certain aspects of cognitive symptoms in humans and rodents, including executive function, attention, learning, and memory (Grayson et al., 2007; Houthoofd et al., 2008; Rajagopal et al., 2014; Baldez et al., 2021).

We have recently reported that acute PCP exerts strong influences on prefrontal-hippocampal neural dynamics in freely moving mice. The psychosis-like states produced by PCP were associated with hypersynchronization of the medial PFC (mPFC), desynchronization of the dorsal HPC (dHPC), and disrupted mPFC-dHPC circuit connectivity. Acute risperidone reduced cortical hypersynchronization but had limited efficacy in restoring hippocampal synchronization and circuit connectivity (Delgado-Sallent et al., 2022). In healthy mice, acute risperidone had an inhibitory effect on the circuit, reducing spiking activity and theta-gamma oscillations in both areas, and it also disrupted the circuit's connectivity (Gener et al., 2019). Here, we investigated the neural correlates of memory and auditory deficits in the sPCP model of schizophrenia and their rescue by chronic risperidone, experimental conditions closer to the clinical settings.

## Materials and methods

### Animals

Experiments were performed in C57BL/6J male mice ($n = 51$) that were 2–3 months old at the start of the experiments. Mice were housed under conditions of controlled temperature ($23 \pm 1°C$) and illumination (12 hours light/dark cycle). All procedures were authorized by the Barcelona Biomedical Research Park (PRBB) Animal Research Ethics Committee and the local government.

### Surgeries

Mice were induced with a mixture of ketamine/xylazine and placed in a stereotaxic apparatus. Anesthesia was induced with 4% isoflurane and maintained at 0.5–2%. Small craniotomies were drilled above the medial PFC and the HPC. Several micro-screws were screwed into the skull to stabilize the implant, and the one on top of the cerebellum was used as a general ground. Three tungsten electrodes, one stereotrode and one single electrode, were implanted in the prelimbic region of the medial PFC (mPFC) and two more were implanted in the CA1 area of the dorsal HPC (dHPC). The electrodes were positioned stereotaxically in the prelimbic cortex (AP: 1.5, 2.1 mm; ML: ± 0.6, 0.25 mm; DV: −1.7 mm from bregma) and the CA1 region (AP: −1.8 mm; ML: −1.3 mm; DV: −1.15 mm). Neural activity was recorded while the electrodes were being lowered down inside the brain to help locate the CA1 region. In addition, three reference electrodes were implanted in the corpus callosum and lateral ventricles (AP: 1, 0.2, −1; ML: 1, 0.8, 1.7; DV: −1.25, −1.4, −1.5, respectively). The electrodes were made with two twisted strands of tungsten wire 25 μm wide (Advent, UK) and were held together using heat insulation. At the time of implantation, the electrodes had an impedance that ranged from 100 to 400 kΩ and were implanted unilaterally with dental cement. Electrode wires were pinned to an adaptor to facilitate their connection to the recording system. After surgery, animals were allowed at least one week to recover during which they were extensively monitored and received both analgesia and anti-inflammatory treatments. Prior to the initiation of the experiments, the animals were handled and familiarized with the implant connected to the recording cable. After the experiments ended, the electrode placements were confirmed histologically by staining the brain slices with Cresyl violet (**Figure 1B**). Electrodes with tips outside the targeted areas were discarded from data analyses.

## Behavioral tests

### Resting states

Recordings during quiet wakefulness were performed in an open field box (50 cm × 40 cm × 20 cm) for 30 min. We harnessed the accelerometer signals integrated within the Intan RHD2132 amplifiers to precisely monitor general mobility of mice. We quantified the variance of the instantaneous acceleration module (ACC; variance (Root square[$X^2$, $Y^2$, $Z^2$])) that was maximum during exploration and decreased as the animals were in quiet alertness (Gener et al., 2019; Delgado-Sallent et al., 2022). Low mobility was determined by a defined threshold in the output of the accelerometer signals and normal movement was defined as above that threshold. The animals typically rested for brief periods between 2 and 10 consecutive seconds.

### Novel object recognition test (NOR)

We quantified recognition memory in a custom-designed T-maze as previously reported (Alemany-González et al., 2020, 2022). The maze was made of aluminum with wider and higher arms than the standard mazes (8 cm wide × 30 cm long × 20 cm high). The maze was shielded and grounded for electrophysiological recordings and was placed on an aluminum platform. The novel-familiar object pairs were previously validated as in Gulinello et al. (2018). The arm of the maze where the novel object was placed in each session was randomly chosen across experiments. The task consisted of a habituation phase, familiarization phase, short-term memory test (STM), and long-term memory test (LTM), each lasting ten minutes (**Figure 1B**). During the habituation phase, the animals explored the maze without objects. Five minutes later, mice were put back in the maze where two identical objects had been placed at the end of the lateral arms for the familiarization phase. Three minutes and twenty-four hours later, a familiar object and a new object were placed in the maze for the STM and LTM tests, respectively. Memory acquisition was investigated by comparing the initial (early) and the last (late) visits to the two identical items in the familiarization phase; memory retrieval and novelty seeking were investigated during the initial visits to familiar and novel objects, respectively, during the STM and LTM tests. Exploratory events were timestamped into the recording files by sending TTL pulses to the acquisition system. This allowed us to quantify the number and duration of the visits. We used this information to estimate the neurophysiological correlates of memory performance. The duration of the initial visits and the visits to the novel objects were typically longer than the last visits of the sessions and to the familiar objects (**Figure 1E**). Because some of the mathematical tools employed are sensitive to the time window used, we concatenated different visits until the accumulated time reached five seconds. We note that familiarization was considered valid when mice visited the objects for at least ten seconds, as in previous studies (Alemany-González et al., 2020, 2022). The exact number of visits used for each analysis was the following: [Familiarization phase] All conditions and objects combined, early: 3.91 ± 0.17, late: 4.86 ± 0.05; BAS, early: 3.81 ± 0.25, late: 4.81 ± 0.1; sPCP, early: 4.25 ± 0.19, late: 5; RIS, early: 3.54 ± 0.45, late: 4.73 ± 0.14; [3 min test] Novel objects, all conditions combined, 3.24 ± 0.2; BAS: 3.07 ± 0.25, sPCP: 3.92 ± 0.25, RIS: 2.29 ± 0.52; Familiar objects, all conditions combined, 4.29 ± 0.13; BAS: 4.5 ± 0.16, sPCP: 4.07 ± 0.25, RIS: 4.29 ± 0.36; [24 h test] Novel objects, all conditions combined, 3.83 ± 0.12; BAS: 3.84 ± 0.21, sPCP: 3.89 ± 0.12, RIS: 3.7 ± 0.26; Familiar objects, all conditions combined, 4.47 ± 0.1; BAS: 4.47 ± 0.15, sPCP: 4.57 ± 0.19, RIS: 4.3 ± 0.15. We also note that we needed to concatenate more visits when they were short to reach five seconds.

### Auditory evoked potential (AEP) and mismatch negativity (MMN) tests

The auditory tests were conducted consecutively in the home cage located inside a soundproof box. We used the Python library simpleaudio to generate the sounds in custom scripts that synchronized the sound with the electrophysiological recordings via an EIB board. Mice were habituated to the environment for 5 min. Next, 100 consecutive clicks separated by 10 s were presented to the mice for a total of 8 min. A click consisted of 15 ms of white noise ("15ms_whitenoise.wav" function in the *simpleaudio* Python library). We next used an auditory oddball paradigm to measure MMN. Mice were presented with a series of standard tones (6 or 8 kHz) in which a target tone (8 or 6 kHz) was presented randomly in 75–25% proportions, respectively. The frequencies of the standard and target tones were switched after 500 trials in a flip-flop design (Hamilton et al., 2018a). Tones lasted 10 ms and were presented with 500 ms intertrial intervals. The protocol consisted in the presentation of 1,000 tones, lasting around 10 min.

## Subchronic PCP model and pharmacology

We used phencyclidine hydrochloride (PCP; Sigma-Aldrich) 10 mg/kg, 5+5 days, as in Rajagopal et al. (2014); risperidone (RIS; Sigma-Aldrich) 0.5 mg/kg, 14 consecutive days. PCP was administered subcutaneously (SC) and risperidone intraperitoneally (IP). The following pharmacological groups were investigated: sPCP ($n$ = 21 mice), sPCP-RIS ($n$ = 9), and their corresponding saline controls: SAL ($n$ = 8), sPCP-SAL ($n$ = 7), SAL-SAL ($n$ = 8; **Figure 1B** and **Supplementary Figure 1**).

## Neurophysiological recordings and data analyses

All the recordings were implemented with the multi-channel Open Ephys system at 0.1–6,000 Hz and a sampling rate of 30 kHz. Recorded signals from each electrode were filtered offline to extract local field potentials (LFPs) and multi-unit activity (MUA).

### Oscillatory activity

To obtain LFPs, recorded signals were detrended, notch-filtered and decimated to 1 kHz offline. The frequency bands considered for the band-specific analyses included: delta (2–5 Hz), slow theta (4–8 Hz), theta (8–12 Hz), low gamma (30–48 Hz), high gamma (52–100 Hz), and HFOs (100–200 Hz). Power spectral density results were calculated using the multi-taper method. Spectrograms were constructed using consecutive Fourier transforms. Phase-amplitude coupling (PAC) was measured following the method

described in Onslow et al. (2011). The parameters used were: phase frequencies = [0, 15] with 1 Hz step and 4 Hz bandwidth, amplitude frequencies = [10, 250] with 5 Hz step and 10 Hz bandwidth. Phase-amplitude coupling quantification results were obtained by averaging the values of selected areas of interest in the comodulograms. The exact frequencies used for each analysis are described in the figure legends. Directionality of signals between areas (PFC→HPC and HPC→PFC) was calculated with the phase slope index (PSI) with a Python translation of MATLAB's data2psi.m (epleng = 60 s, segleng = 1 s) as in Nolte et al. (2008). Briefly, the PSI quantifies the consistency of the phase lag (or lead) as a function of frequency, between two signals. Here, positive slopes suggested the presence of PFC-to-HPC flows of information while negative slopes suggested the opposite signal directionality. The significance of PSI's deviations was tested via surrogate analysis. The surrogate analyses were performed by randomizing the data of two pairs of channels, one in PFC and one in HPC, using all the combinations of different pairs of channels. The data were shuffled across time series and across pair of channels 1,000 times to obtain the correspondent PSI shuffle. Next, to remove chance effects, the randomized data were averaged and subtracted from the original data. To establish significance, a *t*-test was performed between the original data and its shuffle (Puig and Miller, 2015; Lancaster et al., 2018).

### Spiking activity

Multi-unit activity was estimated by first subtracting the raw signal from each electrode with the signal from a nearby referencing electrode to remove artifacts resulting from the animal's movement. Then, continuous signals were filtered between 450 and 6,000 Hz with Python and thresholded at -3 sigma standard deviations with Offline Sorter v4 (Plexon Inc.). We estimated MUA in three-second (quiet alertness) or 10 ms (auditory evoked potentials) non-overlapping windows. Spike-LFP coupling was estimated with the pairwise phase consistency (PPC) method, which is an unbiased parameter to determine the degree of tuning of the neurons' firing to ongoing network activity at specific frequencies (Vinck et al., 2011, p. 20; Zorrilla de San Martín et al., 2020). PPC was determined using the phases of spikes from MUA in 25 s epochs, only considering epochs with at least 250 spikes.

## Statistical analysis

Data are represented in boxplots (*seaborn* function in Python) where the median and the quartiles are shown. We used paired *t*-tests, one-way repeated measures ANOVAs to compare behavioral and neurophysiological measures within animals (baseline-sPCP-RIS), and mixed ANOVAS to compare behavioral and neurophysiological measures between pharmacological groups (baseline-sPCP-SAL). Two-way ANOVAs were used to compare the effects of the sPCP-RIS group with their respective saline controls (sPCP-SAL, SAL-SAL). Paired *t*-tests were used to assess differences between early and late visits to objects (familiarization test), between visits to novel and familiar objects (3-min and 24 h tests), and between PSI and its shuffle. We used Sidak's correction *post hoc* tests in the ANOVAs. We employed Pearson correlations to identify associations between neurophysiological measures and DIs. Statistical analyses were implemented in Python with the Pingouin statistical package (Vallat, 2018).

# Results

## Chronic risperidone prevented sPCP-induced short-term and long-term memory deficits

We administered subchronically to mice the NMDAR antagonist phencyclidine (10 mg/kg SC 5 + 5 days; sPCP group) to model cognitive impairment in schizophrenia. We investigated the neural substrates of the well-established memory and auditory deficits of this model and their subsequent rescue by chronic risperidone (0.5 mg/kg IP for 14 consecutive days; sPCP-RIS group). We recorded neural activities in the prelimbic medial PFC (mPFC) and CA1 region of the dorsal HPC (dHPC), brain regions relevant for cognitive processing and the pathophysiology of schizophrenia (Sigurdsson and Duvarci, 2016). The animals' behaviors and neural activities were characterized during baseline, after sPCP, after risperidone (sPCP-RIS group), and their corresponding saline controls (SAL, sPCP-SAL, and SAL-SAL groups; **Figures 1A, B** and **Supplementary Figure 1**).

We first examined short-term memory (STM) and long-term memory (LTM) abilities of the different pharmacological groups assessed via the NOR task (**Figure 1B**), a well validated memory test that relies on the mice' innate instinct to explore novel objects and depends on hippocampal-prefrontal circuits (Warburton and Brown, 2015; Alemany-González et al., 2020; Wang et al., 2021). Consistent with previous studies, discrimination indices (DIs) for novel versus familiar objects ([time visiting the novel object − time visiting the familiar object]/total exploration time) were positive for all the mice during baseline in the 3-min and 24 h memory tests (DIs = 0.35 ± 0.05 and 0.29 ± 0.04; $n$ = 7, 8 mice, respectively). That is, mice exhibited good STM and LTM at the beginning of the experiment. After sPCP, mice explored novel and familiar objects evenly (DIs = 0.01 ± 0.06 and −0.06 ± 0.06; baseline vs. sPCP: $p < 0.0005$, paired *t*-test) indicating poor recognition memory. This was not observed in controls with saline (SAL group, $n$ = 4 mice). Chronic risperidone rescued both STM deficits (DI = 0.42 ± 0.1; $n$ = 4 mice) and LTM deficits (DI = 0.37 ± 0.07; $n$ = 6 mice; **Figure 1C** and **Table 1**), but not their corresponding saline controls (sPCP-SAL group, $n$ = 7 mice; **Supplementary Figure 1**).

We next analyzed the number and duration of the visits to each object per session. During baseline and risperidone conditions, mice visited the novel items on more occasions than the familiar items ([STM: baseline, risperidone]: $p$ = 0.019, 0.038; [LTM: baseline, risperidone]: $p$ = 0.003, 0.047; paired *t*-tests) and the visits lasted longer, particularly during the STM test ([baseline, risperidone]: $p$ < 0.005, 0.056). In contrast, after sPCP the mice visited both objects evenly by increasing the number and duration of visits to familiar objects, behaving as if they were novel (**Figure 1D**). This indicated poor recognition memory. The duration of the visits decreased within a session as the mice became less interested in the objects, both novel and familiar. A sharp decrease in duration occurred during the first five visits to the novel objects in the two tests and subsequently the duration of the

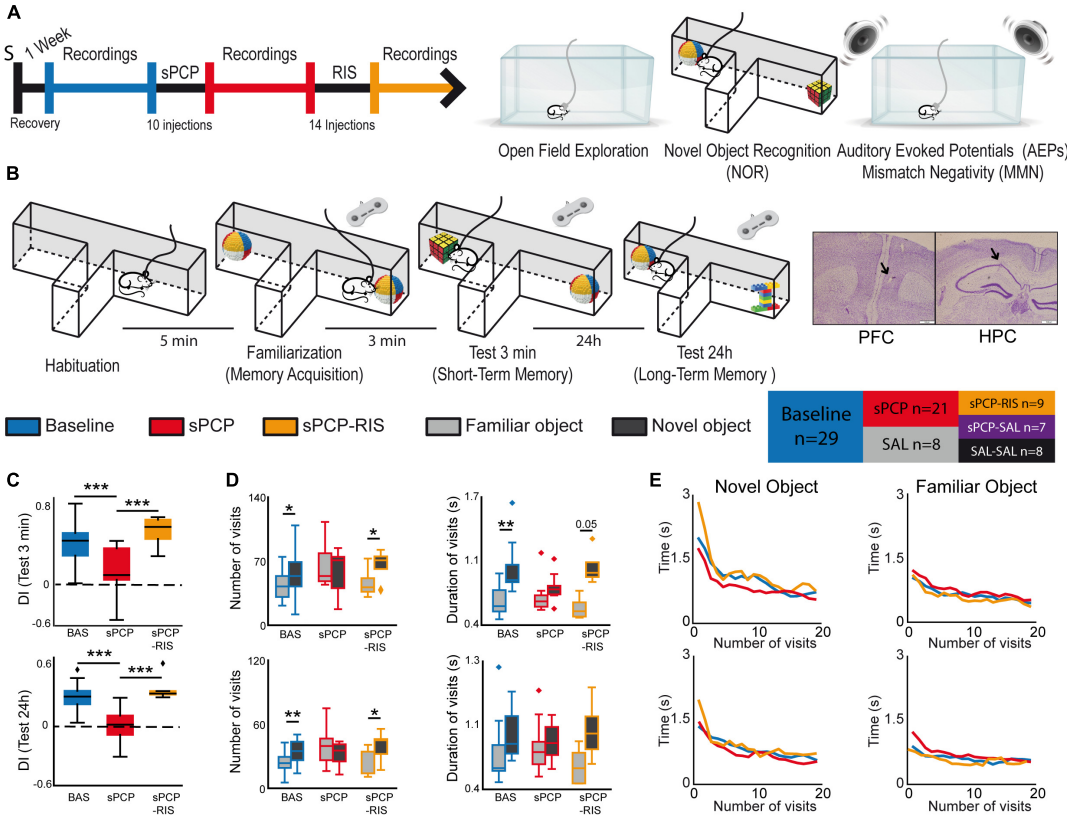


FIGURE 1
Experimental design and main behavioral results. **(A)** Experimental protocol and behavioral tests used. S indicates the date of surgery to implant recording electrodes. **(B)** The novel object recognition test (NOR) in detail. Right and left buttons on a joystick were pressed for the duration of each visit to timestamp the information into the recording files. Representative examples of histological verification of electrode locations within the prelimbic PFC and the CA1 area of the HPC. We recorded neural activities during the surgical implantations to increase the chances of implanting the electrodes within the target areas. At the end of the experiment, before euthanasia, a gentle current was passed through the electrodes to mark the recording areas (arrows). Also shown is a summary table that illustrates the different pharmacological groups of the study and the number of mice used in each group. **(C)** Discrimination indices (DIs) during the 3-min (STM) and the 24 h (LTM) tests. DIs decreased significantly after sPCP and recovered after chronic risperidone (STM, LTM: $F_{(2,6)}$ = 16.64, 15.15, $p$ = 0.004, <0.0005; one-way repeated measures ANOVA, $n$ = 9 mice; the results including all the mice are shown in **Supplementary Figure 1**). **(D)** Number and mean duration of visits to familiar and novel objects during the STM and LTM tests. After sPCP, mice visited both objects evenly by increasing the number of visits to familiar objects, reflecting poor recognition memory ($F_{(1,13)}$ = 15.12, 5.2, $p$ = 0.002, 0.037). **(E)** The duration of the visits decreased within a session as the mice became less interested in the objects ([baseline STM, LTM]: $F_{(2,26)}$ = 3.52, 3.56, $p$ = 0.005, 0.0006; one-way repeated measures ANOVA with novel and familiar objects combined). A sharp decrease in duration occurred during the first 5 visits to both objects in the two tests, and this was more pronounced for novel objects (first 5 visits to novel objects vs. first 5 visits to familiar objects; [STM, LTM]: $F_{(2,26)}$ = 36.03, 11.57, $p$ < 0.0005, 0.002). These behaviors were not overtly disrupted by sPCP or risperidone.

visits declined slowly. These prolonged initial visits did not occur when the mice visited the familiar objects. These behaviors were not overtly disrupted by sPCP or risperidone (Figure 1E).

## Risperidone partially rescued sPCP-induced disruptions of theta and gamma synchronization in prefrontal-hippocampal circuits during quiet alertness

We first aimed to gain insight into the neural dynamics of healthy prefrontal-hippocampal circuits (mPFC-dHPC) during quiet alertness and their impact by sPCP and risperidone. To mitigate the effects of the hyperlocomotion produced by sPCP (Mouri et al., 2012; Castañé et al., 2015) we analyzed neural activities during resting states, brief 3-second episodes of low behavioral activity while the mice explored an open field (see section "Materials and methods"). As we reported previously (Delgado-Sallent et al., 2022), during resting states healthy mice exhibited a strong circuit synchronization at theta frequencies (4–12 Hz): theta oscillations were prominent in the mPFC and there were robust theta oscillations, theta-gamma and spike-theta coupling in the dHPC (Figures 2A–C).

sPCP disrupted theta and gamma rhythms within mPFC-dHPC circuits that were partially restored by risperidone ($n$ = 21 mice). First, sPCP increased high gamma (52–100 Hz) power in the mPFC that was reduced by risperidone. Concomitantly, sPCP decreased high gamma power in the dHPC, however, this was not rescued by risperidone (Figure 2A). In addition, sPCP weakened intrinsic theta-gamma coupling both locally in the dHPC and inter-regionally ($PFC_{phase}$-$HPC_{amp}$) that were partially restored by

TABLE 1 Summary of main results.

| | | sPCP | Risperidone |
|---|---|---|---|
| Quiet alertness | mPFC | Increased high gamma power | Fully rescued |
| | dHPC | Decreased high gamma power and theta-gamma coupling | Coupling partially rescued |
| Memory acquisition | BEHAVIOR | – | – |
| | mPFC | Increased theta power | Not rescued |
| | dHPC | Decreased high gamma power and theta-gamma coupling | Coupling partially rescued |
| | PSI | Disrupted mPFC → dHPC high gamma signals during familiar visits | Not rescued |
| Short-term memory | BEHAVIOR | Decreased discrimination index | Fully rescued |
| | mPFC | Increased theta power | Not rescued |
| | dHPC | Decreased high gamma power and theta-gamma coupling | Partially rescued |
| | PSI | Disrupted mPFC → dHPC high gamma signals during familiar visits | Not rescued |
| Long-term memory | BEHAVIOR | Decreased discrimination index | Fully rescued |
| | mPFC | – | – |
| | dHPC | Decreased high gamma power and theta-gamma coupling | Partially rescued |
| | PSI | Disrupted dHPC → mPFC theta signals during familiar visits | Not rescued |
| Auditory processing | BEHAVIOR | Decreased response ratio | Partially rescued |
| | mPFC-P2 | Decreased spiking activity | Partially rescued |
| | mPFC-P3 | Decreased amplitude and spiking activity | Partially rescued |
| | MMN | MMN not present | Not rescued |

risperidone (Figure 2B). We detected strong correlations between the reductions of hippocampal high gamma power and the two forms of theta-gamma coupling both during baseline ([HPC, circuit] Pearson's R = 0.73, 0.69, $p < 0.0005$) and after sPCP (R = 0.81, 0.76, $p < 0.0005$). These correlations put forward a key role of hippocampal high gamma oscillations in the generation of theta-gamma coupling within the circuit. Moreover, sPCP tended to increase the firing rate of neuron populations (MUA) in the mPFC that was reduced by risperidone ($n$ = 5 mice; Figure 2C). In the dHPC, sPCP did not change the firing rate of neurons but disrupted the coupling of spikes to ongoing theta oscillations ($n$ = 4 mice). Risperidone was unable to restore the spike-theta synchronization and it increased the locking of spikes to delta oscillations (<5 Hz; Figure 2D). No major changes in power, cross-frequency coupling, and spike-LFP coupling were observed at other frequencies in either region. Finally, the directionality of signals within the circuit was not overtly affected by sPCP or risperidone (Figure 2E). These sPCP-induced alterations were not present in saline controls (SAL group, $n$ = 8 mice; Supplementary Figure 2). Together, these findings suggested that risperidone improved sPCP-induced disruption of theta and gamma synchronization in mPFC-dHPC circuits (Figure 2F and Table 1).

## Risperidone partially restored the neural correlates of sPCP-induced poor recognition memory in prefrontal-hippocampal circuits

We first aimed to understand the neural mechanisms underlying memory acquisition in healthy animals ($n$ = 9 mice). We compared the neurophysiological signals during the familiarization phase (Figure 1B) between the initial visits to the two (identical) objects, which imply novelty seeking, and the last visits of the session, when the animals had just acquired a new memory about the objects. More specifically, we compared neurophysiological biomarkers recorded during the first five seconds versus the last five seconds of the total accumulated time of the visits, regardless of object (i.e., located in the right or left arms) or number of visits. On average, the 5-second epochs included 3.91 ± 0.2 early visits and 4.86 ± 0.06 late visits (see section "Materials and methods"). During normal memory acquisition, theta power (8–12 Hz) increased in the mPFC and decreased in the dHPC (early vs. late visits; $p$ = 0.012, 0.024, paired $t$-test; Figures 3A, B), whereas local and inter-regional theta-gamma coupling seemed unchanged (Figures 3C, D). We note that changes in theta power were not simply due to differential locomotion of mice during a session, as the animals' mobility was low while they were visiting the objects both at the beginning and at the end of the sessions. We further investigated whether any flow of information emerged within the circuit during memory acquisition. We focused on theta and gamma frequencies based on previous work from our group (Alemany-González et al., 2020, 2022). We found that mPFC→dHPC high gamma signals tended to emerge during the late visits (Figure 3E). Therefore, memory acquisition was associated with increases of theta power in the mPFC, decreases of theta and gamma power in the dHPC, and mPFC→dHPC high gamma signals (Figure 3F).

sPCP augmented non-specifically theta power in the mPFC and decreased it in the dHPC. In addition, high gamma power also declined in the dHPC after sPCP. None of the power changes were consistently recovered by risperidone, although tendencies were detected in the dHPC (Figures 3A, B). Local and inter-regional theta-gamma did not change during memory acquisition. However,

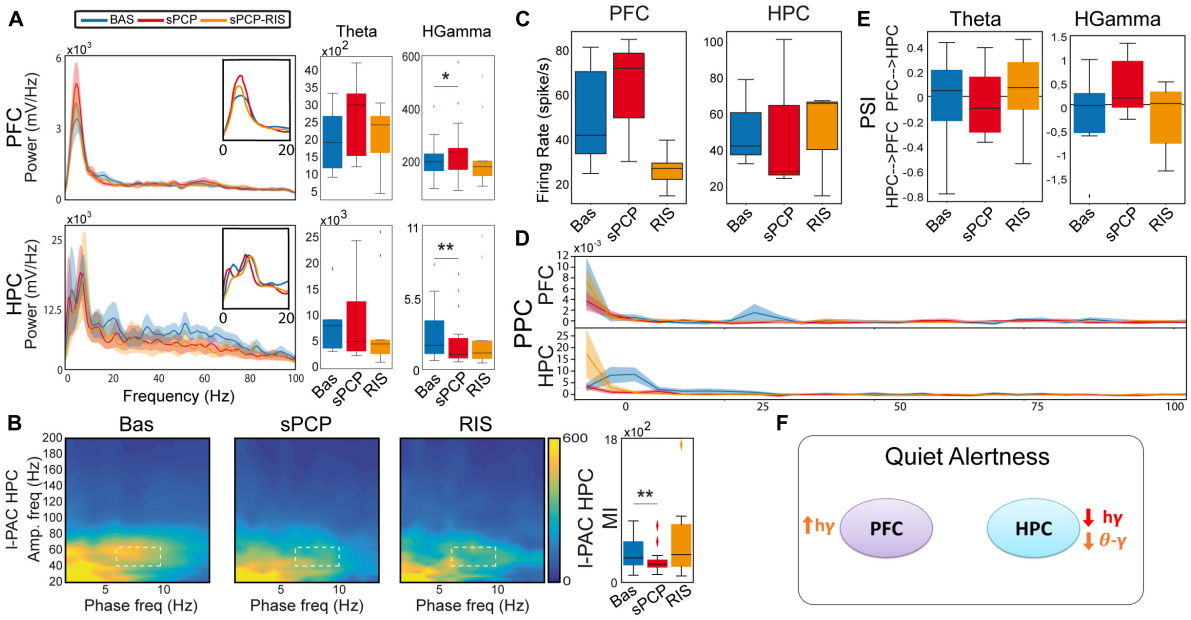


FIGURE 2
sPCP disrupted theta and gamma synchronization in mPFC-dHPC circuits during quiet wakefulness. Some of these alterations were ameliorated by risperidone. **(A)** sPCP increased high gamma power in the mPFC (baseline vs. sPCP: $p = 0.047$, paired $t$-test; $n = 21$ mice) and decreased it in the dHPC ($p = 0.004$). Risperidone rescued aberrant gamma power in the mPFC ($F_{(2,16)} = 0.11$, $p = 0.9$; one-way repeated measures ANOVA; no post-hoc differences between BAS and sPCP-RIS), but not in the dHPC ($F_{(2,14)} = 6.73$, $p = 0.01$). **(B)** sPCP weakened local and inter-regional theta-gamma coupling (6–10 Hz with 40–60 Hz; l-PAC; $p = 0.008$; ir-PAC $PFC_{phase}$-$HPC_{amp}$; $p = 0.001$; one-way repeated measures ANOVA) that were partially restored by risperidone ($F_{(2,14)} = 0.23$, $p = 0.125$; no post-hoc differences between BAS and sPCP-RIS). **(C)** sPCP promoted the spiking activity of neuron populations (multi-unit activity or MUA) in the mPFC that was reduced by risperidone ($F_{(2,6)} = 4.58$, $p = 0.047$). **(D)** sPCP disrupted the coupling of spikes to theta oscillations in the dHPC that was restored by risperidone ($F_{(2,6)} = 19.4$, $p = 0.002$). Risperidone also boosted spike-delta coupling in the dHPC (3–6 Hz, $F_{(2,6)} = 5.39$, $p = 0.046$). Spike-LFP coupling was estimated via the pairwise phase consistency method (PPC). **(E)** sPCP did not significantly affect the directionality of theta and high gamma signals within the circuit, but some tendencies were observed in the high gamma band. Circuit directionality was estimated via the phase slope index (PSI). **(F)** Proposed neural mechanism for the effects of sPCP and risperidone on mPFC-dHPC circuits during quiet alertness. In red, changes produced by sPCP, in orange sPCP-induced deviations ameliorated by risperidone. See also **Supplementary Figure 3**.

as above, and consistent with the reduction of gamma power in the dHPC, both types of theta-gamma coupling weakened after sPCP (differences with SAL controls; **Supplementary Figure 2**). After risperidone, theta-gamma coupling was partially restored (**Figures 3C, D**). Finally, sPCP disrupted the mPFC→dHPC high gamma signals detected during late visits to the objects that were partially corrected by risperidone (**Figure 3E**). Overall, we found that sPCP disrupted all the biomarkers associated with memory acquisition, that were not rescued by risperidone. sPCP further weakened theta-gamma coupling in the dHPC that was partially restored by risperidone (**Figure 3F** and **Table 1**).

We next investigated the neural substrates of STM ($n = 7$ mice). We compared the neurophysiological signals recorded during the first five seconds of visits to the novel and familiar objects during the 3-min tests (**Figure 1B**). On average, these included 3.24 ± 0.2 and 4.29 ± 0.13 visits to novel and familiar objects, respectively (**Figure 1E**). Animals with DIs over 0.2 during the baseline were used in these analyses. Theta power (**Figures 4A, B**) and theta-gamma coupling (**Figures 4C, D**) did not differ during the visits to novel and familiar objects. However, we detected a mPFC→dHPC flow of information at high gamma frequencies during the visits to familiar objects (**Figure 4E**), similar to memory acquisition. This directionality of signals seemed relevant for memory processing as it correlated strongly with memory performances (DI with PSI: Pearson's R = 0.7, $p = 0.026$; **Figure 4F**). Similar again to memory acquisition, sPCP increased theta power in the mPFC and reduced high gamma power in the dHPC (**Figures 4A, B**). Correspondingly, both local and inter-regional theta-gamma coupling were also reduced (**Figures 4C, D**). Risperidone only partially recovered the power and coupling alterations produced by sPCP in the dHPC. The mPFC→dHPC high gamma signals detected during familiar visits when the animals were healthy were also disrupted by sPCP and were not recovered by risperidone (**Figure 4E**). Overall, risperidone attenuated the alterations produced by sPCP in the dHPC but was unable to rescue disrupted neural activities in the mPFC or the flow of information within the circuit (**Figure 4G** and **Table 1**).

We further investigated the neural substrates of LTM ($n = 8$ mice). We compared the neurophysiological signals recorded during the first 5 s of visits to the novel and familiar objects during the 24 h memory tests (**Figure 1B**). On average, these included 3.83 ± 0.12 and 4.47 ± 0.1 visits to novel and familiar objects, respectively (**Figure 1E**). Again, only animals with DIs over 0.2 during baseline were used. Similar to STM, we did not detect changes in power or theta-gamma coupling between visits to novel and familiar objects in either region (**Figures 5A–D**). Furthermore, dHPC→mPFC theta signals were detected during the visits to familiar objects (**Figure 5E**) and correlated inversely

10.3389/fncel.2023.1152248

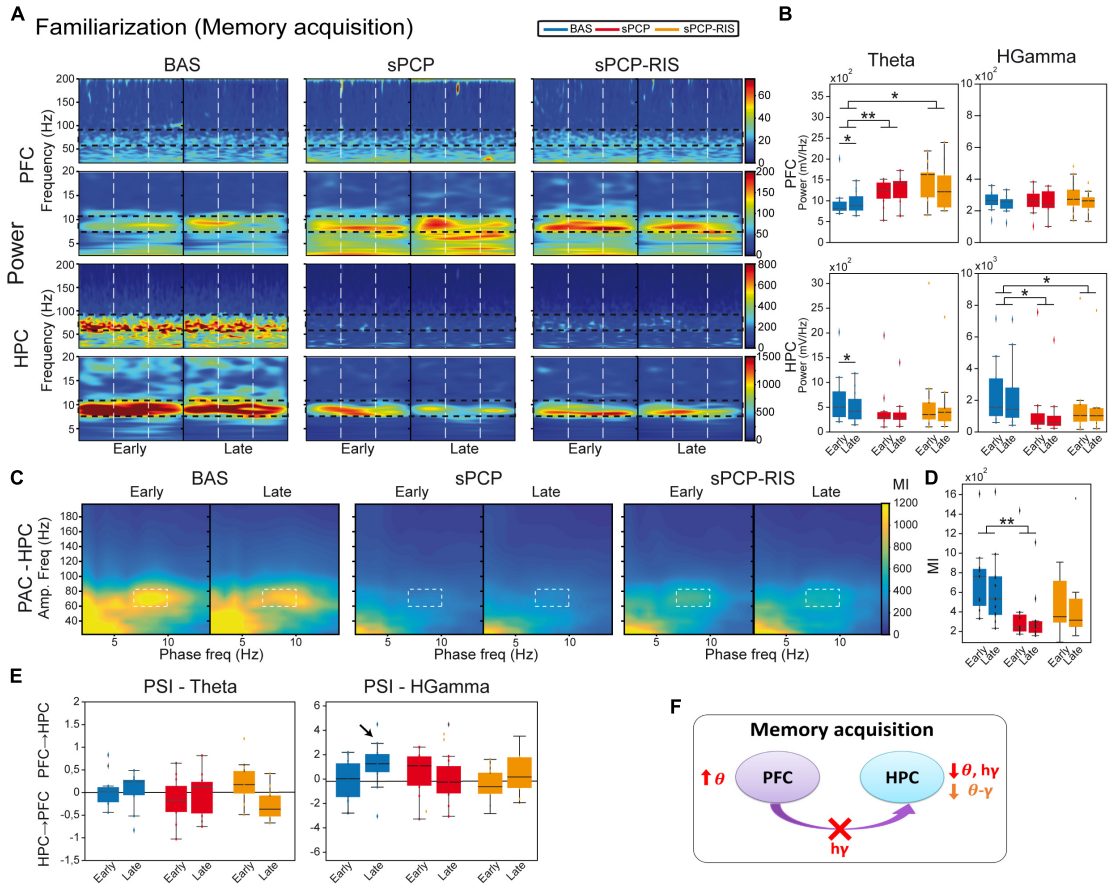


FIGURE 3
Neural substrates of memory acquisition and effects of sPCP and risperidone. **(A)** Power spectra showing the effects of sPCP and risperidone in the mPFC and the dHPC during the familiarization phase. Vertical dashed lines mark the first second upon initiation of the visits. **(B)** Prefrontal theta power increased in healthy animals during the late visits to the objects. sPCP increased non-specifically theta power in the mPFC (baseline vs. sPCP: $F_{(1,10)}$ = 7.46, $p$ = 0.021; mixed ANOVA with time of visits (early vs. late) and treatment (baseline vs. sPCP) as factors) and reduced theta and high gamma power in the HPC (baseline vs. sPCP: $F_{(1,12)}$ = 4.81, 9.59, $p$ = 0.053, 0.011), disrupting the normal neural dynamics of memory acquisition. Risperidone did not rescue these power changes. **(C,D)** Intrinsic dHPC theta-gamma coupling (7–10 Hz with 60–80 Hz) did not change with memory acquisition. sPCP disrupted theta-gamma coordination that was partially rescued by risperidone ([l-PAC] $F_{(1,12)}$ = 37.68, $p < 0.0005$; mixed ANOVAs as above; differences with sPCP-SAL controls: $F_{(1,22)}$ = 6.31, $p$ = 0.02; mixed ANOVA with time of visits (early vs. late) and treatment (SAL vs. sPCP) as factors). Similar results were obtained for inter-regional theta-gamma coupling ([ir-PAC] $F_{(1,12)}$ = 41.09, $p < 0.0005$; data not shown; differences with sPCP-SAL controls: $F_{(1,22)}$ = 4.62, $p$ = 0.024; mixed ANOVAs as above). **(E)** In healthy mice, mPFC→dHPC high gamma signals tended to occur during the late visits to the objects (PSI vs. shuffle, $p$ = 0.069; paired $t$-student; marked with an arrow). sPCP disrupted these flows of information (baseline vs. sPCP, $p$ = 0.096; PSI vs. shuffle, $p$ = 0.49) that were not restored by risperidone (PSI vs. shuffle, $p$ = 0.38). **(F)** Proposed neural mechanism for memory acquisition and effects of sPCP and risperidone. In red, changes produced by sPCP, in orange sPCP-induced deviations ameliorated by risperidone.

with the DIs (Pearson's R = −0.72, $p$ = 0.01; Figure 5F). As above, sPCP decreased dHPC high gamma power when the animals visited both objects (Figures 5A, B). Also as above, both local and inter-regional theta-gamma coupling were reduced by sPCP (Figures 5C, D). Like during STM, risperidone partially rescued sPCP-reduced gamma power and theta-gamma coupling in the dHPC. However, it was unable to restore dHPC→mPFC theta signals (Figure 5G and Table 1).

Together, these results unraveled a contribution of theta and gamma signals within mPFC-dHPC circuits to normal memory acquisition, STM and LTM processes in the context of object recognition memory. sPCP increased theta power in prefrontal microcircuits, disrupted high gamma rhythms in the dHPC and the theta-gamma coupling associated with it, regardless of brain state and cognitive task. That is, sPCP-induced neurophysiological alterations were observed across different days. Risperidone partially rescued some of these disturbances, hippocampal gamma oscillations and theta-gamma coupling in a more consistent way, suggesting a preferential action on this brain region (Table 1).

## Risperidone improved the neurophysiological signatures of auditory processing in sPCP-treated mice but did not reinstate MMN

We finally investigated the effects of sPCP and risperidone on the neural substrates of auditory attention and processing. More specifically, we examined alterations in auditory evoked potentials (AEPs) and mismatch negativity (MMN), as both biomarkers

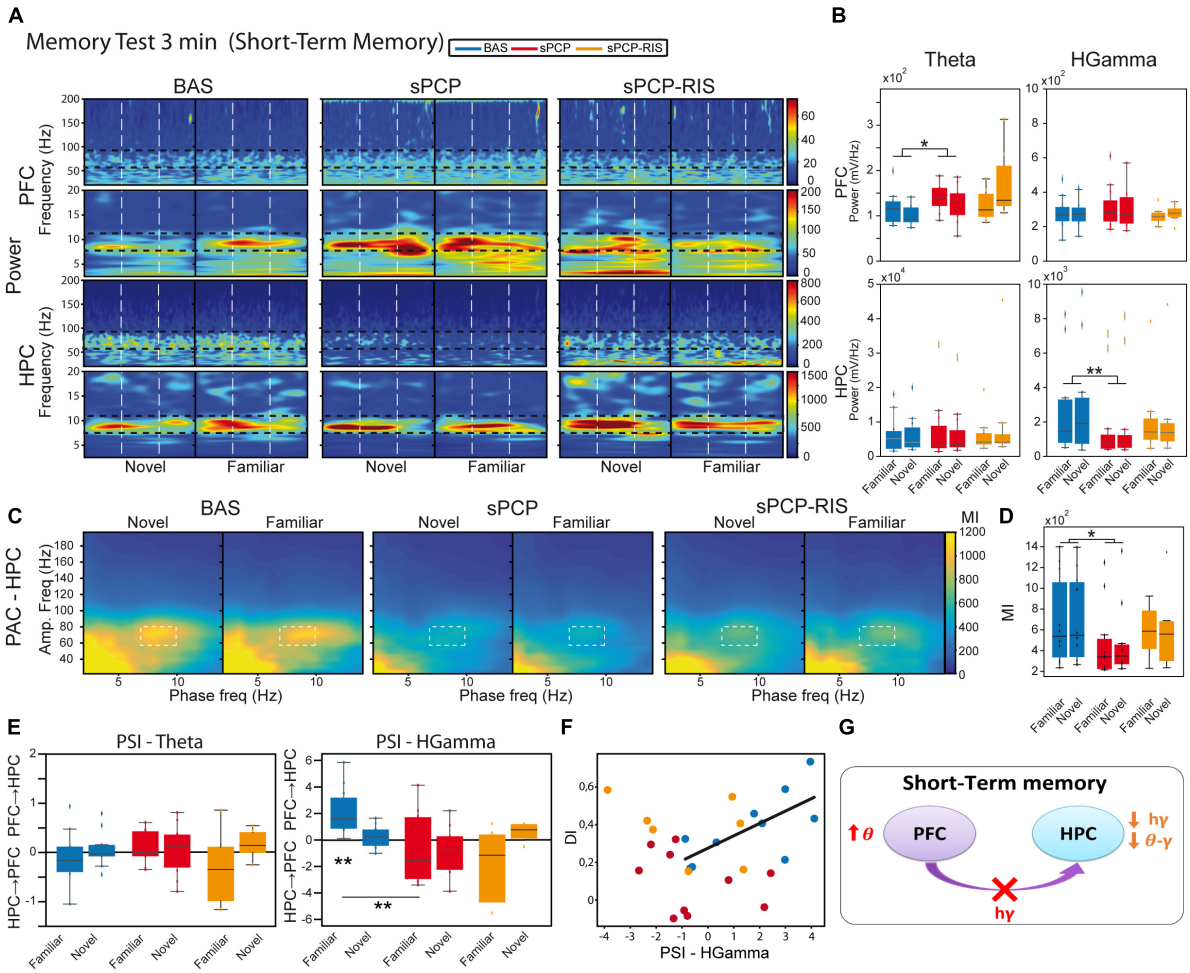


FIGURE 4
Neural substrates of short-term memory and effects of sPCP and risperidone. **(A)** Power spectra in the mPFC and the dHPC during the 3-minute memory test and effects of sPCP and risperidone. Vertical dashed lines mark the first second upon initiation of the visits. **(B)** Theta and high gamma oscillations were similar during the visits to familiar and novel objects in both regions. sPCP increased theta power in the mPFC non-specifically interfering with the normal theta dynamics ($F_{(1,7)}$ = 8.26 $p$ = 0.024; mixed ANOVA with object (familiar vs. novel) and treatment (baseline vs. sPCP) as factors). sPCP also reduced dHPC high gamma power ($F_{(1,12)}$ = 8.37, $p$ = 0.023; differences with sPCP-SAL controls: $F_{(1,20)}$ = 6.44, $p$ = 0.022; mixed ANOVA with object (familiar vs. novel) and treatment (SAL vs. sPCP) as factors) that were partially rescued by risperidone. **(C,D)** Intrinsic hippocampal theta-gamma coupling (7–10 Hz with 60–80 Hz) was similar during visits to familiar and novel objects. sPCP disrupted theta-gamma coordination that was partially rescued by risperidone ([l-PAC] $F_{(1,12)}$ = 10.36, $p$ < 0.009; differences with sPCP-SAL controls; $F_{(1,22)}$ = 19.13, $p$ = < 0.0005; mixed ANOVAs as above). Similar results were obtained for inter-regional theta-gamma coupling ([ir-PAC] $F_{(1,12)}$ = 16.38, $p$ = 0.002, data not shown; differences with sPCP-SAL controls: $F_{(1,22)}$ = 17.5, $p$ < 0.0005; mixed ANOVAs as above). **(E)** In healthy mice, mPFC→dHPC high gamma signals were detected during the visits to the familiar objects (PSI vs. shuffle, $p$ = 0.004; paired $t$-student). sPCP disrupted this flow of information (baseline vs. sPCP, $p$ = 0.008; PSI vs. shuffle, $p$ = 0.19) that was not restored by risperidone (PSI vs. shuffle, $p$ = 0.24). **(F)** mPFC→dHPC PSI at high gamma frequencies during the visits to familiar objects correlated strongly with discrimination indices during baseline (R = 0.7, $p$ = 0.026), but not after sPCP (R = −0.28, $p$ = 0.43) or risperidone (R = −0.39, $p$ = 0.38). **(G)** Proposed neural mechanism for STM and effects of sPCP and risperidone. In red, changes produced by sPCP, in orange sPCP-induced deviations ameliorated by risperidone.

are highly translational between patients and rodent models of schizophrenia (Amann et al., 2010; Nagai et al., 2013; Javitt and Sweet, 2015; Modi and Sahin, 2017). Briefly, mice were placed in a cage surrounded by a sound enclosure with four speakers. The animals were presented with standard auditory stimuli first and subsequently the oddball paradigm in 30-min sessions during baseline, after sPCP and after risperidone treatments as above. Only animals evaluated in the three experiments were included in the analyses. Neural activities were recorded both in the mPFC and the dHPC, but hippocampal responses were inconsistent and highly variable between animals, therefore we only present data collected from the mPFC.

The AEP protocol consisted of 100 trials of white noise, each tone lasting 15 ms with an inter-trial interval of 10 s (**Figure 6A**). During baseline, we detected cortical AEPs in 82.3% of the trials (response ratio: [number of AEPs/number of trials]). The response ratio decreased after sPCP to 64.7%, but not after saline (**Supplementary Figure 4**). Risperidone partially rescued the response ratio to 71.8% (**Figure 6B**). Concomitantly, sPCP-treated mice showed abnormal AEPs with respect to the baseline, specifically the P2 and P3 peaks, analogous to the P200 and P300 peaks in humans. sPCP attenuated the spiking activity associated with the P2 component (40–70 ms) whereas the P3 component (200–300 ms) was reduced both in amplitude and

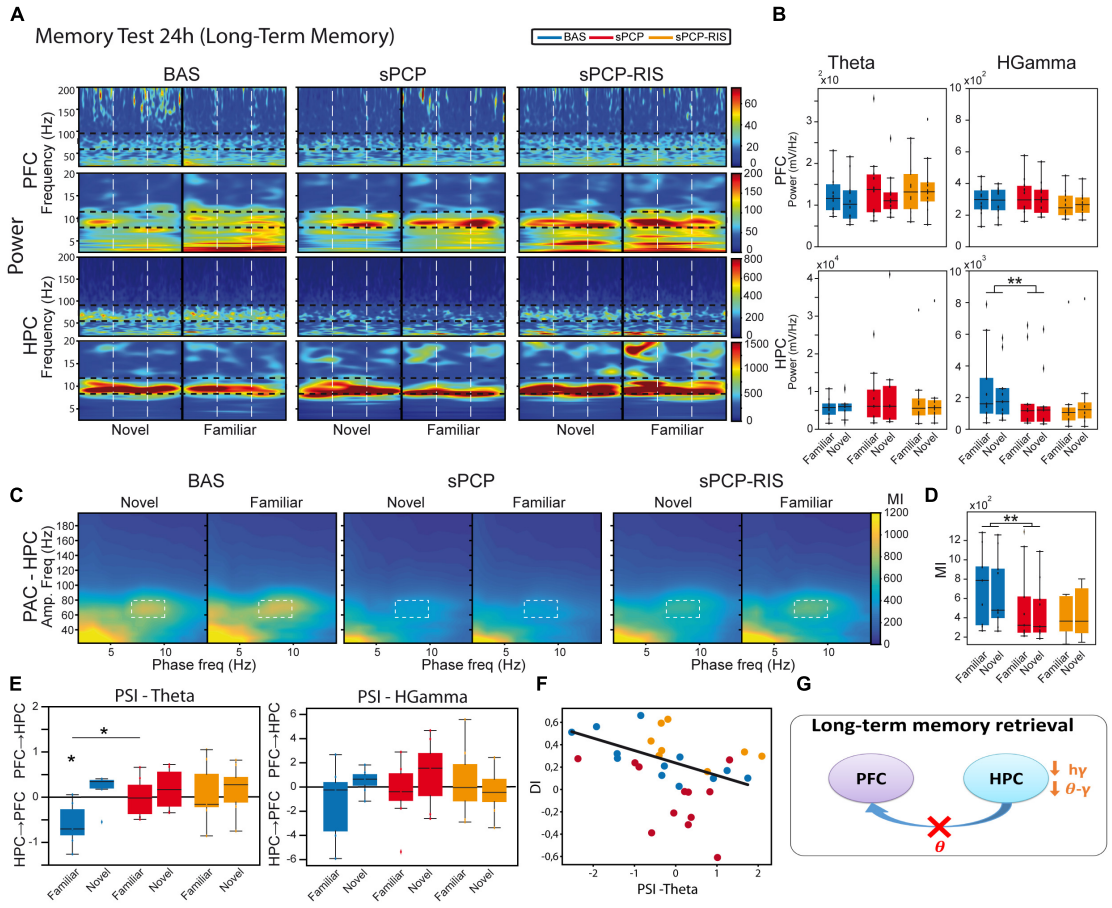


FIGURE 5
Neural substrates of long-term memory and effects of sPCP and risperidone. **(A)** Power spectra in the mPFC and the dHPC during the 24h memory test and effects of sPCP and risperidone. Vertical dashed lines mark the first second upon initiation of the visits. **(B)** Power in the mPFC and the dHPC was similar during visits to familiar and novel objects. sPCP reduced high gamma power in the dHPC non-specifically ($F_{(1,12)}$ = 15.33, $p$ = 0.006; mixed ANOVA with object (familiar vs. novel) and treatment (baseline vs. sPCP) as factors; differences with SAL controls, $F_{(1,20)}$ = 5.28, $p$ = 0.021; mixed ANOVA with object (familiar vs. novel) and treatment (SAL vs. sPCP) as factors). As above, risperidone partially rescued hippocampal gamma power. **(C,D)** Intrinsic hippocampal theta-gamma coupling (7–10 Hz with 60–80 Hz) was similar during visits to familiar and novel objects. sPCP disrupted theta-gamma coordination that was partially rescued by risperidone ([I-PAC] $F_{(1,12)}$ = 15.96, $p$ < 0.003; differences with sPCP-SAL controls: $F_{(1,22)}$ = 6.31, $p$ = 0.021; mixed ANOVAs as above). Similar results were obtained for inter-regional theta-gamma coupling ([ir-PAC] $F_{(1,12)}$ = 33.19, $p$ < 0.0005; differences with sPCP-SAL controls: $F_{(1,22)}$ = 5.97, $p$ = 0.02; data not shown). **(E)** In healthy mice, dHPC→mPFC theta signals were detected during the visits to the familiar objects (PSI vs. shuffle, $p$ = 0.031; paired $t$-student). sPCP disrupted this flow of information (baseline vs. sPCP, $p$ = 0.024; PSI vs. shuffle, $p$ = 0.94) that was not rescued by risperidone (PSI vs shuffle, $p$ = 0.64). **(F)** dHPC→mPFC PSI at theta frequencies during the visits to familiar objects correlated strongly with discrimination indices during baseline (R = −0.72, $p$ = 0.01), but not after sPCP (R = −0.42, $p$ = 0.17) or risperidone (R = −0.47, $p$ = 0.24). **(G)** Proposed neural mechanism for LTM and effects of sPCP and risperidone. In red, changes produced by sPCP, in orange sPCP-induced deviations ameliorated by risperidone.

spiking activity. Risperidone ameliorated the alterations associated with both components (Figure 6C and Table 1).

We finally examined the MMN using a passive oddball paradigm. Mismatch negativity is a component of event-related potentials that reflects preattentive auditory sensory memory. It emerges following deviant auditory stimuli and has been well characterized in patients with schizophrenia. We examined whether sPCP-treated mice exhibited reduced MMN and the rescuing abilities of risperidone. Mice were presented with 500 tones that differed in frequency (6 or 8 kHz) in 25–75% ratios (target and standard stimuli, respectively; Figure 6D). During baseline and in SAL mice, MMN emerged when the 6–8 kHz target-standard tone combination was presented, but not with the 8–6 kHz combination. The MMN was abolished by sPCP and not restored by risperidone (Figure 6E and Supplementary Figure 4). Together, risperidone attenuated the behavioral and neurophysiological alterations associated with the late components of the AEPs but failed to rescue the MMN (Table 1).

## Discussion

We found that subchronic PCP impaired STM, LTM, and auditory processing in mice that were partially rescued by risperidone administered daily for two weeks. The behavioral deficits were accompanied by disrupted dHPC-mPFC neural dynamics that attenuated after risperidone, preferentially in the dHPC. These findings suggest that risperidone may target this circuit, at least in part, to elicit its beneficial actions on cognitive abilities in patients with schizophrenia.

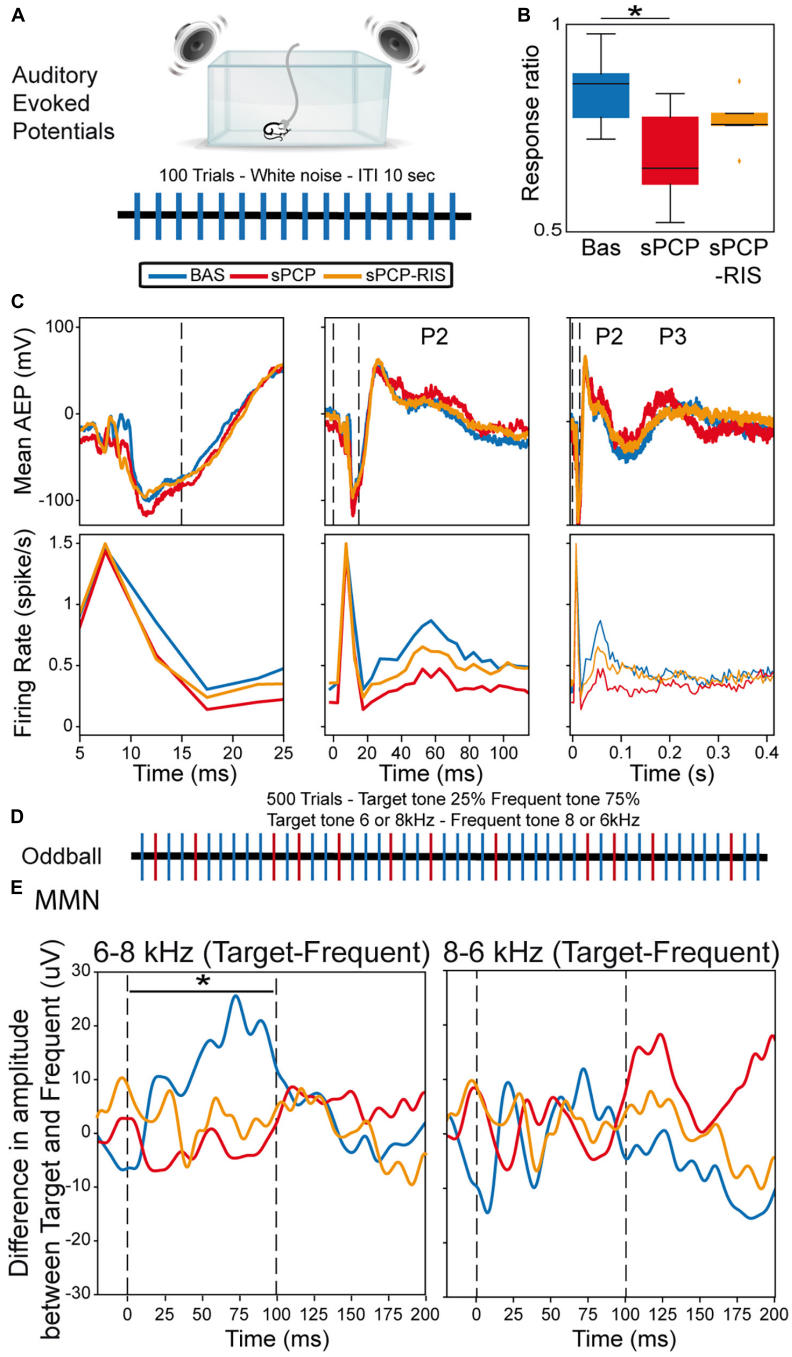


FIGURE 6
Neural substrates of auditory processing in the prelimbic cortex and effects of sPCP and risperidone. **(A)** AEP protocol. **(B)** Ratio of AEP responses detected in the PFC after the auditory stimuli. The ratio decreased in sPCP-treated animals ([baseline vs. sPCP, sPCP vs. saline]: $p$ = 0.024, 0.024, paired and unpaired $t$-test, respectively) and was partially recovered by risperidone. **(C)** Mean AEP and corresponding spiking activity (multi-unit firing rates) at three different timescales. P2 (40-70 ms) was associated with less spiking activity after sPCP ([baseline vs. sPCP, sPCP vs. saline as above]: $p$ = 0.013, 0.068; paired and unpaired $t$-tests, respectively), whereas P3 (200–300 ms) was reduced in amplitude and spiking activity ([baseline vs. sPCP, sPCP vs. saline as above]: amplitude: $p$ = 0.015, 0.055; firing rate: $p$ = 0.024, 0.06). Risperidone increased the spiking activity associated within P2 with respect to sPCP ($F_{(2,10)}$ = 2.49, $p$ = 0.076; one-way repeated measures ANOVA) and augmented the amplitude and spiking activity associated with P3 component ([amplitude, firing rate]: $p$ = 0.065, 0.097; paired and unpaired $t$-tests, respectively). **(D)** Protocol used for the oddball paradigm to assess mismatch negativity (MMN). **(E)** MMN was detected during the presentation of the 6-8 KHz target-frequent combination (left) but not the 8–6 kHz combination (right). Shown is the subtraction of target-frequent responses. MMN was absent in the sPCP-treated group (baseline vs. sPCP area under the curve; $p$ = 0.021, paired $t$-test) and not restored by risperidone. Vertical dashed lines mark the start and end of tone presentation.

The memory impairments produced by sPCP and their rescue by risperidone are in consonance with previous studies reporting that sPCP disrupts recognition memory in rodents that is sensitive to antipsychotic medication (Castañé et al., 2015; Rajagopal et al., 2016; Cadinu et al., 2018). Despite the novel object recognition task being extensively used as a screening tool for memory

abilities in biomedicine, an understanding of its underlying neural mechanisms was missing. Thus, we first investigated whether and how mPFC-dHPC circuits encoded memory acquisition, STM, and LTM in this task. Our findings unraveled a relevant role for the circuit's communication in the encoding of this task during baseline, with limited contribution of local power and theta-gamma coupling. mPFC→dHPC high gamma signals emerged during memory acquisition and the visits to familiar objects in the 3-minute memory test and were strongly associated with STM performance (R = 0.7). Later, dHPC→mPFC theta signals were detected during the visits to familiar objects in the 24 h memory test, which also correlated with LTM retrieval (R = 0.72). We note that the mPFC sends direct afferents to the dHPC in the mouse whereas dHPC→mPFC pathways use the nucleus reuniens of the thalamus as a relay (Sigurdsson and Duvarci, 2016). Our findings suggest that the information about the new object (acquisition) and its short-term storage were encoded by direct mPFC→dHPC connectivity whereas long-term memory retrieval depended on dHPC→mPFC indirect connectivity. This hypothesis is in line with previous studies showing that novel experiences initiate molecular signaling in the PFC that subsequently travel to the HPC (Takehara-Nishiuchi, 2020), where memories are stored (Eichenbaum, 2004). A key contribution of the circuit's connectivity to memory processing was evidenced further by the fact that sPCP impaired STM and LTM and disrupted dHPC-mPFC communication during the three phases of the NOR task. Previous studies from our group have consistently detected that dHPC→mPFC signals are relevant for long-term memory retrieval in wild-type mice of a different genetic background and altered in a mouse model of intellectual disability (Alemany-González et al., 2020, 2022), further supporting the findings presented here. Conflicting results exist on whether recognition memory for objects requires the PFC (Spanswick and Dyck, 2012; Morici et al., 2015). Recent studies using optogenetic interrogation, however, implicate the mPFC in this type of memory and, in fact, identify HPC→mPFC theta coupling as a major neural mechanism involved (Wang et al., 2021; Chao et al., 2022).

The differential effects of sPCP on prefrontal and hippocampal microcircuits may explain the disruption of the flow of information within this pathway. sPCP "disconnected" the circuit by causing opposite effects in the two brain regions: it increased neural synchronization in the mPFC (enhanced theta and gamma power) and desynchronized neural networks in the dHPC (reduced theta, gamma power, and theta-gamma coupling). Prior studies have demonstrated that acute NMDAR hypofunction desynchronizes neural activity in the HPC of rodents, including oscillatory and cross-frequency coupling (Caixeta et al., 2013). Remarkably, we recently reported comparable effects following an acute administration of PCP that generated psychosis-like states in mice (Delgado-Sallent et al., 2022). In that study, acute risperidone attenuated aberrant cortical hypersynchronization but was unable to restore hippocampal desynchronization. This likely reflects risperidone's efficacy in containing psychosis but its inefficiency in ameliorating cognitive abilities in the short term. While acute risperidone has proven to be effective in restoring cognitive deficits in the sPCP mouse model of schizophrenia (Grayson et al., 2007; Meltzer et al., 2011; Cadinu et al., 2018), it was important to assess the effects of a chronic treatment that mimicked more realistically the prescription of antipsychotic drugs to patients. Here, the injection of risperidone for two weeks rescued STM and LTM impairments and attenuated the neural activity reductions observed in the dHPC, albeit it was unable to restore cortical hypersynchronization or the connectivity of the circuit. However, it is plausible that dampening cortical hyperactivity by more prolonged administration of risperidone restores the circuit's communication. Therefore, chronic medication with risperidone may indeed favor healthier dHPC-mPFC neural dynamics in patients with schizophrenia, accounting for their better performance in executive function, attention, learning, and memory (Houthoofd et al., 2008; Baldez et al., 2021).

Furthermore, the findings of this study may help reconcile studies in schizophrenia patients, in which both increases and decreases of gamma oscillations were found to be key biomarkers of the disorder (Uhlhaas and Singer, 2010). Pathological gamma oscillations in the cortex may originate from disinhibition of cortical pyramidal neurons resulting from deficient $PV^+$ interneurons (Sigurdsson, 2016; Guyon et al., 2021; Alemany-González et al., 2022). In contrast, sPCP reduces $PV^+$ density extensively in the HPC (Abdul-Monim et al., 2007; Sabbagh et al., 2013) that, in turn, down-regulates pyramidal neuron activity (Korotkova et al., 2010). This may explain the dampening of gamma oscillations and theta-gamma coupling observed in the dHPC of sPCP-treated mice. Consistent with our findings, abnormal gamma synchrony produced by NMDAR hypofunction in both areas has been linked to cognitive impairment, including tasks assessing STM and object recognition (Tort et al., 2009; Korotkova et al., 2010; Carlén et al., 2012). Further experiments, however, are needed to elucidate the exact neural mechanisms underlying gamma pathology in schizophrenia. Risperidone attenuated sPCP-induced gamma and theta-gamma decreases in the dHPC very consistently. This antipsychotic drug binds to serotonin $5\text{-}HT_{2A}R$ with high affinity for which it is an inverse agonist. Therefore, it is likely that risperidone modulates gamma synchrony via $5\text{-}HT_{2A}R$-expressing $PV^+$ interneurons, which are present both in the mPFC and the dHPC (Puig et al., 2010; Puig and Gulledge, 2011; Puig and Gener, 2015).

We finally investigated the neural correlates of abnormal auditory processing in the frontal cortex of sPCP-treated mice, and the rescuing abilities of risperidone. As above, we found that sPCP impaired auditory processing in the mPFC that was attenuated by risperidone. That is, there was a reduction in the number of AEPs after sPCP, which in turn exhibited smaller P2 and P3 late peaks, the mouse components analogous to the P200 and P300 peaks in humans (Amann et al., 2010; Modi and Sahin, 2017). In addition, abnormal P2 and P3 components were associated with decreased spiking activity. Risperidone partially restored the late components of the AEPs, as observed in patients (Umbricht et al., 1999). We note that we did not detect alterations in the early component of the AEPs (the P1 and N1), which have been associated with positive symptoms (Galderisi et al., 2014), consistent with the lack of psychotic-like symptoms in sPCP-treated animals. However, electrophysiological recordings in the auditory cortex would be necessary to confirm these results as the auditory cortex has shown

more consistent alterations in the early components in patients and rodent models (Wang et al., 2020). sPCP-treated mice also showed reduced MMN, however, it was not rescued by risperidone. Reduced amplitude of the P200 and P300 peaks and the MMN are robust findings in patients with schizophrenia (Galderisi et al., 2014; Javitt and Sweet, 2015; Turetsky et al., 2015; Hamilton et al., 2019; Fitzgerald and Todd, 2020; Koshiyama et al., 2020) and have also been reported in NMDAR hypofunction animal models (Ehrlichman et al., 2008, 2009; Amann et al., 2010). Therefore, our findings on sPCP- and risperidone-produced alterations of AEPs and MMN are highly translational and relevant to human studies.

In conclusion, sPCP impaired recognition memory that was associated with increased mPFC, decreased dHPC neural network activities, and disrupted mPFC-dHPC communication. Risperidone rescued the memory deficits and attenuated hippocampal desynchronization but did not ameliorate mPFC and circuit connectivity alterations. sPCP also impaired auditory attention and its neural correlates in the mPFC, which were also ameliorated by risperidone. Our study suggests that the mPFC and the dHPC disconnect during NMDAR hypofunction, possibly underlying cognitive impairment in schizophrenia, and that risperidone targets this circuit to ameliorate cognitive abilities in patients.

## Data availability statement

The raw data supporting the conclusions of this article will be made available by the authors, without undue reservation.

## Ethics statement

All procedures were conducted in compliance with EU directive 2010/63/EU and Spanish guidelines (Laws 32/2007, 6/2013 and Real Decreto 53/2013) and were authorized by the Barcelona Biomedical Research Park (PRBB) Animal Research Ethics Committee and the local government.

## Author contributions

CD-S, TG, and MVP contributed to conception and design of the study and wrote the final version of the manuscript. CD-S, TG, CL-C, and PN analyzed the data. CD-S and MVP wrote the first draft of the manuscript. All authors contributed to manuscript revision, read, and approved the submitted version.

## Funding

This study was financed by grants SAF2016-80726-R and PID2019-104683RB-I00 to MVP funded by MCIN/AEI/10.13039/501100011033 and by ERDF "A way of making Europe". CD-S was supported by a FI AGAUR predoctoral fellowship from the Catalan Government (Generalitat de Catalunya grant number 2018 FI_B_00112).

## Acknowledgments

We thank Jose A. Garrido and Amanda B. Fath for scientific insight into this study and Patricia Ruiz for administrative support.

## Conflict of interest

The authors declare that the research was conducted in the absence of any commercial or financial relationships that could be construed as a potential conflict of interest.

## Publisher's note

All claims expressed in this article are solely those of the authors and do not necessarily represent those of their affiliated organizations, or those of the publisher, the editors and the reviewers. Any product that may be evaluated in this article, or claim that may be made by its manufacturer, is not guaranteed or endorsed by the publisher.

## Supplementary material

The Supplementary Material for this article can be found online at: https://www.frontiersin.org/articles/10.3389/fncel.2023.1152248/full#supplementary-material

## References

Abdul-Monim, Z., Neill, J. C., and Reynolds, G. P. (2007). Sub-chronic psychotomimetic phencyclidine induces deficits in reversal learning and alterations in parvalbumin-immunoreactive expression in the rat. *J. Psychopharmacol. Oxf. Engl.* 21, 198–205. doi: 10.1177/0269881107067097

Alemany-González, M., Gener, T., Nebot, P., Vilademunt, M., Dierssen, M., and Puig, M. V. (2020). Prefrontal-hippocampal functional connectivity encodes recognition memory and is impaired in intellectual disability. *Proc. Natl. Acad. Sci.* 117, 11788–11798. doi: 10.1073/pnas.1921314117

Alemany-González, M., Vilademunt, M., Gener, T., and Puig, M. V. (2022). Postnatal environmental enrichment enhances memory through distinct neural mechanisms in healthy and trisomic female mice. *Neurobiol. Dis.* 173:105841. doi: 10.1016/j.nbd.2022.105841

Amann, L. C., Gandal, M. J., Halene, T. B., Ehrlichman, R. S., White, S. L., McCarren, H. S., et al. (2010). Mouse behavioral endophenotypes for schizophrenia. *Brain Res. Bull.* 83, 147–161. doi: 10.1016/j.brainresbull.2010.04.008

Baldez, D. P., Biazus, T. B., Rabelo-da-Ponte, F. D., Nogaro, G. P., Martins, D. S., Kunz, M., et al. (2021). The effect of antipsychotics on the cognitive performanc of individuals with psychotic disorders: network meta-analyses of randomized controlled trials. *Neurosci. Biobehav. Rev.* 126, 265–275. doi: 10.1016/j.neubiorev.2021.03.028

Cadinu, D., Grayson, B., Podda, G., Harte, M. K., Doostdar, N., and Neill, J. C. (2018). NMDA receptor antagonist rodent models for cognition in schizophrenia and identification of novel drug treatments, an update. *Neuropharmacology* 142, 41–62. doi: 10.1016/j.neuropharm.2017.11.045

Caixeta, F. V., Cornélio, A. M., Scheffer-Teixeira, R., Ribeiro, S., and Tort, A. B. L. (2013). Ketamine alters oscillatory coupling in the hippocampus. *Sci. Rep.* 3:2348. doi: 10.1038/srep02348

Carlén, M., Meletis, K., Siegle, J. H., Cardin, J. A., Futai, K., Vierling-Claassen, D., et al. (2012). A critical role for NMDA receptors in parvalbumin interneurons for gamma rhythm induction and behavior. *Mol. Psychiatry* 17, 537–548. doi: 10.1038/mp.2011.31

Castañé, A., Santana, N., and Artigas, F. (2015). PCP-based mice models of schizophrenia: differential behavioral, neurochemical and cellular effects of acute and subchronic treatments. *Psychopharmacology* 232, 4085–4097. doi: 10.1007/s00213-015-3946-6

Chao, O. Y., Nikolaus, S., Yang, Y.-M., and Huston, J. P. (2022). Neuronal circuitry for recognition memory of object and place in rodent models. *Neurosci. Biobehav. Rev.* 141:104855. doi: 10.1016/j.neubiorev.2022.104855

Delgado-Sallent, C., Nebot, P., Gener, T., Fath, A. B., Timplalexi, M., and Puig, M. V. (2022). Atypical, but not typical, antipsychotic drugs reduce hypersynchronized prefrontal- hippocampal circuits during psychosis-like states in mice: contribution of 5-HT2A and 5-HT1A receptors. *Cereb. Cortex* 32, 3472–3487. doi: 10.1093/cercor/bhab427

Ehrlichman, R. S., Gandal, M. J., Maxwell, C. R., Lazarewicz, M. T., Finkel, L. H., Contreras, D., et al. (2009). N-methyl-d-aspartic acid receptor antagonist-induced frequency oscillations in mice recreate pattern of electrophysiological deficits in schizophrenia. *Neuroscience* 158, 705–712. doi: 10.1016/j.neuroscience.2008.10.031

Ehrlichman, R. S., Maxwell, C. R., Majumdar, S., and Siegel, S. J. (2008). Deviance-elicited changes in event-related potentials are attenuated by ketamine in mice. *J. Cogn. Neurosci.* 20, 1403–1414. doi: 10.1162/jocn.2008.20097

Eichenbaum, H. (2004). Hippocampus: cognitive processes and neural representations that underlie declarative memory. *Neuron* 44, 109–120. doi: 10.1016/j.neuron.2004.08.028

Fitzgerald, K., and Todd, J. (2020). Making sense of mismatch negativity. *Front. Psychiatry* 11:468. doi: 10.3389/fpsyt.2020.00468

Galderisi, S., Vignapiano, A., Mucci, A., and Boutros, N. N. (2014). Physiological correlates of positive symptoms in schizophrenia. *Curr. Top. Behav. Neurosci.* 21, 103–128. doi: 10.1007/7854_2014_322

Gener, T., Tauste-Campo, A., Alemany-González, M., Nebot, P., Delgado-Sallent, C., Chanovas, J., et al. (2019). Serotonin 5-HT1A, 5-HT2A and dopamine D2 receptors strongly influence prefronto-hippocampal neural networks in alert mice: contribution to the actions of risperidone. *Neuropharmacology* 158, 107743–107743. doi: 10.1016/j.neuropharm.2019.107743

Grayson, B., Idris, N., and Neill, J. (2007). Atypical antipsychotics attenuate a sub-chronic PCP-induced cognitive deficit in the novel object recognition task in the rat. *Behav. Brain Res.* 184, 31–38. doi: 10.1016/j.bbr.2007.06.012

Gulinello, M., Mitchell, H. A., Chang, Q., Timothy O'brien, W., Zhou, Z., Abel, T., et al. (2018). Rigor and reproducibility in rodent behavioral research. *Neurobiol. Learn. Mem.* 165:106780. doi: 10.1016/j.nlm.2018.01.001

Guyon, N., Zacharias, L. R., Oliveira, E. F. D., Kim, H., Leite, J. P., Lopes-Aguiar, C., et al. (2021). Network asynchrony underlying increased broadband gamma power. *J. Neurosci.* 41, 2944–2963. doi: 10.1523/JNEUROSCI.2250-20.2021

Hamilton, H. K., D'Souza, D. C., Ford, J. M., Roach, B. J., Kort, N. S., Ahn, K.-H., et al. (2018a). Interactive effects of an N-methyl-d-aspartate receptor antagonist and a nicotinic acetylcholine receptor agonist on mismatch negativity: implications for schizophrenia. *Schizophr. Res.* 191, 87–94. doi: 10.1016/j.schres.2017.06.040

Hamilton, H. K., Perez, V. B., Ford, J. M., Roach, B. J., Jaeger, J., and Mathalon, D. H. (2018b). Mismatch negativity but not P300 is associated with functional disability in schizophrenia. *Schizophr. Bull.* 44, 492–504. doi: 10.1093/schbul/sbx104

Hamilton, H. K., Woods, S. W., Roach, B. J., Llerena, K., McGlashan, T. H., Srihari, V. H., et al. (2019). Auditory and visual oddball stimulus processing deficits in schizophrenia and the psychosis risk syndrome: forecasting psychosis risk with P300. *Schizophr. Bull.* 45, 1068–1080. doi: 10.1093/schbul/sby167

Houthoofd, S. A. M. K., Morrens, M., and Sabbe, B. G. C. (2008). Cognitive and psychomotor effects of risperidone in schizophrenia and schizoaffective disorder. *Clin. Ther.* 30, 1565–1589. doi: 10.1016/j.clinthera.2008.09.014

Javitt, D. C., and Sweet, R. A. (2015). Auditory dysfunction in schizophrenia: integrating clinical and basic features. *Nat. Rev. Neurosci.* 16, 535–550. doi: 10.1038/nrn4002

Kaar, S. J., Angelescu, I., Marques, T. R., and Howes, O. D. (2019). Pre-frontal parvalbumin interneurons in schizophrenia: a meta-analysis of post-mortem studies. *J. Neural Transm. Vienna Austria* 1996, 1637–1651. doi: 10.1007/s00702-019-02080-2

Konradi, C., Yang, C. K., Zimmerman, E. I., Lohmann, K. M., Gresch, P., Pantazopoulos, H., et al. (2011). Hippocampal interneurons are abnormal in schizophrenia. *Schizophr. Res.* 131, 165–173. doi: 10.1016/j.schres.2011.06.007

Korotkova, T., Fuchs, E. C., Ponomarenko, A., von Engelhardt, J., and Monyer, H. (2010). NMDA receptor ablation on parvalbumin-positive interneurons impairs hippocampal synchrony, spatial representations, and working memory. *Neuron* 68, 557–569. doi: 10.1016/j.neuron.2010.09.017

Koshiyama, D., Kirihara, K., Tada, M., Nagai, T., Fujioka, M., Usui, K., et al. (2020). Reduced auditory mismatch negativity reflects impaired deviance detection in schizophrenia. *Schizophr. Bull.* 46, 937–946. doi: 10.1093/schbul/sbaa006

Lancaster, G., Iatsenko, D., Pidde, A., Ticcinelli, V., and Stefanovska, A. (2018). Surrogate data for hypothesis testing of physical systems. *Phys. Rep.* 748, 1–60. doi: 10.1016/j.physrep.2018.06.001

Lee, G., and Zhou, Y. (2019). NMDAR hypofunction animal models of schizophrenia. *Front. Mol. Neurosci.* 12:185. doi: 10.3389/fnmol.2019.00185

Lewis, D. A., Hashimoto, T., and Volk, D. W. (2005). Cortical inhibitory neurons and schizophrenia. *Nat. Rev. Neurosci.* 6, 312–324. doi: 10.1038/nrn1648

Meltzer, H. Y., Horiguchi, M., and Massey, B. W. (2011). The role of serotonin in the NMDA receptor antagonist models of psychosis and cognitive impairment. *Psychopharmacology* 213, 289–305. doi: 10.1007/s00213-010-2137-8

Modi, M. E., and Sahin, M. (2017). Translational use of event-related potentials to assess circuit integrity in ASD. *Nat. Rev. Neurol.* 13, 160–170. doi: 10.1038/nrneurol.2017.15

Morici, J. F., Bekinschtein, P., and Weisstaub, N. V. (2015). Medial prefrontal cortex role in recognition memory in rodents. *Behav. Brain Res.* 292, 241–251. doi: 10.1016/j.bbr.2015.06.030

Mouri, A., Koseki, T., Narusawa, S., Niwa, M., Mamiya, T., Kano, S., et al. (2012). Mouse strain differences in phencyclidine-induced behavioural changes. *Int. J. Neuropsychopharmacol.* 15, 767–779. doi: 10.1017/S146114571100085X

Nagai, T., Tada, M., Kirihara, K., Araki, T., Jinde, S., and Kasai, K. (2013). Mismatch negativity as a "translatable" brain marker toward early intervention for psychosis: a review. *Front. Psychiatry* 4:115. doi: 10.3389/fpsyt.2013.00115

Nolte, G., Ziehe, A., Nikulin, V. V., Schlögl, A., Krämer, N., Brismar, T., et al. (2008). Robustly estimating the flow direction of information in complex physical systems. *Phys. Rev. Lett.* 100, 234101–234101. doi: 10.1103/PhysRevLett.100.234101

Onslow, A. C. E., Bogacz, R., and Jones, M. W. (2011). Quantifying phase-amplitude coupling in neuronal network oscillations. *Prog. Biophys. Mol. Biol.* 105, 49–57. doi: 10.1016/j.pbiomolbio.2010.09.007

Puig, M. V., and Gener, T. (2015). Serotonin modulation of prefronto-hippocampal rhythms in health and disease. *ACS Chem. Neurosci.* 6, 1017–1025. doi: 10.1021/cn500350e

Puig, M. V., and Gulledge, A. T. (2011). Serotonin and prefrontal cortex function: neurons, networks, and circuits. *Mol. Neurobiol.* 44, 449–464. doi: 10.1007/s12035-011-8214-0

Puig, M. V., and Miller, E. K. (2015). Neural substrates of dopamine D2 receptor modulated executive functions in the monkey prefrontal cortex. *Cereb. Cortex* 1991, 2980–2987. doi: 10.1093/cercor/bhu096

Puig, M. V., Watakabe, A., Ushimaru, M., Yamamori, T., and Kawaguchi, Y. (2010). Serotonin modulates fast-spiking interneuron and synchronous activity in the rat prefrontal cortex through 5-HT1A and 5-HT2A receptors. *J. Neurosci.* 30, 2211–2222. doi: 10.1523/JNEUROSCI.3335-09.2010

Rajagopal, L., Massey, B. W., Huang, M., Oyamada, Y., and Meltzer, H. Y. (2014). The novel object recognition test in rodents in relation to cognitive impairment in schizophrenia. *Curr. Pharm. Des.* 20, 5104–5114. doi: 10.2174/13816128196661312161142 40

Rajagopal, L., Massey, B. W., Michael, E., and Meltzer, H. Y. (2016). Serotonin (5-HT)1A receptor agonism and 5-HT7 receptor antagonism ameliorate the subchronic phencyclidine-induced deficit in executive functioning in mice. *Psychopharmacology* 233, 649–660. doi: 10.1007/s00213-015-4137-1

Sabbagh, J. J., Murtishaw, A. S., Bolton, M. M., Heaney, C. F., Langhardt, M., and Kinney, J. W. (2013). Chronic ketamine produces altered distribution of parvalbumin-positive cells in the hippocampus of adult rats. *Neurosci. Lett.* 550, 69–74. doi: 10.1016/j.neulet.2013.06.040

Sigurdsson, T. (2016). Neural circuit dysfunction in schizophrenia: insights from animal models. *Neuroscience* 321, 42–65. doi: 10.1016/j.neuroscience.2015.06.059

Sigurdsson, T., and Duvarci, S. (2016). Hippocampal-prefrontal interactions in cognition, behavior and psychiatric disease. *Front. Syst. Neurosci.* 9:190. doi: 10.3389/fnsys.2015.00190

Spanswick, S. C., and Dyck, R. H. (2012). Object/context specific memory deficits following medial frontal cortex damage in mice. *PloS One* 7:e43698. doi: 10.1371/journal.pone.0043698

Takehara-Nishiuchi, K. (2020). Prefrontal-hippocampal interaction during the encoding of new memories. *Brain Neurosci. Adv.* 4:2398212820925580. doi: 10.1177/2398212820925580

Tort, A. B. L., Komorowski, R. W., Manns, J. R., Kopell, N. J., and Eichenbaum, H. (2009). Theta-gamma coupling increases during the learning of item-context associations. *Proc. Natl. Acad. Sci.* 106, 20942–20947. doi: 10.1073/pnas.0911331106

Turetsky, B. I., Dress, E. M., Braff, D. L., Calkins, M. E., Green, M. F., Greenwood, T. A., et al. (2015). The utility of P300 as a schizophrenia endophenotype and predictive biomarker: clinical and socio-demographic modulators in COGS-2. *Schizophr. Res.* 163, 53–62. doi: 10.1016/j.schres.2014.09.024

Uhlhaas, P. J., and Singer, W. (2010). Abnormal neural oscillations and synchrony in schizophrenia. *Nat. Rev. Neurosci.* 11, 100–113. doi: 10.1038/nrn2774

Umbricht, D., Javitt, D., Novak, G., Bates, J., Pollack, S., Lieberman, J., et al. (1999). Effects of risperidone on auditory event-related potentials in schizophrenia. *Int. J. Neuropsychopharmacol.* 2, 299–304. doi: 10.1017/S1461145799001595

Vallat, R. (2018). Pingouin: statistics in python. *J. Open Source Softw.* 3:1026. doi: 10.21105/joss.01026

Vinck, M., Oostenveld, R., Wingerden, M. V., Battaglia, F., and Pennartz, C. M. A. (2011). An improved index of phase-synchronization for electrophysiological data in the presence of volume-conduction, noise and sample-size bias. *NeuroImage* 55, 1548–1565. doi: 10.1016/j.neuroimage.2011.01.055

Wang, C., Furlong, T. M., Stratton, P. G., Lee, C. C. Y., Xu, L., Merlin, S., et al. (2021). Hippocampus–prefrontal coupling regulates recognition memory for novelty discrimination. *J. Neurosci.* 41, 9617–9632. doi: 10.1523/JNEUROSCI.1202-21.2021

Wang, X., Li, Y., Chen, J., Li, Z., Li, J., and Qin, L. (2020). Aberrant auditory steady-state response of awake mice after single application of the NMDA receptor antagonist MK-801 into the medial geniculate body. *Int. J. Neuropsychopharmacol.* 23, 459–468. doi: 10.1093/ijnp/pyaa022

Warburton, E. C., and Brown, M. W. (2015). Neural circuitry for rat recognition memory. *Behav. Brain Res.* 285, 131–139. doi: 10.1016/j.bbr.2014.09.050

Zorrilla de San Martín, J., Donato, C., Peixoto, J., Aguirre, A., Choudhary, V., et al. (2020). Alterations of specific cortical GABAergic circuits underlie abnormal network activity in a mouse model of down syndrome. *eLife* 9:e58731. doi: 10.7554/eLife.58731

frontiers | Frontiers in Cellular Neuroscience

TYPE Original Research
PUBLISHED 20 April 2023
DOI 10.3389/fncel.2023.1143319



OPEN ACCESS

EDITED BY
Ji Chen,
Zhejiang University, China

REVIEWED BY
Eckart Förster,
Ruhr University Bochum, Germany
Yuh-Man Sun,
Retired, London, United Kingdom
Martine Ammassari-Teule,
National Research Council (CNR), Italy

*CORRESPONDENCE
Eduardo Soriano
✉ esoriano@ub.edu
Yasmina Manso
✉ ymansosanz@ub.edu

†PRESENT ADDRESSES
Sara Gregorio,
Institute for Research in Biomedicine (IRB), Barcelona, Spain
Alba Vílchez-Acosta,
Department of Biomedical Sciences, Faculty of Biology and Medicine, University of Lausanne, Lausanne, Switzerland
Mónica Pardo,
Genetic Counseling Unit in Hereditary Cancer, Hospital del Mar, Barcelona, Spain

‡These authors have contributed equally to this work and share last authorship

SPECIALTY SECTION
This article was submitted to Cellular Neuropathology, a section of the journal Frontiers in Cellular Neuroscience

RECEIVED 12 January 2023
ACCEPTED 27 March 2023
PUBLISHED 20 April 2023

CITATION
Pardo M, Gregorio S, Montalban E, Pujadas L, Elias-Tersa A, Masachs N, Vílchez-Acosta A, Parent A, Auladell C, Girault J-A, Vila M, Nairn AC, Manso Y and Soriano E (2023) Adult-specific Reelin expression alters striatal neuronal organization: implications for neuropsychiatric disorders. *Front. Cell. Neurosci.* 17:1143319. doi: 10.3389/fncel.2023.1143319



# Adult-specific Reelin expression alters striatal neuronal organization: implications for neuropsychiatric disorders

Mònica Pardo[1,2†], Sara Gregorio[1,2†], Enrica Montalban[3], Lluís Pujadas[1,2,4,5], Alba Elias-Tersa[1,2], Núria Masachs[1,2], Alba Vílchez-Acosta[1,2†], Annabelle Parent[6], Carme Auladell[1,2], Jean-Antoine Girault[3], Miquel Vila[2,6,7,8,9], Angus C. Nairn[10], Yasmina Manso[1,2*‡] and Eduardo Soriano[1,2*‡]

[1]Developmental Neurobiology and Regeneration Laboratory, Department of Cell Biology, Physiology and Immunology, Institute of Neurosciences, Universitat de Barcelona, Barcelona, Spain, [2]Centro de Investigación Biomédica en Red Enfermedades Neurodegenerativas (CIBERNED), Instituto de Salud Carlos III, Madrid, Spain, [3]Institut du Fer à Moulin UMR-S 1270, INSERM, Sorbonne University, Paris, France, [4]Department of Experimental Sciences and Methodology, Faculty of Health Science and Welfare, University of Vic – Central University of Catalonia (UVic-UCC), Vic, Spain, [5]Tissue Repair and Regeneration Laboratory (TR2Lab), Institut de Recerca i Innovació en Ciències de la Vida i de la Salut a la Catalunya Central (IRIS-CC), Barcelona, Spain, [6]Neurodegenerative Diseases Research Group, Vall d'Hebron Research Institute, Barcelona, Spain, [7]Department of Biochemistry and Molecular Biology, Autonomous University of Barcelona (UAB), Barcelona, Spain, [8]Institució Catalana de Recerca i Estudis Avançats (ICREA), Barcelona, Spain, [9]Aligning Science Across Parkinson's (ASAP) Collaborative Research Network, Chevy Chase, MD, United States, [10]Department of Psychiatry, Yale University School of Medicine, New Haven, CT, United States

In addition to neuronal migration, brain development, and adult plasticity, the extracellular matrix protein Reelin has been extensively implicated in human psychiatric disorders such as schizophrenia, bipolar disorder, and autism spectrum disorder. Moreover, heterozygous *reeler* mice exhibit features reminiscent of these disorders, while overexpression of Reelin protects against its manifestation. However, how Reelin influences the structure and circuits of the striatal complex, a key region for the above-mentioned disorders, is far from being understood, especially when altered Reelin expression levels are found at adult stages. In the present study, we took advantage of complementary conditional gain- and loss-of-function mouse models to investigate how Reelin levels may modify adult brain striatal structure and neuronal composition. Using immunohistochemical techniques, we determined that Reelin does not seem to influence the striatal patch and matrix organization (studied by μ-opioid receptor immunohistochemistry) nor the density of medium spiny neurons (MSNs, studied with DARPP-32). We show that overexpression of Reelin leads to increased numbers of striatal parvalbumin- and cholinergic-interneurons, and to a slight increase in tyrosine hydroxylase-positive projections. We conclude that increased Reelin levels might modulate the numbers of striatal interneurons and the density of the nigrostriatal dopaminergic projections, suggesting that these changes may be involved in the protection of Reelin against neuropsychiatric disorders.

KEYWORDS

**Reelin, striatum, interneurons, dopamine projections, schizophrenia, Tourette's syndrome**

# 1. Introduction

Reelin is an extracellular matrix protein important for neuronal migration and layer formation during neocortical development (D'Arcangelo et al., 1995; Alcántara et al., 1998; Rice and Curran, 2001; Soriano and Del Río, 2005; Cooper, 2008; Hirota and Nakajima, 2017; Vílchez-Acosta et al., 2022). Besides its role during development, the Reelin pathway is also active in the adult brain, controlling glutamatergic neurotransmission, dendritic spine formation, synaptic plasticity and adult neurogenesis (Chen et al., 2005; Herz and Chen, 2006; Qiu et al., 2006b; Groc et al., 2007; Niu et al., 2008; Pujadas et al., 2010; Teixeira et al., 2012; Bosch et al., 2016). Reelin binds to apolipoprotein E receptor 2 (ApoER2) and very-low-density lipoprotein receptor (VLDLR), leading to the phosphorylation and activation of the intracellular adaptor protein Disabled 1 (Dab1), which triggers a complex signaling cascade involving members of the Src kinase family, PI3K, Erk1/2 and GSK3 kinases, and Cullin-5-dependent degradation, amongst others (Howell et al., 1997, 1999; D'Arcangelo et al., 1999; Hiesberger et al., 1999; Beffert et al., 2002; Arnaud et al., 2003; Benhayon et al., 2003; Ballif et al., 2004; Strasser et al., 2004; González-Billault et al., 2005; Simó et al., 2007, 2010; Yasui et al., 2010; Molnár et al., 2019).

Genetic studies have associated the Reelin gene (*RELN*) with a number of psychiatric diseases, including schizophrenia, bipolar disorder, and autism spectrum disorder (Impagnatiello et al., 1998; Fatemi et al., 2001, 2005; Persico et al., 2001; Grayson et al., 2005; Ovadia and Shifman, 2011; Wang et al., 2014; Baek et al., 2015; Lammert and Howell, 2016). This link is also supported by studies showing that Reelin levels are reduced in patients with schizophrenia and bipolar disorder (Fatemi et al., 2000; Torrey et al., 2005; Ruzicka et al., 2007), and can be altered by psychotropic medication (Fatemi et al., 2009). In fact, Reelin haploinsufficiency models, based on the suppression or reduction of Reelin expression (or its downstream pathway), manifest features related to neuropsychiatric disorders, such as cognitive impairments, psychosis vulnerability, and learning deficits that frequently coexist with evident alterations in hippocampal plasticity (Tueting et al., 1999; Krueger et al., 2006; Marrone et al., 2006; Qiu et al., 2006a; Ammassari-Teule et al., 2009; Folsom and Fatemi, 2013). Conversely, overexpression of Reelin protects against psychiatric disease-related phenotypes in mice, since it reduces cocaine sensitization, disruption of pre-pulse inhibition (PPI) and the time spent floating in the forced swim test (Teixeira et al., 2011). Furthermore, Reelin also regulates adult neurogenesis and synaptogenesis (Kim et al., 2002; Pujadas et al., 2010; Teixeira et al., 2012; Bosch et al., 2016), whose disruption is considered to be involved in the pathogenesis of psychiatric disorders (Kempermann, 2008; Zhao et al., 2008).

The striatum plays a critical function in motor control and regulation of motivated behaviors (Bolam et al., 2000). Its neuronal population is composed of 5–10% interneurons but the large majority (90–95%) are efferent neurons, the GABAergic medium spiny neurons (MSNs). The latter can be classified into striatonigral or striatopallidal subtypes based on their axonal projections to the internal globus pallidus (iGP) and substantia nigra (SN) or to the external globus pallidus (eGP), respectively. They can be distinguished by the expression of the dopamine D1 receptor (striatonigral MSNs) or the dopamine D2 receptor (striatopallidal MSNs) (Bolam, 1984; Schiffmann et al., 1991; Gerfen, 1992; Smith et al., 1998). Although the striatum exhibits a relatively uniform appearance, it presents a complex organization based in two different compartments: the patches or striosomes (stained by μ-opioid receptor MOR) and the matrix, which surrounds the patches (Olson et al., 1972; Graybiel and Ragsdale, 1978; Herkenham and Pert, 1981). A proper cellular and compartmental organization is essential for a correct striatal function (Crittenden and Graybiel, 2011).

Despite the involvement of the striatum (including the nucleus accumbens) and its circuitry in psychiatric disorders such as major depression, schizophrenia, and obsessive-compulsive disorder, few studies addressing how Reelin influences striatal structure and circuits are available (de Guglielmo et al., 2022). Most of these studies use heterozygous *reeler* mice as a model, which have reduced Reelin expression also during development. Here we investigate how altering Reelin levels, specifically at late postnatal and adult stages, may lead to cellular and compartmental changes in the striatum that could be related to neuropsychiatric disorders. We used gain- and loss-of-function conditional mouse models to investigate how Reelin levels may modify striatal structure and neuronal composition. Our results suggest that whereas Reelin does not seem to influence the patch-matrix striatal organization and the numbers of MSNs, overexpression of Reelin leads to increased numbers of striatal interneurons and to a slight increase in the dopaminergic projections.

# 2. Materials and methods

## 2.1. Animals

The TgRln is a conditionally regulated transgenic line that overexpresses Reelin from postnatal (P) day 5–10 by means of a transactivator (tTA) under the control of the calcium–calmodulin-dependent kinase II α promoter (pCaMKIIα) (Pujadas et al., 2010). Reelin transgenic littermates, which have an inactive form of the Reelin gene insertion without the transactivator tTA, were used as controls. For the generation of the Reelin conditional knockout mouse line, homozygous floxed Reelin (fR/fR) mice, with the exon 1 of the Reln gene flanked by loxP sites, were crossed with a heterozygous UbiCreERT2 line [B6.Cg-Tg(UBC-cre/ESR1)1Ejb/J, stock #008085, The Jackson Laboratory], both on a C57BL/6J background (Vílchez-Acosta et al., 2022). The UbiCreERT2 line displays a ubiquitous expression of the Cre recombinase fused to a modified estrogen receptor ligand-binding domain that retains the Cre at the cytoplasm. Administration of an estrogen receptor antagonist (tamoxifen) at P45–60 induces the nuclear translocation of Cre recombinase and the ubiquitous scission of the floxed gene sequence (*Reln*) in all tissues at adult stages. The resultant offspring (Cre fR/fR) was used for the experiments, and fR/fR littermates were used as controls. In both transgenic lines, 4–5 months old female and male mice were used for the experiments.

Male, 8–10-week old, Drd2-EGFP ($n$ = 20 Swiss-Webster and 6 C57BL/6N background, founder S118), Drd1a-EGFP ($n$ = 4 Swiss-Webster and $n$ = 4 C57BL/6N background, founder X60) hemizygous mice were also used in this study. BAC Drd2- and Drd1a-EGFP mice, that express the reporter protein enhanced green fluorescent protein under the control of the D2 and D1

receptor promoters, were generated by GENSAT (Gene Expression Nervous System Atlas) at the Rockefeller University (New York, NY, USA) (Gong et al., 2007).

Mice were bred, studied, and processed at the animal research facility of the Faculty of Pharmacy of the University of Barcelona and at the animal research facility of the Rockefeller University. Animals were provided with food and water *ad libitum* and maintained in a temperature-controlled environment in a 12/12 h light-dark cycle. All the experiments involving animals were performed in accordance with the European Community Council directive 2010/63/EU, the National Institute of Health guidelines for the care and use of laboratory animals, and the Rockefeller University's Institutional Animal Care and Use Committee (protocol 14753-H). Experiments were also approved by the local ethical committees.

## 2.2. PCR genotyping

DNA was extracted from tail biopsies by adding 100 µl sodium hydroxide (50 mM), and incubating at 100°C during 15 min. Then, samples were kept on ice for 10 min and stored at −20°C until use.

The PCR was performed with the GoTaq® Green Master Mix (Promega), and the primers used for genotyping were as follows. Cre fR/fR line: for homozygous floxed Reelin detection, FloxA (5′CGAGGTGCTCATTTCCCTGCACATTGC3′) and FloxB (5′ CACCGACCAAAGTGCTCCAATCTGTCG 3′) primers were used. Homozygous fR/fR mice present only one band of 613 bp whereas heterozygous mice present an additional band at 496 bp. To determine the presence of UbiCre, the primers UbiCre1(5′ GCG GTC TGG CAG TAA AAA CTA TC 3′) and UbiCre2 (5′ GTC AAA CAG CAT TGC TGT CAC TT 3′) which are specific for UbiCreERT2, and UbiCre3 (5′ CTA GGC CAC AGA ATT GAA AGA TCT 3′) and UbiCre4 (5′ GTA GGT GGA AAT TCT AGC ATC ATC C 3′) as internal positive control were used. Mice heterozygous for Cre (Cre fR/fR) had a double band at 324 and 100 bp while mice negative for Cre only amplified the 100 bp band. TgRln line: the primers RLTG-gen-F (5′-TTGTACCAGGTTCCGCTGGT-3′) and RLTG-gen-R (5′-GCA CAT ATC CAG GTT TCA GG-3′) were used to amplify both the endogenous Reelin gene (720 bp) and the transgenic DNA (320 bp); the primers nTTA-C (5′-ACT AAG TCA TCG CGA TGG AG-3′) and nTTA-F (5′-CGA AAT CGT CTA GCG CGT C-3′), were used to detect the transactivator tTA transgene (Pujadas et al., 2010).

## 2.3. Tamoxifen administration

Inactivation of Reelin expression was induced at postnatal day 45–60 by daily intraperitoneal injections of tamoxifen dissolved in 10% alcohol-90% sunflower oil for 3 consecutive days (180 mg/kg/day; Sigma-Aldrich).

## 2.4. Immunohistochemistry

For immunohistochemistry, 4–5 months old mice were perfused transcardially with 4% paraformaldehyde (PFA) in PB 0.1 M. Brains were quickly removed, fixed overnight in PFA, and then transferred to 30% sucrose in PBS 0.1 M and stored at 4°C (48 h). Brains were frozen with methylbutane (Honeywell) at −42°C and stored at −80°C until use. Thirty-µm coronal sections were obtained with a freezing microtome (Leica SM2010R) and were kept in a cryoprotective solution at −20°C. Immunohistochemistry was performed on free-floating sections. The sections were inactivated for endogenous peroxidases with 3% $H_2O_2$ in 10% methanol and PBS for 15 min. After three washes with PBS and three washes with PBS-0.2% Triton (PBS-T), sections were blocked for 2 h at room temperature (RT) with PBS-T containing 10% of normal horse serum (NHS) and 0.2% of gelatin. For Reelin immunostaining, anti-mouse unconjugated F(ab′)2 fragments (1:300, Jackson ImmunoResearch), were added in the blocking step. After three washes with PBS-T, tissue sections were incubated with a primary antibody with PBS-T containing 5% of NHS and 0.2% of gelatine, overnight at 4°C.

The commercial primary antibodies used were: anti-Reelin (clone G10, MAB5364, Merck Millipore, 1:1,000), anti-choline acetyltransferase (ChAT AB144P, Merck Millipore, 1:500), anti-µ opioid receptor (MOR, 1:2,000, rabbit, AB5511, Merck Millipore), anti-parvalbumin (PV, 1:500, Rabbit, PV27, Swant), anti-dopamine- and cAMP-regulated phosphoprotein, 32 kDa (DARPP-32, 1:500, mouse, 611520, BD Transduction Laboratories), anti-tyrosine hydroxylase (TH, 1:1,000, Rabbit, AB152, Merck Millipore). Sections were washed with PBS-T and then incubated for 2 h at RT with biotinylated secondary antibody (1:200, Vector Laboratories). After subsequent washes with PBS-T, the sections were incubated for 2 h at RT with streptavidin-HRP (1:400, GE Healthcare UK). After washing, the staining was developed using 0.03% diaminobenzidine (DAB) and 0.01% $H_2O_2$, with 0.1% nickel ammonium sulfate added to the solution. Finally, sections were dehydrated and mounted with Eukitt mounting medium (Sigma-Aldrich).

For immunofluorescence staining a similar procedure was followed using Alexa Fluor 488 secondary antibody (1:500, Invitrogen, ThermoFisher) (excluding peroxidase inactivation), counterstained with Bisbenzimide (1:500) for 30 min at RT, mounted with Mowiol and stored at −20°C.

## 2.5. D1-/D2-cell specific mRNA extraction

Cell-type specific translated-mRNA purification (TRAP), was performed as previously described (Heiman et al., 2008) with a few modifications. Each sample consisted of a pool of 2–3 mice. BAC-TRAP transgenic mice (Drd2- and Drd1a-EGFP) were sacrificed by decapitation. The brain was quickly dissected out and placed in a cold buffer and was then transferred to an ice-cold mouse brain matrix to cut thick slices from which the nucleus accumbens (NAcc) and the dorsal striatum (DS) were punched out using ice-cold stainless-steel cannulas. Each sample was homogenized in 1 ml of lysis buffer (20 mM HEPES KOH (pH 7.4), 5 mM $MgCl_2$, 150 mM KCl, 0.5 mM dithiothreitol, 100 µg/ml CHX protease and RNAse inhibitors) with successively loose and tight glass-glass 2-ml Dounce homogenizers. Each homogenate was centrifuged at 2,000 × *g*, at 4°C, for 10 min. The supernatant was

separated from cell debris and supplemented with NP-40 (EDM Biosciences) to a final concentration of 1% and DHPC (Avanti Polar lipids) to a final concentration of 30 mM. After mixing and incubating on ice for 5 min, the lysate was centrifuged for 10 min at 20,000 × *g* to separate the supernatant from the insolubilized material. A mixture of streptavidin-coated magnetic beads was incubated with biotinylated protein L and then with GFP antibody that was added to the supernatant and incubated ON at 4°C with gentle end-over rotation. After incubation, beads were collected with a magnetic rack and washed 5 times with high-salt washing buffer (20 mM HEPES-KOH (pH 7.4), 5 mM $MgCl_2$, 350 mM KCl, 1% NP-40) and immediately placed in "RTL plus" buffer (Qiagen). The mRNA was purified using the RNase micro KIT (Qiagen). RNA integrity was checked with the Bionalyzer (agilent 2100 Bioanalyzer, Agilent RNA 6000 nano kit). Five nanograms of mRNA from each sample were used for retro-transcription, performed with the Reverse Transcriptase III (Life Technologies) following the manufacturer's instructions.

## 2.6. Real-time PCR

Quantitative real time PCR, was performed using SYBR Green PCR kit in 96-well plates according to the manufacturer's instructions. Results are presented as normalized to the indicated house-keeping genes and the delta-threshold cycle (Ct) method was used to obtain a fold change. mRNA levels are presented relative to D2. The housekeeping gene for normalization was beta-myosin heavy chain gene (Myh7).

## 2.7. Western blot

Brains were quickly extracted, frozen in liquid nitrogen and stored at −80°C until use. Brain tissue was processed as previously described (Pujadas et al., 2010). After incubation with antibodies, membranes were developed with the ECL system.

## 2.8. Immunohistochemical analysis

For DARPP-32 cell counting, sections were scanned using NanoZoomer 2.0-HT (Hamamatsu). We used FIJI software to crop the striatal profile from the image. DARPP-32-positive cells were counted with the cell nuclei assistant TMarker software.

The images of PV and ChAT interneurons were acquired with a Nikon E600 microscope attached to an Olympus DP72 camera, and images were reconstructed using MosaicJ from the Fiji software (Fiji is Just ImageJ – NIH). The intermediate striatum was subdivided into four sub-regions: dorso-medial (DM), dorso-lateral (DL), ventro-medial (VM), and ventro-lateral (VL) (see Gernert et al., 2000; Ammassari-Teule et al., 2009) taking slices from Bregma 1.34 to 0.02 mm, to identify possible changes in the neuronal distribution inside the different striatal regions. Cell density studies were performed with FIJI tools to measure the area and to count cells (cell counter).

To measure TH intensity, slides were scanned with SilverFast at 600 ppm and SigmaPlot was used to measure the intensity of the different striatal areas. The results are expressed as % from control which was considered as 1 in each independent experiment to avoid deviations caused by differences in the DAB development procedure.

TH-positive synaptic bouton images were taken with 63X oil immersion objective and counted selecting randomly an 11 mm × 11 mm ROI using Fiji.

For each mouse transgenic line we analyzed 3–14 animals and for each animal and average of 6–8 images were analyzed.

## 2.9. Statistics

All statistical analyses were performed using GraphPad Prism 5.0 software (GraphPad Software, Inc.). Data were analyzed with unpaired, two-tailed Student's *t*-tests and statistical significance was set at $p$-value $< 0.05$. Unless otherwise stated, all values are presented as mean ± the standard error of the mean (SEM). The number of animals used in each experiment is detailed in the figure legend.

# 3. Results

## 3.1. Reelin is highly expressed in striatonigral MSNs

To determine the effects of Reelin levels in the mouse striatal organization, we first studied Reelin expression in a Reelin overexpressing and a knockout mouse line. Control mice from both lines exhibited numerous Reelin-positive cell bodies that were distributed throughout the striatum (**Figures 1A, D**), whereas the tamoxifen-inducible conditional knockout mouse line (Cre fR/fR) presented a drastic reduction of Reelin protein as detected by immunohistochemistry (**Figure 1B**) and by Western blot (**Figure 1C**). In contrast, Reelin overexpressing mice (TgRln) showed a dramatic increase of Reelin protein in the striatum (**Figure 1E**) which was apparent in both cell bodies and neuropil (see also Pujadas et al., 2010).

Reelin has been described to co-localize with Calbindin D-28k-positive neurons (Sharaf et al., 2015), a well-known marker of striatal MSNs. Hence, we used the TRAP technology (Heiman et al., 2008) to determine a possible enrichment of Reelin mRNA in D1- or D2-receptor expressing MSNs in both DS and NAcc. BAC-TRAP-D1 and –D2 mice, were used to specifically immunoprecipitate mRNAs from D1 (striatonigral) or D2 (striatopallidal) neuronal populations from the DS and the NAcc. Reelin mRNA levels were compared to the housekeeping beta-myosin heavy chain gene. Results indicated that Reelin mRNA is enriched in D1-MSNs, in both the DS and the NAcc (**Figures 1F, G**). The expression of Dab1, a key downstream effector of the Reelin pathway, was also higher in D1 MSNs of the DS and NAcc (**Figures 1H, I**). These results suggest that the striatonigral D1 MSNs population is the main producer of striatal Reelin.

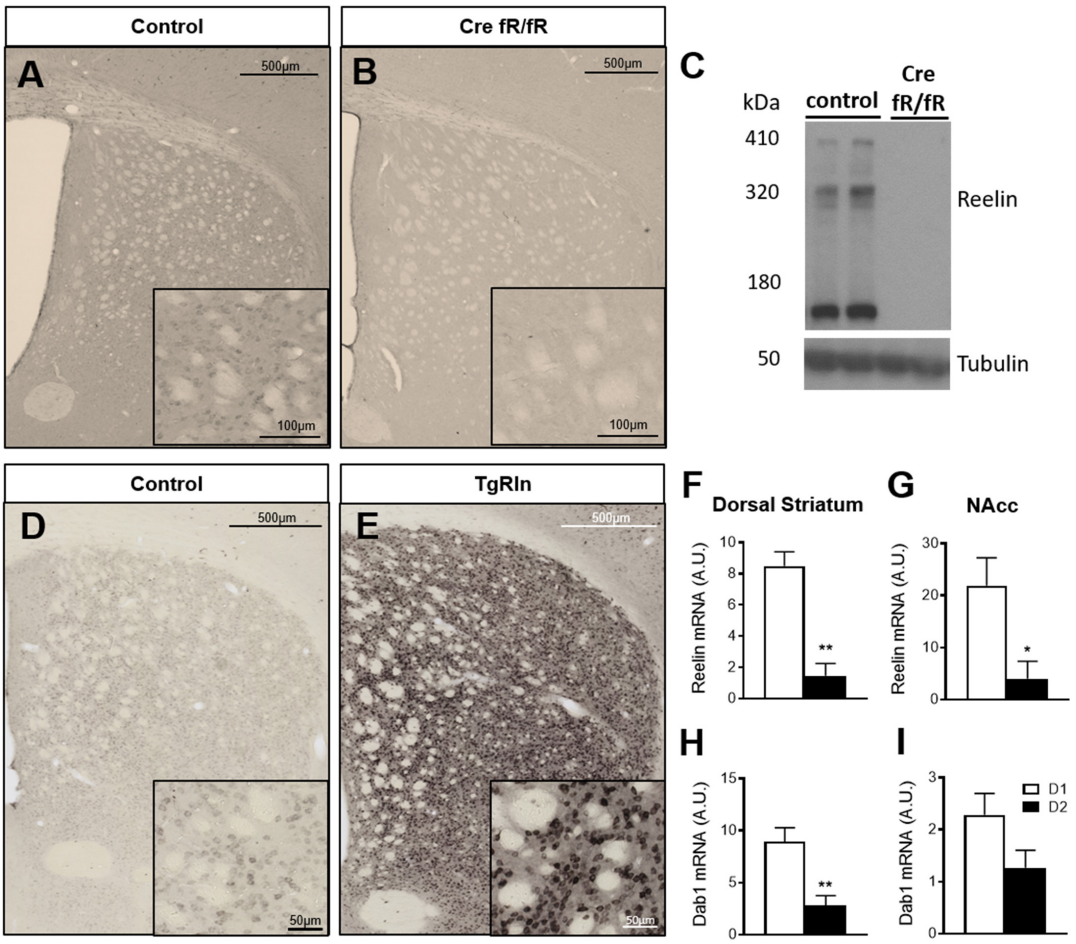


FIGURE 1
Reelin in the striatum is mainly expressed by D1 striatonigral MSNs. **(A–E)** Immunohistochemistry and Western blot for Reelin show that it is absent in Cre fR/fR mice **(B,C)** compared to the fR/fR littermates (control, **A,C**) while it is clearly overexpressed in the striatum of TgRln mice **(E)** compared to transgenic littermates with an inactive form of the Reelin gene insertion without tTA (controls, **D**). **(F,G)** Quantification of Reelin mRNA levels in the dorsal striatum **(F)** and NAcc **(G)** of D1/D2-TRAP mice ($n$ = 3–4). **(H,I)** Quantification of Dab1 mRNA levels in the dorsal striatum **(H)** and NAcc **(I)** of D1/D2-TRAP mice ($n$ = 4–7). Scale bar: **(A,B,D,E)**, 500 μm; high magnification insets **(A,B)**, 100 μm, **(D,E)**, 50 μm. NAcc, nucleus accumbens; D1, dopamine 1 receptor; D2, dopamine 2 receptor. Statistical analysis was performed using Student's $t$-test; significant differences were established at $^{*}p < 0.05$, $^{**}p < 0.01$. Data represent means ± SEM.

## 3.2. Striatal MSNs organization is independent of Reelin expression levels

To determine whether Reelin expression levels could modify DS MSN populations, we first immunostained sections with DARPP-32, a marker of MSNs, and quantified the density of striatal MSNs in the Cre fR/fR (Figures 2A, B) and TgRln (Figures 2C, D) mouse models. Results indicated that neither the absence nor the overexpression of Reelin altered the density of striatal DARPP-32 positive neurons in the striatum of Cre fR/fR (Figures 2A, B, E) or TgRln mice (Figures 2C, D, F).

Since Reelin controls neuronal migration, we next wanted to determine whether Reelin levels could affect the DS patch organization. Immunostaining of the striosomes with MOR showed striatal patches with a similar spatial distribution in all genotypes, suggesting that striatal MSNs density and organization are not affected by alterations of Reelin expression levels (Figures 2G–I).

## 3.3. Reelin overexpression alters striatal interneuron population

In addition to MSNs, the striatum also contains ChAT+ and GABAergic interneurons, the PV-expressing ones being the best known. To assess the number and distribution of ChAT+ interneurons in the different transgenic lines, we subdivided the DS in four sub-regions: DM, DL, VM, and VL (Figure 3A). Analysis of the density and distribution of ChAT+ cells showed no differences in Cre fR/fR mice compared to controls (Figures 3A–F). In contrast, the density of ChAT+ cells was increased in Reelin overexpressing mice compared to controls, reaching significance in 3 of the striatal sub-regions analyzed (Figures 3G–L).

We also analyzed the density and distribution of PV striatal interneurons. In line with the ChAT+ interneuron data, no changes in the density and distribution of PV+ interneurons (Figures 4A, B) were observed in any of the DS regions of Cre fR/fR mice compared to controls (Figures 4C–F). However, analysis of PV+ interneuron

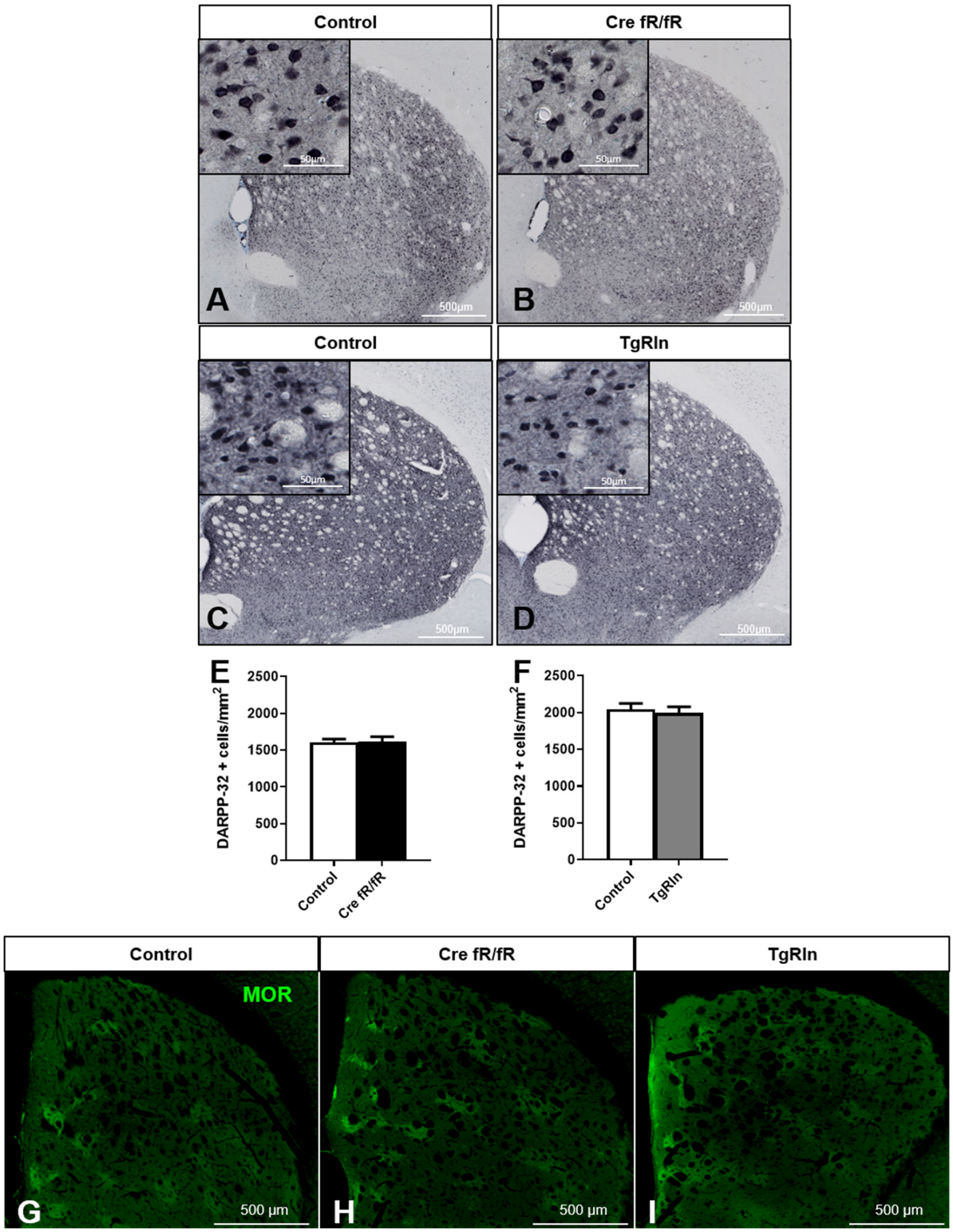


FIGURE 2
Striatal MSNs density and organization is not affected by Reelin levels. **(A–D)** Representative images of DARPP-32 immunohistochemistry (striatal MSNs) in coronal sections of control and Cre fR/fR **(A,B)** and control and TgRln **(C,D)** striatum (respective controls as in Figure 1). **(E,F)** Quantification of DARPP-32-positive cell density shows no alterations of striatal MSNs neither in Cre fR/fR ($n$ = 5–6) **(E)** nor in TgRln ($n$ = 6) **(F)** mice. **(G–I)** Immunofluorescence for μ-opioid receptor (MOR) in coronal sections of control **(G)**, Cre fR/fR **(H)**, and TgRln **(I)** striatum showing a similar organization of striatal patches in all the models. Scale bar: **(A–D)**, 500 μm; high magnification insets 50 μm; **(G–I)**, 500 μm. Statistical analysis was performed using Student's t-test. Data are represented as means ± SEM.

10.3389/fncel.2023.1143319

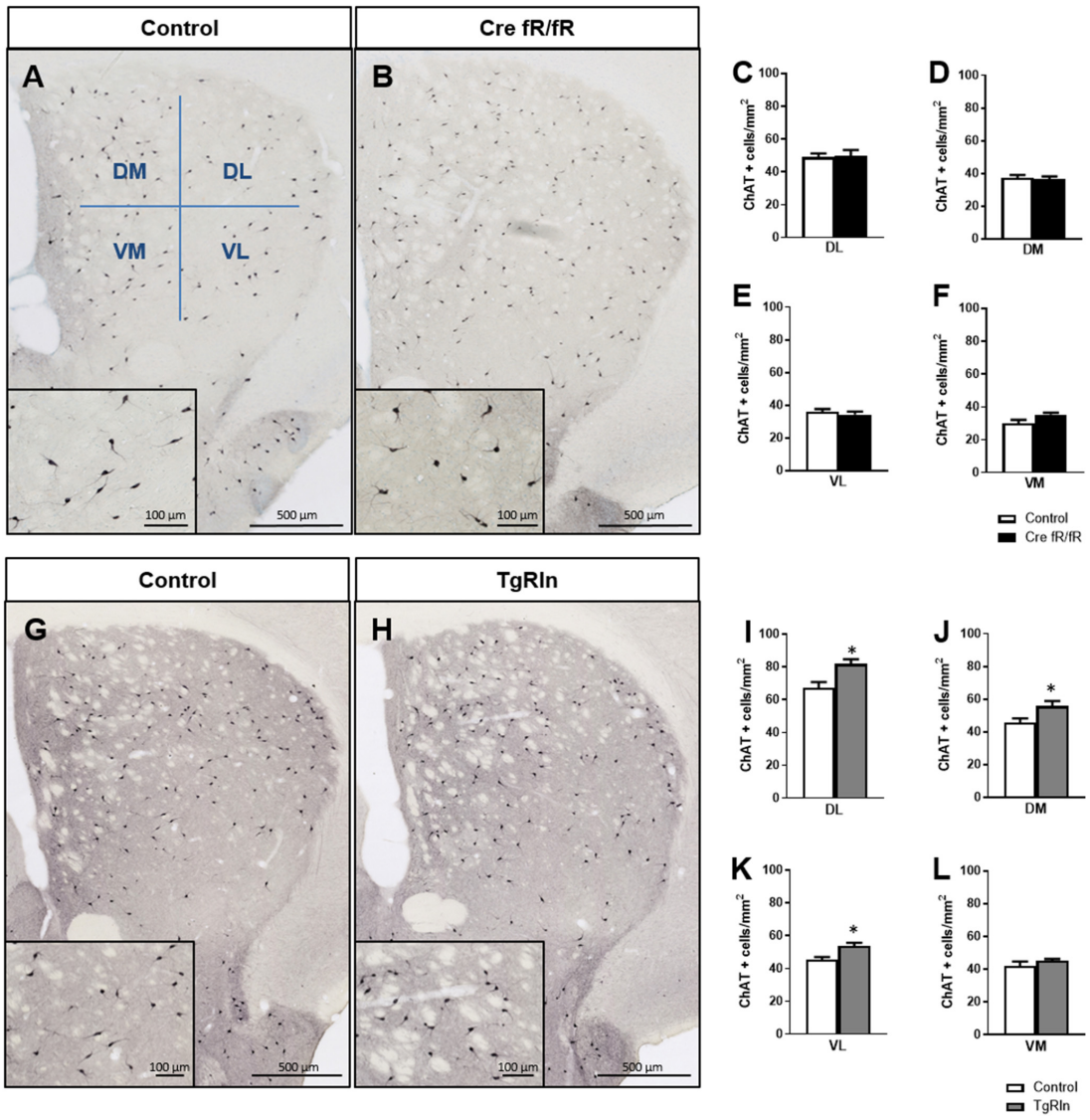


FIGURE 3
Reelin overexpression increases the density of striatal cholinergic interneurons. **(A,B)** Immunohistochemistry of ChAT in striatal coronal sections of control and Cre fR/fR mice, with representative subdivision of the striatum in four regions (DM, dorsal-medial; DL, dorsal-lateral; VM, ventral-medial; VL, ventral-lateral). **(C–F)** Quantification of ChAT+ neurons density in the striatal subdivisions shows no differences between control and Cre fR/fR mice ($n$ = 4). **(G,H)** Representative images of ChAT immunohistochemistry in the striatum of control and TgRln mice, with higher magnification insets showing increased ChAT+ neuronal density in the TgRln mice. **(I–L)** Quantification of ChAT+ cell density indicates a significant increase in the DL, VL, and DM striatal regions of TgRln mice ($n$ = 4–6). Scale bar: **(A,B,G,H)**, 500 µm; high magnification insets 100 µm. Statistical analyses were performed using Student's $t$-test; *$p < 0.05$. Data are represented as means ± SEM.

density in TgRln mice showed a statistically significant increase in the VL striatum (Figures 4G, H, K) but not in other striatal regions (Figures 4G–J, L) as compared to controls. Altogether, our results indicated that Reelin overexpression increased the number of DS interneurons.

## 3.4. Reelin levels control dopaminergic projections

Next, we analyzed whether the expression of Reelin could influence dopaminergic projections. Thus, we performed immunohistochemistry for TH to detect dopaminergic projections that reach the striatum from the SN and the ventral tegmental area (VTA). We quantified TH intensity in the DS and the ventral striatum (VS), including the NAcc and the olfactory tubercle (OT). In the Cre fR/fR model, we observed no alterations in the dopaminergic intensity in all three striatal regions studied (Figures 5A–E) compared to controls. However, in the OT of Cre fR/fR mice, we observed a tendency toward a reduction in TH intensity compared to controls (Figure 5E). In contrast, in Reelin overexpressing mice, quantification of TH immunostaining (Figures 5F, G) showed a significant increase of TH intensity in both the NAcc and OT regions compared to controls (Figures 5H–J).

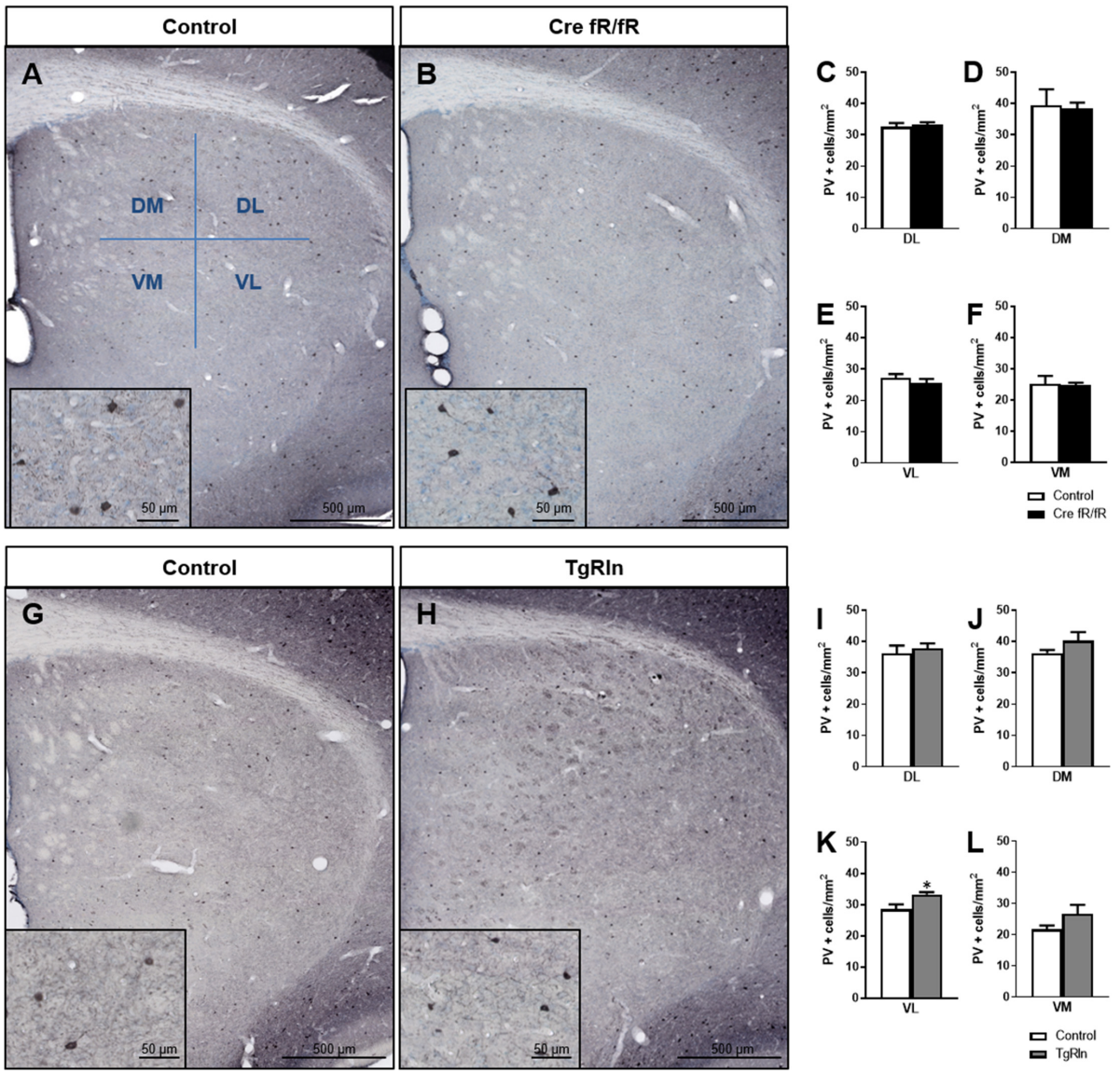


FIGURE 4
Increased levels of Reelin alter the density of parvalbumin interneurons in the ventral-medial striatum. **(A,B)** Immunohistochemistry for PV in coronal sections of control and Cre fR/fR striatum, subdividing the striatum in four regions (as in Figure 3). **(C–F)** Quantification of the density of PV+ interneurons indicated no differences between the control and Cre fR/fR mice ($n$ = 4). **(G,H)** Representative images of PV immunostaining in the striatum of control and TgRln mice. Quantification of PV immunohistochemistry indicated an increase in the density of PV positive cells in the VL striatum of TgRln mice ($n$ = 4–5) **(K)** with no differences in the other striatal regions **(I,J,L)**. Scale bar: **(A,B,G,H)**, 500 µm; high magnification insets 50 µm. Statistical analyses were performed using Student's $t$-test; *$p < 0.05$. Data are represented as means ± SEM.

Finally, we also wanted to quantify synaptic boutons of striatal dopaminergic projections. Thus, we determined the density of TH-positive synaptic boutons in the DS, NAcc, and OT, dividing the DS into dorsal and ventral regions. In the Cre fR/fR mice, the density of synaptic boutons in all the regions was similar to that of control mice (DS dorsal: fR/fR 0.28 ± 0.017 vs. Cre fR/fR 0.30 ± 0.014; DS ventral: fR/fR 0.27 ± 0.016 vs. Cre fR/fR 0.27 ± 0.023; NAcc: fR/fR 0.26 ± 0.013 vs. Cre fR/fR 0.25 ± 0.034; OT: fR/fR 0.24 ± 0.013 vs. Cre fR/fR 0.25 ± 0.018; $n$ = 4 mice/genotype, mean ± SD). In contrast, the density of dopaminergic synaptic boutons were all increased in the tested regions (**Figures 6A–L**), but only the NAcc showed a statistically significant increase (**Figures 6C, G, K**) in the TgRln mice as compared to controls. These results suggest that higher Reelin levels might modulate dopaminergic fibers and synaptic boutons, mainly in the NAcc.

## 4. Discussion

Variations in Reelin expression levels have been shown to be important for the development of neuropsychiatric disorders (Impagnatiello et al., 1998; Fatemi et al., 2000, 2001, 2005; Persico et al., 2001; Grayson et al., 2005; Torrey et al., 2005; Ruzicka et al., 2007; Ovadia and Shifman, 2011; Wang et al., 2014; Baek et al., 2015; Lammert and Howell, 2016); however, we still lack a precise understanding of the mechanistic insights of this

10.3389/fncel.2023.1143319

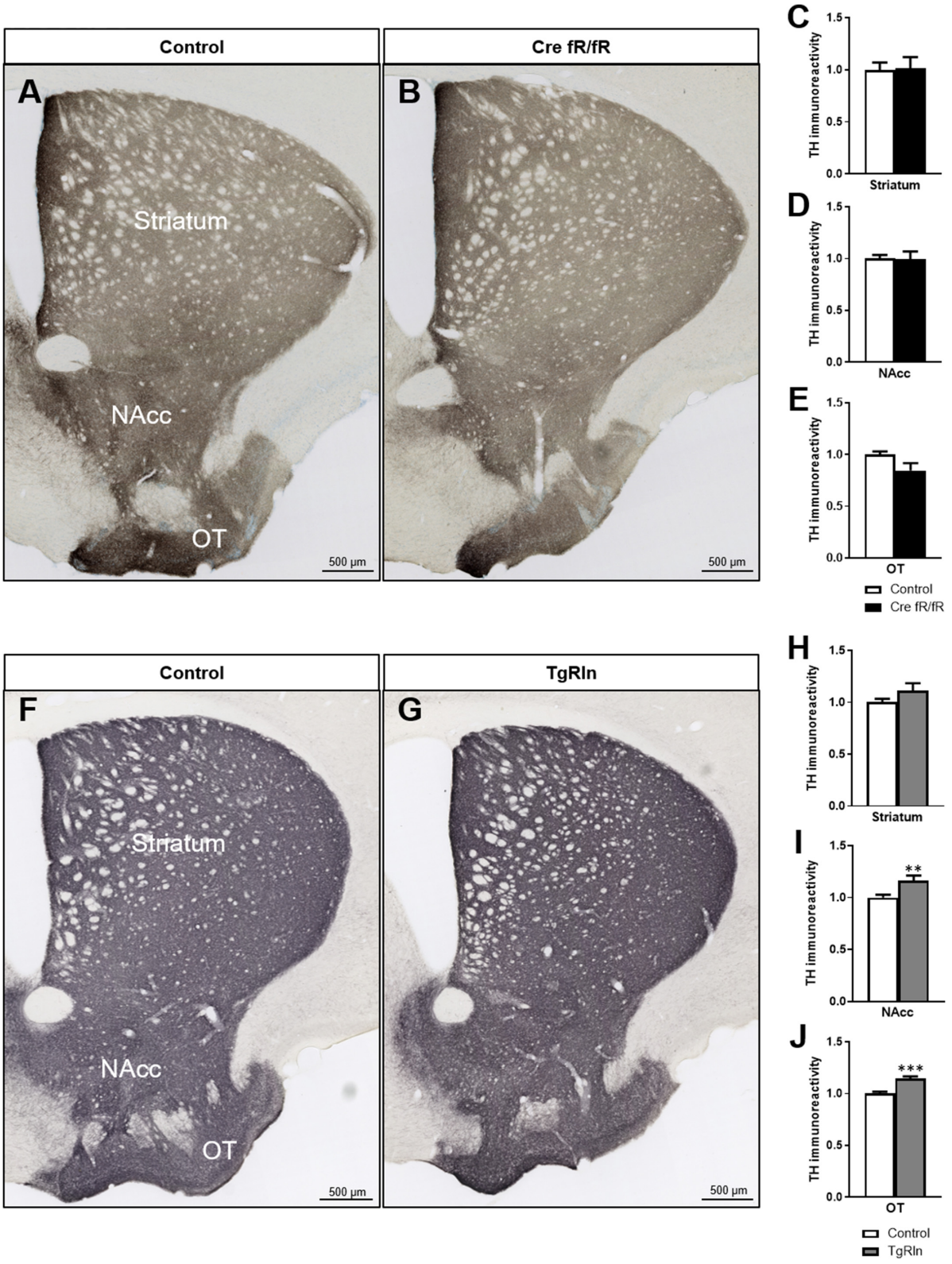


FIGURE 5
Increased levels of Reelin elevates dopaminergic projections in the ventral striatum. **(A,B)** Immunohistochemistry for TH to stain dopaminergic projections in coronal sections of the DS, NAcc, and OT of control and Cre fR/fR mice. TH intensity remains constant in the striatum **(C)**, NAcc **(D)**, and OT **(E)** of Cre fR/fR mice compared to controls ($n$ = 4). **(F,G)** Immunohistochemistry for TH in control and TgRln mice. After quantification, increased TH immunoreactivity was detected in the NAcc **(I)** and OT **(J)**, but not in the DS **(H)** of TgRln mice compared to controls ($n$ = 8–14). Scale bar: **(A,B,F,G)**, 500 µm. NAcc, nucleus accumbens; OT, olfactory tubercle. Statistical analyses were performed using Student's $t$-test; $^{**}p < 0.01$; $^{***}p < 0.001$. Results represent the means ± SEM.

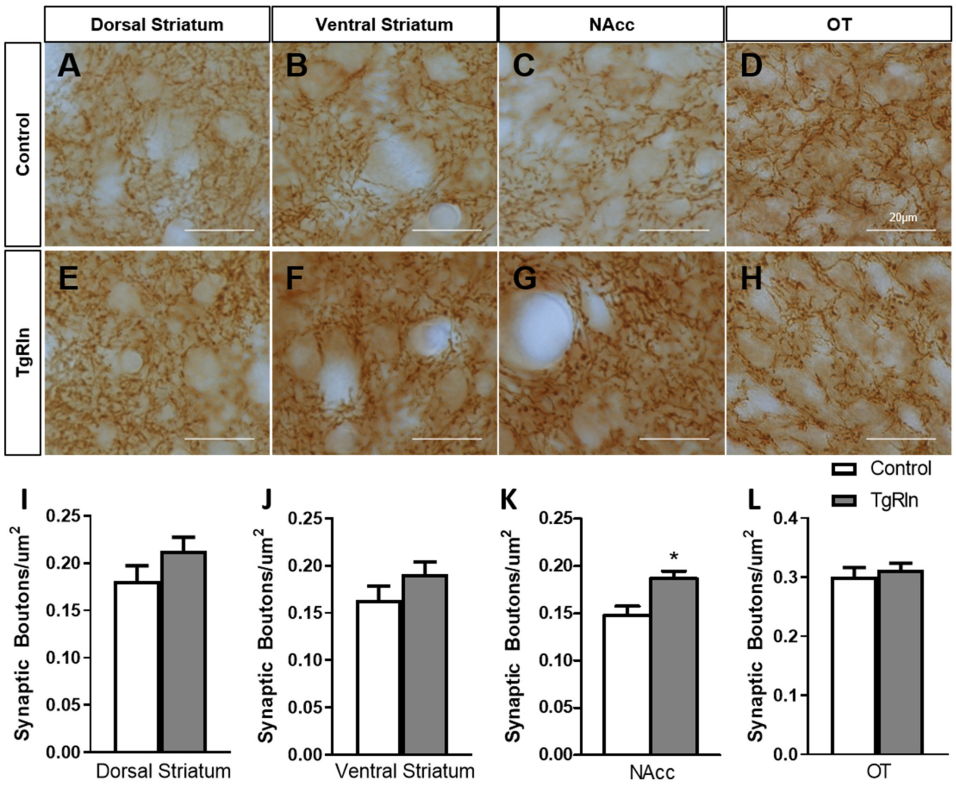


FIGURE 6
Increased number of dopaminergic synaptic boutons in the NAcc of TgRln mice. **(A–H)** Immunohistochemistry for TH staining dopaminergic synaptic boutons in the dorsal **(A,E)** and ventral regions **(B,F)** of the DS, NAcc **(C,G)**, and OT **(D,H)** of TgRln mice and its controls. **(I–L)** Quantification of the density of dopaminergic boutons evidenced a higher density of synaptic boutons in the NAcc **(K)** of TgRln mice compared to its controls while no differences were observed in the rest of the analyzed structures **(I,J,L)**. Scale bar: **(A–H)**, 20 μm. DS, dorsal striatum; NAcc, nucleus accumbens; OT, olfactory tubercle. Statistical analyses were performed using Student's *t*-test; $*p < 0.05$. Data are represented as means ± SEM.

correlation. Here we focused our attention on the striatum as a key region participating in the pathogenesis of psychiatric diseases (McCutcheon et al., 2021). We thus characterized specific striatal neuronal populations as well as the dopaminergic mesolimbic innervation in two different mouse models either overexpressing or deficient for Reelin. In previous studies we reported that TgRln mice were more resilient to stressors implicated in the genesis of psychiatric diseases (chronic stress and psychostimulant administration) (Teixeira et al., 2011), suggesting a role for Reelin in preventing behavioral symptoms related with these disorders. Here we show that Reelin-depletion at adult stages does not lead to significant changes either in the striatal composition or in dopaminergic innervation, suggesting that during adulthood Reelin is not essential for the maintenance of striatal organization. However, postnatal Reelin overexpression increases interneuron populations as well as the density of dopaminergic striatal projections from the VTA, suggesting the participation of postnatal Reelin expression in the fine structural tuning of the striatal area (**Figure 7**).

## 4.1. A role for Reelin in the striatum

The role of Reelin in the cortex and the hippocampus has been extensively studied including the expression pattern in GABAergic interneurons and the regulation in glutamatergic synapses (Alcántara et al., 1998; Herz and Chen, 2006; Jossin, 2020). Indeed, it has been shown that Reelin controls several structural and functional properties of the glutamatergic synapses including the strength of glutamate neurotransmission (Beffert et al., 2005; Qiu et al., 2006b), protein composition of presynaptic boutons (Hellwig et al., 2011), structural properties of dendritic spines (Bosch et al., 2016) as well as trafficking of glutamate receptor subunits (Sinagra et al., 2005; Groc et al., 2007). Several studies also support a key role of Reelin in the correct organization of the basal ganglia. Blockade of Reelin or its signaling pathway leads to a severe disorganization of the tangentially migrating midbrain dopaminergic (mDA) neurons, which fail to reach their final position in the SN pars compacta (SNc) and accumulate instead in the VTA, resulting in a conspicuous reduction of mDA neurons in the SNc, despite no overall changes in the number of mDA neurons (Nishikawa et al., 2003; Kang et al., 2010; Sharaf et al., 2013; Bodea et al., 2014). Interestingly, alterations in the radial and tangential fibers that guide migrating mDA neurons have been described in *reeler* mice (Nishikawa et al., 2003; Kang et al., 2010) and specific inactivation of Reelin signaling in mDA neurons indicates a direct role of Reelin by promoting fast-laterally directed migration and stabilization of their leading process (Vaswani et al., 2019). Despite these organization abnormalities in the SNc, no significant alterations have been described in the nigrostriatal

A

| | Control | Cre fR/fR | TgRln |
|---|---|---|---|
| DARPP-32+ MSNs | ++ | ++ | ++ |
| Striosomes | evenly organized | evenly organized | evenly organized |
| ChAT+ interneurons | ++ | ++ | +++ |
| PV+ interneurons | ++ | ++ | +++ |
| TH DS/VS | ++/++ | ++/++ | ++/+++ |
| Synaptic boutons | ++ | ++ | +++ (*NAcc) |

B

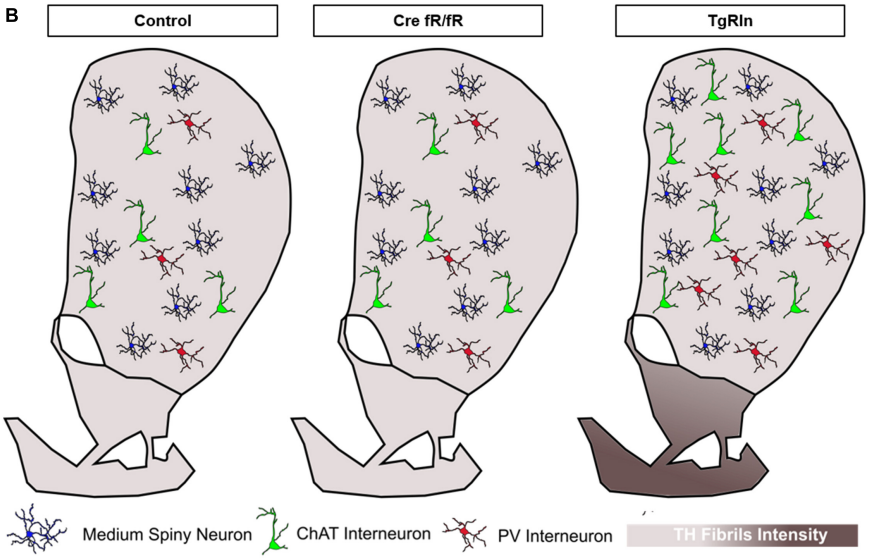


FIGURE 7
Schematic summary of the striatal organization in different Reelin mouse models. **(A)** Summary table indicating the main changes observed in striatal organization in the different strains. **(B)** Graphic summary of the striatal organization per strain. Density of striatal MSNs is preserved between the control, Cre fR/fR, and TgRln striatums. Although the density of striatal PV+ and ChAT+ interneurons is maintained between control and Cre fR/fR mice, it is increased in the DS of TgRln mice. Increased numbers of ChAT+ interneurons are present in the dorsal striatum and higher numbers of PV+ interneurons are distributed in the ventral medial striatum sub-region. Dopaminergic projections are represented with different gradient of brown color, showing a specific increase of TH fibers in the NAcc and OT of the TgRln mice compared with controls.

pathway of *reeler*, *reeler-like* mutants or heterozygous *reeler* mice (Nishikawa et al., 2003; Sharaf et al., 2013; Vaswani et al., 2019). In contrast, defects in cortico-striatal plasticity (Marrone et al., 2006) and in the dopaminergic system (Matsuzaki et al., 2007) have been reported in *reeler* mice. Moreover, decreased levels of Reelin have been associated with alterations in striatal composition, such as reductions in the number of striatal PV+ neurons along the rostro-caudal axis (Marrone et al., 2006; Ammassari-Teule et al., 2009), decreases in TH immunoreactivity in the striatum, VTA, and NAcc (Ballmaier et al., 2002; Nullmeier et al., 2014) and increases in the density of ChAT (Sigala et al., 2007) and the expression of D1, D2, and serotonin 5-HT2A receptors (Matsuzaki et al., 2007; Varela et al., 2015). Importantly, it is still controversial whether these striatal alterations are attributable either to a role of Reelin during development or to an acute effect at adult stages. Given that very few studies have addressed this issue (Matsuzaki et al., 2007), here we use a conditional KO model (Cre fR/fR) in which neurodevelopment is preserved, which allowed us to specifically analyze the contribution of adult Reelin expression to the cellular and anatomical organization of the striatum. Our results indicate no significant changes either in the cell densities of CHAT+ and PV+ interneurons or in the density of DARPP32+ MSNs, suggesting that Reelin expression is critical for striatal composition during development, but not for the maintenance of cellular pools during adulthood. Moreover, mapping of the TH+ immunoreactivity in DS, VTA, and NAcc areas in Cre fR/fR mice showed no differences from controls, although there was a trend in the OT, supporting that at adult stages Reelin is largely dispensable for the maintenance of the dopaminergic innervation from the SN/VTA to the striatum.

## 4.2. Reelin, psychiatric behavioral phenotypes, and drug sensitization

Alterations in Reelin levels have been associated with psychiatric-related behavioral phenotypes in rodents, including visual attention-related deficits in reversal learning (Brigman et al., 2006), decreased inhibition, emotionality, and motor impulsivity starting from adolescence (Ognibene et al., 2007), sensorimotor gating impairments (Barr et al., 2008) or altered latent inhibition (Ammassari-Teule et al., 2009), although these

results are controversial since many labs have failed to reproduce them (Podhorna and Didriksen, 2004; Teixeira et al., 2011; Lossi et al., 2019). Interestingly, pharmacological supplementation or genetic overexpression of Reelin, prevent some of these deficits (e.g., associative learning, sensorimotor gating) (Teixeira et al., 2011; Rogers et al., 2013) and support the idea of boosting Reelin levels as a therapeutic approach in psychiatric disorders. Moreover, several studies relate Reelin deficits with exacerbated behavioral abnormalities in response to drug consumption (Romano et al., 2014; Iemolo et al., 2021; de Guglielmo et al., 2022) and we have previously reported that Reelin overexpression prevents psychomotor effects associated with chronic psychostimulant administration (Teixeira et al., 2011), supporting a role for Reelin in drug sensitization. Importantly, there is a high comorbidity between substance use disorders (cannabis, nicotine, alcohol, and stimulants) and schizophrenia, with an estimated prevalence of 41.7% (Hunt et al., 2018).

It has been widely described that the mesolimbic system is the major neurochemical pathway controlling the rewarding effects of drugs of abuse (Wise and Rompre, 1989). Disturbances in the dopaminergic mesolimbic system including altered immunoreactivity and mRNA levels of TH and dopamine receptors (D2 and D3) in the VTA and the VS have been reported in heterozygous *reeler* mice (Ballmaier et al., 2002) and could be related to some of the behavioral deficits observed in this model. In this regard, our results show an increased immunoreactivity of dopaminergic fibers in the NAcc and OT of the TgRln mice which could be indicative of increased dopamine (DA) release from the VTA. The NAcc, is one of the main projection sites of the VTA, and the release of DA in this region is associated with reward and motivated behaviors (Robison et al., 2020). The OT, on the other hand, is markedly connected with sensory and arousal/reward centers and is critical for multisensory integration and hedonic responses (Wesson and Wilson, 2011). Human imaging studies, pharmacology and preclinical models indicate that the integration of the reward circuitry is affected in schizophrenia (Robison et al., 2020) and a higher reactivity of dopamine release appears to play a role in schizophrenia positive symptoms through its action on D2 receptors, including the NAcc (see Simpson et al., 2022 for a review). Importantly, there are studies involving other striatal elements, such as the striatal patch-matrix organization and striatal interneurons, in the control of reward and drug abuse, making the characterization of the striatal organization in TgRln mice essential to further understand the mechanisms underlying drug sensitization. Despite the fact that the gross structure of the striatal architecture was not altered in TgRln mice, the study of striatal interneurons, which represent 5–10% of the striatal cell population, clearly suggests that Reelin is able to modulate interneuron densities. Reelin overexpression leads to increased densities of PV+ and ChAT+ cells, suggesting a specific response of these neurons to increased amounts of Reelin. Noteworthy, schizophrenic patients present reduced densities of ChAT+ interneurons in the caudate nucleus, the VS and in the striatum as a whole (Holt et al., 1999, 2005).

Decreased density of PV+ interneurons in the dorsomedial and ventromedial striatum of heterozygous *reeler* mice have been paralleled with deficits in some behaviors strongly disrupted in schizophrenic patients (Ammassari-Teule et al., 2009). Moreover, cocaine sensitization correlates with transient increases in the number of PV+ neurons in striatum, which is reduced below the normal number after a 2-week cocaine withdrawal period (Todtenkopf et al., 2004). The fact that TgRln mice, which show reduced sensitization to cocaine, also show increased densities of PV+ interneurons could appear contradictory; nevertheless, here the increased number of PV+ interneurons is sustained, while upon cocaine administration the increase is transient, and eventually, related to compensatory responses. In addition, recent data suggest that increased acetylcholine signaling reduces the acute and sensitized motor responses to cocaine (Lewis et al., 2020) supporting the idea that the increased PV+ and ChAT+ interneuron density observed in TgRln mice could be involved in the reduction of cocaine sensitization described in these mice (Teixeira et al., 2011).

It has been described that after cocaine administration, there is an specific increase in the ERK pathway in striatonigral MSNs (Bertran-Gonzalez et al., 2008), a pathway that is also activated by Reelin (Simó et al., 2007; Lee et al., 2014). Interestingly, an increased Fos activation in the dorsal medial striatum but not in the NAcc of heterozygous *reeler* mice after the administration of cocaine has been reported (de Guglielmo et al., 2022). Increases in Fos activation are thought to be the result of the cocaine-induced upregulation in dopamine levels in the striatum (Di Chiara and Imperato, 1988), which is hypothesized to alter the activity of MSNs by activating D1 and D2 receptors. Experiments in mice lacking D1 receptor indicate a clear role for this receptor in the psychomotor effects of cocaine. In this study we describe a preferential expression of Reelin mRNA in a specific subpopulation of MSNs of the striatum, the D1 neurons, corroborating previous studies using FISH (de Guglielmo et al., 2022) or genome-wide translatome (Montalban et al., 2022). The fact that the expression of both Reelin and its main downstream effector Dab1 are higher in striatonigral D1 MSNs than in striatopallidal D2 MSNs, suggests that Reelin may function in an autocrine manner in D1 MSNs and could be somehow modulating its function and hence influencing cocaine-induced psychomotor effects which are reduced in Reelin overexpressing mice (Teixeira et al., 2011) and increased when Reelin levels are reduced (de Guglielmo et al., 2022).

Although the mechanisms by which Reelin overexpression leads to increased numbers of PV and CHAT neurons remain unknown, it is important to remark that CAMKII promoter drives expression of Reelin in the striatum from the end of the first postnatal week onward (P5–P10) (Pujadas et al., 2010). Hence, we discard direct actions of Reelin overexpression on neurogenesis and migration, since those processes take place mainly at embryonic stages (Knowles et al., 2021). Several recent studies using conditional Reelin inactivation either from postnatal stages or specifically targeting interneurons, have indicated that Reelin participates in the fine tuning of cortical and hippocampal layering (Pahle et al., 2020; Vílchez-Acosta et al., 2022) and in dendritic growth control of specific interneuronal subsets through the regulation of presynaptic neurotransmitter release and $Ca^{2+}$ influx (Hamad et al., 2021). It has been recently reported that PV+ and ChAT+ striatal interneurons undergo extensive apoptosis during the first and second postnatal weeks, with the main changes occurring between P5 and P10 (Sreenivasan et al., 2022), coinciding with the onset of Reelin overexpression in our model. The survival of these particular interneuronal populations has been related with their specific afferent connectivity, being

PV+ interneurons controlled by long-range cortical inputs whilst local inputs from MSNs control ChAT+ interneurons. Our data indicate that Reelin overexpression does not influence the total number of DARPP-32+ MSNs, however, as described in other brain regions such as the hippocampus (Pujadas et al., 2010), Reelin overexpression could be modulating neuronal activity levels and hence affecting interneuron survival. Moreover, it is also possible that Reelin influences positively the maturation and survival of these interneurons, through Reelin/Dab1 associated pathways that are known to influence these processes (Simó et al., 2007; Lee et al., 2014). Nevertheless, since PV and ChAT expressions can be modulated by many factors, we cannot completely exclude the possibility that Reelin overexpression might be increasing PV and ChAT expression and therefore making visible interneurons that otherwise express very low marker levels in control mice.

### 4.3. Reelin as a possible therapeutic target for psychiatric diseases

Reelin has been placed as a top candidate gene associated with several neuropsychiatric diseases. This link is supported by several studies showing that Reelin levels are reduced in patients with schizophrenia, bipolar disorder, and autism spectrum disorder (Impagnatiello et al., 1998; Fatemi et al., 2000, 2001, 2005; Persico et al., 2001; Grayson et al., 2005; Torrey et al., 2005; Ruzicka et al., 2007; Ovadia and Shifman, 2011; Wang et al., 2014; Baek et al., 2015; Lammert and Howell, 2016). Excitatory/inhibitory unbalances have been widely reported in schizophrenia patients and mouse models (Gao and Penzes, 2015). Current data indicates decreased GABA and increased glutamate levels in schizophrenic patients (Rowland et al., 2013; Song et al., 2014; Chiu et al., 2018) that most likely lead to hyperexcitability in certain brain circuits. Interestingly, the increased density in GABAergic PV+ and ChAT+ interneurons observed in TgRln mice presumably intensifies the inhibitory input onto striatal MSNs, reducing in turn the excitability in the striatal circuitry and perhaps counteracting in part the excitatory/inhibitory imbalance typically found in schizophrenia.

It is interesting to note that the striatal changes observed in TgRln mice are opposite to those found in patients with Tourette's syndrome which present a clear decrease in the density of PV+ and ChAT+ interneurons in the DS with no alterations in the density and number of MSNs (Kataoka et al., 2010). The fact that GWAS studies have identified RELN genetic variants in Tourette's syndrome (Li et al., 2012) together with our findings in the TgRln model suggest that Reelin overexpression could reverse some of the symptoms of this disorder, although altered Reelin expression or signaling should be explored in patients affected by Tourette's syndrome.

## Data availability statement

The original contributions presented in this study are included in the article/supplementary material, further inquiries can be directed to the corresponding authors.

## Ethics statement

This animal study was reviewed and approved by the University of Barcelona Animal Ethics Committee and the Rockefeller University's Institutional Animal Care and Use Committee.

## Author contributions

ES contributed to conception and design of the study. MP, SG, EM, LP, AE-T, NM, AV-A, and YM performed the experiments. MP, SG, EM, CA, and YM analyzed the data and performed the statistical analysis. AN contributed to new reagents/analytic tools. MP, LP, YM, and ES wrote the first draft of the manuscript. EM, AP, J-AG, CA, and MV wrote sections of the manuscript. YM and ES reviewed and edited the final version. All authors contributed to manuscript revision, read, and approved the submitted version.

## Funding

This work was supported by grants from the Spanish MINECO and MICIN (SAF2016-76340R and PID2019-106764RB-C21, Excellence Unit 629, María de Maeztu/Institute of Neurosciences) to ES and LP, and by CIBERNED (Project: 2019-09; ISCIII, Spanish Ministry of Health) to ES, Aligning Science Across Parkinson's through the Michael J. Fox Foundation for Parkinson's Research, United States (ASAP-020505 to MV), Ministry of Science and Innovation (MICINN), Spain (PID2020-116339RB-I00 to MV), and EU Joint Programme Neurodegenerative Disease Research (JPND), Instituto de Salud Carlos III, EU/Spain (AC20/00121 to MV).

## Acknowledgments

We thank Daniela Rossi and Ashraf Muhaisen for help in the management of mouse colonies.

## Conflict of interest

The authors declare that the research was conducted in the absence of any commercial or financial relationships that could be construed as a potential conflict of interest.

## Publisher's note

# References


Alcántara, S., Ruiz, M., D'Arcangelo, G., Ezan, F., de Lecea, L., Curran, T., et al. (1998). Regional and cellular patterns of Reelin mRNA expression in the forebrain of the developing and adult mouse. *J. Neurosci.* 18:7779. doi: 10.1523/JNEUROSCI.18-19-07779.1998

Ammassari-Teule, M., Sgobio, C., Biamonte, F., Marrone, C., Mercuri, N. B., and Keller, F. (2009). Reelin haploinsufficiency reduces the density of PV+ neurons in circumscribed regions of the striatum and selectively alters striatal-based behaviors. *Psychopharmacology (Berl)* 204, 511–521. doi: 10.1007/s00213-009-1483-x

Arnaud, L., Ballif, B. A., and Cooper, J. A. (2003). Regulation of protein tyrosine kinase signaling by substrate degradation during brain development. *Mol. Cell. Biol.* 23, 9293–9302. doi: 10.1128/MCB.23.24.9293-9302.2003

Baek, S. T., Copeland, B., Yun, E.-J., Kwon, S.-K., Guemez-Gamboa, A., Schaffer, A. E., et al. (2015). An AKT3-FOXG1-Reelin network underlies defective migration in human focal malformations of cortical development. *Nat. Med.* 21, 1445–1454. doi: 10.1038/nm.3982

Ballif, B. A., Arnaud, L., Arthur, W. T., Guris, D., Imamoto, A., and Cooper, J. A. (2004). Activation of a Dab1/CrkL/C3G/Rap1 pathway in Reelin-stimulated neurons. *Curr. Biol.* 14, 606–610. doi: 10.1016/j.cub.2004.03.038

Ballmaier, M., Zoli, M., Leo, G., Agnati, L. F., and Spano, P. (2002). Preferential alterations in the mesolimbic dopamine pathway of heterozygous reeler mice: An emerging animal-based model of schizophrenia. *Eur. J. Neurosci.* 15, 1197–1205. doi: 10.1046/j.1460-9568.2002.01952.x

Barr, A. M., Fish, K. N., Markou, A., and Honer, W. G. (2008). Heterozygous reeler mice exhibit alterations in sensorimotor gating but not presynaptic proteins. *Eur. J. Neurosci.* 27, 2568–2574. doi: 10.1111/j.1460-9568.2008.06233.x

Beffert, U., Morfini, G., Bock, H. H., Reyna, H., Brady, S. T., and Herz, J. (2002). Reelin-mediated signaling locally regulates protein kinase B/Akt and glycogen synthase kinase 3beta. *J. Biol. Chem.* 277, 49958–49964. doi: 10.1074/jbc.M209205200

Beffert, U., Weeber, E. J., Durudas, A., Qiu, S., Masiulis, I., Sweatt, J. D., et al. (2005). Modulation of synaptic plasticity and memory by Reelin involves differential splicing of the lipoprotein receptor Apoer2. *Neuron* 47, 567–579. doi: 10.1016/j.neuron.2005.07.007

Benhayon, D., Magdaleno, S., and Curran, T. (2003). Binding of purified Reelin to ApoER2 and VLDLR mediates tyrosine phosphorylation of disabled-1. *Brain Res. Mol. Brain Res.* 112, 33–45. doi: 10.1016/s0169-328x(03)00032-9

Bertran-Gonzalez, J., Bosch, C., Maroteaux, M., Matamales, M., Hervé, D., Valjent, E., et al. (2008). Opposing patterns of signaling activation in dopamine D1 and D2 receptor-expressing striatal neurons in response to cocaine and haloperidol. *J. Neurosci.* 28, 5671–5685. doi: 10.1523/JNEUROSCI.1039-08.2008

Bodea, G. O., Spille, J.-H., Abe, P., Andersson, A. S., Acker-Palmer, A., Stumm, R., et al. (2014). Reelin and CXCL12 regulate distinct migratory behaviors during the development of the dopaminergic system. *Development* 141, 661–673. doi: 10.1242/dev.099937

Bolam, J. P. (1984). Synapses of identified neurons in the neostriatum. *Ciba Found. Symp.* 107, 30–47.

Bolam, J. P., Hanley, J. J., Booth, P. A., and Bevan, M. D. (2000). Synaptic organisation of the basal ganglia. *J. Anat.* 196, 527–542.

Bosch, C., Masachs, N., Exposito-Alonso, D., Martínez, A., Teixeira, C. M., Fernaud, I., et al. (2016). Reelin regulates the maturation of dendritic spines, synaptogenesis and glial ensheathment of newborn granule cells. *Cereb. Cortex* 26, 4282–4298. doi: 10.1093/cercor/bhw216

Brigman, J. L., Padukiewicz, K. E., Sutherland, M. L., and Rothblat, L. A. (2006). Executive functions in the heterozygous reeler mouse model of schizophrenia. *Behav. Neurosci.* 120, 984–988. doi: 10.1037/0735-7044.120.4.984

Chen, Y., Beffert, U., Ertunc, M., Tang, T.-S., Kavalali, E. T., Bezprozvanny, I., et al. (2005). Reelin modulates NMDA receptor activity in cortical neurons. *J. Neurosci.* 25, 8209–8216. doi: 10.1523/JNEUROSCI.1951-05.2005

Chiu, P. W., Lui, S. S. Y., Hung, K. S. Y., Chan, R. C. K., Chan, Q., Sham, P. C., et al. (2018). In vivo gamma-aminobutyric acid and glutamate levels in people with first-episode schizophrenia: A proton magnetic resonance spectroscopy study. *Schizophr. Res.* 193, 295–303. doi: 10.1016/j.schres.2017.07.021

Cooper, J. A. (2008). A mechanism for inside-out lamination in the neocortex. *Trends Neurosci.* 31, 113–119. doi: 10.1016/j.tins.2007.12.003

Crittenden, J. R., and Graybiel, A. M. (2011). Basal ganglia disorders associated with imbalances in the striatal striosome and matrix compartments. *Front. Neuroanat.* 5:59. doi: 10.3389/fnana.2011.00059

D'Arcangelo, G., Homayouni, R., Keshvara, L., Rice, D. S., Sheldon, M., and Curran, T. (1999). Reelin is a ligand for lipoprotein receptors. *Neuron* 24, 471–479.

D'Arcangelo, G., Miao, G., Chen, S., Soares, H., Morgan, J., and Curran, T. (1995). A protein related to extracellular matrix proteins deleted in the mouse mutant reeler. *Nature* 374, 719–723. doi: 10.1038/374719a0

de Guglielmo, G., Iemolo, A., Nur, A., Turner, A., Montilla-Perez, P., Martinez, A., et al. (2022). Reelin deficiency exacerbates cocaine-induced hyperlocomotion by enhancing neuronal activity in the dorsomedial striatum. *Genes Brain Behav.* 21:e12828. doi: 10.1111/gbb.12828

Di Chiara, G., and Imperato, A. (1988). Drugs abused by humans preferentially increase synaptic dopamine concentrations in the mesolimbic system of freely moving rats. *Proc. Natl. Acad. Sci. U.S.A.* 85, 5274–5278. doi: 10.1073/pnas.85.14.5274

Fatemi, S. H., Earle, J. A., and McMenomy, T. (2000). Reduction in Reelin immunoreactivity in hippocampus of subjects with schizophrenia, bipolar disorder and major depression. *Mol. Psychiatry* 5, 654–663. doi: 10.1038/sj.mp.4000783

Fatemi, S. H., Kroll, J. L., and Stary, J. M. (2001). Altered levels of Reelin and its isoforms in schizophrenia and mood disorders. *Neuroreport* 12, 3209–3215.

Fatemi, S. H., Reutiman, T. J., and Folsom, T. D. (2009). Chronic psychotropic drug treatment causes differential expression of Reelin signaling system in frontal cortex of rats. *Schizophr. Res.* 111, 138–152. doi: 10.1016/j.schres.2009.03.002

Fatemi, S. H., Snow, A. V., Stary, J. M., Araghi-Niknam, M., Reutiman, T. J., Lee, S., et al. (2005). Reelin signaling is impaired in autism. *Biol. Psychiatry* 57, 777–787. doi: 10.1016/j.biopsych.2004.12.018

Folsom, T. D., and Fatemi, S. H. (2013). The involvement of Reelin in neurodevelopmental disorders. *Neuropharmacology* 68, 122–135. doi: 10.1016/j.neuropharm.2012.08.015

Gao, R., and Penzes, P. (2015). Common mechanisms of excitatory and inhibitory imbalance in schizophrenia and autism spectrum disorders. *Curr. Mol. Med.* 15, 146–167. doi: 10.2174/1566524015666150303003028

Gerfen, C. R. (1992). The neostriatal mosaic: Multiple levels of compartmental organization. *Trends Neurosci.* 15, 133–139.

Gernert, M., Hamann, M., Bennay, M., Löscher, W., and Richter, A. (2000). Deficit of striatal parvalbumin-reactive GABAergic interneurons and decreased basal ganglia output in a genetic rodent model of idiopathic paroxysmal dystonia. *J. Neurosci.* 20, 7052–7058. doi: 10.1523/JNEUROSCI.20-18-07052.2000

Gong, S., Doughty, M., Harbaugh, C. R., Cummins, A., Hatten, M. E., Heintz, N., et al. (2007). Targeting CRE Recombinase to specific neuron populations with bacterial artificial chromosome constructs. *J. Neurosci.* 27, 9817–9823. doi: 10.1523/JNEUROSCI.2707-07.2007

González-Billault, C., Del Río, J. A., Ureña, J. M., Jiménez-Mateos, E. M., Barallobre, M. J., Pascual, M., et al. (2005). A role of MAP1B in Reelin-dependent neuronal migration. *Cereb. Cortex* 15, 1134–1145. doi: 10.1093/cercor/bhh213

Graybiel, A. M., and Ragsdale, C. W. (1978). Histochemically distinct compartments in the striatum of human, monkeys, and cat demonstrated by acetylthiocholinesterase staining. *Proc. Natl. Acad. Sci. U.S.A.* 75, 5723–5726. doi: 10.1073/pnas.75.11.5723

Grayson, D. R., Jia, X., Chen, Y., Sharma, R. P., Mitchell, C. P., Guidotti, A., et al. (2005). Reelin promoter hypermethylation in schizophrenia. *Proc. Natl. Acad. Sci. U.S.A.* 102, 9341–9346. doi: 10.1073/pnas.0503736102

Groc, L., Choquet, D., Stephenson, F. A., Verrier, D., Manzoni, O. J., and Chavis, P. (2007). NMDA receptor surface trafficking and synaptic subunit composition are developmentally regulated by the extracellular matrix protein Reelin. *J. Neurosci.* 27, 10165–10175. doi: 10.1523/JNEUROSCI.1772-07.2007

Hamad, M. I. K., Petrova, P., Daoud, S., Rabaya, O., Jbara, A., Melliti, N., et al. (2021). Reelin restricts dendritic growth of interneurons in the neocortex. *Development* 148:dev199718. doi: 10.1242/dev.199718

Heiman, M., Schaefer, A., Gong, S., Peterson, J. D., Day, M., Ramsey, K. E., et al. (2008). A translational profiling approach for the molecular characterization of CNS cell types. *Cell* 135, 738–748. doi: 10.1016/j.cell.2008.10.028

Hellwig, S., Hack, I., Kowalski, J., Brunne, B., Jarowyj, J., Unger, A., et al. (2011). Role for Reelin in neurotransmitter release. *J. Neurosci.* 31, 2352–2360. doi: 10.1523/JNEUROSCI.3984-10.2011

Herkenham, M., and Pert, C. B. (1981). Mosaic distribution of opiate receptors, parafascicular projections and acetylcholinesterase in rat striatum. *Nature* 291, 415–418. doi: 10.1038/291415a0

Herz, J., and Chen, Y. (2006). Reelin, lipoprotein receptors and synaptic plasticity. *Nat. Rev. Neurosci.* 7, 850–859. doi: 10.1038/nrn2009

Hiesberger, T., Trommsdorff, M., Howell, B. W., Goffinet, A., Mumby, M. C., Cooper, J. A., et al. (1999). Direct binding of Reelin to VLDL receptor and ApoE receptor 2 induces tyrosine phosphorylation of disabled-1 and modulates tau phosphorylation. *Neuron* 24, 481–489. doi: 10.1016/s0896-6273(00)80861-2

Hirota, Y., and Nakajima, K. (2017). Control of neuronal migration and aggregation by Reelin signaling in the developing cerebral cortex. *Front. Cell Dev. Biol.* 5:40. doi: 10.3389/fcell.2017.00040

Holt, D. J., Bachus, S. E., Hyde, T. M., Wittie, M., Herman, M. M., Vangel, M., et al. (2005). Reduced density of cholinergic interneurons in the ventral striatum in schizophrenia: An in situ hybridization study. *Biol. Psychiatry* 58, 408–416. doi: 10.1016/j.biopsych.2005.04.007

Holt, D. J., Herman, M. M., Hyde, T. M., Kleinman, J. E., Sinton, C. M., German, D. C., et al. (1999). Evidence for a deficit in cholinergic interneurons in the striatum in schizophrenia. *Neuroscience* 94, 21–31.

Howell, B. W., Hawkes, R., Soriano, P., and Cooper, J. A. (1997). Neuronal position in the developing brain is regulated by mouse disabled-1. *Nature* 389, 733–737. doi: 10.1038/39607

Howell, B. W., Herrick, T. M., and Cooper, J. A. (1999). Reelin-induced tyrosine [corrected] phosphorylation of disabled 1 during neuronal positioning. *Genes Dev.* 13, 643–648.

Hunt, G. E., Large, M. M., Cleary, M., Lai, H. M. X., and Saunders, J. B. (2018). Prevalence of comorbid substance use in schizophrenia spectrum disorders in community and clinical settings, 1990-2017: Systematic review and meta-analysis. *Drug Alcohol Depend.* 191, 234–258. doi: 10.1016/j.drugalcdep.2018.07.011

Iemolo, A., Montilla-Perez, P., Nguyen, J., Risbrough, V. B., Taffe, M. A., and Telese, F. (2021). Reelin deficiency contributes to long-term behavioral abnormalities induced by chronic adolescent exposure to Δ9-tetrahydrocannabinol in mice. *Neuropharmacology* 187:108495. doi: 10.1016/j.neuropharm.2021.108495

Impagnatiello, F., Guidotti, A. R., Pesold, C., Dwivedi, Y., Caruncho, H., Pisu, M. G., et al. (1998). A decrease of Reelin expression as a putative vulnerability factor in schizophrenia. *Proc. Natl. Acad. Sci. U.S.A.* 95, 15718–15723.

Jossin, Y. (2020). Reelin functions, mechanisms of action and signaling pathways during brain development and maturation. *Biomolecules* 10:964. doi: 10.3390/biom10060964

Kang, W.-Y., Kim, S.-S., Cho, S.-K., Kim, S., Suh-Kim, H., and Lee, Y.-D. (2010). Migratory defect of mesencephalic dopaminergic neurons in developing reeler mice. *Anat. Cell Biol.* 43, 241–251. doi: 10.5115/acb.2010.43.3.241

Kataoka, Y., Kalanithi, P. S. A., Grantz, H., Schwartz, M. L., Saper, C., Leckman, J. F., et al. (2010). Decreased number of parvalbumin and cholinergic interneurons in the striatum of individuals with Tourette syndrome. *J. Comp. Neurol.* 518, 277–291. doi: 10.1002/cne.22206

Kempermann, G. (2008). The neurogenic reserve hypothesis: What is adult hippocampal neurogenesis good for? *Trends Neurosci.* 31, 163–169. doi: 10.1016/j.tins.2008.01.002

Kim, H. M., Qu, T., Kriho, V., Lacor, P., Smalheiser, N., Pappas, G. D., et al. (2002). Reelin function in neural stem cell biology. *Proc. Natl. Acad. Sci. U.S.A.* 99, 4020–4025. doi: 10.1073/pnas.062698299

Knowles, R., Dehorter, N., and Ellender, T. (2021). From progenitors to progeny: Shaping striatal circuit development and function. *J. Neurosci.* 41, 9483–9502. doi: 10.1523/JNEUROSCI.0620-21.2021

Krueger, D. D., Howell, J. L., Hebert, B. F., Olausson, P., Taylor, J. R., and Nairn, A. C. (2006). Assessment of cognitive function in the heterozygous reeler mouse. *Psychopharmacology (Berl)* 189, 95–104. doi: 10.1007/s00213-006-0530-0

Lammert, D. B., and Howell, B. W. (2016). RELN mutations in autism spectrum disorder. *Front. Cell. Neurosci.* 10:84. doi: 10.3389/fncel.2016.00084

Lee, G. H., Chhangawala, Z., von Daake, S., Savas, J. N., Yates, J. R., Comoletti, D., et al. (2014). Reelin induces Erk1/2 signaling in cortical neurons through a non-canonical pathway. *J. Biol. Chem.* 289, 20307–20317. doi: 10.1074/jbc.M114.576249

Lewis, R. G., Serra, M., Radl, D., Gori, M., Tran, C., Michalak, S. E., et al. (2020). Dopaminergic control of striatal cholinergic interneurons underlies cocaine-induced psychostimulation. *Cell Rep.* 31:107527. doi: 10.1016/j.celrep.2020.107527

Li, M. J., Wang, P., Liu, X., Lim, E. L., Wang, Z., Yeager, M., et al. (2012). GWASdb: A database for human genetic variants identified by genome-wide association studies. *Nucleic Acids Res.* 40, D1047–D1054. doi: 10.1093/nar/gkr1182

Lossi, L., Castagna, C., Granato, A., and Merighi, A. (2019). The reeler mouse: A translational model of human neurological conditions, or simply a good tool for better understanding neurodevelopment? *J. Clin. Med.* 8:2088. doi: 10.3390/jcm8122088

Marrone, M. C., Marinelli, S., Biamonte, F., Keller, F., Sgobio, C. A., Ammassari-Teule, M., et al. (2006). Altered cortico-striatal synaptic plasticity and related behavioural impairments in reeler mice. *Eur. J. Neurosci.* 24, 2061–2070. doi: 10.1111/j.1460-9568.2006.05083.x

Matsuzaki, H., Minabe, Y., Nakamura, K., Suzuki, K., Iwata, Y., Sekine, Y., et al. (2007). Disruption of Reelin signaling attenuates methamphetamine-induced hyperlocomotion. *Eur. J. Neurosci.* 25, 3376–3384. doi: 10.1111/j.1460-9568.2007.05564.x

McCutcheon, R. A., Brown, K., Nour, M. M., Smith, S. M., Veronese, M., Zelaya, F., et al. (2021). Dopaminergic organization of striatum is linked to cortical activity and brain expression of genes associated with psychiatric illness. *Sci. Adv.* 7:eabg1512. doi: 10.1126/sciadv.abg1512

Molnár, Z., Clowry, G. J., Šestan, N., Alzu'bi, A., Bakken, T., Hevner, R. F., et al. (2019). New insights into the development of the human cerebral cortex. *J. Anat.* 235, 432–451. doi: 10.1111/joa.13055

Montalban, E., Giralt, A., Taing, L., Schut, E. H. S., Supiot, L. F., Castell, L., et al. (2022). Translational profiling of mouse dopaminoceptive neurons reveals region-specific gene expression, exon usage, and striatal prostaglandin E2 modulatory effects. *Mol. Psychiatry* 27, 2068–2079. doi: 10.1038/s41380-022-01439-4

Nishikawa, S., Goto, S., Yamada, K., Hamasaki, T., and Ushio, Y. (2003). Lack of Reelin causes malpositioning of nigral dopaminergic neurons: Evidence from comparison of normal and Reln(rl) mutant mice. *J. Comp. Neurol.* 461, 166–173. doi: 10.1002/cne.10610

Niu, S., Yabut, O., and D'Arcangelo, G. (2008). The Reelin signaling pathway promotes dendritic spine development in hippocampal neurons. *J. Neurosci.* 28, 10339–10348. doi: 10.1523/JNEUROSCI.1917-08.2008

Nullmeier, S., Panther, P., Frotscher, M., Zhao, S., and Schwegler, H. (2014). Alterations in the hippocampal and striatal catecholaminergic fiber densities of heterozygous reeler mice. *Neuroscience* 275, 404–419. doi: 10.1016/j.neuroscience.2014.06.027

Ognibene, E., Adriani, W., Granstrem, O., Pieretti, S., and Laviola, G. (2007). Impulsivity-anxiety-related behavior and profiles of morphine-induced analgesia in heterozygous reeler mice. *Brain Res.* 1131, 173–180. doi: 10.1016/j.brainres.2006.11.007

Olson, L., Seiger, A., and Fuxe, K. (1972). Heterogeneity of striatal and limbic dopamine innervation: Highly fluorescent islands in developing and adult rats. *Brain Res.* 44, 283–288. doi: 10.1016/0006-8993(72)90385-x

Ovadia, G., and Shifman, S. (2011). The genetic variation of RELN expression in schizophrenia and bipolar disorder. *PLoS One* 6:e19955. doi: 10.1371/journal.pone.0019955

Pahle, J., Muhia, M., Wagener, R. J., Tippmann, A., Bock, H. H., Graw, J., et al. (2020). Selective inactivation of Reelin in inhibitory interneurons leads to subtle changes in the dentate gyrus but leaves cortical layering and behavior unaffected. *Cereb. Cortex* 30, 1688–1707. doi: 10.1093/cercor/bhz196

Persico, A. M., D'Agruma, L., Maiorano, N., Totaro, A., Militerni, R., Bravaccio, C., et al. (2001). Reelin gene alleles and haplotypes as a factor predisposing to autistic disorder. *Mol. Psychiatry* 6, 150–159. doi: 10.1038/sj.mp.4000850

Podhorna, J., and Didriksen, M. (2004). The heterozygous reeler mouse: Behavioural phenotype. *Behav. Brain Res.* 153, 43–54. doi: 10.1016/j.bbr.2003.10.033

Pujadas, L., Gruart, A., Bosch, C., Delgado, L., Teixeira, C. M., Rossi, D., et al. (2010). Reelin regulates postnatal neurogenesis and enhances spine hypertrophy and long-term potentiation. *J. Neurosci.* 30, 4636–4649. doi: 10.1523/JNEUROSCI.5284-09.2010

Qiu, S., Zhao, L. F., Korwek, K. M., and Weeber, E. J. (2006b). Differential Reelin-induced enhancement of NMDA and AMPA receptor activity in the adult hippocampus. *J. Neurosci.* 26, 12943–12955. doi: 10.1523/JNEUROSCI.2561-06.2006

Qiu, S., Korwek, K. M., Pratt-Davis, A. R., Peters, M., Bergman, M. Y., and Weeber, E. J. (2006a). Cognitive disruption and altered hippocampus synaptic function in Reelin haploinsufficient mice. *Neurobiol. Learn. Mem.* 85, 228–242. doi: 10.1016/j.nlm.2005.11.001

Rice, D. S., and Curran, T. (2001). Role of the Reelin signaling pathway in central nervous system development. *Annu. Rev. Neurosci.* 24, 1005–1039. doi: 10.1146/annurev.neuro.24.1.1005

Robison, A. J., Thakkar, K. N., and Diwadkar, V. A. (2020). Cognition and reward circuits in schizophrenia: Synergistic, not separate. *Biol. Psychiatry* 87, 204–214. doi: 10.1016/j.biopsych.2019.09.021

Rogers, J. T., Zhao, L., Trotter, J. H., Rusiana, I., Peters, M. M., Li, Q., et al. (2013). Reelin supplementation recovers sensorimotor gating, synaptic plasticity and associative learning deficits in the heterozygous reeler mouse. *J. Psychopharmacol.* 27, 386–395. doi: 10.1177/0269881112463468

Romano, E., De Angelis, F., Ulbrich, L., De Jaco, A., Fuso, A., and Laviola, G. (2014). Nicotine exposure during adolescence: Cognitive performance and brain gene expression in adult heterozygous reeler mice. *Psychopharmacology (Berl)* 231, 1775–1787. doi: 10.1007/s00213-013-3388-y

Rowland, L. M., Kontson, K., West, J., Edden, R. A., Zhu, H., Wijtenburg, S. A., et al. (2013). In vivo measurements of glutamate, GABA, and NAAG in schizophrenia. *Schizophr. Bull.* 39, 1096–1104. doi: 10.1093/schbul/sbs092

Ruzicka, W. B., Zhubi, A., Veldic, M., Grayson, D. R., Costa, E., and Guidotti, A. (2007). Selective epigenetic alteration of layer I GABAergic neurons isolated from prefrontal cortex of schizophrenia patients using laser-assisted microdissection. *Mol. Psychiatry* 12, 385–397. doi: 10.1038/sj.mp.4001954

Schiffmann, S. N., Jacobs, O., and Vanderhaeghen, J. J. (1991). Striatal restricted adenosine A2 receptor (RDC8) is expressed by enkephalin but not by substance P neurons: An in situ hybridization histochemistry study. *J. Neurochem.* 57, 1062–1067. doi: 10.1111/j.1471-4159.1991.tb08257.x

Sharaf, A., Bock, H. H., Spittau, B., Bouché, E., and Krieglstein, K. (2013). ApoER2 and VLDLr are required for mediating Reelin signalling pathway for normal migration and positioning of mesencephalic dopaminergic neurons. *PLoS One* 8:e71091. doi: 10.1371/journal.pone.0071091

Sharaf, A., Rahhal, B., Spittau, B., and Roussa, E. (2015). Localization of Reelin signaling pathway components in murine midbrain and striatum. *Cell Tissue Res.* 359, 393–407. doi: 10.1007/s00441-014-2022-6

Sigala, S., Zoli, M., Palazzolo, F., Faccoli, S., Zanardi, A., Mercuri, N. B., et al. (2007). Selective disarrangement of the rostral telencephalic cholinergic system in

heterozygous reeler mice. *Neuroscience* 144, 834–844. doi: 10.1016/j.neuroscience.2006.10.013

Simó, S., Jossin, Y., and Cooper, J. A. (2010). Cullin 5 regulates cortical layering by modulating the speed and duration of Dab1-dependent neuronal migration. *J. Neurosci.* 30, 5668–5676. doi: 10.1523/JNEUROSCI.0035-10.2010

Simó, S., Pujadas, L., Segura, M. F., La Torre, A., Del Río, J. A., Ureña, J. M., et al. (2007). Reelin induces the detachment of postnatal subventricular zone cells and the expression of the Egr-1 through Erk1/2 activation. *Cereb. Cortex* 17, 294–303. doi: 10.1093/cercor/bhj147

Simpson, E. H., Gallo, E. F., Balsam, P. D., Javitch, J. A., and Kellendonk, C. (2022). How changes in dopamine D2 receptor levels alter striatal circuit function and motivation. *Mol. Psychiatry* 27, 436–444. doi: 10.1038/s41380-021-01253-4

Sinagra, M., Verrier, D., Frankova, D., Korwek, K. M., Blahos, J., Weeber, E. J., et al. (2005). Reelin, very-low-density lipoprotein receptor, and apolipoprotein E receptor 2 control somatic NMDA receptor composition during hippocampal maturation in vitro. *J. Neurosci.* 25, 6127–6136. doi: 10.1523/JNEUROSCI.1757-05.2005

Smith, Y., Bevan, M. D., Shink, E., and Bolam, J. P. (1998). Microcircuitry of the direct and indirect pathways of the basal ganglia. *Neuroscience* 86, 353–387.

Song, J., Viggiano, A., Monda, M., and De Luca, V. (2014). Peripheral glutamate levels in schizophrenia: Evidence from a meta-analysis. *Neuropsychobiology* 70, 133–141. doi: 10.1159/000364828

Soriano, E., and Del Río, J. A. (2005). The cells of cajal-retzius: Still a mystery one century after. *Neuron* 46, 389–394. doi: 10.1016/j.neuron.2005.04.019

Sreenivasan, V., Serafeimidou-Pouliou, E., Exposito-Alonso, D., Bercsenyi, K., Bernard, C., Bae, S.-E., et al. (2022). Input-specific control of interneuron numbers in nascent striatal networks. *Proc. Natl. Acad. Sci. U.S.A.* 119:e2118430119. doi: 10.1073/pnas.2118430119

Strasser, V., Fasching, D., Hauser, C., Mayer, H., Bock, H. H., Hiesberger, T., et al. (2004). Receptor clustering is involved in Reelin signaling. *Mol. Cell. Biol.* 24, 1378–1386.

Teixeira, C. M., Kron, M. M., Masachs, N., Zhang, H., Lagace, D. C., Martinez, A., et al. (2012). Cell-autonomous inactivation of the Reelin pathway impairs adult neurogenesis in the hippocampus. *J. Neurosci.* 32, 12051–12065. doi: 10.1523/JNEUROSCI.1857-12.2012

Teixeira, C. M., Martín, E. D., Sahún, I., Masachs, N., Pujadas, L., Corvelo, A., et al. (2011). Overexpression of Reelin prevents the manifestation of behavioral phenotypes related to schizophrenia and bipolar disorder. *Neuropsychopharmacology* 36, 2395–2405. doi: 10.1038/npp.2011.153

Todtenkopf, M., Stellar, J., Williams, E., and Zahm, D. (2004). Differential distribution of parvalbumin immunoreactive neurons in the striatum of cocaine sensitized rats. *Neuroscience* 127, 35–42. doi: 10.1016/j.neuroscience.2004.04.054

Torrey, E. F., Barci, B. M., Webster, M. J., Bartko, J. J., Meador-Woodruff, J. H., and Knable, M. B. (2005). Neurochemical markers for schizophrenia, bipolar disorder, and major depression in postmortem brains. *Biol. Psychiatry* 57, 252–260. doi: 10.1016/j.biopsych.2004.10.019

Tueting, P., Costa, E., Dwivedi, Y., Guidotti, A., Impagnatiello, F., Manev, R., et al. (1999). The phenotypic characteristics of heterozygous reeler mouse. *Neuroreport* 10, 1329–1334.

Varela, M. J., Lage, S., Caruncho, H. J., Cadavid, M. I., Loza, M. I., and Brea, J. (2015). Reelin influences the expression and function of dopamine D2 and serotonin 5-HT2A receptors: A comparative study. *Neuroscience* 290, 165–174. doi: 10.1016/j.neuroscience.2015.01.031

Vaswani, A. R., Weykopf, B., Hagemann, C., Fried, H.-U., Brüstle, O., and Blaess, S. (2019). Correct setup of the substantia nigra requires Reelin-mediated fast, laterally-directed migration of dopaminergic neurons. *Elife* 8:e41623. doi: 10.7554/eLife.41623

Vílchez-Acosta, A., Manso, Y., Cárdenas, A., Elias-Tersa, A., Martínez-Losa, M., Pascual, M., et al. (2022). Specific contribution of Reelin expressed by cajal-retzius cells or GABAergic interneurons to cortical lamination. *Proc. Natl. Acad. Sci. U.S.A.* 119:e2120079119. doi: 10.1073/pnas.2120079119

Wang, Z., Hong, Y., Zou, L., Zhong, R., Zhu, B., Shen, N., et al. (2014). Reelin gene variants and risk of autism spectrum disorders: An integrated meta-analysis. *Am. J. Med. Genet. B Neuropsychiatr. Genet.* 165, 192–200. doi: 10.1002/ajmg.b.32222

Wesson, D. W., and Wilson, D. A. (2011). Sniffing out the contributions of the olfactory tubercle to the sense of smell: Hedonics, sensory integration, and more? *Neurosci. Biobehav. Rev.* 35, 655–668. doi: 10.1016/j.neubiorev.2010.08.004

Wise, R. A., and Rompre, P. P. (1989). Brain dopamine and reward. *Annu. Rev. Psychol.* 40, 191–225. doi: 10.1146/annurev.ps.40.020189.001203

Yasui, N., Nogi, T., and Takagi, J. (2010). Structural basis for specific recognition of Reelin by its receptors. *Structure* 18, 320–331. doi: 10.1016/j.str.2010.01.010

Zhao, C., Deng, W., and Gage, F. H. (2008). Mechanisms and functional implications of adult neurogenesis. *Cell* 132, 645–660. doi: 10.1016/j.cell.2008.01.033

# Frontiers in
# Cellular Neuroscience

**Leading research in cellular mechanisms underlying brain function and development**

Part of the world's most cited neuroscience journal series that advances our understanding of the cellular mechanisms underlying cell function in the nervous system across all species.

---

## Discover the latest Research Topics

See more →

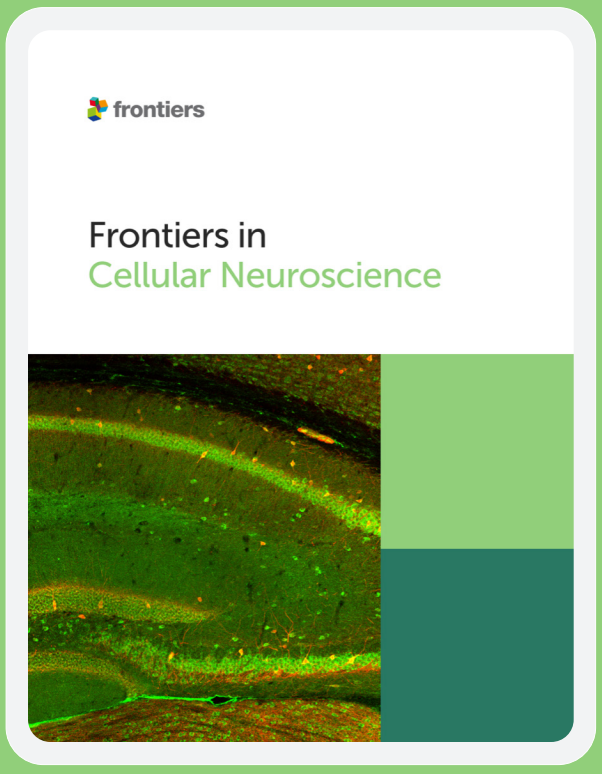


**Frontiers**

Avenue du Tribunal-Fédéral 34
1005 Lausanne, Switzerland
frontiersin.org

**Contact us**

+41 (0)21 510 17 00
frontiersin.org/about/contact